THREE DIMENSIONAL COMPUTATIONAL FLUID DYNAMICS MODELS OF FUGITIVE DUST DISPERSION IN HIGH-LATITUDE OPEN-PIT MINES

By

Taraprasad Bhowmick

RECOMMENDED:

Dr. Rajive Ganguli

Dr. G. Javier Fochesatto

Dr. Tathagata Ghosh

Dr. Sukumar Bandopadhyay
Advisory Committee Chair

Dr. Margaret Darrow
Chair, Department of Mining and Geological Engineering

APPROVED:

Dr. Doug Goering
Dean, College of Engineering & Mines

Dr. John C. Eichelberger
Dean of the Graduate School

12/17/15
Date

THREE DIMENSIONAL COMPUTATIONAL FLUID DYNAMICS MODELS OF FUGITIVE DUST DISPERSION IN HIGH-LATITUDE OPEN-PIT MINES

A

THESIS

Presented to the Faculty

of the University of Alaska Fairbanks

in Partial Fulfillment of the Requirements

for the Degree of

MASTER OF SCIENCE

By

Taraprasad Bhowmick, B.E.

Fairbanks, AK

December 2015

Abstract

The Arctic region contains vast mineral resources and mining of these resources is a major activity in several countries, including the United States. With the advancement of open-pit mining technology, the depth to which minerals can be profitably mined has increased, resulting in deeper pits than ever before. This increase in depth has several inherent challenges for mining operations. The ventilation of an open-pit mine is mostly dependent on natural airflow patterns. The dispersion behavior of the pollutants generated in a mine is also dependent on the atmospheric conditions. The control of fugitive dust in high-latitude open-pit mines is challenging due to unique atmospheric phenomena resulting in complicated flow regimes as well as atmospheric inversion due to the lack of adequate insolation during prolonged winter seasons.

The development of a computational fluid dynamics (CFD) model of an open-pit mine is challenging due to the presence of several sharp and irregular features at the pit surface. A good quality mesh of the model domain is a prerequisite for convergence in solution. Besides good quality meshing, choices of various simulation setup parameters have significant impact in convergence or divergence of the simulation. Appropriate choices of simulation type, boundary and initial conditions, time stepping and various convergence criteria are important for realistic simulation of a model domain.

Environmental conditions in the mine vary from season to season; hence, fugitive dust dispersion simulations using a commercial CFD software are conducted for various seasonal conditions along with several cloud conditions. Clear sky and cloudy sky conditions result in different radiative and turbulent energy fluxes. In each scenario, fugitive dust particles varying in size ($PM_{0.1}$ to PM_{10}) and concentrations are generated at various locations of the selected mine. The simulation results predict a speedy removal of fugitive dust in summer. However, during winter, the presence of an inversion layer in the open-pit results in extensive retention of fugitive dust. For removal of the atmospheric inversion during winter, it is observed that the presence of cloud cover and convective wind are the most important factors.

Table of Contents

List of Figures

List of Tables

Acknowledgments

This research was supported by the National Institute for Occupational Safety and Health (NIOSH), and Dr. Sukumar Bandopadhyay served as the principal investigator for the project. I would like to express my deep sense of gratitude and indebtedness to Dr. Sukumar Bandopadhyay for suggesting the problem for this research. Without his encouragements, patience and the guidance this study would not have been completed. I wish to thank the support of our industrial partner for sharing the operational and meteorological data, access to the mine, and in-kind financial support in setting up the instruments at the mine. Assistance of the technical support team of CRADLE North America is also gratefully acknowledged.

I would also like to thank the members of the graduate advisory committee: Dr. Rajive Ganguli, and Dr. Tathagata Ghosh for their support. I especially thank Dr. Javier Fochesatto, a member of the graduate advisory committee, for his valuable suggestions during this research.

I would also take this opportunity to thank my fellow graduate student, Dr. Kumar Vaibhav Raj, for his valuable suggestions and constructive criticisms in this research.

Chapter 1 Introduction

1.1 Background

The generation and entrainment of dust is inherent to many of the unit and auxiliary operations of mining. In surface mining, in general, most of these operations are carried out in open atmosphere and the resulting dust is generally released to the atmosphere. Dusts generated from these open sources are, by definition, fugitive dusts and the sources, fugitive sources. Many communities and countries have set environmental standards for ambient airborne dust concentrations produced by mining operations; these are enforced by their respective regulatory agencies (e.g. Mine Safety and Health Administration (MSHA) and Environmental Protection Agency (EPA) in the United States). Even where there are no standards, or comparatively less stringent regulations, there is increasing recognition of the health, safety, environmental and economic benefits yielded by a well-designed particulate control program.

Fugitive dusts can be a source of threats to the health and safety of miners and communities. The particular threat is dependent on the type of dust. Coal, silica and metallic dusts have been associated with serious health consequences. When mineral operations take place close to populated communities, effects on the general public, livestock, and vegetation are major issues. Fugitive dusts also have the potential to affect production and productivity in a number of ways: they can cause poor visibility for operators; they affect the moving parts of machinery, leading to failures, downtime and repairs; dusts can settle on various surfaces and structures, creating both waste and a need for regular clean-up. Finally, they can be a public relations nightmare, a major cause for bad publicity, damaging the image of mining companies in the local and national media.

An additional concern to the mining industry is the potential for fugitive dust to contain metals. Along with total suspended solids, metals are also regulated and must be assessed as a component of a site's fugitive emissions. In addition, many mine sites in Arctic regions often undergo strong atmospheric inversions during the winters, which are characterized by extremely cold temperatures and little wind, conditions that tend to intensify the effects of fugitive emissions. These inversions are common during Arctic winters due to a lack of insolation and atmospheric conditions. In general, fine dust seems to be generated more often in the winter from mid-October to May.

As opposed to dust sources in other industrial activities, dust sources in mining are multiple in number, spatially distributed, generally non-point, and present several challenges to successful prediction and control of dust. The amount and the characteristics of the dusts generated and dispersed are affected by a number of natural and cultural factors such as the topography, meteorological conditions, dust sources and the amount of dust produced determined by such factors as material mined, mining method, and methods used to load and haul the mined materials, as well as the control measures in place. While haul roads account for the bulk of fugitive dust, all operations such as top soil removal, drilling, blasting, loading and dumping generate and entrain dust. Particle sizes ranges from under 10 μm to over 100 μm. Though programs for dust control incorporate well-known methods of prevention, suppression, reduction and isolation strategies, often in combination, it has been difficult to fully control the generation and entrainment of dust.

The entrained dust is dispersed by small-scale airflows and transported to farther distances by larger scale airflows. This dispersion and transport by wind in an open-pit environment is a complex process, making the open-pit airborne dust assessment and control very challenging. Developing more effective methods for dust control requires the application of computer-oriented mathematical simulation models of pollutant dispersion.

While governmental agencies in the U.S. and elsewhere are in the forefront of atmospheric dispersion modeling, much of their work is focused on large-scale regional or global issues affecting public policy and safety. For example, the U.S. EPA has developed and approved models such as AERMOD, CALPUFF and ISC3 for atmospheric dispersion studies and these have been applied extensively in many industrial settings in both the United States and abroad. Reed [2005] has provided an excellent summary of significant dust dispersion models for mining operations, noting the importance of variability of airflow velocities and directions in surface mining and the difficulty in interpreting model results. The performance of these models when applied to surface mining sources has been questionable, often over-predicting concentrations [Cole and Zapert, 1995; Long, 2011].

Advances in mathematical and computational technology in recent years have enabled better modeling of the dust dispersion phenomenon around mines using computational fluid dynamics (CFD). However, there is a need for a good understanding of the physical, mathematical and

computational aspects and limitations. The importance of the location of the emission sources, the direction and strength of the prevailing wind, and the pit configuration were identified as major factors by Lowndes et al. [2008] in their CFD model study of dust dispersion in a limestone quarry. Silvester et al. [2009] developed and applied a CFD model to study the dispersion and deposition of fugitive mineral dust particles generated during rock blasting operations. While this study concluded that depending on the location of the bench blast within the quarry and the direction of the wind, a mass fraction ranging from 0.3 to 0.6 of the emitted mineral particles was retained within the quarry, the stability of the prevailing atmospheric conditions would also be an influencing factor on deposition. Flores et al. [2013a, 2013b] applied a CFD modeling approach to study dust dispersion in the Chuquicamata copper open-pit.

This brief literature review underscores the need for more comprehensive data collection and analytical procedures to address the surface mine dust dispersion problem. Indeed, Reed [2005] explicitly notes in his specific study of mining dispersion models that dust dispersion modeling of mining facilities needs to be advanced. This research outlines a new approach combining several advances in computer modeling, data collection and analytical procedures to predict dispersion of fugitive dust in open-pit mines at high latitudes.

1.2 Problem Statement

Surface mining is an important component of the mining sector. In the United States, more than 60% of the coal and over 90% metal and non-metallic minerals are mined by this method. Surface mines have grown larger in terms of the excavated area, the area affected by the mine operation, the size of equipment used, and the production rates. Whether it is a surface coal mine in the Powder River Basin in Wyoming, a copper open-pit in Arizona, or an aggregate quarry in Western Pennsylvania, the issue of emission control encompasses all on-site and off-site unit operations. Understanding the dust generation process helps to evaluate the environmental impact of the emission and to select a suitable dust emission reduction and control approach. However, the magnitude of the problem and the approaches to solutions are very much dependent on local natural conditions.

Field experiments remain the ideal method to understand the aerodynamic phenomenon. It is generally very expensive from time and cost viewpoints to collect extensive data on dust generation and dispersion for each new mine site. Further, the changing conditions of operations

(both mining and weather), limited measuring points, and the accuracy of the collected data make it difficult to establish a correlation between weather conditions and dust dispersion. Numerical models are important tools for assessing dust particle dispersion and deposition and for designing and evaluating mitigation strategies for diverse dust emission situations, weather conditions and topographies. However, significant effort is required to improve the accuracy of numerical models so that they accurately capture the macro- and micro- level aspects of the dust dispersion problem.

The number of models applicable to aerodynamic analyses of fugitive dust dispersion in the complicated topographic domain common to open-pit mines is rather limited. This is because the processes governing emissions and transport by wind flows over an open-pit mine are, as already stated, very complex. Terrain morphology causes difficulties in estimating the dust emission rate and determining dust transport. The dust particles are often driven by meso-scale to synoptic-scale systems over long distances. At the more local spatial scale of an open-pit mine and neighboring areas, a more precise spatio-temporal modeling of the open-pit surfaces and wind flows is needed for better predictions of fugitive dust transport. CFD simulation can be used to quantitatively and qualitatively analyze dust dispersion according to various weather conditions. As stated previously, dispersion of fugitive dust is mainly affected by particle size and wind speed as well as wind direction. CFD accuracy could be improved by incorporating topographical design, mesh structure, particle generation and computational process [Flores et al., 2013a, 2013b].

1.3 Scope of this Research

In the past three decades, the development of CFD has made it possible to understand pollutant flow in open-pit mines better. As particulate matter, such as fugitive dust, is suspended in the air, the fugitive dust transportation and distribution are highly associated with the convective airflow and the turbulence. Hence, the CFD is the most suitable modeling approach to study the spatial distribution of dust in open-pit mines.

CFD can be used to predict air flow and pollutant distribution. The majority of these CFD programs are based on Navier-Stokes (N-S) equations, the turbulent kinetic energy equation, the mass conversion, and transport equations for turbulent viscosity. CFD models provide a pattern of air flow, distribution of pollutant concentration, and temperature within an open-pit. CFD

modeling has been widely used in atmospheric pollution studies in urban areas. However, none of these models or studies has addressed ventilation design for deep, open-pit mines in general and especially in Arctic or sub-Arctic conditions. The complexity of the problem varies from the irregularities of the topography to the influences of the climate. It is understood that the generation and transport of fugitive dust in open-pit mines are sensitive to various time-dependent parameters. The development of airflow inside an open-pit mine is dependent on two fundamental mechanisms: (1) mechanical turbulence and (2) thermal buoyancy. The mechanical turbulence is dependent on several factors, such as: (1) wind speed, (2) wind direction, (3) topography, (4) aspect ratio, and (5) surface roughness. The thermal buoyancy is also dependent on several factors, such as: (1) atmospheric stability, (2) radiation balance in the domain, and (3) the presence of absence of cloud covers [Chinthala and Khare, 2011].

The phenomenon of buoyancy driven flow in an open-pit is an important issue of mass and energy transport between the incoming air and the stagnant air mass under Arctic inversion. Very few CFD studies of air flow in open-pit mines have been reported for the Arctic region.

There are three methods generally used to study the air flow distribution and contaminant transport in open-pit mines: (1) empirical models, (2) experimental measurements, and (3) CFD. Most researchers use scale model measurements and empirical models to study the pollutant distribution driven by convection and diffusion only. Although these models are simple, they cannot account for the highly transient and complicated behavior of the Atmospheric Boundary Layer (ABL), interaction with solar radiation, and pit geometry of open-pit mines. Therefore, full-scale experimental investigation is critically important. Nevertheless, due to the extensive size of an open-pit mine, experimental measurements are expensive in terms of time and cost, and are therefore deemed impractical.

CFD is an alternative approach to study the fugitive dust dispersion in high-latitude open-pit mines. Any solution to the problem of fugitive dust propagation in open-pit mines will require an extensive understanding of the interaction of the aerodynamic movement of air, air temperature inversion, meteorology, dust source and transport phenomena in open-pit mines. The CFD modeling effort proposed here is to develop and solve the coupled conservation equations of mass, momentum, and energy with appropriate initial and boundary equations.

In this thesis, the CFD work is performed using a fluid dynamics software package SC/Tetra of software CRADLE to import and mesh open-pit geometry and to model the propagation of fugitive dust in open-pit mines. The computer software (SC/Tetra) uses finite volume method (FVM) based code for fluid flow simulation.

Meshing is one of the most critical steps in getting good simulation results. For geometry import and meshing, the 'Preprocessor' of SC/Tetra is used. Meshing is a step to discretize a continuous domain into discrete grid points; however, due to the complexity of open-pit geometry, the mesh may not be of desired mesh quality for better model convergence and reasonable simulation outcomes. Once a good quality mesh is obtained, it is brought into the SC/Tetra solver for turbulent modeling.

For predicting the transport of fugitive dust in the model domain, a coupled simulation approach is selected. To solve the airflow inside the open-pit domain, various turbulent flow methods and turbulence models are applied in the Eulerian reference frame. The Eulerian method develops the conservations equations on a control volume (mesh elements) basis and solves the airflow parameters at each mesh element. The parameters, such as, gravity, velocity, pressure of the airflow are calculated using the Eulerian method. These airflow parameters are calculated as a function of the location and the time in the Eulerian method. However, for solving the turbulent dispersion of fugitive dust particles, the Lagrangian algorithm is used. A Lagrangian stochastic model characterizes the advection and the diffusion processes of an individual dust particle as a function of time only.

Turbulence is a stochastic motion that exists at higher Reynolds numbers. Turbulence has a wide spectrum of scales that can be interpreted as eddy motion of a given size interval with an associated spectrum of fluctuation in the frequency domain. The large eddies have sizes of the same magnitude as the flow domain, have low frequencies, and are affected by the flow conditions at the boundaries and the mean flow.

The Reynolds-Averaged Navier-Stokes (RANS) equations represent transport equations for the mean flow quantities only, with all scales of turbulence being resolved. The RANS approach is generally adopted for practical engineering calculations and uses models such as (Kappa-Epsilon) κ-ε and its variants.

Unlike Reynolds averaging, which relies on ensemble-averaging in its mathematical formulations to calculate mean flow characteristics, Large Eddy Simulation (LES) models divide the overall flow structure into large and small scale motions. The large scale motions are directly calculated, while the small scale motions are modeled.

LES provides the solution for time-dependent and three-dimensional flows. In LES, the large scale turbulence is not modeled, and only eddies smaller than the mesh size need to be represented by a so-called sub-grid scale (SGS) model. Therefore, it is important that the grids are fine enough to account for the small eddies. The mean flow quantities predicted from transient calculations need sufficient time to obtain a steady solution. Thus, the LES contains the time-dependent evolution of eddies in three dimensions.

The methodology developed in this research will be useful in any open-pit mine ventilation situation; however, the scope of this research is limited only to fugitive dust dispersion in deep open-pit mines in high-latitude. The tasks undertaken in this study are: (1) investigating various atmospheric parameters controlling the development of airflow in an open-pit mine; (2) identifying and categorizing the factors influencing fugitive dust propagation; (3) reviewing literature and developing appropriate CFD models to simulate airflow in open-pit mines; (4) collecting atmospheric data from an operating open-pit mine; (5) simulating dust dispersion in open-pit domains using appropriate choices of initial and boundary conditions; and (6) synthesizing the results of the research into a set of recommendations.

1.4 Organization of the Thesis

The research work is presented in several chapters of this thesis.

Chapter 2 Literature Review and Previous Modeling Approaches: This chapter presents a review of the published research on characterization of fugitive dust in open-pit mines and a review of various modeling approaches to simulate fugitive dust dispersion.

Chapter 3 Data Collection: Prior to building the fugitive dust dispersion model, characterization of various modeling parameters is important. The input values of various atmospheric parameters are required for defining the initial and the boundary conditions for simulation of the model domain. The collection of data for the fugitive dust dispersion model is presented in this chapter.

Chapter 4 Model Development: Following the data collection, the open-pit domain of the selected open-pit mine is meshed and the various simulation setup parameters are evaluated for the model domain. The development of the model domain is presented in this chapter.

Chapter 5 Simulation Setup: For simulation of fugitive dust dispersion in open-pit mines the open-pit domain meshed in Chapter 4 is selected for simulation. Various simulation parameters are defined and the results are evaluated to select the appropriate choices of simulation parameters. The selection of various simulation setup parameters are presented in this chapter.

Chapter 6 Simulation of Fugitive Dust Propagation in Open-Pit Mines: The idealized and the actual open-pit domains of the selected open-pit mine are simulated for various seasonal conditions to predict the fugitive dust dispersion. The simulation results of various simulation domains for various climatic conditions are presented in Chapter 6.

Chapter 7 Mitigation of Dust Retention during Air Temperature Inversion: This chapter presents the simulation results of a mitigation approach to remove the atmospheric inversion in the selected open-pit mine.

Chapter 8 Summary and Conclusions: This chapter presents a summary and conclusions of the research and suggestions for future work.

Chapter 2 Literature Review and Previous Modeling Approaches

In the past three decades, several modeling approaches were proposed and explored to predict fugitive dust dispersion in open-pit and underground mines. These dust propagation models and the associated mathematical algorithms were developed incrementally to predict the dust dispersion phenomenon inside and around the mines.

Airborne Respirable Dust (ARD) is a significant public health issue. In the United States, 250 workers die each year because of silicosis [U.S. Department of Labor, 1996]. The EPA has statistically found that a 50 $\mu g/m^3$ increase in 24-hr average PM_{10} concentration in the general public will result in 2.5-8.5% increase in mortality rates [EPA 1996]. Air quality in the U.S., at various mining operations is regulated by two different agencies (1) the EPA and (2) the MSHA. The two legislative acts regulating the air quality from mining operations are: (1) the Federal Coal Mine Health and Safety Act of 1969, which was amended by the Federal Mine Safety and Health Act of 1977, and (2) the Clean Air Act of 1970, which was amended in 1977 and 1990. The Federal Coal Mine Health and Safety Act of 1969 established the amount of dust allowable in the air for health and safety purposes. The Clean Air Amendment of 1990 regulates the air emissions from facilities from an environmental perspective [Reed, 2005].

2.1 Dust Propagation Models and Mathematical Algorithms

PEDCo Environmental, Inc. prepared a "Review of Atmospheric Dispersion Modeling Procedures for Surface Coal Mines" for the U.S. Department of the Interior, Office of Surface Mining Reclamation and Enforcement to address the applicable dispersion models to predict the impact of western coal mining operations on air quality, and recommended procedures for identifying and quantifying emissions that could be used as input to the model and the methods to calibrate the model [PEDCo, 1979].

It was suggested that Particle categorization can be done in two ways: (1) coarse radii$>$ 1 μm and fine radii$<$ 1 μm, and (2) primary particles that do not change form after emission and secondary particles that are substantially formed by in situ chemical reactions. The two numerical modeling approaches available during that period were: (1) Gaussian Diffusion Model (normal distribution horizontally and vertically away from the plume) and (2) Mass Conservation Model (predict concentration of photo reactive pollutants). PEDCo recommended the Long-term

(averaged annual) and the Short-term (24-hr) Gaussian Diffusion models for estimation purposes. PEDCo concluded that only the Environmental Research and Technology Air Quality Model (ERTAQ) model out of all the long-term Gaussian models explicitly incorporates fallout or a deposition function for coarse particles and explicitly accommodates line sources.

The size distribution of the generated dust particles in an open-pit metal or non-metal mine is dependent on the physical-mechanical properties of the host rock, and the physicochemical characteristics of the dust particles is dependent on the type of the rock being mined. Perezhilov et al. [1993] observed that the expected dust concentration in the working-zone can be categorized by (1) the technological parameters such as the rate of the operation, and the predicted size of the comminution product; (2) the properties of the material such as the density, and the internal friction and (3) the type of destructive load such as the comminution characteristics of the material, establishing the relation between the specific surface work of the cohesional forces of the particles and the degree of pulverization of the initial material. The researchers concluded that the dust-flux localization is most effective when the angle of slope of the material being transported is equal to its angle of internal friction.

Jones et al. [2003] studied the physicochemical characterization of dust clouds in a limestone quarry, blasted with Ammonium Nitrate Fuel Oil (ANFO), slurry explosive Powergel 2000, and Powergel 3000 which are primed with a cast pentolite primer and two U500 Nonel detonators. Two different components ((a) minerals and (b) diesel soot) were found to be the components of the dust cloud under high-resolution electron microscopy. A size distribution of the quarry dust particles showed that soot particles dominate the assemblage of respirable dust under 2.5 μm (about 91%). Whereas the mineral grains are more abundant in the inhalable 2.5-10 μm 'coarse' fractions compared to the soot particles.

Page et al. [2008] assembled a full-scale drill rig mockup to investigate the parameters that influence the respirable dust production at drilling operations. Limestone dust, fed by a screw type feeder, was used as a dust source. Gravimetric samplers were used to measure the resulting dust concentrations in the test chambers. Dimensional analysis was used to determine the important variables affecting the dust entrainment and to derive a functional relationship between the Buckingham $\prod$ parameters. The important variables considered were: dust feed rate, ARD concentration (the dependent variable), bailing air flow, collector air flow, open shroud-to-

ground gap height, shroud height, effective shroud height, cross-sectional area of drill deck shroud, and leakage area of deck shroud [Page et al., 2008].

Thirty-six experimental runs with the drill deck model were performed. The functional relationships developed from dimensional analysis showed excellent (R^2 ranging from 0.8-0.95) agreement with the experimental results. It was concluded that the functional relationships derived in this study can be used to predict ARD concentrations from a drill rig by knowing the values of a few basic variables only [Page et al., 2008].

In addition to the research on dust generation, a vast amount of research was devoted to the development and application of dust dispersion modeling in open-pit mines. In a NIOSH Information Circular (IC 9478), Reed [2005] summarized the mathematical concepts used in various dispersion modeling. According to Reed, the basic mathematical algorithms used in dispersion models are: the box model, Gaussian model, Eulerian model, and the Lagrangian model.

The box model is the simplest of the modeling algorithms. It assumes the air-shed is in the shape of a box. The air inside the box is assumed to have a homogeneous concentration in space. Although useful, this model has several limitations. It assumes that the pollutant is homogeneous across the air-shed, and it is used to estimate average pollutant concentrations over a very large area. The ability of the mathematical model to predict dispersion of the pollutant over an air-shed is limited primarily due to its inability to use spatial information [Collett and Oduyemi, 1997].

The Gaussian models are the most common mathematical models in dust dispersion studies. Gaussian models are based upon the assumption that the pollutant will disperse according to the normal statistical distribution [Beychok, 1994]. However, there are a number of assumptions that are made in order for the dispersion equation and predicted results to be valid: (1) the emissions must be constant and uniform, (2) the wind direction and speed are constant, (3) downwind diffusion is negligible compared to vertical and crosswind diffusion, (4) the terrain is relatively flat, i.e., no crosswind barriers, (5) there is no deposition or absorption of the pollutant, (6) the vertical and crosswind diffusion of the pollutant follow a Gaussian distribution, (7) the shape of the plume can be represented by an expanding cone, and (8) the use of the horizontal and vertical standard deviations requires the turbulence of the plume to be homogeneous throughout the

entire plume [Beychok, 1994]. It seems clear that the conditions imposed by the modeling are too restrictive to be a realistic representation of the open-pit problem.

Eulerian models solve a conservation of mass equation for a given pollutant. The Eulerian method develops the conservations equations on a control volume (mesh elements) basis and solves the airflow parameters at each mesh element. According to Collett and Oduyemi [1997], the conservation of mass equation can be computationally expensive to solve and requires some form of optimization in order to reduce the solution time. Numerical solutions of Eulerian dispersion models have been achieved quickly, by reducing the problem to one and two dimensions rather than using three dimensions.

Lagrangian models, on the other hand, predict pollutant dispersion based on a shifting reference grid. This shifting reference grid is generally based on the prevailing wind direction, vector, or the general direction of the dust plume movement. A Lagrangian model has limitations due to the dynamic nature of the model. Actual measurements are generally made at stationary points, whereas the model predicts pollutant concentration based upon a shifting reference grid. This makes it difficult to validate a model during its initial use. To compensate for this limitation, the Lagrangian models are generally modified by adding an Eulerian reference grid; it incorporates a static reference grid into the model. Incorporation of a static reference grid allows a better comparison of the model predicted results with the actual measurements [Collett and Oduyemi, 1997].

Reed [2005] also presented several modeling approaches specifically used for fugitive dust estimation in underground or surface mining operations. Cole and Fabrick [1984] worked on pit retention of dust from surface mining operations. In their report, they mentioned that approximately one-third of the emissions from mining activities escape the open-pit. This was a very simplistic model that is representative of the box model algorithm.

Several open-pit dust models are discussed in a study by TRC [TRC Environmental Consultants, 1995], which was conducted for the U.S. EPA. The study includes the models previously discussed by Cole and Fabrick [1984], which was a computer simulation model based on finite-element analysis. The FEM model accounted for many factors such as wind conditions, surface roughness, complex terrain, atmospheric stability, pollutant sources, particulate terminal settling and deposition velocities, and surface particulate accumulation. One of the limitations

identified in the studies that FEM models may not result in good prediction for open-pit mines with ultimate pit slope angles greater than 35^{O} or in the case of stable atmospheres.

Pereira et al. [1997] used a Gaussian dispersion equation to predict dust concentrations from stockpiles of an operating surface mine in Portugal. The Gaussian equation was used to create risk maps of air quality for locations surrounding the mine site. According to Reed [2005], however, no experimental validation was performed to determine the accuracy of these maps to actual conditions.

Dust dispersion modeling for surface mining operations for air quality compliance studies is generally conducted using an established model, such as, the Industrial Source Complex Model (ISC3) developed by the EPA. No other dust dispersion model has impacted the surface mining industry as much as the ISC3 model [Reed, 2005]. The ISC3 model to predict pollutant dispersion from industrial facilities is available from the EPA website [EPA, 2005]. The pollutants for which it is designed include CO, NO_X, SO_X, VOC, Pb, and PM_{10}.

Characterization of the emissions source in the ISC3 model is significantly important before dispersion modeling of the pollutants. Incorrect characterization of the type of pollutant source can impact modeled concentrations by an order of magnitude. In addition, incorrect dimensions of the pollutant source can cause large variances in modeled concentrations. The mischaracterization of the emissions source in the ISC3 model is a common cause of inaccuracy [Heinerikson, 2004].

An EPA study [1995] documented that ISC3 model tends to over-predict the PM_{10} emissions from the surface coal mining operation significantly. Significant over-prediction is defined as an over-prediction that is more than a factor of 2 at a single site [EPA, 1994]. In this study, no attempt was made to determine the source of the over-prediction of PM_{10}. Consequently, it is not known whether the over-prediction was caused by the emission estimation methods (AP-42) or by the dispersion model [Reed, 2005].

Reed et al. [2001] completed a study on the ISC3 model using a theoretical rock quarry. It was concluded that hauling operations contributed the majority of the PM_{10} concentrations. It was hypothesized that the haul truck emissions factors may be the reason of the over-prediction of PM_{10} concentrations by the ISC3 model. However, further analysis of the data provided by

Cole and Zapert [1995] presented another hypothesis explaining the cause of the ISC3 model's over-prediction. It is known that the majority of the PM_{10} sources at surface mining operations are the moving or mobile sources. The ISC3 model is designed for predicting dust dispersion from stationary sources, and therefore cannot accurately predict dust concentrations from mining operations. This led to further investigations on dust dispersion modeling at surface mining operations, focusing on modeling the dispersion of dust generated from haul trucks. In his latter research, Reed [2003] described a model termed as the Dynamic Component Program, which can be used for predicting dust dispersion from haul trucks. This model is a modification of the ISC3 model and was validated at two surface mining operations. The model is primarily based on a Gaussian equation similar to that used by the ISC3 model [Reed et al., 2002].

Two other dispersion models, although not developed specifically for the mining industry, have been used to model pollutant dispersion at surface mines: CALPUFF and AERMOD. These models are also available from the EPA website [EPA, 2005]. CALPUFF is an EPA-preferred air quality model. The CALPUFF model is a Lagrangian model that uses continuous puffs to simulate emissions from sources [EPA, 1998b]. It has applicability for many different pollutants, including PM_{10}. The CALPUFF model has the ability to simulate the effects of temporally and spatially varying meteorological conditions that occur more often over long pollutant transport distances. This makes it suitable for the prediction of long-range pollutant dispersion (>50 km). Conversely, the ISC3 model is appropriate for short-range pollutant dispersion because it requires constant steady-state meteorological conditions (<50 km) (40 CFR 51, appendix A of appendix W) [EPA, 1998a].

AERMOD is the EPA-proposed replacement for the ISC3 model [EPA, 2003a]. A comparative evaluation of the AERMOD model indicated that AERMOD-predicted pollutant concentrations were closer to the actual concentrations than that of the ISC3 model. The two models produce relatively similar results for flat terrain. However, the largest amount of improvement was accomplished when comparing the two models in complex terrain [EPA, 2003b].

Advances in mathematical and computational technology in recent years have enabled better modeling of pollutant dispersion phenomena around mines using various complex dust generation and dispersion models. Tandon [1998] performed a study to simulate the propagation

of fugitive dust, and to quantify the pit retention/ escape fraction of fugitive dust in Bingham Canyon mine, Utah using Fluid Dynamic Analysis Package (FIDAP 7.5). Due to extremely small fraction of particles with respect to the volume of the carrier phase (air) in the pit, the assumption of one way coupling was applied. This means that the dynamics of the carrier phase (air) drives the motion of the dispersed phase (particulate). The presence of the dispersed phase has no effect on the dynamics of the carrier phase. The simulation was done in sequence, i.e., first the flow field for the carrier phase was solved, and then the particle dynamics equations were solved based on the simulated flow field [Tandon, 1998].

In the Bingham pit model, the boundaries were chosen to be sufficiently far from the area of interest, and a uniform profile was used to describe the wind on the upstream boundary. Before the flow enters the area of interest (the emission points), a velocity boundary layer develops in the wind profile depending on the terrain due to the no-slip boundary condition of the ground. In this study, the parametric studies were conducted to understand the effects of: (1) wind speed, (2) wind direction, (3) atmospheric stability, (4) source location and height; and (5) particle size on dust dispersion and retention [Tandon, 1998].

Bhaskar and Tandon [1998] concluded that two separate mechanisms contribute to the pit retention phenomenon. First of all, the decoupling of the wind-velocity field at the pit-rim from the wind field at the surface suppresses the vertical transport of the particulate from the bottom of the pit to the surface. This phenomenon is more pronounced during low wind speed conditions (Night-time wind field). The second mechanism is the deposition of dust particles on the mine pit surface and the pit walls. The thesis concluded that the presence (or absence) of the recirculatory vortex is dependent on topography of the pit. The idealized pit geometry (trapezoidal or rectangular cross-section) resulted in flow separation at the upwind edge of the pit, which resulted in a recirculatory wind profile inside the mine [Tandon, 1998].

The simulation results of a three-dimensional non-hydrostatic model by Shi et al. [2000] showed that both the mechanical and thermal forces are important mechanisms, for the development of a flow regime inside an open-pit mine.

Using an EPA developed Fugitive Dust Model (FDM) Arpacıoğlu and Er [2003] estimated fugitive dust emission from a gold mine in Costa Rica. The study parameters included in the study were: (1) wind speed, (2) wind direction, (3) ambient temperature, (4) rainfall amount, and

(5) atmospheric stability. The simulated depletion of the particulates was achieved using the process of dry deposition. The deposition of particle was simulated in a FDM by two parameters: (1) the gravitational settling velocity and (2) the deposition velocity [Arpacıoğlu and Er, 2003].

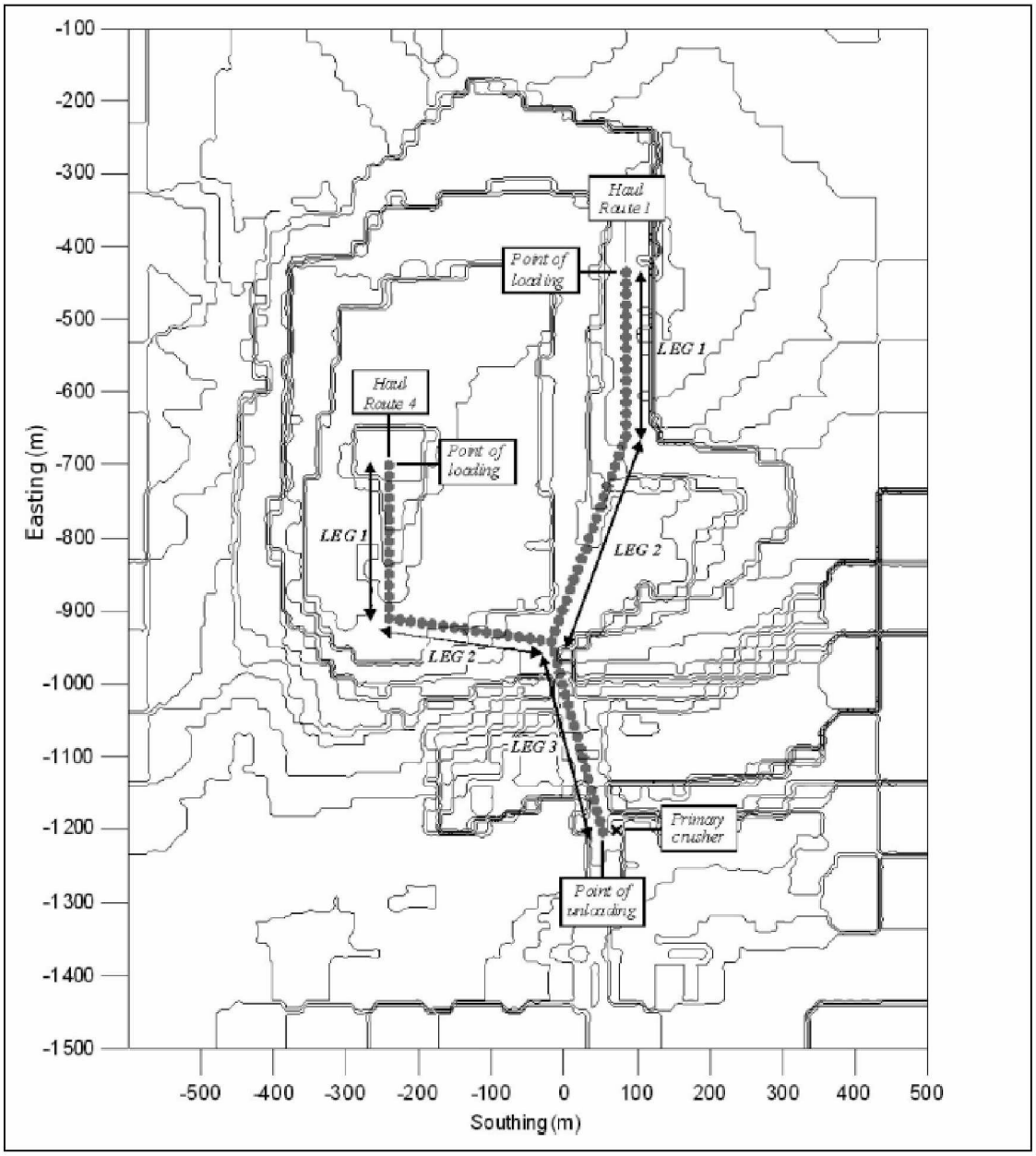

Figure 2.1: Location of HR1 and HR4 haul roads within Old Moor Quarry [Appleton et al., 2006]

Appleton et al. [2006] used ADMS 3 to simulate fugitive dust dispersion from primary in-pit quarry operations. In order to simulate the influence of terrain on dust-plume dispersion and

deposition, the 'Hills module' of ADMS 3 was used. The Hills module allows the import of specific terrain elevation data. However, the application of the hills module is limited to modeling the dispersion from point sources only. Figure 2.1 presents the combinations of point dust sources in the haul roads of the model. To simulate the dispersion of a particulate dust-plume, the ADMS 3 model input is a particulate size distribution. A representative dust particle size distribution employed in all the ADMS 3 models should be comprised of PM_{10} distribution (50% of the particulates by mass) as suggested by the Michigan Department for Environmental Quality. The inclusion of the pit terrain enhanced the dispersion-behavior of the particulate plume. The most concentrated region of both the airborne plume and the deposition plume are observed nearby the point of emission. The orientation of the benches, however, altered the trajectory of dispersion (Figure 2.2) [Appleton et al., 2006].

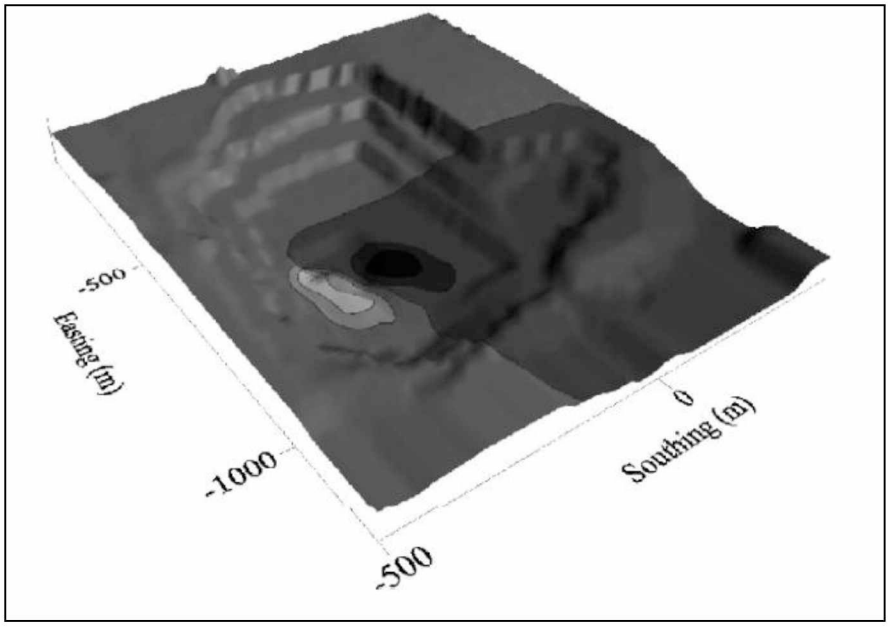

Figure 2.2: The effect of in-pit terrain on the dust deposition plume. Case: Blast 4, wind direction 60^{O}, stability class G [Appleton et al., 2006].

Zhang and Chen [2007] used Eulerian and Lagrangian models to simulate particle dispersion in a "clean room" to study particle dispersion in enclosed spaces. The domain was defined with constant ventilation rates, contaminant source terms (steady state) and an airliner cabin with a coughing passenger (unsteady state). For the steady state condition, experimental data was available for validation of the CFD model. In each case, it was assumed that the particle

concentrations were sufficiently small so that the particle movement did not impact the turbulent structures of the airflow ("one-way coupling of flow to particles"). No attempt was made to model the deposition of particles on the interior surfaces.

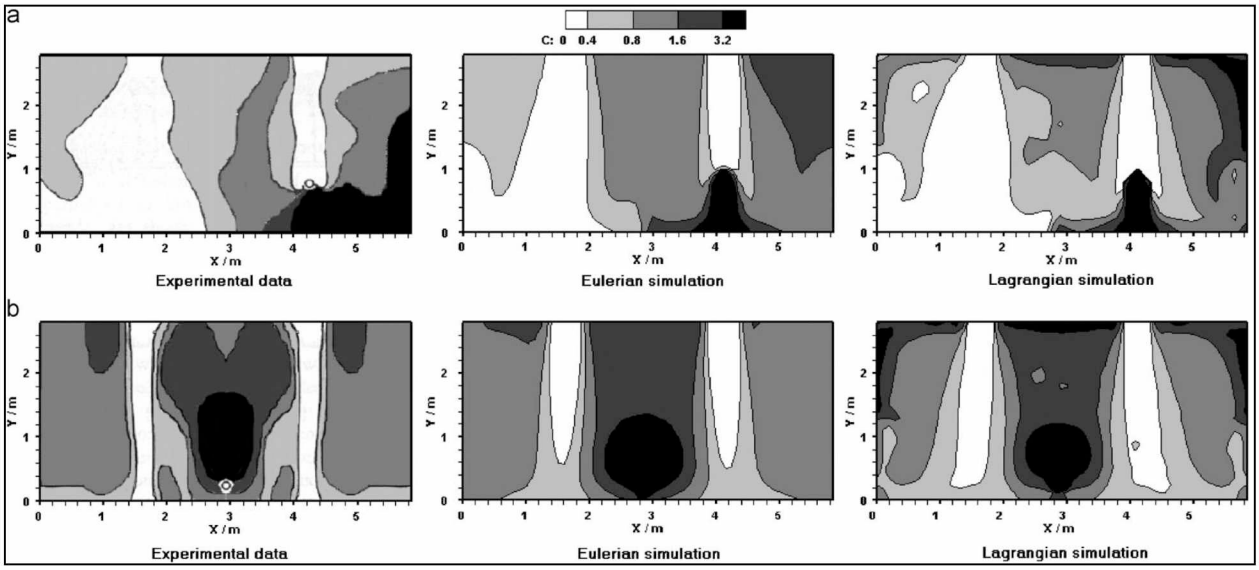

Figure 2.3: A comparison of simulated particle concentration distributions by Eulerian and Lagrangian methods with experimental data in the measurement section. (a) Source 1: particle source below the right air supply. (b) Source 2: particle source above the floor at the center [Zhang and Chen, 2007].

Zhang and Chen [2007] concluded that both the Eulerian and Lagrangian models are able to satisfactorily predict the contaminant concentration distribution under steady state conditions. For steady state conditions, the Lagrangian method proved to be much more computationally intensive than the Eulerian method. For the Lagrangian model, a large number of particles needed to be introduced into the model domain to ensure statistical stability. Figure 2.3 describes the comparison of the simulated particle concentration by Eulerian and Lagrangian methods with experimental data in a measured section. For the unsteady state conditions, the Lagrangian model was much more computationally efficient than the Eulerian model. It was concluded that the Eulerian model was impractical for tracking the particles over long time periods under unsteady conditions. This was due to the requirement of small time steps and large number of iterations for model convergence. No validation data for the unsteady state case was presented to validate the findings [Zhang and Chen, 2007].

Alvarez et al. [2007] developed a CFD model for estimation of dust dispersion in a medium-sized limestone quarry that was operated with the drill and blast method. The fugitive dust sources were defined with the use of several video recordings of blasts and dust concentration field measurements by 'light scattering' dust collector. Several iso-surfaces of varying dust concentrations at different times (55s and 75s) using the post-processor of ANSYS CFX-Solver were presented. The authors concluded that the higher concentration disappears from the domain with time.

A similar study was performed by Torno et al. [2010] and introduced more sophisticated simulation parameters to improve upon the work of Alvarez et al. [2007]. In this study, using SolidWorks, 3D models were generated and the domain was adequately meshed using ICEM CFD 10.0. The ANSYS CFX 10.0 was used for modeling and analysis. In this CFD model, three characteristics of particulate material were considered: (1) dust particle size distribution, (2) quantity of dust dispersed and (3) the locations of the injection points. Six different dust injection sources were considered for a particular blasting zone in a bench. The dust sources from different bench surfaces and the concentric hemispherical dust injection sources were considered for defining the sources (Figure 2.4). Two "light scattering" E-samplers from Met-One Instruments, Inc. were used for dust concentration measurement at 120 m and 200 m distance from the source.

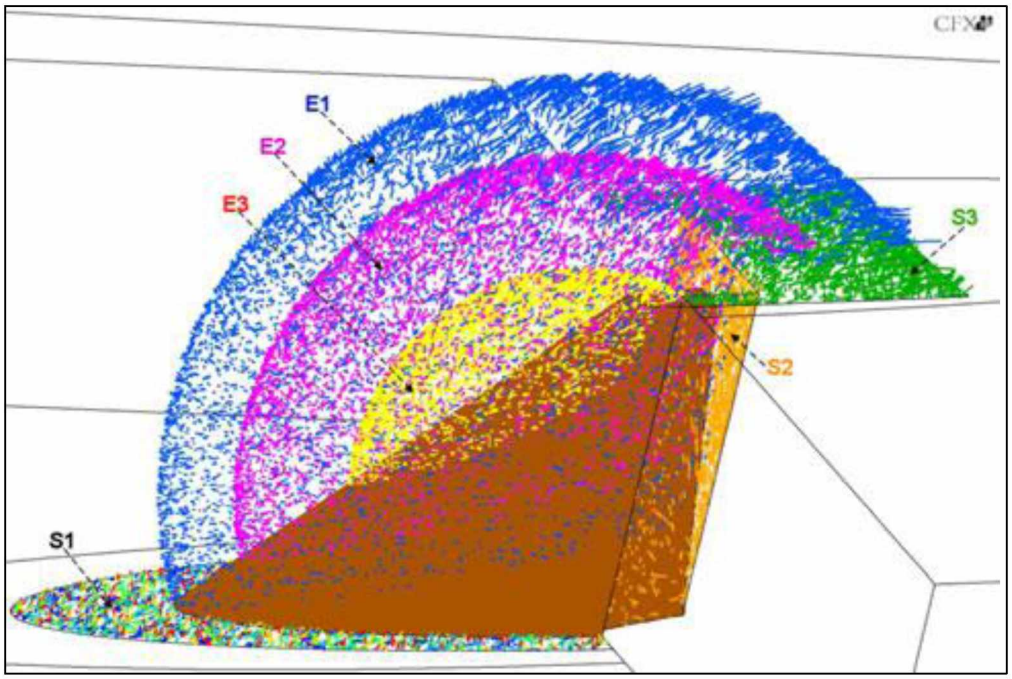

Figure 2.4: Distribution of the dust injection areas [Torno et al., 2010].

In ANSYS CFX 10.0, a dispersed phase (particles) that follows the Lagrangian approach was modeled inside a continuous phase (air), which was then solved with Eulerian approach to calculate both the pressure and the velocity of the airflow. Figure 2.5 presents the movement of dust clouds with respect to time [Torno et al., 2010].

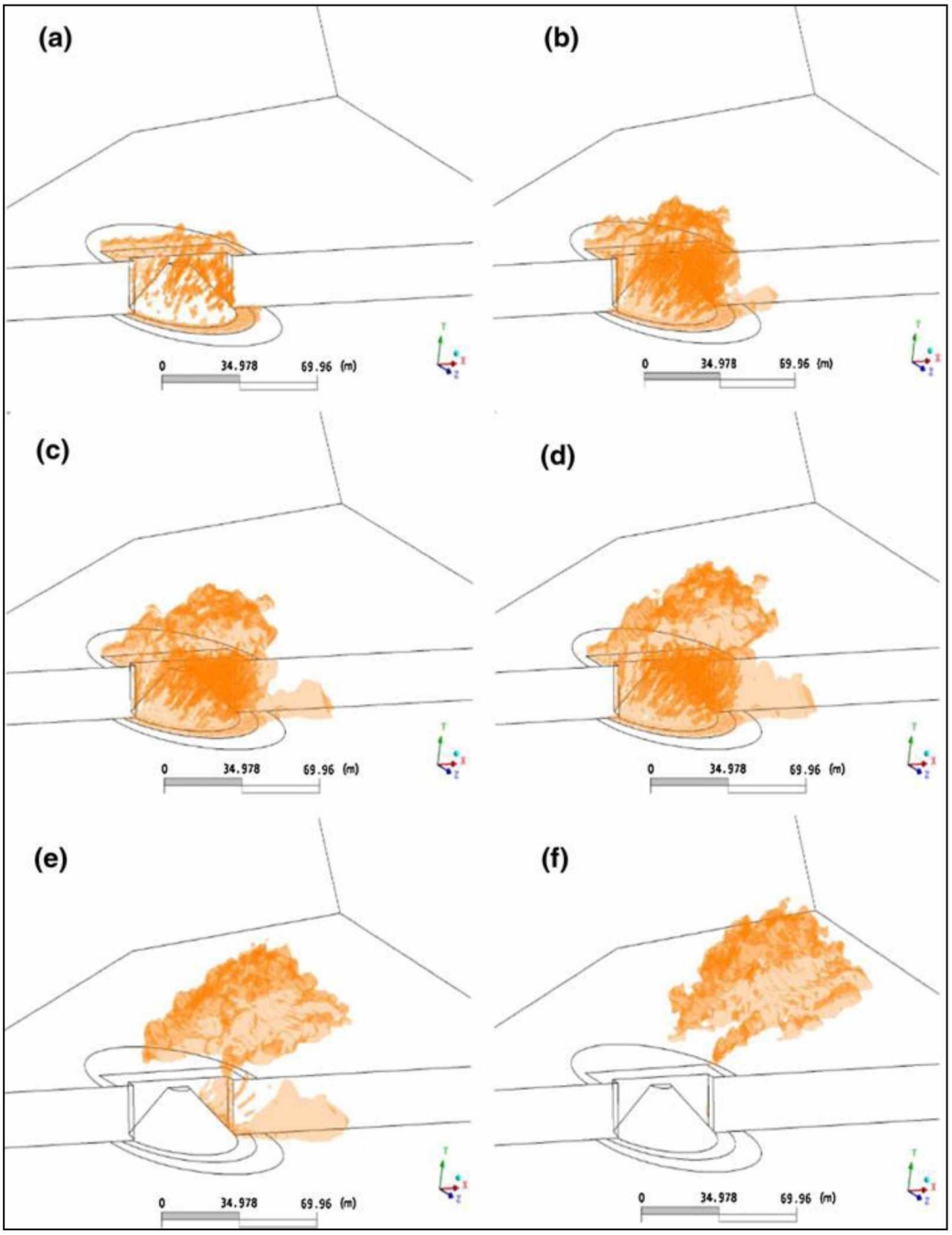

Figure 2.5: Dust cloud movement versus time elapsed: (a) 3.5s, (b) 14s, (c) 24.5s, (d) 35s, (e) 55s and (f) 75s [Torno et al., 2010].

Lowndes et al. [2008] applied CFD as a modeling tool to predict the dispersion and deposition of fugitive dust within and around surface mining operations (Figure 2.6). This study considered the presence of (1) complex internal inhomogeneous flow surfaces, (2) the influence of the external atmospheric boundary layer upon the air recirculation inside the open-pit, and (3) the influences of slope radiation on the open-pit microclimate, resulting in the formation of local temperature inversions and local winds. Three scale-modeling approaches are presented in the study: (1) The development of an improved dust emission model, followed by (2) the development of a more complex CFD model taking the pit microclimate into account, and then (3) the development of an interface between the open-pit and the far field downwind flow. This research concluded that the dispersion and the deposition of fugitive dust emission are governed by the location of the emission sources, the prevailing wind direction and the wind speed which is characterized by the atmospheric boundary layer (ABL). Silvester et al. [2009] used four particle sizes of 2.5, 10, 30, and 75μm diameters, at mass fractions of 0.05, 0.45, 0.3, and 0.2, respectively, to simulate the fugitive dust emission sources within a quarry. The quantity of dust released from each fugitive dust source (such as bench blasting, loading, truck haulage) was calculated using the emission factors. At each blast location, a series of stochastic trajectories were calculated for each particle released from each of the 2000 injection points. The researchers concluded that under the neutral conditions, the retention of fugitive dust within the quarry ranged between 30% and 60% depending on the direction of the wind.

The formation of recirculatory patterns in the airflow inside the open-pit is dependent on the aspect ratio of the pit. Cavity flows can be classified as: (1) open type (L (Length of the open-pit in downwind direction) / D (Depth of the open-pit) <10) and (2) closed type (L/D>13) of cavity according to the aspect ratio [Chinthala and Khare, 2011]. In the closed type of cavity, the shear layer generated at the leading edge collides with the cavity floor. Then the layer is reflected from the floor, which forms the expansion waves and allows the flow to escape eventually through the trailing edge. In the open type of cavity, free stream shear layer divides the flow into internal and external flow and is reattached at the trailing edge. For modeling the flow dynamics of deep open-pit coal mines, Chinthala and Khare [2011] recommended several factors that need consideration: (1) topographic factors, (2) meteorological effects and (3) thermal effects.

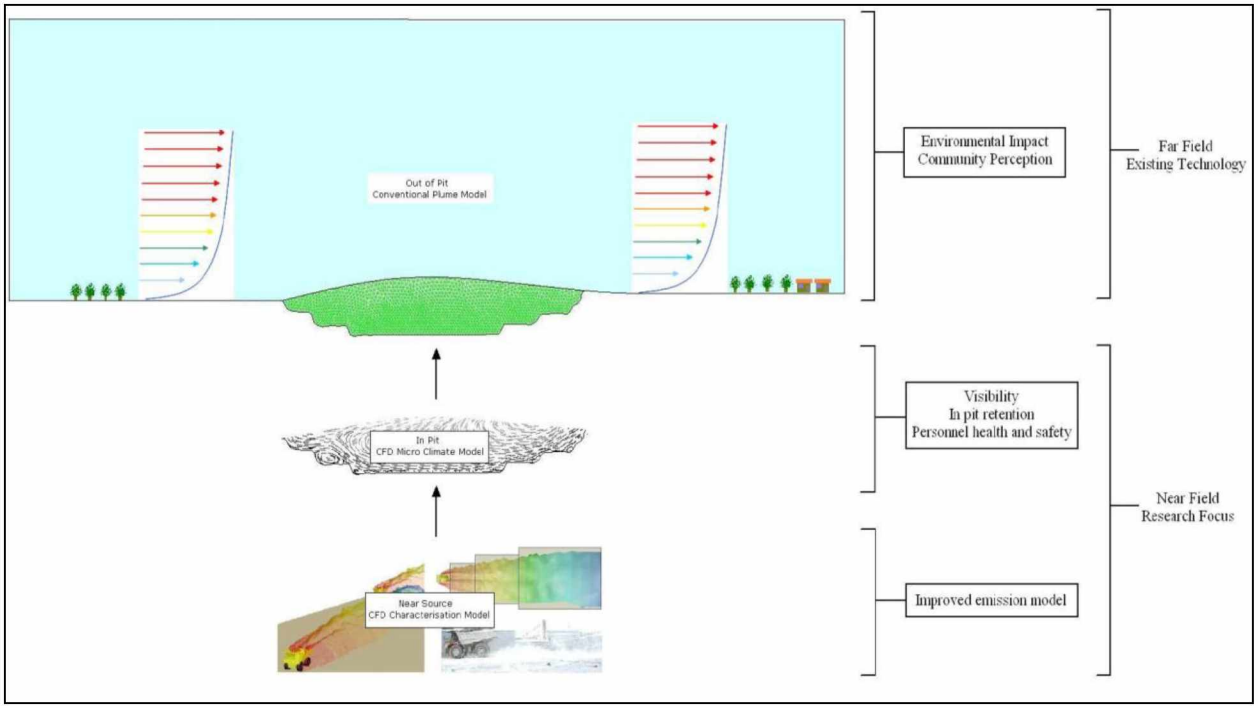

Figure 2.6: The development of a multiscale modelling methodology to improve the prediction of the effects of fugitive dust emissions within and around an open-pit [Lowndes et al., 2008].

Topographic factors are sub-divided into: (1) slopes and benches, (2) the depth of the open-pit coal mine, (3) width and breadth of deep open-pit coal mine, (4) aspect ratio, and (5) the effect of overburden dumps. The meteorological effects are sub-divided into two groups: (1) wind speed and direction; and (2) stability. Thermal effects are dependent on the thermal inhomogeneity [Chinthala and Khare, 2011]. The paper concluded that the fundamental understanding of the microclimate along with the mechanical and the thermal forces in the deep open-pit mine are essential to develop a dynamic inverse hill numerical model that can be used to investigate the complex wind flows and dispersion mechanisms [Chinthala and Khare, 2011].

Flores et al. [2013b] used an OpenFOAM CFD simulation package to simulate and predict pollutant dispersion in an idealized and an actual open-pit mine in Chile with an intense insolation condition. The model was simulated for three varying conditions: (1) air advection (10 m/s) driven mechanical turbulence; (2) surface heat flux (240 W/m^2) driven thermal buoyancy; and (3) both air advection and surface heat flux driven conditions. The results of the simulations showed that the buoyant currents contribute to the removal of a large percentage of the dust particles, as well as modify the purely mechanical-turbulence induced flow pattern and reduce

the particle residence time, commonly observed in a purely mechanical turbulent flow (non-buoyant case).

It may be clear that a large amount of research is available on production, transport and dispersion of fugitive dusts in open-pit mines in the temperate regions. However, the information on the dust generation, transport and dispersion in open-pit mines at higher latitudes is very limited. In the former USSR, studies have been conducted on generation and dispersion of fugitive dust in open-pit mines in the North. Most of this literature is not in the public domain, and therefore is not included in this review. Few publications in the area that are available are reviewed for completeness.

In their research, Grainger and Meroney [1992] concluded that the pollutant dispersions from coal pit combustion during night time inversion may result in a stagnant accumulation of smoke and dangerous gases that might inhibit mining operations. It was hypothesized that the concentration levels would reach the maximum levels during stably stratified night-time situations, since the mixing and flushing are minimal during inversion. A wind-tunnel study was conducted to identify the range of flow and the mixing conditions when stably stratified flows pass over a large open-pit, since flow penetration into the pit is dependent upon the approaching flow stability (Froude number) and the strength of thermal inversion within the coal pit [Grainger and Meroney, 1992]. In this study, the related studies of valley flows, nocturnal drainage flows in mountain basins, and the nature of mixing across inversions were also examined prior to using linear perturbation methods and numerical modeling. The wind speed, temperatures, and dispersion data were collected over a 1:600 scale model of a coal pit [Grainger and Meroney, 1992].

In his research, Baklanov [1995] concluded that the airflow pattern inside a domain is not always a typical ABL problem; the hydrodynamics and the meso-meteorology may also need to be considered as well. This approach is most common for developing airflow inside complex domains such as mountain valleys and deep open-pit mines. In this research, the author presented three numerical experiments with two to three variants in each experiment. In the first experiment, the influence of meso-scale process under normal condition as well as under inversion was simulated with a dominant background flow velocity. In the second experiment, the influence of micro-climate on the open-pit was estimated with three types of variants. In this

experiment, the radiation and thermal budget for an orographically-inhomogeneous soil surface was used. In the final experiment, the variants of the first and the second experiments were combined to reflect much of the real world situation.

2.2 Prospective Research Areas in Dust Dispersion Modeling

Fugitive dust dispersion in an open-pit mine is a day to day problem for the mine operations and involves the health and safety concerns of the mine workers and the population in the vicinity of the mine. Prior research activities have accounted for several fugitive dust estimation techniques. However, due to the complexity of the problem, none of the techniques are able to predict the amount of fugitive dust dispersion in the open-pit mines adequately. The complexity of the problem varies from the irregularities of the topography to the influences of the climatology. It is understood that the generation and transport of fugitive dust in open-pit mines are sensitive to various time-dependent parameters.

Among all the developed dust propagation models, the Gaussian model is one of the most explored models for estimation of fugitive dust. According to Beychok [1994], the Gaussian model is a good estimator of fugitive dust dispersion only if some of the basic assumptions are applicable. In most cases, however, several of these assumptions may not be valid. The ISC3 model developed by the EPA is one of the very few approved surface fugitive dust propagation models [Reed, 2005]. Though the ISC3 model is most extensively used for the mine permitting process, the model has several built-in assumptions that may always not be true for every surface mine.

It may be clear from the prior discussions [Shi et al., 2000] that the development of airflow inside an open-pit domain is dependent on two fundamental mechanisms: (1) mechanical turbulence and (2) thermal buoyancy. The mechanical turbulence is dependent on several factors, such as: (1) wind speed, (2) wind direction, (3) topography, (4) aspect ratio, and (5) surface roughness. The thermal buoyancy is also dependent on several factors, such as, (1) atmospheric stability, (2) radiation balance in the domain, and (3) presence or absence of cloud covers [Chinthala and Khare, 2011].

The ISC3 model, which is based on the Gaussian dispersion equations, calculates the wind velocity profile based on the atmospheric stability criteria for defining the input to the model. The atmospheric stability criteria of the ISC3 model are dependent on the (1) surface wind speed

(measured at 10 m height) and (2) the availability of insolation (strong, moderate or nighttime cloudiness). However, it is understood that the atmospheric stability is dependent on the balance of the shear force (due to air advection) and the buoyant forces (due to radiation balance in the domain) [Stull, 1988]. As a result, the atmospheric stability criteria in the ISC3 model are considered simplified, and the wind velocity profile may not simulate the thermal buoyancy inside the domain efficiently. The surface roughness and the topography of an open-pit domain results in the formation of airflow recirculation (eddies) that has influence on the dispersion of the dust particles. Another limitation of the ISC3 model is its inability to incorporate the influences of the airflow recirculation on the propagation of dust particles in the domain.

Advances in mathematical and computational technology in recent years have enabled better modeling of pollutant dispersion phenomena around open-pit mines using CFD. The research by Alvarez et al. [2007], Lowndes et al. [2008], Silvester et al. [2009], Torno et al. [2010], Collingwood et al. [2012], Raj et al. [2013] and Flores et al. [2013b] have made important contributions for the development of CFD models to predict dust dispersion in open-pit mines. The CFD models are able to simulate the development of airflow inside open-pit domains based on the (1) mechanical turbulence and (2) thermal buoyancy. The mechanical turbulence and the thermal buoyancy, however, vary based on the atmospheric conditions, such as, wind speed, insolation, and cloud covers. The seasonal fluctuations in the atmospheric conditions result in the variance in the retention of fugitive dust inside open-pit mines.

In this thesis, the propagation and the retention of fugitive dust in a high latitude open-pit mine is simulated using the SC/Tetra software developed by the software CRADLE. The open-pit domain of the selected mine is meshed using the Preprocessor of the SC/Tetra. The meshed model domain is solved using the Solver of the SC/Tetra. For solving the model domain, coupled simulation approach is selected. To solve the airflow inside the open-pit domain, various turbulent flow methods and turbulence models are applied in the Eulerian reference frame. The Eulerian method develops the conservations equations on a control volume (mesh elements) basis and solves the airflow parameters at each mesh elements. The parameters, such as, gravity, velocity, pressure of the airflow are solved using the Eulerian method. These airflow parameters are calculated as a function of location and time in the Eulerian method. However, for solving the turbulent dispersion of the fugitive dust particles, the Lagrangian algorithm is applied to the

dust particles. The Lagrangian stochastic model characterizes the advection and the diffusion processes of the individual dust particles as a function of time only.

Due to the extremely small fraction of particles with respect to the volume of the carrier phase (air) in the pit, the assumption of one-way coupling is applied. This means that the dynamics of the carrier phase (air) drives the motion of the dispersed phase (particulate). The presence of the dispersed phase has no effect on the dynamics of the carrier phase.

As a first step, prior to building the fugitive dust dispersion model, important variables were characterized, and input values of various atmospheric parameters were collected for defining the initial and the boundary conditions for simulation of the model domain. The collection of data for the fugitive dust dispersion model is presented in Chapter 3.

Chapter 3 Data Collection

For simulation of dust dispersion in open-pit mines, various input conditions are necessary for defining the boundaries of the simulation domain. The input conditions applicable to the domain boundaries are termed as boundary conditions. The validity and the accuracy of a model-generated prediction depend on the accurate definition of the initial and the boundary conditions. For simulating the dispersion and the retention of fugitive dust in a high-latitude open-pit mine various input conditions were characterized for defining the initial and the boundary conditions.

The selected open-pit mine is located at high-latitude (Figure 3.1), and the simulation domain is presented in Figure 3.2. The dimensions of the open-pit are 1800 m in the East-West direction, 760 m in the North-South direction, with a depth of 480 m as shown in Figure 3.2. For estimating the air flow patterns inside the open-pit, the simulation model domain is extended beyond the open-pit mine. The dimensions of the modeled domain is 4405 m in East-West direction, 2750 m in North-South direction and the height of the topmost boundary of the domain is 1000 m from the surface at the East boundary (Figure 3.2). The domain has several defined boundaries according to its location, such as, East, West, North, South and Pit surface boundary.

Figure 3.1: Picture of the open-pit mine under study during the winter months.

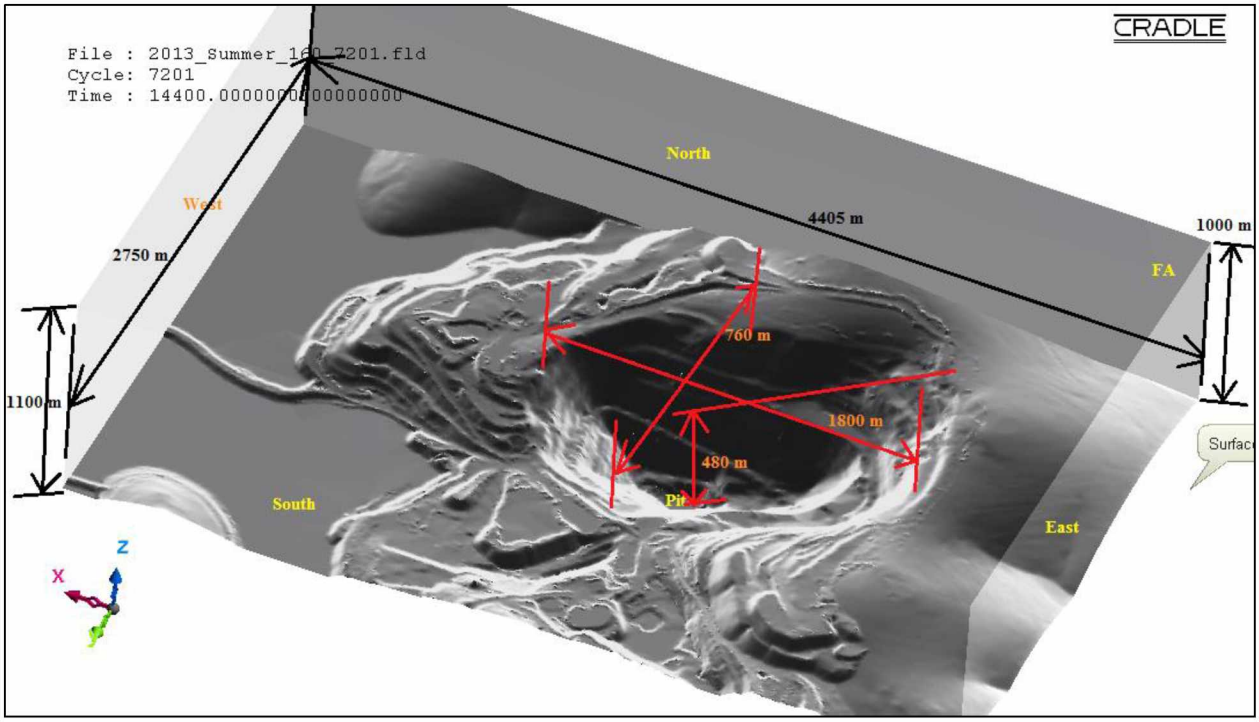

Figure 3.2: The simulation model domain of the selected open-pit, surface scanned in 2013.

In order to simulate the airflow inside the open-pit domain, several boundary conditions and input conditions are required, such as: (1) inlet boundary conditions, (2) outlet boundary conditions, (3) conditions of the roughness boundary, which is the open-pit surface, and (4) conditions for the remaining boundaries in the domain. For defining the inlet boundary conditions, the wind speed, wind direction and the airflow temperature data are collected. The outlet boundary conditions are defined by using the available outlet boundary conditions in the CFD software. For defining the roughness boundary conditions, the amount of equivalent roughness of the open-pit surface and the amount of available sensible heat flux from this surface are required. For the other remaining boundaries, the available wall boundary conditions in the CFD software are used.

3.1 Wind Speed, Wind Direction and Airflow Temperature Data

The wind speed, wind direction and the airflow temperature data are collected from a weather station located nearby the selected open-pit. The wind speed, wind direction and the airflow temperature data collected from the weather station over the time period from December 1, 2013 to January 31, 2014 are presented in Figure 3.3.

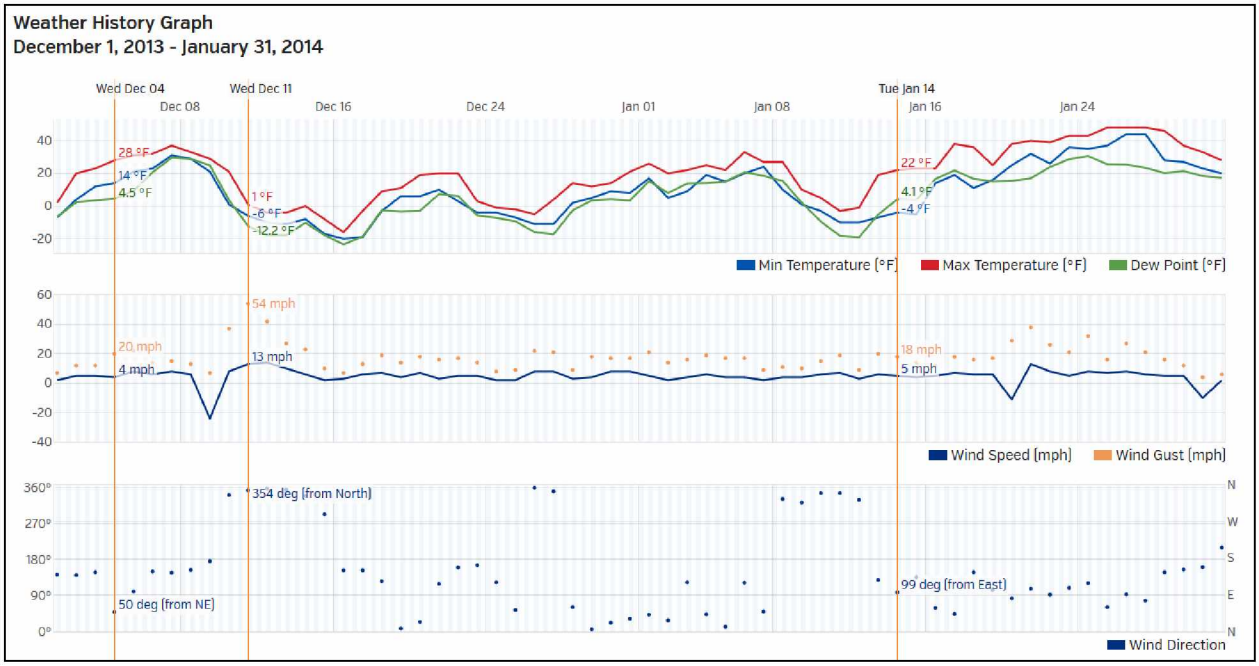

Figure 3.3: Wind speed, wind direction and air temperature variation from Dec. 1, 2013 to Jan. 31, 2014. (Source: www.wunderground.com, Weather Station ID: MCLRA2, Latitude / Longitude: N 65 ° 3 ' 1 ", W 147 ° 26 ' 49 ").

Similarly the wind speed, wind direction and the airflow temperature data over the time period from March 1, 2014 to April 30, 2014, and from June 1, 2014 to July 31, 2014, respectively, are shown in Figure 3.4 and Figure 3.5. Due to technical problems in the weather station, as shown in the Figure 3.5, no data was recorded from June 6 to July 24, 2014.

In this research, for defining the input conditions of the model domain, several seasonal conditions are selected. For each season, the data are collected for duration of two months. For simulating the winter season, for example, the input data are collected from December 1, 2013 to January 31, 2014 (Figure 3.3). For the spring season, the input data are collected from March 1, 2014 to April 30, 2014 (Figure 3.4). For the summer season, the input data is collected from June 1, 2014 to July 31, 2014 (Figure 3.5). For the fall season, the input data are collected from September 1, 2014 to October 31, 2014.

In Figure 3.3 and Figure 3.4, it is observed that the airflow temperature (maximum, minimum and dew point temperatures) fluctuates over the period of the two selected months for both the winter and the spring seasons. Due to the unavailability of weather data from June 6 to July 24,

2014, the fluctuating behavior of the airflow temperature in Figure 3.5 is not clearly visible. Similar fluctuating behavior is also observed for the wind direction profile during the two seasons (winter and spring). It can be noted, however, that the wind speed remained mostly within a range of 2 to 10 mph during the two (winter and spring) seasons.

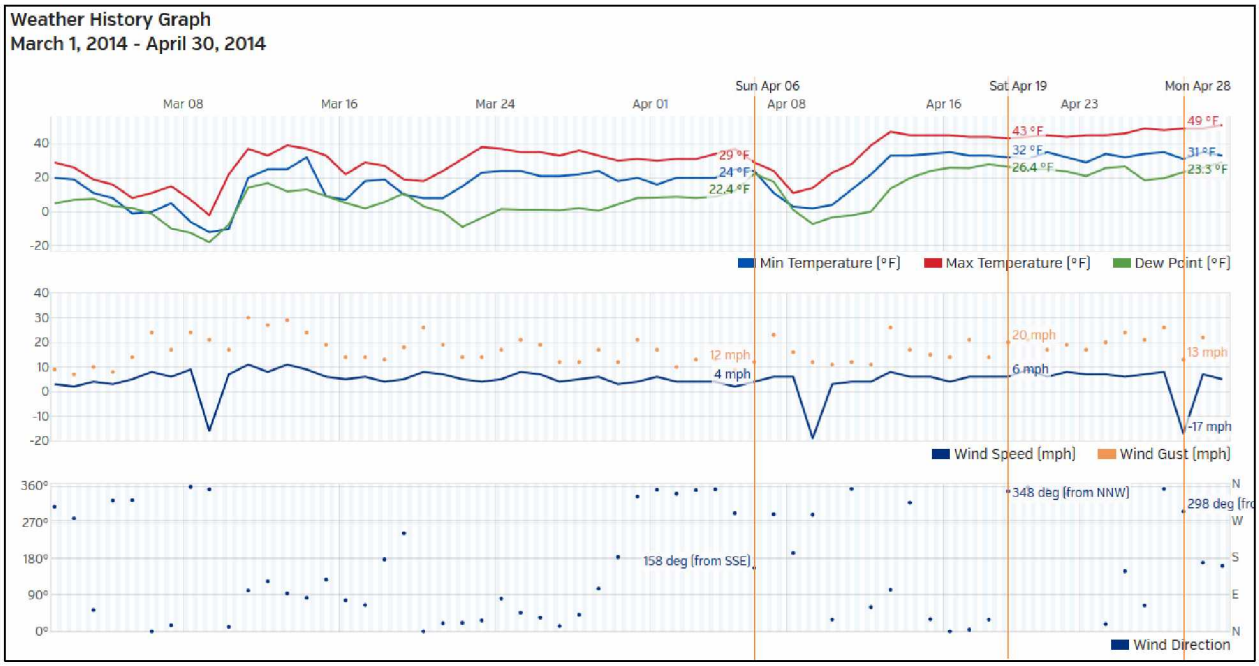

Figure 3.4: Wind speed, wind direction and air temperature variation from Mar. 1 to Apr. 30, 2014. (Source: www.wunderground.com, Weather Station ID: MCLRA2, Latitude / Longitude: N 65 ° 3 ' 1 ", W 147 ° 26 ' 49 ").

For defining the wind speed and the air temperature values for the simulation model, the wind speed and the air temperature data are averaged for each season, and the averaged wind speed and the averaged air temperature are used as the inlet boundary conditions. Table 3.1 presents the highest, lowest and the average value of the temperature, humidity, and wind speed recorded during the winter and the summer months at the weather station. It can be observed (Table 3.1) that during winter months, the average air temperature in the mine is around -10 °C. While, the average air temperature in the mine during the summer months is around 10 °C. A small increment in the average wind speed is observed from the winter to the summer season. Due to the unavailability of weather data from June 6 to July 24, 2014 the average wind speed and the average air temperature is compared with the average values from previous and following years [2013 and 2015]. In the summer months of 2013, the recorded average wind

speed and the average air temperature are 2.01 m/s and 15.56 °C, respectively. While during summer months of 2015, the recorded average wind speed and the average air temperature are 2.32 m/s and 13.89 °C, respectively. Since no significant difference is observed in the average values during the summer months (2013, 2014 and 2015), the 2014 average wind speed and the average air temperature values are used in the simulation.

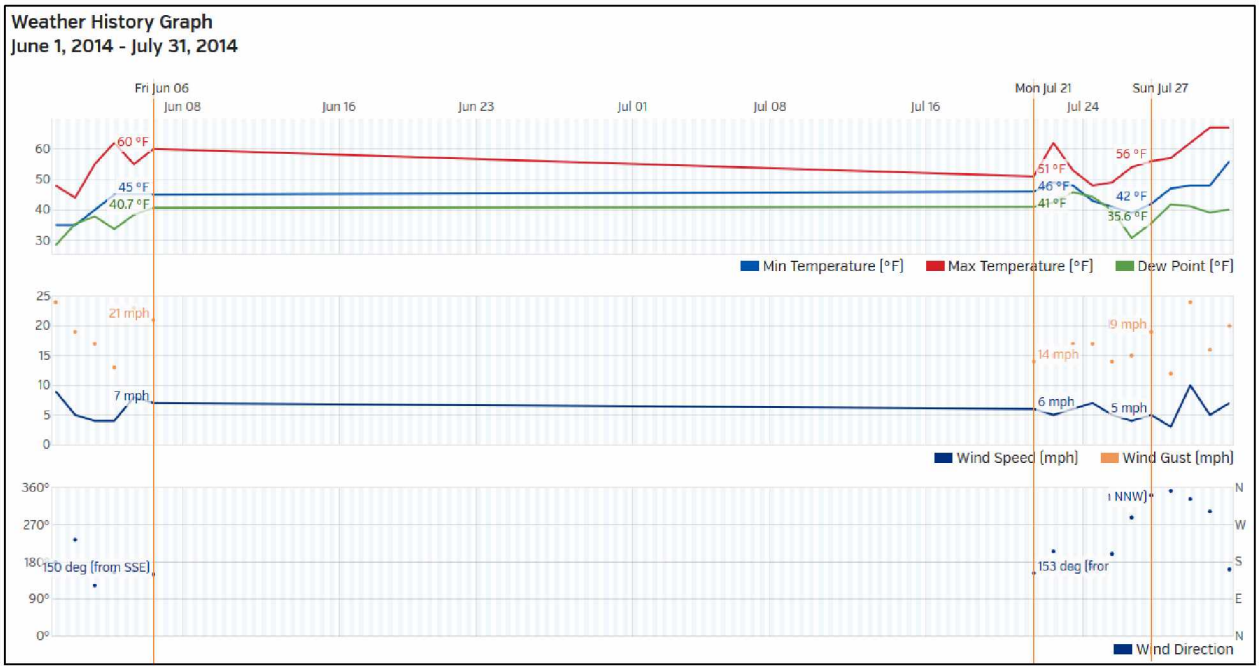

Figure 3.5: Wind speed, wind direction and air temperature variation from Jun. 1 to Jul. 31, 2014. (Source: www.wunderground.com, Weather Station ID: MCLRA2, Latitude / Longitude: N 65 ° 3 ' 1 ", W 147 ° 26 ' 49 ").

Table 3.1: Temperature, humidity, and wind speed values during the months of the winter and the summer seasons.

Seasons	Winter, 2013-2014			Summer, 2014		
	High	Low	Average	High	Low	Average
Temperature	8.89 °C	-28.89 °C	-9.61 °C	19.4 °C	1.67 °C	9.44 °C
Humidity	96%	34%	70.50%	96%	32%	70.30%
Wind Speed	9.39 m/s	--	2.1 m/s	7.6 m/s	--	2.5 m/s
Wind Direction	--	--	SSE	--	--	SW

Table 3.2 presents the highest, lowest and the average values of the temperature, humidity, and wind speed during the spring and the fall seasons. It can be observed that the average wind speed during the spring of 2014 is very close to the average wind speed during the winter, 2013-2014 season. The average wind speed during the fall of 2014 is similar to the average wind speed during the summer of 2014. Although the wind speed values are very similar, a significant difference is observed in the average air temperature values of all the seasons.

For calculation of the radiation balance, several days (vertical lines in the figures) are randomly selected as shown in the Figure 3.3, Figure 3.4 and Figure 3.5. The net radiation profile is plotted to estimate the radiation balance in the open-pit domain.

Table 3.2: Temperature, humidity, and wind speed values during the months of the spring and the fall seasons.

Seasons	Spring, 2014			Fall, 2014		
	High	Low	Average	High	Low	Average
Temperature	10.57 °C	-24.44 °C	-3.56 °C	19.44 °C	-13.33 °C	0.28 °C
Humidity	97%	20%	53.30%	96%	29%	68.40%
Wind Speed	8.05 m/s	--	2.06 m/s	12.07 m/s	--	2.5 m/s
Wind Direction	--	--	South	--	--	South

3.2 Equivalent Surface Roughness of Pit Surface

Open-pit surface topography is generally rough and uneven. The pit surface of the open-pit generates turbulence when the air flows over the pit surfaces. The roughness of the pit surface provides resistance to the advective air flow, and this disturbs the viscous sublayer in the airflow, resulting in the formation of mechanical turbulence.

In order to simulate the mechanical turbulence generated by the rough surface, the wall boundary condition of the pit surface needs to be defined with an equivalent roughness value. Stull [1988] defined the equivalent roughness or the aerodynamic roughness length (k_s) as the distance (in meter) measured from the rough surface interface to that airflow sublayer, where the wind speed becomes zero due to the presence of the roughness in the surface. According to Stull [1988], the wind velocity profile under neutral conditions at a surface follows a logarithmic wind profile. The logarithmic wind profile used in this research [Software Cradle Co. Ltd., 2013d], is:

$$\frac{u}{u_*} = \left(\frac{1}{k}\right) \ln\left(\frac{y}{k_s}\right) + B \tag{3.1}$$

Where, u is the wind speed at the y height, u_* is the friction (shear) velocity, k is the von Kármán constant with a value of 0.41, B is a constant (on a fully rough surface, B = 8.5), and k_s is the aerodynamic roughness length or the equivalent roughness.

In the CFD software used in this research (SC/Tetra), the input variables KS, SK, and SB stand for the variables k_s, k and B, respectively in Equation 3.1. It can be noted that only the parameter value of KS is needed for defining the rough surface, which is the value of the equivalent or the aerodynamic roughness length. The roughness length is composed of a weighted sum of the roughness lengths of the individual roughness elements. The aerodynamic roughness lengths for various terrain types are given by Stull [1988] (Figure 3.6). However, no specific value of the equivalent roughness for an open-pit surface is available. In the absence of any representative data, a comparative equivalent roughness value is selected. The open-pit surface may not have roughness similar to many hedges or many trees at a surface, and not as smooth as uncut grassland (the red circled region in Figure 3.6). Therefore, an equivalent roughness value of $2 * 10^{-2}$ is selected for the open-pit surface, which represents a roughness value in between the isolated trees and uncut grassland. However, during the winter season, due

to presence of accumulated snow on the pit surface, the equivalent roughness of the snow covered surface is reduced significantly ($1 * 10^{-3}$).

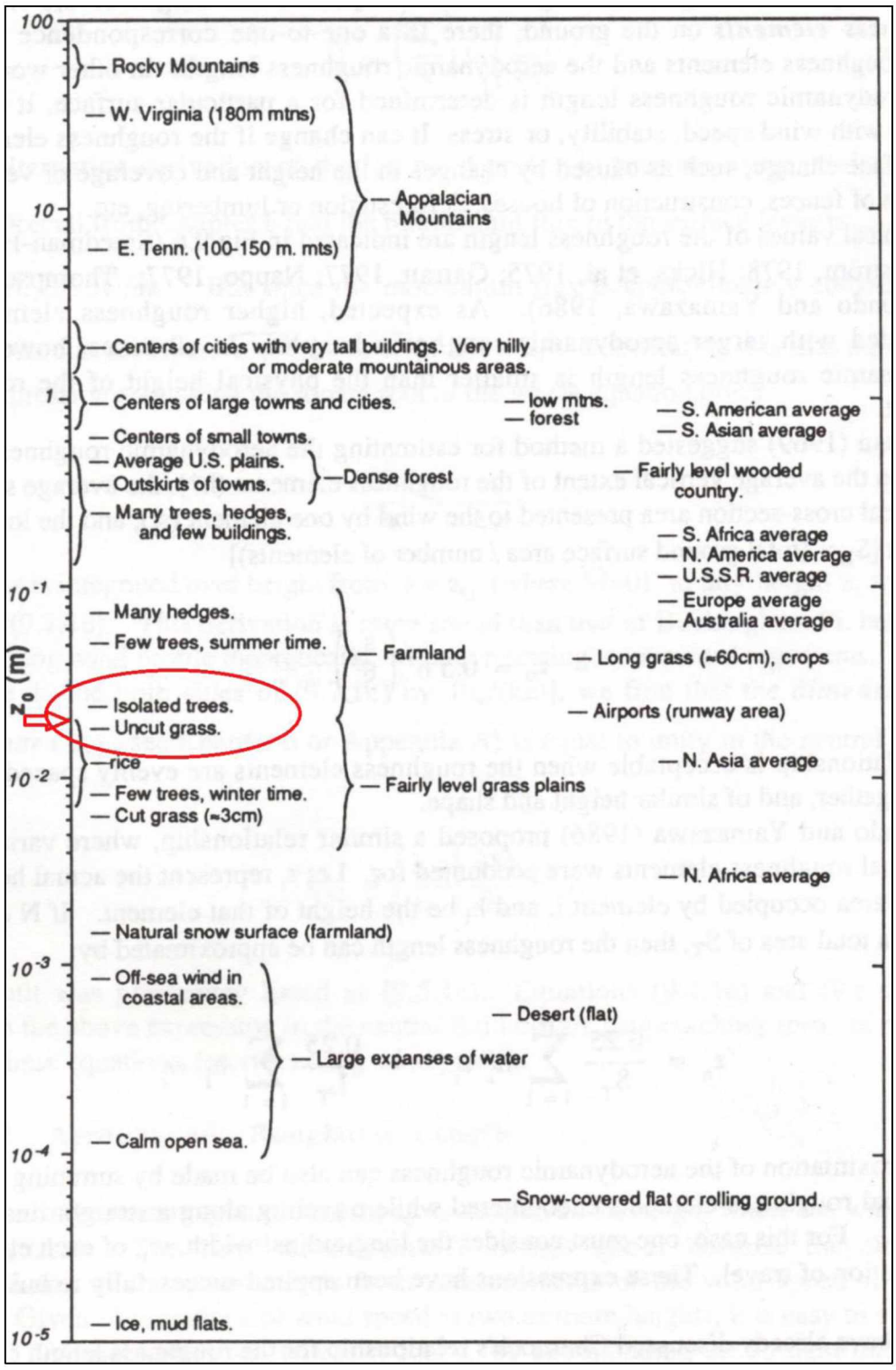

Figure 3.6: Aerodynamic roughness lengths for typical terrain types [Stull, 1988].

3.3 Sensible Heat Flux from the Pit Surface

The ABL is the part of the troposphere that is directly influenced by the presence of the earth's surface and responds to the surface forcing in a time scale of about one hour or less [Stull, 1988]. The ABL flows at small scales are developed due to the (1) surface energy balance, (2) surface roughness, and (3) the influences of mesoscale and synoptic-scale flows in the atmosphere. In micro-scale flow the surface energy balance and the surface roughness play dominant roles due to the shorter spatial and temporal scales of the micrometeorology. For fugitive dust dispersion in an open-pit domain, the development of micro-scale ABL flow in the domain is rather important, since the dust dispersion is directly influenced by it.

As the ABL is directly affected by diurnal cycles at the surface, it is a turbulent layer that is characterized by irregular eddies. The turbulent eddy motions are generated by two mechanisms: wind shear and buoyancy [Stull, 1988]. Figure 3.7 presents the effects of diurnal cycles on the boundary layer structure over land surfaces in high pressure regions. As shown in the Figure 3.7, the boundary layer structure has three major components during a diurnal cycle: (1) a mixed layer, (2) a residual layer, and (3) a stable boundary layer.

The surface energy balance results from net radiation (RN), ground heat flux (G), sensible heat flux (H), and latent heat flux (LE) (Equation 3.2).

$$RN - G = H + LE \tag{3.2}$$

Figure 3.8 (a) shows a typical day time scenario of energy balance, where the RN is of the highest magnitude and pointing towards the ground surface. However, the actual magnitudes of the various fluxes depend on several factors such as the medium type and its characteristics (moisture content, texture, vegetation, etc.), the season, the time of day, the weather conditions, and the geographical location. Figure 3.8 (b) shows a typical night time scenario of energy balance. The RN component in the energy balance equation (Equations 3.3) is resulted due to short-wave (SW) and long-wave (LW) radiation both down-welling (DN) and up-welling (UP). Figure 3.9 presents an illustration of net radiation fluxes according to Equation 3.3.

$$RN = SW_{DN} + SW_{UP} + LW_{UP} + LW_{DN} \tag{3.3}$$

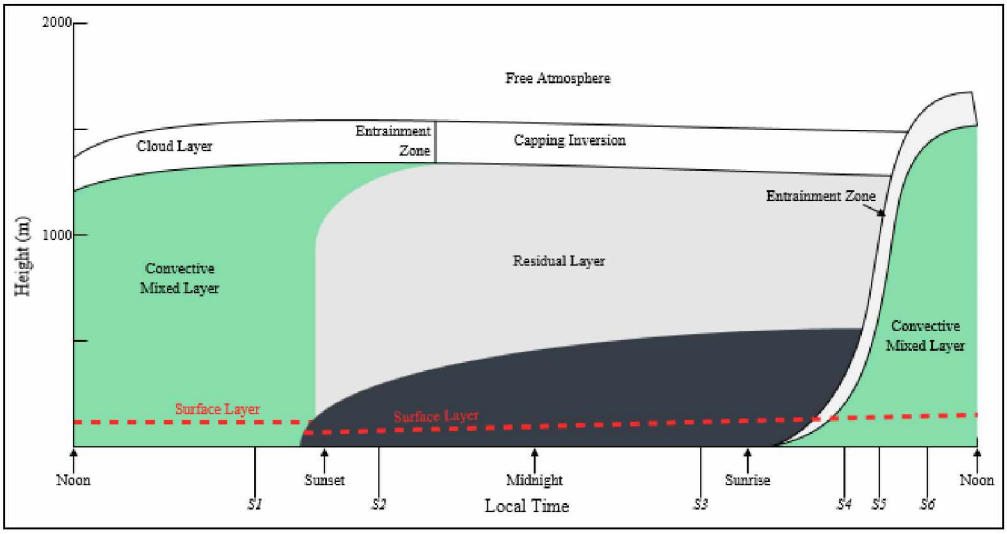

Figure 3.7: The effects of diurnal cycles on the boundary layer structure [Stull, 1988].

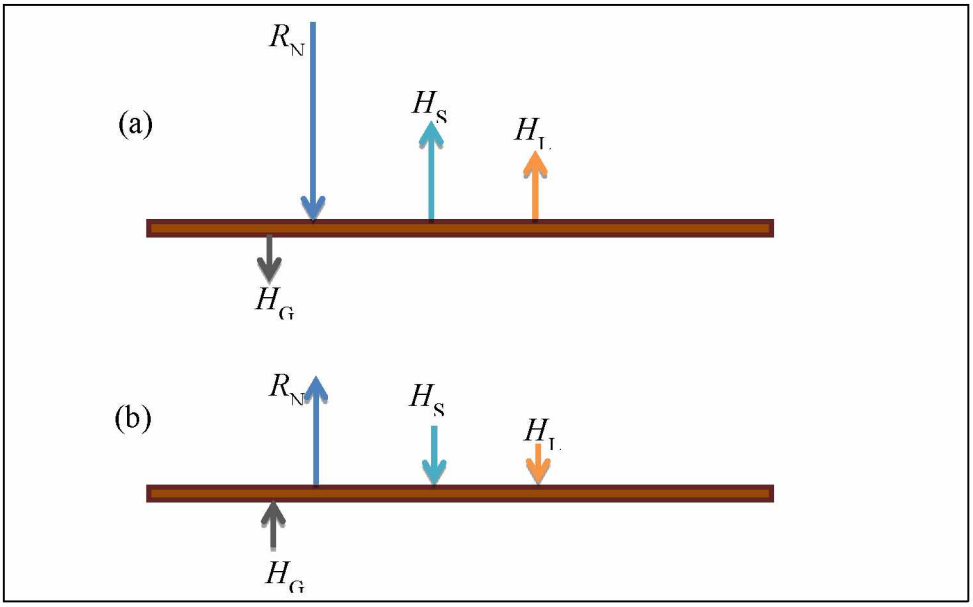

Figure 3.8: A typical energy balance during (a) Day-time (b) Night-time [Raj, 2015].

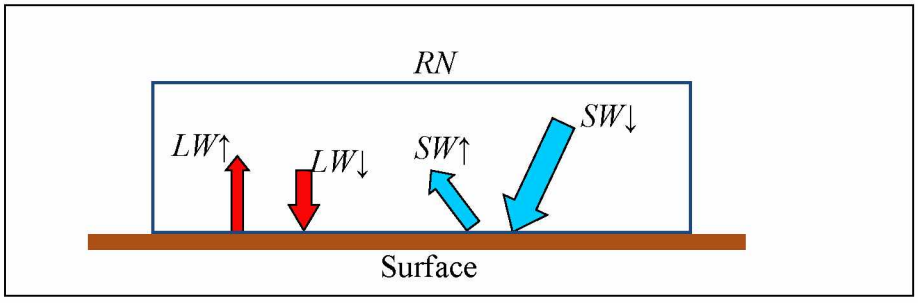

Figure 3.9: An illustration of net radiation fluxes [Raj, 2015].

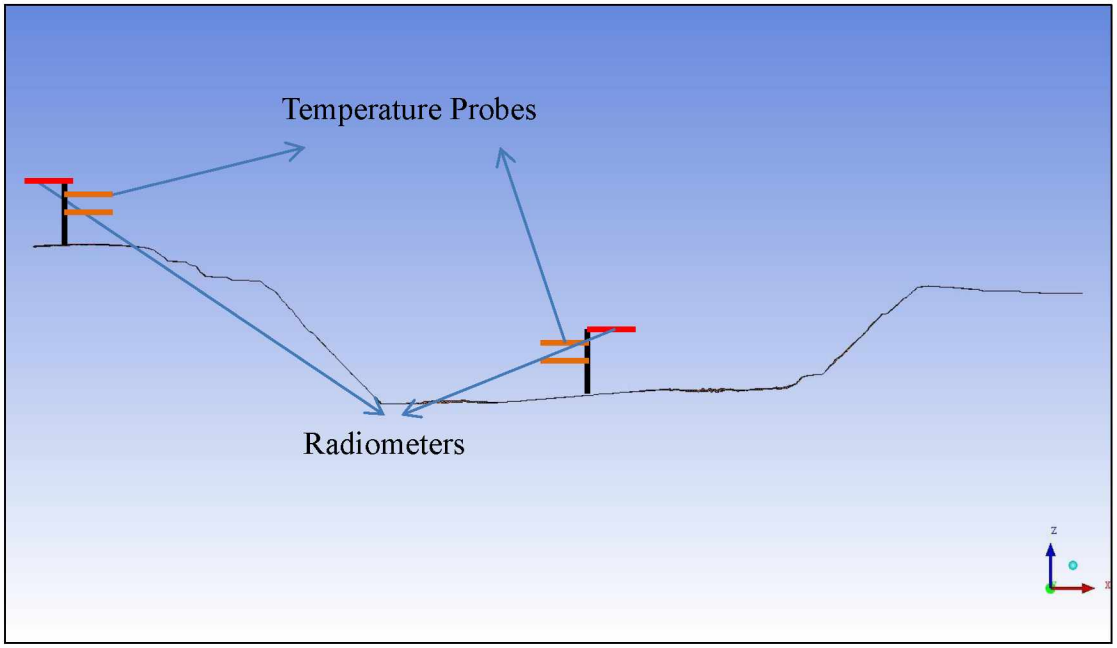

Figure 3.10: Schematic for the instrumentation in the mine [Raj, 2015].

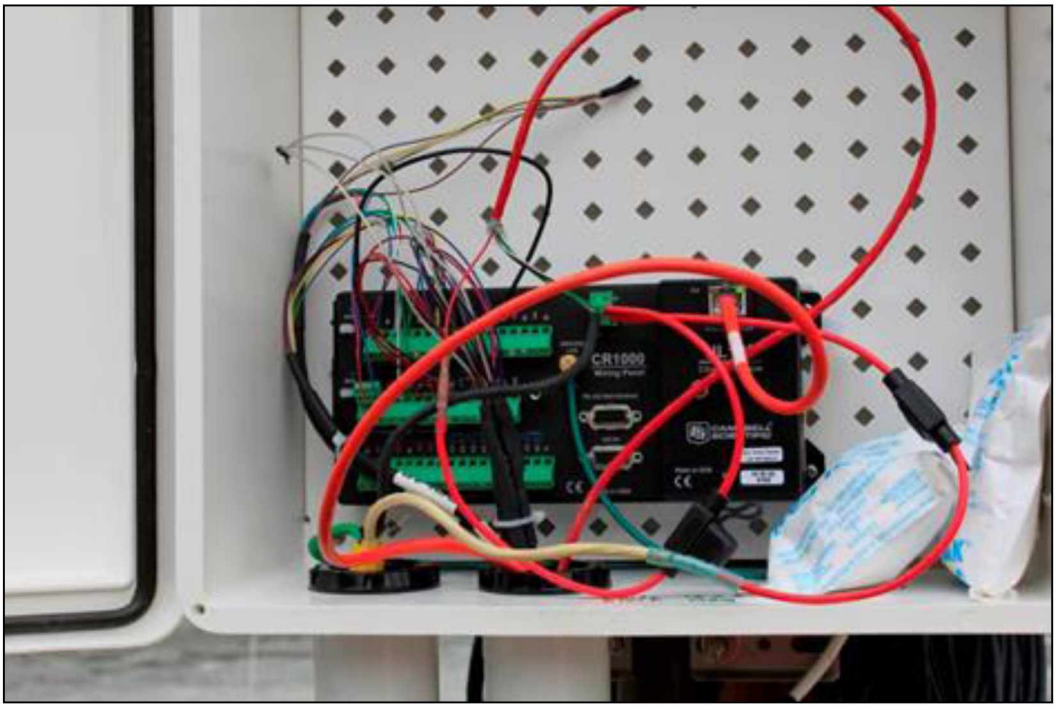

Figure 3.11: Data logger at pit-bottom [Raj, 2015].

In the selected open-pit mine, no water surface is present. Therefore, the LE component in Equation 3.2 is ignored due to absence of any latent heat. The G component, which is a small fraction of RN, is also ignored for simplification. From Equation 3.2, it is clear that the RN from

the open-pit surface is used entirely as H, which results in temperature variation in airflow inside the open-pit mine.

Figure 3.12: Ten meter tower with temperature probes and radiometer at the pit-bottom [Raj, 2015].

A schematic of the instrument setup at the selected open-pit mine is given in Figure 3.10. Two set of instruments are installed at pit-bottom and pit-rim. The radiometers collect the short-wave and the long-wave radiation data at the pit-bottom and at the pit-rim. Three temperature probes at varying heights of 1.5 m (5 ft.), 3.6 m (12 ft.) and 10 m (35 ft.) are installed at the pit-bottom to obtain temperature profile in the vertical direction. Similarly, two temperature probes at the heights of 1.5 m (5 ft.) and 3.6 m (12 ft.) are installed at the pit-rim. The radiation and temperature data at the pit-rim and pit-bottom provide an understanding of the existing thermal conditions inside the open-pit domain. Figure 3.11 and Figure 3.12 shows the data logger instrument setup at the pit-bottom.

A plot of SW and LW radiation obtained from the 4-component radiometer installed inside the selected open-pit on 4th December, 2013 is presented in Figure 3.13. The wind speed, wind direction, and the temperature data for 4th December, 2013 were shown in Figure 3.3.

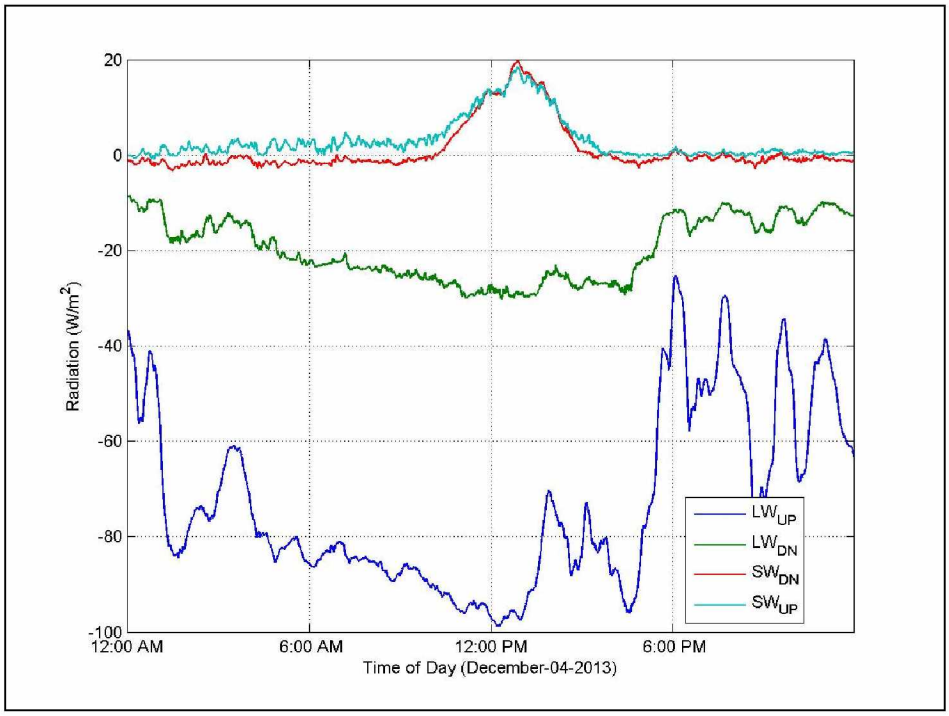

Figure 3.13: SW and LW radiation plot inside the open-pit on December 4, 2013.

The resultant RN from the SW and LW radiation on 4th December, 2013 at the pit-rim and pit-bottom is given in Figure 3.14 and Figure 3.15, respectively. A significant difference is observed in the RN temporal series. Between midnight (12:00 AM) to afternoon (3:00 PM), the RN series for the pit-rim (Figure 3.14) shows fluctuations ranging in between -45 W/m^2 to -72 W/m^2. A considerably high negative magnitude values in the fluctuations can be observed. During that same time period at the pit-bottom (Figure 3.15), however, the RN series show fluctuations in the positive range varying between 5 W/m^2 to 18 W/m^2. This opposing phenomenon indicates the formation of a stable boundary layer at the pit-rim. While at the same time the formation of an unstable boundary layer is developing at the pit-bottom. The average net radiation at the pit-rim is calculated as -55 W/m^2, while at the pit-bottom the average net radiation is 9.52 W/m^2.

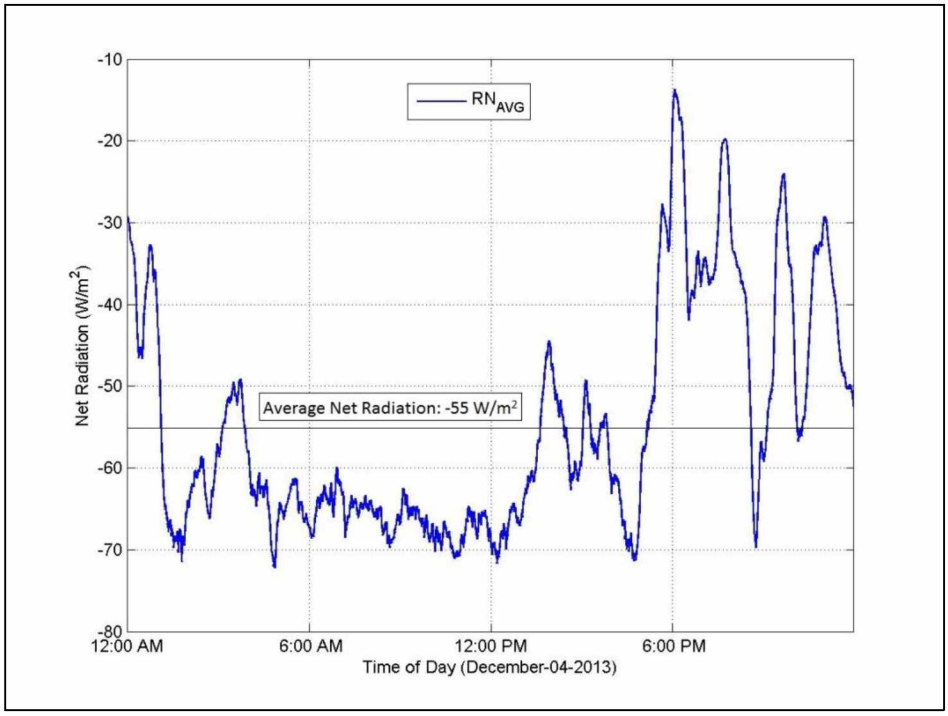

Figure 3.14: RN plot inside the open-pit at the pit-rim on December 4, 2013.

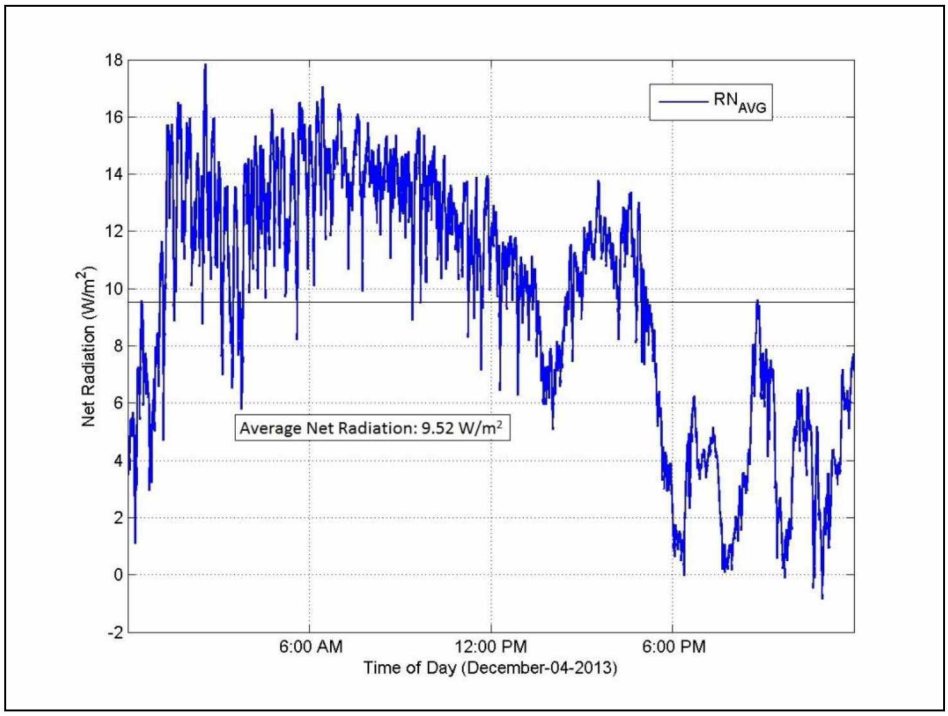

Figure 3.15: RN plot inside the open-pit at the pit-bottom on December 4, 2013.

The randomly selected days shown in Figure 3.3, Figure 3.4 and Figure 3.5 are used for calculation of the radiation balance. The temporal series of the net radiation data at the pit-rim and the pit-bottom are plotted for 16th December, 14th January, 6th April, 19th April, 28th April, and 11th June. In the following discussion, the RN temporal series for various days are plotted to find the similarity in the net RN trends and to quantify the net radiation input parameters for the dispersion models.

The RN temporal series for the 16th December, 2014 shows similar trends in the temporal series at the pit-rim and at the pit-bottom. For the initial part of the day, the RN values are positive indicating an unstable nature of the boundary layer in the open-pit domain. The RN values gradually decrease to negative values with time. This indicates the transition of the boundary layer from an unstable boundary layer to a stable boundary layer (negative RN). The average net radiation at the pit-rim (Figure 3.16) is calculated as 2.92 W/m^2, and at the pit-bottom (Figure 3.17) the average net radiation is 1.78 W/m^2.

Significant differences can be observed in the RN temporal series for the 14th January, 2014. In the early half of the day (until noon), the temporal series for both the pit-rim and the pit-bottom show RN magnitudes close to zero (0 W/m^2). Between noon (12:00 PM) and evening (9:00 PM), however, the RN series for the pit-rim (Figure 3.18) show fluctuating high negative values ranging from -20 W/m^2 to -35 W/m^2. The RN temporal series during that time period at the pit-bottom shows a trend which is completely different. The RN series for the pit-bottom (Figure 3.19) fluctuates in the positive range from 3 W/m^2 to 17 W/m^2. The radiometer data (Figure 3.18) indicates radiative cooling at the pit-rim between noon (12:00 PM) and evening (9:00 PM), which might develop a stable boundary layer depending on the state of mechanical turbulence at the open-pit. While the net radiometer data at the pit-bottom (Figure 3.19) indicates that an unstable boundary layer formation is present in the open-pit domain during that corresponding time period. A similar phenomenon was observed for the RN temporal series for 4th December, 2013 (Figure 3.14 and Figure 3.15).

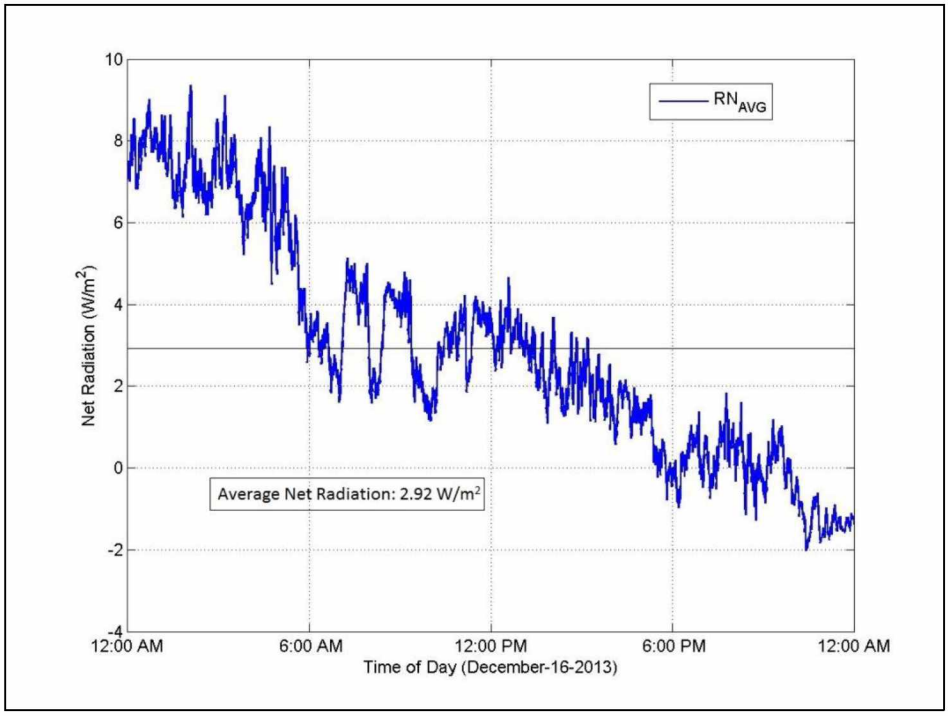

Figure 3.16: RN plot inside the open-pit at the pit-rim on December 16, 2013.

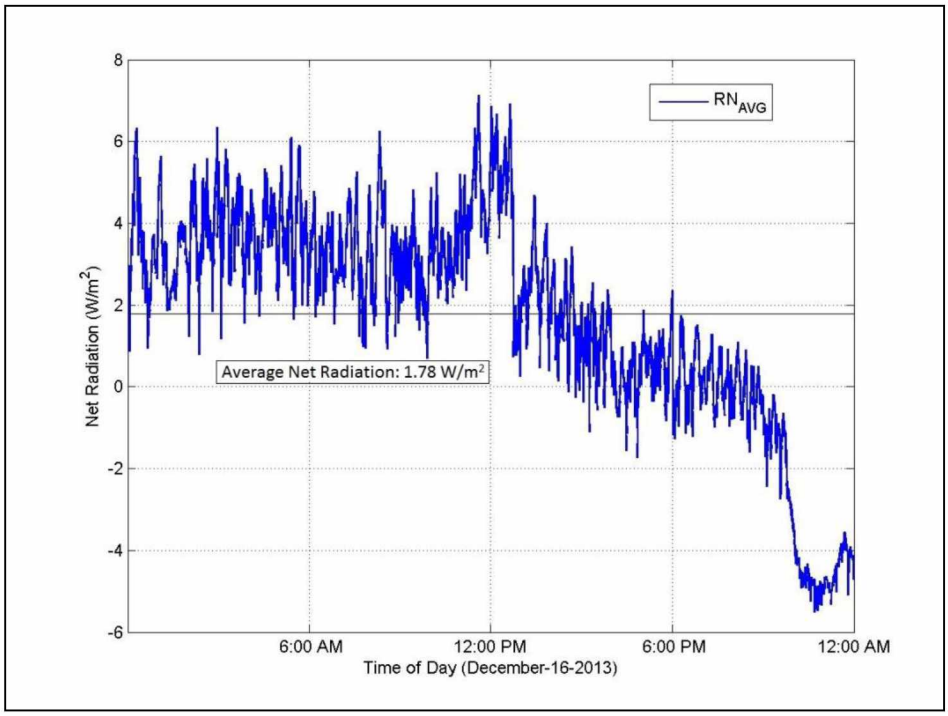

Figure 3.17: RN plot inside the open-pit at the pit-bottom on December 16, 2013.

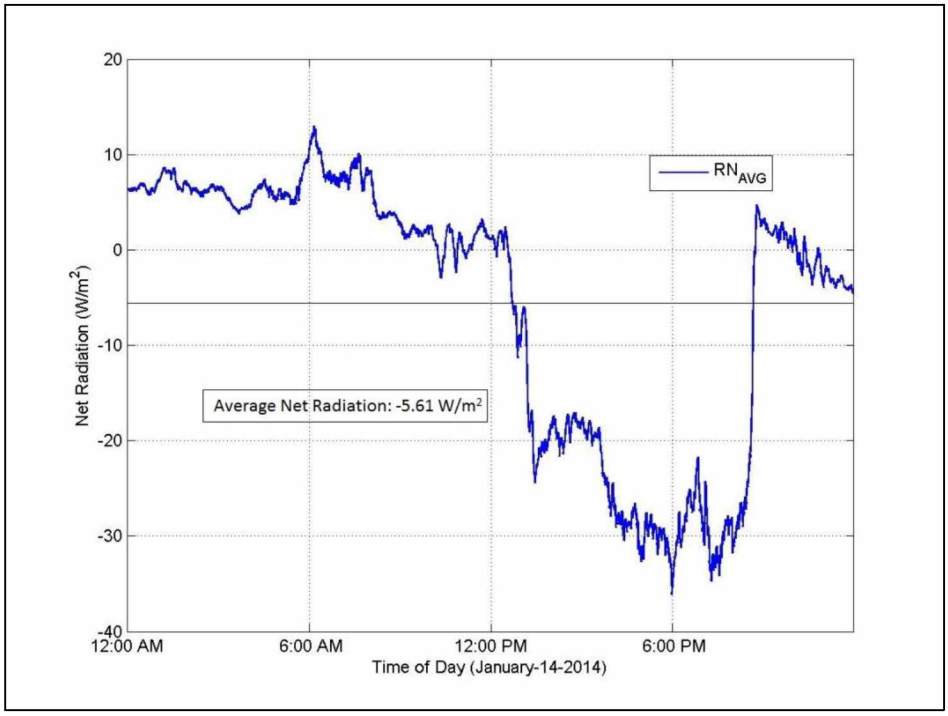

Figure 3.18: RN plot inside the open-pit at the pit-rim on January 14, 2014.

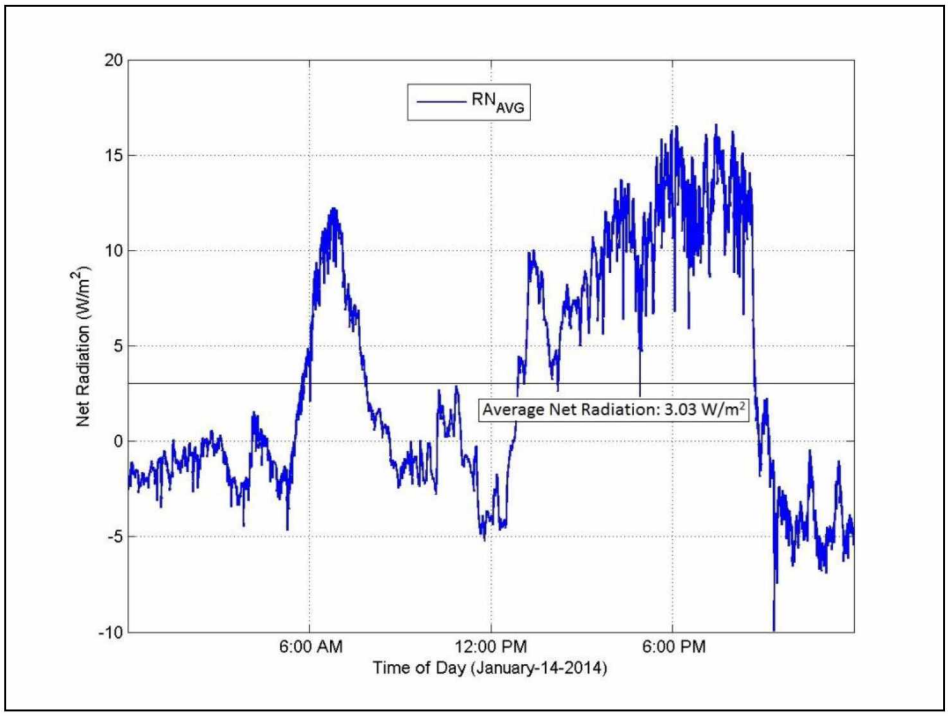

Figure 3.19: RN plot inside the open-pit at the pit-bottom on January 14, 2014.

It can be seen from Figure 3.14 to Figure 3.19, that none of the RN temporal series display any diurnal evolution. This is due to the absence of insolation during the winter months (December and January) at high latitudes, such as Alaska. Due to the very short span of a winter-day and lack of insolation, the shortwave radiation does not have any significant influence on the net radiation balance at high latitudes. With increasing span of daylights, and the availability of relatively higher insolation in the domain, the shortwave down-welling radiation plays a dominant role in the radiation balance. This results in the diurnal evolution of radiation balance during the daytime for the remaining months. Figure 3.20 presents a plot of SW and LW radiation series for 28th April, 2014, obtained from the 4-component radiometer installed inside the selected open-pit. A prominent diurnal evolution of the shortwave down-welling radiation can be observed. The shortwave down-welling radiation varies between zero (0 W/m^2) to 600 W/m^2. The bell shaped temporal series reaches the maximum value around noon (12:00 Noon) when the insolation is maximum.

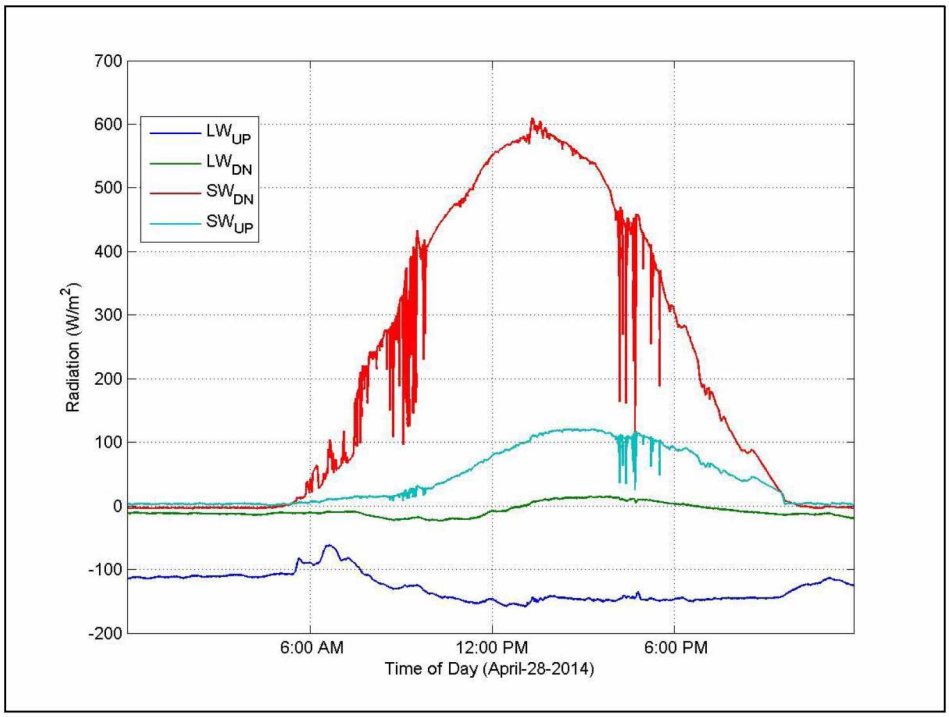

Figure 3.20: SW and LW radiation plot inside the open-pit on April 28, 2014.

Figure 3.21 and Figure 3.22 present the RN temporal series for 6th April, 2014, respectively at the pit-rim and at the pit-bottom. The diurnal evolution of the net radiation profile is observed in both the figures. The profiles, however, exhibit several spikes when the maximum values of the RN series are reached. The shape of net radiation profile for the pit-rim is under-developed as compared to the profile at the pit-bottom. The average net radiation at the pit-rim (Figure 3.21) is calculated as 16.38 W/m^2, and at the pit-bottom (Figure 3.22) the average net radiation is 51.54 W/m^2.

The RN temporal series at the pit-rim and pit-bottom for 19th April, 2014 are presented in Figure 3.23 and Figure 3.24, respectively. A well-developed diurnal evolution of the net radiation in the domain as calculated at the pit-rim is presented in Figure 3.23. The RN profile (Figure 3.23) reaches the maximum value around noon (12:00 PM). Although the RN profile from the pit-bottom starts with a well-defined shape with increasing net radiation value, it abruptly drops down to a zero value (0 W/m^2) just before the mid-day, and this trend continues until afternoon (3:00 PM). The profile again reaches the maximum value very abruptly, and then follows a bell shaped curve. This abrupt drop is believed to be due to some mining unit operations nearby the radiometer at the pit-bottom. Similar patterns of abrupt drop in net radiation value are also observed for other days. The exact cause for this hindrance is not examined thoroughly.

Figure 3.25 and Figure 3.26 present the RN temporal series at the pit-rim and at the pit-bottom for 28th April, 2014, respectively. Similar to the Figure 3.23, Figure 3.25 presents a well-developed diurnal evolution of the net radiation in the domain as calculated at the pit-rim. Figure 3.26 presents similar abrupt drops in net radiation magnitude at the pit-bottom. In contrast, the drop in the net radiation value in Figure 3.26 is around -100 W/m^2. The cause for this very highly negative radiation is not examined, but observed during some other days as well.

The RN temporal series at the pit-rim and pit-bottom for 11th June, 2014 are presented in Figure 3.27 and Figure 3.28, respectively. An extensively fluctuating diurnal evolution of net radiation values can be observed in Figure 3.27. Similar fluctuations in the net radiation are also observed in Figure 3.28. The fluctuating net radiation is perhaps due to the frequent low level clouds.

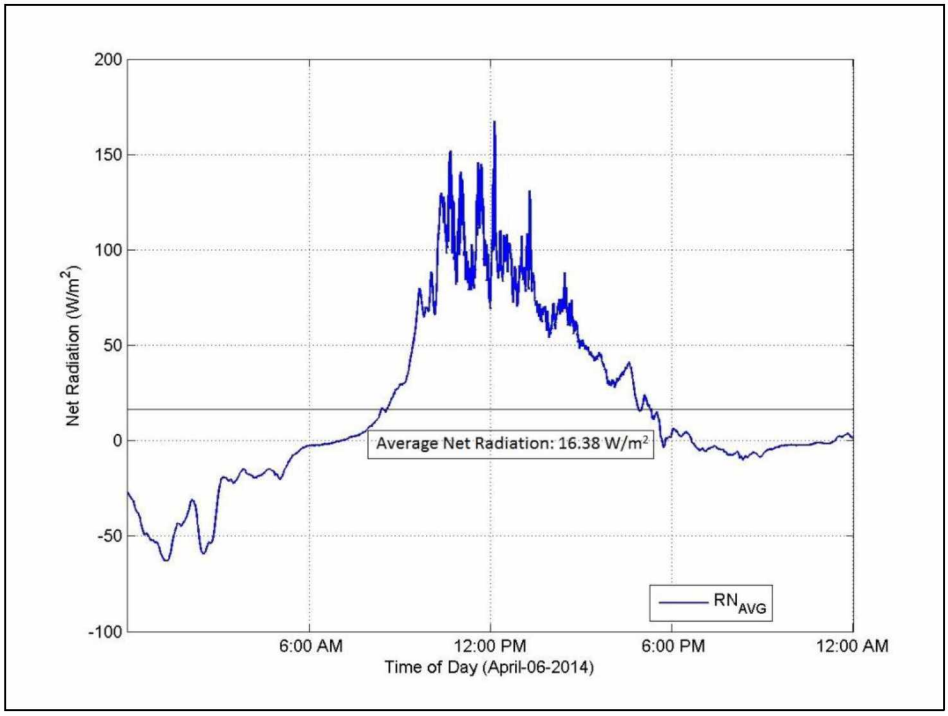

Figure 3.21: RN plot inside the open-pit at the pit-rim on April 6, 2014.

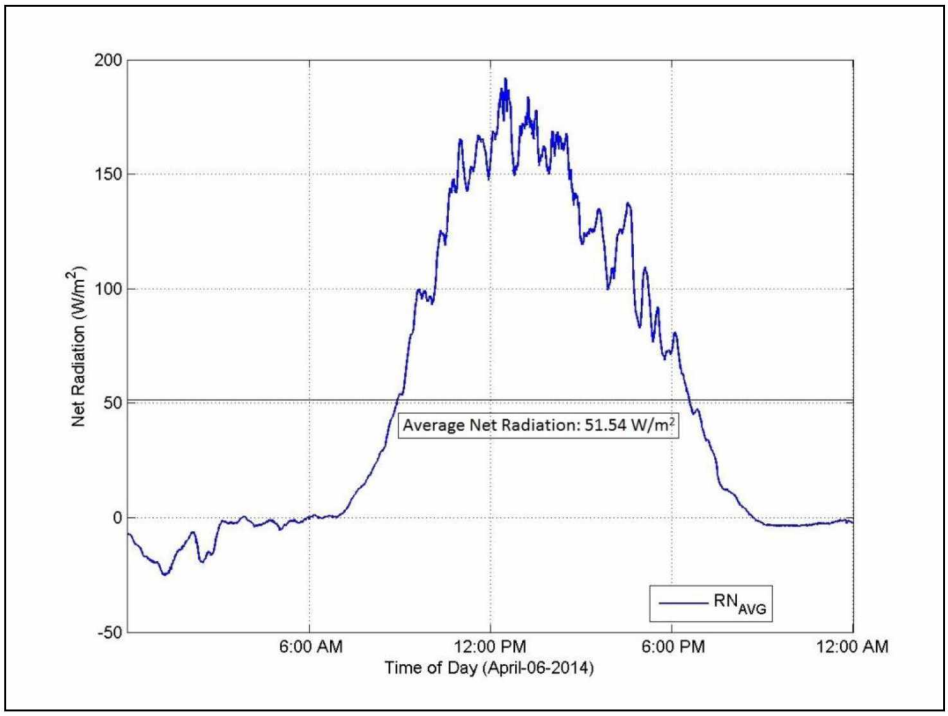

Figure 3.22: RN plot inside the open-pit at the pit-bottom on April 6, 2014.

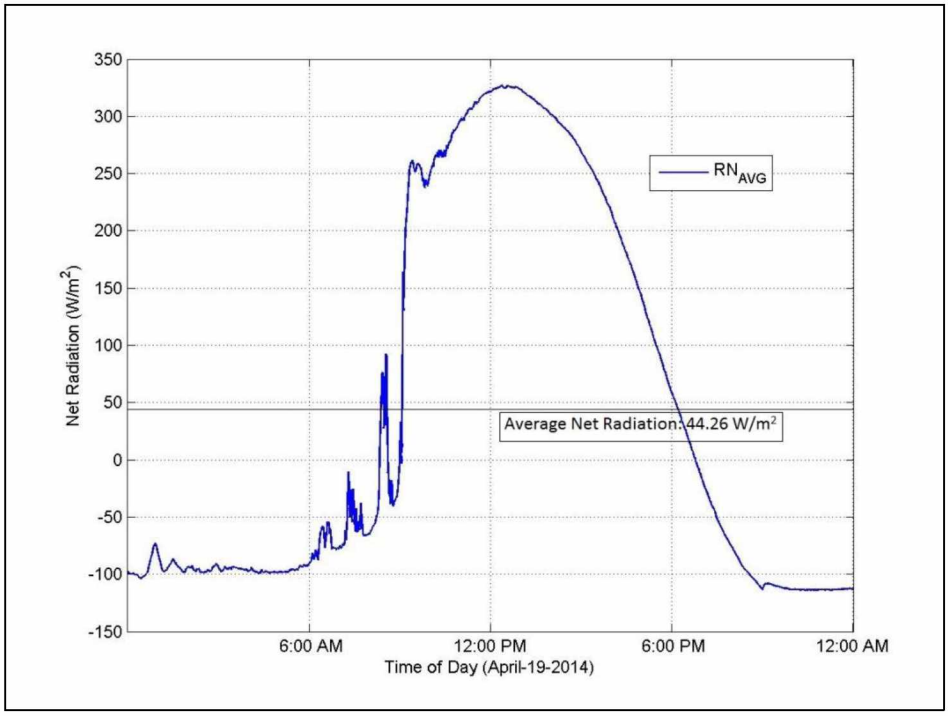

Figure 3.23: RN plot inside the open-pit at the pit-rim on April 19, 2014.

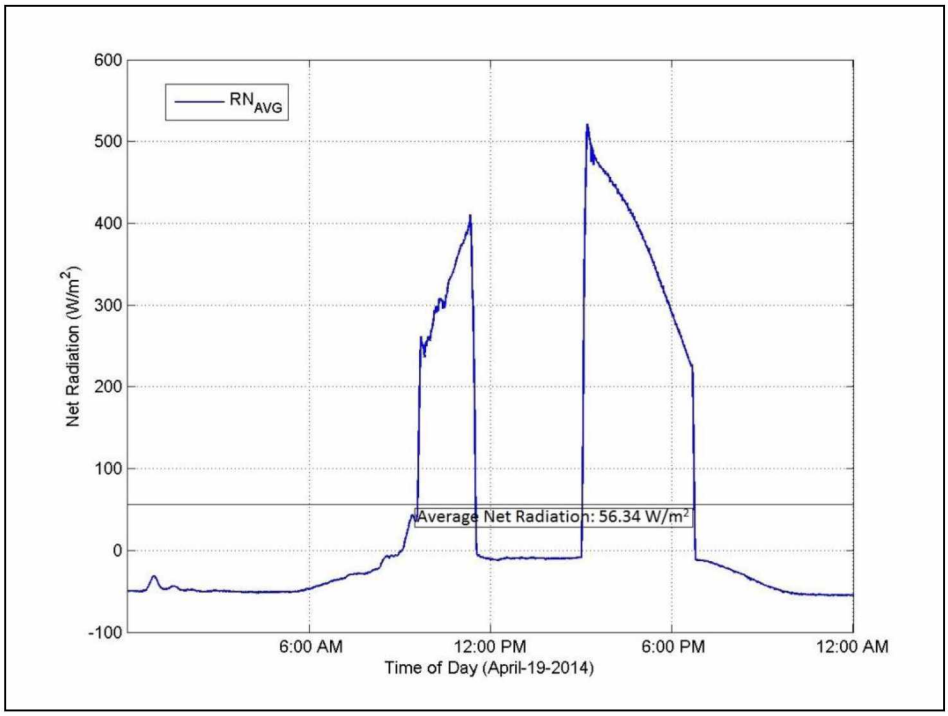

Figure 3.24: RN plot inside the open-pit at the pit-bottom on April 19, 2014.

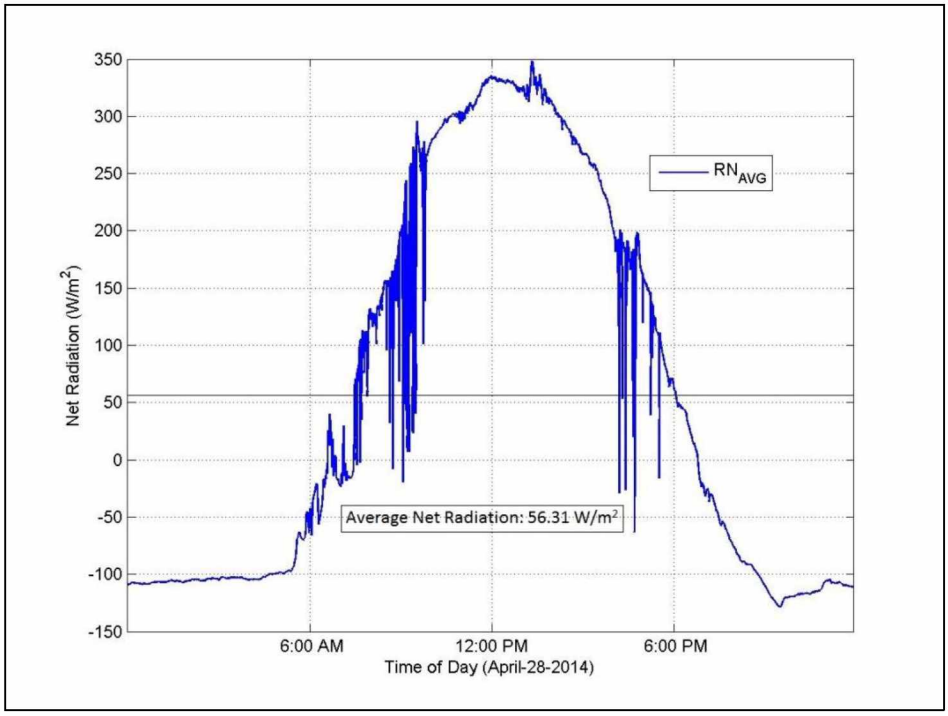

Figure 3.25: RN plot inside the open-pit at the pit-rim on April 28, 2014.

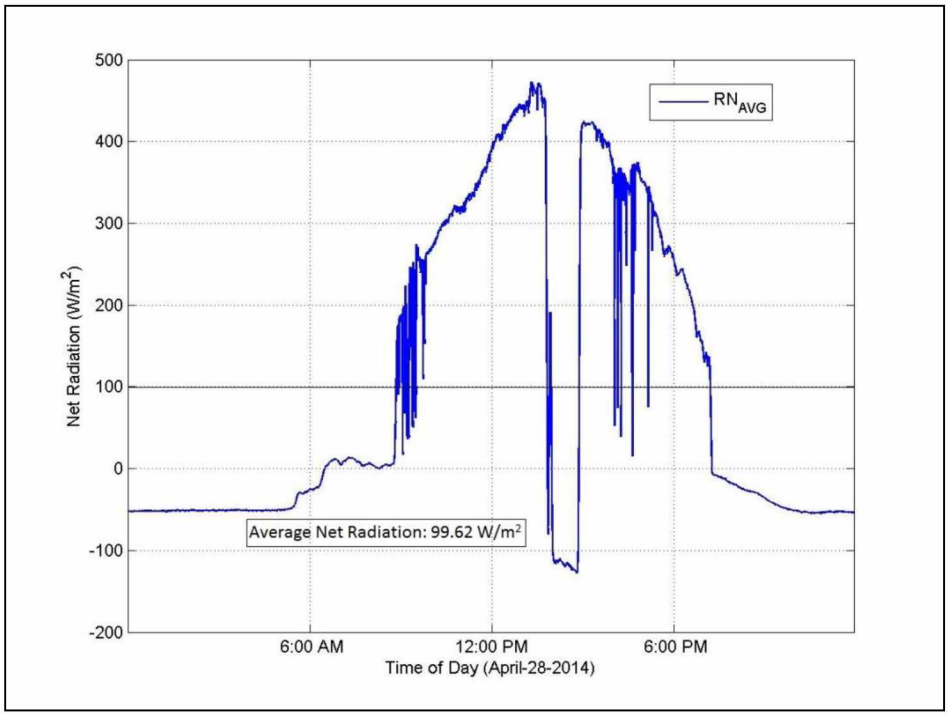

Figure 3.26: RN plot inside the open-pit at the pit-bottom on April 28, 2014.

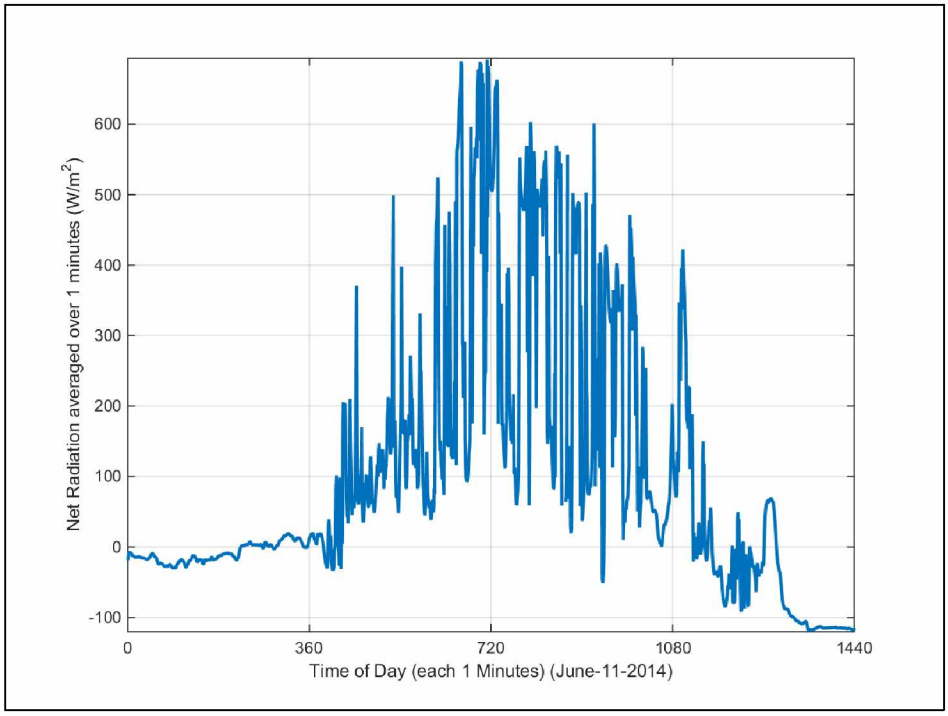

Figure 3.27: RN plot inside the open-pit at the pit-rim on June 11, 2014.

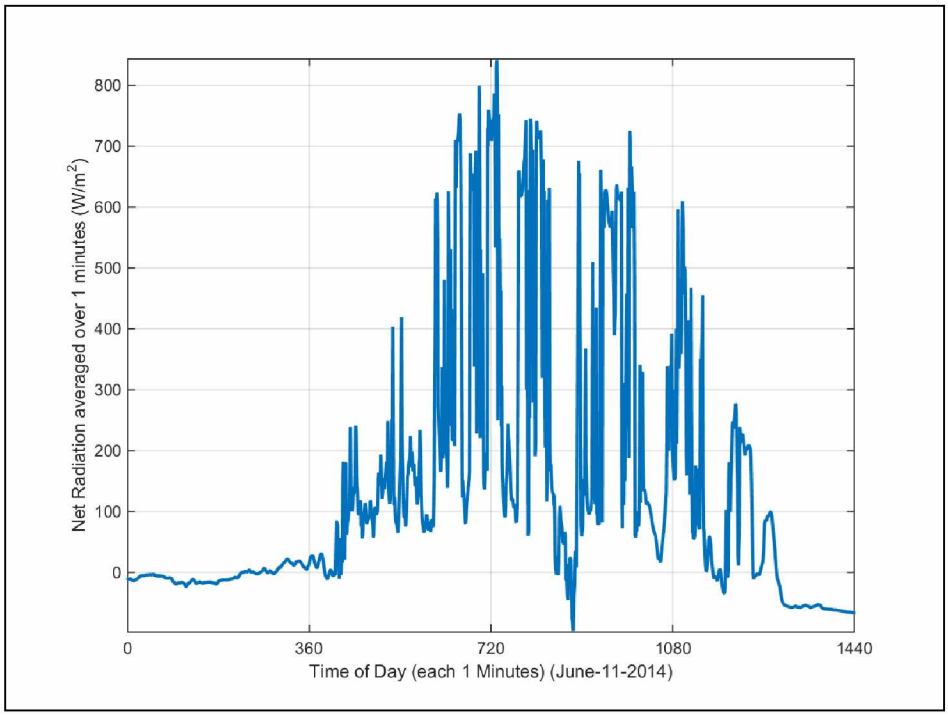

Figure 3.28: RN plot inside the open-pit at the pit-bottom on June 11, 2014.

The sensible heat flux from the pit surface is an important input parameter for simulation of the model domain, and therefore, the collected radiometer data need to be processed. From the discussions in the previous section, it can be seen that the temporal series of net radiation highly fluctuates and varies from day to day and season to season as well. Since the collected net radiation data is of high frequency (sampling interval every 10 seconds), the temporal series for each day is averaged over one minute. The averaged data for all the temporal series for the winter and the summer seasons are plotted together to characterize the seasonal variability in the net radiation. Figure 3.29 and Figure 3.30 present the temporal series of net radiation data for the winter season collected consecutively at the pit-rim and at the pit-bottom.

It can be seen from Figure 3.29 and Figure 3.30 that the net radiation series for the winter days vary over a wide range of magnitudes, and no distinct pattern is visible in these series. The majority of the temporal series vary in the range of -20 W/m^2 to 20 W/m^2. Sixty-two temporal series (number of sampled winter days) at the pit-rim and fort-four temporal series at the pit-bottom are available for analysis (Figure 3.29 and Figure 3.30).

To process the temporal data, the temporal series are averaged over the length of the day for each day during the winter season. Figure 3.31 presents the averaged net radiation data for the winter temporal series at the pit-rim. The red and the blue data points in Figure 3.31 are the mean and the median of the temporal series of each day at the pit-rim. Figure 3.32 presents the averaged net radiation data over each day of the temporal series at the pit-bottom. It can be seen from Figure 3.31 and Figure 3.32, that the averaged net radiation (over the entire day) during the winter season highly fluctuates and varies from as high as 20 W/m^2 to as low as -100 W/m^2 for the pit-rim. At the pit-bottom, the range of fluctuation is between 10 W/m^2 and -60 W/m^2.

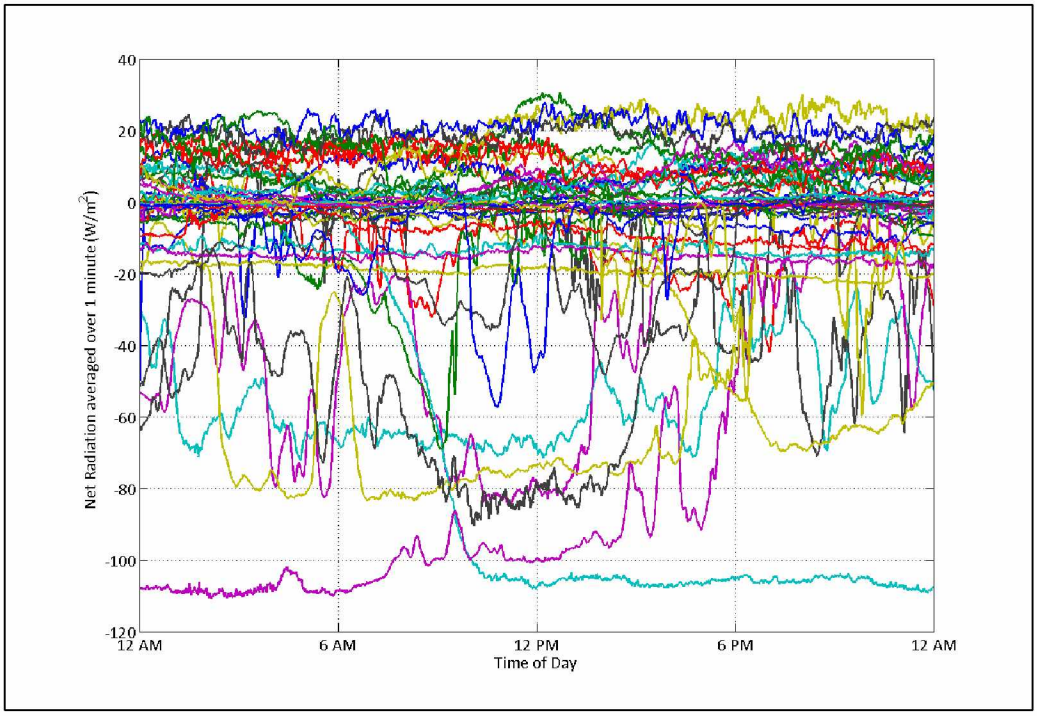

Figure 3.29: Temporal series of net radiation data for the winter season at pit-rim.

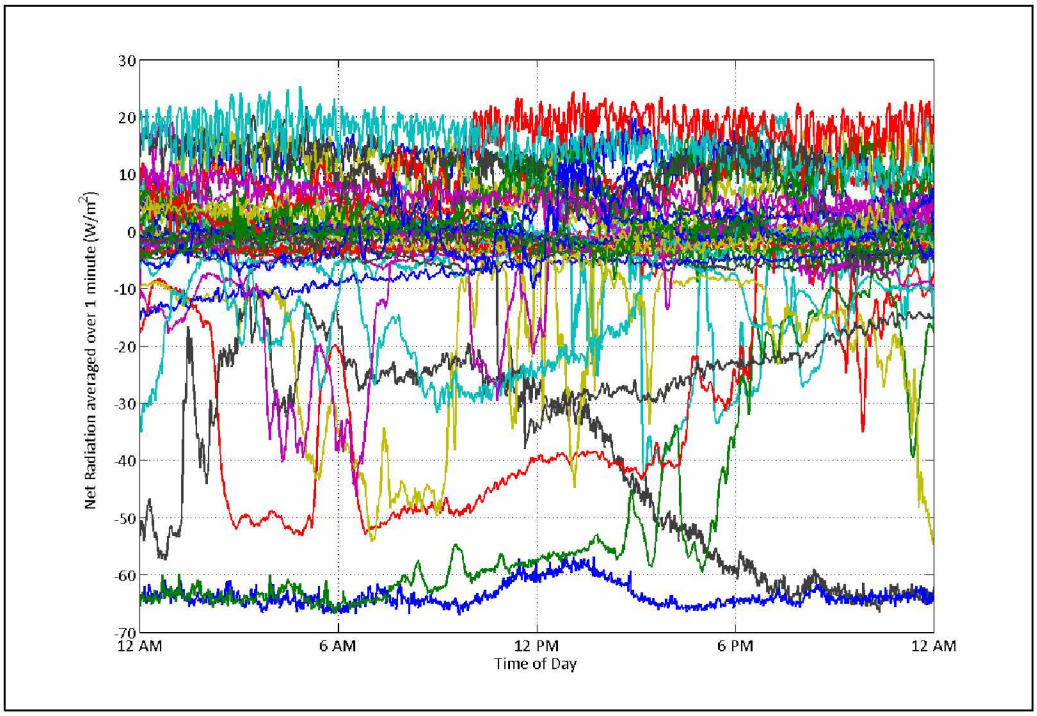

Figure 3.30: Temporal series of net radiation data for the winter season at pit-bottom.

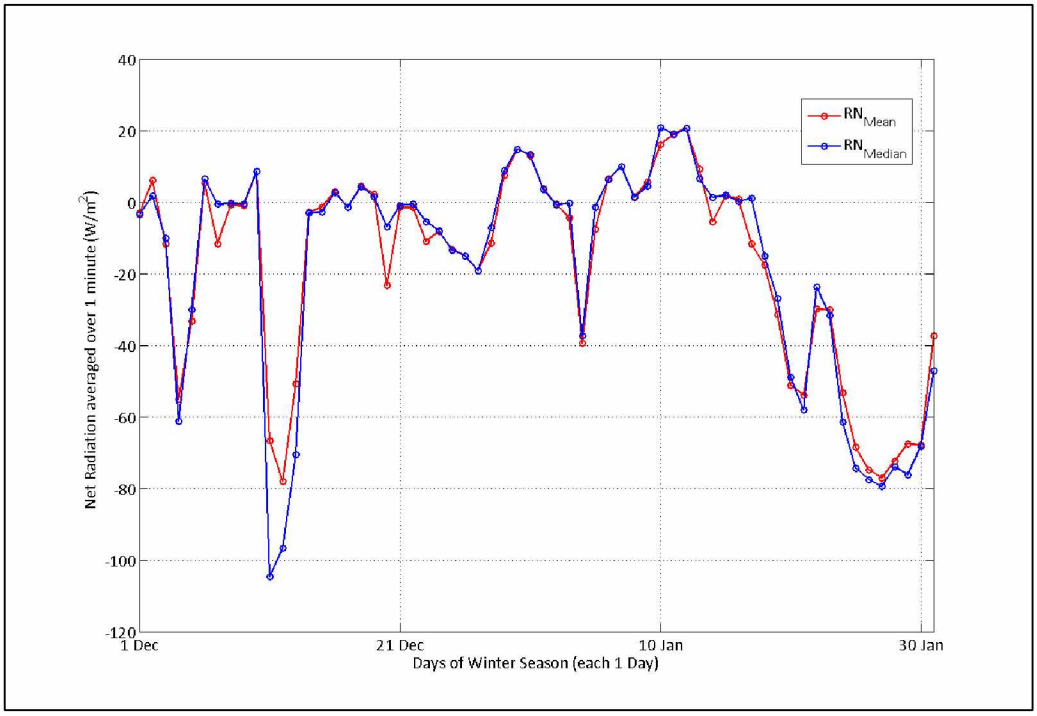

Figure 3.31: Net radiation averaged over each day for the winter temporal series at the pit-rim.

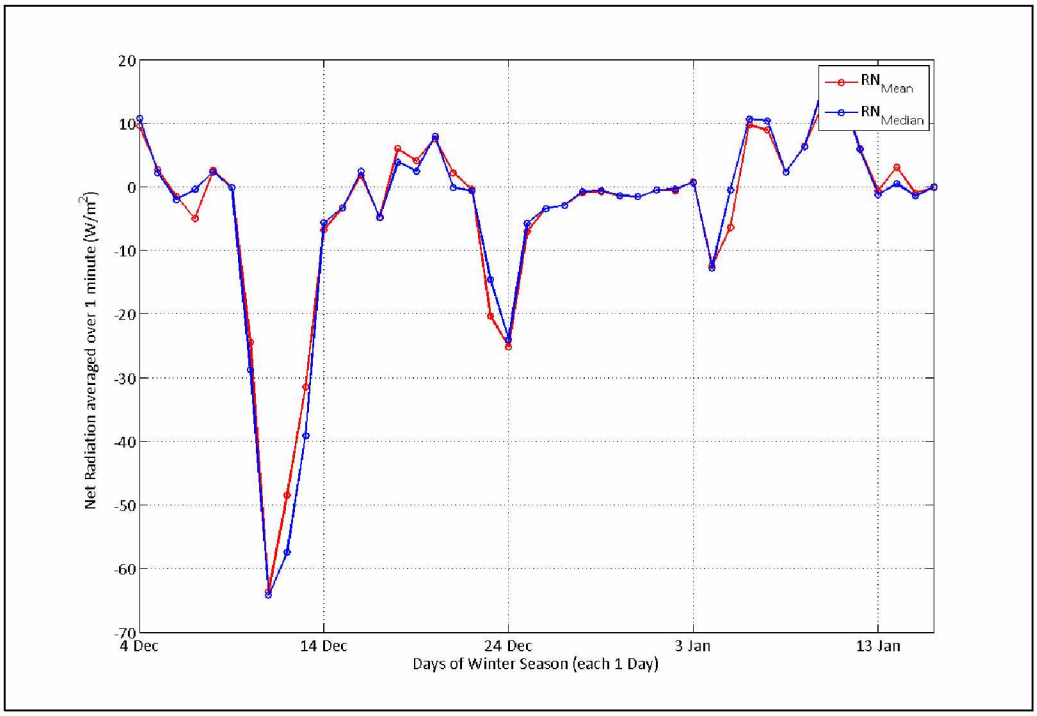

Figure 3.32: Net radiation averaged over each day for the winter temporal series at the pit-bottom.

Using another approach, the temporal series of the net radiation data is averaged for every minute of a day (over all the temporal series) to calculate the mean and the median value of net radiation. Figure 3.33 and Figure 3.34 present the net radiation temporal series for the duration of the day for all the winter days. Therefore, in Figure 3.33, the mean and the median values for each minute of the duration of the day is the average of the entire 62 days of temporal series. Similarly, in Figure 3.34, each data point is the average of the entire 44 days of temporal series for the winter season at the pit-bottom.

It can be observed in both the figures (Figure 3.33 and Figure 3.34), that the mean and the median net radiation temporal series are far apart. It was seen that the net radiation temporal series (Figure 3.29 and Figure 3.30) are most concentrated around the -20 W/m^2 to 20 W/m^2 range. Therefore, the medians of the net radiation values which are averaged over all the temporal series of winter days are observed to fluctuate around zero (0 W/m^2) magnitude. However, the means of the net radiation values are affected by extreme values of a net radiation temporal series. Therefore, the mean temporal series of the net radiation is located below the median temporal series of the net radiation and has higher negative magnitudes.

It is generally accepted that dispersion modeling of fugitive dust during the winter season at high latitudes requires longer simulation time (minimum 24 hrs. of simulation) to account for the formation of a stable boundary and its effect on dust retention in the model domain. Therefore the net radiation values averaged over each day are preferable over the net radiation values averaged over all the temporal series. For dispersion modeling of fugitive dust in winter season, two sensible pit surface heat flux values (the amount of available net radiation) are defined. As shown in Figure 3.31 and Figure 3.32, the values of the average net radiation mostly occur around zero (0 W/m^2); however a heat flux of 0 W/m^2 represents a neutral atmospheric condition in the ABL. The magnitude of -20 W/m^2 heat flux is observed for several days (Figure 3.31 and Figure 3.32); and therefore is considered as a moderate or common winter condition for the selected open-pit mine. However, a magnitude of -40 W/m^2 heat flux or less is not so common in these figures, and therefore is considered as input for extreme winter. As a result, the heat flux for a moderate winter season is defined as -20 W/m^2, and the heat flux input for an extreme winter season is defined as -40 W/m^2.

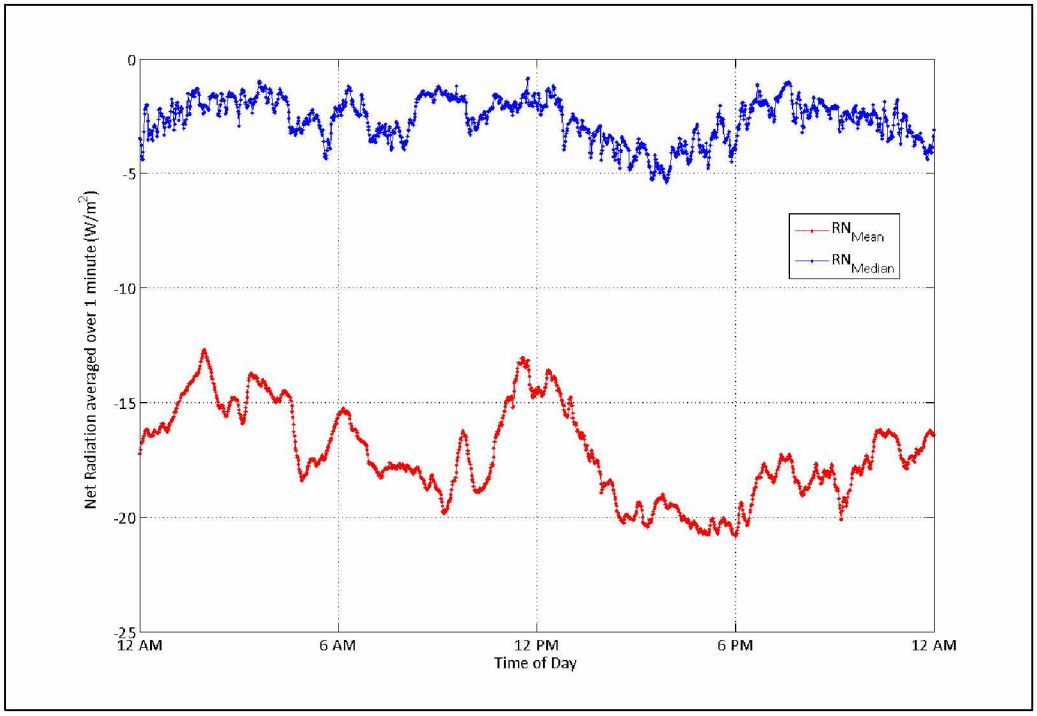

Figure 3.33: Net radiation averaged over the entire winter temporal series at the pit-rim.

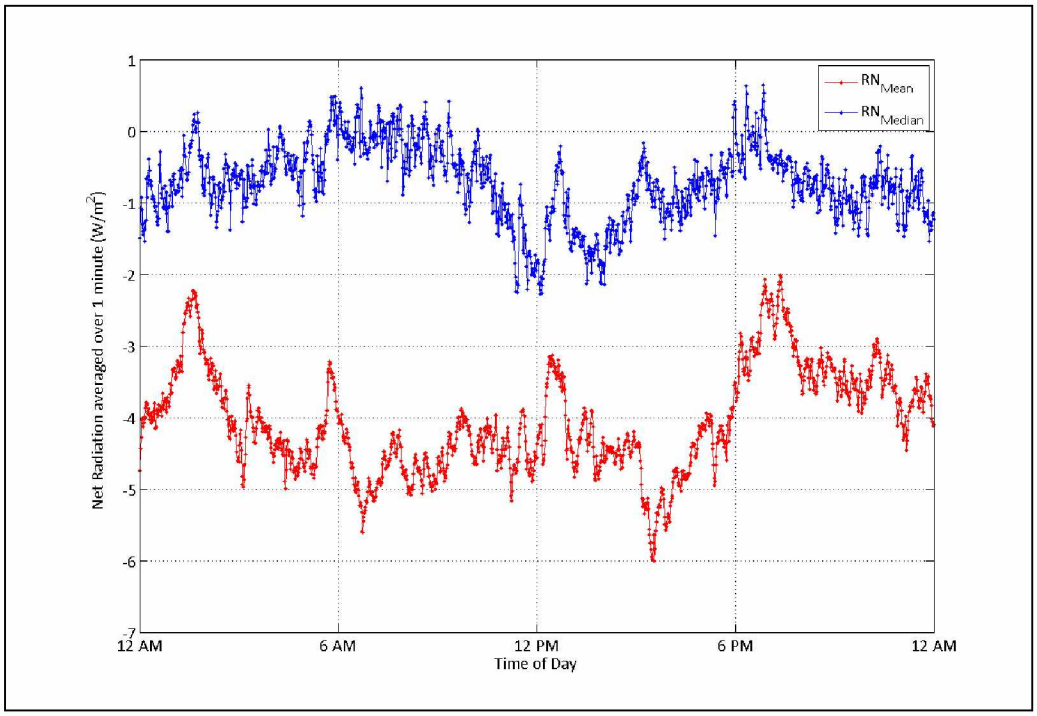

Figure 3.34: Net radiation averaged over the entire winter temporal series at the pit-bottom.

The temporal series of net radiation data for the summer season were also collected both at the pit-rim and at the pit-bottom and are presented in Figure 3.35 and Figure 3.36, respectively. It can be seen from Figure 3.35 and Figure 3.36 that the net radiation series for the summer days also vary widely but show a prominent pattern of diurnal evolution. For the summer season, twenty-five temporal series (number of sampled summer days) at the pit-rim and thirty-four temporal series at the pit-bottom are available. Therefore, Figure 3.35 summarizes the 25 summer-temporal series at the pit-rim, while Figure 3.36 presents the 34 summer temporal series at pit-bottom.

The summer temporal series are also averaged using the two previously discussed approaches: (1) The temporal series averaged over the length of the day for each day during the summer season, and (2) the temporal series averaged over all the temporal series of all the summer days for each second of a day. Figure 3.37 and Figure 3.38 present the net radiation values of the various summer days averaged over the length of the day for each day. In contrast with the winter season, the summer season mean and the median net radiation values fluctuates (Figure 3.37 and Figure 3.38), and vary between 20 W/m^2 and 190 W/m^2 at the pit-bottom. Therefore the heat flux for (1) the fair insolation day (fair summer days) is defined as 60 W/m^2; (2) for the moderate insolation day (moderate summer days) is defined as 100 W/m^2; and (3) the extreme insolation day (extreme summer days) is defined as 160 W/m^2.

Figure 3.39 and Figure 3.40 present the net radiation temporal series for duration of the day, which is created by averaging the one-minute averaged temporal series of all the summer days. In contrast with the winter season, the mean and the median net radiation values for the summer season are close to each other. In the absence of a stable boundary layer, and due to formation of convective boundary layer in the domain, modeling of the fugitive dust dispersion during the summer season requires comparatively less simulation time. It can be seen in Figure 3.39 and Figure 3.40, that (1) net radiation of 60 W/m^2 can be noted around 7:00 AM and around 8:00 PM; (2) net radiation of 100 W/m^2 can be noted around 8:30 AM and 6:00 PM; and (3) net radiation of 160 W/m^2 can be noted as around 10:00 AM and 3:30 PM in the open-pit domain. Therefore these input values also represent the input heat flux during various times in a summer day.

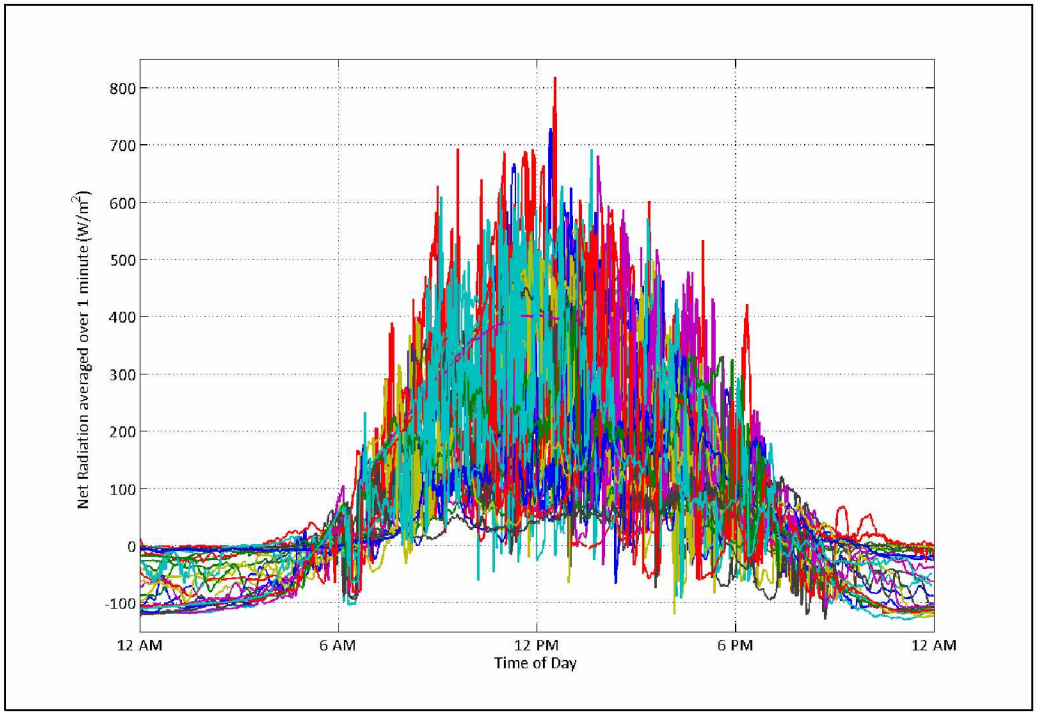

Figure 3.35: Temporal series of net radiation data for the summer season at pit-rim.

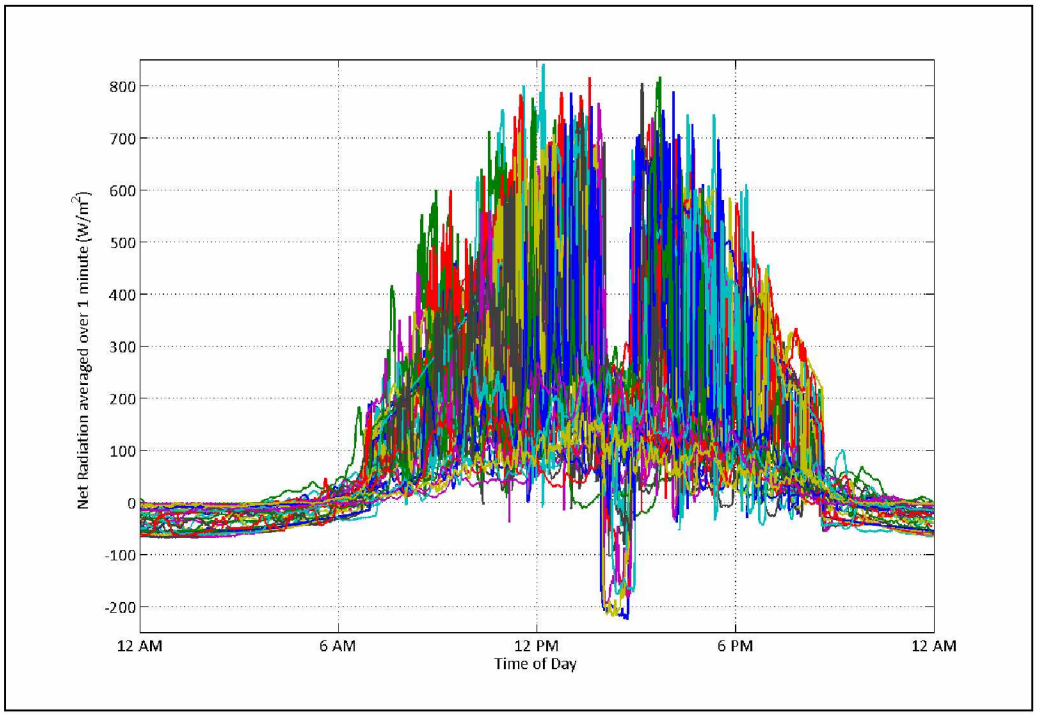

Figure 3.36: Temporal series of net radiation data for the summer season at pit-bottom.

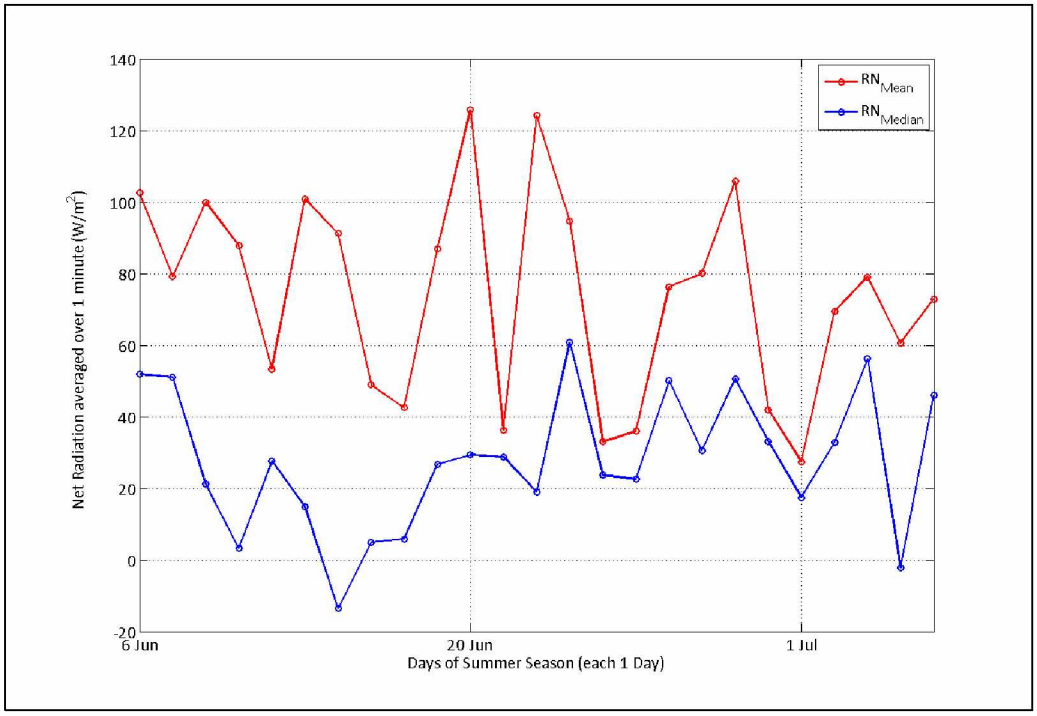

Figure 3.37: Net radiation averaged over each day for the summer temporal series at the pit-rim.

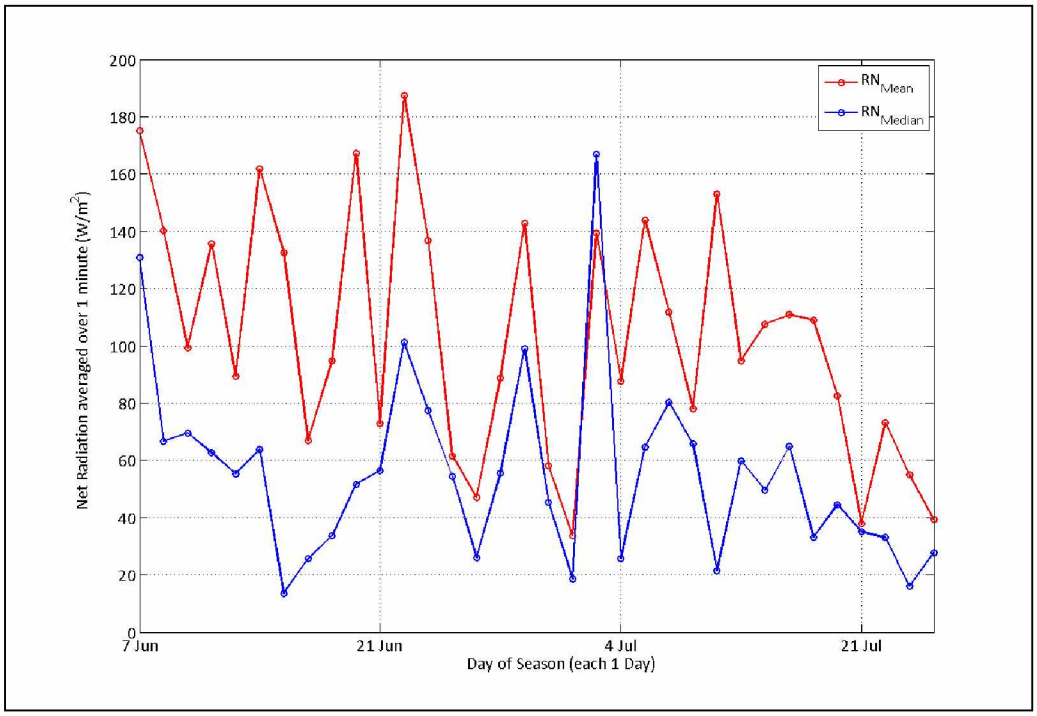

Figure 3.38: Net radiation averaged over each day for the summer temporal series at the pit-bottom.

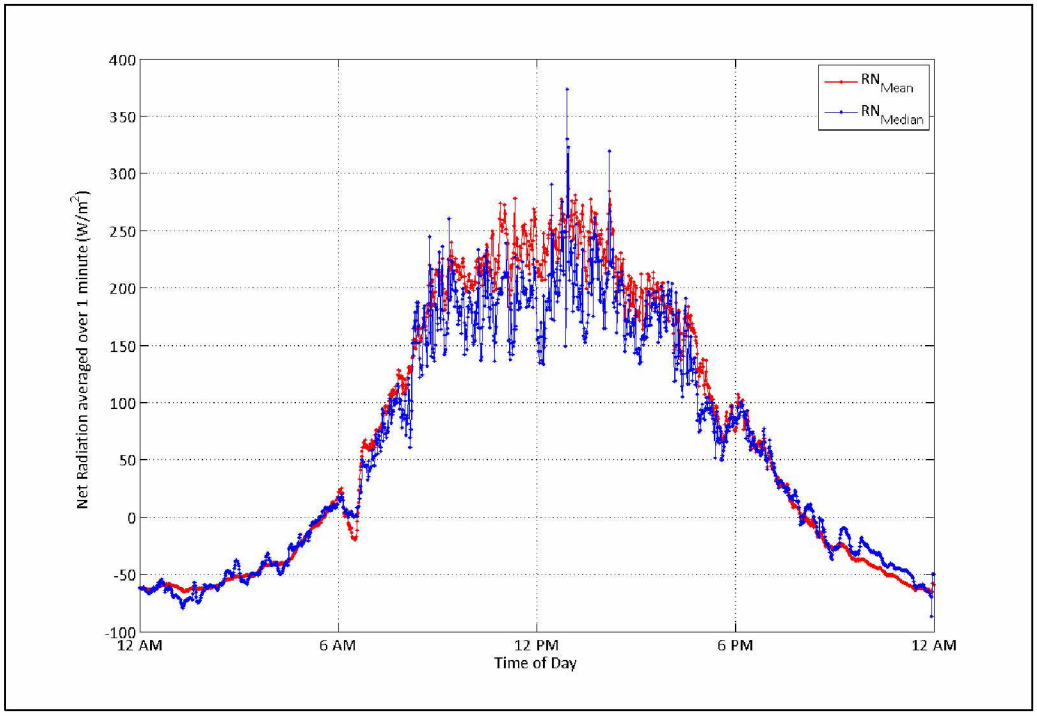

Figure 3.39: Net radiation averaged over the entire summer temporal series at the pit-rim.

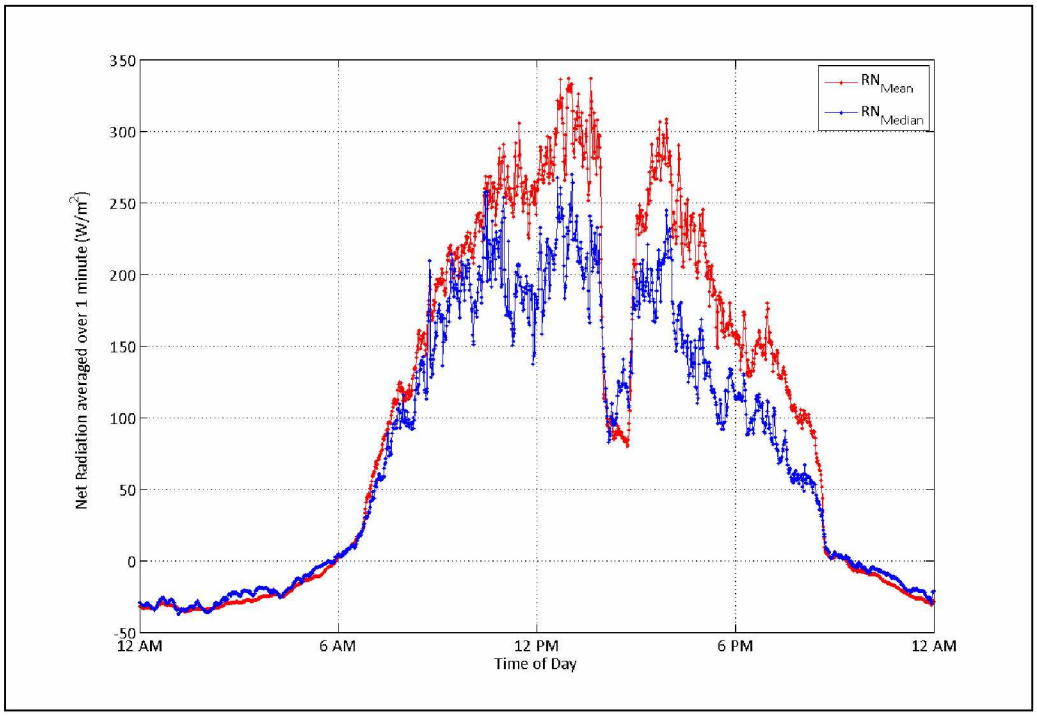

Figure 3.40: Net radiation averaged over the entire summer temporal series at the pit-bottom.

An abrupt drop in the net radiation temporal series can also be observed (Figure 3.36 and Figure 3.40) at around 2:00 PM to 3:00 PM. This phenomenon was exhibited most of the days during the summer months. This abrupt drop is due to some hindrance as a result of mining unit operations that were occurring nearby the radiometer at the pit-bottom.

3.4 Summary of Input Data

The wind speed, the airflow temperature, and the net radiation data are categorized into various seasonal input conditions for defining the initial and the boundary conditions for the simulation of the open-pit domain. Table 3.3 presents the simulation input values for the winter and the summer seasons.

Following the data collection, the open-pit domain of the selected open-pit mine is meshed and the various simulation setup parameters are evaluated for the model domain. The development of the model domain is presented in Chapter 4.

Table 3.3: Simulation input values for the winter and the summer seasons.

Season	Intensity	Wind Speed	Initial Temp.	Heat Flux (W/m^2)
Winter	Moderate Winter	2.1 m/s	-10 C	-20
	Extreme Winter	2.1 m/s	-10 C	-40
Summer	Fair Insolation	2.5 m/s	10 C	60
	Moderate Insolation	2.5 m/s	10 C	100
	Extreme Insolation	2.5 m/s	10 C	160

Chapter 4 Model Development

Development of a three-dimensional open-pit model domain is always challenging due to several reasons, such as, the presence of irregular faceted features at the pit surface. However, these challenges are also software dependent. A large number of commercial CFD software packages are available for simulation of fluid flow. CFD packages such as ANSYS CFX, ANSYS FLUENT developed by the ANSYS; OpenFOAM distributed by the OpenFOAM Foundation; COMSOL Multiphysics, COMSOL Server developed by the COMSOL; SC/Tetra, SC/Stream developed by the software CRADLE are examples of the available CFD software.

For modeling a large open-pit mine with faceted and sharp features in the geometry and complex topography, the SC/Tetra software of CRADLE provides many advantages in comparison with other commercial CFD software (ANSYS, COMSOL). Although not independently verified, some of the comparative advantages reported by the SC/Tetra are: (1) Robustness in meshing, (2) high speed meshing, (3) high speed calculations with competitive resolution and (4) overall efficiency of the software [Cradle North America Technical Support team, Personal Communication., 2014]. In this chapter, development of a three-dimensional CFD model for estimation of fugitive dust retention in an open-pit mine is presented using the SC/Tetra software of the software CRADLE.

The following discussion has been modified from a document [Bhowmick et al., 2015a] originally written for and published in the SME Annual Meeting, 2015, with coauthors Raj, K. V. and Bandopadhyay, S.

4.1 Open-Pit Geometry Import

Figure 4.1 presents a generic flow chart for the steps involved in a CFD simulation. Development of a CFD model in SC/Tetra involves: (1) preprocessing, (2) solving and (3) post-processing. In the preprocessing stage, a three-dimensional volume of the open-pit geometry of a selected deep open-pit mine (Figure 4.2) is imported into the preprocessor. Following the importation of the three-dimensional open-pit geometry, the enclosing walls of the pit geometry are defined as 'Pit'; and the East, the West, the North, and the South, which are created perpendicularly at the four edges of this topography. The Free-Atmosphere (FA) boundary is then added at the top of the three-dimensional geometry to create a three-dimensional volume.

In order to characterize the simulation parameters and variables, two idealized geometries are initially used for the simulation purpose. The idealized pits have several advantages over an actual open-pit domain: (1) idealized domains contain no faceted topography due to a simplified geometry; (2) mesh quality is excellent due to the absence of vertices and ridges; (3) good resolution in solution can be achieved with comparatively larger elements compared to an actual pit domain, due to a planar pit surface; (4) less number of mesh elements; and (5) steady state is reached more quickly than an actual pit domain.

Thus, simulation of idealized pit domains, using the same boundary and initial conditions of an actual pit domain, provides quick results which can be utilized to evaluate various processes, which are influential for the development of air flow and recirculation within the pit domain. Furthermore, the requirement for mesh resizing for a required resolution and an understanding of fugitive dust dispersion phenomena inside the open-pit mine can be realized.

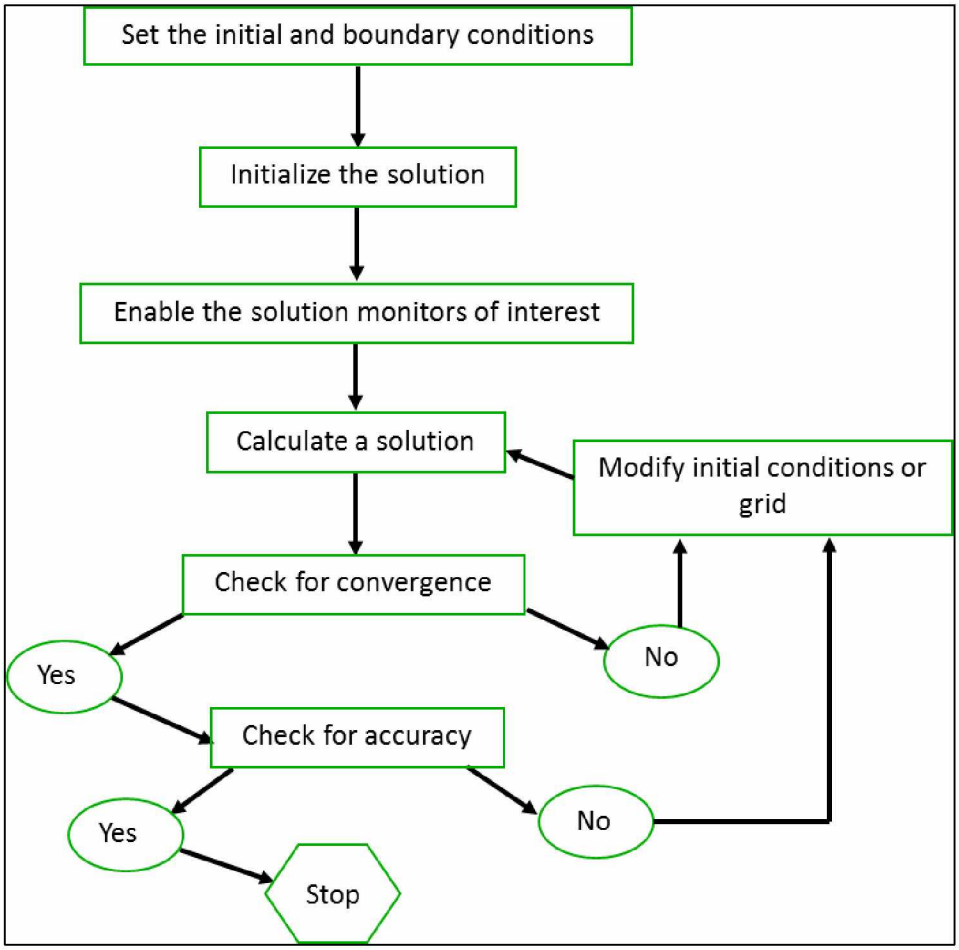

Figure 4.1: Generic flow chart for CFD modeling [Raj, 2015].

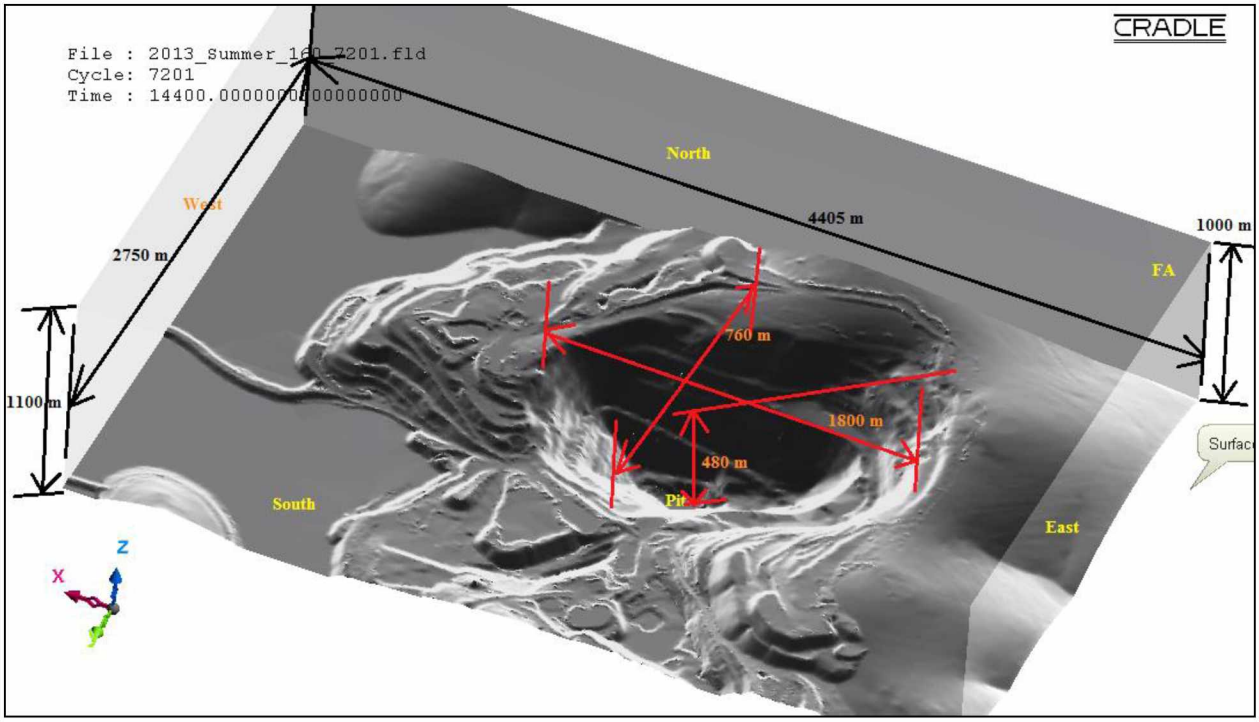

Figure 4.2: The imported model domain of the selected open-pit.

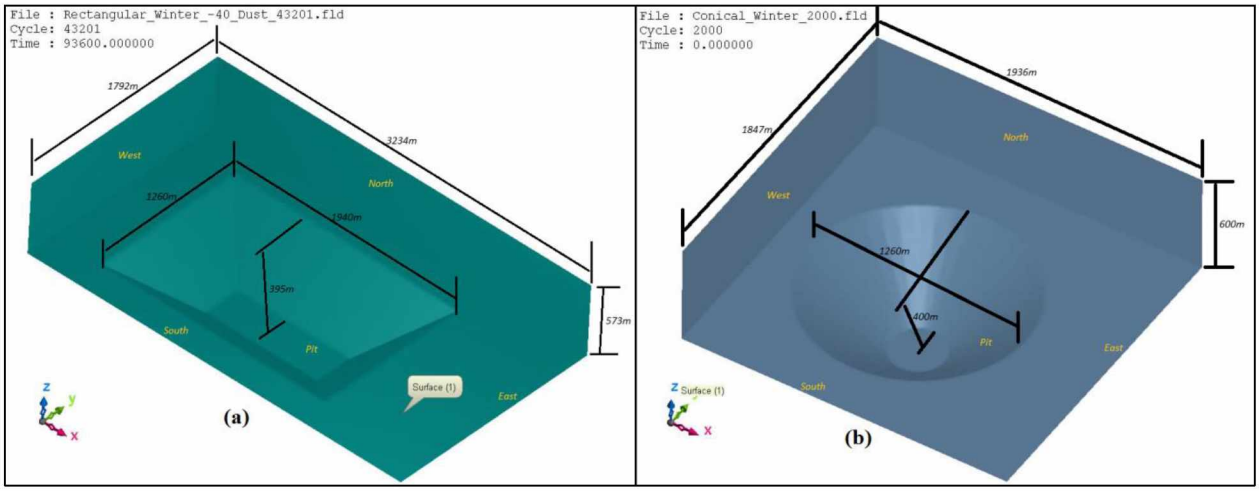

Figure 4.3: The imported model domain of the idealized (a) trapezoidal and (b) conical open-pit.

The two idealized trapezoidal and conical open-pit domains used for this study are presented in Figure 4.3(a), and Figure 4.3(b), respectively. The pit cavities approximately contain the same volume similar to an actual open-pit domain. The ultimate pit slope is 40° for both the geometries. The agreement in simulation results of both the idealized domains reflects the appropriate choice of simulation setup. Due to the geometrical aspects of the domains, it is

presumed that the dust dispersion phenomena will be of reduced duration in the conical domain as compared to the trapezoidal domain. Since the actual geometry of an open-pit is far more complex compared to idealized geometries, fugitive dust retention would be expected to be different in the actual pit domain as compared to the idealized domains.

4.2 Octree

Meshing is a step to discretize a continuous domain into discrete grid points. In SC/Tetra, the volume of the model domain is meshed with tetrahedral elements to fill up the entire volume. Surface meshes are created at the boundaries of the domain and are formed of triangle elements.

In SC/Tetra, various types of elements are available for volume meshing. In general, basic three-dimensional mesh elements are of four types. Figure 4.4 displays these four types of element. Tetra elements extensively form volume mesh; while prism elements form layers at the roughness boundary and resolve boundary layers most efficiently. Velocity and thermal boundary layers are developed due to the presence of roughness and thermal gradient at the stationary walls. Pyramid elements are used as transition elements in between two different types of elements, for example, tetra and prism; and hexa elements are mostly used in structured grids and have the highest accuracy of solution.

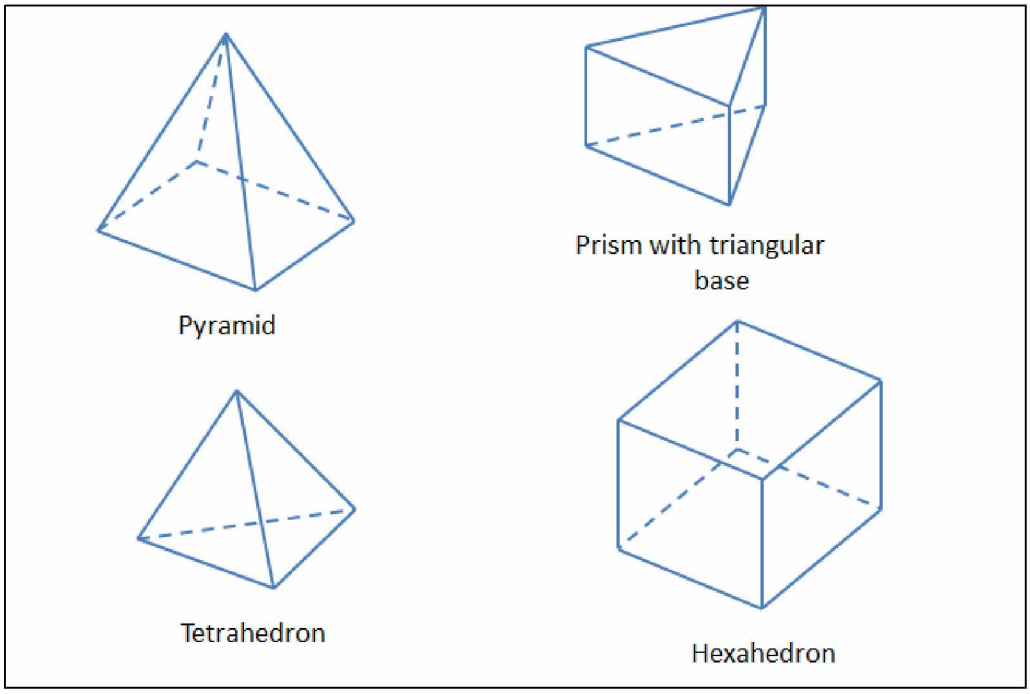

Figure 4.4: Basic three-dimensional elements.

The second step of preprocessing in SC/Tetra is to define an Octree around the open-pit model domain. Octree controls the three-dimensional size of the mesh elements. At the initial step, a cube (root octant) surrounds the entire model domain. The cube is then divided into eight cubes recursively to create a set of sub-cubes which fills up the entire model domain. Each sub-cube is called an octant. The surface and the volume meshes are created based on the size of the octants [Software Cradle Co. Ltd., 2013b].

Figure 4.5 presents an octree used for meshing the selected open-pit domain. The sizes of the octants are smallest at the pit boundary and the size gradually increases away from the pit boundary. Small size mesh elements at the pit-bottom capture the turbulent airflow patterns more accurately than it would be possible with larger size elements. For the selected model domain, the size of the smallest octant at the pit boundary is 11.92 m and the size of the largest octant at the FA boundary is 190.76 m. The size of the smallest octant is selected based on: (1) the convergence criteria of the solution, and (2) the required resolution.

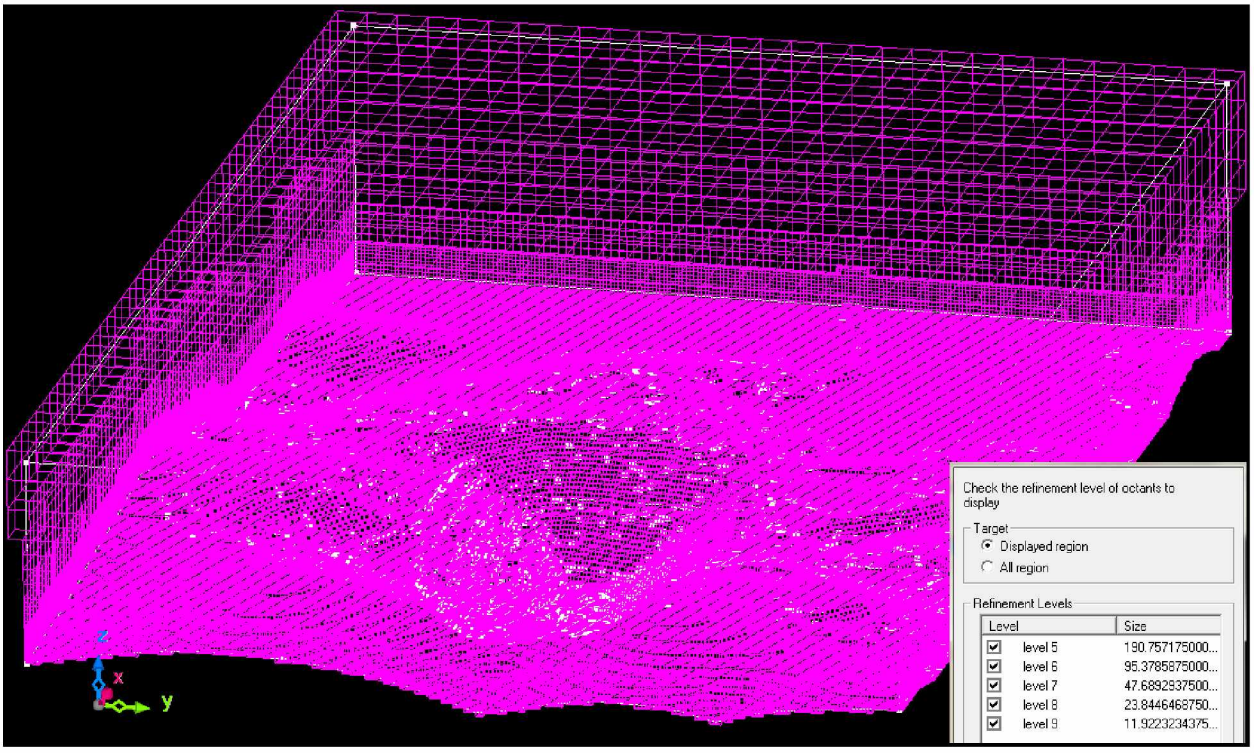

Figure 4.5: The octree used for meshing the domain.

The volume of open-pit domain is meshed with tetrahedral (tetra) elements. A few layers of prism elements are inserted at the pit boundary. Prism elements efficiently capture the

mechanical turbulence due to the surface roughness and the thermal buoyancy generated due to heat flux. This results in development of appropriate velocity and thermal boundary layers at the pit boundary [Bhowmick et al., 2015a].

A good quality mesh of a model domain is a prerequisite for model convergence. The quality of mesh elements in SC/Tetra is defined by the 'h-ratio' for the tetrahedral elements and by the 'shape factor' for the hybrid elements. The 'h-ratio' is the ratio of the radii of the inscribed circle and the circumscribed circle of a triangle. A ratio of 0.5 resembles the best triangle shape (equilateral triangle), and it approaches to zero as the shape of the elements worsen, such as, in the case of a skewed triangle [Software Cradle Co. Ltd., 2013c]. The quality of hybrid elements such as prism elements is defined by the 'shape factor'. The best quality element has a shape factor of one (1.0) and the factor approaches to zero as the shape of a prism deteriorates.

4.3 Meshing in Faceted Mine Geometry

The third step of preprocessing is meshing the open-pit model domain using the specification of an octree. Meshing an open-pit domain using the SC/Tetra software presents some novel challenges. The initial attempts of creating a volume mesh in the model domain, for example, were not successful due to the presence of (1) intersecting surfaces and (2) vertices and ridges at the pit boundary. In the following, the challenges and the approaches used to mesh the domain are presented.

4.3.1 Intersecting Surfaces

Intersecting surfaces are generated when multiple vertices are present inside the same octant. Figure 4.6 presents examples of intersecting surfaces at the pit boundary of the model domain. While creating the volume mesh, the presence of the intersecting surfaces result in overlap/collision in between the tetra elements. Therefore, it is essential that all intersecting surfaces must be removed prior to creating a volume mesh inside the model domain. In this thesis, all intersecting surfaces of the selected model domain are removed by strategical merging of nodes.

A volume mesh is created after removal of all the intersecting surfaces. The Auto execution option in SC/Tetra is initially used to create the volume mesh and subsequently, the surface mesh and the prism layers are created. The quality of the mesh elements are evaluated based on the h-ratio and the shape factor. A number of poor quality tetra elements are observed in the generated

volume mesh. Figure 4.7(a) presents the poor quality tetra elements (tetrahedrons colored in pink) with h-ratio in the range of 0.000 to 0.060. Figure 4.7(b) presents the element quality of the volume mesh of the model domain.

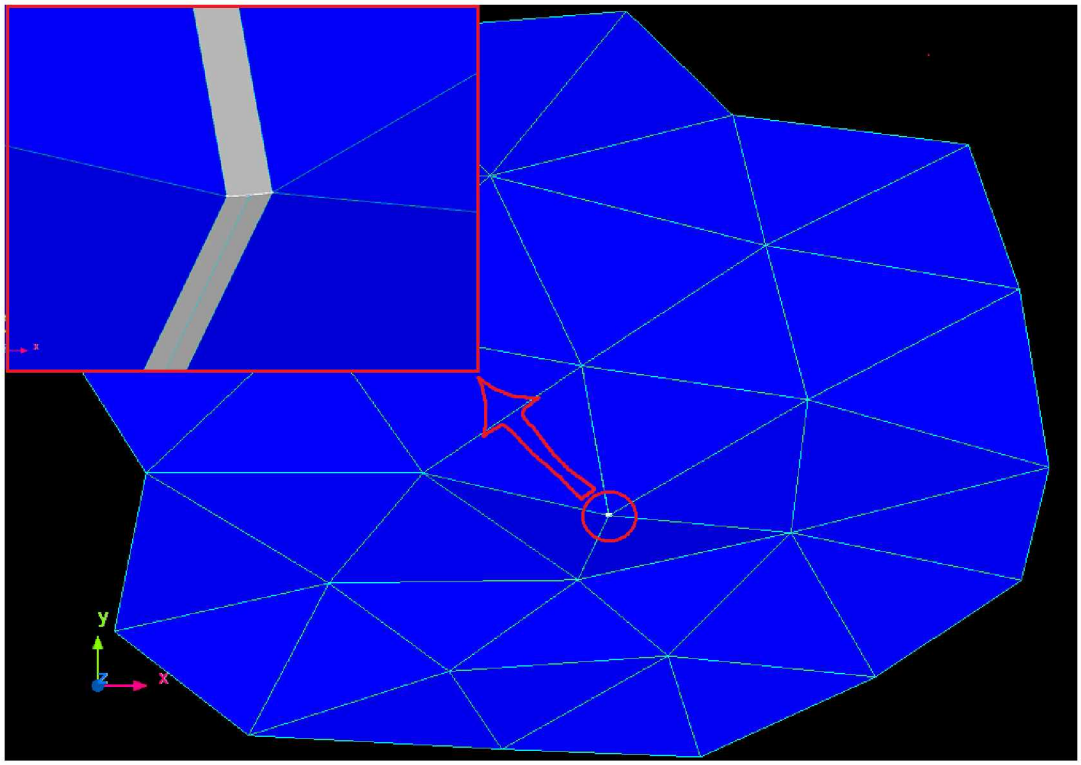

Figure 4.6: Intersecting surface at the pit boundary and its enlarged view.

4.3.2 Vertices and Ridges at the Pit Boundary

The white points and lines in Figure 4.7(a) are the vertices and the ridges at the pit boundary. The poor quality tetra elements (pink colored tetrahedrons), as shown in Figure 4.7(a), are formed due to the presence of vertices and ridges. The preprocessor attempts to create the volume mesh following these vertices and the ridges at the boundary. This results in excessive skewedness in some of the tetra elements which are attached to a vertex or a ridge. Since one of the four vertices or an end of these tetra elements are always attached to a vertex or a ridge of the boundary, these elements have very limited degrees of freedom to improve the element quality. When the prism layers are inserted, the tetra elements of the volume mesh shrink and shift away from the boundary making room for the prism layers. However, the poor quality tetra elements, attached to some of the vertices and ridges of the boundary cannot shift away from the boundary. Therefore, no prism elements can be inserted at those vertices and the ridges. This results in the

formation of holes in the prism layers. The presence of poor quality tetra elements and the holes in the prism layers results in excessive divergence during simulation. Figure 4.8 shows examples of holes formed in the prism layers at the pit boundary.

Figure 4.7: (a) Poor quality tetra elements in the volume mesh and (b) element quality of the entire volume mesh.

Therefore, removal of all unwanted vertices and ridges at the pit boundary is important for good quality meshing. In this thesis, the vertices and the ridges are removed by (1) strategically merging and moving the nodes, and by (2) swiping and splitting the edges. The entire model domain is then re-meshed, and the element quality of the new volume mesh is examined. Removal of all unwanted vertices and ridges significantly improved the element quality. Figure 4.9(a) shows the prism layers at the pit boundary of the selected open-pit domain following the removal of all the vertices and the ridges. In this new meshed model domain, 99.99% of the entire pit boundary is inserted with 3-layers of Prism elements without any holes. Figure 4.9(b) shows the h-ratio of the re-meshed volume of the model domain. It is noted that an insignificant number of bad quality elements are still present.

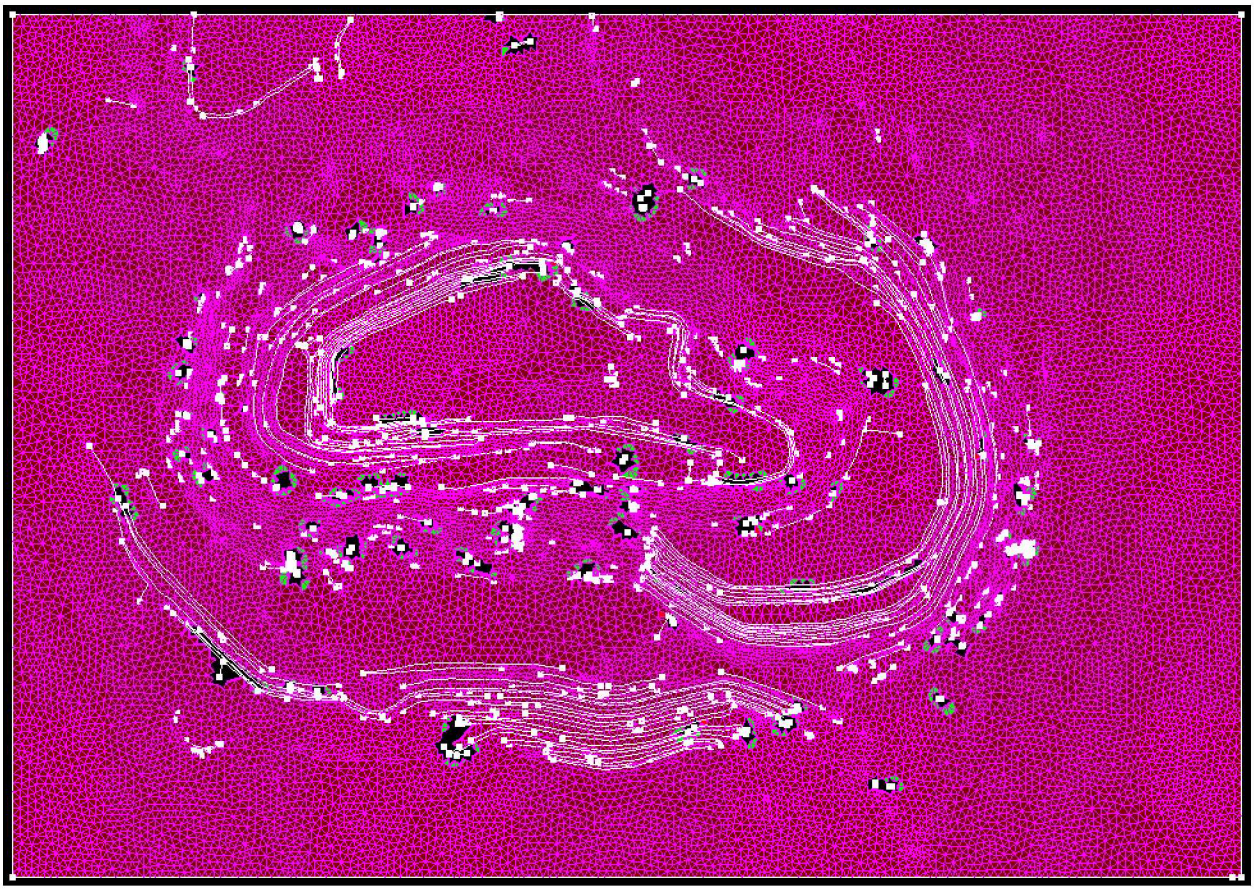

Figure 4.8: Holes in pit boundary prism layers.

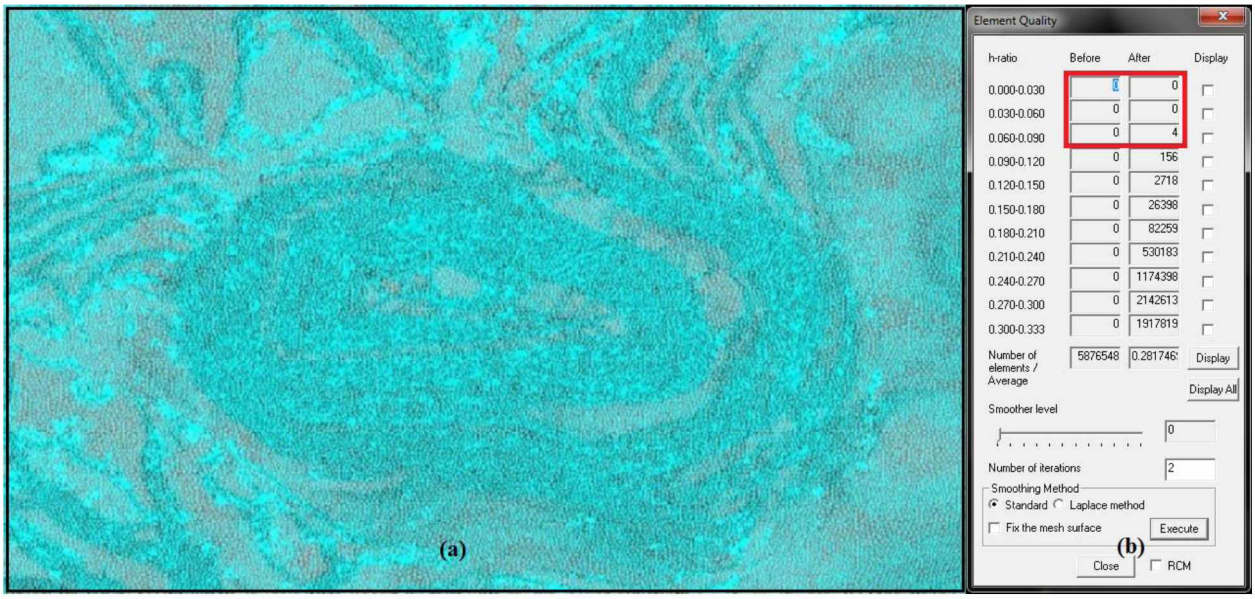

Figure 4.9: (a) The prism layers at pit boundary, when the vertices and the ridges are removed and (b) the element quality of the new volume mesh.

Good quality meshing helps the solver in convergence of a solution. Occasionally, a single bad element could be enough to cause extensive divergence of a numerical solution. Figure 4.10 shows the velocity min/max plot of a steady state analysis of the meshed pit with few bad tetra elements and holes in the prism layers. An extensive fluctuation in the velocity magnitudes represents a poor quality meshing of the model domain.

Figure 4.11 shows the velocity min/max plot of a good quality mesh of the same geometry with similar boundary conditions. A steady state is reached at the 628th cycle. Almost a linear pattern of the plot (Figure 4.11) at the final stage indicates a good convergence and a very low fluctuation in the residuals.

Number of mesh elements is in the order of 1.2 million and 1.3 million for the idealized trapezoidal and the conical domains. Whereas, the actual domain of the 2013 open-pit geometry contains around 6 million mesh elements. The mesh elements at the roughness boundary for the domains range from 6 m to 12 m, which resulted in the y+ distribution [Flores et al., 2013b] ranging from 30 to 10,000. The y+ is the distance between the centroid of the first cell and the wall in wall units.

The height of the domain was based on the location of the FA boundary in Arctic regions. In high-latitude open-pit mines, the convective boundary layers may reach an elevation ranging from 300 to 600 m during the winter [Hartmann and Wendler, 2005; Malingowski et al., 2014]. The FA boundaries of the idealized domains are placed at 600 m from the surface. For simulation of the boundary layers during summer in the actual pit geometry, however, the average height of the FA boundary is increased to 1050 m. The increased height of the FA boundary provides sufficient room for simulation of the unstable convective boundary layers during the summer months, which may reach a height more than 600 meters (Winter ABL).

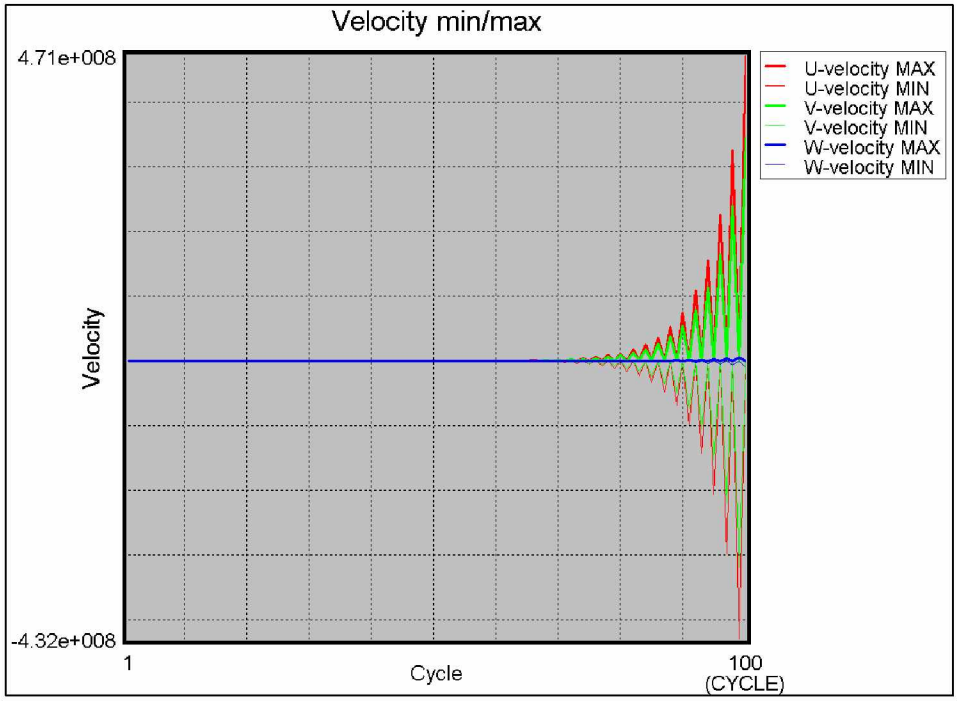

Figure 4.10: Velocity min/max plot of poorly meshed pit.

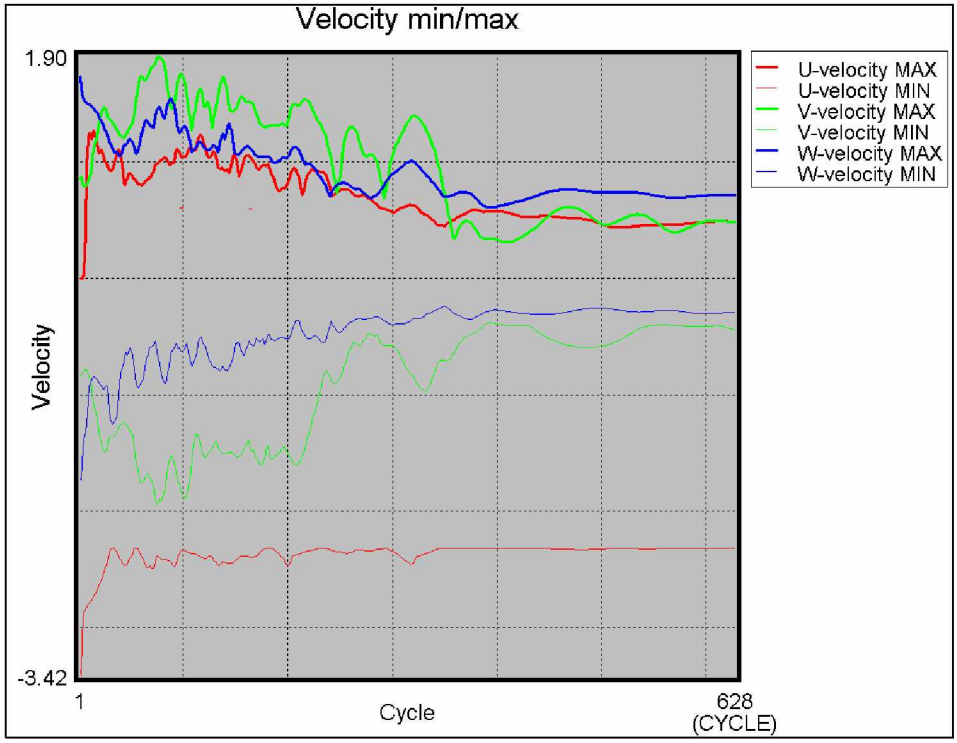

Figure 4.11: Velocity min/max plot of good quality mesh.

To examine the significance of prism layers in a domain, two different meshes of the selected domain is simulated with similar simulation setup. In one mesh, no prism layers are inserted, while in the other, three layers of prism elements are inserted at the pit boundary. Figure 4.12 presents the velocity vector profiles at the Y = 1290 m plane in the selected model domain, meshed with prism elements. Various re-circulatory eddies can be observed in the model domain.

To evaluate the accuracy of the solution, the formation of velocity and thermal boundary layers are evaluated at the pit boundary. The magnitude of the velocity and temperature profiles along the selected straight lines at various locations (line 1-2, 3-4, and 5-6 in Figure 4.12) at the pit boundary are plotted and analyzed. Figure 4.13 presents the magnitude of velocity and temperature profiles in both the meshes with and without the prism layers for the line 1-2 (Figure 4.13(a) and Figure 4.13(b)) in the left and line 3-4 (Figure 4.13(c) and Figure 4.13(d)). The magnitude of velocity profiles (Figure 4.13(a) and Figure 4.13(c)) of both the model domains display the formation of well-defined velocity boundary layers at the pit boundary. Since no computational points or nodes are present at the pit boundary for the mesh with prism layers, the magnitude of velocity profile does not converge to a value of zero (m/s) unlike the profile exhibited with the mesh without prism layers. However, the model domain with prism layers manifested the heat flux at the pit boundary better than the model domain without prism layers. The gradient of the temperature profiles (Figure 4.13(b) and Figure 4.13(d)) in the model domain with prism layers represent a well-defined formation of a thermal boundary layer, while the temperature gradients in the model domain without the prism layers are very steep and hence seem unrealistic. This phenomenon simultaneously affects the convective motion of air inside the model domain. An abrupt rise/drop in the air temperature in the domain without prism layers is observed near the pit boundary, which resulted in unexpected flow due to thermal buoyancy.

For simulation of fugitive dust dispersion in open-pit mines, the open-pit domain meshed with a few layers of prism elements at the pit-bottom is selected. Various simulation parameters are defined for simulation of the domain and the simulation results are evaluated to select the appropriate choices of simulation parameters. The selection of various simulation parameters are presented in Chapter 5.

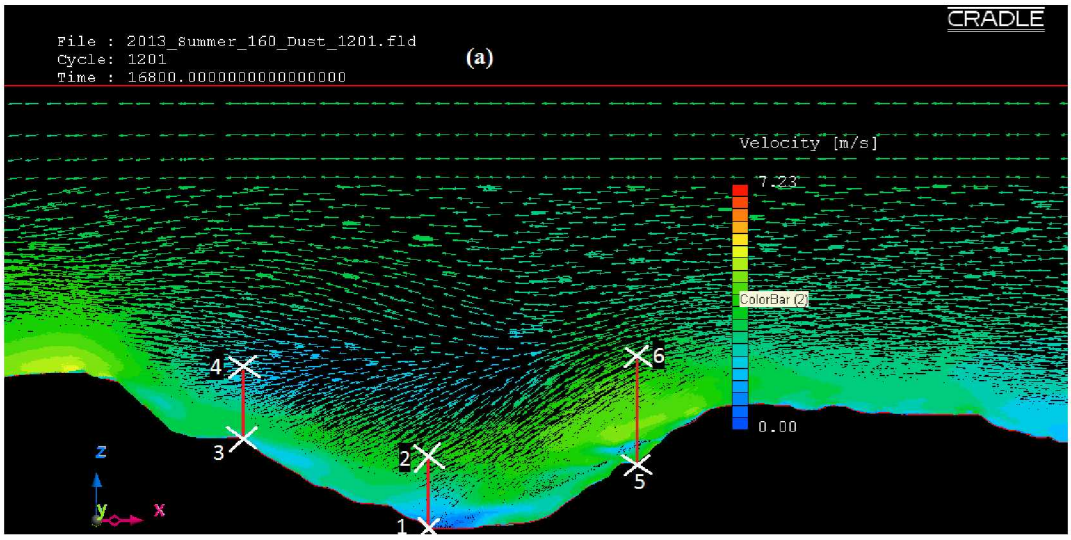

Figure 4.12: Velocity vector profiles in the open-pit domain during the summer months.

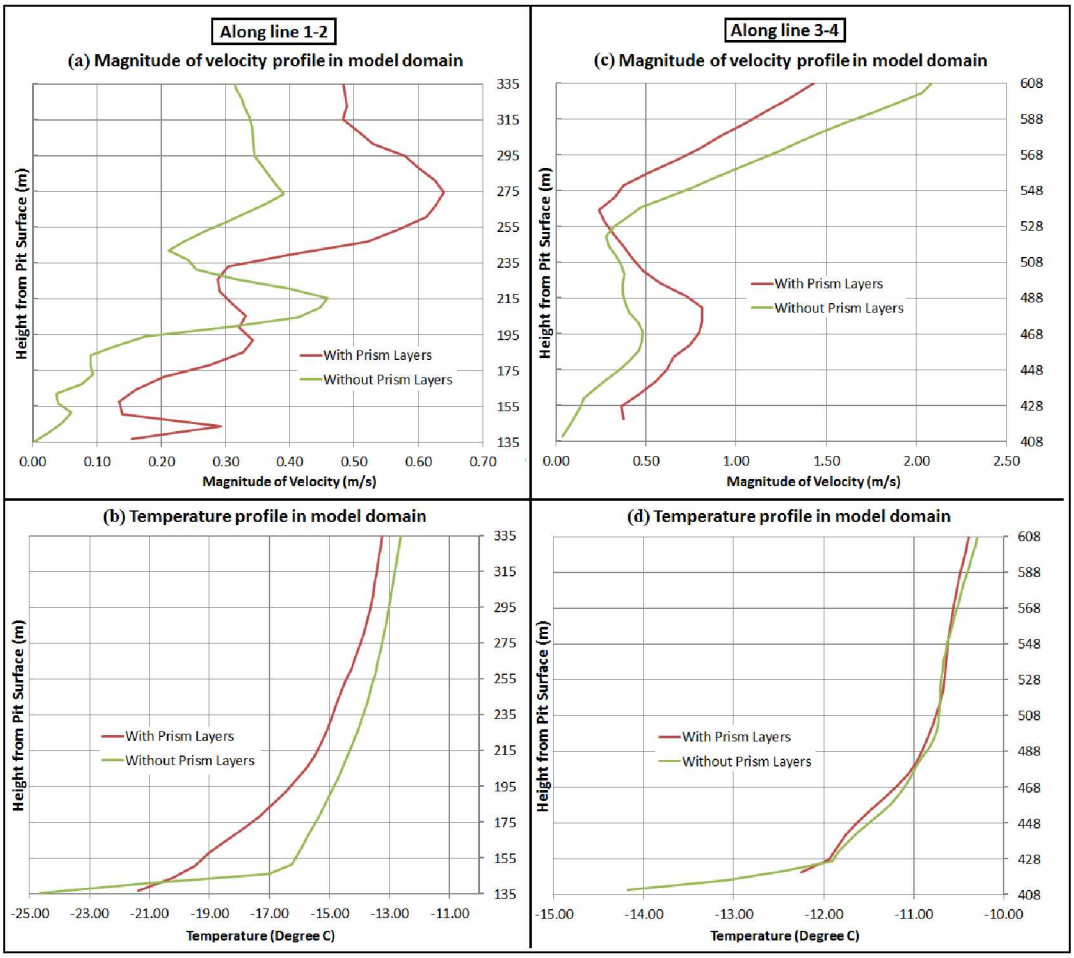

Figure 4.13: The magnitudes of velocity and temperature profiles in both the mesh with and without the prism layers for the line 1-2 ((a) and (b)) and line 3-4 ((c) and (d)).

Chapter 5 Simulation Setup

The final step of preprocessing is defining various simulation parameters using the 'analysis conditions' wizard of the preprocessor. Properties of the fluid, simulation type, initial and boundary conditions, time stepping, turbulence model, source conditions, and various solver settings are defined using this "analysis conditions" wizard. In this thesis, the fluid in the model domain is defined as incompressible air. The Navier-Stokes equations with the Boussinesq approximation are used for estimation of the turbulent heat convection or the thermal buoyancy in the airflow. In this approximation, the air density is assumed to be a function of air temperature at a constant pressure only in the vertical direction. Both the steady and the transient types of simulations are used. The steady state simulation is used for solving the mechanical turbulence in the airflow within the model domain, which is created due to the surface roughness. Transient simulation is used subsequently to solve the modified airflow due to both the mechanical turbulence and the thermal buoyancy. Thermal buoyancy is created due to the convective heat flux from the Pit surface.

In this thesis, one-way coupled Eulerian-Lagrangian simulation approach is selected for solving the model domain. To solve the airflow inside the open-pit domain, various turbulent flow methods and turbulence models are applied in the Eulerian reference frame. The Eulerian method develops the conservations equations on a control volume (mesh elements) basis and solves the airflow parameters at each mesh elements. The parameters, such as, gravity, velocity, pressure of the airflow is solved using the Eulerian method. These airflow parameters are calculated as a function of location and time in the Eulerian method. However, for solving the turbulent dispersion of the fugitive dust particles, the Lagrangian algorithm is applied to the dust particles. The Lagrangian stochastic model characterizes the advection and the diffusion processes of the individual dust particles as a function of time only.

5.1 Boundary Conditions

The selected open-pit model domain has six boundaries. All the boundaries are defined with appropriate boundary conditions to initiate a simulation. An inlet (East) and an outlet (West) boundary along with various wall boundaries (North, South, Pit and FA) are defined in the simulation. The inlet wind velocity in an open-pit mine varies in magnitude over the height. In order to capture this variability in the wind velocity, the inlet boundary is defined as the velocity

boundary with a power law profile of velocity [Flores et al., 2013b] acting normally to the East boundary. The power-law equation of velocity profile is given by Equations 5.1.

$$U = u \,.\left(\frac{dz_i}{dZ_{ref}}\right)^{\frac{1}{7}} \tag{5.1}$$

Where, U is the velocity at height z; u is the velocity at Z_{ref}; dz_i is the distance between the *i*th and the lowest points; and dZ_{ref} is the distance between Z_{ref} and the lowest point.

Figure 5.1 presents the power-law profile of velocity at the East boundary based on the weather station data discussed in Chapter 3. A wind velocity of zero m/s is assigned to the z-coordinate of 397.8 m since the selected z-coordinate value is the lowest point at the East boundary.

The pit boundary, which is the surface of the mine, is defined as a rough wall with an equivalent roughness of $2 * 10^{-2}$ m (Section 3.2 Equivalent Surface Roughness of Pit Surface), along with a constant heat flux (W/m^2) generated from this interface. The equivalent roughness generates mechanical turbulences due to interaction with the wind speed. The constant heat flux generates RN at the pit surface which results in H inside the air volume. This H warms or cools down the air and as a result, develops thermal buoyancy inside the open-pit domain.

Velocity (m/s)	Coordinate (z)
0	397.8
1.39	402.8
1.54	407.8
1.7	417.8
1.94	447.8
2.14	497.8
2.37	597.8
2.5	690.8
2.7	897.8
2.83	1097.8
3.02	1497.8
3.06	1597.8

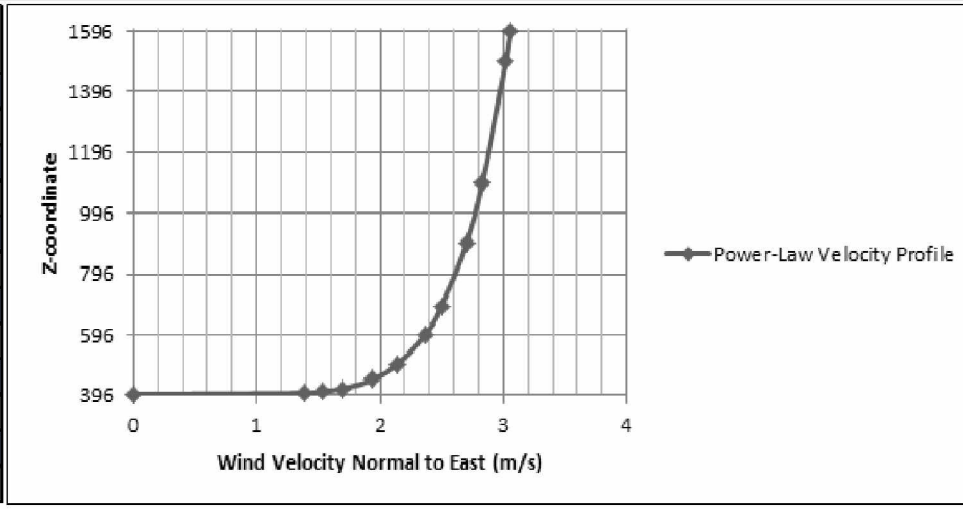

Figure 5.1: Power-law velocity profile at East boundary.

The North, South, and FA boundaries are defined as free-slip wall boundaries, along with an adiabatic heat transfer condition. The North, South, and FA boundaries enclose the volume of the domain. A free slip wall condition is used to model these boundaries as a symmetry plane.

A clear sky condition assumes zero reflected LW radiation from the FA boundary. In this thesis, the adiabatic heat transfer conditions are used to model these boundaries for a clear sky condition.

The choice of the outlet boundary (West) condition has significant influences on the convergence/divergence of the numerical solution. The selection of a static pressure outlet boundary condition (Figure 5.2) results in an extreme magnitude of velocity at the West boundary, and as a result the solution collapses immediately. While keeping the other boundary conditions unchanged, the outlet boundary condition is modified to natural inflow/outflow boundary condition with inflow suppression (Figure 5.3); and this resulted in the convergence of the numerical solution at each time step of the simulation run.

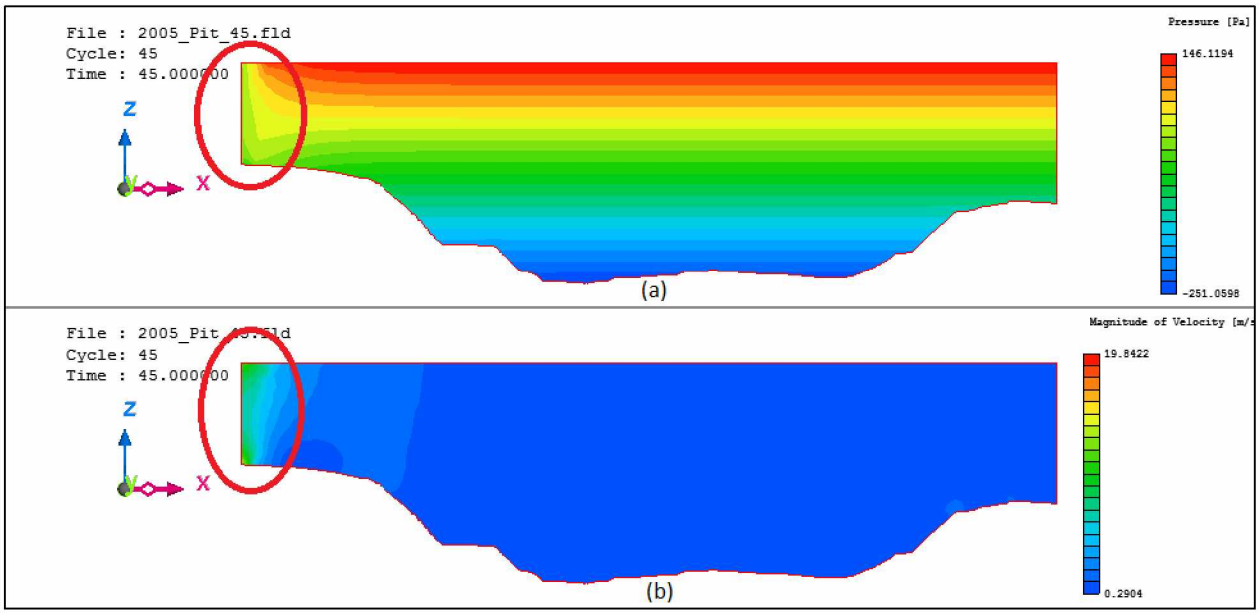

Figure 5.2: (a) Pressure and (b) magnitude of velocity contour plot for static pressure outlet boundary condition.

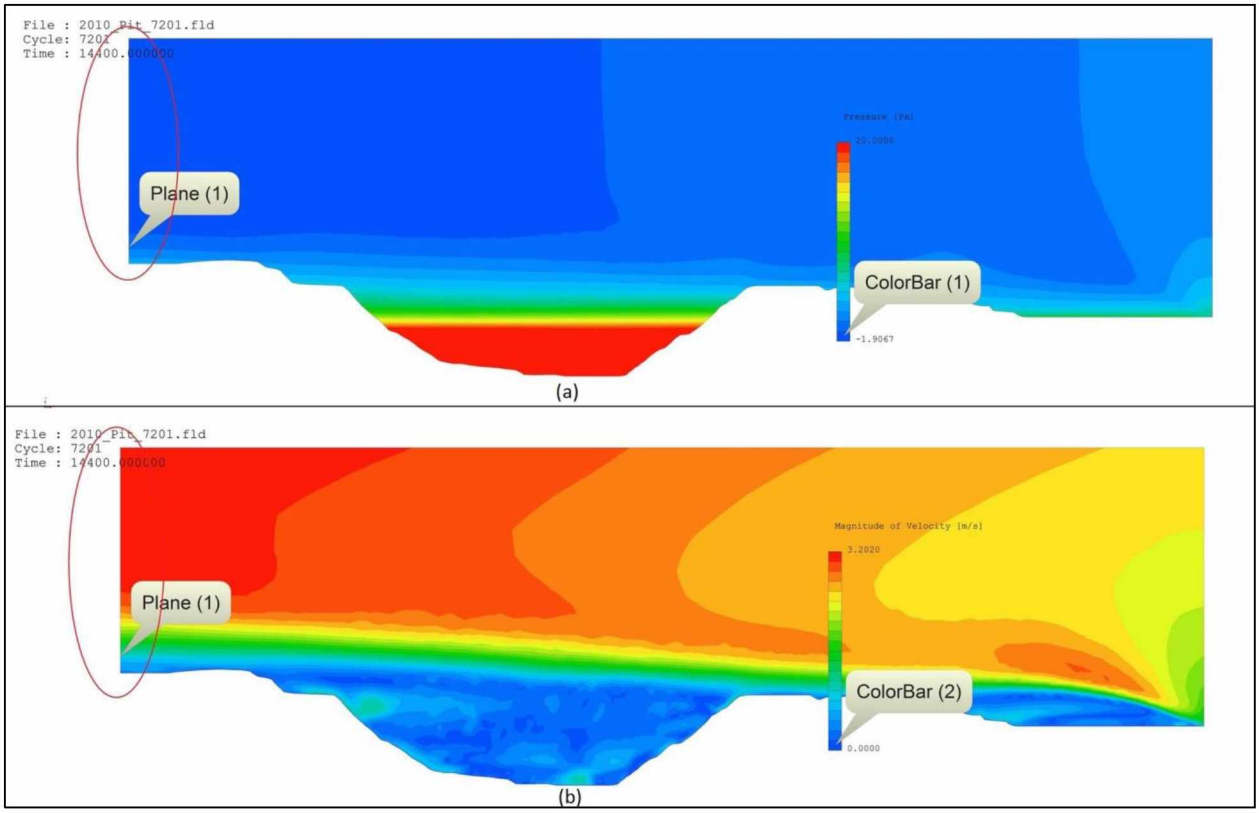

Figure 5.3: (a) Pressure and (b) magnitude of velocity contour plot for natural inflow/outflow outlet boundary condition.

5.2 Initial Conditions

Initial conditions need to be defined for a transient analysis. The airflow profile from the prior steady state simulation is used as an initial airflow profile for subsequent transient simulations. The steady state simulation only considers the surface roughness of the pit boundary, and therefore, defines only the topography-induced downwind recirculation due to mechanical turbulence within the model domain. In the transient simulation, however, the time dependent variables such as the temperature and the heat flux values are introduced.

To develop the thermal boundary layers and the flow for various temperatures regimes inside the pit, the simulation was run for two to four initial hours with a constant heat flux and temperature. The simulation develops the turbulence due to thermal buoyancy while the mechanical turbulence in the domain was developed at the steady state. Before the dust particles sources are introduced in the simulation domain, the calculation of a fully developed background flow is required. This means that unsteady state simulation of background flow is needed for an

extensive period of time, until all eddies in the entire model domain are fully developed. The fugitive dust particles, therefore, are injected after two to four hours of initial simulation so that the transport of fugitive dust is carried out by the developed airflow.

Figure 5.4 displays a velocity vector profile of the trapezoidal domain along the Y = 896 m plane, after two hours of simulation. The thermal buoyancy modified the purely mechanical-turbulence induced flow pattern and an enlarged recirculation pattern is visible inside the open-pit domain.

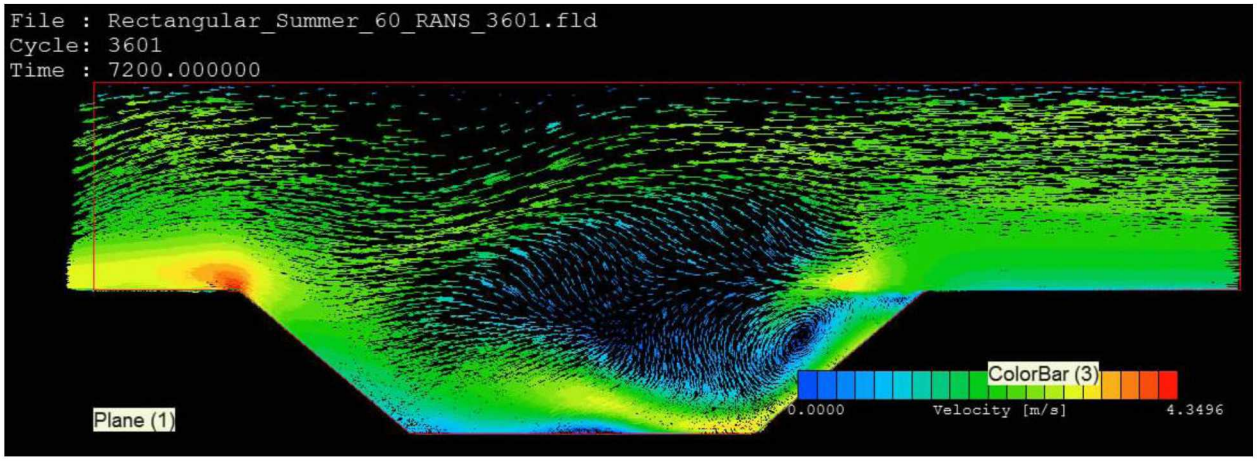

Figure 5.4: The velocity vector profile of the trapezoidal domain after two hours of simulation.

5.3 Time Step in the Transient Simulation

In an open-pit mine, fugitive dust dispersion is a time dependent phenomenon and therefore, requires a transient analysis. In a transient simulation, the simulation clock advances with a specified time step. Two different approaches are available in the SC/Tetra for defining the time step: (1) time step in temporal units and (2) time step based on a Courant number. In the first approach, the time step can be defined either as a constant time step or as a variable time step, which would be a function of the simulation time. In the second approach, the time step can also be defined either as a constant Courant number or as a variable Courant number. The time step defined by the Courant number is an adaptive time step scheme, where the time step is determined by the Courant-Friedrich-Levy (CFL) criterion [Software Cradle Co. Ltd., 2013a].

For convergence of the numerical solution, ideally, the time step should be small. The choice of the time step should result in a CFL number of one; however, a very small time step is required to achieve that. Therefore, a fixed time step is used. Various constant time step duration

is initially selected to evaluate the convergence and stability of the solution. With a time step greater than two seconds, however, the solution did not converge and resulted in instability. Therefore, a constant time step of two seconds is applied throughout the simulation.

5.4 Fugitive Dust Sources and Particle Tracking

Seasonal variation in the amount of dust retention in open-pit mines is well known. To study the seasonally varying fugitive dust dispersion phenomenon inside the selected open-pit mine, sources of dust are defined for all possible working locations in the mine. For the entire open-pit domain, a total of 25 dust source polygons are defined. The dust source polygons are positioned to represent various possible combinations of working locations. Thus, the simulation results estimate the fugitive dust retention from all possible sources. Each source is positioned approximately 10 m above the pit surface. This positioning of the dust sources takes into account two very important considerations: (1) close to the pit surface level, the airflow velocity is approximately zero and the dust particles lying on the pit surface are not generally the source of fugitive dust (no re-entrainment); and (2) the sources of fugitive dust, such as blasting, create dust volumes at various heights from the surface. The particles are thrown upwards by the kinetic energy during blasting and small diameter particles (PMs) stay in suspension in the air, and eventually are dispersed by the natural airflow. Figure 5.5 displays the 25 dust sources with the number of dust particles in the trapezoidal domain.

The particle tracking function of the Cradle SC/Tetra has several options for defining the particles inside the CFD domain. Particle tracking function can generate particles of two types [Software Cradle Co. Ltd., 2013c]: (1) Marker particles: these particles have no mass and the velocity of a particle is the sum of the flow velocity and the sedimentation velocity. Since the sedimentation velocity of a marker particle is zero, these particles move with the airflow. (2) Mass particles: these particles have mass, and they interact with the flow. Each source needs to be defined with the number of particles it generates. Due to the extensive requirement of computational space, the number of particles from each source is kept to 100 particles. In this thesis, all particles were defined by the mass of the particle since dust particles have density and settling velocity. Four types of particles were generated from each source: the $PM_{0.1}$, the $PM_{2.5}$, the PM_5, and the PM_{10}. The number of each particle type from each source is 25, which is called the effective number [Software Cradle Co. Ltd., 2013c] and can be correlated based on the field

data. If the amount of retention of dust from a dust source after two hours of simulation is 20 particles out of a total of 100 particles, this simulation result estimates 20% retention of the fugitive dust for that specific climatic condition, which can be cross-verified with the dust sampling data [Bhowmick et al., 2015b].

Figure 5.5: Dust sources in the trapezoidal domain.

5.5 Turbulent Flow and Turbulence Model

Since the exact flow situation in an open-pit mine is not known a-priori; various turbulence models are evaluated to identify the appropriate model that would simulate the flow phenomena within the pit with reasonable accuracy. Turbulence models differ in their assumptions, structures, and in algorithm. Therefore the predictions vary from one model to another.

There are relatively few known applications of CFD in the three-dimensional modeling of airflow in large open-pit mines. However, two equation turbulence closure formulations of

Kappa-Epsilon (κ-ε) model, and Large Eddy Simulation (LES) [Lesieur et al., 2005]; have been used to solve stable boundary layer (SBL) problems in atmospheric sciences. Because an exact flow situation in open-pit mines is not known a priori, it is necessary to investigate various turbulent models to identify the model that would simulate flow phenomena and predict fugitive dust distributions within the pit with reasonable accuracy. Dispersion models differ in their assumptions and structures as well as in the algorithm used; as a result, the simulated predictions vary from model to model. Furthermore, it is also important to investigate the performance of a CFD model when simulating complex phenomena such as the transport and distribution of fugitive dust in an open-pit mine. The simulation of an enhanced period of turbulence in SBL is of particular interest because traditional fugitive dust dispersion models cannot explicitly treat such intermittent events, and yet the SBL is often the worst-case scenario in open-pit for fugitive dust dispersion.

The majority of the CFD models are based on the solutions of the Navier-Strokes (N-S) equations, the energy equation, the mass and concentration equations as well as transport equations for turbulent viscosity and its scale in a well-defined domain. In this thesis, the CFD simulation is performed using the SC/Tetra software package developed by software CRADLE, which is a finite volume (FVM) based code for fluid flow simulation, importing and meshing the open-pit geometry and modeling contaminant transport. Most of the turbulence models available in SC/Tetra are based on Reynolds averaging of the turbulent quantities using the Reynolds-averaged Navier-Stokes (RANS) equations. The RANS equations are formulated in terms of the time-averaged flow field (velocity, pressure, density and temperature). This averaging concept for theN-S equations significantly reduces the complexity of simulating turbulent flow. This simplification, however, results in the additional Reynolds stress tensor that appears in the RANS equation as a result of the nonlinear terms of the underlying N-S equations [Versteeg and Malalasekera, 1995].

Two equation κ-ε model is one of the most widely used turbulence models for simulating industrial flow problems such as wing-body, pipe flow, etc. Apart from the solution to the industrial flow problem, the κ-ε model has found wide acceptability in atmospheric science [Richards and Hoxey, 1993; Blocken et al., 2007]. The κ-ε model provides a quick solution to many flow problems with reasonable accuracy at relatively low computational cost. However,

the κ-ε model is incapable of capturing the internally induced fluctuations of the flow field on which the transport of pollutants depends [Menter, 2012]. Therefore, to account for turbulent mixing, other turbulent models need to be examined.

In recent years, with advancement in computation power LES is becoming an attractive alternative to the flow problems where the κ-ε models lack accuracy. LES has been widely used in simulating the ABL structure [Kosović and Curry, 2000; Basu and Porté-Agel, 2006]. LES resolves the fluctuations of flow variables, which are shown to vary significantly over time, thus capturing the transient mixing. The simulated wind fields can then be used to study transport and dispersion under a variety of atmospheric conditions. Therefore, a LES modeling of the open-pit mine is also studied.

The CFD software SC/Tetra Thermal-Fluid analysis system of software CRADLE provides options for selecting (1) turbulence model and (2) turbulent flow in the Preprocessor. A number of turbulence models are available in SC/Tetra, such as: (1) standard k-ε; (2) re-normalization group (RNG) k-ε; (3) modified production (MP) k-ε and (4) realizable k-ε, for solving high-Reynold's number (Re) flow. Turbulent flow parameters simultaneously can be solved with several approximations such as: (1) Reynolds-Averaged Navier-Stokes (RANS); (2) Detached Eddy Simulation (DES); (3) Very Large Eddy Simulation (VLES), and (4) Large Eddy Simulation (LES) [Software Cradle Co. Ltd., 2013a and 2013c].

5.5.1 Comparison of Turbulence Models: Solving Airflow

In this research, the open-pit model domain is simulated with various flow methods using the standard k-ε turbulence model. The LES flow method does not need a turbulence model for solving the model domain. In the default k-ε turbulence model, the model solves two-transport-equations where k is solving for kinetic energy and ε is solving for turbulent dissipation. The standard k-ε turbulence model is: (1) robust is calculation, (2) extensively used, (3) easy to simulate, and (4) comparatively computationally efficient. However, the standard k-ε turbulence model has limitations, such as: (1) inefficient performance in solving complex flows involving severe pressure gradient, separation, and strong streamline curvature, etc.; and (2) the lack of sensitivity to adverse pressure gradients [Menter, 1993 and 1994].

During the summer months with positive heat flux from the pit boundary, various downwind recirculation profiles are observed (Figure 5.6) in various turbulent flow methods. The velocity

vector profiles in the Y = 1290 m plane, respectively for the RANS and LES method in the selected model domain are presented in Figure 5.6. From this figure, numerous re-circulatory eddies can be observed in the model domain. The location and the profile of eddies are, however, different from one method of turbulent flow to another. During the winter months with negative heat flux from the pit boundary, the airflow profiles inside the domain vary based on the selection of turbulent flow method. The negative heat flux from the pit boundary results in the formation of a temperature-based air inversion zone within the pit cavity, which causes the detachment of the airflow inside the cavity from the airflow outside of the cavity. All the methods of turbulent flow predict the formation of an air temperature inversion zone inside the model domain. Since the downwind recirculation inside the pit cavity is almost absent, the airflow profiles are stagnant for all the methods of turbulent flow for the winter months.

To identify an appropriate modeling approach, the solutions of various turbulent flow methods are evaluated based on the formation of velocity and thermal boundary layers at the pit boundary. Since the pit boundary is the source of mechanical turbulence and thermal convective forcing in the domain, the formation of velocity and thermal boundary layers at the pit boundary are needed to be precise for the estimation of the airflow inside the domain. Figure 5.7 displays the magnitude of velocity profiles and the temperature profiles along the line 1-2 (Figure 5.7(a) and Figure 5.7(b)) and line 3-4 (Figure 5.7(c) and Figure 5.7(d)) for the respective DES, LES, RANS and VLES methods. The magnitude of velocity and the temperature profiles near the Pit surface (Close to 135 m of elevation for line 1-2 and 420 m of elevation for line 3-4) represent the formation of the velocity boundary layer and the thermal boundary layer at the pit boundary.

It is understood that the magnitude of wind velocity at the surface in reality is zero. Due to the absence of any computational points or nodes located exactly at the Pit surface, the magnitudes of velocity profiles in Figure 5.7(a) and Figure 5.7(c) do not converge to zero (m/s) value. The magnitude of velocity profiles (Figure 5.7(a) and Figure 5.7(c)) for all the methods of turbulent flow display a well-defined and almost similar pattern of velocity boundary layer at the pit boundary. The magnitude of velocity profiles, very close to the Pit surface, shows very slow increment; however, the profile shows rapid increment away from the surface. This phenomenon corresponds to a velocity boundary layer feature of a rough surface. The temperature profile along line 1-2 (Figure 5.7(b)), predicted by the LES method indicates a reasonable temperature

gradient close to the Pit surface. While for the other methods of turbulent flow, the temperature gradients are very steep. The exhibited temperature profile along line 3-4 (Figure 5.7(d)), by the LES as well as the DES and VLES methods, indicates an expected temperature gradient; while the RANS method predicts lesser values of temperature. Most importantly, it is observed that the LES method calculates a reasonable temperature gradient at the deepest regions of the Pit as compared to the other methods. Therefore, it can be said that the LES method exhibits a better resolution for the thermal boundary layers at the Pit surface for all the domains.

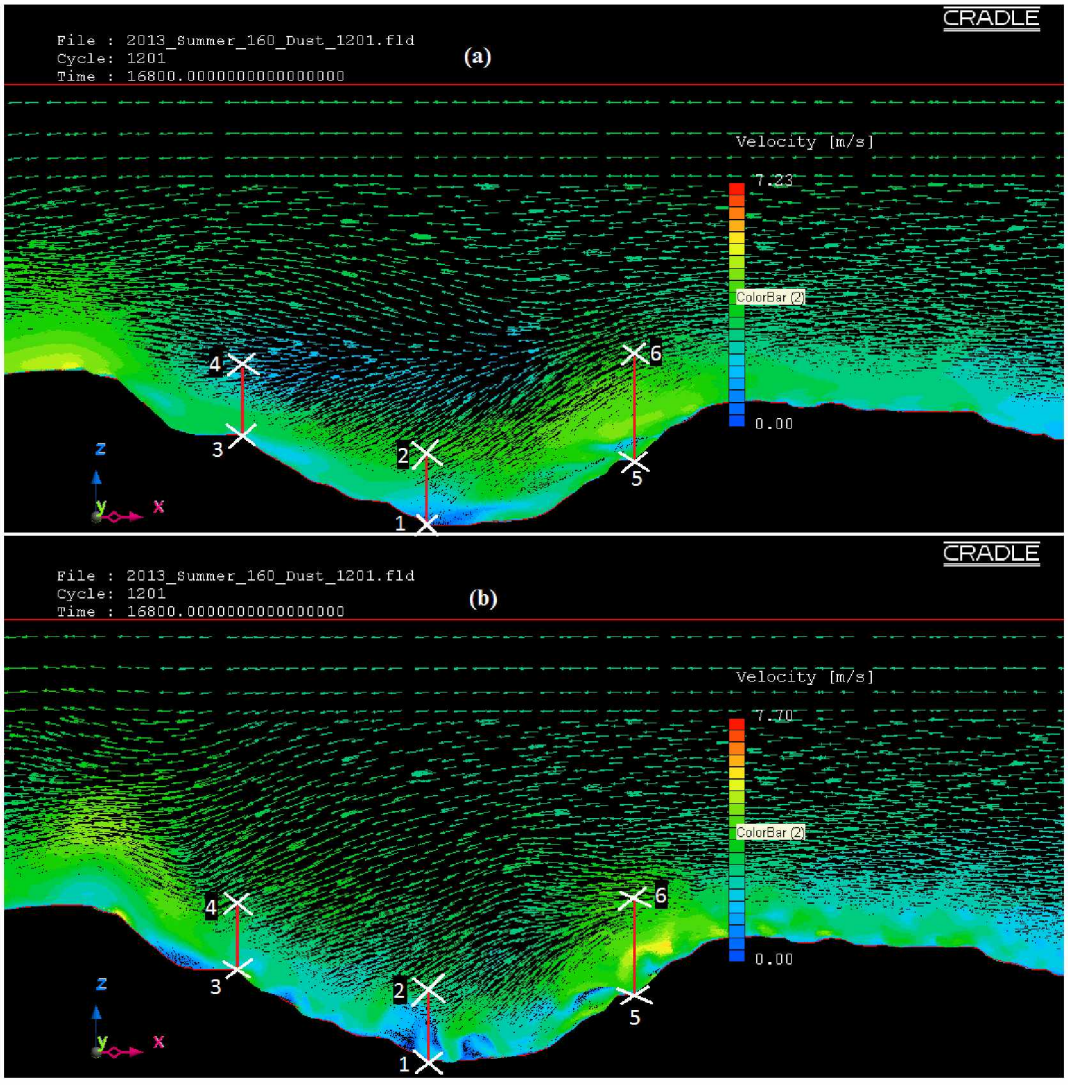

Figure 5.6: Velocity vector profiles during the summer months for (a) RANS and (b) LES methods of turbulent flow.

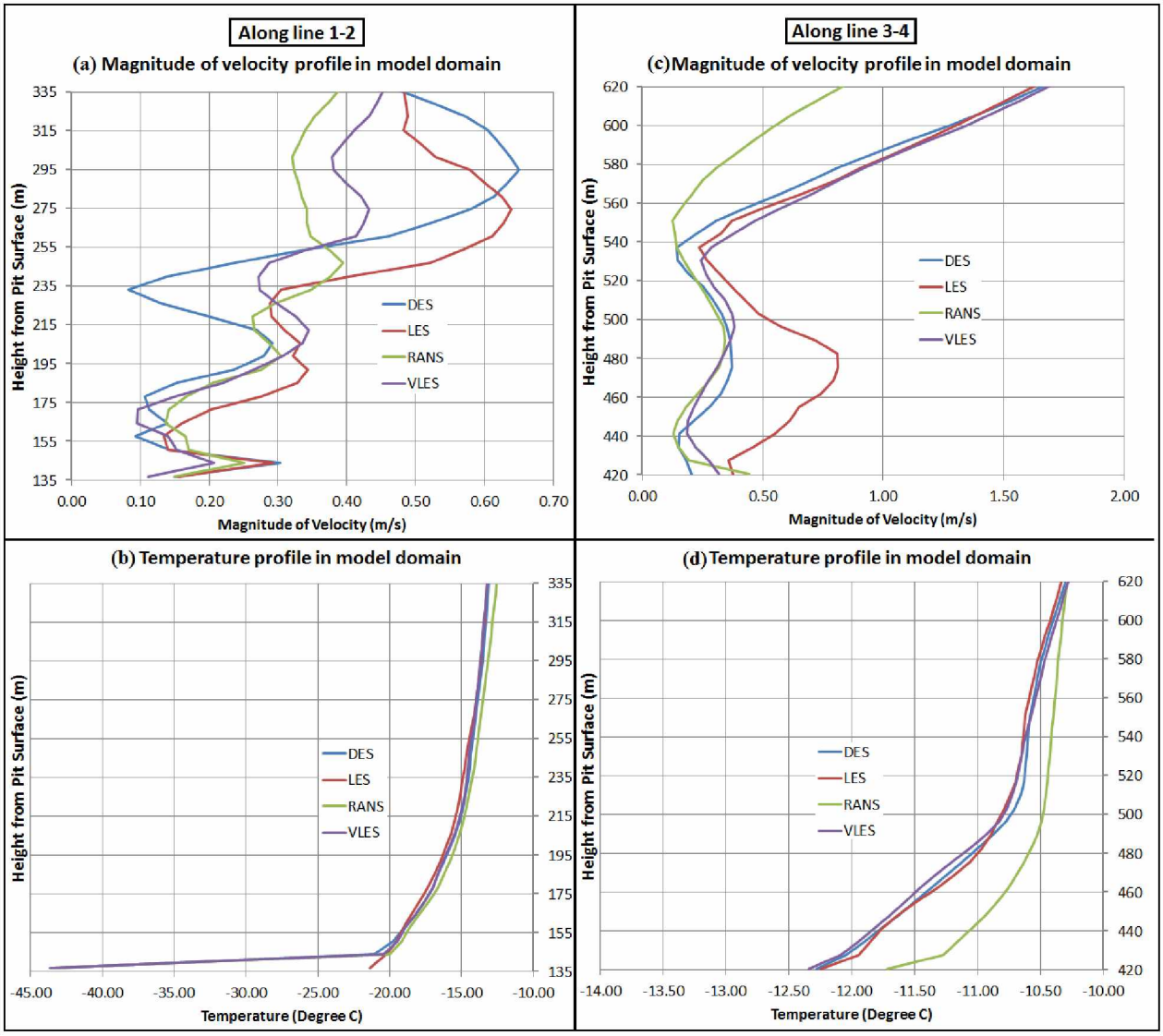

Figure 5.7: Magnitude of velocity and temperature profiles along the line 1-2 ((a) and (b)) and line 3-4 ((c) and (d)), during the winter months for DES, LES, RANS and VLES methods of turbulent flow.

5.5.2 Comparison of Turbulence Models: Solving Particle Propagation

The following discussion has been modified from a document [Bhowmick and Bandopadhyay, 2015] originally written for and published in the Proceedings of 15th North American Mine Ventilation Symposium, 2015, with coauthor Bandopadhyay, S.

Based on the simulation results in the previous sub-section, it seems that RANS and LES would be the appropriate models to consider for fugitive dust dispersion modeling. Therefore, the dust dispersion phenomenon under clear sky conditions is simulated using both the RANS

and the LES methods. The amount of dust retention and the time required for the dust particles to clear out of the domain depend on the turbulence model. To compare the selected turbulence models, the initial downfall and the pathlines of the dust particles are analyzed [Bhowmick and Bandopadhyay, 2015].

With the RANS simulation, an extensive amount of dust particles settles down at the pit surface within the initial four minutes of simulation. Whereas in the LES simulation; the settling of dust particles is more realistic. Table 5.1 presents the initial downfall of dust particles for the two methods. An extensive initial downfall of dust particles in the RANS simulation results in reduced dust retention and a shorter time for the dust particles to clear out of the pit.

Figure 5.8 presents the pathlines for LES and RANS simulation. The pathlines of the dust particles for the RANS simulation show small scale irregularities on their way out of the domain. Whereas, the pathlines of the dust particles in the LES simulation; follow well-developed smooth re-circulatory patterns. The pathlines in LES simulation resembles the re-circulatory patterns of the airflow inside the model domain. The irregular pathlines in RANS simulation represents the lack of accuracy in the calculation of the net resultant forces on the dust particles.

Following the generation of the dust particles, the pathlines in the RANS simulation also display a very complicated pattern at the initial stage of dust dispersion. Some of the pathlines also collapse abruptly at the pit surface after being dispersed for a short duration. The initial downfalls of the dust particles are due to the lack of accuracy in the net resultant force.

Table 5.1: The initial downfall of dust particles in RANS and LES simulations.

Season	Intensity	Settled dust particle (out of 2460 particles)		Live dust particle (out of 2460 particles)	
		RANS	LES	RANS	LES
Winter	Moderate Winter	705	138	1755	2322
	Extreme Winter	574	132	1886	2328
Summer	Fair Insolation	1498	36	962	2424
	Moderate Insolation	1726	25	734	2435
	Extreme Insolation	1609	83	851	2377

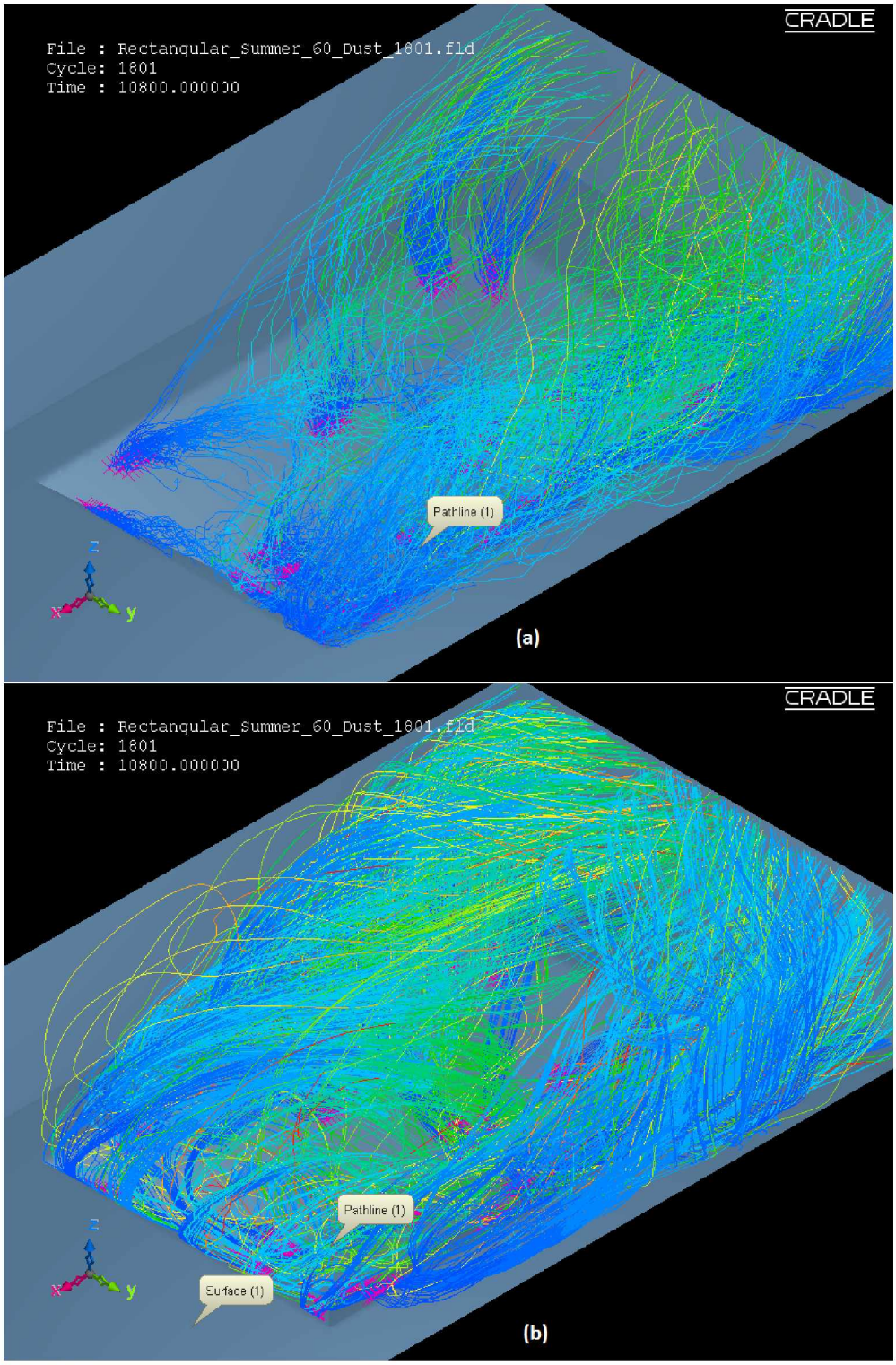

Figure 5.8: Pathlines of the dust particles for (a) RANS and (b) LES simulations.

The initial downfall of dust particles in the RANS simulation has a significant effect on the estimates of (1) the particles, settled down at the pit surface, (2) the particles, transported outside the pit domain, and (3) the duration of dust retention within the pit. While in LES simulation, since the quantity of initial downfall of dust particles is comparatively small, the simulation requires longer duration to clear the dispersed dust particles out of the pit.

The simulation results of clear sky condition using both the RANS and LES methods are shown in Table 5.2. The results of the RANS simulation predict that the gravitational settling is the foremost mechanism for removal of the fugitive dust particles. The result of LES simulation suggests that the re-circulatory airflow inside the domain is the primary mechanism for removal of the fugitive dust in all the model domains.

The RANS simulation result for the fair insolation condition in the conical model domain predicted that a maximum of 45% of the particles would be removed. While the LES simulation results for the summer conditions predicted more than 95% of the particles would be removed. The settling time calculated from the terminal gravitational settling velocities of PM_{10} and smaller particles indicates that the downfall of a large percentage of fugitive dust particles within a short duration is not feasible. Therefore the LES method seems to be a better choice than the RANS method.

The simulation results of the winter conditions in both the domains show extensive fugitive dust retention. This is due to the existence of air temperature inversion, which results from the negative heat flux at the pit surface. However, the LES simulation predicts a more feasible percentage of fugitive dust particles settling down at the pit surface. The number of predicted dust particles trapped below the inversion layer is also larger than the RANS simulation. The absence of a strong re-circulatory airflow within the inversion layer results in extensive fugitive dust retention for a long duration. The simulated time to clear out the dust particles during the winter condition is beyond the scope of this thesis.

Various simulation parameters are categorized based on the various simulation outcomes as described in this chapter. The simulation parameters are extensively used for simulation of both the idealized and the actual open-pit domains for prediction of fugitive dust retention in the selected open-pit mine depending on the various seasonal conditions. The simulation results of the open-pit domains are presented in Chapter 6.

Table 5.2: The simulation results of clear sky condition using the RANS and the LES simulation.

Domain	Climate Condition	Heat Flux (W/m^2)	% settled down		% reported outside		Time to clear out	
			RANS	LES	RANS	LES	RANS	LES
Trapezoidal	Moderate Winter	-20	~92	~23	4.10 (6 hrs.)	2.68 (6 hrs.)	Unknown	Unknown
	Extreme Winter	-40	~96	~27.8	0.12 (6 hrs.)	1.2 (6 hrs.)	Unknown	Unknown
	Fair Insolation	60	73	1.8	27	98.2	52 min	116 min
	Moderate Insolation	100	81	3	19	97	48 min	144 min
	Extreme Insolation	160	75	4.6	25	95.4	53 min	80 min
Conical	Moderate Winter	-20	~89	~25.2	6.06 (6 hrs.)	18.66 (6 hrs.)	Unknown	Unknown
	Extreme Winter	-40	~88	~26.14	0.53 (6 hrs.)	2.1 (6 hrs.)	Unknown	Unknown
	Fair Insolation	60	55	0.07	45	99.93	36 min	80 min
	Moderate Insolation	100	61	1.18	39	98.82	32 min	80 min
	Extreme Insolation	160	72	1.07	28	98.93	48 min	104 min

Chapter 6 Simulation of Fugitive Dust Propagation in Open-Pit Mines

Modeling fugitive dust transport is an important step for assessing the pollutant concentrations within an open-pit mine. The airflow in open-pit mines can be considered to be in an unbounded volume of a large scale and does not strictly follow the principles of pipe flow The airflow problems in actual open-pit mines are far more complex. As dust particles are suspended in air, the transportation and distribution of fugitive dust are highly associated with the convective motion of the air and the turbulence. Hence the computational fluid dynamics is the most suited modeling approach to study the spatial distribution of fugitive dust in open-pit mines. Computational fluid dynamics (CFD) models provide detailed information about the airflow pattern and air velocity distribution, temperature, and fugitive dust concentration within the enclosed domain of an open-pit.

The atmospheric boundary layer flow over rough terrain, such as an open-pit mine, is classified as entirely rough because the roughness elements are so large that the laminar sub-layer is mostly eliminated. This is, however, the case for airflow in the upstream and downstream portion of the computational model domain, but not necessarily for the airflow over the explicitly modeled surfaces with small-scale roughness in the central part of an open-pit domain.

Two idealized and an actual open-pit domain of the selected open-pit mine are simulated with various simulation parameters to predict fugitive dust retention in a selected open-pit mine. As discussed earlier, a coupled simulation approach is selected for predicting the fugitive dust dispersion in the model domain.

To calculate the airflow parameters inside the open-pit domain, various turbulent flow methods and turbulence models are applied in the Eulerian reference frame. The Eulerian method develops the conservations equations on a control volume (mesh elements) basis and solves the airflow parameters at each mesh elements. The parameters, such as, gravity, velocity, pressure of the airflow are calculated using the Eulerian method. The Eulerian method develops the conservations equations on a control volume (mesh elements) basis and solves the airflow parameters at each mesh elements. These airflow parameters are calculated as a function of location and time in the Eulerian method. However, for solving the turbulent dispersion of the fugitive dust particles, the Lagrangian algorithm is applied to the dust particles. The Lagrangian

stochastic model characterizes the advection and the diffusion processes of the individual dust particles as a function of time only.

Two turbulent flow methods are used for solving the airflow inside the domains. (1) RANS (Reynolds-Averaged Navier-Stokes) using standard k-ε turbulence models and (2) LES (Large Eddy Simulation) using SGS/WALE (Sub-Grid-Scale/Wall-Adapting Local Eddy-viscosity) models are used to model the turbulent dispersion of fugitive dust in the selected domains.

The turbulent flow in the k-ε turbulence model is treated through Reynolds averaging. In Reynolds averaging, the transitional and the unsteady physical phenomena are time-averaged and divided into their mean values and fluctuating components. Whereas, Large Eddy Simulation (LES) models the various sizes of turbulence eddies generated by the cascading process of turbulence [Software Cradle Co., Ltd., 2013a].

The model domains are simulated to capture the micro-scale ABL flow due to the surface roughness induced mechanical turbulence and surface radiation induced thermal buoyancy. The surface roughness results in formation of velocity boundary layers. The sensible heat flux of the surface radiation results in formation of thermal boundary layers. In order to model the thermal forces, Boussinesq approximation is used in both the simulations. For resolving the thermal boundary layers, the LES method shows better resolution than other turbulent methods (presented in Chapter 5).

The following discussion has been modified from a document [Bhowmick et al., 2015b] originally written for and published in the Mining Engineering journal of SME, Vol. 67, with coauthors Raj, K. V. and Bandopadhyay, S.

The simulation results in this chapter are organized in two sub-sections. In the first sub-section, the simulation results of the idealized domains are presented. In the second sub-section, the simulation results of the actual open-pit domains are presented.

6.1 Simulation Results of the Idealized Domains

In simulation of the two idealized open-pit domains, the steady state wind velocity profile is used as the initial velocity profile for the transient simulation. Before the dust particles are introduced in the flow domain, the calculation of fully developed background flow is required. This is accomplished in the initial two hours of the transient simulation of the background flow,

and all eddies in the entire flow domain are fully developed. The fugitive dust particles were then injected, and the simulation was run until the last dust particle is removed from the pit. To analyze the dust dispersion phenomenon, a good understanding of the airflow regimes is necessary since the retention of fugitive dust inside the domain is directly affected by the flow inside the domain.

6.1.1 Airflow Regimes: Winter Climatic Conditions

The airflow pattern inside the domain changes from summer to winter due to the amount of sensible heat flux. The airflow patterns vary from domain to domain based on the aspects of the geometry even for the similar simulation set up. In an extreme insolation condition, different airflow patterns are exhibited as compared to a moderate or a fair insolation condition such as during the summer months.

Figure 6.1 and Figure 6.2 present the airflow patterns along the middle of domain for a moderate winter condition (-20 W/m^2) after three hours of simulation inside the trapezoidal and the conical domains respectively. A flow separation can be observed near the pit-rim in both the domains, which is caused due to the formation of an atmospheric inversion inside the open-pit. The airflow inside the domain is stagnant and completely detached from the airflow outside the open-pit. The airflow pattern during an extreme winter condition (-40 W/m^2 heat flux) inside the trapezoidal and the conical domains are presented in Figure 6.3 and Figure 6.4, respectively. Similar flow separation phenomena such as in the moderate winter condition can be observed in these figures.

As observed in Figure 6.1 to Figure 6.4, the presence of an air temperature inversion in the open-pit domains may result in higher retention of fugitive dust. Since the airflow inside the domain is completely stagnant for the winter conditions and detached from the airflow outside the domain, the dust particles inside the open-pit may remain suspended for a very long duration.

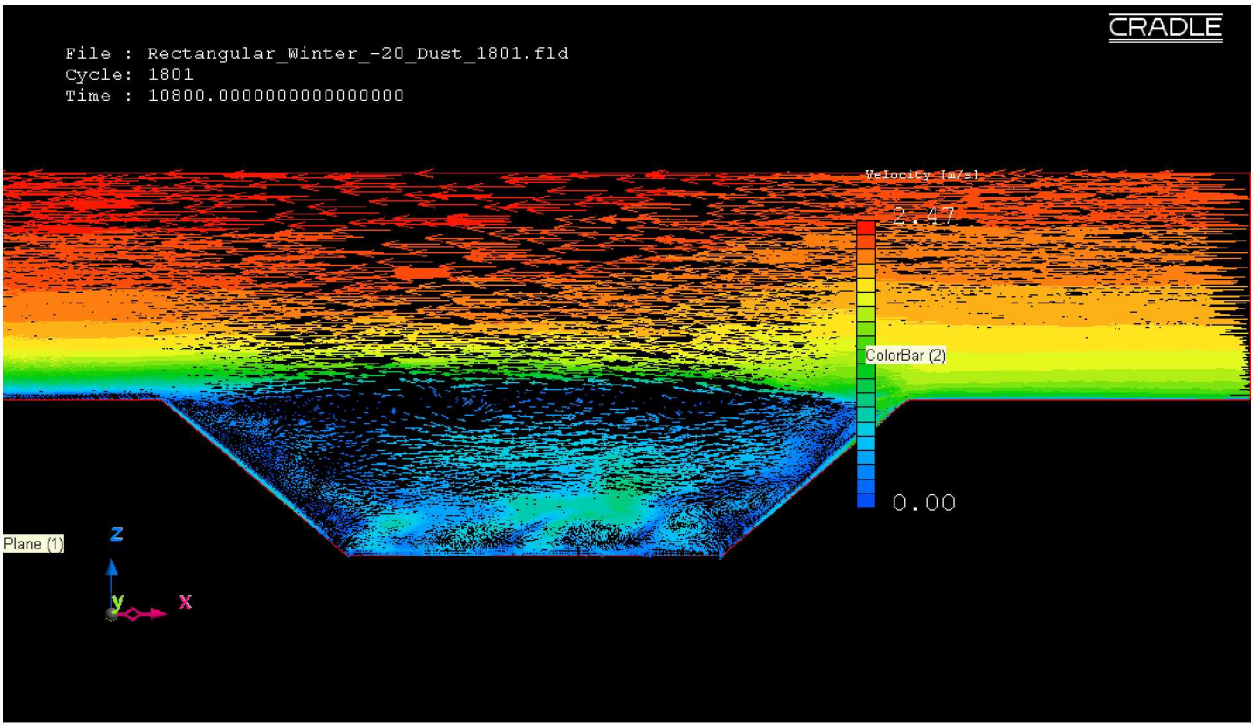

Figure 6.1: Velocity vector profile in the trapezoidal domain for moderate winter condition.

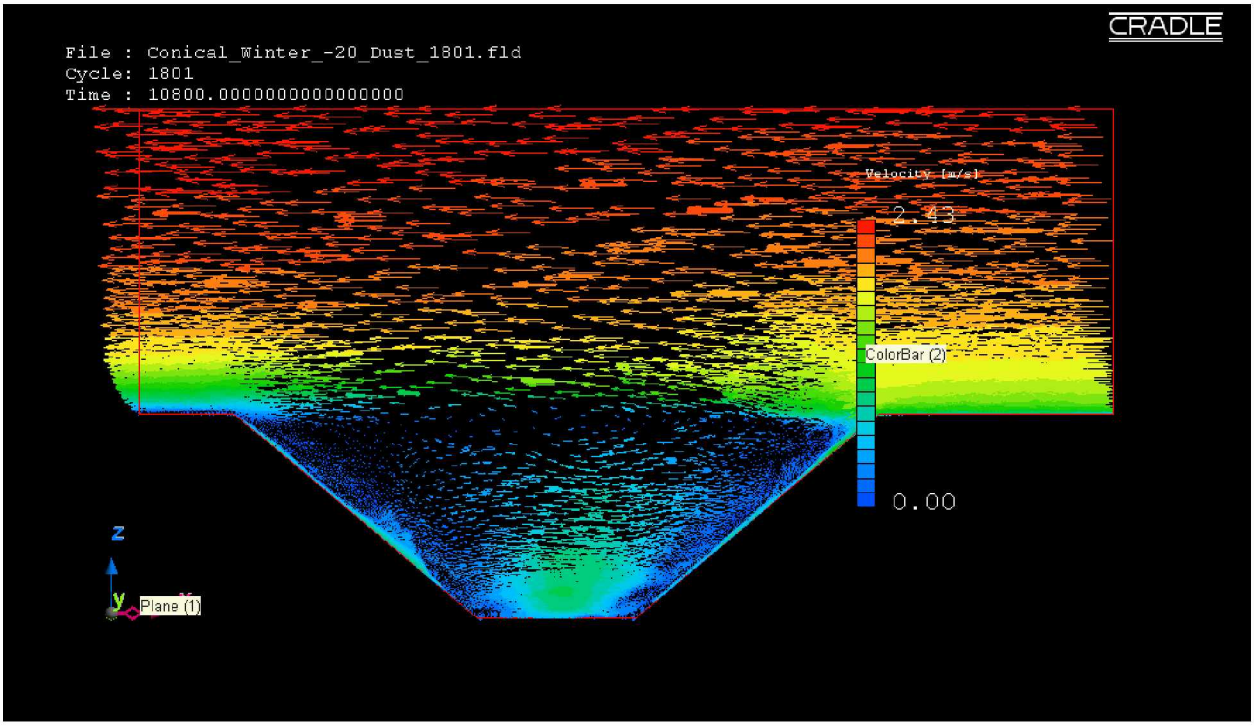

Figure 6.2: Velocity vector profile in the conical domain for moderate winter condition.

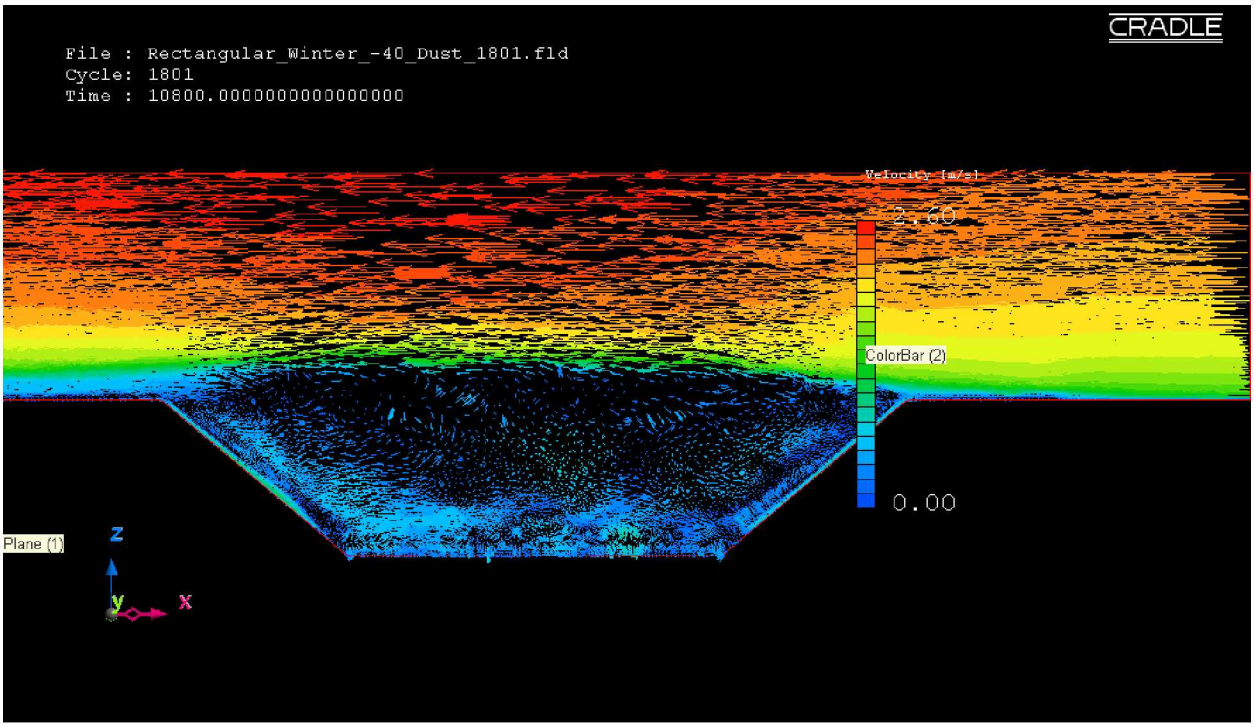

Figure 6.3: Velocity vector profile in the trapezoidal domain for extreme winter condition.

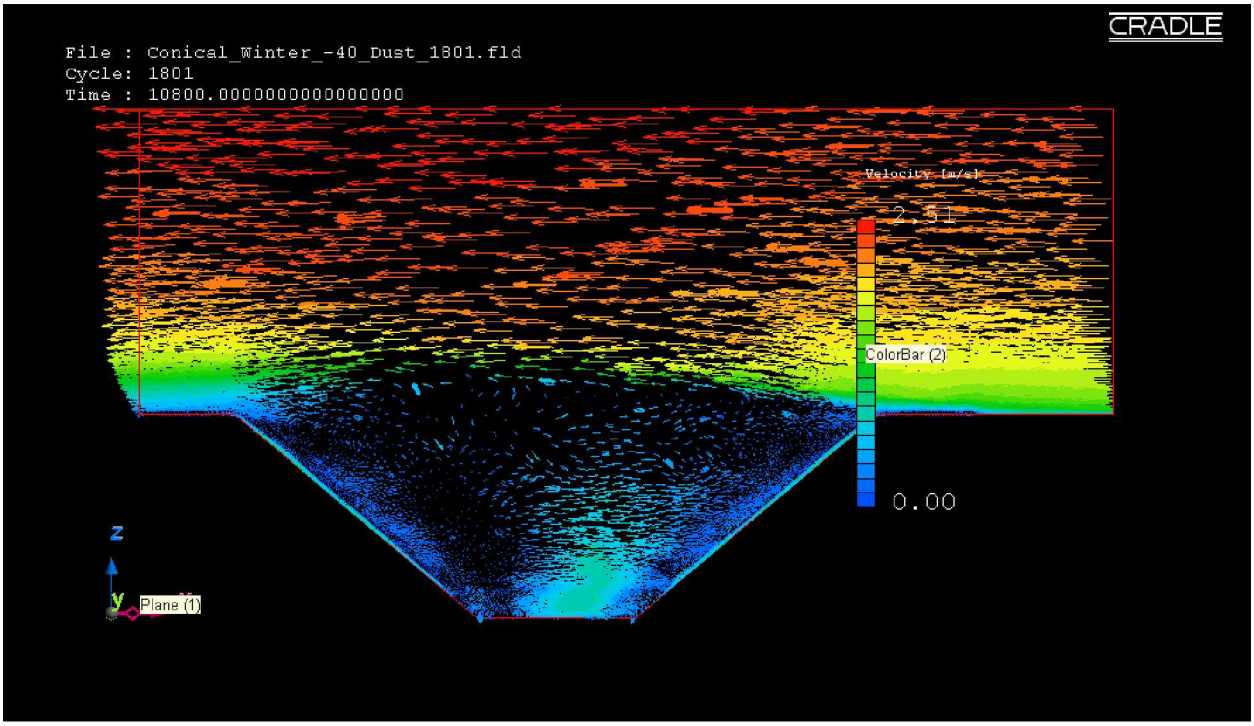

Figure 6.4: Velocity vector profile in the conical domain for extreme winter condition.

6.1.2 Airflow Regimes: Summer Climatic Conditions

Airflow patterns along the middle of domain after three hours of simulation for a fair insolation condition (60 W/m^2 heat flux) inside the trapezoidal and the conical domains respectively are presented in Figure 6.5 and Figure 6.6. The recirculation profiles inside the open-pit domain (Figure 6.5 and Figure 6.6) indicate the formation of a convective (unstable) boundary layer. The locations of the convective eddies are, however, varying from one domain to another based on the aspects of the domain geometry.

Airflow patterns inside the trapezoidal and the conical domains during a moderate insolation condition (100 W/m^2 heat flux) are presented in Figure 6.7 and Figure 6.8, respectively. The formation of a convective (unstable) boundary layer can be noted.

Airflow patterns for an extreme insolation condition (160 W/m^2 heat flux) inside the trapezoidal and the conical domains respectively are presented in Figure 6.9 and Figure 6.10. A similar convective boundary layer with numerous turbulent eddies are observed within the domains.

It can be observed (Figure 6.5 to Figure 6.10) that the height of the convective boundary layer during summer is dependent on the sensible heat flux in the domain. The height of the convective boundary layer and the air recirculation in both the domains, in particular in the trapezoidal domain, is a function of the sensible heat flux.

During the summer, (Figure 6.5 to Figure 6.10), the convective (unstable) motion in the airflow inside the domains may carry most of the dust particles out of the domains in a comparatively short duration. The propagation of the dust particles in the idealized simulation domains are presented in the next section.

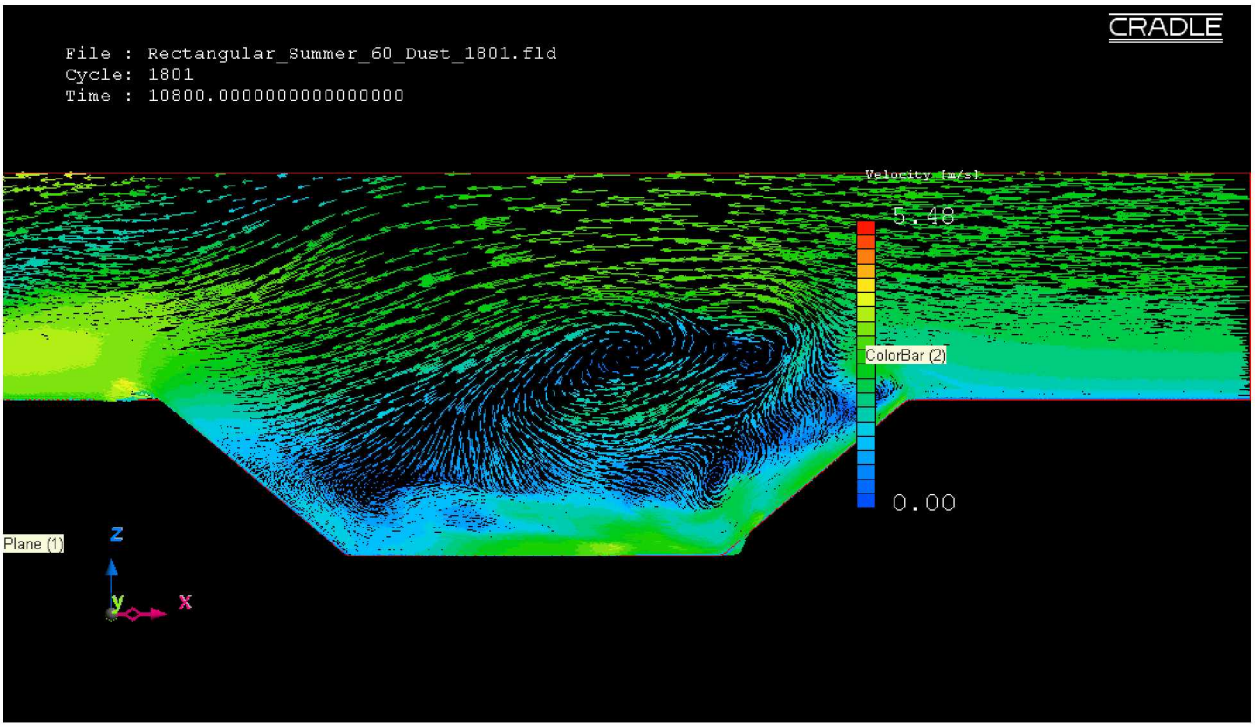

Figure 6.5: Velocity vector profile in the trapezoidal domain for fair insolation condition.

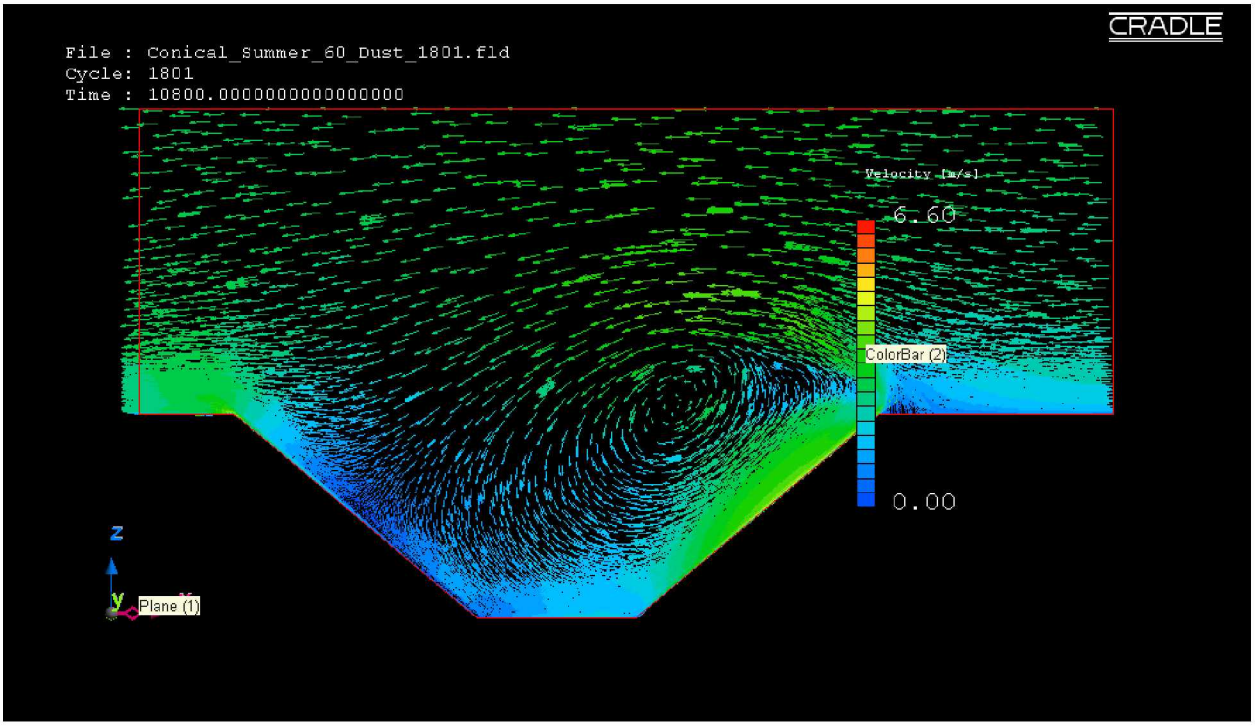

Figure 6.6: Velocity vector profile in the conical domain for fair insolation condition.

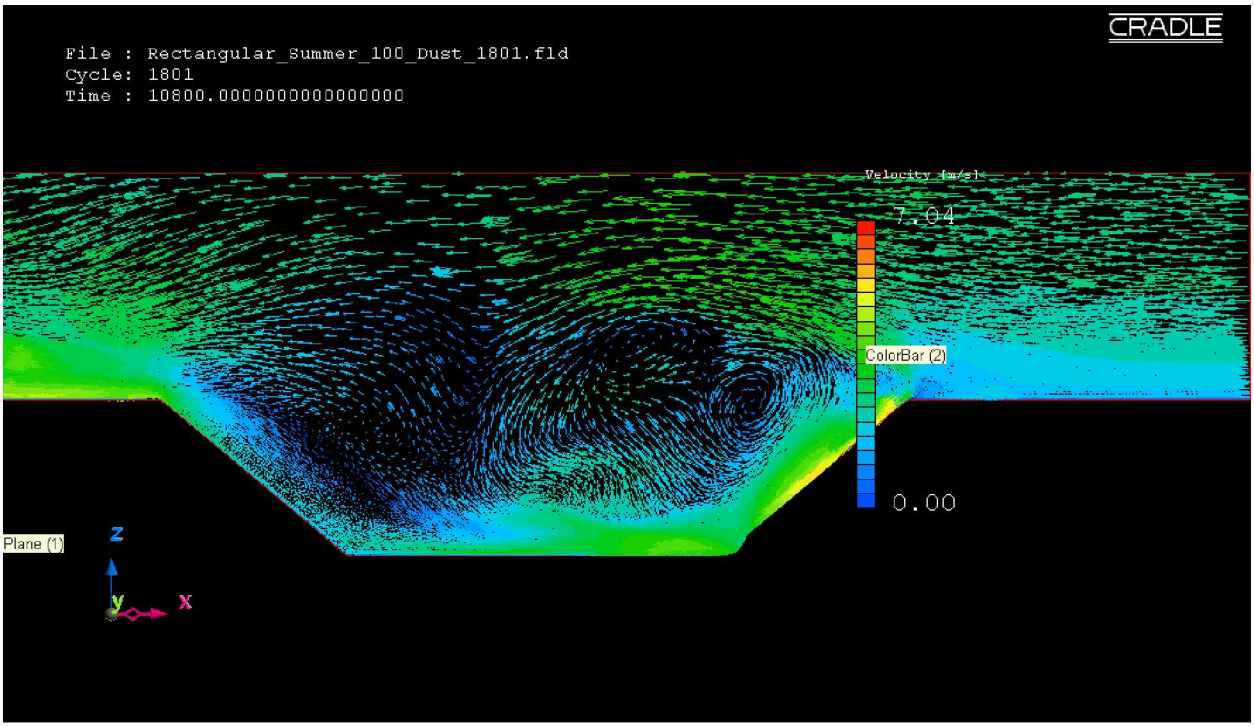

Figure 6.7: Velocity vector profile in the trapezoidal domain for moderate insolation condition.

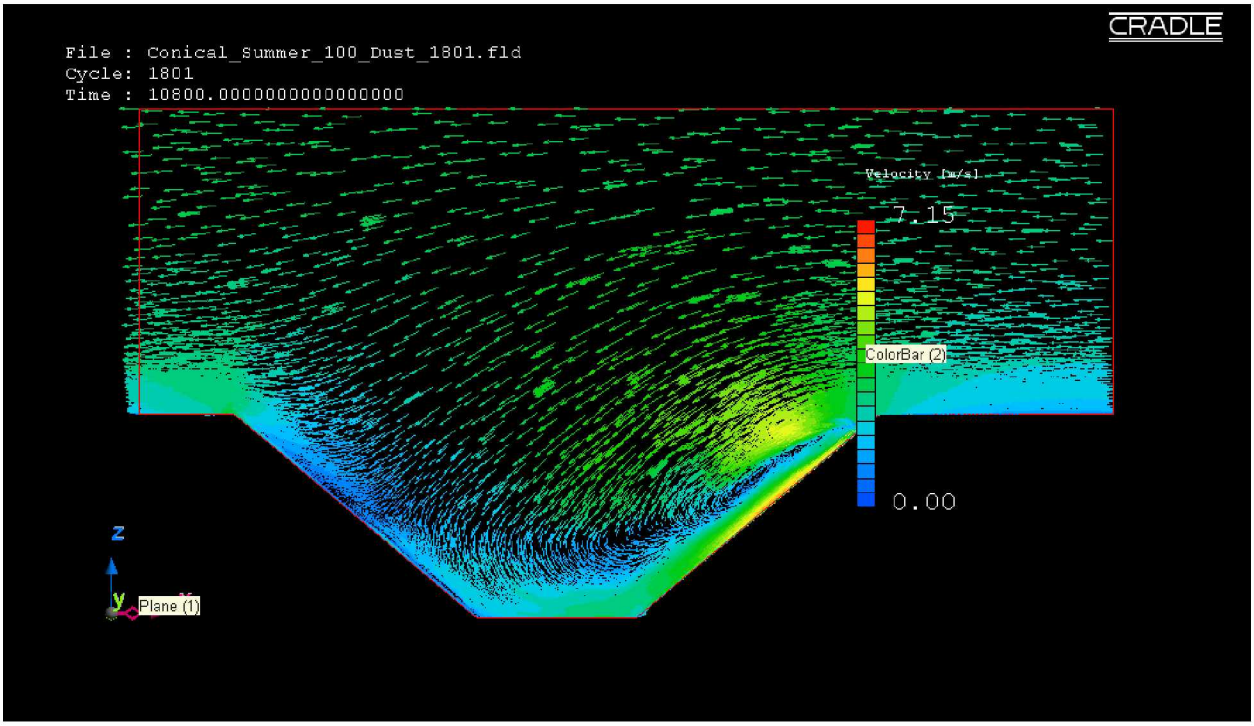

Figure 6.8: Velocity vector profile in the conical domain for moderate insolation condition.

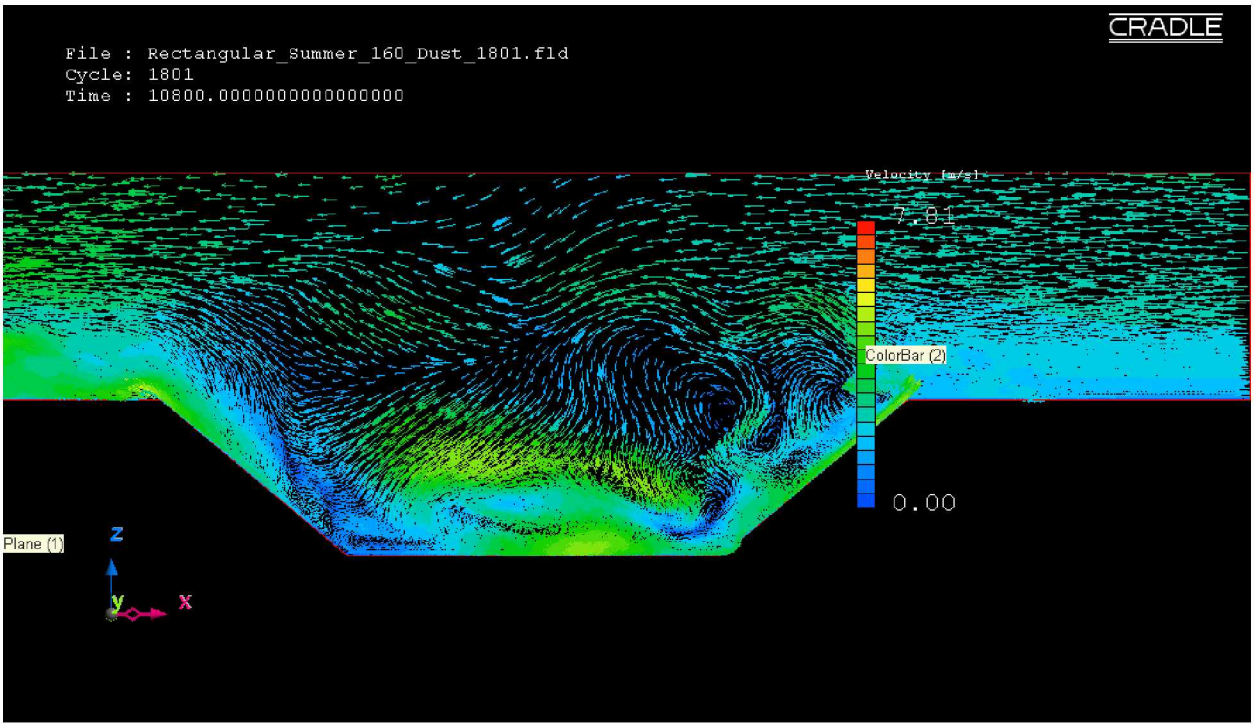

Figure 6.9: Velocity vector profile in the trapezoidal domain for extreme insolation condition.

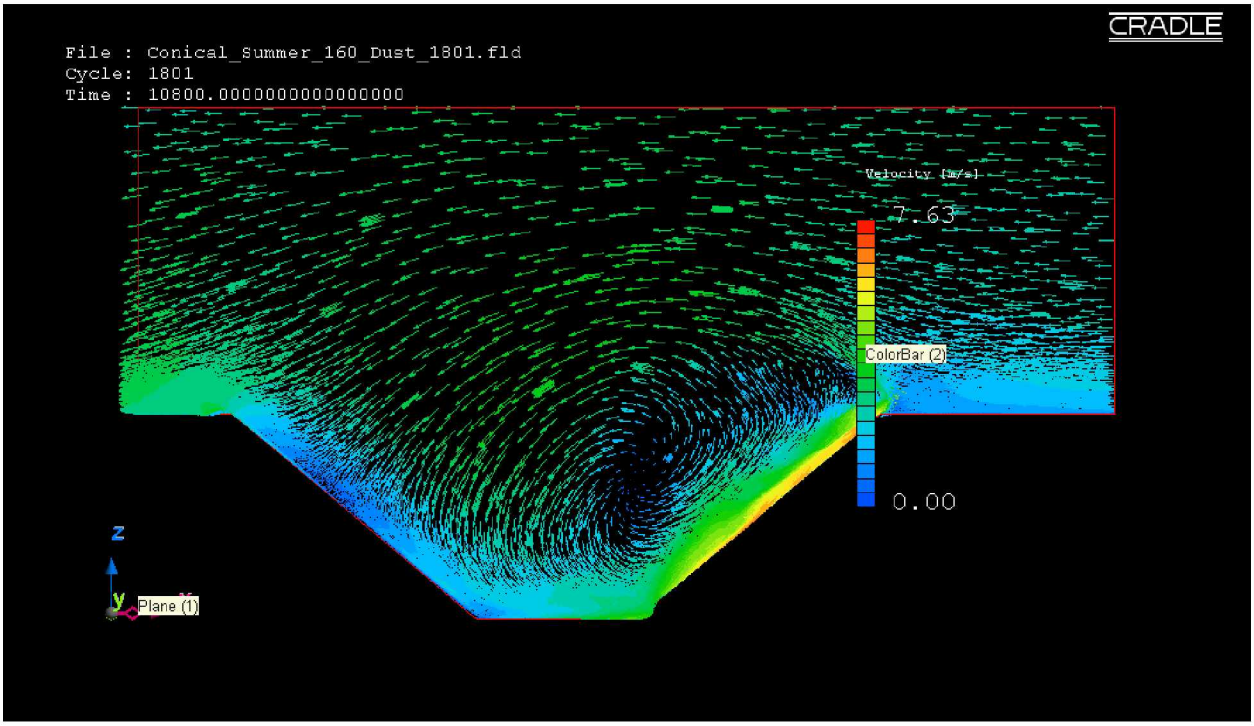

Figure 6.10: Velocity vector profile in the conical domain for extreme insolation condition.

6.1.3 Dust Propagation in the Idealized Domains: Winter Climatic Conditions

In SC/Tetra, the positions of particles are updated during each time step. For solving the turbulent dispersion of the fugitive dust particles, the Lagrangian algorithm is applied. The Lagrangian stochastic model characterizes the advection and the diffusion processes of individual dust particle as a function of time. In this research, the locations of the particles during the simulation are reported at 10 minutes intervals.

Figure 6.11 and Figure 6.12 present the temperature contour plots and the locations of dust particles (as black dots) after three hours of simulation (one hour after particle injection) for a moderate winter condition (-20 W/m^2) inside the respective domains. The temperature contours represent the formation of an atmospheric inversion inside the open-pit. The dense air volume occupies the entire pit. As described in the previous section, airflow inside the domain is stagnant and completely detached from the airflow outside the open-pit. These phenomena resulted in very high retention of fugitive dust particles inside the open-pit domain. The temperature contour plots and the locations of dust particles during an extreme winter condition (-40 W/m^2) inside the two domains are presented in Figure 6.13 and Figure 6.14. Similar stratification in the temperature contours and presence of cold and dense air mass inside the pit can also be observed in Figure 6.13 and Figure 6.14.

As observed from Figure 6.11 to Figure 6.14, presence of the air temperature inversion in the open-pit domains resulted in very high retention of the fugitive dust. Since the airflow inside the domain is completely stagnant for the winter conditions and detached from the airflow outside the domain, the dust particles inside the open-pit remained suspended for a very long duration.

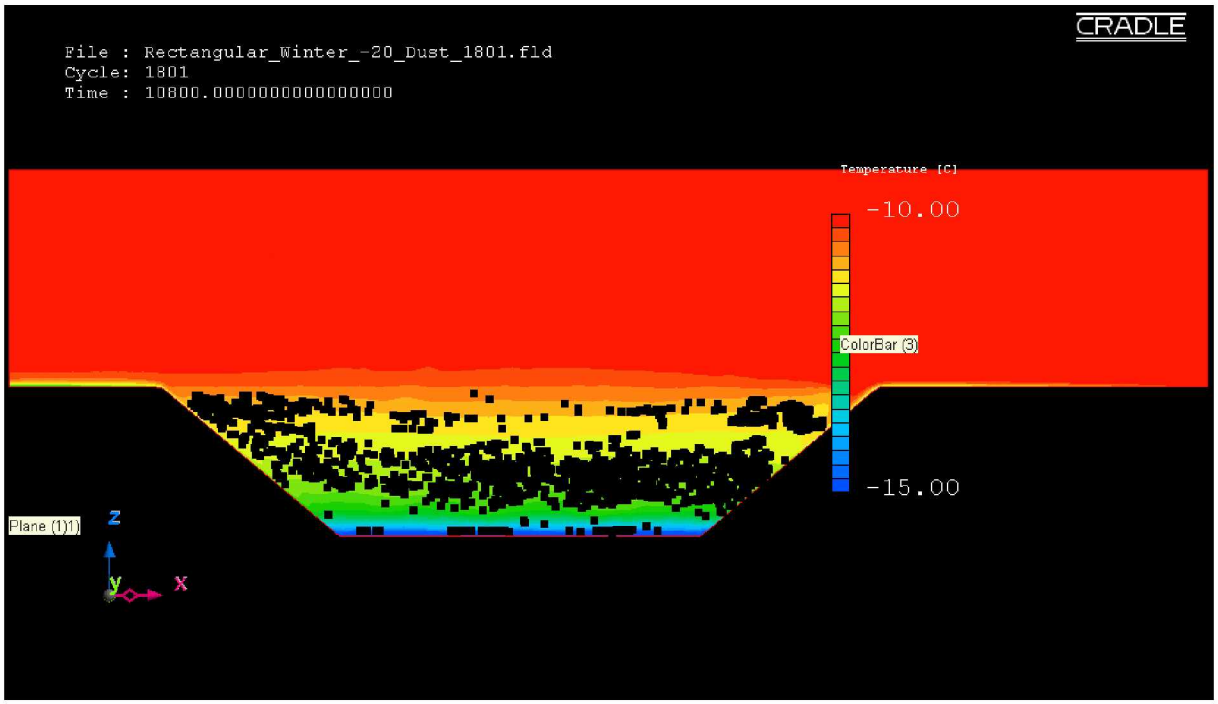

Figure 6.11: Temperature contour profile and locations of dust particles (black dots) in the trapezoidal domain for moderate winter condition.

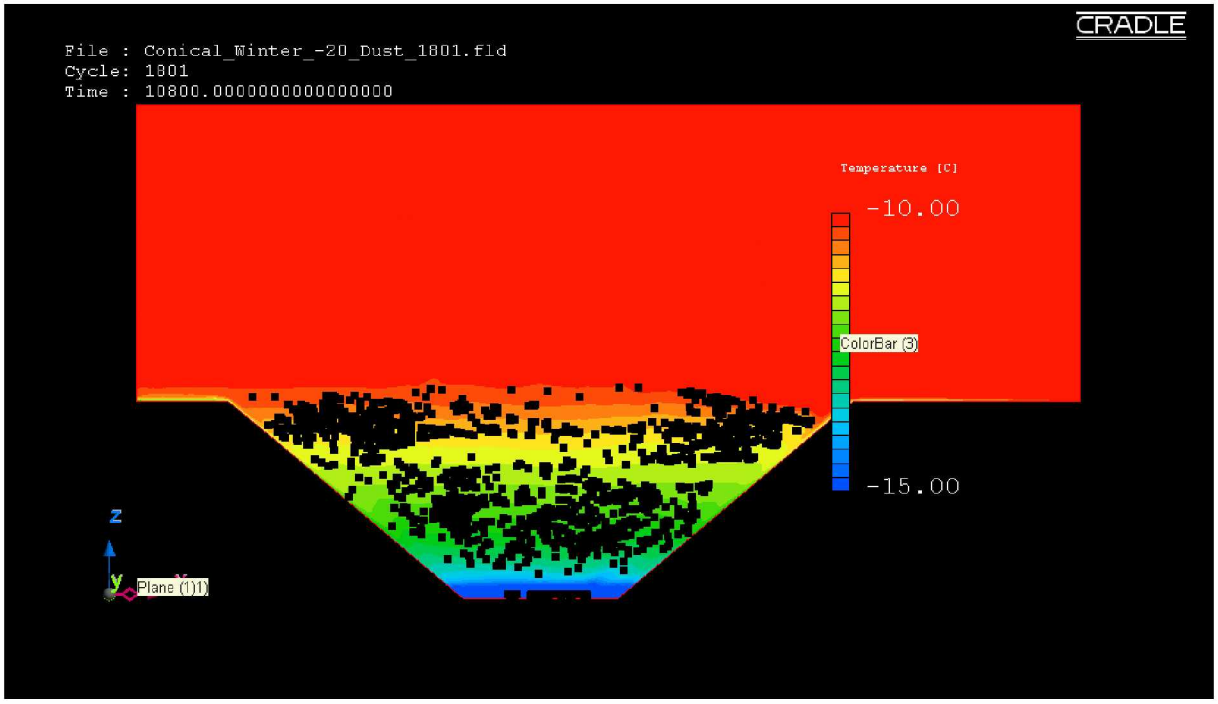

Figure 6.12: Temperature contour profile and locations of dust particles (black dots) in the conical domain for moderate winter condition.

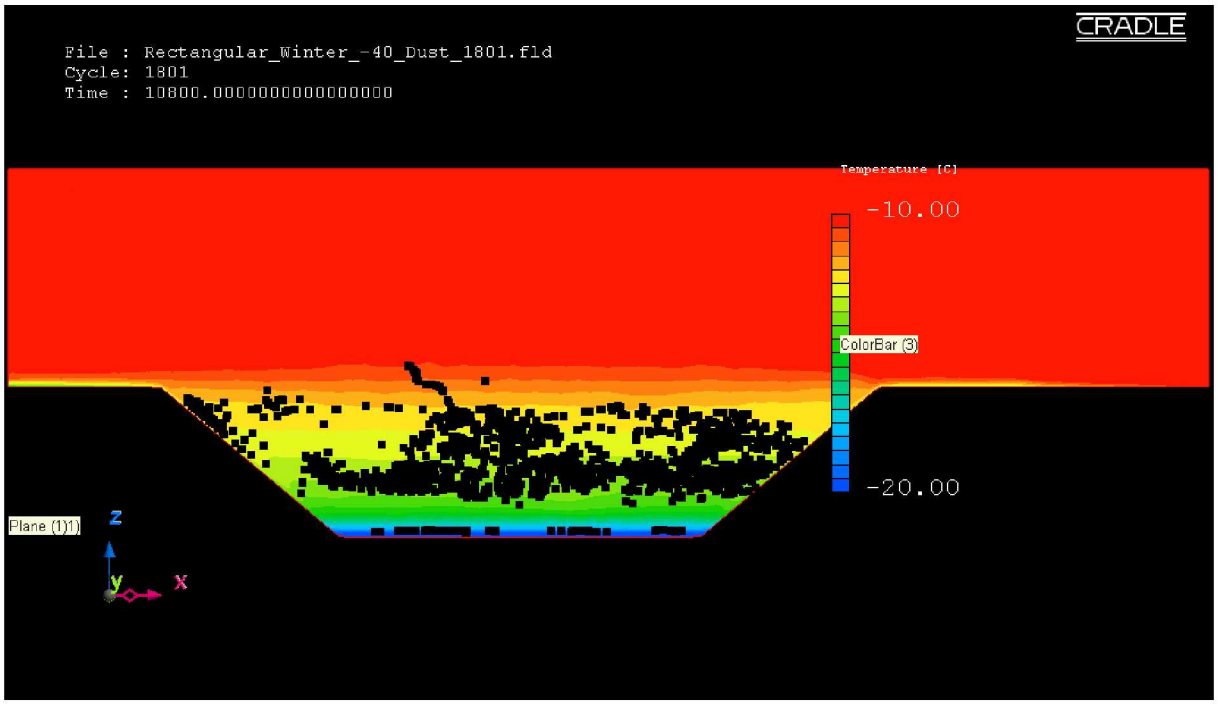

Figure 6.13: Temperature contour profile and locations of dust particles (black dots) in the trapezoidal domain for extreme winter condition.

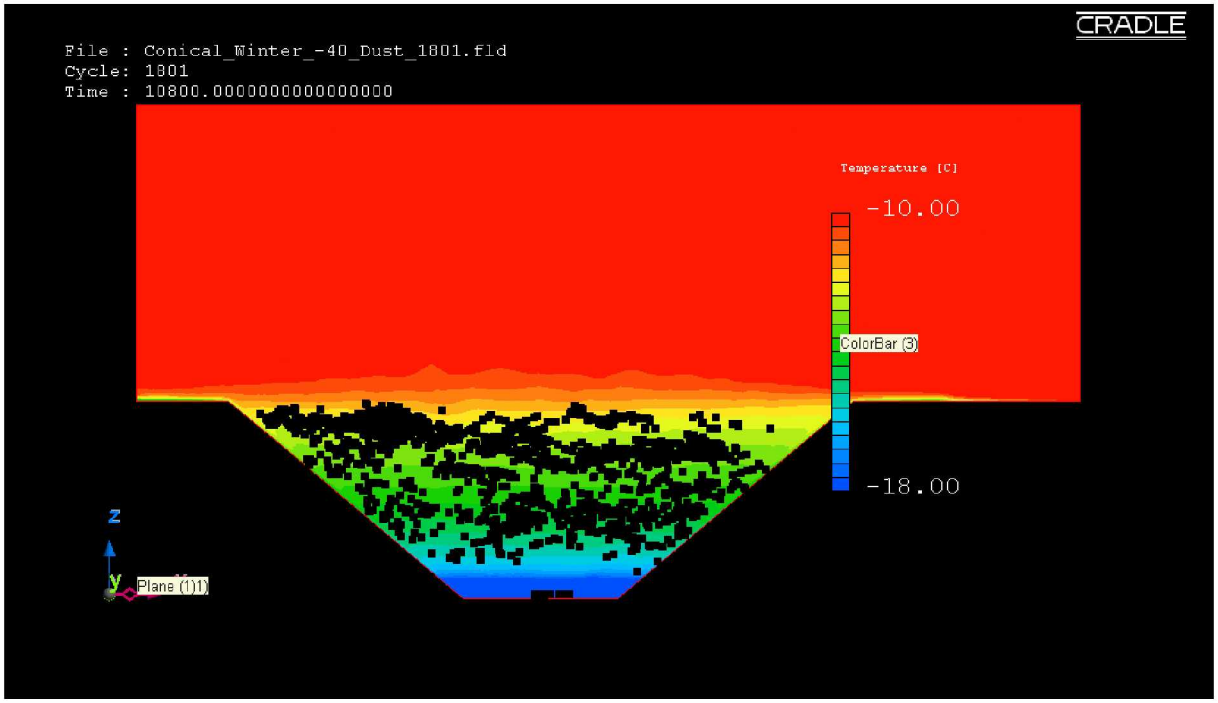

Figure 6.14: Temperature contour profile and locations of dust particles (black dots) in the conical domain for extreme winter condition.

6.1.4 Dust Propagation in the Idealized Domains: Summer Climatic Conditions

Figure 6.15 and Figure 6.16 present the temperature contour plots and the locations of dust particles (as black dots) after three hours of simulation (one hour after particle injection) for a fair insolation condition (60 W/m^2 heat flux) inside the idealized domains. The temperature contours in the domain show profiles that can be correlated with the location of the air recirculation observed in Figure 6.5 and Figure 6.6. The turbulent eddies in the domains are due to the buoyancy flow. The buoyancy results from the temperature difference in the air layers, and is created due to positive heat flux from the pit boundary. Due to formation of the convective (unstable) boundary layer in the domain, the presence of very few dust particles are observed inside the domain. Most of the dust particles are conveyed out of the domain within the first hour after the dust particles are injected. It can be noted that due to the aspects of the domain geometry, the conical domain has much lower dust retention as compared to the trapezoidal domain.

The temperature contour plots and the locations of dust particles inside the idealized domains during a moderate insolation condition (100 W/m^2 heat flux) are presented in Figure 6.17 and Figure 6.18. Due to the well dispersed characteristics of the convective (unstable) boundary layer, most of the remaining dust particles are dispersed all around the domain.

Figure 6.19 and Figure 6.20 present the temperature contour plots and the locations of dust particles for an extreme insolation condition (160 W/m^2 heat flux) inside the idealized domains. As noted previously, the conical domain shows reduced dust retention due to the aspects of the domain geometry.

During summer (Figure 6.15 to Figure 6.20), the convective (unstable) motion of the airflow inside the domains transported most of the dust particles out of the domains within one to two hours after fugitive dusts are generated. A summary of the simulation results for the idealized domains are presented in Table 6.1.

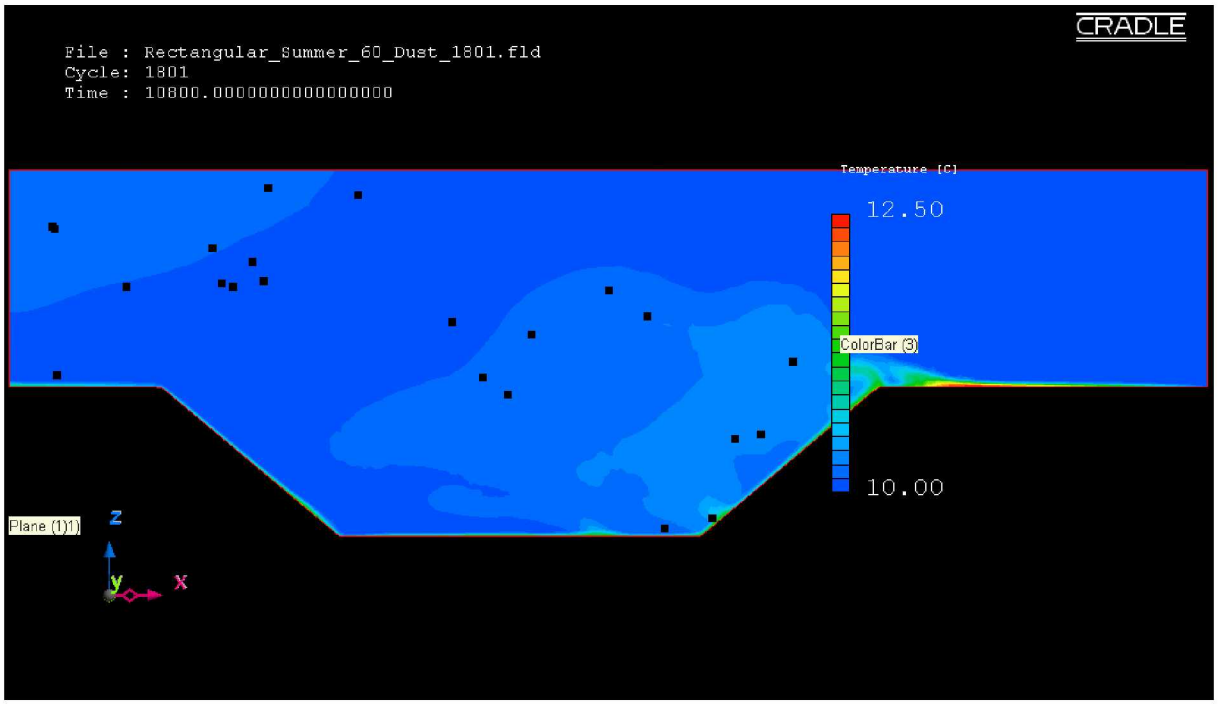

Figure 6.15: Temperature contour profile and locations of dust particles (black dots) in the trapezoidal domain for fair insolation condition.

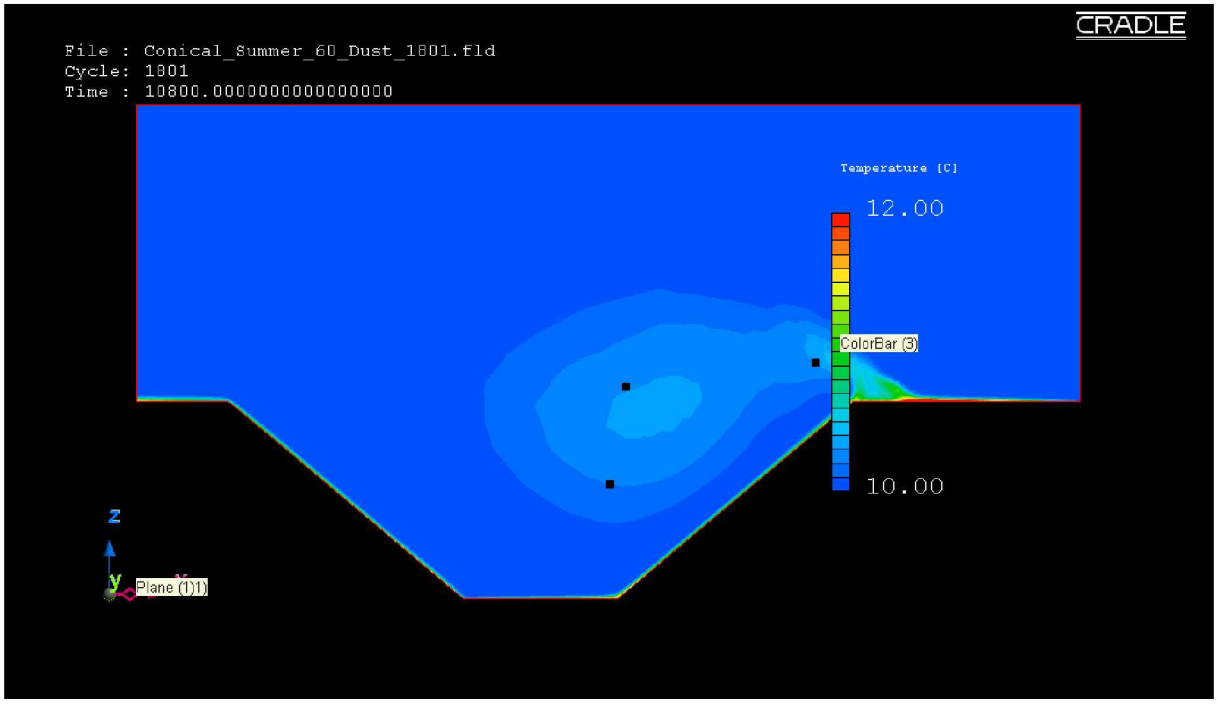

Figure 6.16: Temperature contour profile and locations of dust particles (black dots) in the conical domain for fair insolation condition.

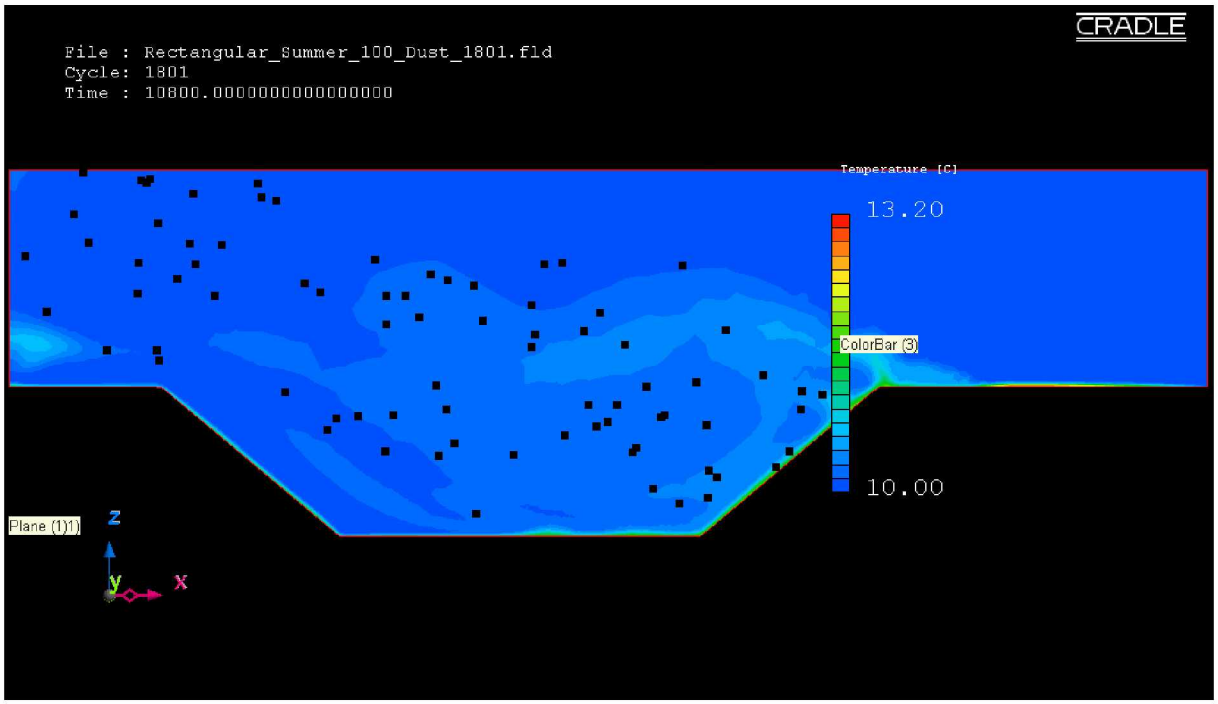

Figure 6.17: Temperature contour profile and locations of dust particles (black dots) in the trapezoidal domain for moderate insolation condition.

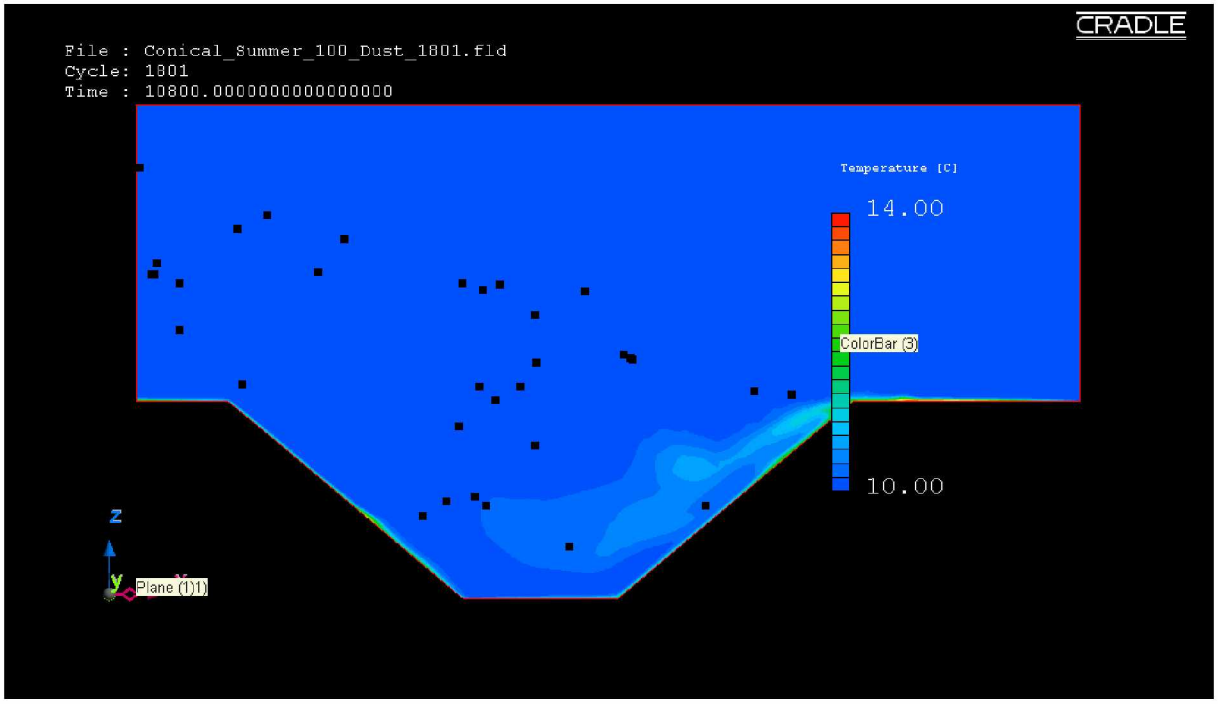

Figure 6.18: Temperature contour profile and locations of dust particles (black dots) in the conical domain for moderate insolation condition.

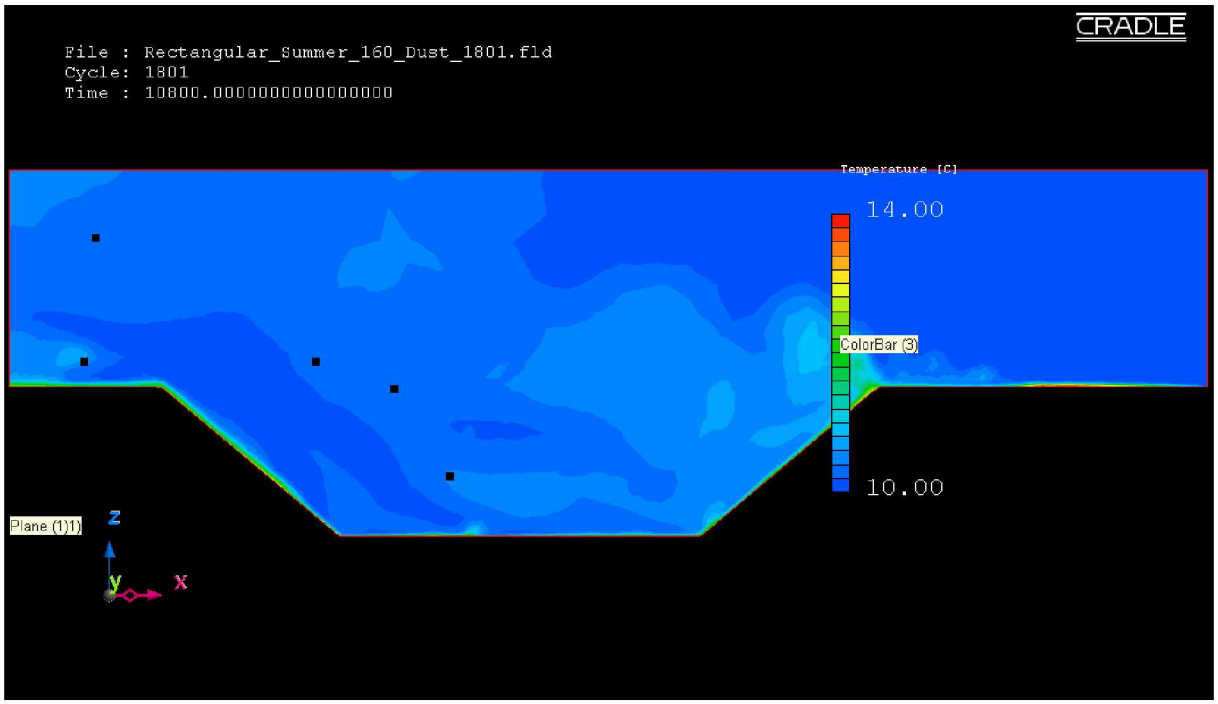

Figure 6.19: Temperature contour profile and locations of dust particles (black dots) in the trapezoidal domain for extreme insolation condition.

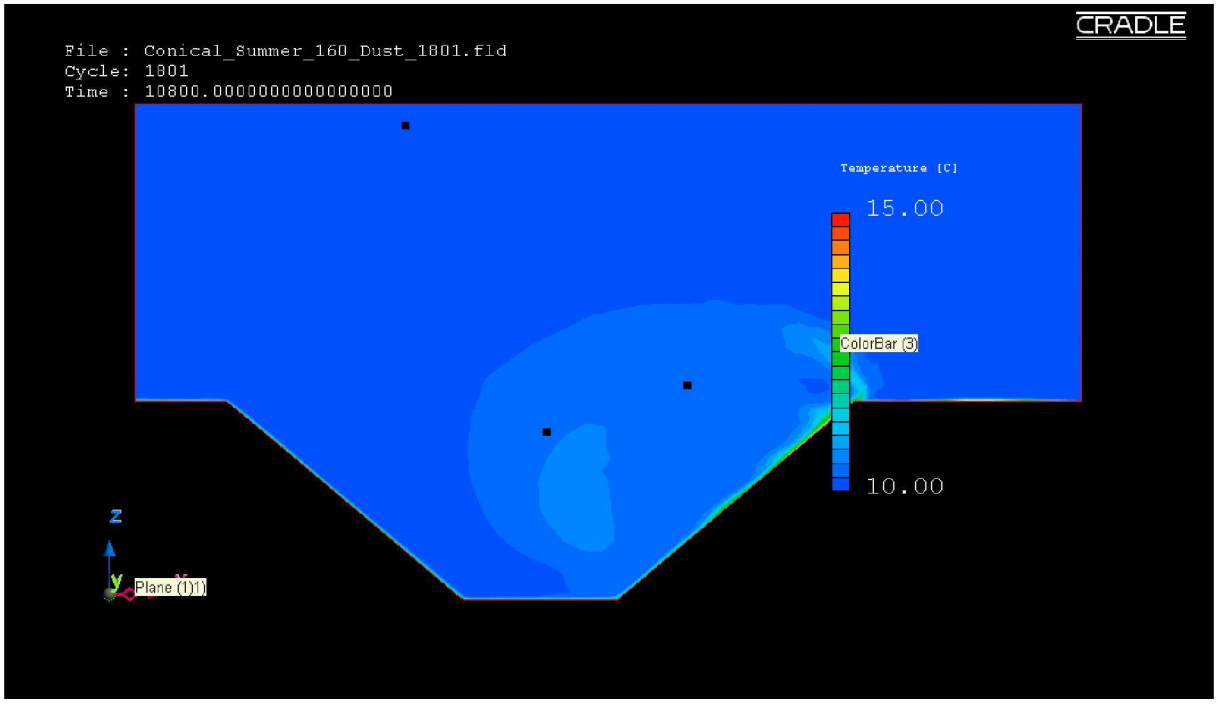

Figure 6.20: Temperature contour profile and locations of dust particles (black dots) in the conical domain for extreme insolation condition.

Table 6.1: A summary of simulation results for the idealized domains using LES method.

Domain	Climate Condition	Heat Flux (W/m^2)	% settled down	% reported outside	Time to clear out
Trapezoidal	**Moderate Winter**	-20	~23	2.68 (6 hrs.)	Unknown
	Extreme Winter	-40	~27.8	1.2 (6 hrs.)	Unknown
	Fair Insolation	60	1.8	98.2	116 min
	Moderate Insolation	100	3	97	144 min
	Extreme Insolation	160	4.6	95.4	80 min
Conical	**Moderate Winter**	-20	~25.2	18.66 (6 hrs.)	Unknown
	Extreme Winter	-40	~26.14	2.1 (6 hrs.)	Unknown
	Fair Insolation	60	0.07	99.93	80 min
	Moderate Insolation	100	1.18	98.82	80 min
	Extreme Insolation	160	1.07	98.93	104 min

Formation of atmospheric air temperature inversion inside the domains during both the moderate and the extreme winter conditions resulted in a very high retention of fugitive dust particles. The simulation results of the winter season (Table 6.1) show extensive entrapment of dust particles in the domain. Few particles (less than 20%) are transported outside the model domain for the entire period of the simulation run.

During summer conditions, due to formation of a convective (unstable) boundary layer inside the open-pit domains, almost all of the dust particles (more than 95%) are transported out of the domain by the airflow. As previously noted, retention of fugitive dust is also dependent on the aspects of a domain. It is observed that fugitive dust particles clear out of the conical open-pit domain sooner than the trapezoidal domain.

6.2 Simulation Results of the Actual Open-Pit Domain

Similar simulation parameters, as in the case of idealized domains, are used for prediction of fugitive dust retention in the model domain of the selected open-pit mine. In simulating the actual 2013 open-pit domain, initially, a steady state wind velocity profile is used as the initial velocity profile for the transient simulation. To develop the flow regimes, the model domain is simulated for four hours of initial transient simulation with heat flux and airflow temperature.

6.2.1 Airflow Regimes: Winter Climatic Conditions

The airflow pattern inside the actual open-pit domain is observed to change for various seasonal conditions due to the variability in the amount of sensible heat flux. Similar variations were also observed for the idealized domains.

Figure 6.21 and Figure 6.22 present the airflow patterns in the actual open-pit domain along the X-Z (Y = 1290 m) plane after initial four hours of simulation for a moderate winter condition (-20 W/m^2) using the RANS and the LES methods respectively. A flow separation can be observed near the pit-rim in both the domains, which is caused due to the formation of an atmospheric inversion inside the open-pit. Airflow inside the domain is stagnant and completely detached from airflow outside the open-pit. It can be observed (Figure 6.21 and Figure 6.22) that the height of the inversion layer predicted by the LES method is higher than predicted by the RANS method due to formation of large eddies by the LES method. Airflow patterns during an extreme winter condition (-40 W/m^2) inside the actual open-pit domain using the RANS and the LES methods are presented in Figure 6.23 and Figure 6.24, respectively. Similar flow separation phenomena can be observed in Figure 6.23 and Figure 6.24.

As can be observed from Figure 6.21 to Figure 6.24, the presence of the air temperature inversion in the open-pit domain may result in higher retention of fugitive dust. Since the airflow inside the domain is completely stagnant for the winter conditions, and detached from the airflow outside the domain, dust particles inside the open-pit may remain suspended for a very long duration.

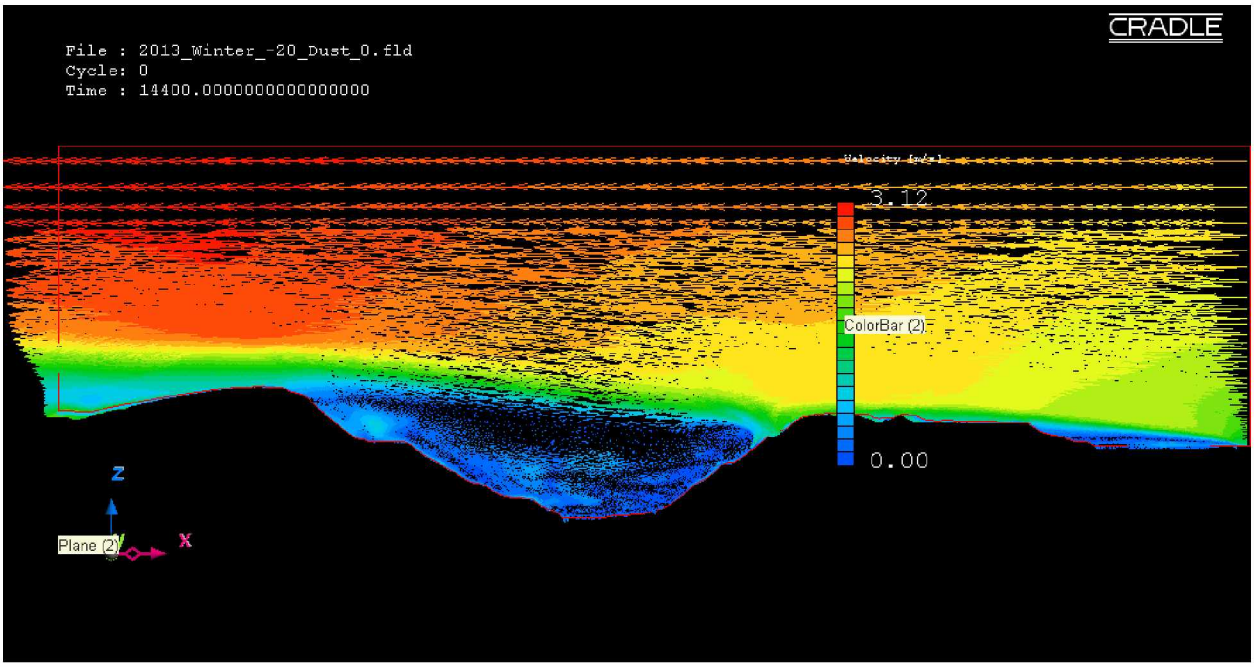

Figure 6.21: Velocity vector profile in the actual open-pit domain for moderate winter condition using the RANS method.

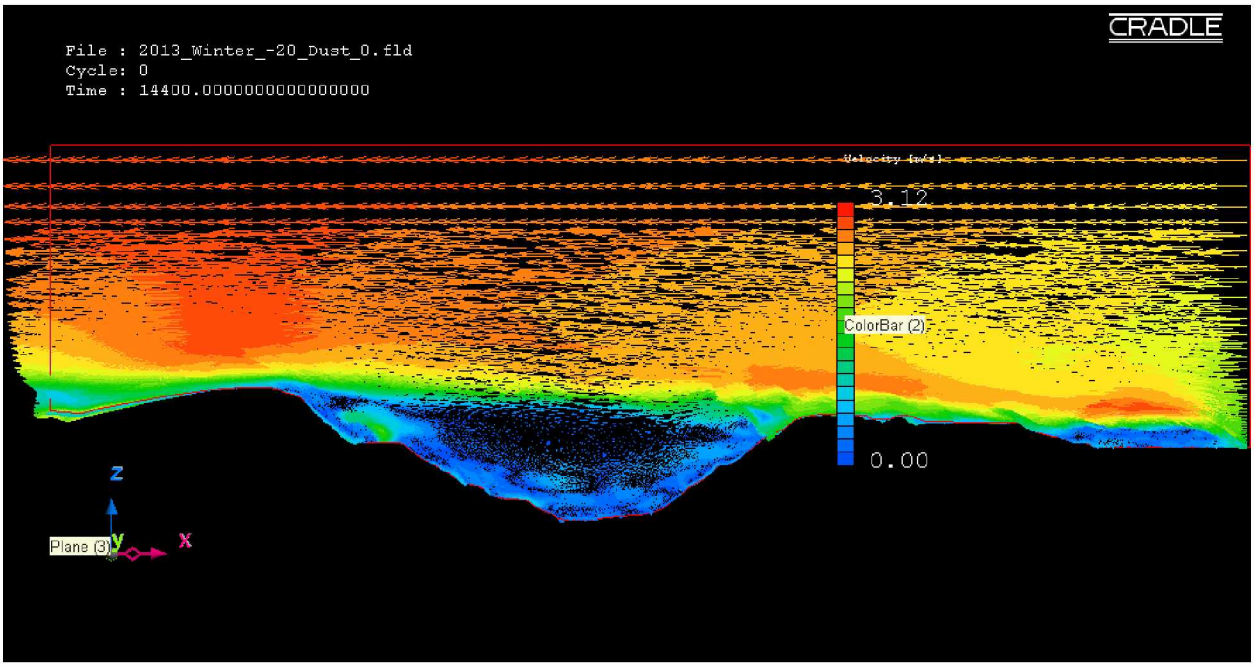

Figure 6.22: Velocity vector profile in the actual open-pit domain for moderate winter condition using the LES method.

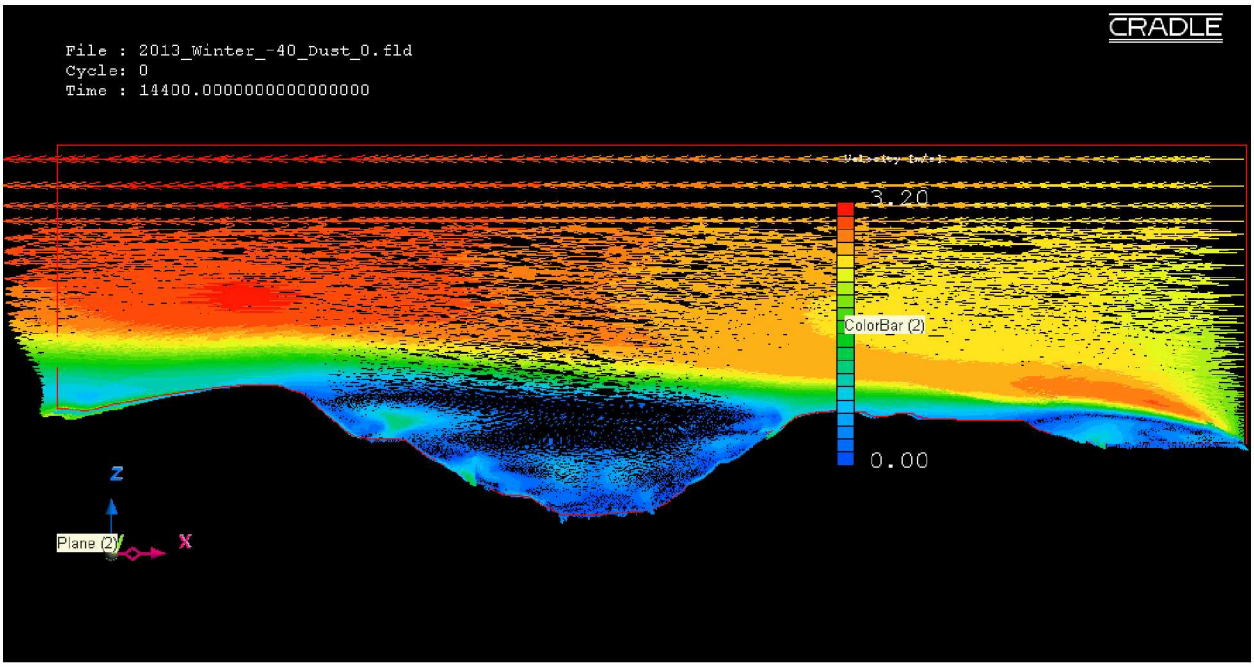

Figure 6.23: Velocity vector profile in the actual open-pit domain for extreme winter condition using the RANS method.

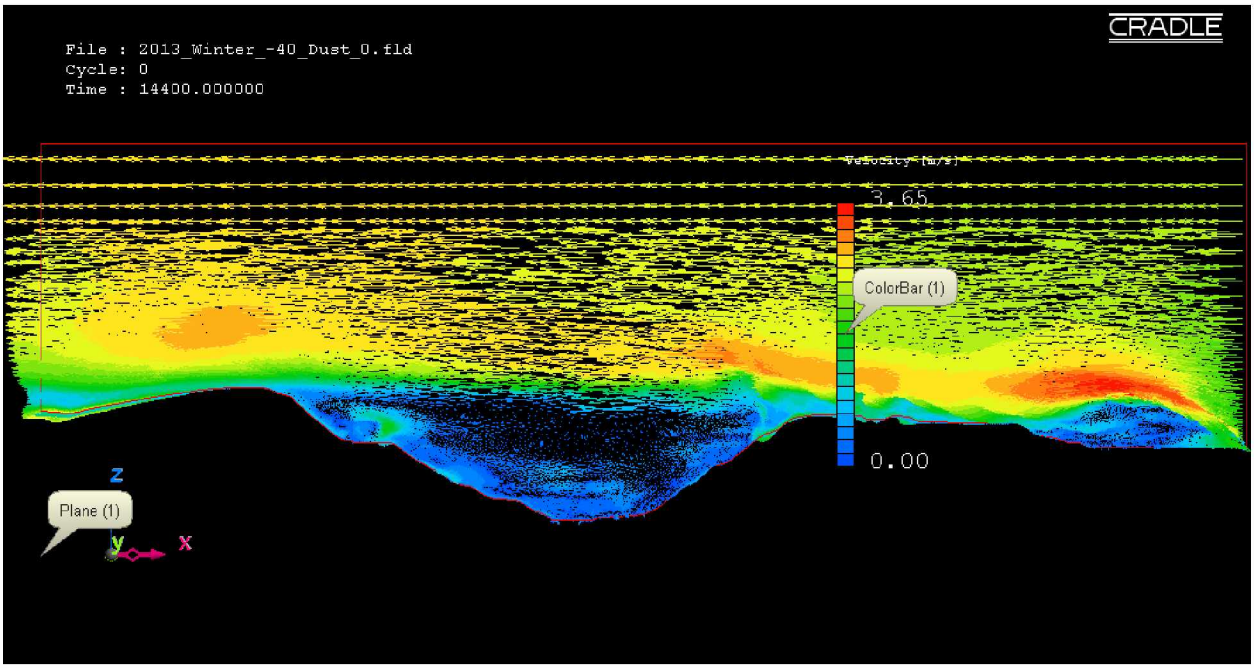

Figure 6.24: Velocity vector profile in the actual open-pit domain for extreme winter condition using the LES method.

6.2.2 Airflow Regimes: Summer Climatic Conditions

Figure 6.25 and Figure 6.26 present the airflow patterns along an X-Z (Y = 1290 m) plane after four and half hours of simulation (30 minutes after dust particle injection) for a fair insolation condition (60 W/m^2) using the RANS and the LES methods respectively. Recirculation profiles inside the open-pit domain indicate the formation of a convective (unstable) boundary layer. The locations of the convective eddies vary, however, based on the choice of the turbulence method.

Airflow patterns predicted by the RANS and the LES methods during a moderate insolation condition (100 W/m^2) in the actual open-pit mine are presented in Figure 6.27 and Figure 6.28. Formation of a convective (unstable) boundary layer with various turbulent eddies can be observed in the model domain.

Figure 6.29 and Figure 6.30 present airflow patterns for an extreme insolation condition (160 W/m^2) inside the actual open-pit domain using the RANS and the LES methods. Similar convective boundary layer with numerous turbulent eddies is observed inside the domain. .

During summer conditions (Figure 6.25 to Figure 6.30), a convective (unstable) motion in the airflow inside the domains may carry most of the dust particles out of the domains in relatively short duration. The eddy viscosity regimes in the selected simulation domain are presented in Section 6.2.3.

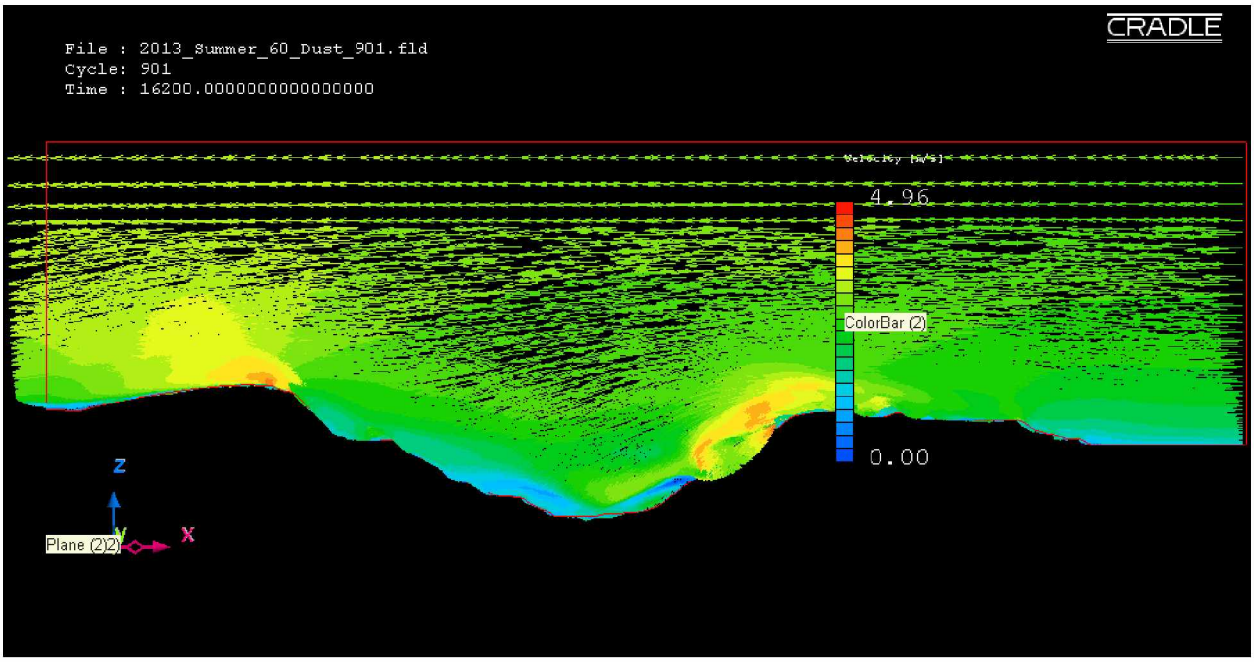

Figure 6.25: Velocity vector profile in the actual open-pit domain for fair insolation condition using the RANS method.

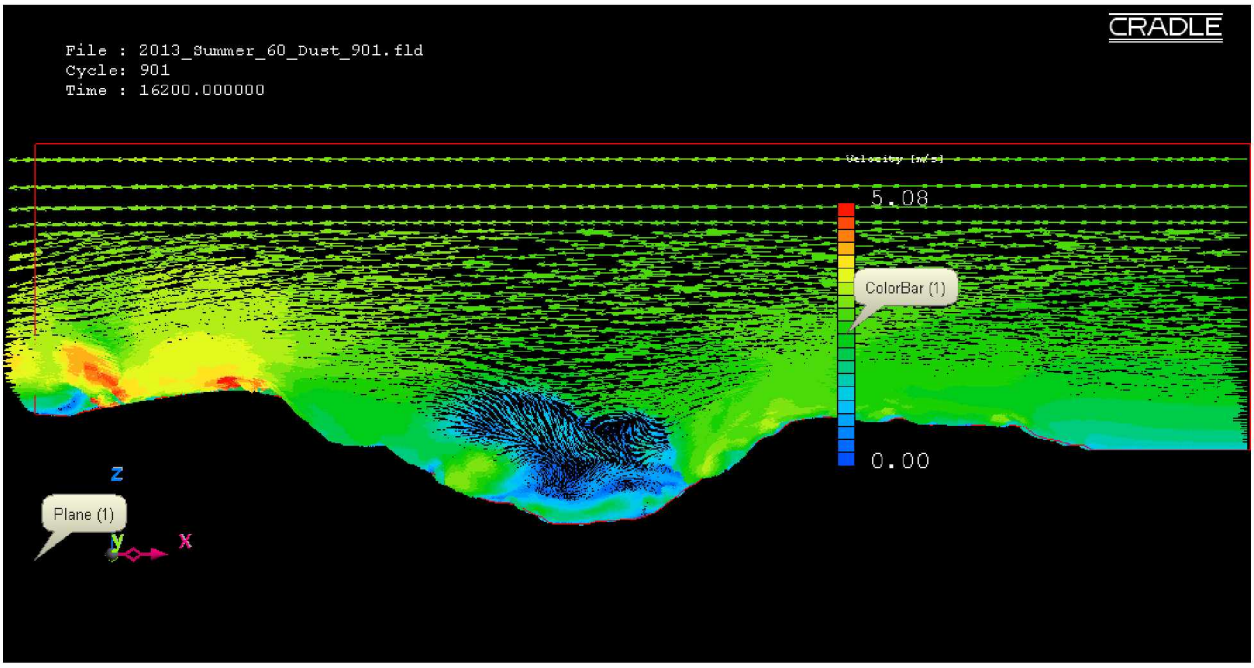

Figure 6.26: Velocity vector profile in the actual open-pit domain for fair insolation condition using the LES method.

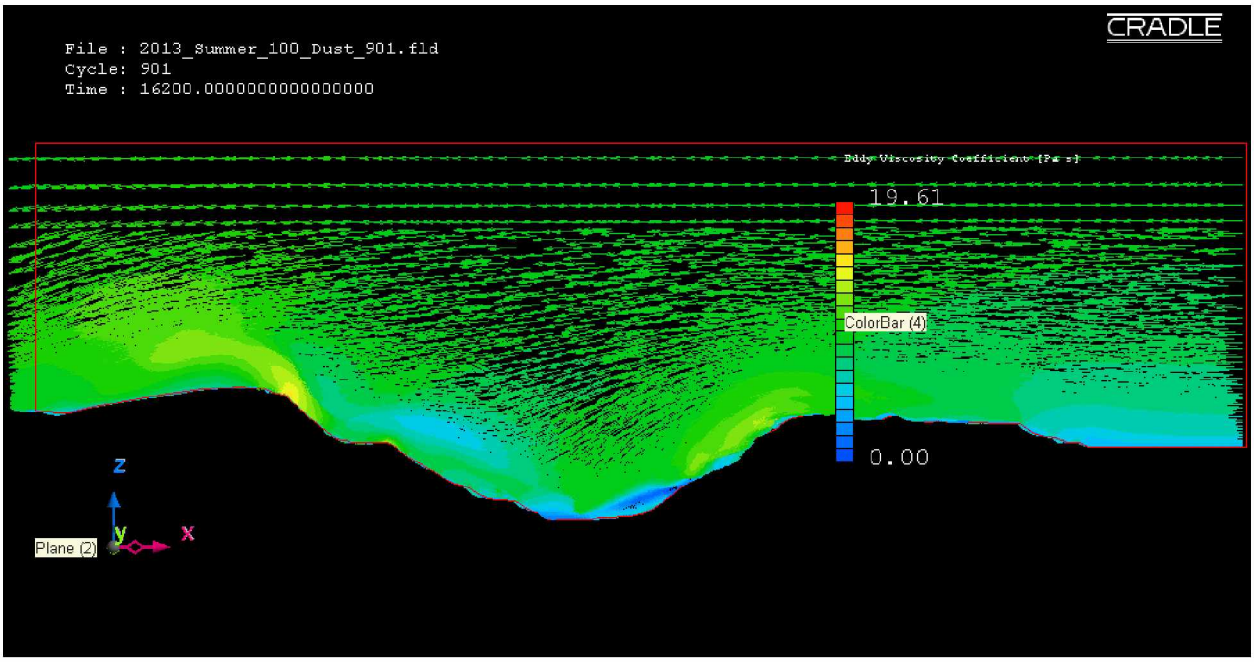

Figure 6.27: Velocity vector profile in the actual open-pit domain for moderate insolation condition using the RANS method.

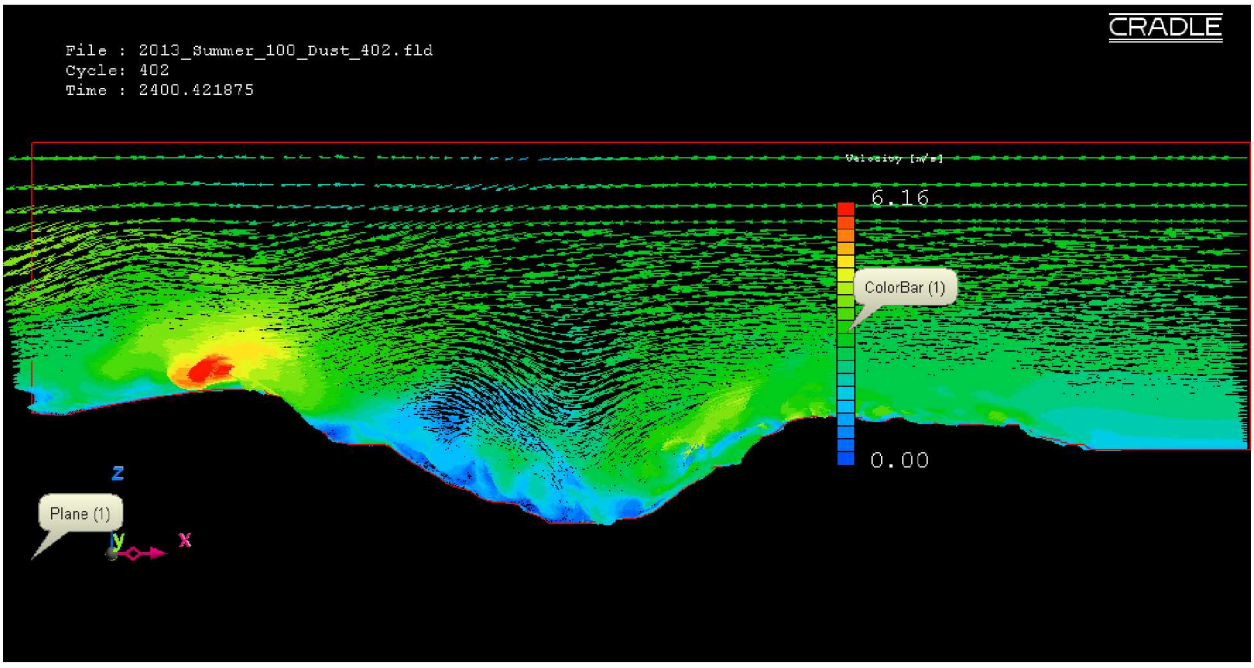

Figure 6.28: Velocity vector profile in the actual open-pit domain for moderate insolation condition using the LES method.

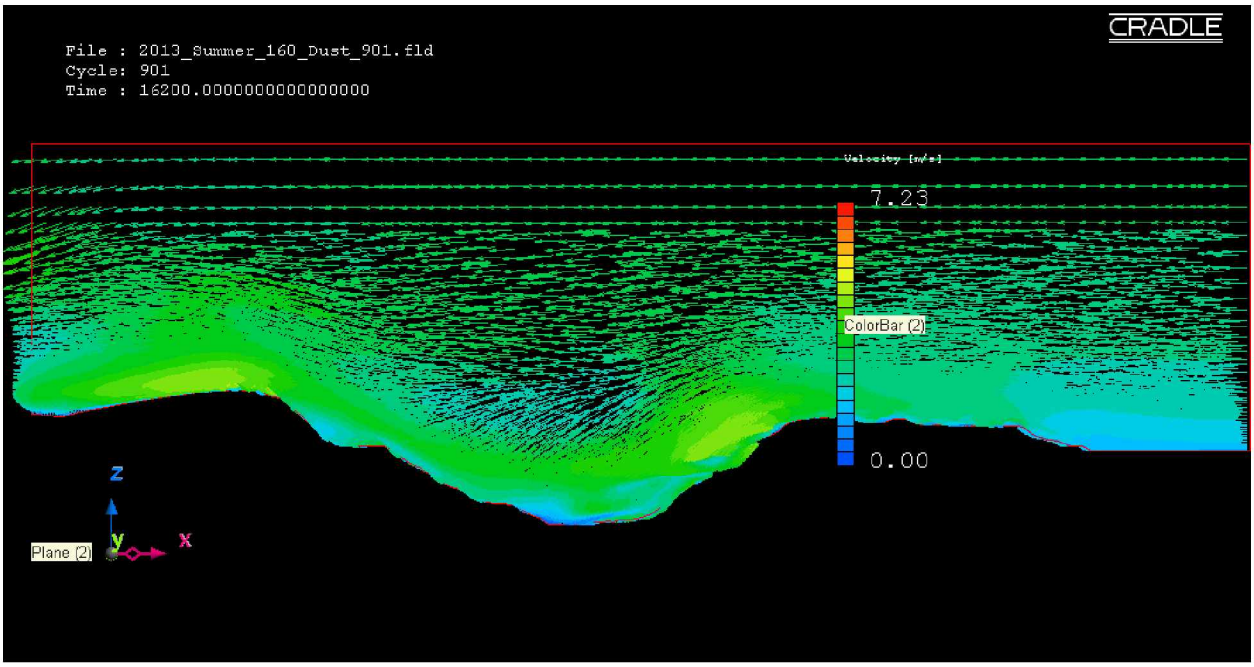

Figure 6.29: Velocity vector profile in the actual open-pit domain for extreme insolation condition using the RANS method.

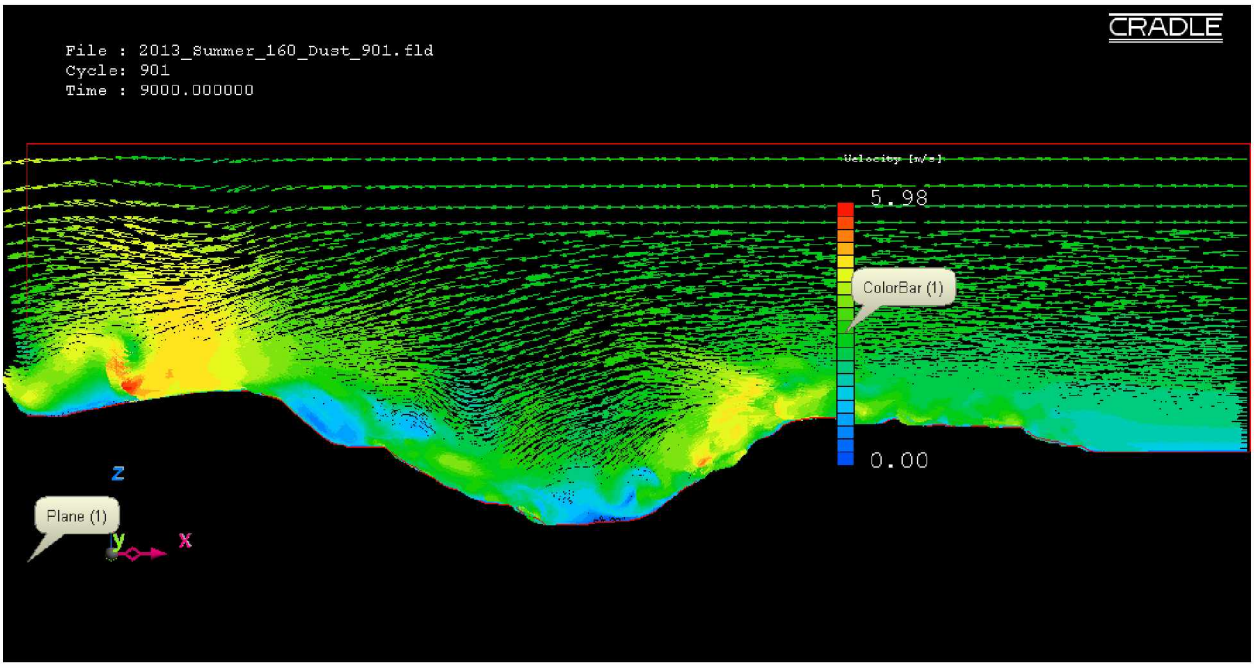

Figure 6.30: Velocity vector profile in the actual open-pit domain for extreme insolation condition using the LES method.

6.2.3 Eddy Viscosity Regimes: Winter Climatic Conditions

Figure 6.31 and Figure 6.32 present the eddy viscosity regimes in the actual open-pit domain along an X-Z (Y = 1290 m) plane after the initial four hours of simulation for a moderate winter condition (-20 W/m^2) using the RANS and the LES methods respectively. The turbulent transfer of momentum by turbulent eddies give rise to an internal fluid friction inside the fluid flow, which is quantified as eddy viscosity. The airflow separation discussed earlier resulted in stratification of high magnitude eddy viscosity contours near the pit-rim. The top of the atmospheric inversion is also located at the pit-rim. The airflow inside the domain is stagnant and completely detached from the airflow outside the open-pit. As a result, very limited variations in the eddy viscosity contours can be observed inside the pit cavity. It can be observed (Figure 6.31 and Figure 6.32) that the eddy viscosity contours for the RANS method show very high magnitude stratification in comparison to the LES method. The stratification of the high magnitude eddy viscosity contours extends across the length of the pit to the outlet boundary for the RANS method. While for the LES method, the high magnitude eddy viscosity contours only extend across the pit-rim. The continuation of the eddy viscosity contours across the pit to the outlet boundary is due to the high magnitude resulted from RANS method.

Eddy viscosity regimes developed by RANS and LES methods during an extreme winter condition (-40 W/m^2) within the actual open-pit domain are presented in Figure 6.33 and Figure 6.34. As in the case of moderate winter condition, similar stratification of the eddy viscosity contours can be observed in Figure 6.33 and Figure 6.34.

The presence of an atmospheric air temperature inversion (Figure 6.31 to Figure 6.34) can also be noted in the open-pit domain which may result in higher retention of fugitive dust. The turbulent energy contours inside the open-pit domain for the winter conditions are presented in Appendix A (Figure A.1, Figure A.3, Figure A.5 and Figure A.7). The corresponding magnitudes of turbulent energy (Figure A.2, Figure A.4, Figure A.6 and Figure A.8) are plotted along two vertical lines: one is located at the pit-bottom and the other is located near the pit-rim. The turbulent energy contours and the profiles (Figure A.1 to Figure A.8) show an increment in the magnitudes of turbulent energy at an elevation of 615 m. The pit-rim of the open-pit mine is located at that elevation. High magnitude of turbulent energy indicates an increase in turbulence near the pit-rim, which is due to the shear in between the cold stratified air inside the cavity and

the airflow above the pit-rim. The turbulent energy contours and the turbulent energy profiles (Figure A.1 to Figure A.8), therefore, resemble the presence of an atmospheric air temperature inversion inside the open-pit domain for winter conditions.

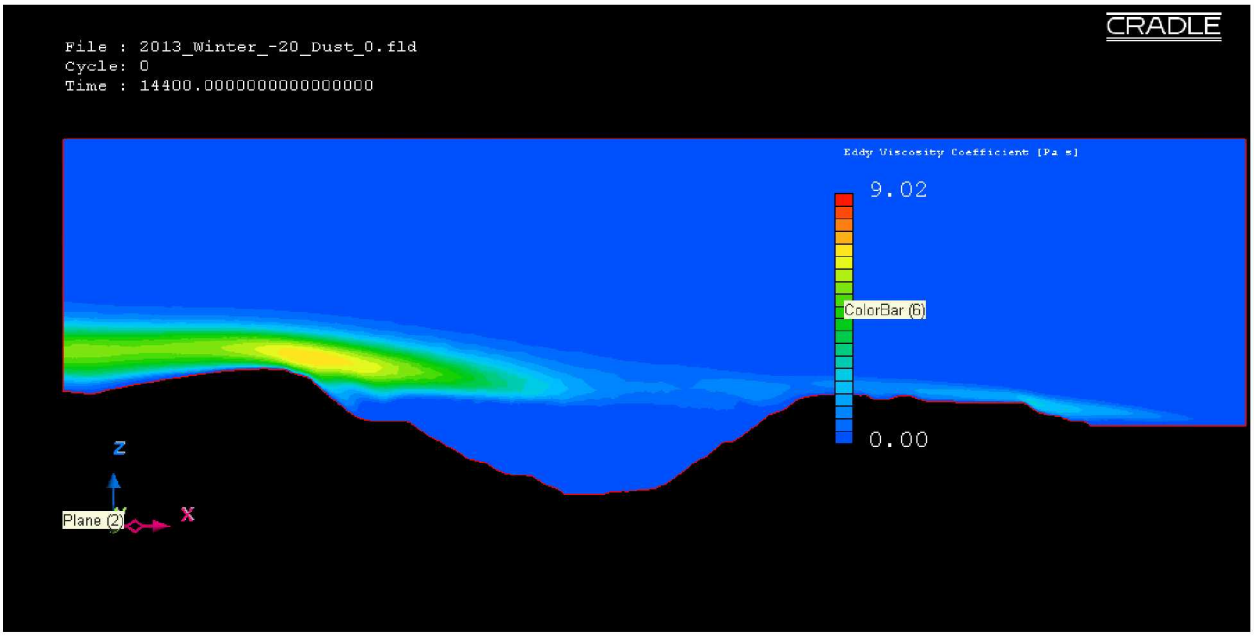

Figure 6.31: Eddy viscosity regimes in the actual open-pit domain for moderate winter condition using the RANS method.

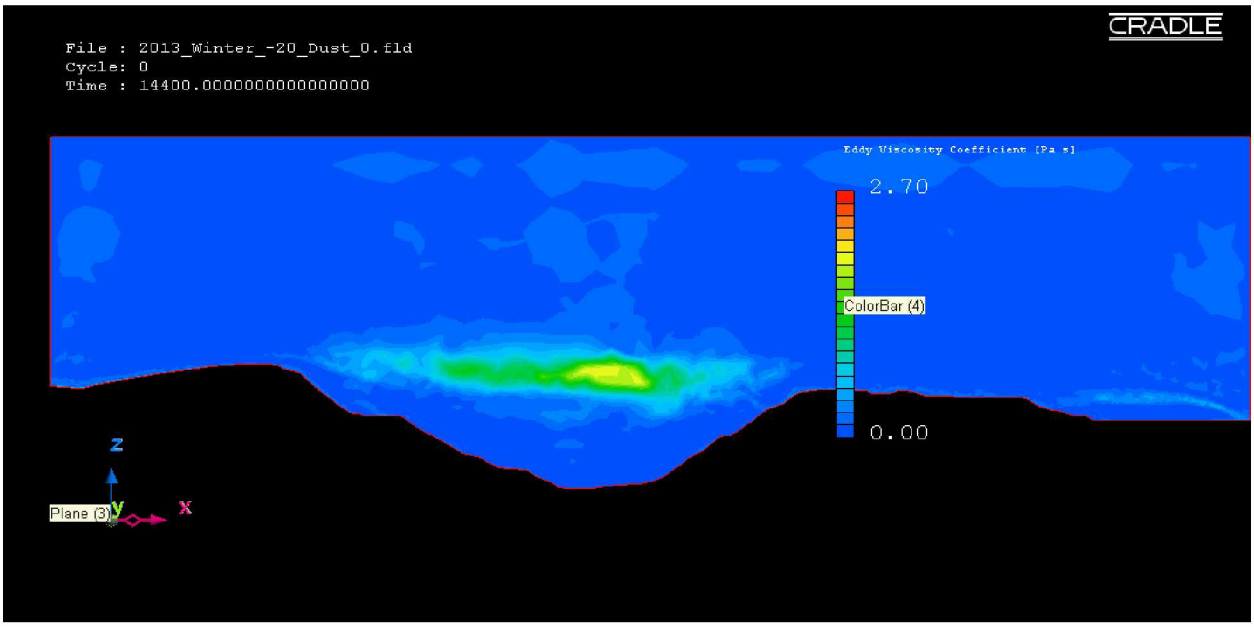

Figure 6.32: Eddy viscosity regimes in the actual open-pit domain for moderate winter condition using the LES method.

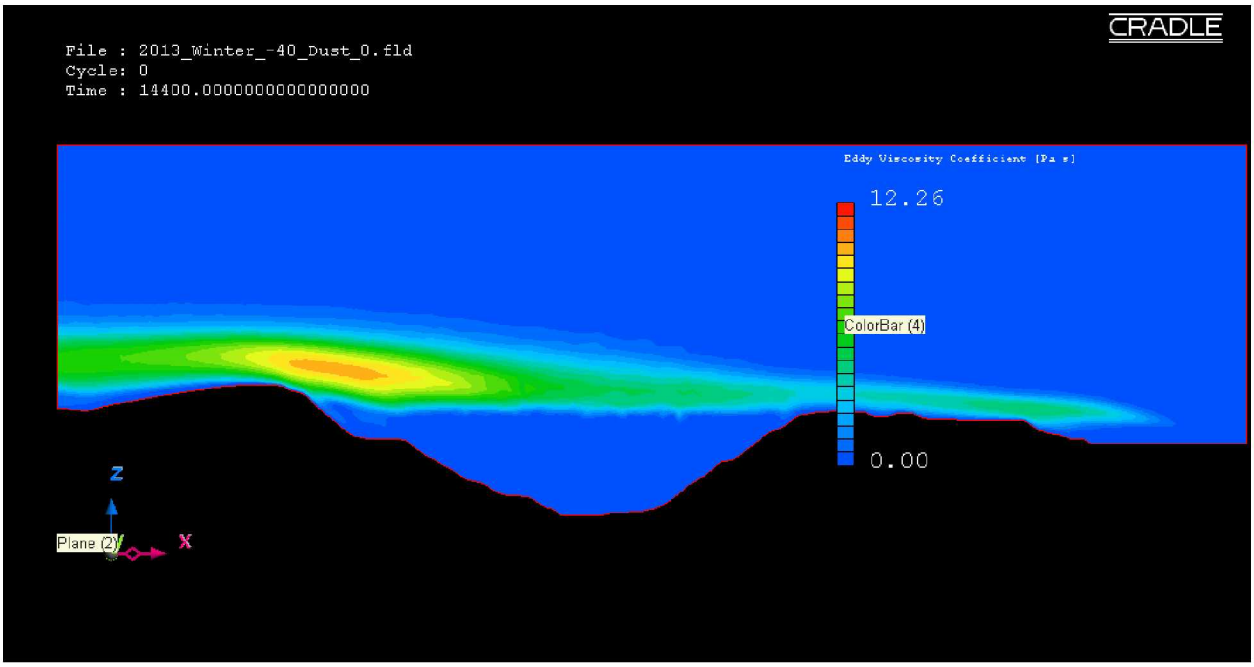

Figure 6.33: Eddy viscosity regimes in the actual open-pit domain for extreme winter condition using the RANS method.

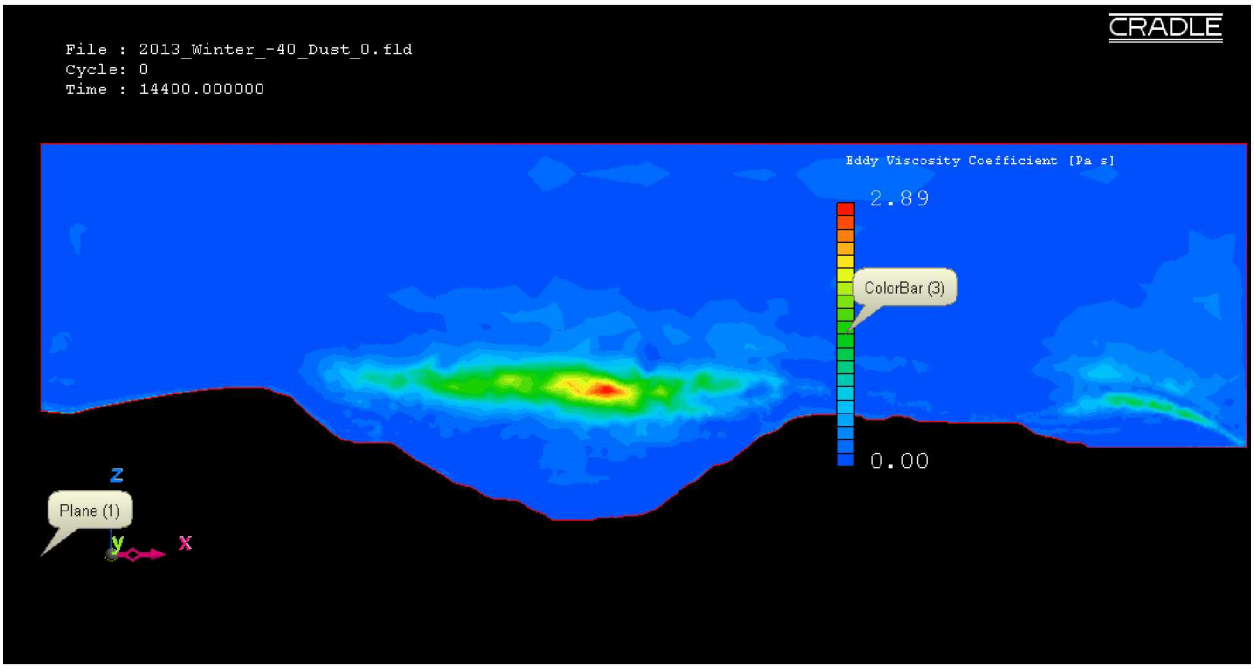

Figure 6.34: Eddy viscosity regimes in the actual open-pit domain for extreme winter condition using the LES method.

6.2.4 Eddy Viscosity Regimes: Summer Climatic Conditions

Figure 6.35 and Figure 6.36 present the respective eddy viscosity regimes along X-Z (Y = 1290 m) plane after four and half hours of simulation (30 minutes after dust particle injection) for a fair insolation condition (60 W/m^2) using the RANS and the LES methods. The locations of the high magnitude eddy viscosity contours can be correlated with the locations of the recirculation profiles where the internal fluid frictions are higher. However, the eddy viscosity contours from RANS method show very high magnitudes of fluid frictions in areas which are close to the pit-bottom. From the contour plot of the eddy viscosity parameter (Figure 6.35), an absence of the convective boundary layer is evident. Whereas, the eddy viscosity contours from the LES method resemble the formation of the convective (unstable) boundary layer in the open-pit domain.

Eddy viscosity regimes predicted by the RANS and the LES methods during a moderate insolation condition (100 W/m^2) in the actual open-pit mine are presented in Figure 6.37 and Figure 6.38. As in the case of the fair insolation condition, similar phenomena (Figure 6.35 and Figure 6.36) of stratified eddy viscosity contours can be observed.

Figure 6.39 and Figure 6.40 present the eddy viscosity regimes for an extreme insolation condition (160 W/m^2) inside the actual open-pit domain using the RANS and the LES methods. The stratification of the eddy viscosity contours resembling the formation of numerous turbulent eddies is similar to the previous two insolation conditions.

During summer, (Figure 6.35 to Figure 6.40), formation of a convective (unstable) motion in the airflow inside the domains can be noted, which may transport most of the dust particles out of the domains in a relatively short duration. The turbulent energy contours inside the open-pit domain and the corresponding magnitudes of turbulent energy along two vertical lines (one at the pit-bottom and the other near the pit-rim) for the summer conditions are presented in Appendix A (Figure A.9 to Figure A.20). The turbulent energy profiles from Figure A.9 to Figure A.20 show an increment in magnitudes of turbulent energy inside the open-pit cavity. High turbulent energy inside the pit cavity indicates presence of convective eddies inside the open-pit domain. The turbulent energy contours and the profiles, therefore, resemble the formation of a convective (unstable) boundary layer inside the open-pit domain for summer conditions. The propagation of the dust particles in the selected simulated domain is presented in the next sections.

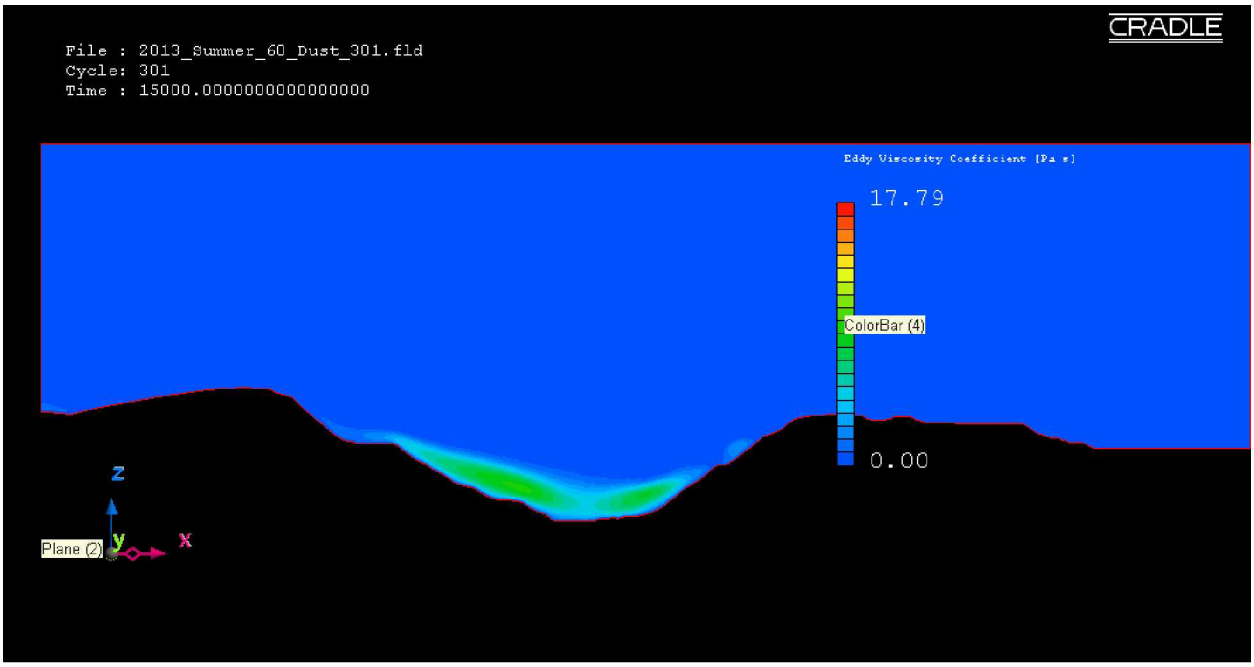

Figure 6.35: Eddy viscosity regimes in the actual open-pit domain for fair insolation condition using the RANS method.

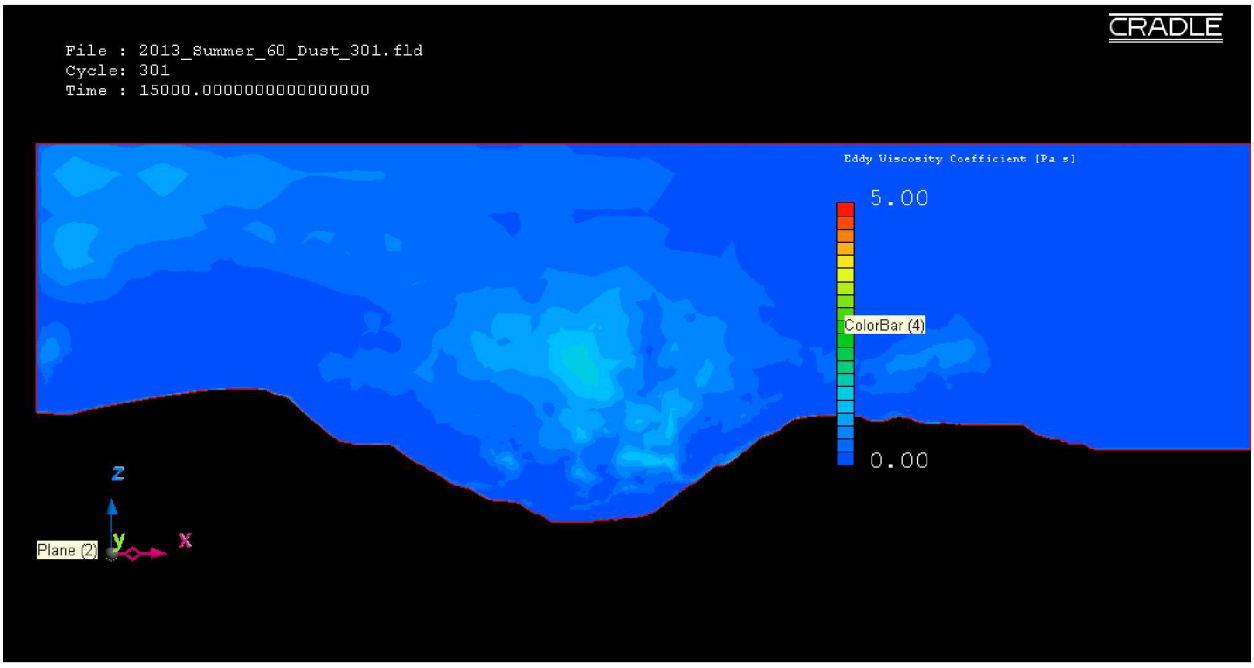

Figure 6.36: Eddy viscosity regimes in the actual open-pit domain for fair insolation condition using the LES method.

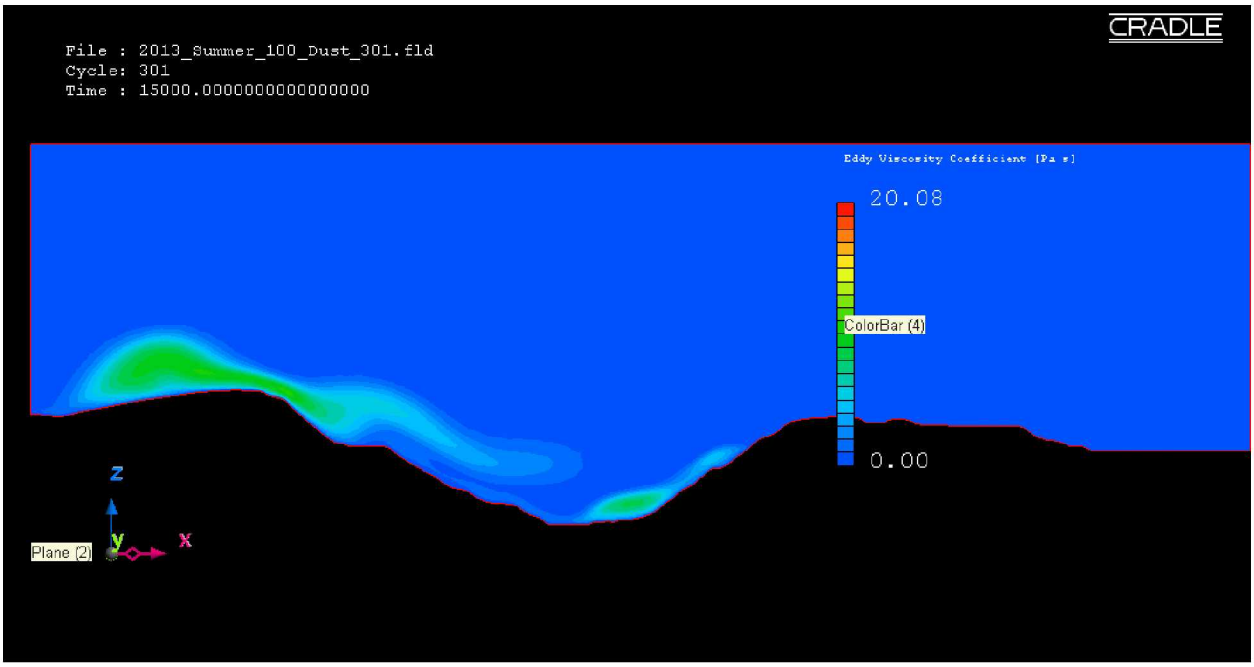

Figure 6.37: Eddy viscosity regimes in the actual open-pit domain for moderate insolation condition using the RANS method.

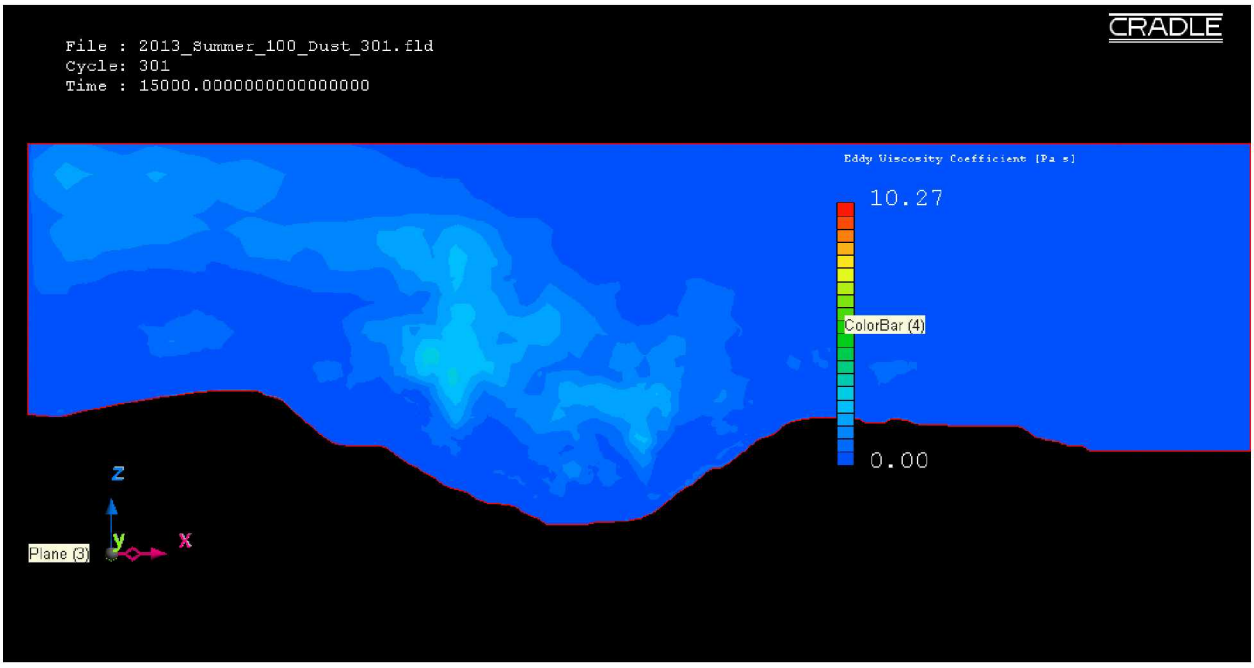

Figure 6.38: Eddy viscosity regimes in the actual open-pit domain for moderate insolation condition using the LES method.

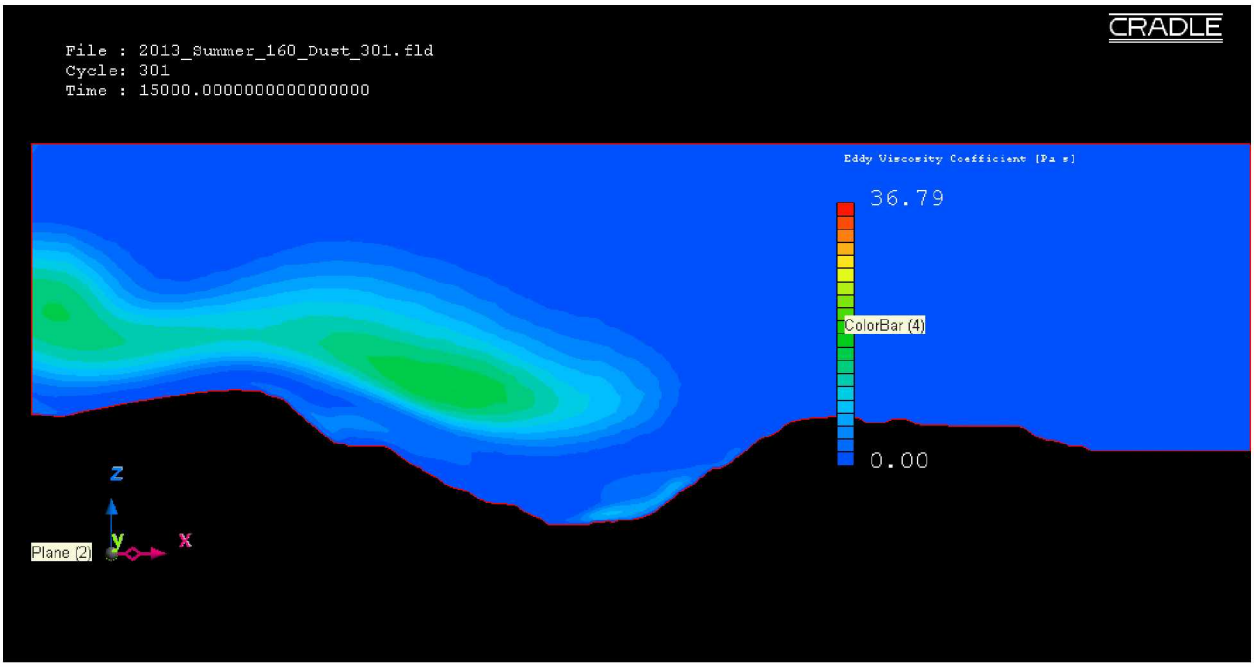

Figure 6.39: Eddy viscosity regimes in the actual open-pit domain for extreme insolation condition using the RANS method.

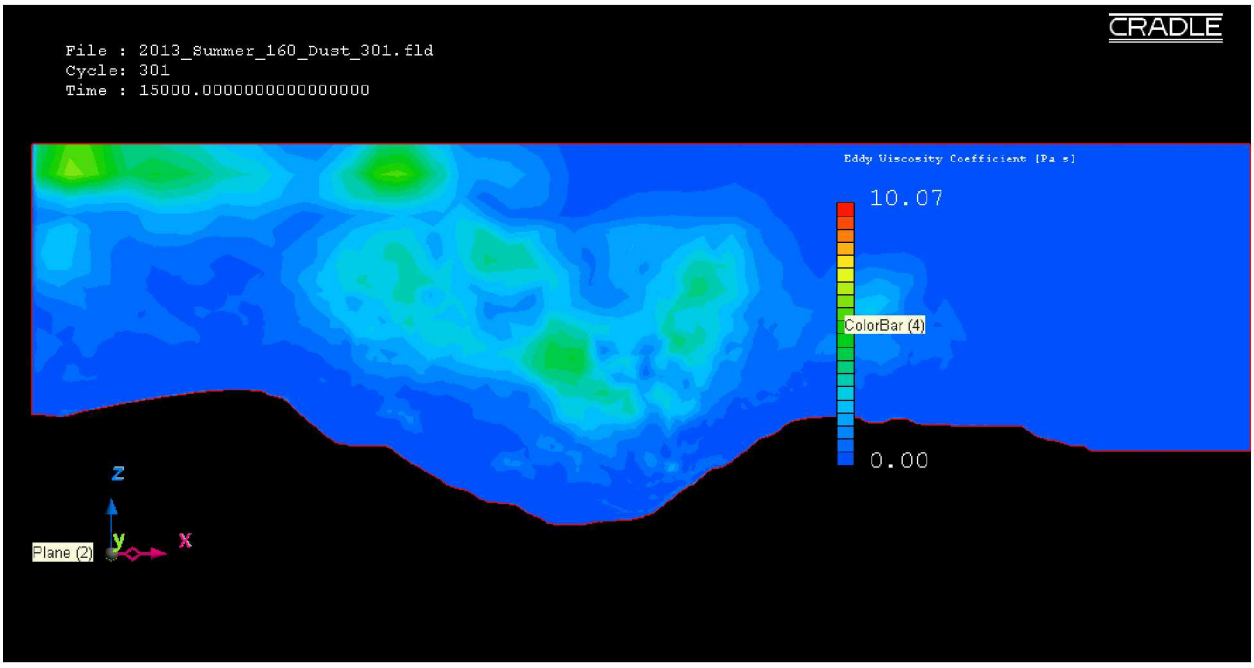

Figure 6.40: Eddy viscosity regimes in the actual open-pit domain for extreme insolation condition using the LES method.

6.2.5 Dust Propagation in the Actual Domains: Winter Climatic Conditions

In SC/Tetra, the locations of particles are updated during each time step. For solving the turbulent dispersion of the fugitive dust particles, the Lagrangian algorithm is used. The Lagrangian stochastic model characterizes the advection and the diffusion processes of an individual dust particle as a function of time. In this research, the locations of the particles during the simulation are reported at an interval of 10 minutes.

For a moderate winter condition (-20 W/m^2), Figure 6.41 and Figure 6.42 present the temperature contour plots and the locations of the dust particles (in black dots) along X-Z (Y = 1290 m) plane after four and half hours of simulation (30 minutes after dust particle injection) using the RANS and the LES methods. The temperature contours indicate the formation of an atmospheric inversion inside the open-pit, and a cold and dense air volume occupies the entire pit. As described in the previous sections, airflow inside the open-pit domain during an air temperature inversion is stagnant and completely detached from the airflow outside the open-pit. These phenomena resulted in very high retention of fugitive dust particles inside the open-pit.

During an extreme winter condition (-40 W/m^2), Figure 6.43 and Figure 6.44 show the temperature contour plots and the locations of the dust particles (as black dots) using the RANS and the LES methods respectively. As in the case of moderate winter condition, similar stratification in the temperature contours and presence of cold and dense air mass inside the pit can also be observed (Figure 6.43 and Figure 6.44).

It was shown that (Figure 6.41 to Figure 6.44), the presence of the air temperature inversion in the open-pit domain resulted in a very high retention of fugitive dust. Since the airflow inside the domain is completely stagnant and detached from the airflow outside the domain, the dust particles inside the open-pit remain suspended for a very long duration.

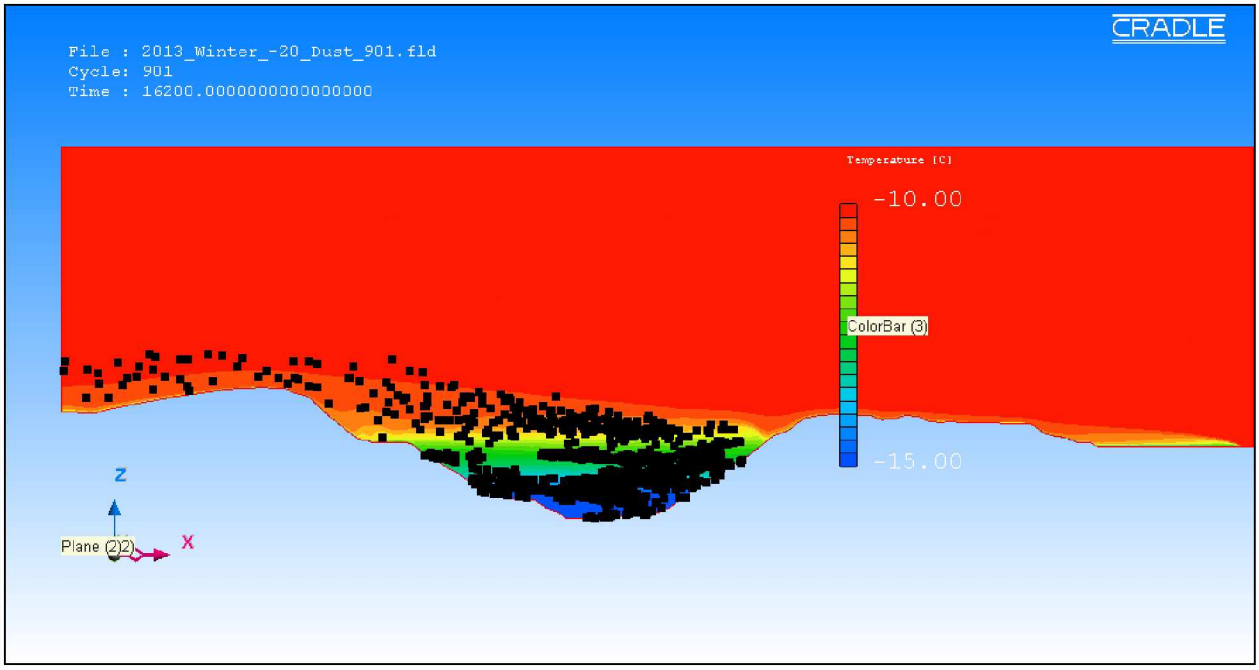

Figure 6.41: Temperature contour profile and locations of dust particles (black dots) in the actual open-pit domain for moderate winter condition using the RANS method.

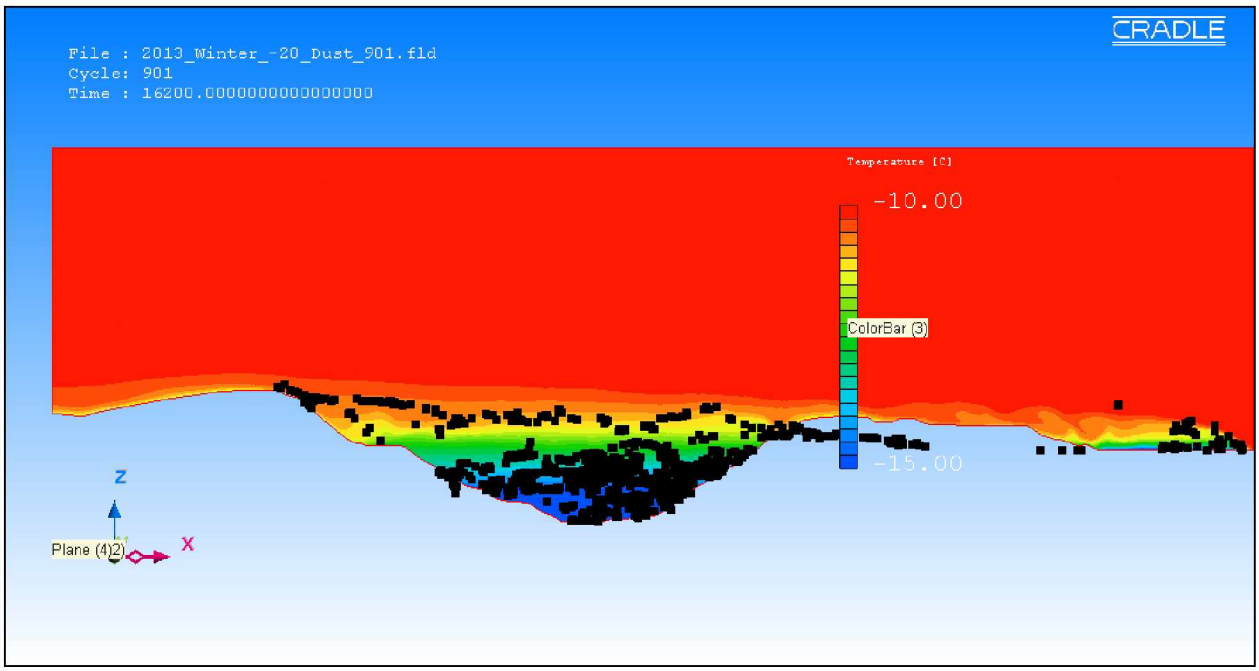

Figure 6.42: Temperature contour profile and locations of dust particles (black dots) in the actual open-pit domain for moderate winter condition using the LES method.

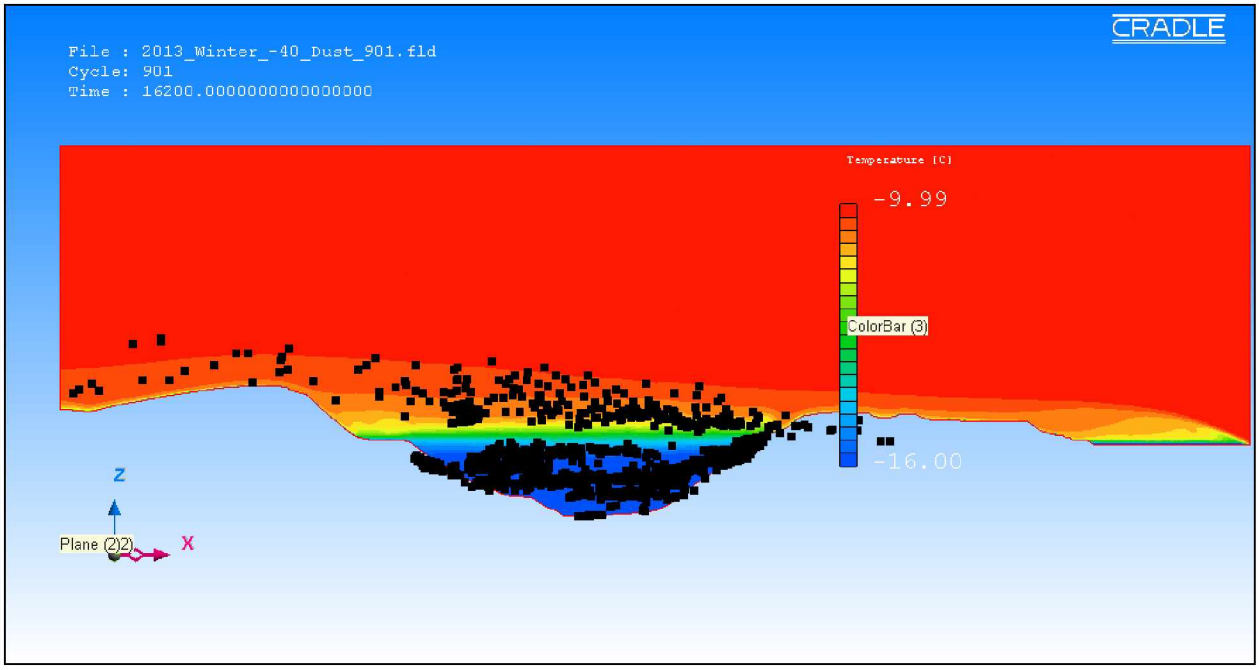

Figure 6.43: Temperature contour profile and locations of dust particles (black dots) in the actual open-pit domain for extreme winter condition using the RANS method.

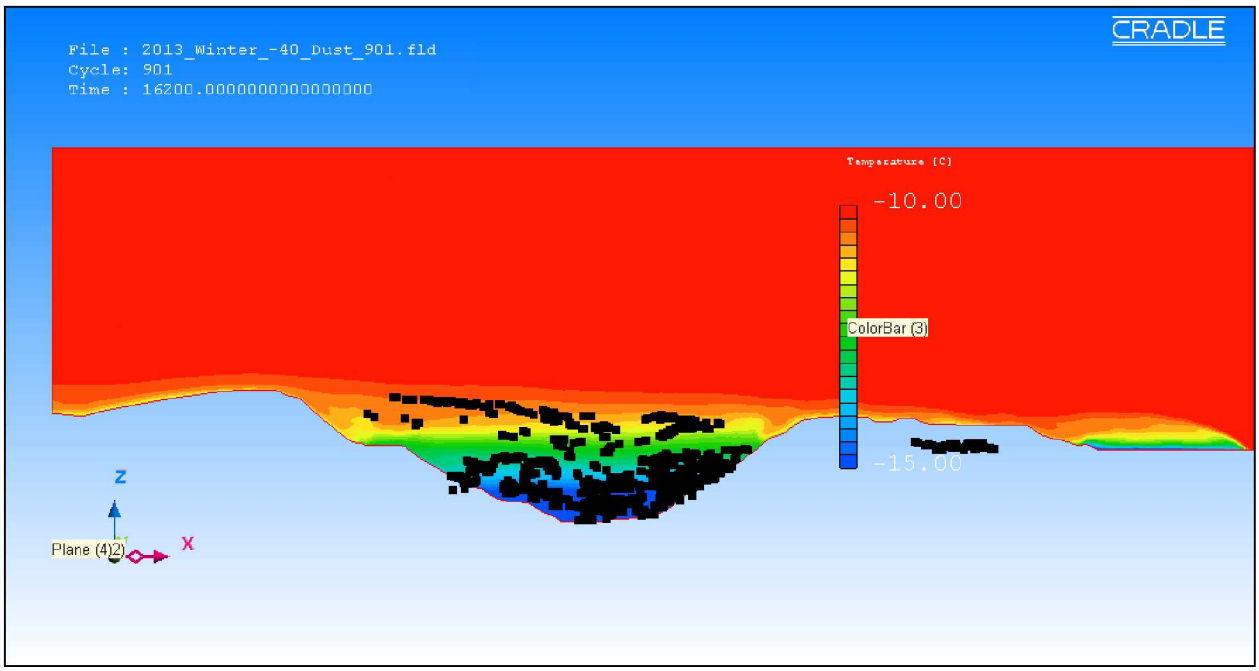

Figure 6.44: Temperature contour profile and locations of dust particles (black dots) in the actual open-pit domain for extreme winter condition using the LES method.

6.2.6 Dust Propagation in the Actual Domains: Summer Climatic Conditions

For a fair insolation condition (60 W/m^2), using the RANS and the LES methods, Figure 6.45 and Figure 6.46 present the temperature contour plots and the locations of dust particles (as black dots) along X-Z (Y = 1290 m) plane after four hours and ten minutes of simulation (10 minutes after dust particle injection). Before the dust sources are introduced in the flow domain, the calculation of fully developed background flow is required. This is accomplished in the initial four hours of the transient simulation of the background flow and all eddies in the entire flow domain are fully developed.

The temperature contours in the domain show the profiles that can be correlated with the location of the air recirculation profiles (Figure 6.25 and Figure 6.26). As in the case of the idealized domains, the turbulent eddies in the domain are due to the buoyancy flow. Most of the dust particles are transported out of the domain within the first hour after the dust particles are injected.

During a moderate insolation condition (100 W/m^2); Figure 6.47 and Figure 6.48 present the temperature contour plots and the locations of dust particles inside the actual open-pit. Due to the well dispersed characteristics of the convective (unstable) boundary layer, most of the remaining dust particles are dispersed all around the domain.

Figure 6.49 and Figure 6.50 present the temperature contour plots and the locations of dust particles for an extreme insolation condition (160 W/m^2 heat flux) inside the actual open-pit domain. As noted previously, the dust particles are dispersed all around the domain, and propagate towards the outlet boundary.

During summer (Figure 6.45 to Figure 6.50), the convective (unstable) motion of the airflow inside the domains transport most of the dust particles out of the pit within one hour after the fugitive dusts are generated. A summary of the simulation results for the actual open-pit domains is presented in Table 6.2.

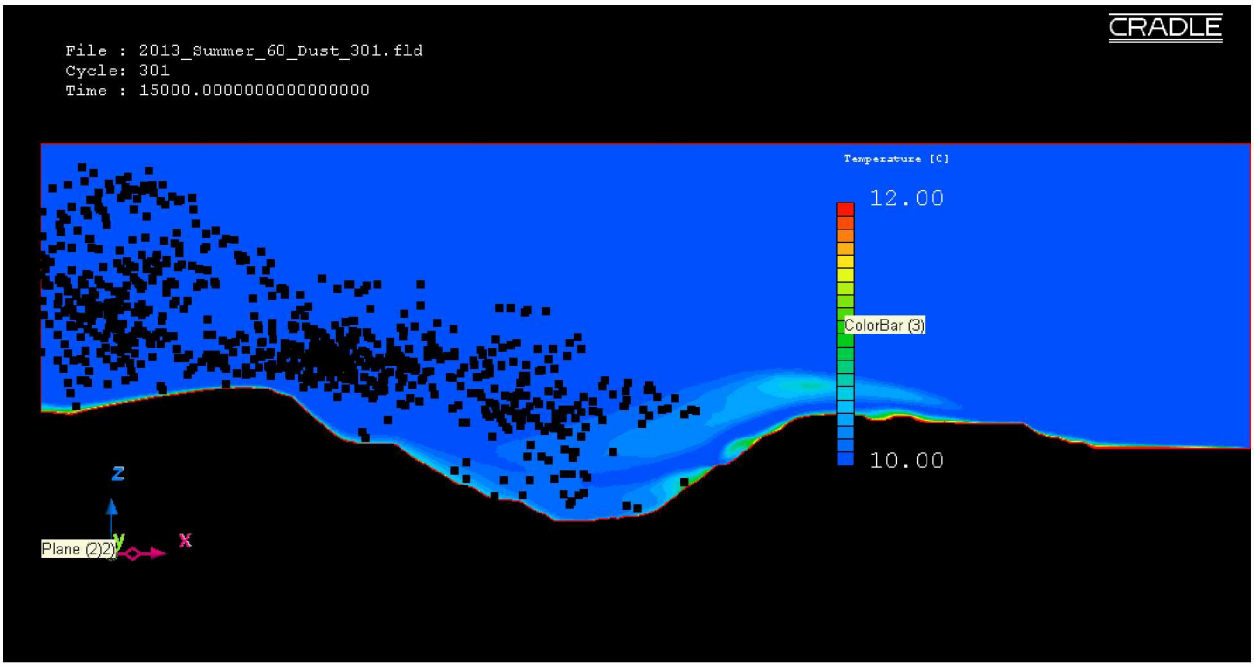

Figure 6.45: Temperature contour profile and locations of dust particles (black dots) in the actual open-pit domain for fair insolation condition using the RANS method.

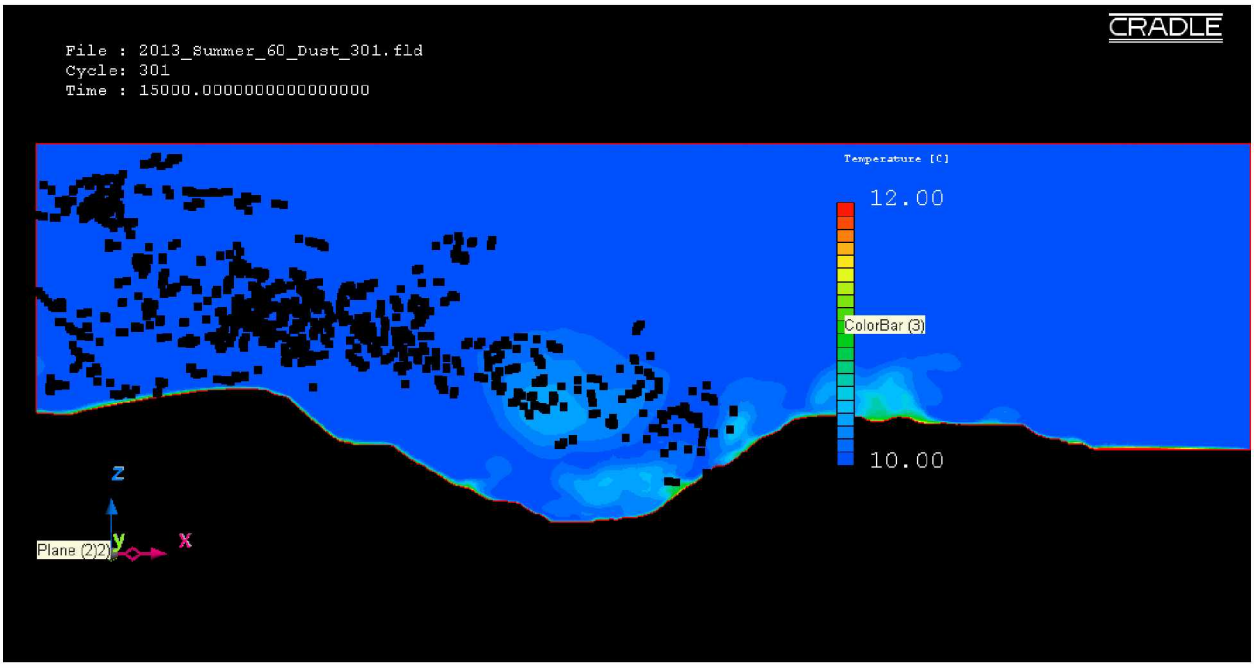

Figure 6.46: Temperature contour profile and locations of dust particles (black dots) in the actual open-pit domain for fair insolation condition using the LES method.

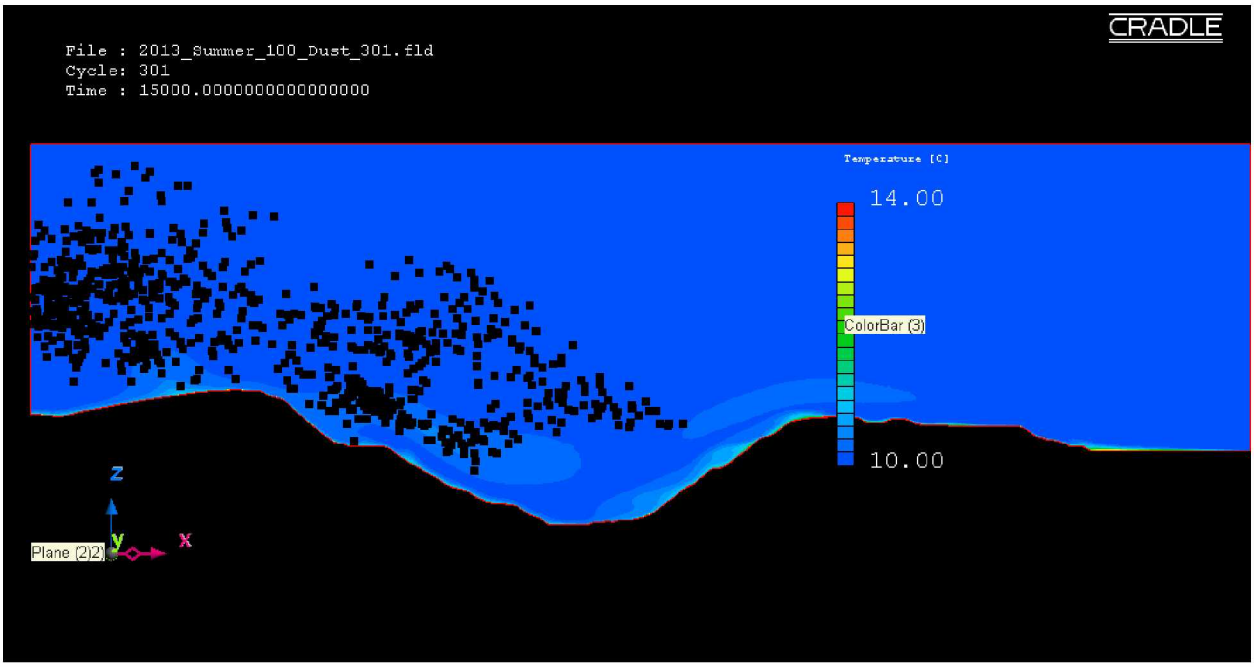

Figure 6.47: Temperature contour profile and locations of dust particles (black dots) in the actual open-pit domain for moderate insolation condition using the RANS method.

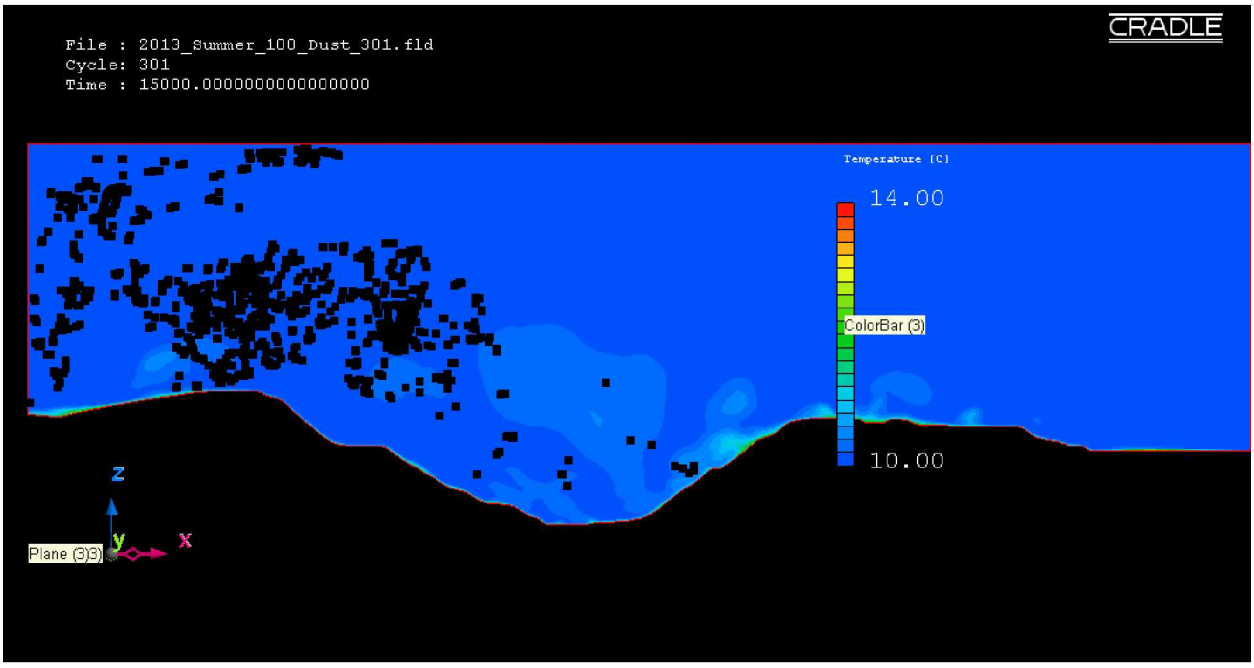

Figure 6.48: Temperature contour profile and locations of dust particles (black dots) in the actual open-pit domain for moderate insolation condition using the LES method.

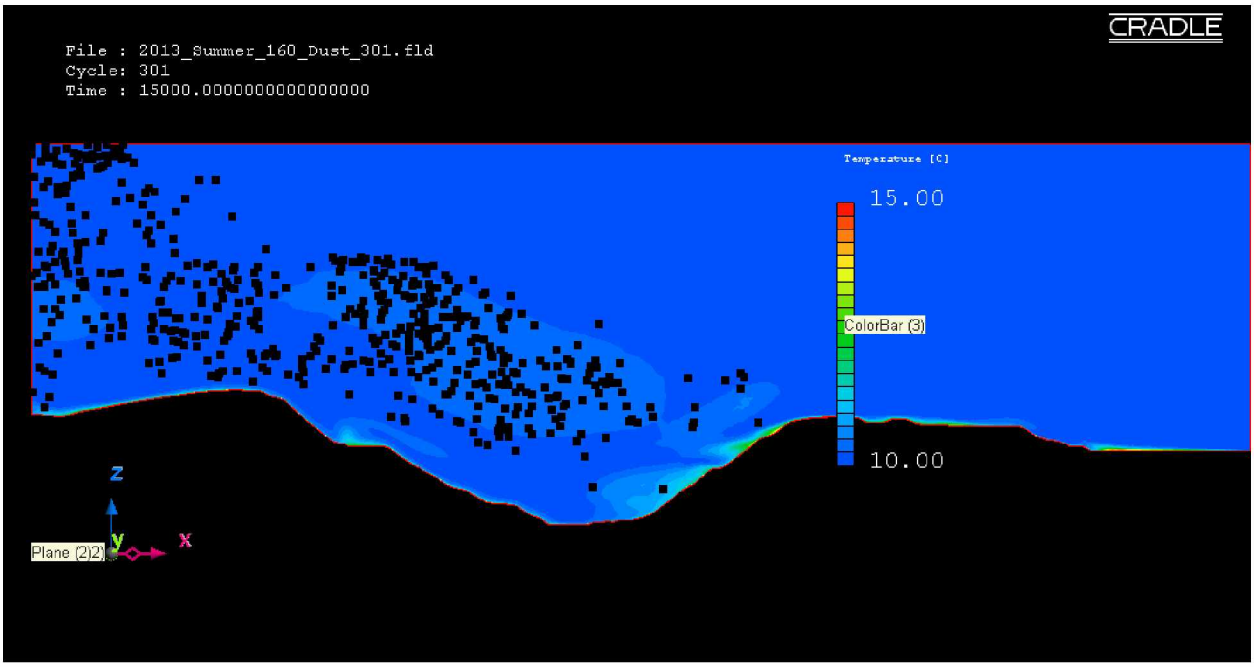

Figure 6.49: Temperature contour profile and locations of dust particles (black dots) in the actual open-pit domain for extreme insolation condition using the RANS method.

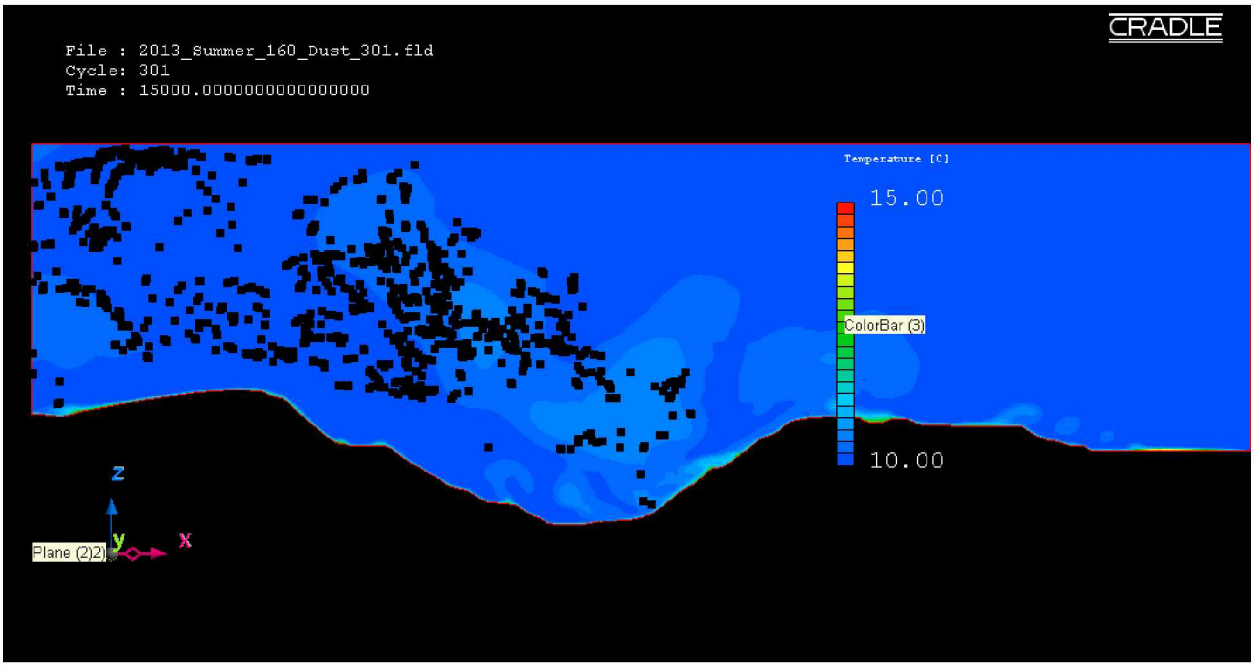

Figure 6.50: Temperature contour profile and locations of dust particles (black dots) in the actual open-pit domain for extreme insolation condition using the LES method.

Table 6.2: A summary of simulation results for the actual open-pit domain using the RANS and the LES method.

Domain	Climate Condition	Heat Flux (W/m^2)	% settled down		% reported outside		Time to clear out	
			RANS	LES	RANS	LES	RANS	LES
2013 Open-pit	Moderate Winter	-20	~76	~18	0.07 (12 hrs.)	0.08 (12 hrs.)	Unknown	Unknown
	Extreme Winter	-40	~86	~24	0.06 (12 hrs.)	0.05 (12 hrs.)	Unknown	Unknown
	Fair Insolation	60	70	7.4	30	92.6	24 min	60 min
	Moderate Insolation	100	63	4.5	37	95.5	30 min	44 min
	Extreme Insolation	160	70	4.2	30	95.8	28 min	36 min

Formation of an atmospheric air temperature inversion inside the domain during moderate and extreme winter conditions resulted in a very high retention of fugitive dust particles. The simulation results for the winter (Table 6.2) show extensive entrapment of dust particles. Very few particles (less than 1%) are transported outside the model domain for the entire period of the simulation run.

During summer, due to the formation of a convective (unstable) boundary layer inside the open-pit domain, almost all of the dust particles (more than 92% for the LES method) are transported out of the domain by the convective airflow. The dispersion of the individual dust particles ($PM_{0.1}$ to PM_{10}) from various fugitive dust sources are presented in Appendix B. The pathlines of dust particles from various dust sources (Figure B.1 to Figure B.202, Appendix B) inside the actual open-pit domain are compared for the fair insolation and the extreme insolation conditions. The pathlines of the dust particles for the extreme insolation condition show a higher degree of recirculation in comparison to the fair insolation condition. The larger amount of convective eddies for the extreme insolation condition resulted in a higher degree of recirculation in the pathlines; and transported the dust particles out of the open-pit domain in short duration.

As previously noted, retention of fugitive dust is also dependent on the choice of turbulence models. It is observed that fugitive dust particles predicted by the RANS method clear out of the actual open-pit domain sooner than the LES method. Extensive settlement of dust particles on

the pit surface is predicted by the RANS method. As a result, the amount of time it takes to transport all the dust particles out is less.

Even with a fully developed background flow, the results of spatial dispersion in LES may vary depending on the selection of the moment of particle injection. Dispersion of particles in buoyancy driven flow is highly influenced by the eddy dynamics. Consequently, the particle dispersion may vary if the particles arrive in the eddy region before or after the eddy passes through that region, causing the dust-particle pathlines to move in one direction or another.

With RANS, averaging of velocities and the applied particle dispersion model causes most probable particle dispersion patterns that can be captured in a single simulation. Overall, the study results show the potential for increased accuracy with a one-way coupled Eulerian-Lagrangian approach for particle modeling with LES.

Chapter 7 Mitigation of Dust Retention during an Air Temperature Inversion

7.1 Extensive Fugitive Dust Retention during an Air Temperature Inversion

Formation of an atmospheric air temperature inversion inside the idealized and the actual open-pit domains resulted in an extensive retention of fugitive dust particles for a prolonged duration. Atmospheric air temperature inversion at the selected Arctic open-pit mine is due to the negative heat flux from the pit surface during the winter months.

Simulation results of dust dispersion in the idealized open-pit domain during the winter season (Table 6.1) predicted an extensive entrapment of dust particles. Very few particles (less than 20%) are transported outside the model domain. In the actual open-pit domain also an extensive entrapment of dust particles during the winter (Table 6.2) is also predicted. Very few particles (less than 1%) are transported outside the model domain.

While, during the summer, due to formation of a convective (unstable) boundary layer within the open-pit domain, almost all of the dust particles are transported out of the domain within a very short duration (within one to two hours after the dust particles are introduced). The dust dispersion during the summer, therefore, does not present a severe health and safety problem.

7.2 Air Temperature Inversion Mitigation Approaches: Mechanical Ventilation

Raj [2015] conducted an extensive study on pollutant mitigation approaches to remove an air temperature inversion from a selected open-pit domain. Several approaches including a field experiment with a helicopter to mitigate pollutants in the selected open-pit are presented. CFD modeling approaches included in the analysis are: (1) use of several mechanical ventilators for local dilution of the pollutants, (2) mechanical ventilators in exhaust mode, and (3) a push-pull ventilation scheme. However, none of these mitigation approaches resulted in the removal of pollutants from the selected open-pit mine. A detailed discussion of these mitigation approaches can be found in Raj [2015], and hence are not detailed in this thesis. A major portion of his Raj's [2015] research is reproduced here to build a foundation for the present work for mitigation of dust in open-pit mines.

7.3 Air Inversion Mitigation Approaches: Effect of Cloud Cover on Air Inversion

The research by Raj [2015] concluded that the presence of cloud cover above the open-pit domain would help in removal of atmospheric inversion of an Arctic open-pit mine. The removal

of atmospheric inversion results in development of turbulence in airflows inside the domain, which helps the pollutants to clear out of the pit. Since clouds are infrared sensitive, most of the infrared radiation emitted from the ground is reflected by the cloud cover. The snow-covered pit surface also reflects most of the incident radiation due to high albedo of snow. However out of the available infrared radiation, some amount of radiation is absorbed by water vapor, CO_2, and other greenhouse gases [Arya, 2001].

Figure 7.1 and Figure 7.2 present Infrared Radiation (IR) measurements at the pit-bottom and the pit-rim under cloud cover in the selected open-pit. As shown in Figure 7.1, the incoming and the outgoing infrared radiation overlap each other at around 6:00 AM (red outlined region, October 29, 2013) and continue until the evening at 6:00 PM. The incoming and the outgoing infrared radiation values at the pit-rim also display similar trends (red outlined region, Figure 7.2) during that same time. This phenomenon of both the incoming and outgoing radiations converging to zero (W/m^2) represents a cloud cover above the open-pit domain [Raj, 2015]. The presence of cloud cover is cross-verified with the RADAR base reflectivity data (Figure 7.3) and the dew point temperature data (Table 7.1 and Table 7.2) during the same time, which also verifies the presence of cloud above the selected open-pit. The green shade over the selected open-pit mine (red outlined region) in Figure 7.3 indicates the presence of cloud cover [Raj, 2015]. Table 7.1 and Table 7.2 present air temperature, dew point temperature, and the relative humidity data from the two weather stations located near the selected open-pit mine. The saturation in the water vapor content or a very high relative humidity (close to 100%) indicates formation of cloud [Raj, 2015].

Raj [2015] presented several other additional data from various dates to provide support for the discussions presented above. Analysis of the data indicates that there is a change in the infrared radiation during cloud cover. The presence of cloud cover results in the convergence of the incoming and the outgoing longwave radiation values to zero. Thus, providing a basis for modeling the presence of cloud cover over an open-pit. It must be noted that in practice, the longwave radiation value cannot be exactly zero.

The following discussion has been modified from a document [Bhowmick et al., 2015] originally written for and published in the WIT Transactions on The Built Environment, Vol. 168, Sustainable Development, Vol. 2, with coauthors Bandopadhyay, S. and Ghosh, T.

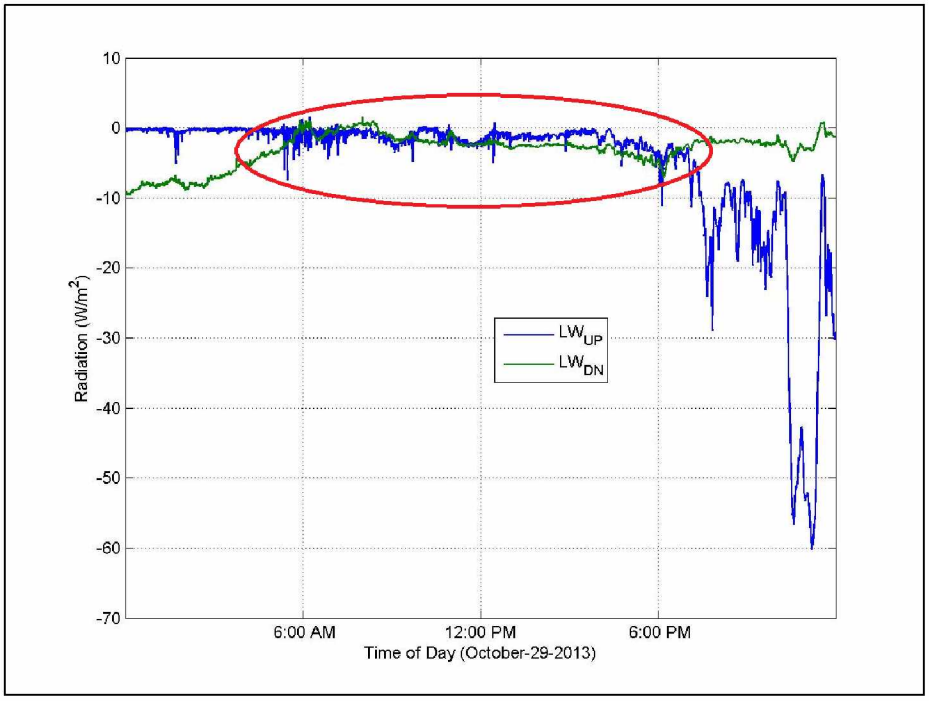

Figure 7.1: Infrared radiation measurements at pit-bottom during cloud cover (October 29, 2013) [Modified from Raj, 2015].

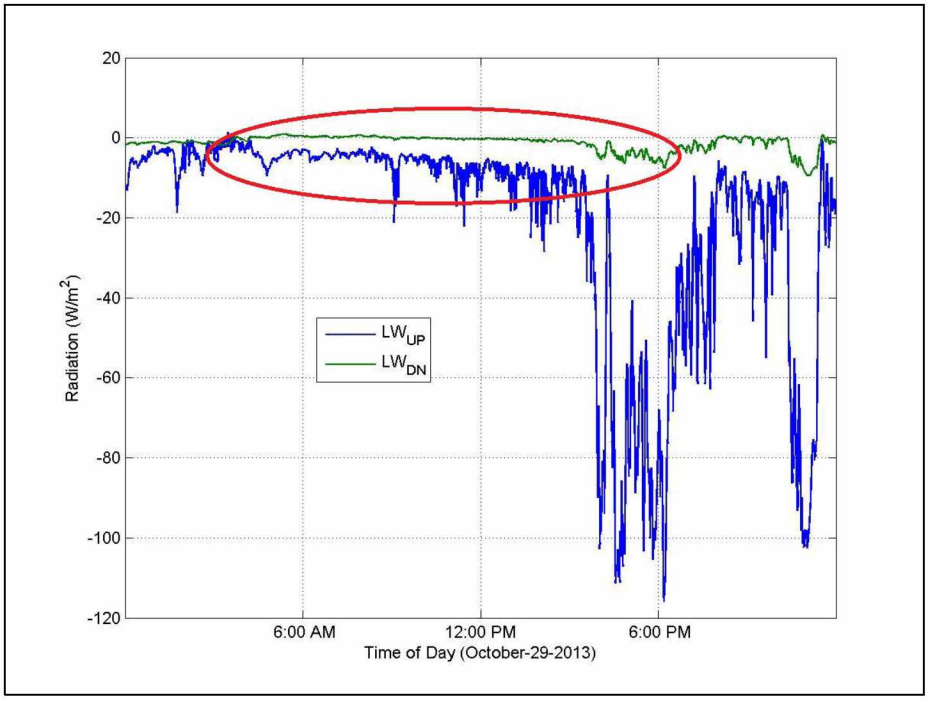

Figure 7.2: Infrared radiation measurements at pit-rim during cloud cover (October 29, 2013) [Modified from Raj, 2015].

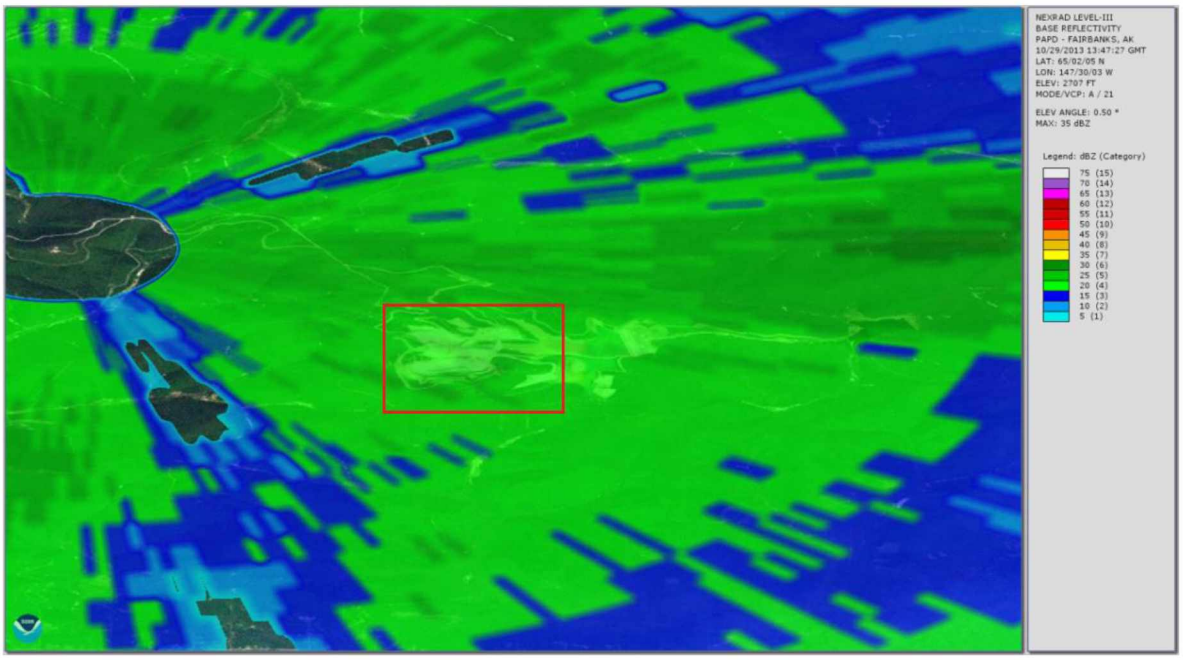

Figure 7.3: RADAR base reflectivity data on October 29, 2013 (http://www.ncdc.noaa.gov/nexradinv/) [Raj, 2015].

Table 7.1: Weather Station 1 data on October 29, 2013 (http://www.wunderground.com/) [Raj, 2015].

	High	Low	Average
Temperature (°C)	1.67	-1.67	-0.67
Dew Point (°C)	1.67	-1.67	0.67
Relative Humidity (%)	100	100	100

Table 7.2: Weather Station 2 data on October 29, 2013 (http://www.wunderground.com/) [Raj, 2015].

	High	Low	Average
Temperature (°C)	1.11	-2.78	-1.06
Dew Point (°C)	0.56	-3.33	-1.61
Relative Humidity (%)	96	95	96

7.3.1 Simulation Setup for Modeling the Cloud Cover

A novel simulation approach is adapted in this thesis to evaluate the effect of cloud cover for mitigation of fugitive dust in open-pit mines. Initially, to model the effect of cloud cover, the domain was simulated with radiation simulation (flux method) using heat flux at the cloud condensation level (CCL) and at the pit boundary. During a complete overcast condition, the net radiation balance in the CCL and Pit boundaries eventually reaches to zero. However, the longwave incoming and the outgoing radiation magnitudes are not always zero as soon as a cloud arrives above the open-pit. The domain has a temperature gradient due to the convective heat transfer from the Pit surface. This results in temperature differences between the air layers resulting in longwave radiation. The outgoing longwave radiation reflects back in presence of a cloud cover. This phenomenon is simulated by introducing a similar magnitude of heat flux (W/m^2) at the CCL as well as at the pit boundary. For example, to simulate an intense winter condition, a heat flux of 40 W/m^2 from the Pit surface and 40 W/m^2 from the CCL are used to simulate a complete overcast condition. It is understood that the heat flux from the Pit surface is negative which results in convective cooling of air layers while the positive heat flux from the CCL results in convective heating of the air layers. Therefore, the total amount of energy inside the domain remains constant. However as the time progresses, the physics dictates that the heat flux values need to reach a zero magnitude (Figure 7.1 and Figure 7.2) at both the pit boundary and the CCL boundary. To reflect that state of the open-pit domain, a modified heat flux of zero magnitude (W/m^2) is introduced at both the boundaries. These modified boundary conditions imply that net radiation is zero at each boundary. The incoming and the outgoing solar (short wave) radiations are close to zero and therefore neglected [Bhowmick et al., 2015].

As stated previously, initial conditions, boundary conditions, choices of the turbulence models, the turbulent parameters along with the generation and tracking process of fugitive dust particles, are important criteria for the simulation setup. The simulation setup for the mitigation model is defined using the 'Analysis Condition' wizard of CRADLE SC/Tetra Preprocessor.

7.3.2 Boundary Conditions for Modeling the Cloud Cover

All the model boundaries are required to be defined to initiate a simulation. An Inlet (East) and an Outlet (West) boundary with various Wall boundaries are used for the simulation. Inlet boundary is defined as the velocity boundary with a power law profile of velocity. Table 7.3

presents the input values used for various boundary conditions for simulating dust dispersion in the winter session. The model domain is simulated for various overcast cloud conditions: (1) clear sky, (2) partial cloudy sky, and (3) complete overcast sky conditions to analyze the effects of cloud cover on dust dispersion:

(1) Clear Sky Condition: During clear sky conditions, no overcast cloud cover is present above the open-pit domain. To simulate clear sky conditions, the FA boundary is defined as an adiabatic free surface. The adiabatic property of the FA boundary restricts any heat transfer through this boundary. The free surface simulates the FA boundary as a virtual surface, which has no influence on the airflow pattern at the boundary. That means that any viscous sublayer in airflow close to the FA boundary is not impacted by the presence of the FA boundary.

Table 7.3: Input values of the Pit surface wall boundary and the FA wall boundary for various cloud conditions during the winter.

Season	Intensity	Wind Speed	Initial Temp.	Pit Boundary Heat Flux	FA Boundary Heat Flux : Clear Sky	FA Boundary Heat Flux : Partial Cloudy Sky	FA Boundary Heat Flux : Complete Overcast Sky
Winter	Moderate Winter	2.1 m/s	-10 C	-20 W/m^2	Adiabatic	10 W/m^2	20 W/m^2
	Extreme Winter	2.1 m/s	-10 C	-40 W/m^2	Adiabatic	20 W/m^2	40 W/m^2

(2) Partial Cloudy Sky Condition: During partial cloudy sky conditions, an overcast cloud partially covers the domain. During the winter seasons, in the presence of a cloud cover, the longwave radiation, emitted from the surface is reflected back. This results in warming of the air under the cloud covered domain.

It is assumed that one-half of the area of pit domain is covered with low level cloud. Thus, the partial cloudy sky condition is simulated with heat flux generated from the FA boundary which is half of the pit boundary heat flux magnitude. The generation of heat flux requires the physical existence of the boundary. Whereas, the free surface boundary condition models the boundary as a virtual boundary. The free surface boundary condition in the CRADLE-CFD is not

compatible with the heat flux boundary condition. Therefore for partial cloudy sky simulation, the FA boundary in CRADLE-CFD is modeled as a smooth boundary with heat flux.

A cloud cover, modeled with smooth wall boundary condition with heat flux, has several limitations. In general, clouds move with the airflow, floating at the cloud condensation level (CCL). While, a smooth wall boundary condition simulates the FA boundary as a static boundary with negligible roughness. This results in the formation of a velocity boundary layer at the FA boundary, and generates unrealistic mechanical turbulence.

(3) Complete Overcast Sky Condition: During a winter season, a cloudy sky condition warms up the air within the cloud covered domain. Table 7.3 presents the simulation input values of the Pit surface wall boundary and the FA wall boundary for winter season and varying cloud conditions for the initial step of the simulation.

7.3.3 Simulation Results of Open-Pit Domains under Various Cloud Conditions

The initial simulation results using a similar magnitude of heat flux at the Pit and the FA boundaries indicate that the choice of sensible heat flux input from the cloud cover has negligible effect in the removal of the fugitive dust. This is predicted irrespective of the sky conditions.

To evaluate the influence of the sensible heat flux, a temperature profile of the air mass inside the open-pit is plotted along a vertical line (line 1-3, Figure 7.4) in the trapezoidal domain. Figure 7.5 is a plot of temperature profiles for various levels of cloudiness during extreme winter conditions after an initial 6 hours of simulation. No significant variation is observed in these temperature profiles. The simulation of cloud cover with heat flux as an input did not have any impact on the stratified cold air mass, and did not lift the air temperature inversion even after 6 hrs. of simulation.

Following the initial stage of simulation, the presence of cloud cover is then modeled with zero heat fluxes (W/m^2) from the Pit surface and the FA boundary. The simulation results indicate that the warm air mass from the inlet is penetrating the air temperature inversion layer very slowly close to the pit-rim. The cold air mass inside the pit cavity, however, remains almost stagnant and still detached from the airflow above the pit. Since the air flow inside the pit is almost stationary, the stratification of the cold air mass within the pit remains for a prolonged duration, with a very slight change in the temperature profile over time.

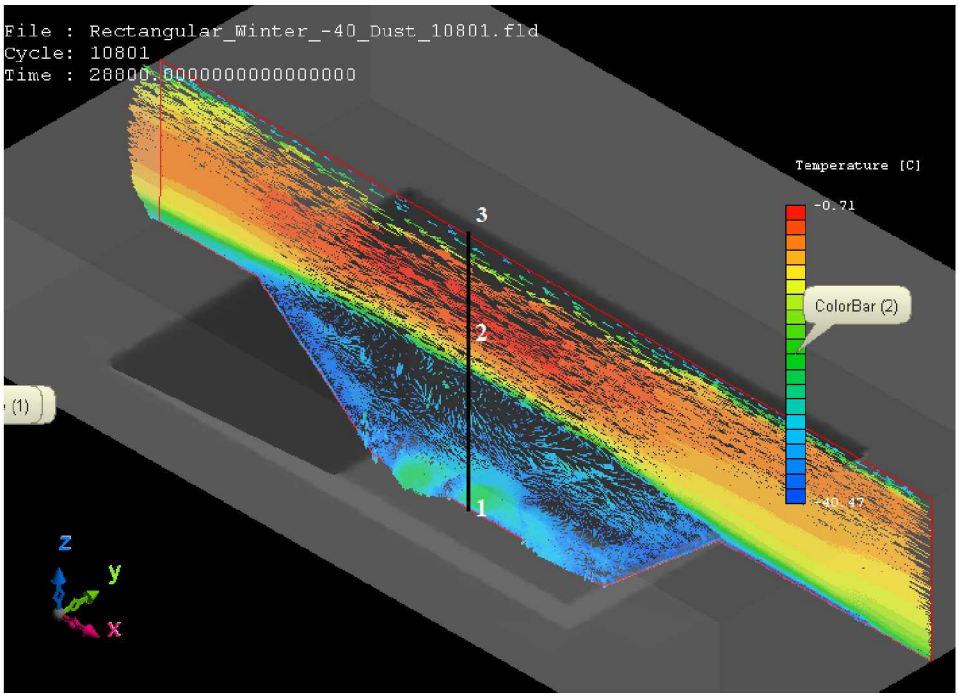

Figure 7.4: Temperature profile in the trapezoidal domain the velocity vector profile along the Y = 900 m plane and the vertical line 1-3.

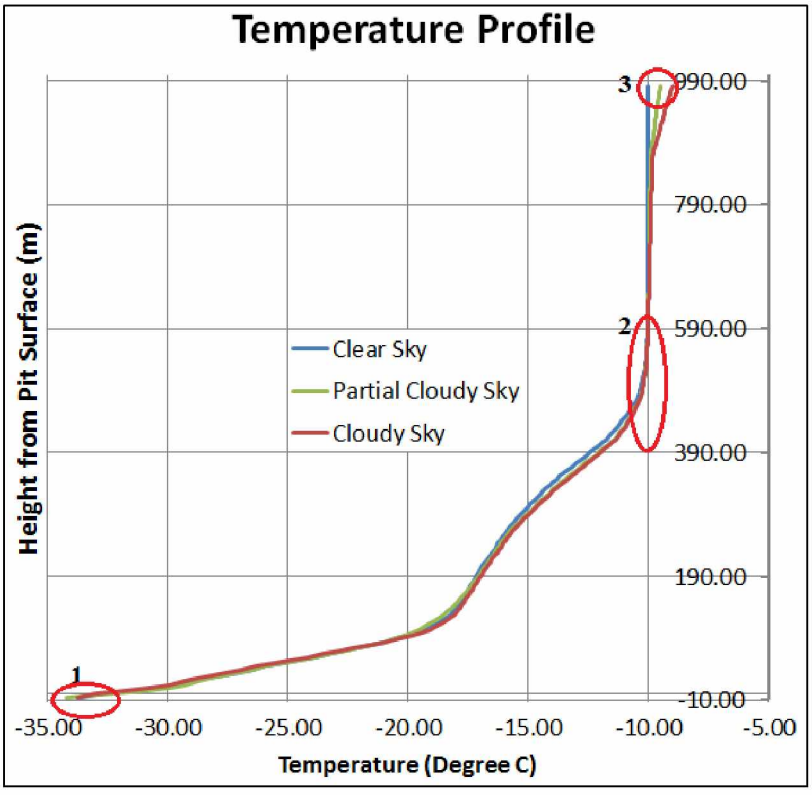

Figure 7.5: Temperature profile along line 1-3 in Figure 7.4.

The temperature profiles of the idealized domains with zero heat flux from the Pit surface and the FA boundary are presented in Figure 7.6 and Figure 7.7. The temperature profiles for both the domains show some changes over time near the Pit surface (region 1); however, the overall stratification of the cold air mass in the pit (region 1 to 2) is almost unchanged.

Following the simulations of the two idealized open-pit domains, an actual open-pit domain is simulated initially using a similar heat flux as input, and then, the zero heat flux as input from the FA and the pit boundary for various levels of cloudiness. The simulation results replicate the results of the idealized domain. From the simulation results, for the geometry of the open-pit domains, and the boundary conditions considered, it appears that a cloud cover alone may weaken the air temperature inversion at a very slow rate, however, would not be able to remove the dust particles from the open-pits.

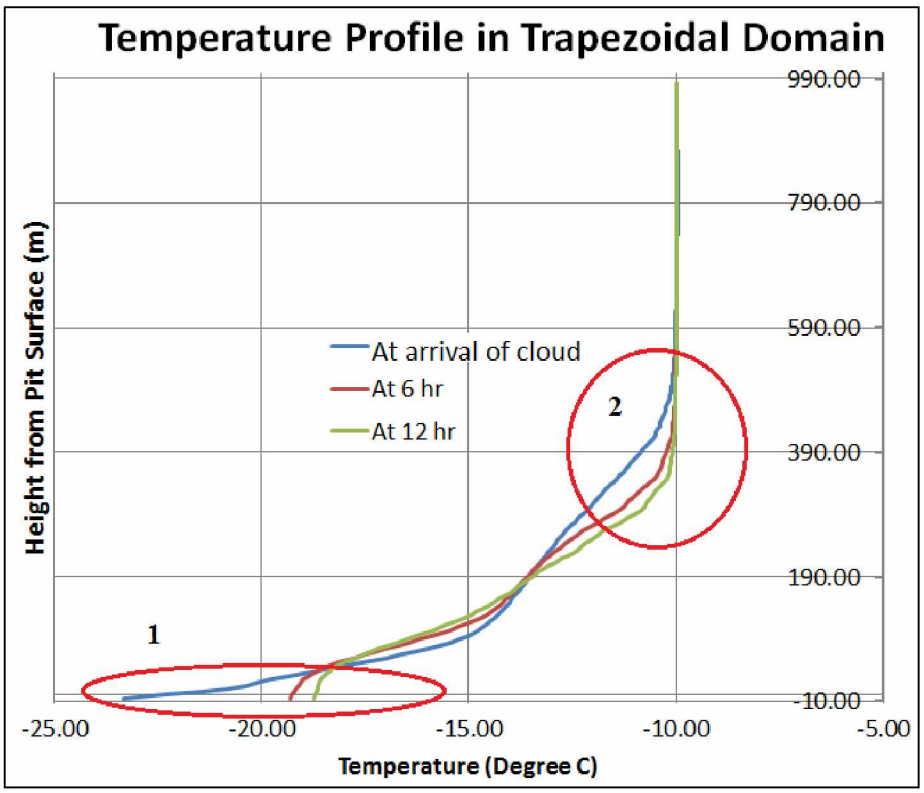

Figure 7.6: Temperature profiles in zero heat flux input from the Pit surface and the FA boundary along a vertical line in the trapezoidal domain.

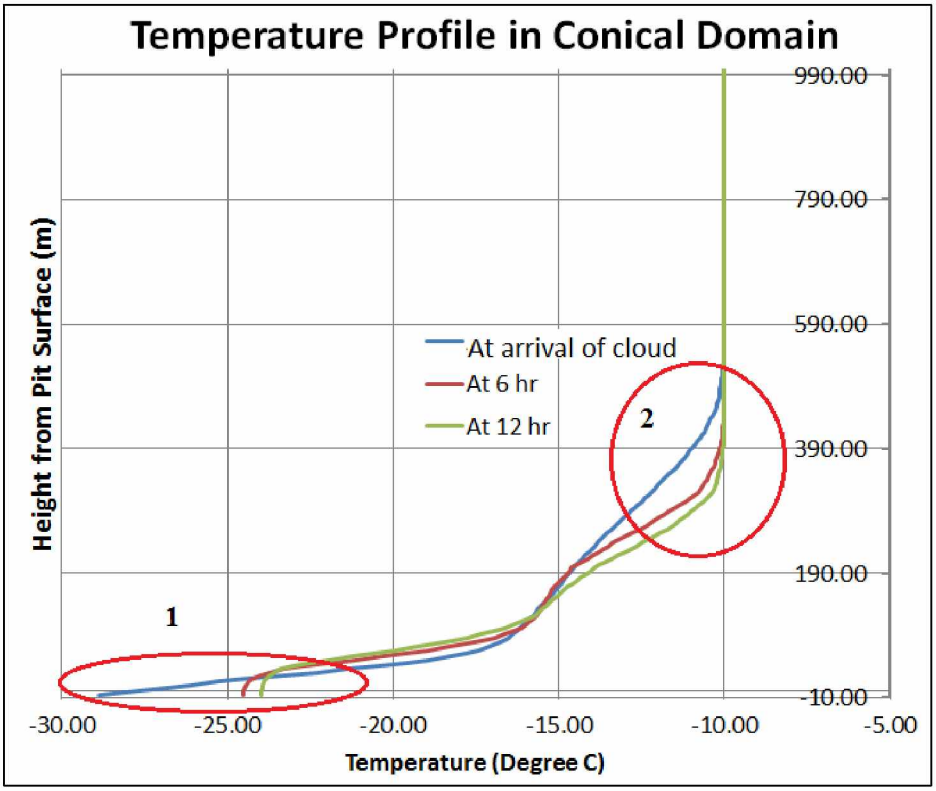

Figure 7.7: Temperature profiles in zero heat flux input from the Pit surface and the FA boundary along a vertical line in the conical domain.

7.3.4 Simulation of the Open-Pit Domains with Increased Wind Speed at Inlet

To evaluate the effect of wind speed along with the cloud cover, all the idealized and the actual domains with strong stratified inversion layers are simulated with increased wind speed at the inlet boundary. The reference wind speed at the inlet boundary is increased from 2.1 m/s to 3.5 m/s and then, to 5 m/s, with all other boundary conditions remaining the same.

The simulation results show an extensive penetration of the inversion layer in case of the actual open-pit (2013 open-pit) domain. While in the idealized domains the penetration of the inversion layer is also observed; but at a slower rate than the actual domain. The slower rate of penetration of the inversion layer in the idealized domains is due to the symmetry and regularity of the idealized domains, which results in limited topography-induced recirculation. While the irregularities in the topography of an actual domain produce various types of recirculation and mechanical forces that enhance the penetration of the inversion layer. The aspect ratio of the actual open-pit domain is very different than the idealized domains, and may have influenced the outcome. Air temperature

profiles for various inlet wind speeds in the actual 2013 open-pit domain are presented in Figure 7.8, Figure 7.9, and Figure 7.10. With increased inlet wind speed along with the cloud cover (complete overcast sky), the stratification in the cold air mass (red circle regions) weakens.

Fugitive dust particles trapped within the pit start to clear out of the open-pit as the stratification weakens. Therefore, for natural removal of the inversion layers and for mitigation of fugitive dust, the presence of cloud covers and a good convective wind are required. Without a cloud cover, thermal buoyancy forces from the Pit surface enhance the stratification. In the absence of a strong convective wind, the mechanical forces do not have the potential to penetrate the cold air layers. The critical wind speed for removal of the air temperature inversion depends on (1) topography and the aspect ratio of the domain; (2) the temperature gradient of the stratified layers; and (3) the net radiation balance.

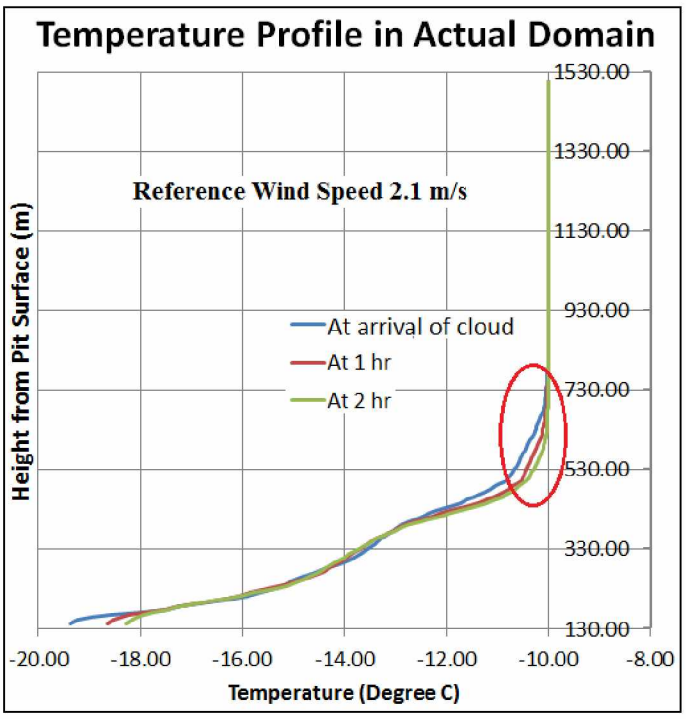

Figure 7.8: Temperature profiles along a vertical line in the actual domain (2013 open-pit) for reference wind speed of 2.1 m/s.

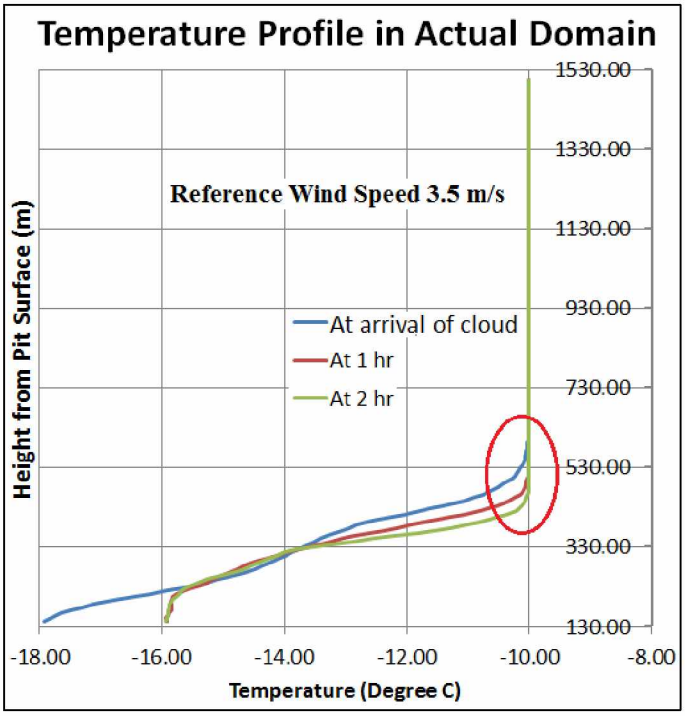

Figure 7.9: Temperature profiles along a vertical line in the actual domain (2013 open-pit) for reference wind speed of 3.5 m/s.

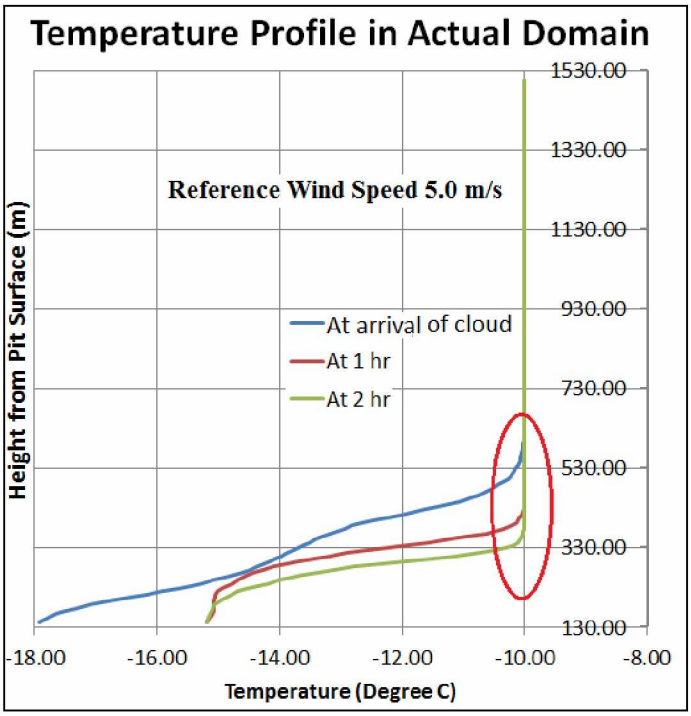

Figure 7.10: Temperature profiles along a vertical line in the actual domain (2013 open-pit) for reference wind speed of 5.0 m/s.

Chapter 8 Summary and Conclusions

8.1 Summary

The Arctic region contains vast mineral resources and mining of these resources is a major activity in several countries, including the United States. With the advancement of open-pit mining technology, the depth to which minerals can be profitably mined has increased, resulting in deeper pits than ever before. This increase in depth has several inherent challenges for mining operations. One of the challenges for deep open-pit mining in a cold climate is atmospheric air temperature inversion. Air temperature inversion, a meteorological phenomenon, occurs mainly due to the negative net radiation balance at the earth's surface. The temperature of the air mass at the pit-bottom cools more rapidly than the air mass above it, leading to an increase in air temperature with altitude. Due to the emission of gases and particulates during the mining process, the air within the pit can be severely and sometimes quickly contaminated, leading to serious health and safety problems. To maintain and enhance the health and safety of the mine workers, effective measures are necessary both to minimize fugitive dust emissions and adequately ventilate the pit to dilute, disperse, and remove the fugitive dust particles.

The development of a computational fluid dynamics (CFD) model of an open-pit mine is challenging due to the presence of several sharp and irregular features at the pit surface. A good quality mesh of the model domain is a prerequisite for convergence in solution. Meshing of a typical open-pit domain generally consists of a combination of different types of mesh elements. Meshing of an open-pit domain with tetrahedral and prism mesh elements is complicated due to the presence of numerous vertices and ridges. Presence of vertices and ridges results in poor quality tetra elements and holes in prism layers, which cause instability in the simulation. Besides good quality meshing, choices of various simulation setup parameters have significant impact in convergence or divergence of the simulation. Appropriate choices of simulation type, boundary and initial conditions, time stepping and various convergence criteria are important for realistic simulation of a model domain. The CFD software provides various turbulent flow methods and turbulence models for simulation of the model domain. It is essential that the various methods are evaluated to identify the appropriate method that would simulate the flow phenomena within the domain with reasonable accuracy. Various constraints and the

consequences in development of a three-dimensional CFD model for estimation of fugitive dust propagation in an open-pit mine are evaluated using the SC/Tetra software of CRADLE.

Three-dimensional geometry of an open-pit mine is imported into the preprocessor of SC/Tetra for development of a CFD model for estimation of pollutant transport in open-pit mines. For meshing the domain, octree was used to define and control the size of the mesh elements. However, meshing the imported open-pit geometry was challenging due to presence of several sharp features at the pit surface. These features resulted in formation of several vertices and ridges at the pit boundary. The presence of several vertices and ridges resulted in intersecting surfaces during meshing the domain. Therefore to create a volume mesh, all the intersecting surfaces were removed. The presence of vertices and ridges also degraded the qualities of the tetra element at the pit boundary and created holes in the prism layers at the pit boundary. Therefore all the unwanted vertices and ridges were removed from the pit boundary to improve the quality of the mesh elements and to create well-defined prism layers at the pit boundary. Insertion of good quality prism layers at the roughness boundary significantly improved the formation of velocity and thermal boundary layers at the pit surface.

Following the meshing of a domain, various simulation setup parameters are defined using the 'analysis condition' wizard of the preprocessor. However, the choice of outlet boundary condition is observed to create either convergence or divergence. Natural inflow/outflow boundary condition at the outlet boundary resulted in convergence in solution. For initiating the transient simulation, a steady state airflow profile within the domain is used as initial velocity condition. The steady state airflow profile defined the topography induced downwind recirculation profile within the domain. To identify an appropriate model for simulation, various turbulent flow methods and turbulence models are used for simulating the same domain with similar simulation setup but with various methods of turbulent flow. The LES method represented better resolution in resolving the surface roughness and the heat flux at the pit boundary, and simulated the velocity and the thermal boundary layers better than the other methods of turbulent flow.

The four-component net radiation sensors and temperature sensors, installed inside an open-pit mine, and the weather stations data provided input information for modeling the dust dispersion. Based on the various climatic conditions, different input parameters were categorized

for simulation. The winter condition is simulated for moderate and extreme winter conditions. While for summer, the model domains are simulated for fair, moderate and extreme summer insolation conditions.

Since an exact flow situation in open-pit mines is not known a priori, it is necessary to investigate various turbulent models to identify the model that would simulate flow phenomena and predict fugitive dust distributions within the pit with reasonable accuracy. Dispersion models differ in their assumptions and structures as well as in the algorithm used; as a result, the simulated predictions vary from model to model. Furthermore, it is also important to investigate the performance of a CFD model when simulating complex phenomena such as the transport and distribution of fugitive dust in an open-pit mine.

To compare the effects of various turbulence models and turbulent flow methods on dust dispersion, two idealized open-pit domains are simulated for various weather conditions. The input values for the initial and the boundary conditions are obtained from net radiation sensors, temperature sensors and weather stations data. The modeling domains are simulated to capture the ABL and the micrometeorological flow inside the open-pit. Following the simulation of the airflow pattern, fugitive dust particles are generated from various dust sources inside the model domain. Two different methods, namely the RANS using Standard k-ε turbulence models and the LES using the SGS/DSGS/WALE modeling, are used for simulation with the similar simulation setup. The simulation results for the LES and the standard k-ε RANS turbulence models are not in agreement in the prediction of the fugitive dust retention in the model domain.

The analysis of results of the standard k-ε RANS turbulence model shows an extensive settling of the dust particles during the initial stage of simulation. This phenomenon significantly reduces the number of dispersed dust particles in the airflow. Excessive downfall of the dust particles during summer also reduces the duration to clear the dust particles out of the domain. While the LES shows negligible settling of dust particles during the initial stage. The settling time based on the terminal gravitational settling velocities of PMs also suggests that the LES provides a more feasible estimate than the RANS model. The pathlines of the dust particles in the RANS model also show small scale irregularities which represent the lack of accuracy in the calculation of the net resultant force on the dust particle. Whereas, the pathlines of the dust particles in the LES method follow a well-developed, smooth re-circulatory pattern that

resembles the re-circulatory pattern of the airflow. The results of the RANS simulation predict the gravitational settling as the foremost mechanism for removal of the fugitive dust. While in the LES simulation, the re-circulatory airflow inside the domain is the primary mechanism for removal of the fugitive dust. Based on the results of this research, the LES seemed to be a better choice than the RANS model.

Even with a fully developed background flow, the results of spatial dispersion in LES may vary depending on the selection of the moment of particle injection. Dispersion of particles in buoyancy driven flow is highly influenced by the eddy dynamics. Consequently, the particle dispersion may vary if the particles arrive in the eddy region before or after the eddy passes through that region, causing the dust-particle pathlines to move in one direction or another.

With RANS, averaging of velocities and the applied particle dispersion model causes most probable particle dispersion pattern that can be captured in a single simulation. Two idealized and actual open-pit domains are simulated for various weather conditions to predict the retention of fugitive dust generated due to various mining unit operations. Completely different dust dispersion phenomena during summer and winter conditions are displayed. In winter conditions, development of an atmospheric inversion significantly affected the amount of dust retention inside the open-pit domain. While during summer, airborne dust particles were transported out of the open-pit domain within a short time.

The presence of low level cloud in the open-pit mine, results in a different radiation energy balance, which helps in the removal of atmospheric inversion in open-pit mines during the winter. A novel approach was used to simulate the effect of cloud cover. A specific magnitude of heat flux was initially introduced in the CCL and the pit boundary to simulate the effects of cloud cover. Following the initial state; a heat flux of zero magnitude was introduced at both the CCL and the pit boundary. The simulation results of all the domains, however, do not show any changes in the stratified cold air mass inside the open-pit and do not lift the inversion layer. While a negligible amount of fugitive dust is removed, the continued presence of an inversion layer results in extensive fugitive dust retention within the pit.

An increased wind speed at the inlet boundary along with cloud covers, significantly changes the stratified cold air mass inside the pit, and penetrates the air temperature inversion layers. Since the irregularities result in higher mechanical turbulences, the irregularities in the

topography of an actual domain help in weakening the inversion. Therefore the presence of cloud cover and a good convective wind are required for removal of the stratified cold air mass and the trapped fugitive dust within the open-pit mine.

8.2 Conclusions

8.2.1 Atmospheric Boundary Layer

The dust propagation in a high-latitude open-pit mine is dependent on the Atmospheric Boundary Layer (ABL) and the flows at micro-scales inside the open-pit. The modeling domains must, therefore, be simulated to capture the micro-scales of ABL flow inside the open-pit. Under the winter conditions, negative heat flux from the pit surface results in the formation of an atmospheric inversion inside the open-pit. Whereas, during the summer, positive heat flux from the pit surface develops a convective (unstable) boundary layer in the open-pit domains.

8.2.2 Computational Resource

An assessment of computational resources requirement is important before conducting a CFD simulation of a deep open-pit. It is advisable to have a computational resource that can handle fine grid size. Thus, the use of high performance computing (HPC) is needed in CFD simulation of deep open-pit mines.

8.2.3 Preprocessing of the Model

A good-quality and appropriately sized mesh is required to obtain good results from a CFD simulation. Any strategy for CFD modeling starts with the geometry. If the geometry is simple, then meshing usually is not a problem. In the case of a highly unstructured and irregular geometry, as described in this study, a considerable amount of time and a significant effort are required to generate a good-quality mesh. Instead of depending on automatic meshing processes, it is preferable to edit the mesh manually to achieve the desired quality.

8.2.4 One Way Coupled Eulerian-Lagrangian Simulation Approach

In this thesis, the propagation and the retention of fugitive dust in a high latitude open-pit mine is simulated using the SC/Tetra software developed by the software CRADLE. For solving the model domain, a coupled simulation approach is selected. To solve the airflow inside the open-pit domain, various turbulent flow methods and turbulence models are applied in the Eulerian reference frame. The Eulerian method develops the conservations equations on a control volume (mesh elements) basis and solves the airflow parameters at each mesh elements.

The parameters, such as, gravity, velocity, pressure of the airflow is solved using the Eulerian method. These airflow parameters are calculated as a function of location and time in the Eulerian method. However, for solving the turbulent dispersion of the fugitive dust particles, the Lagrangian algorithm is applied to the dust particles. The Lagrangian stochastic model characterizes the advection and the diffusion processes of the individual dust particles as a function of time only.

Due to an extremely small fraction of particles with respect to the volume of the carrier phase (air) in the pit, the assumption of one way coupling is applied. This means that the dynamics of the carrier phase (air) drives the motion of the dispersed phase (particulate). The presence of the dispersed phase has no effect on the dynamics of the carrier phase.

8.2.5 Modeling Results using Standard k-ε RANS Turbulence Model and LES Method

The analysis of results of the standard k-ε RANS turbulence model shows an extensive settling of the dust particles during the initial stage of simulation. This phenomenon significantly reduces the number of dispersed dust particles in the airflow. Excessive downfall of the dust particles during summer also reduces the duration to clear the dust particles out of the domain. The LES shows negligible settling of dust particles during the initial stage. The settling time based on the terminal gravitational settling velocities of PMs also suggests that the LES provides a more feasible estimate than the RANS model. The pathlines of the dust particles in the RANS model also show small scale irregularities which represent the lack of accuracy in the calculation of the net resultant force on the dust particle. Whereas, the pathlines of the dust particles in the LES method follow a well-developed, smooth re-circulatory pattern which resembles the re-circulatory pattern of the airflow. The results of the RANS simulation predict the gravitational settling as the foremost mechanism for removal of the fugitive dust. In the LES simulation, the re-circulatory airflow inside the domain is the primary mechanism for removal of the fugitive dust. Based on the results of this research, the LES seemed to be a better choice than the RANS model.

Even though a large body of fundamental and theoretical work has already been published, existing theoretical models are incapable of predicting the dispersion of dust in open pit mine accurately. This difficulty is inherent in the phenomena involved in the dust source estimation, entrainment, as well as the aero-dynamic forces exhibit a stochastic distribution. Coherent

structures in the air flow play an important role on the threshold entrainment conditions as well as entrainment rates. As a result, entrainment rate is not constant under specified conditions, but varies as a function of time.

8.2.6 Mitigation of Dust Retention during Air Temperature Inversion

For natural removal of the inversion layers, the presence of cloud cover and a good convective wind are important. Without a cloud cover, the thermal forces from the Pit surface enhance the stratification. In absence of a convective wind, the mechanical forces do not have the potential to penetrate the cold air layers. The critical wind speed for removal of the air temperature inversion is dependent on (1) the topography and the aspect ratio of the domain; (2) the temperature gradient of the stratified layers; and (3) the net radiation balance.

8.3 Limitations of the Study

This research revealed serious gaps in the available information:

(i) Very few studies on ventilation of deep open-pit mines, especially in the Arctic, have been conducted.

(ii) There was a lack of weather data (velocity, turbulence parameters) at the mine.

(iii) The model domain of an open-pit mine is extremely large, and requires extensive computational resources.

(iv) There was a lack of continuously monitored data of fugitive dust concentrations at various locations in the pit.

(v) The simulation results are not validated due to unavailability of dust concentration data during this research.

8.4 Future Research

Based on the research presented here, it is suggested that further studies are conducted in several areas:

(i) Continuous monitoring data of pollution concentrations and wind velocity from the open-pit mine are needed for accurate model simulation.

(ii) Air temperature inversions affecting mining operations at various open-pit mines in the Arctic, and other regions should be further explored to provide a better understanding of the problem.

References

Alvarez, J.T., Alvarez, I.D., Lougedo, S.T. and Hevia, B.G. (2007), "A CFD Lagrangian particle model to analyze the dust dispersion problem in quarries blast", Computational Methods in Multiphase Flow IV, WIT Transactions on Engineering Sciences, Vol 56, © 2007 WIT Press, ISSN 1743-3533 (on-line), pp. 9-18.

Appleton, T. J., Kingman, S. W., Lowndes, I. S., and Silvester, S. A. (2006), *"The development of a modeling strategy for the simulation of fugitive dust emission from in-pit quarrying activities a UK case study"*, International Journal of Mining, Reclamation and Environment, Vol. 20, No. 1, March 2006, pp. 57 – 82.

Arpacıoğlu, C. B. and Er, C. (2003), *"Estimation of Fugitive Dust impact of Open Pit mine on Local Air Quality_A case study, Bellavista Gold Mine, Costa Rica"*, Proceedings of 18th International Mining Congress and Exhibition of Turkey-IMCET 2003, © 2003, ISBN 975-395-605-3, pp. 229-235.

Arya, P. S. (2001), *"Introduction to Micrometeorology"*, Vol. 79: Academic press.

Baklanov, A.A. (1995), *"Numerical modelling of atmosphere processes in mountain cirques and open pits"*, Transactions on Ecology and the Environment vol 6, © 1995 WIT Press, www.witpress.com, ISSN 1743-3541, pp. 231-238.

Basu, S., and Porté-Agel, F. (2006), "Large-Eddy Simulation of Stably Stratified Atmospheric Boundary Layer Turbulence: A Scale-Dependent Dynamic Modeling Approach." Journal of the Atmospheric Sciences no. 63 (8), pp. 2074-2091.

Beychok, M. R. (1994), *"Fundamentals of Stack Gas Dispersion"*, 3rd ed., Milton R. Beychok: Newport Beach, CA.

Bhaskar, R. and Tandon, N. (1998), *"A Three-dimensional Finite Element Model to Predict Airflow and Pit Retention for an Open-Pit Mine"*, Environmental Impact of Mining Activities- Emphasis on Mitigation and Remedial Measures, Edited by José M. Azcue, ISBN 3-540-64344-3, pp. 69-82.

Bhowmick, T. and Bandopadhyay, S. (2015), *"Comparison of Turbulence Models for Estimation of Fugitive Dust Retention in Open-Pit Mines"*, Proceedings of 15th North American Mine Ventilation Symposium, 2015, Blacksburg, Virginia, pp. 1-6.

Bhowmick, T., Bandopadhyay, S. and Ghosh, T. (2015), *"Three-dimensional CFD modeling approach to approximate air pollution conditions in high latitude open-pit mines"*, WIT Transactions on The Built Environment, Vol. 168, Sustainable Development, Vol. 2, ISSN 1743-3509 (on-line), ISBN: 978-1-78466-157-1, doi:10.2495/SD150652, pp. 741-753.

Bhowmick, T., Raj, K. V. and Bandopadhyay, S. (2015a), *"Constraints and Consequences In 3-Dimensional CFD Modeling Of Open-Pit Mines"*, Preprint 15-018, SME Annual Meeting (2015), Denver, CO, pp. 1–6.

Bhowmick, T., Raj, K. V. and Bandopadhyay, S. (2015b), *"Three-dimensional modeling of fugitive dust dispersion in idealized openpit mines"*, Mining Engineering, Vol. 67, No. 10, pp. 45-52.

Blocken, B., Stathopoulos, T. and Carmeliet, J. (2007), "CFD Simulation of the Atmospheric Boundary Layer: Wall Function Problems." Atmospheric Environment no. 41 (2), pp. 238-252.

Chinthala, S. and Khare, M. (2011), "*Particle dispersion within a deep opencast coal mine",* Air Quality - Models and Applications, ISBN 978-953-307-307-1, Edited by Prof. Dragana Popovic, pp. 81-98.

Cole, C. F. and Fabrick, A. J. (1984), *"Surface mine pit retention"*, Journal of Air Pollution Control Association, Vol 34, No. 6, pp. 674–675.

Cole, C. F. and Zapert, J. G. (1995), *"Air quality dispersion model validation at three stone quarries"*, Englewood, CO: TRC Environmental Corp, TRC project No. 14884 for the National Stone Association, Washington DC.

Collett, R. S. and Oduyemi, K. (1997), *"Air Quality Modeling: A Technical Review Of Mathematical Approaches"*, Meteorol Applic 4(3), pp. 235-246.

Collingwood, W., Raj, K. V., Choudhury, A. and Bandopadhyay, S. (2012), *"CFD Modeling of Air Flow in an Open Pit Mine"*, Mining Engineering, Vol. 64, No. 2, pp. 44-50.

EPA (1994), *"Modeling fugitive dust impacts from surface coal mining operations: phase II – model evaluation protocol"*, Research Triangle Park, NC: U.S. Environmental Protection Agency, Office of Air Quality Planning and Standards, Technical Support Division, EPA publication No. EPA–454/ R–94–025.

EPA (1995), *"Modeling fugitive dust impacts from surface coal mining operations: phase III – evaluating model performance"*, Research Triangle Park, NC: U.S. Environmental Protection Agency, Office of Air Quality Planning and Standards, Emissions, Monitoring, and Analysis Division, EPA publication No. EPA–454/R–96–002.

EPA (1996), *"Executive summary. In: Air quality criteria for particulate matter. Vol. I"*, Research Triangle Park, NC, U.S. Environmental Protection Agency, National Center for Environmental Assessment, EPA publication No. EPA/600/P–95/001aF, pp. 1–1 to 1–21.

EPA (1998a), *"A comparison of CALPUFF modeling results to two tracer field experiments"*, Research Triangle Park, NC: U.S. Environmental Protection Agency, Office of Air Quality Planning and Standards, Emissions, Monitoring, and Analysis Division, EPA publication No. EPA–454/ R–98–009.

EPA (1998b), *"A comparison of CALPUFF with ISC3"*, Research Triangle Park, NC: U.S. Environmental Protection Agency, Office of Air Quality Planning and Standards, EPA publication No. EPA–454/R–98–020.

EPA (2003a), *"AERMOD: Latest features and evaluation results"*, Research Triangle Park, NC: U.S. Environmental Protection Agency, Office of Air Quality Planning and Standards, Emissions, Monitoring, and Analysis Division, EPA publication No. EPA–454/R–03–003.

EPA (2003b), *"Comparison of regulatory design concentrations: AERMOD vs ISCST3, CTDMPLUS, ISC-PRIME"*, Research Triangle Park, NC: U.S. Environmental Protection Agency, Office of Air Quality Planning and Standards, Emissions, Monitoring, and Analysis Division, EPA publication No. EPA–454/R–03–002.

EPA (2005), *"Technology transfer network support center for regulatory air models"*, [http://www.epa.gov/scram001/tt22.htm].

Flores F., Garreaud R. and Muñoz, R. C. (2013a), "CFD simulations of turbulent buoyant atmospheric flows over complex geometry: solver development in OpenFOAM", Computers & Fluids, Vol. 82, pp. 1-13.

Flores, F., Garreaud, R. and Muñoz, R. C. (2013b), *"OpenFOAM applied to the CFD simulation of turbulent buoyant atmospheric flows and pollutant dispersion inside large open pit mines under intense insolation"*, Computers & Fluids, Vol. 90 (2014) © 2013 Elsevier Ltd, pp. 72–87.

Grainger, C. and Meroney, R. N. (1992), *"Dispersion in an open-cut coal mine in stably stratified flow"*, Prepared for Submission to Journal of Boundary Layer Meteorology, CEP91-92CG-RNM-5, pp. 1-13.

Hartmann, B., and Wendler, G. (2005), *"Climatology of the winter surface temperature inversion in Fairbanks, Alaska"*, 85th AMS Annual Meeting, San Diego, CA, p. 187.

Heinerikson, A. (2004), *"Memorandum of June 3, 2004, from Arron Heinerikson, Trinity Consultants, Olathe, KS, to W. R. Reed"*, NIOSH Pittsburgh Research Laboratory, Pittsburgh, PA.

Jones, T., Morgan, A. and Richards, R. (2003), *"Primary blasting in a limestone quarry: physicochemical characterization of the dust clouds"*, Mineralogical Magazine, April 2003, Vol. 67(2), pp. 153–162.

Kosović, B., and Curry, J. A. (2000), "A Large Eddy Simulation Study of a Quasi-Steady, Stably Stratified Atmospheric Boundary Layer." Journal of the Atmospheric Sciences no. 57 (8), pp. 1052-1068.

Lesieur, M., Métais, O., and Comte, P. (2005), *"Large-Eddy Simulations of Turbulence"*. Cambridge; New York: Cambridge University Press.

Long, M. E. (2011), *"Air Quality Modeling and Impacts on the Mining Industry: An Overview"*, Minexpo.

Lowndes, I.S., Silvester, S.A., Kingman, S.W. and Hargreaves D.M. (2008), *"The application of an improved multi-scale computational modelling technique to predict fugitive dust dispersion and deposition within and from surface mining operations"*, 12th U.S./North American Mine Ventilation Symposium 2008 – Wallace (ed.), ISBN 978-0-615-20009-5, pp. 359-366.

Malingowski, J., Atkinson, D., Fochesatto, J., Cherry, J., and Stevens, E. (2014), *"An observational study of radiation temperature inversions in Fairbanks, Alaska"*, Polar Science, Vol. 8, pp. 24-39, doi: 10.1016/j.polar.2014.01.002.

Menter, F. R. (1993), *"Zonal Two Equation k-w Turbulence Models for Aerodynamic Flows"*, AIAA Paper 93-2906, 24th Fluid Dynamics, Plasmadynamics, and Lasers Conference.

Menter, F. R. (1994), *"Two-Equation Eddy-Viscosity Turbulence Models for Engineering Applications"*, AIAA Journal, vol. 32, no. 8, pp. 1598-1605.

Menter, F. R. (2012), Best Practice: Scale-Resolving Simulations in ANSYS CFD.

Page, S. J., Reed, R. and Listak, J. M. (2008), *"An expanded model for predicting surface coal mine drill respirable dust emissions"*, International Journal of Mining, Reclamation and Environment, Vol. 22, No. 3, September 2008, ISSN 1748-0930 print/ISSN 1748-0949 online, pp. 210–221.

PEDCo Environmental, Inc. (1979), *"Review of Atmospheric Dispersion Modelling Procedures for Surface Coal Mines"*, Prepared for U.S. Department of the Interior, Office of Surface Mining Reclamation and Enforcement, Washington, D.C. Contract no. 68-02-2535.

Pereira, M. J., Soares, A. and Branquinho, C. (1997), *"Stochastic simulation of fugitive dust emissions"*, Baafi EY, Schofield NA, eds., Wollongong 1996, Fifth International Geostatistics Congress, Vol. 2, Dordrecht, Netherlands: Kluwer Academic Publishers, pp. 1055–1065.

Perezhilov, A. E., Khar'kovskii, V. S., Novik, G. Ya., Burchakov, A. S. and Grashchenkov, N. F. (1993), *"Control of dust flows in transporting material"*, Journal of Mining Science, March–April, 1993, Volume 29, Issue 2, pp 158-162.

Raj, K. V., Collingwood, W. and Bandopadhyay, S. (2013), *"Challenges In CFD Modeling Of Air Flow In Open-Pit Mines"*, Transactions of the SME, Vol. 334, No. 1, pp. 449-456.

Raj, K.V. (2015), *"Three Dimensional Computational Fluid Dynamics Models of Pollutant Transport in a Deep Open Pit Mine Under Arctic Air Inversion and Mitigation Measures"*, PhD Thesis, University of Alaska Fairbanks, Fairbanks, Alaska.

Reed, W. R., Westman. E. C. and Haycocks, C. (2001), *"An improved model for estimating particulate emissions from surface mining operations in the eastern United States"*, Securing the Future – Proceedings of the International Conference on Mining and the Environment (Skellefteå, Sweden, June 25–July 1, 2001). Stockholm, Sweden: Swedish Mining Association, pp. 693–702.

Reed, W. R., Westman, E. C. and Haycocks, C. (2002), "The introduction of a dynamic component to the ISC3 model in predicting dust emissions from surface mining operations", Bandopadhyay, S. ed., Application of Computers and Operations Research in the Mineral Industry: Proceedings of the 30th International Symposium, Littleton, CO: Society for Mining, Metallurgy, and Exploration, Inc., pp. 659–667.

Reed, W. R. (2003), *"An improved model for prediction of PM_{10} from surface mining operations"*, PhD Thesis, Virginia Polytechnic Institute and State University, Blacksburg, VA.

Reed, W. R. (2005), *"Significant Dust Dispersion Models for Mining Operations"*, Information Circular 9478, Department of Health and Human Services, NIOSH, DHHS (NIOSH) Publication No. 2005-138.

Richards, P. J., and Hoxey, R. P. (1993), "Appropriate Boundary Conditions for Computational Wind Engineering Models using the k-ε Turbulence Model." In *Computational Wind Engineering 1*, edited by S. Murakami, Oxford: Elsevier, pp. 145-153.

Shi, Y., Feng, X., and Wei, F. (2000), *"Three-dimensional non-hydrostatic numerical simulation for the PBL of an open-pit mine*", Boundary-Layer Meteorology, Vol. 94, Issue 2, pp. 197-224.

Silvester, S.A., Lowndes, I.S. and Hargreaves, D.M. (2009), *"A computational study of particulate emissions from an open pit quarry under neutral atmospheric conditions",* Atmospheric Environment 43 (2009) © 2009 Elsevier Ltd., pp. 6415–6424.

Software Cradle Co., Ltd. (2013a), *"User's Guide Basics of CFD Analysis"*, SC/Tetra Version 11.

Software Cradle Co., Ltd. (2013b), *"User's Guide Operation Manual"*, SC/Tetra Version 11.

Software Cradle Co., Ltd. (2013c), *"User's Guide Preprocessor Reference"*, SC/Tetra Version 11.

Software Cradle Co., Ltd. (2013d), *"User's Guide Solver Reference"*, SC/Tetra Version 11.

Stull, R. (1988), *"An Introduction to Boundary Layer Meteorology"*, Kluwer Academic Publishers, p. 380.

Tandon, N. (1998), *"Airflow Patterns and Pit Retention of Fugitive dust for a large open pit mine",* (MS Thesis), Department of Mining Engineering, university of Utah, Salt Lake City, Utah.

Torno, S.; Torano, J.; Menendez, M. and Gent, M. (2010), *"CFD simulation of blasting dust for the design of physical barriers"*, Environ Earth Sci (2011) 64 © Springer-Verlag 2010, DOI 10.1007/s12665-010-0818-6, pp. 73–83.

TRC Environmental Consultants, Inc. (1995), *"Dispersion of airborne particulates in surface coal mines: data analysis"*, Washington, DC, U.S. Environmental Protection Agency, Office of Air and Radiation, Office of Air Quality Planning and Standards.

Versteeg, H. K., and Malalasekera, W. (1995), "*An Introduction to Computational Fluid Dynamics: The Finite Volume Method"*, Longman Scientific & Technical, England.

U.S. Department of Labor (1996), *"Preventing silicosis"*, Washington, DC, U.S. Department of Labor, October 31.

Zhang, Z. and Chen, Q. (2007), *"Comparison of the Eulerian and Lagrangian methods for predicting particle transport in enclosed spaces"*, Atmospheric Environment 41 (2007) © 2007 Elsevier Ltd., pp. 5236–5248.

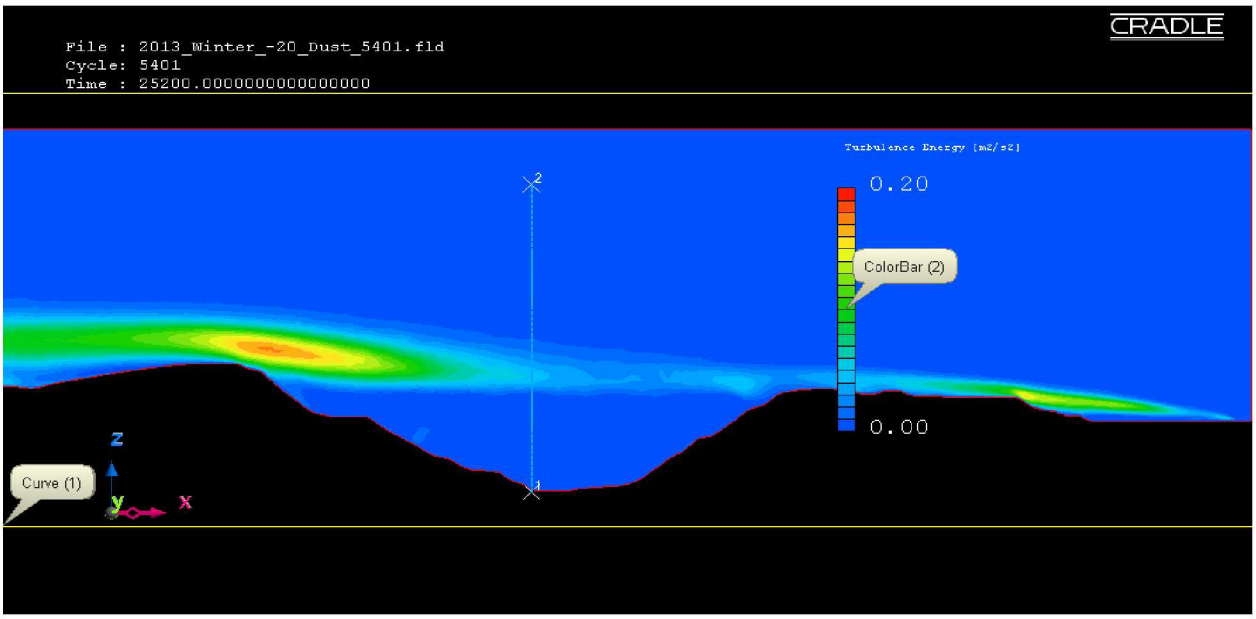

Figure A.1: Turbulent energy profile in the actual open-pit domain for moderate winter condition using the RANS method and a vertical line 1-2 at the pit-bottom.

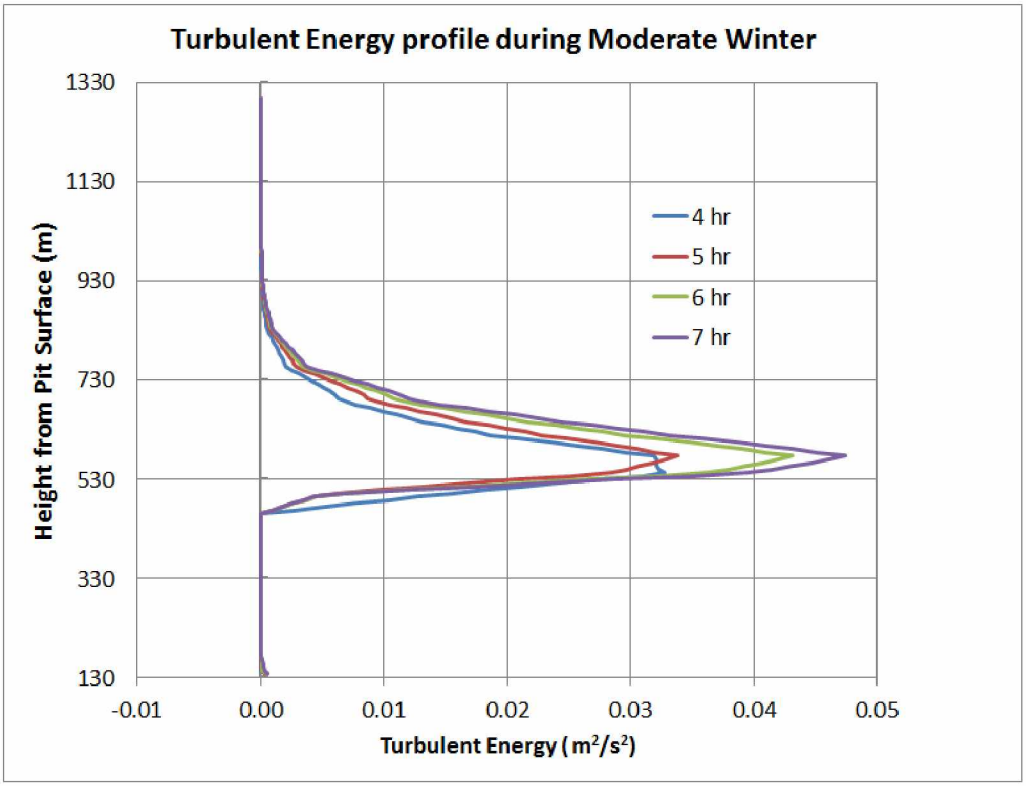

Figure A.2: Turbulent energy profile along line 1-2 for moderate winter condition.

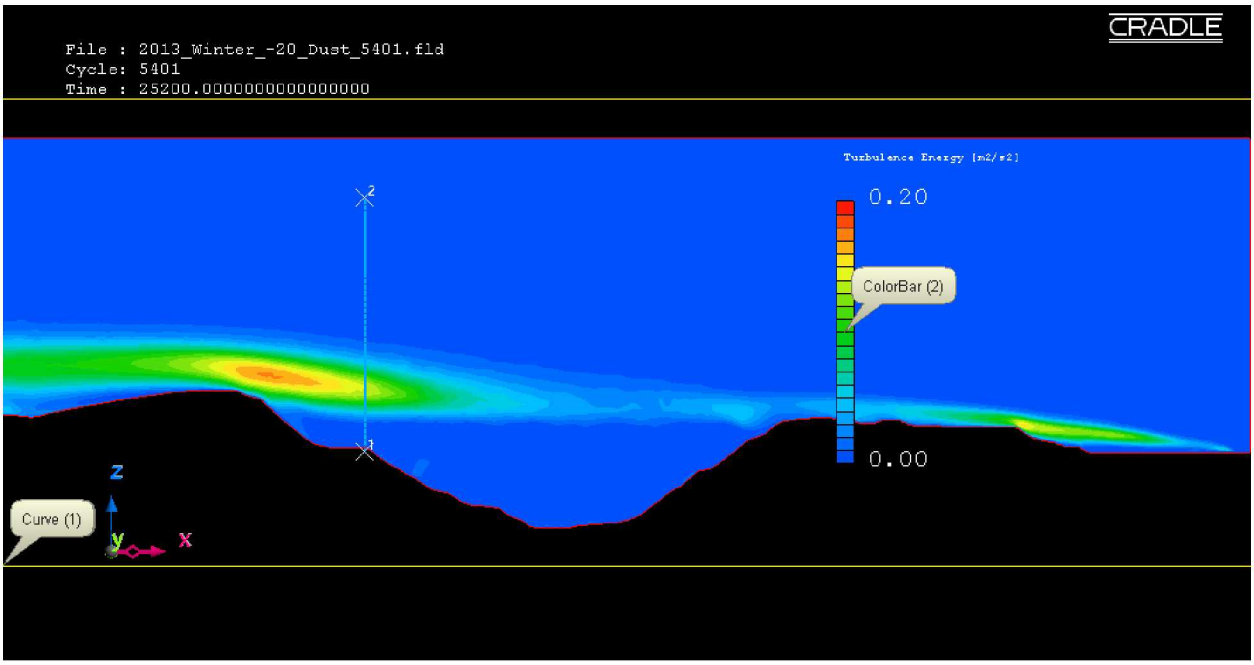

Figure A.3: Turbulent energy profile in the actual open-pit domain for moderate winter condition using the RANS method and a vertical line 1-2 near the pit-rim.

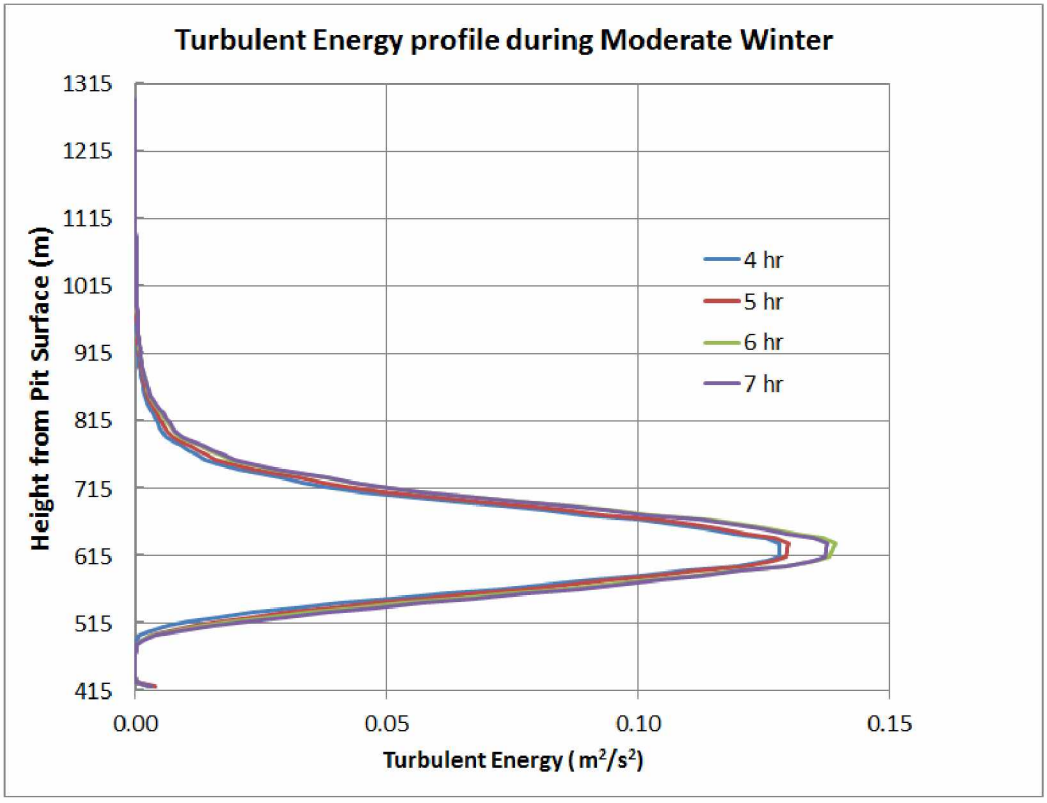

Figure A.4: Turbulent energy profile along line 1-2 for moderate winter condition.

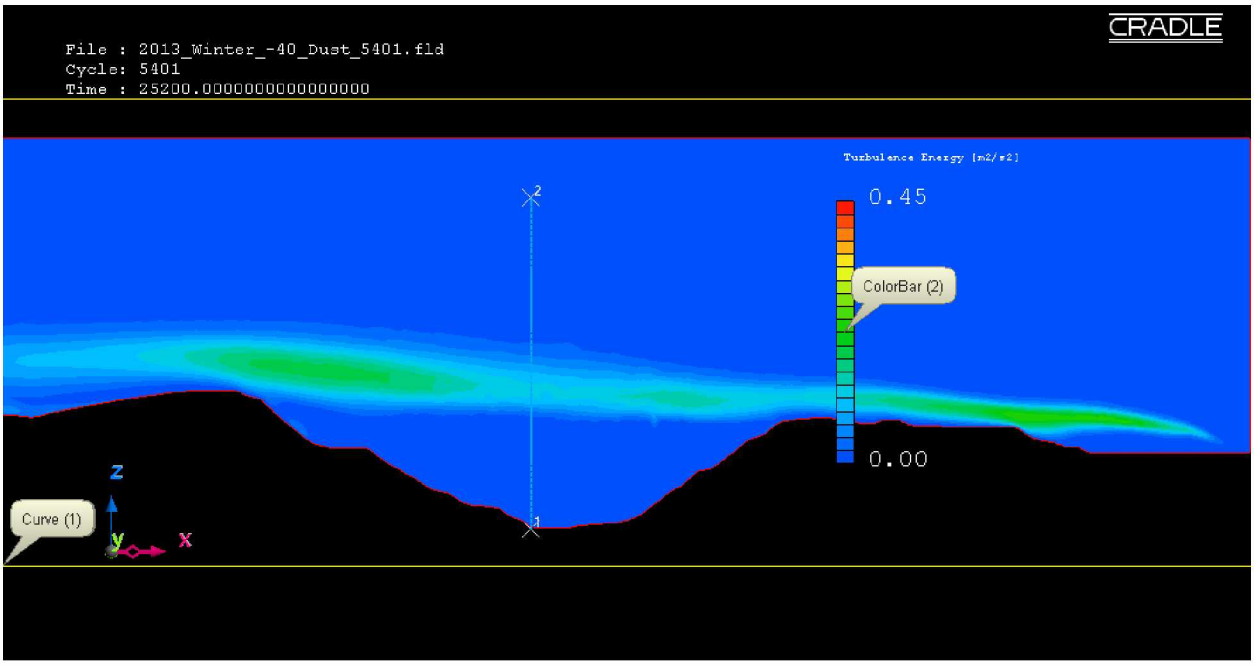

Figure A.5: Turbulent energy profile in the actual open-pit domain for extreme winter condition using the RANS method and a vertical line 1-2 at the pit-bottom.

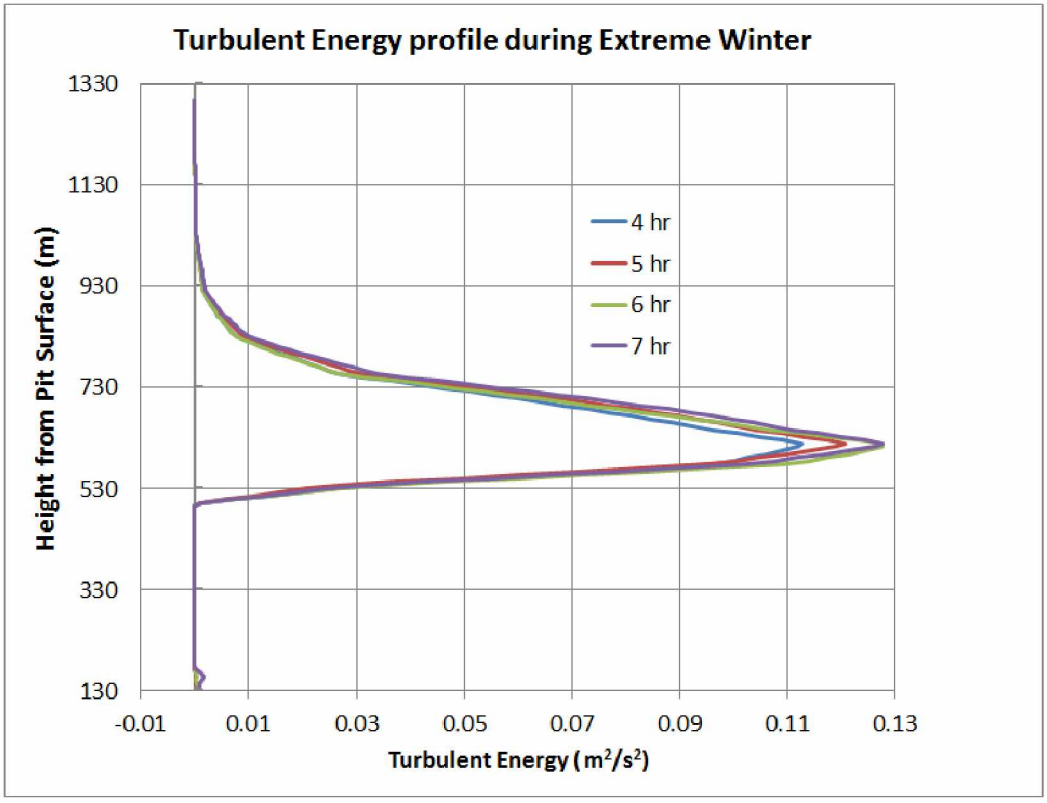

Figure A.6: Turbulent energy profile along line 1-2 for extreme winter condition.

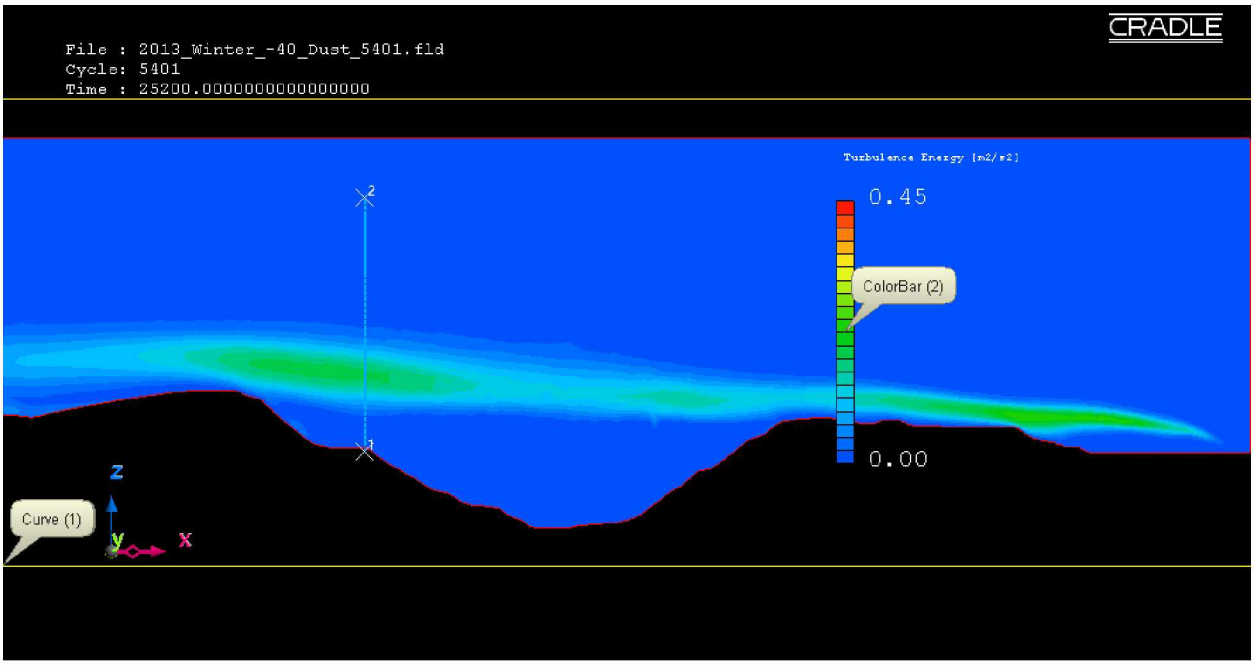

Figure A.7: Turbulent energy profile in the actual open-pit domain for extreme winter condition using the RANS method and a vertical line 1-2 near the pit-rim.

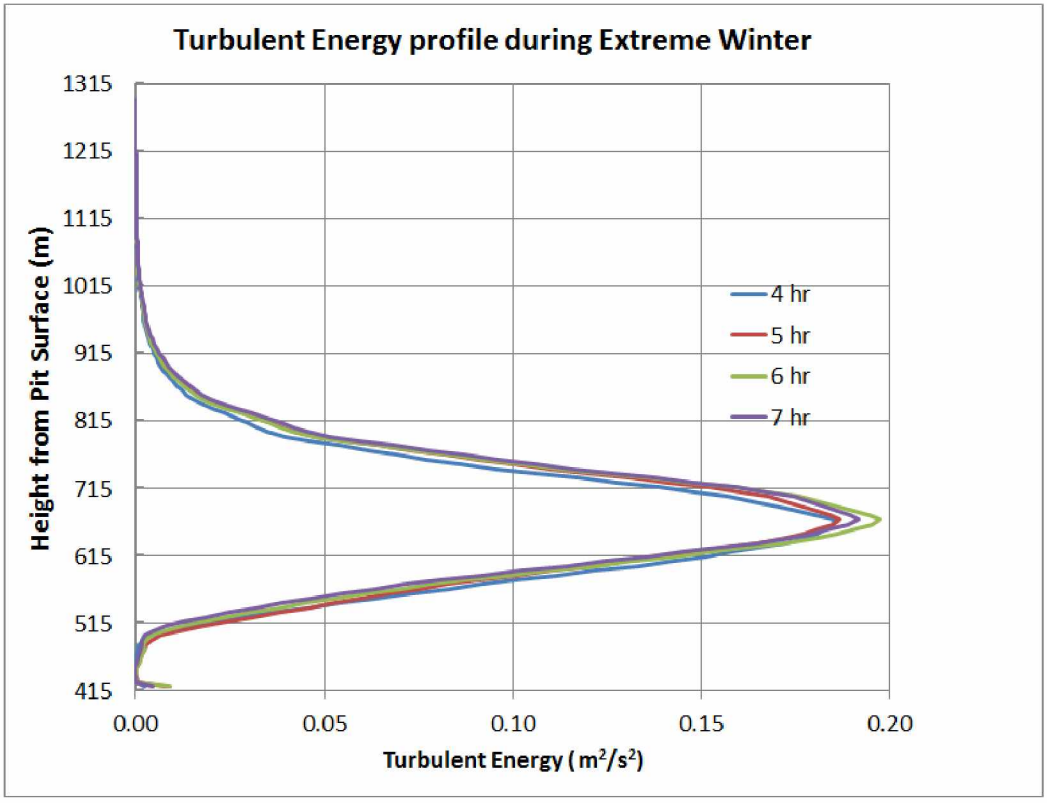

Figure A.8: Turbulent energy profile along line 1-2 for extreme winter condition.

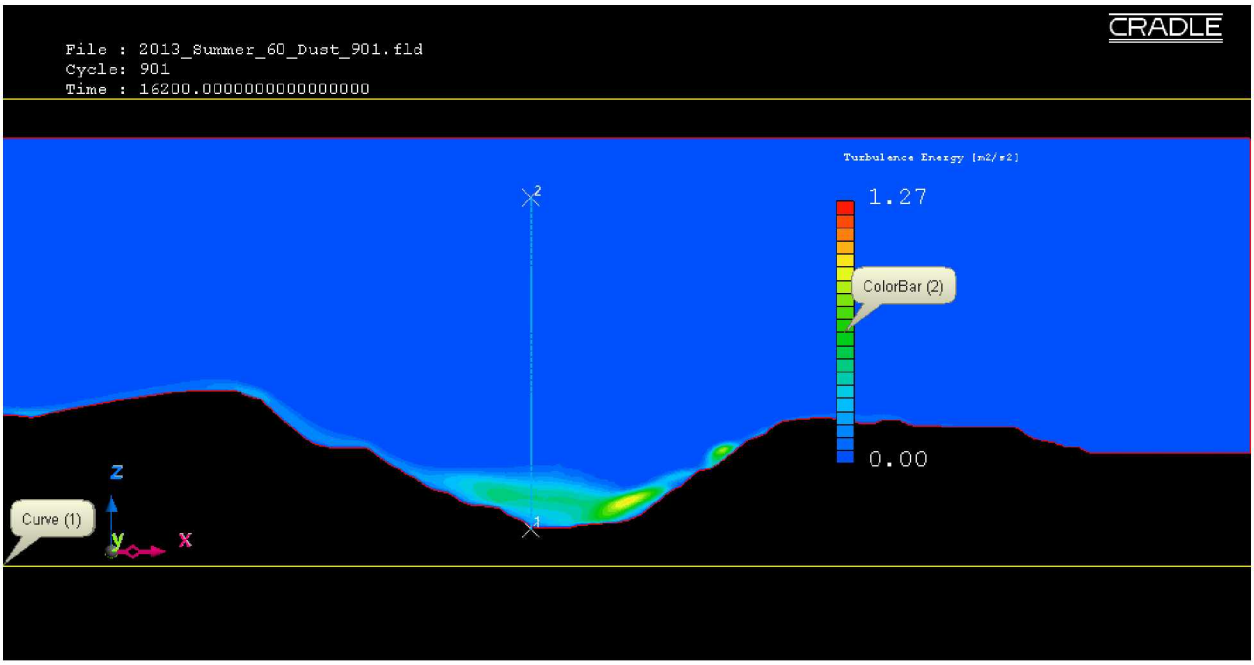

Figure A.9: Turbulent energy profile in the actual open-pit domain for fair insolation condition using the RANS method and a vertical line 1-2 at the pit-bottom.

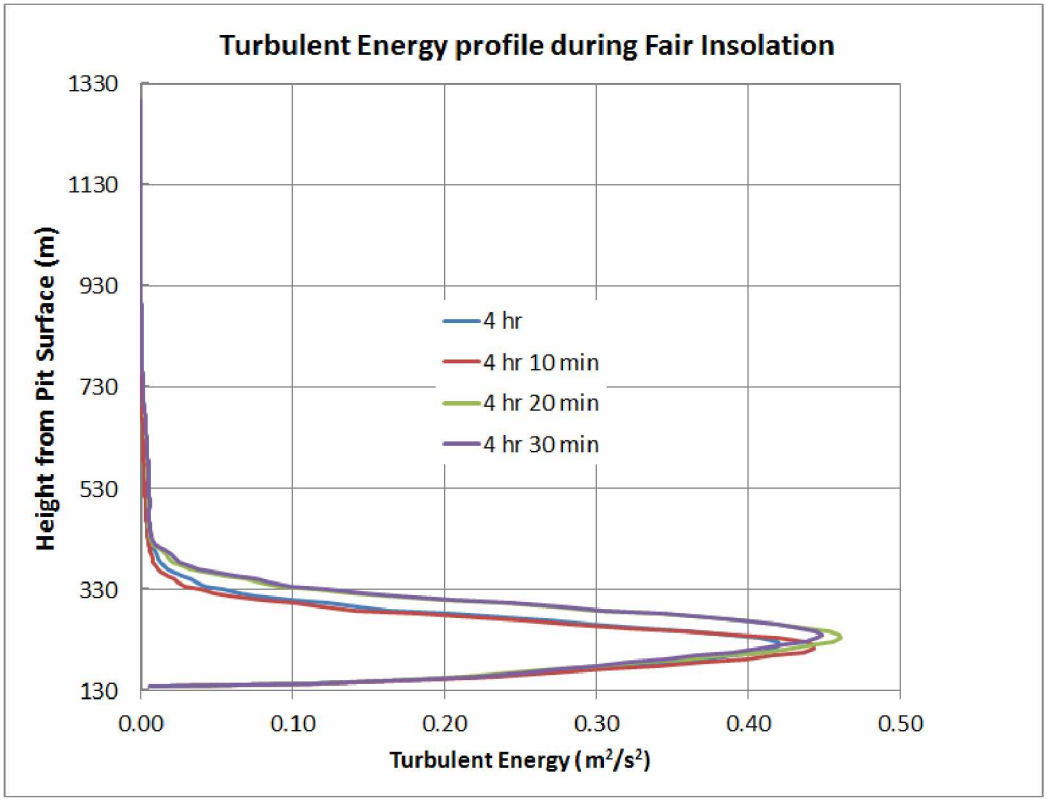

Figure A.10: Turbulent energy profile along line 1-2 for fair insolation condition.

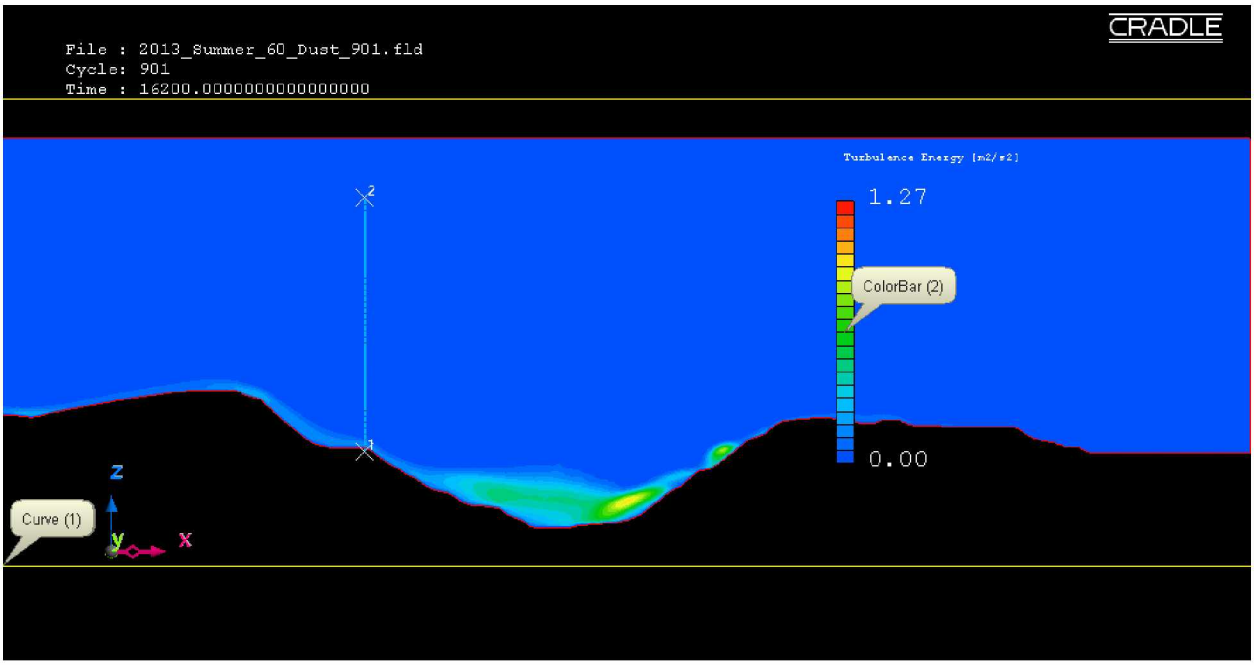

Figure A.11: Turbulent energy profile in the actual open-pit domain for fair insolation condition using the RANS method and a vertical line 1-2 near the pit-rim.

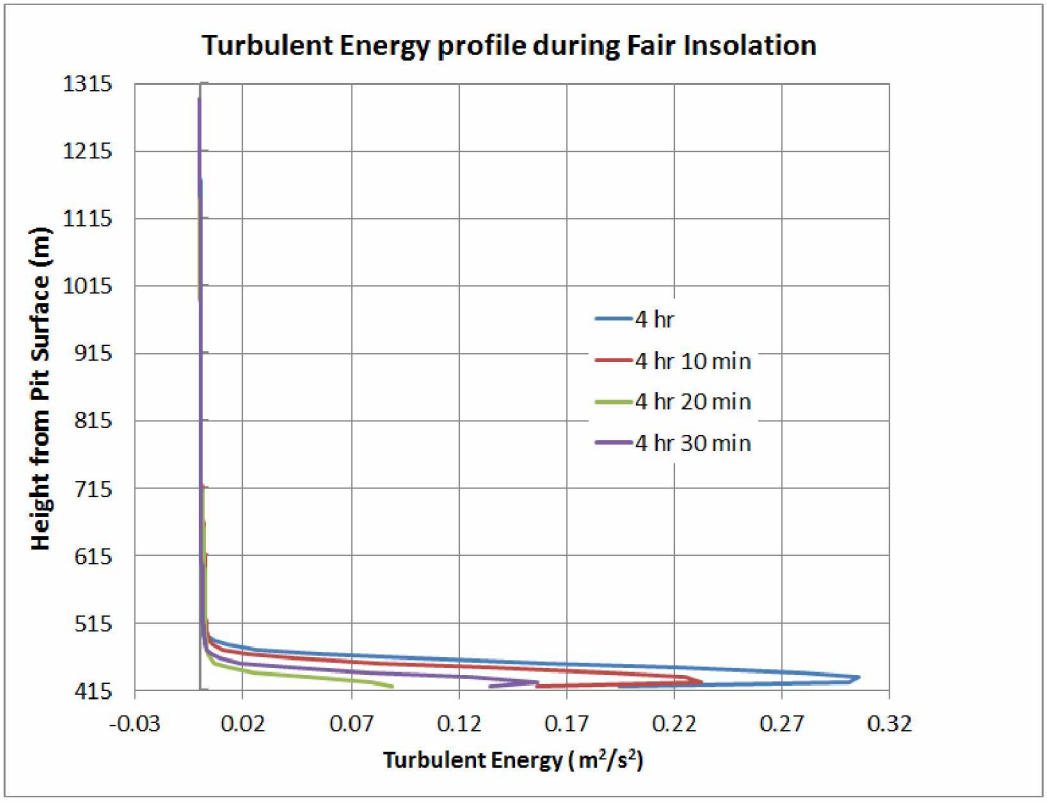

Figure A.12: Turbulent energy profile along line 1-2 for fair insolation condition.

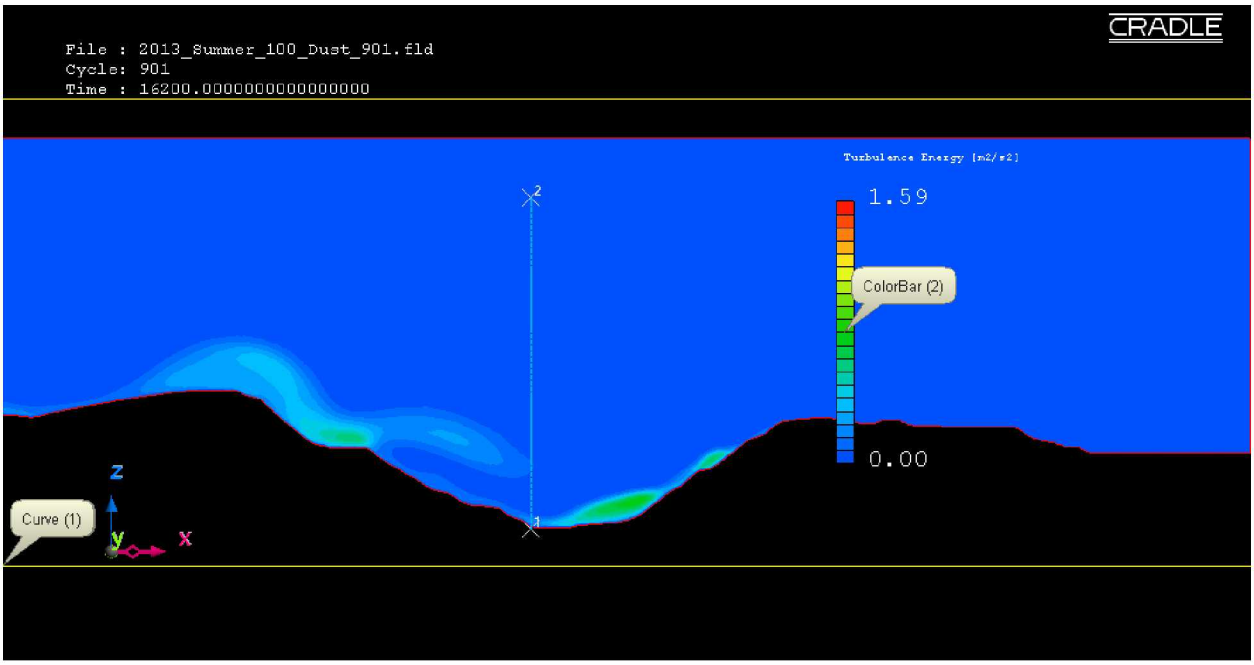

Figure A.13: Turbulent energy profile in the actual open-pit domain for moderate insolation condition using the RANS method and a vertical line 1-2 at the pit-bottom.

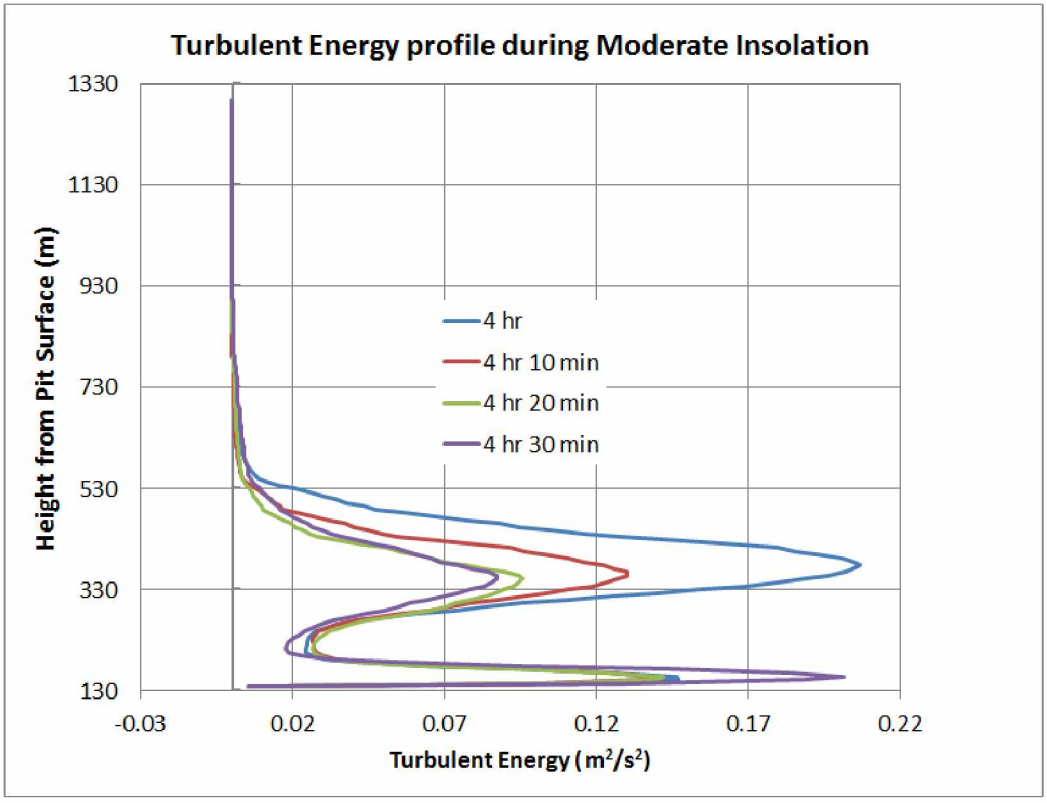

Figure A.14: Turbulent energy profile along line 1-2 for moderate insolation condition.

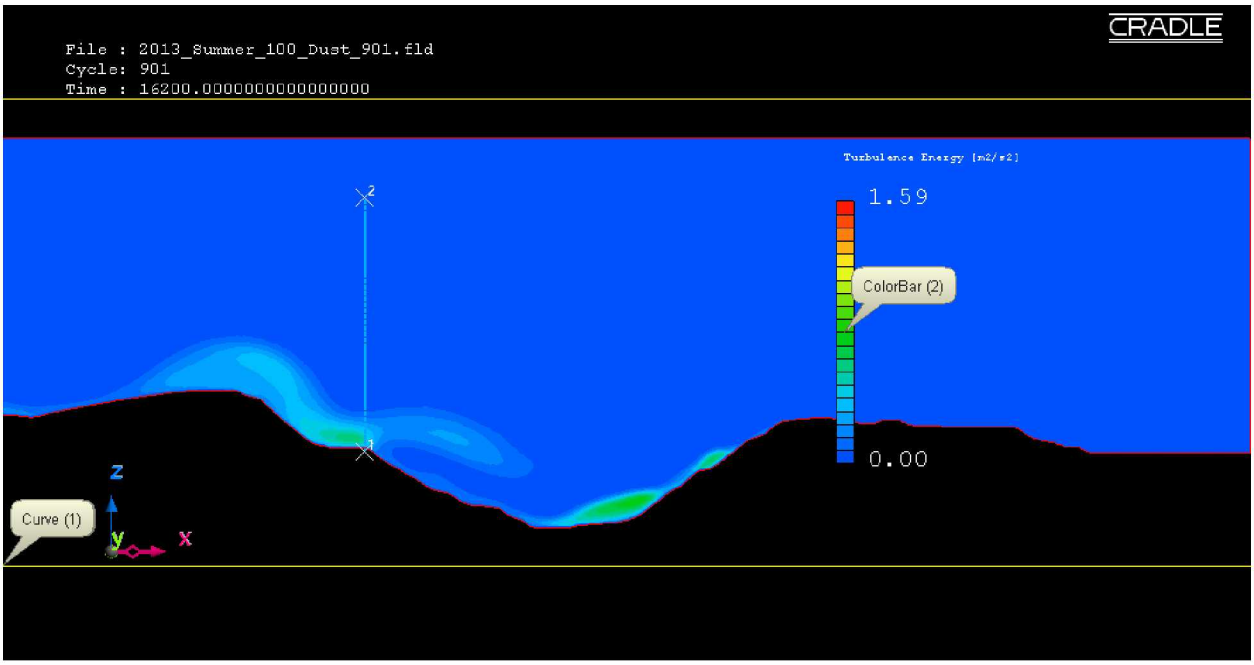

Figure A.15: Turbulent energy profile in the actual open-pit domain for moderate insolation condition using the RANS method and a vertical line 1-2 near the pit-rim.

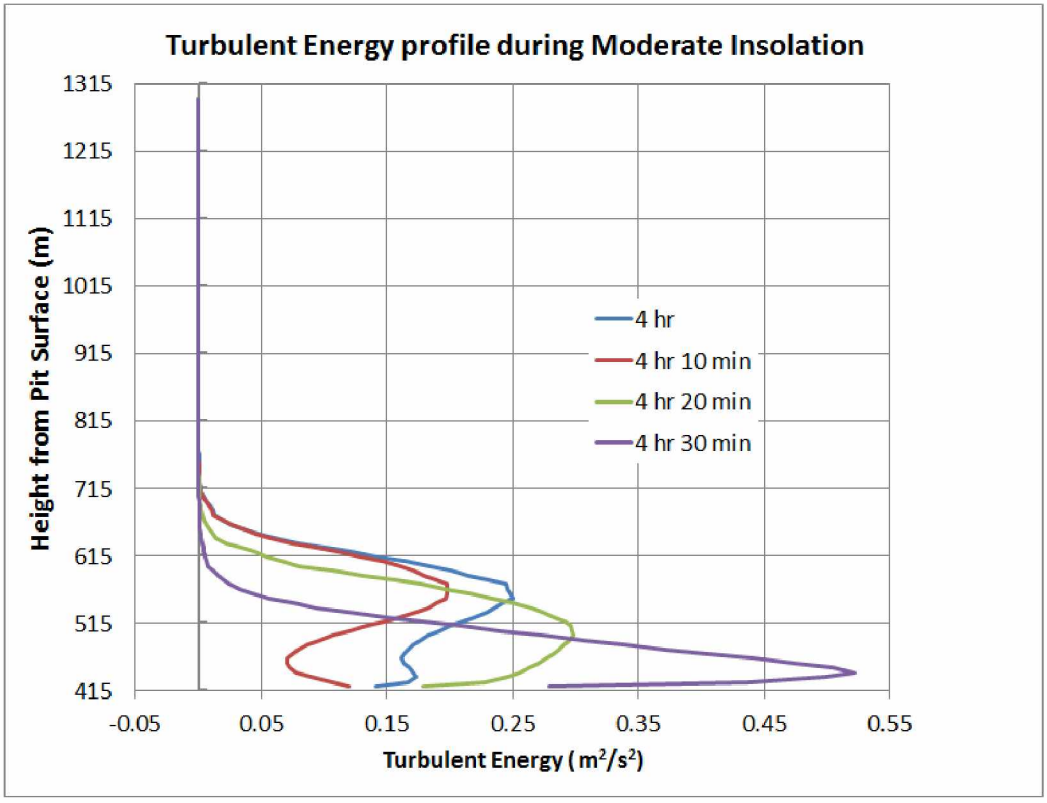

Figure A.16: Turbulent energy profile along line 1-2 for moderate insolation condition.

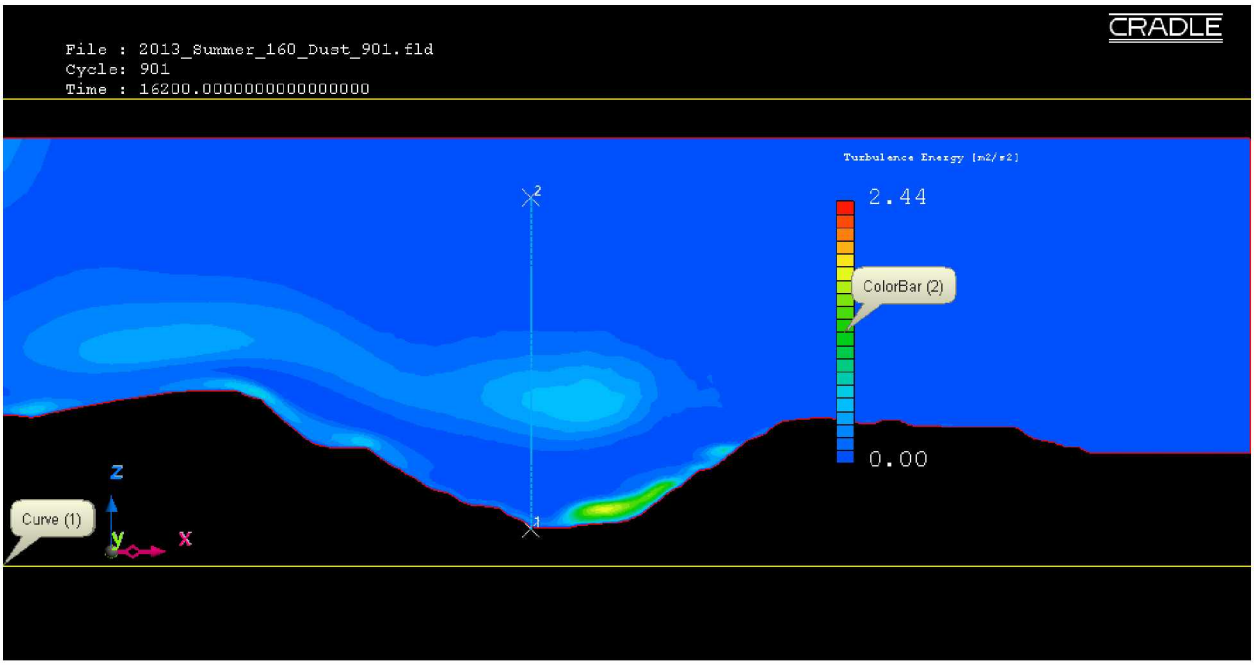

Figure A.17: Turbulent energy profile in the actual open-pit domain for extreme insolation condition using the RANS method and a vertical line 1-2 at the pit-bottom.

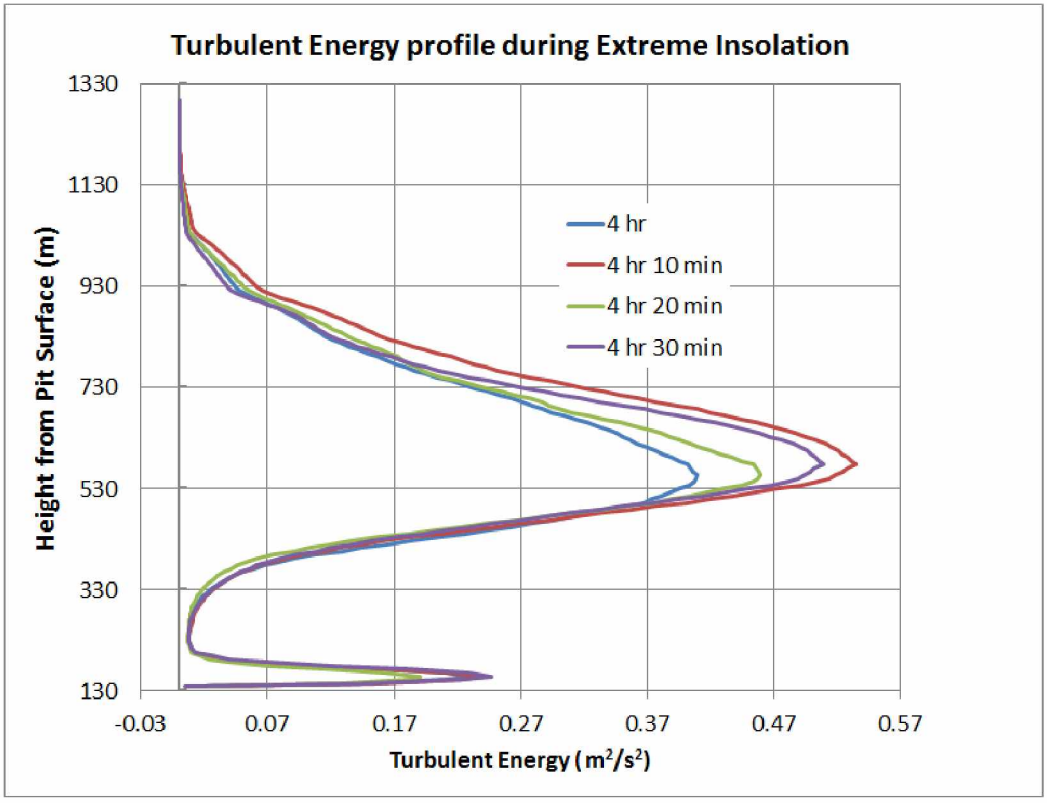

Figure A.18: Turbulent energy profile along line 1-2 for extreme insolation condition.

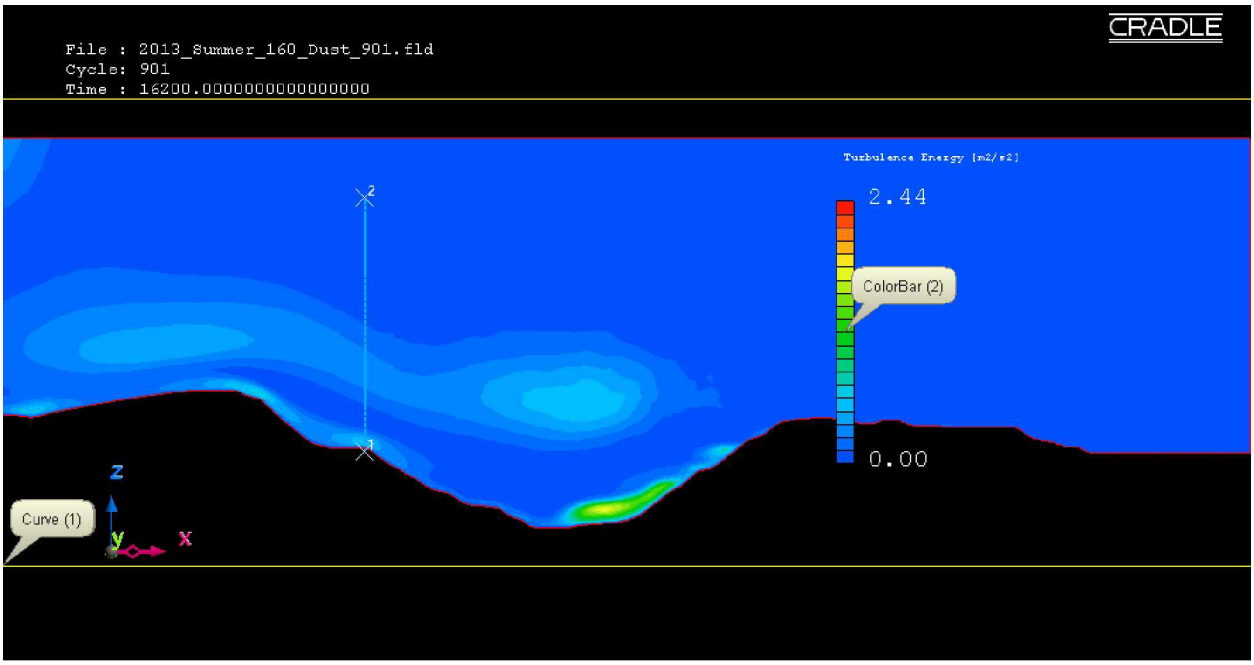

Figure A.19: Turbulent energy profile in the actual open-pit domain for extreme insolation condition using the RANS method and a vertical line 1-2 near the pit-rim.

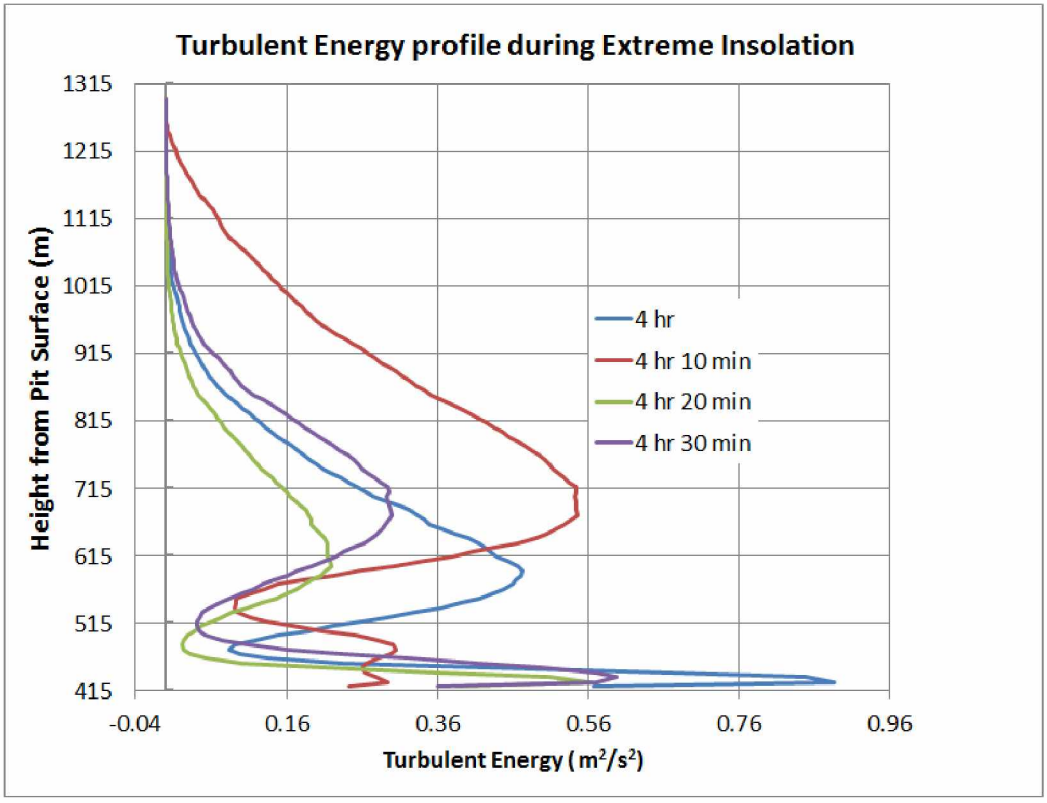

Figure A.20: Turbulent energy profile along line 1-2 for extreme insolation condition.

Appendix B

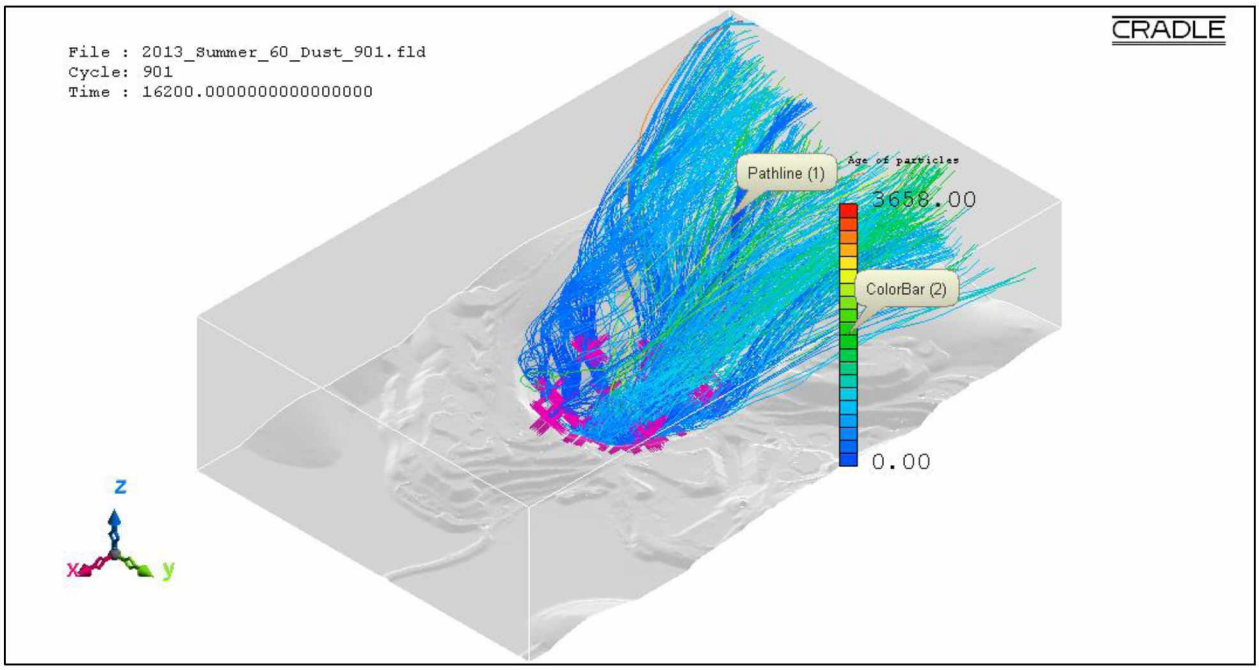

Figure B.1: Pathlines of all the generated dust particles in the actual open-pit domain for fair insolation summer condition using the LES method.

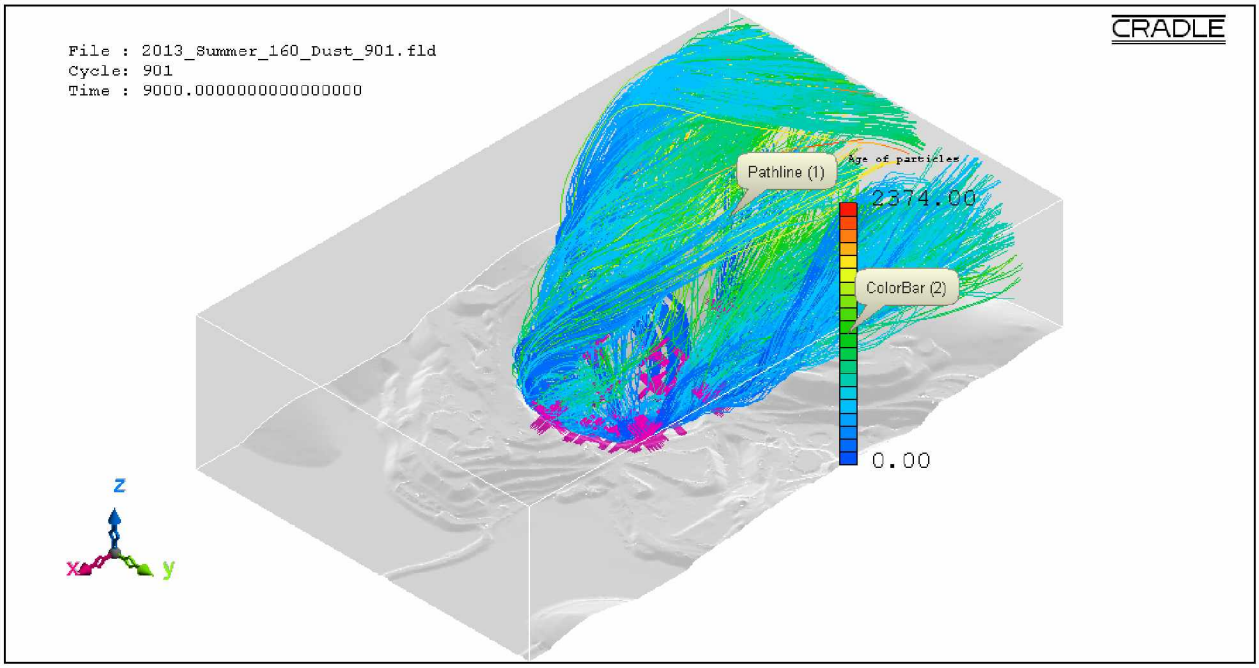

Figure B.2: Pathlines of all the generated dust particles in the actual open-pit domain for extreme insolation summer condition using the LES method.

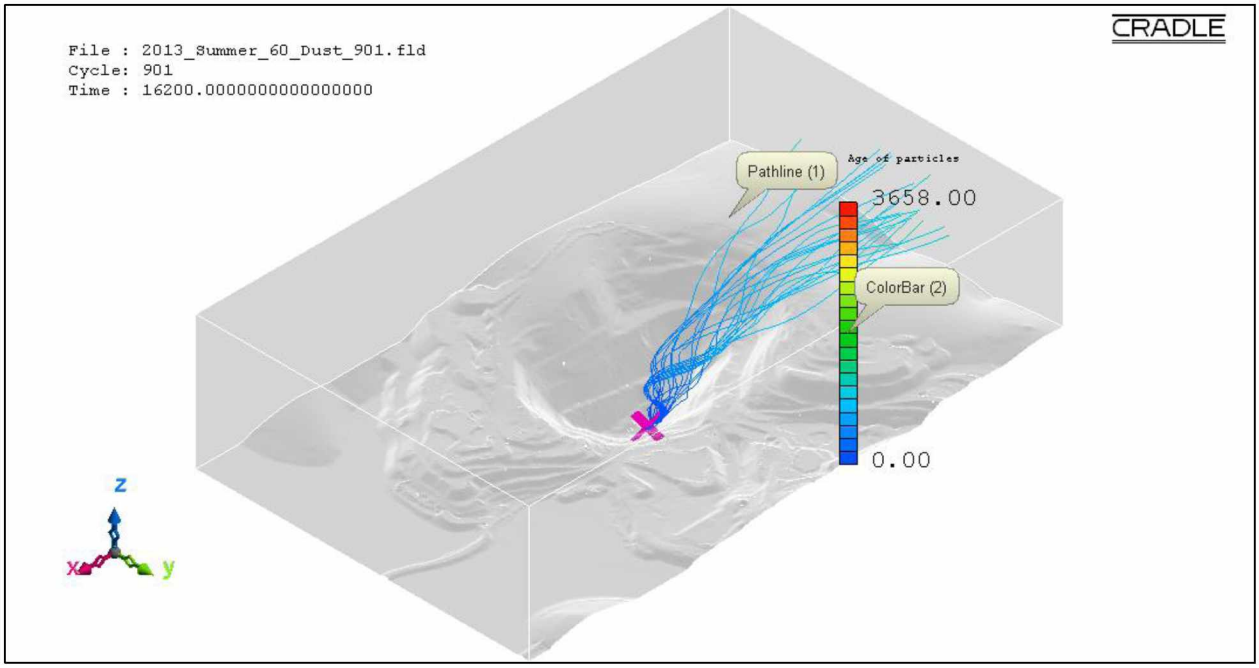

Figure B.3: Pathlines of $PM_{0.1}$ dust particles from source location 1 in the actual open-pit domain for fair insolation summer condition using the LES method.

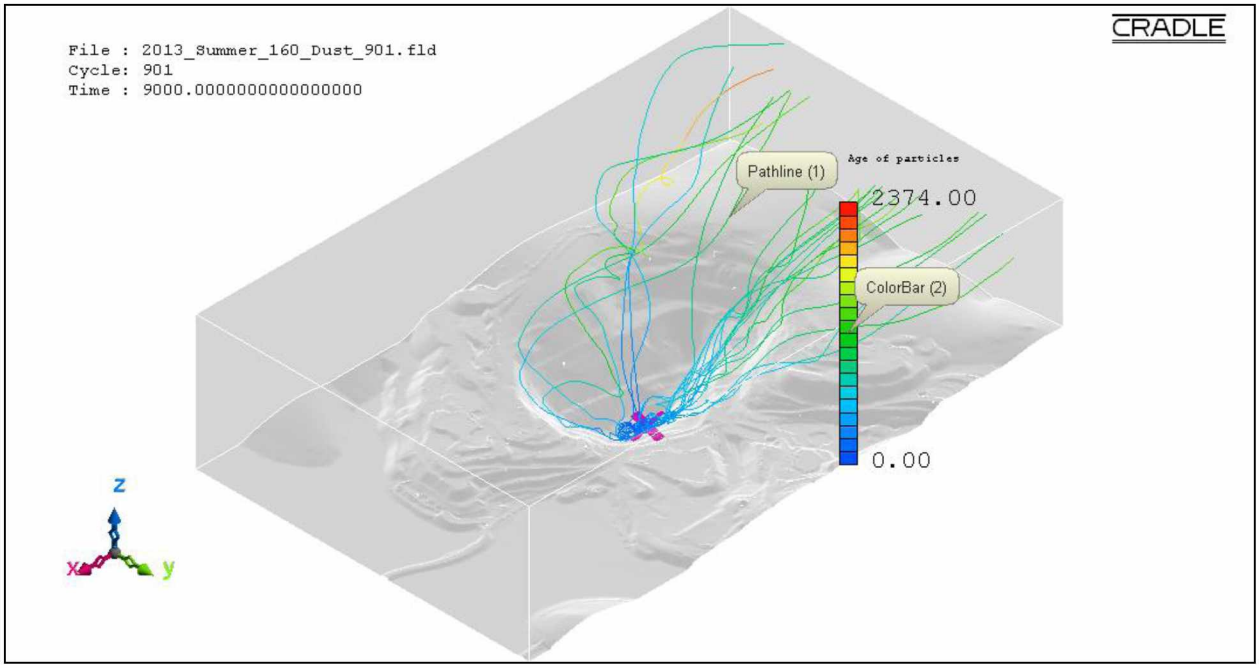

Figure B.4: Pathlines of $PM_{0.1}$ dust particles from source location 1 in the actual open-pit domain for extreme insolation summer condition using the LES method.

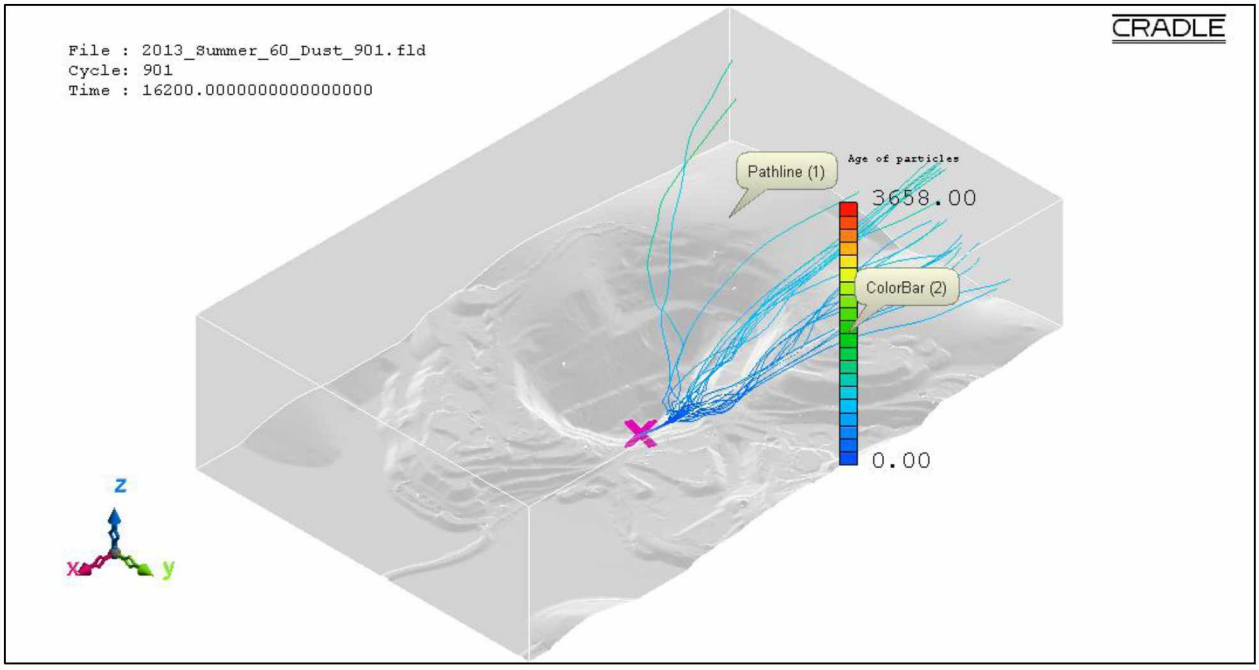

Figure B.5: Pathlines of $PM_{0.1}$ dust particles from source location 2 in the actual open-pit domain for fair insolation summer condition using the LES method.

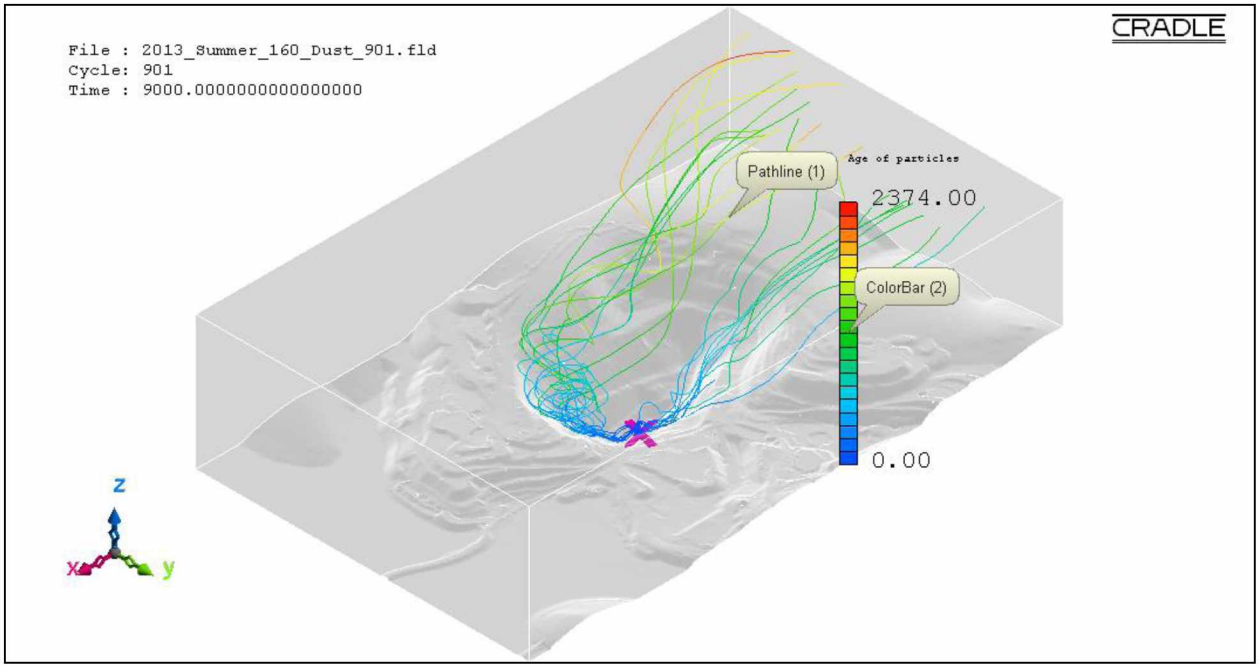

Figure B.6: Pathlines of $PM_{0.1}$ dust particles from source location 2 in the actual open-pit domain for extreme insolation summer condition using the LES method.

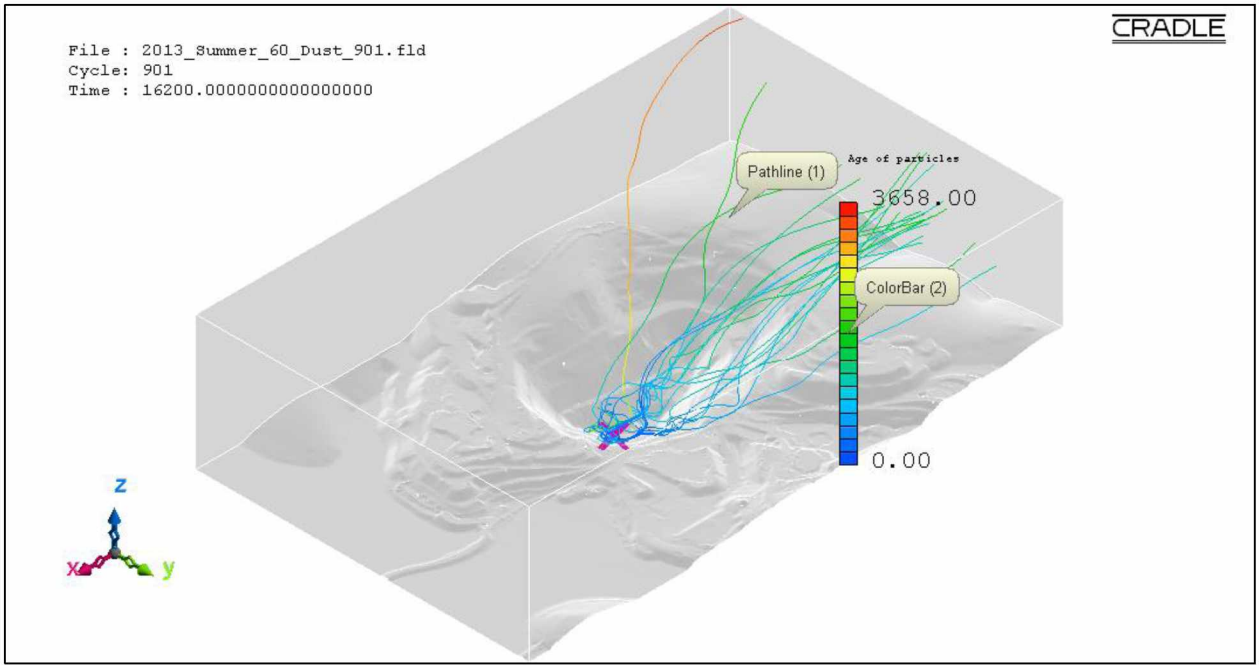

Figure B.7: Pathlines of $PM_{0.1}$ dust particles from source location 3 in the actual open-pit domain for fair insolation summer condition using the LES method.

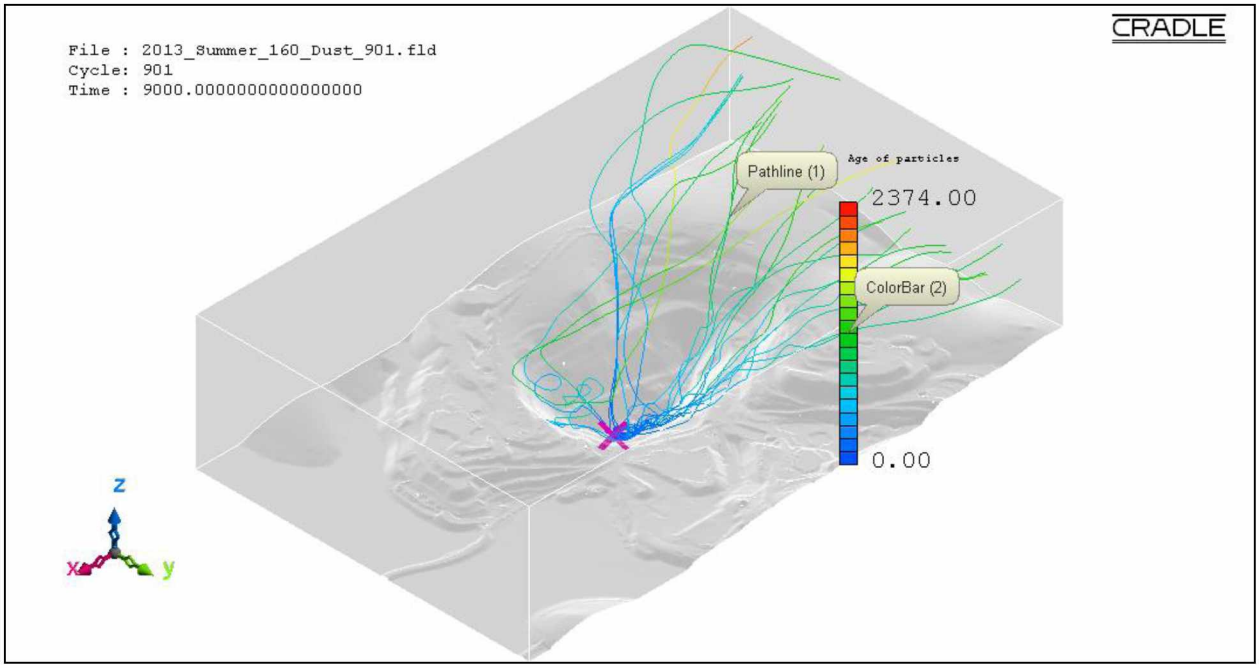

Figure B.8: Pathlines of $PM_{0.1}$ dust particles from source location 3 in the actual open-pit domain for extreme insolation summer condition using the LES method.

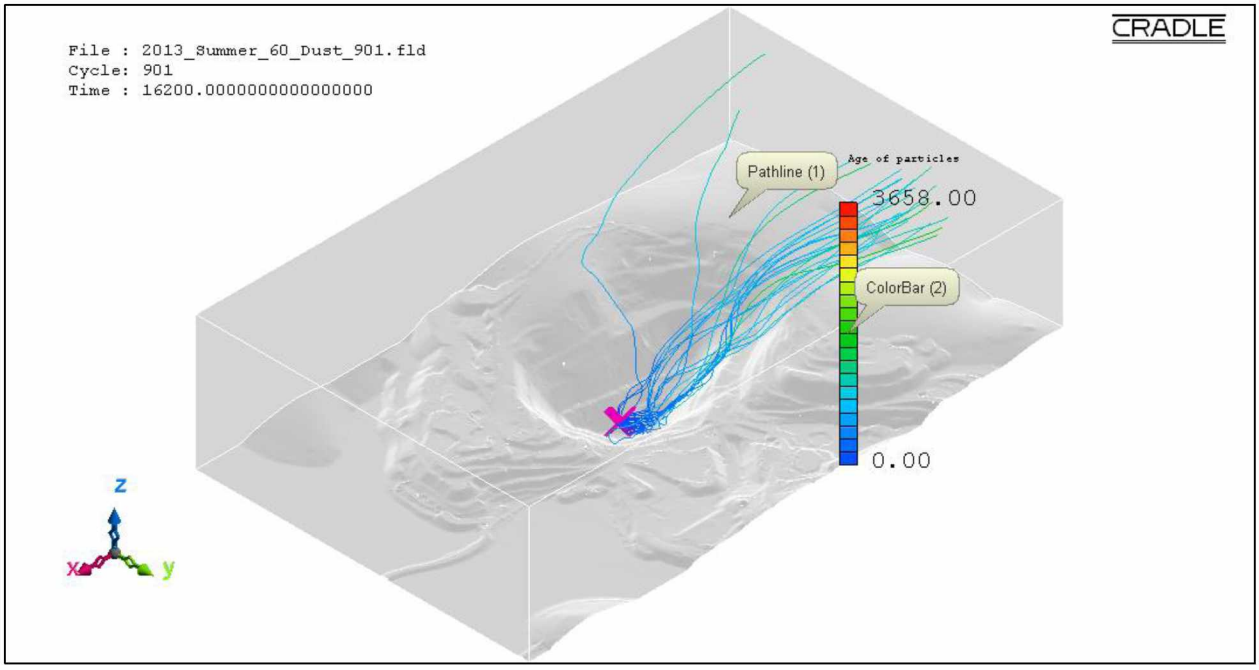

Figure B.9: Pathlines of $PM_{0.1}$ dust particles from source location 4 in the actual open-pit domain for fair insolation summer condition using the LES method.

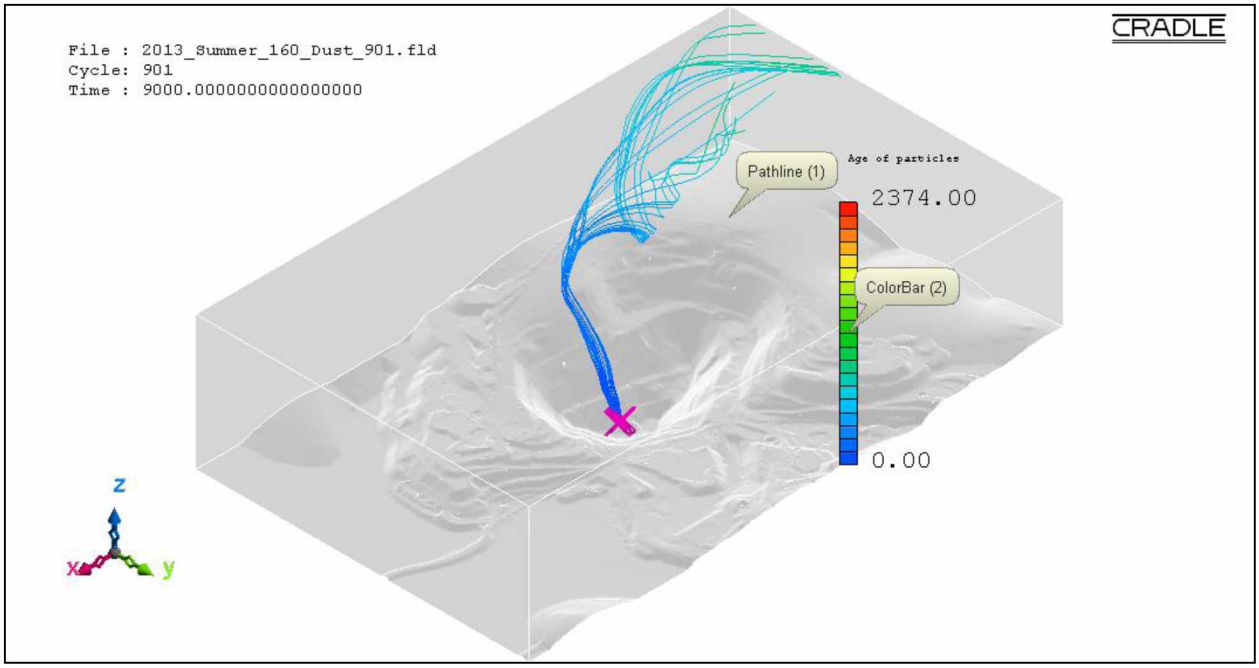

Figure B.10: Pathlines of $PM_{0.1}$ dust particles from source location 4 in the actual open-pit domain for extreme insolation summer condition using the LES method.

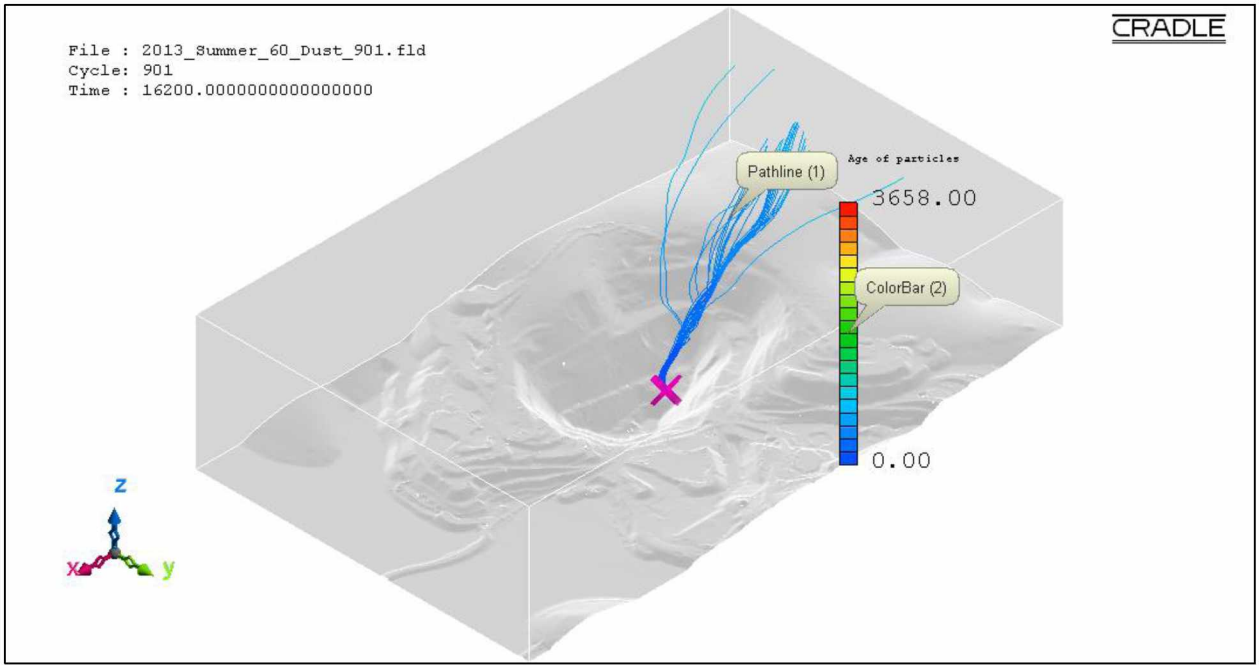

Figure B.11: Pathlines of $PM_{0.1}$ dust particles from source location 5 in the actual open-pit domain for fair insolation summer condition using the LES method.

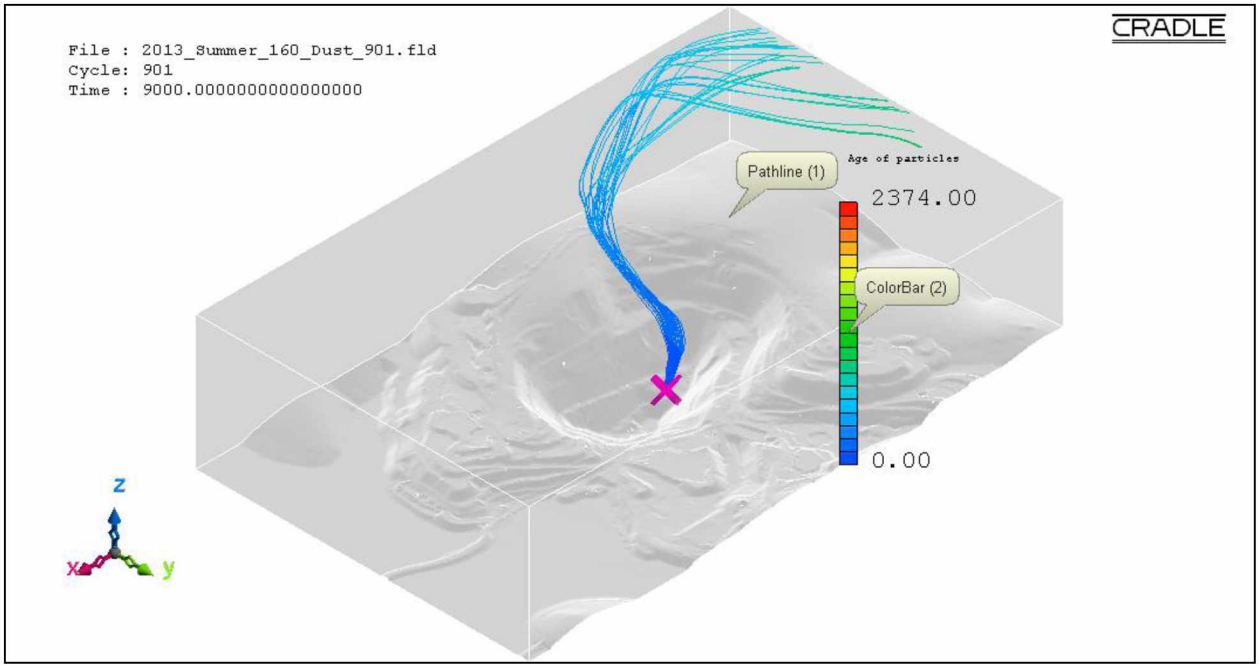

Figure B.12: Pathlines of $PM_{0.1}$ dust particles from source location 5 in the actual open-pit domain for extreme insolation summer condition using the LES method.

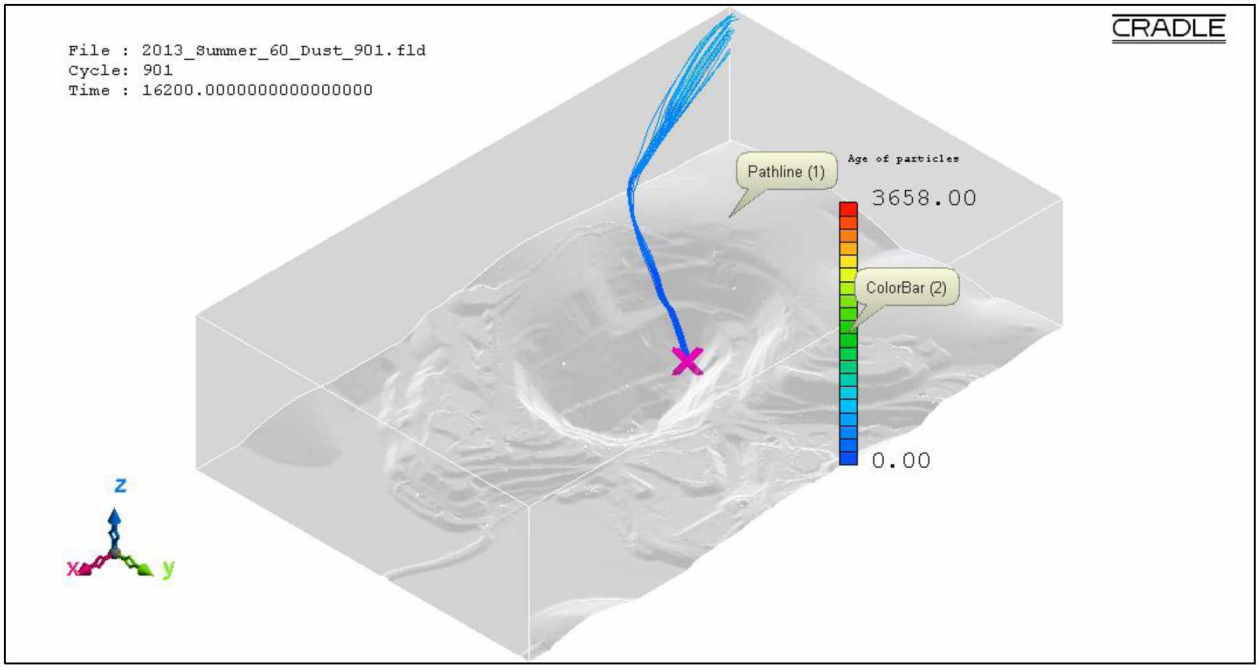

Figure B.13: Pathlines of $PM_{0.1}$ dust particles from source location 6 in the actual open-pit domain for fair insolation summer condition using the LES method.

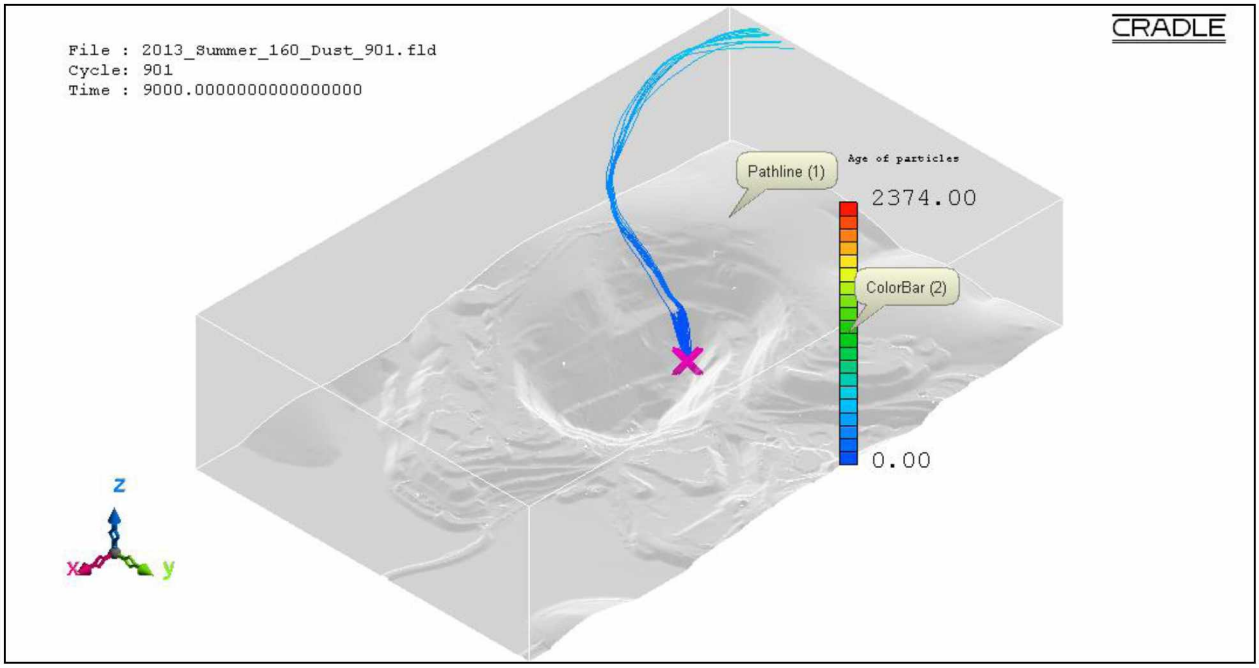

Figure B.14: Pathlines of $PM_{0.1}$ dust particles from source location 6 in the actual open-pit domain for extreme insolation summer condition using the LES method.

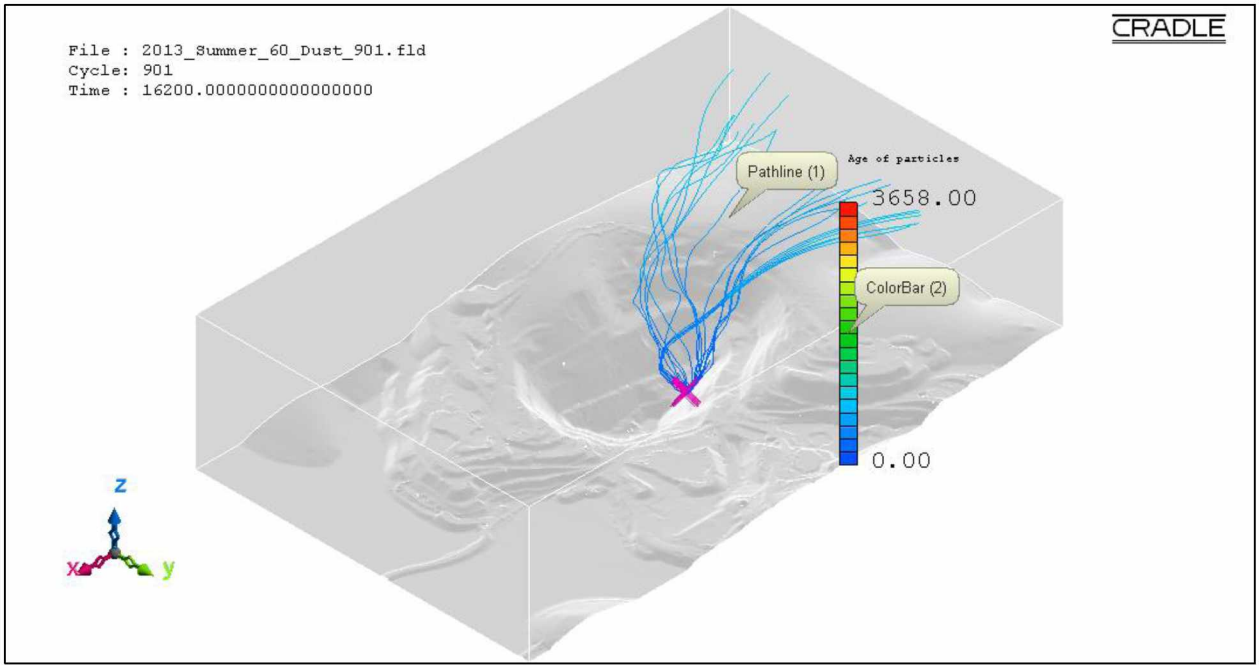

Figure B.15: Pathlines of $PM_{0.1}$ dust particles from source location 7 in the actual open-pit domain for fair insolation summer condition using the LES method.

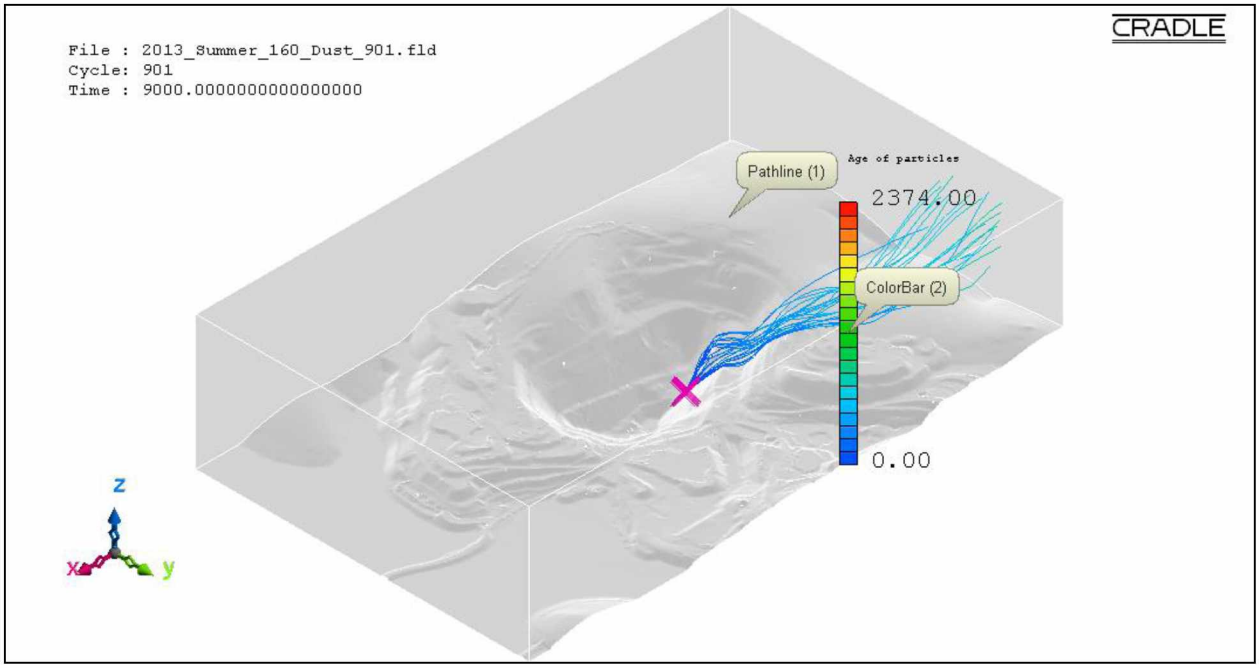

Figure B.16: Pathlines of $PM_{0.1}$ dust particles from source location 7 in the actual open-pit domain for extreme insolation summer condition using the LES method.

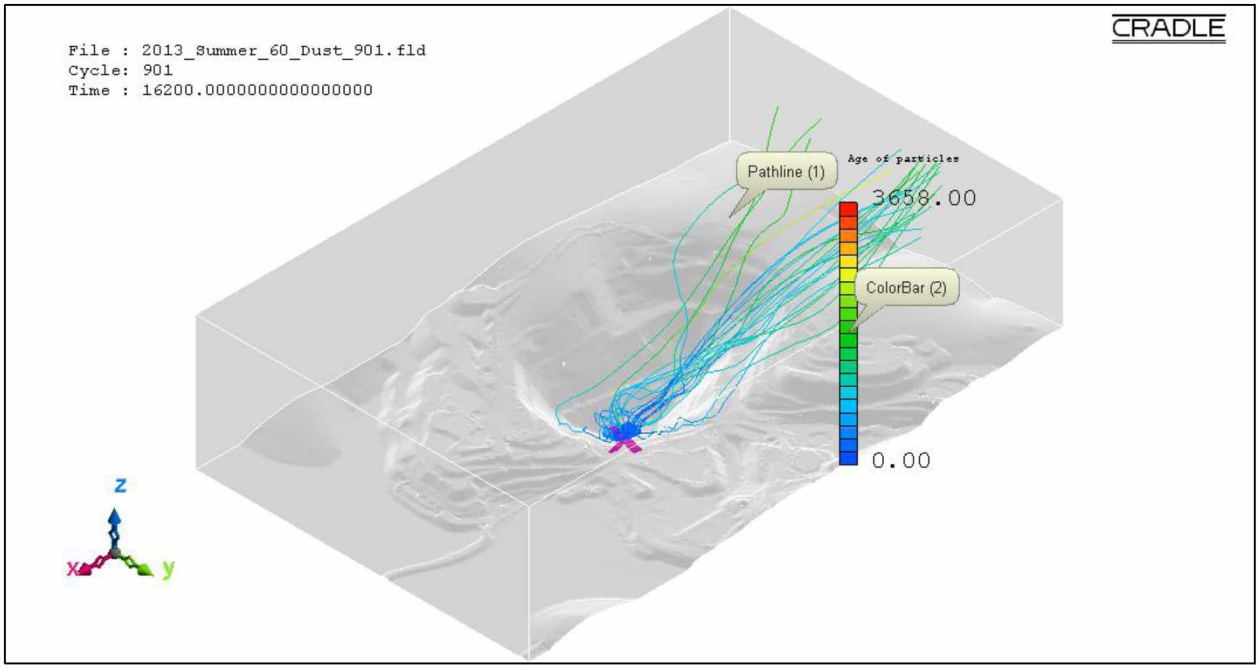

Figure B.17: Pathlines of $PM_{0.1}$ dust particles from source location 8 in the actual open-pit domain for fair insolation summer condition using the LES method.

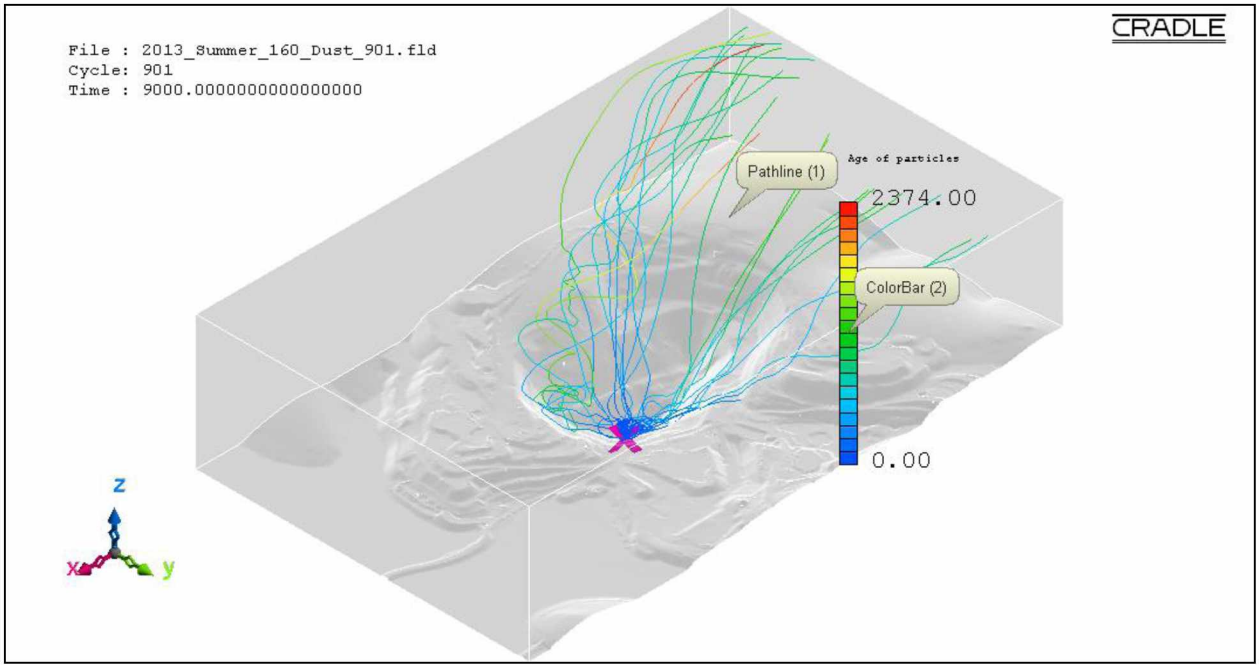

Figure B.18: Pathlines of $PM_{0.1}$ dust particles from source location 8 in the actual open-pit domain for extreme insolation summer condition using the LES method.

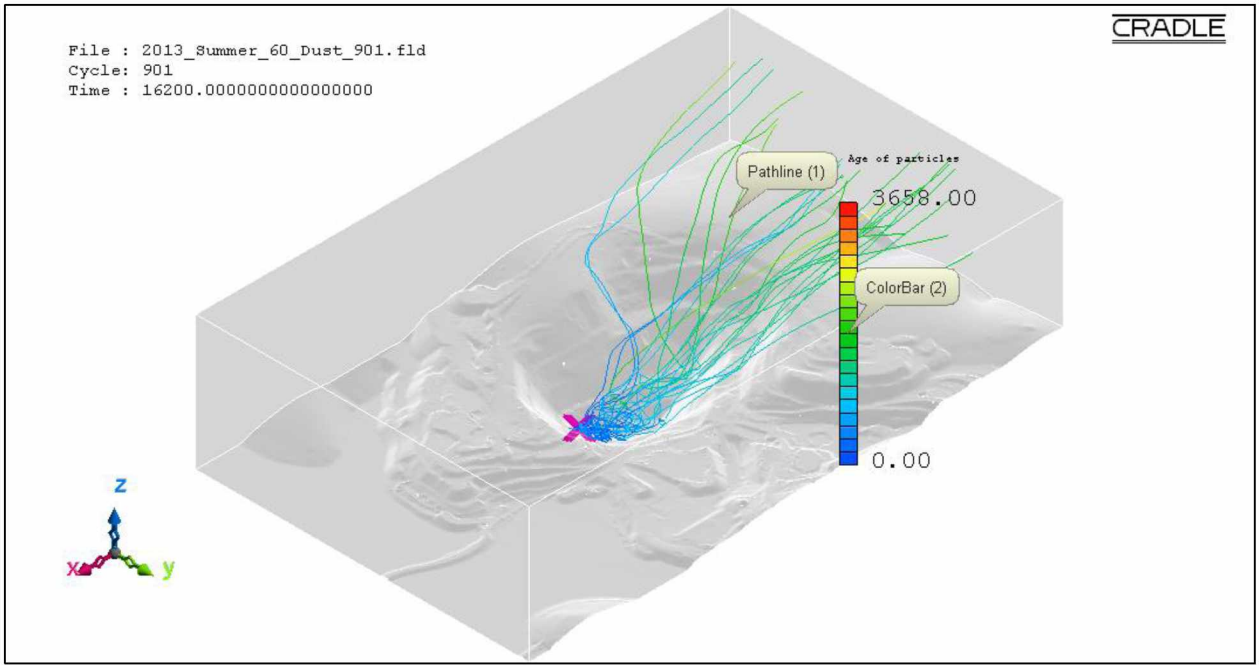

Figure B.19: Pathlines of $PM_{0.1}$ dust particles from source location 9 in the actual open-pit domain for fair insolation summer condition using the LES method.

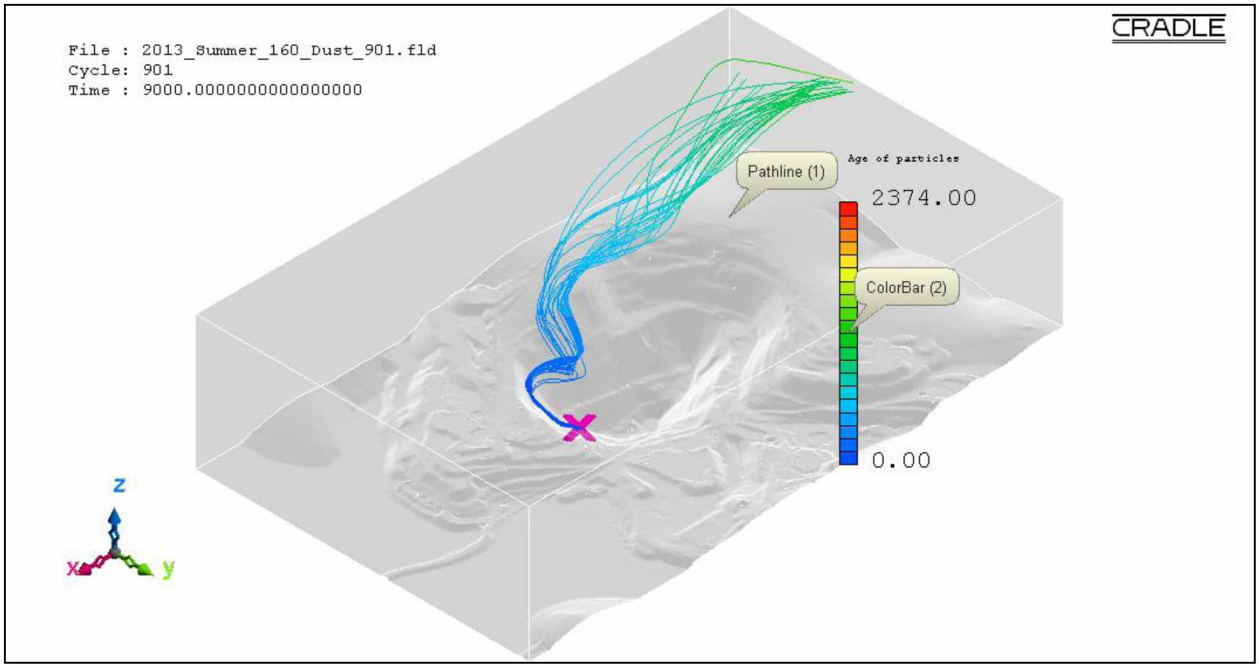

Figure B.20: Pathlines of $PM_{0.1}$ dust particles from source location 9 in the actual open-pit domain for extreme insolation summer condition using the LES method.

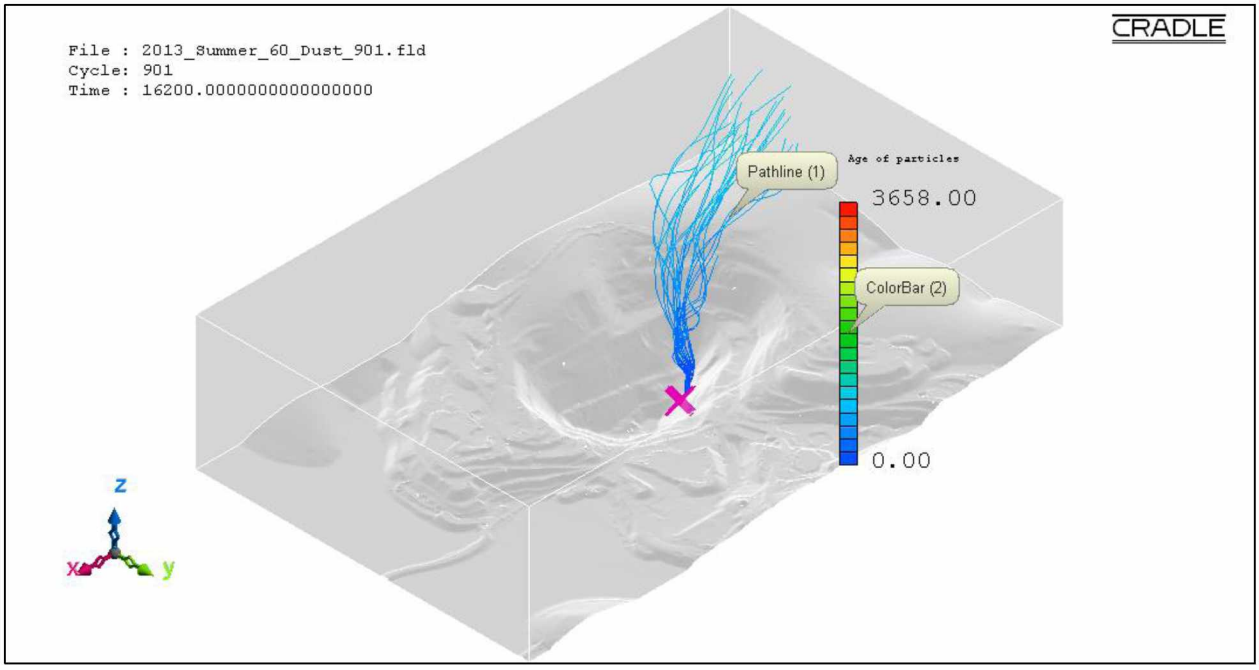

Figure B.21: Pathlines of $PM_{0.1}$ dust particles from source location 10 in the actual open-pit domain for fair insolation summer condition using the LES method.

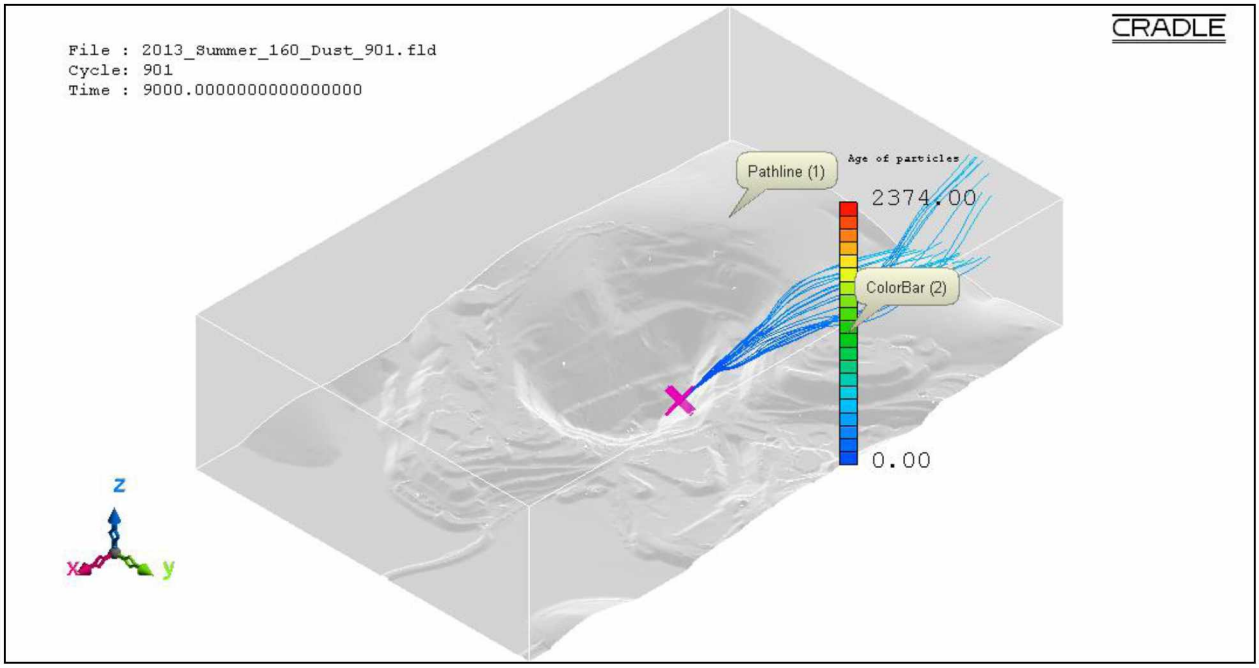

Figure B.22: Pathlines of $PM_{0.1}$ dust particles from source location 10 in the actual open-pit domain for extreme insolation summer condition using the LES method.

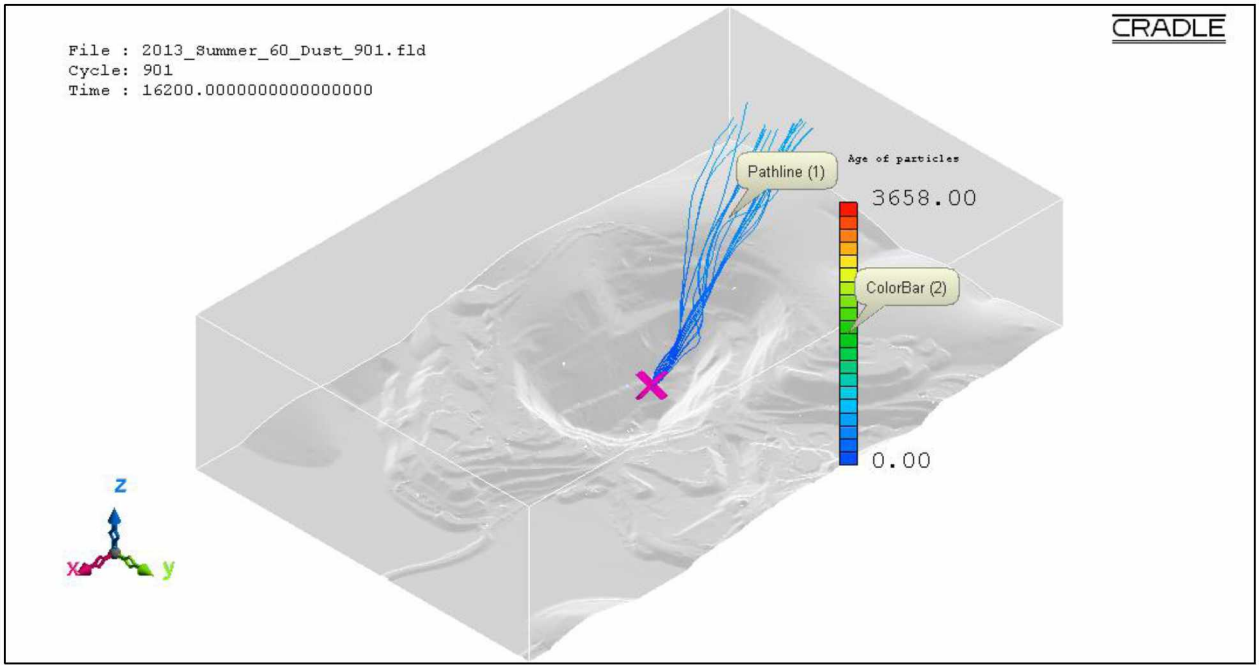

Figure B.23: Pathlines of $PM_{0.1}$ dust particles from source location 11 in the actual open-pit domain for fair insolation summer condition using the LES method.

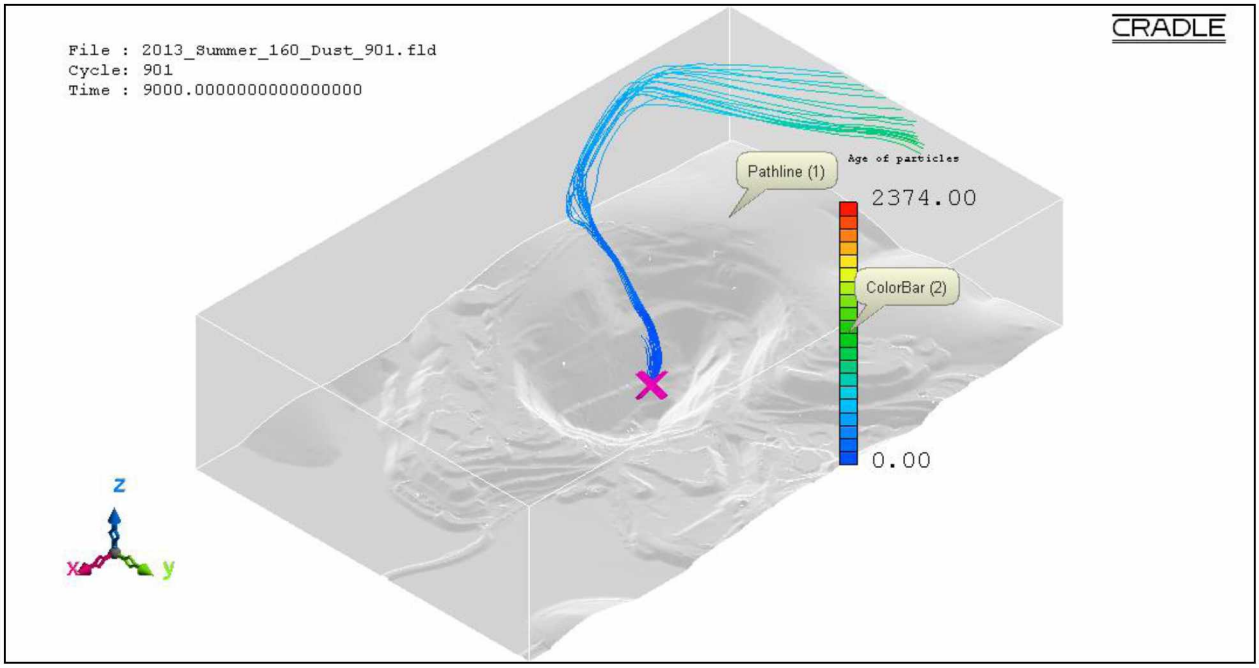

Figure B.24: Pathlines of $PM_{0.1}$ dust particles from source location 11 in the actual open-pit domain for extreme insolation summer condition using the LES method.

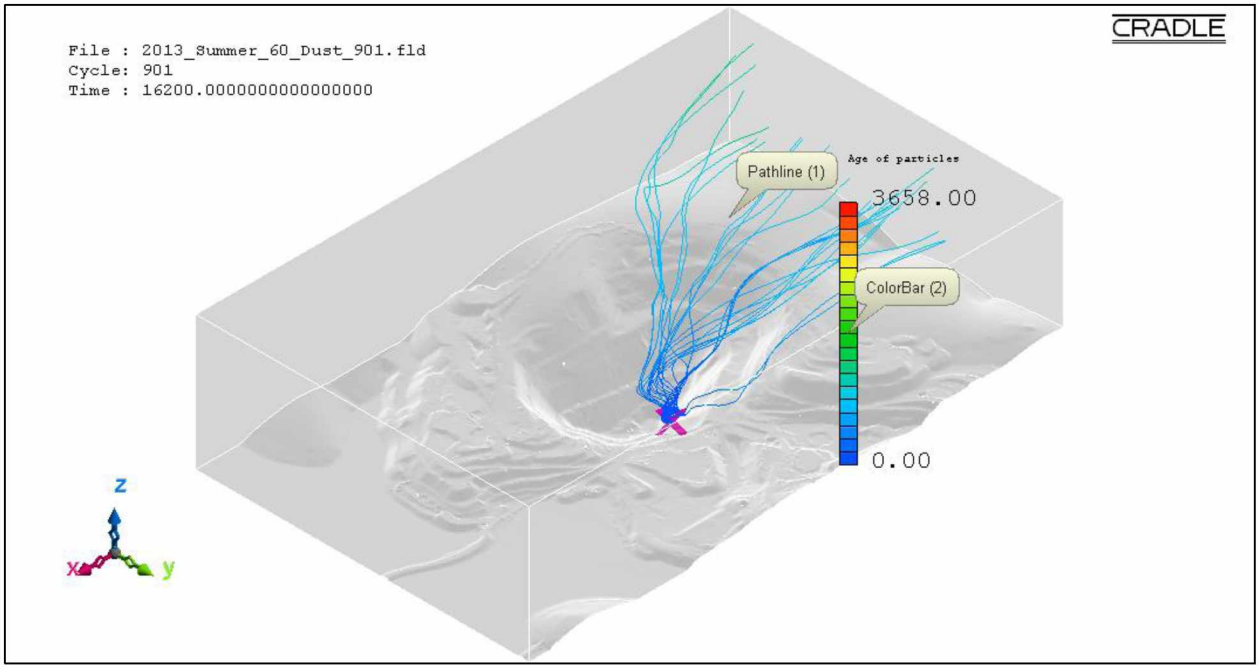

Figure B.25: Pathlines of $PM_{0.1}$ dust particles from source location 12 in the actual open-pit domain for fair insolation summer condition using the LES method.

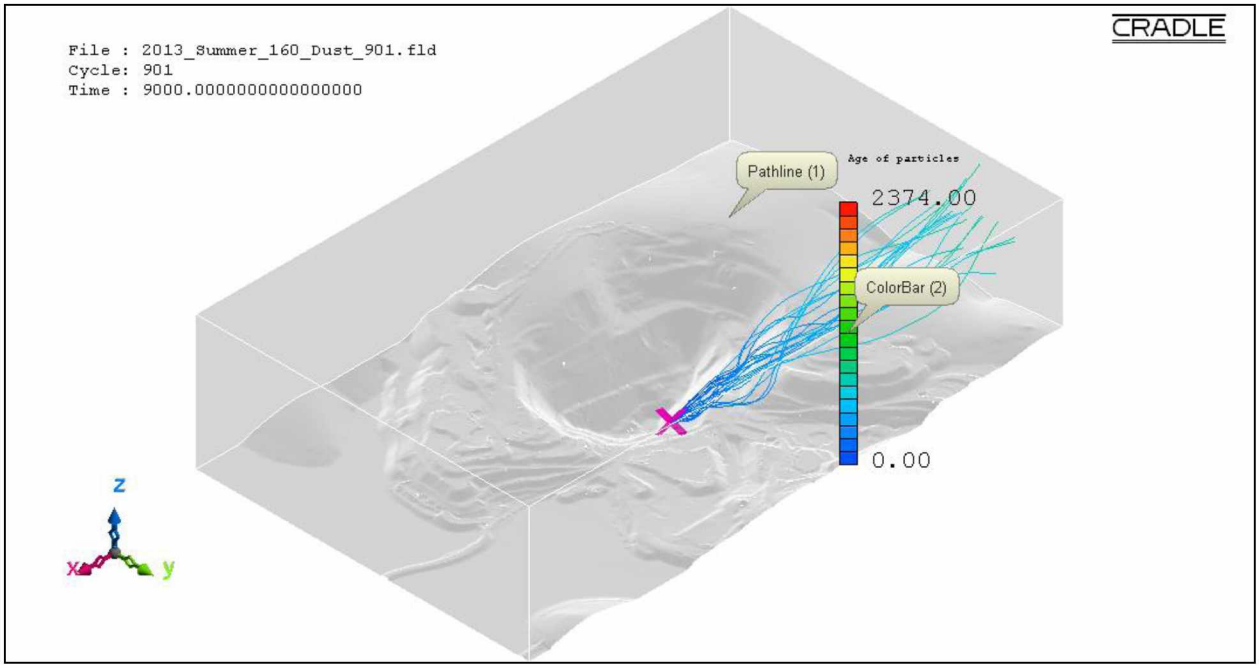

Figure B.26: Pathlines of $PM_{0.1}$ dust particles from source location 12 in the actual open-pit domain for extreme insolation summer condition using the LES method.

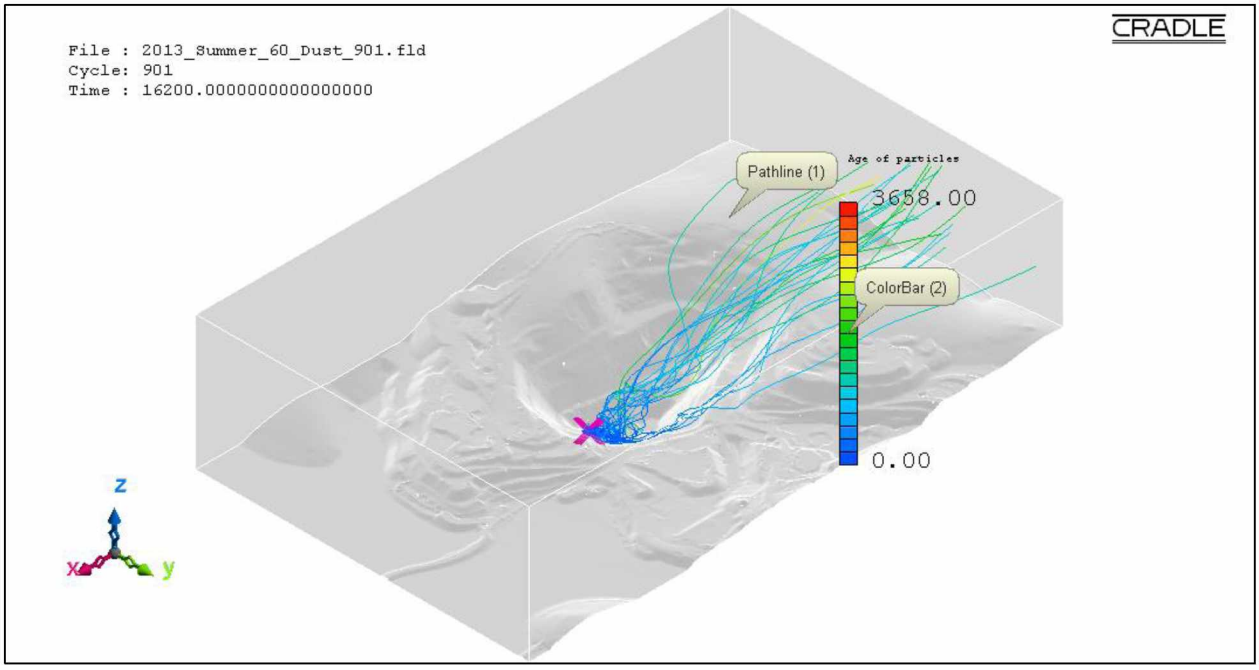

Figure B.27: Pathlines of $PM_{0.1}$ dust particles from source location 13 in the actual open-pit domain for fair insolation summer condition using the LES method.

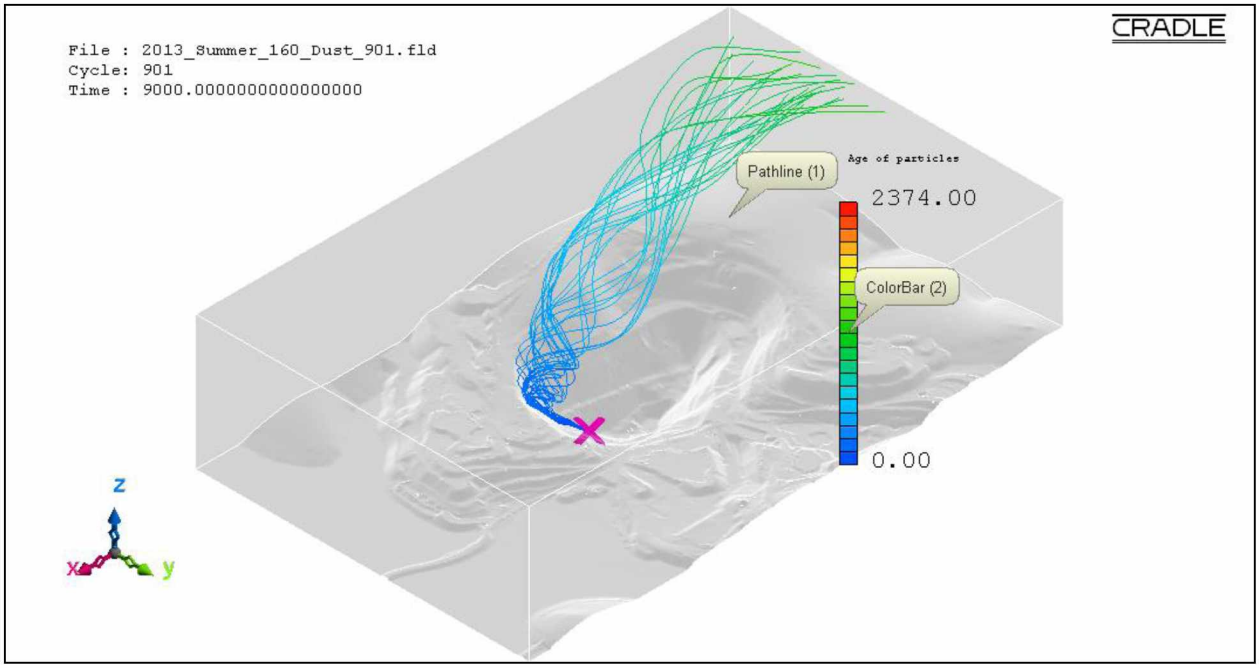

Figure B.28: Pathlines of $PM_{0.1}$ dust particles from source location 13 in the actual open-pit domain for extreme insolation summer condition using the LES method.

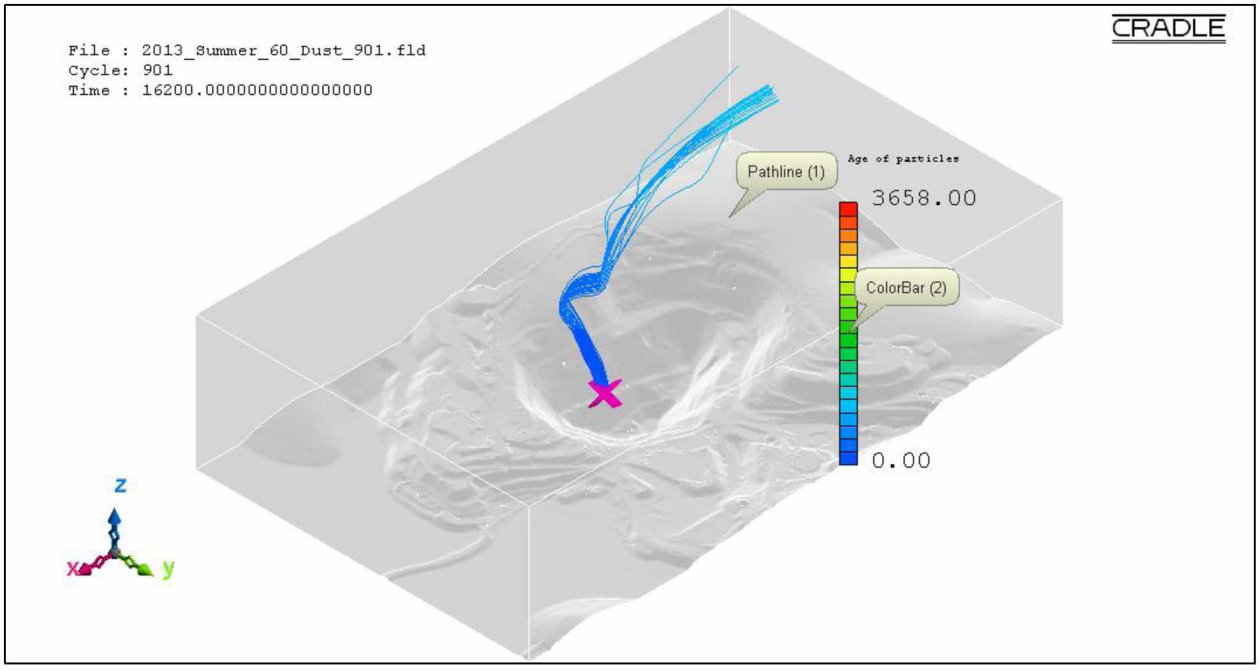

Figure B.29: Pathlines of $PM_{0.1}$ dust particles from source location 14 in the actual open-pit domain for fair insolation summer condition using the LES method.

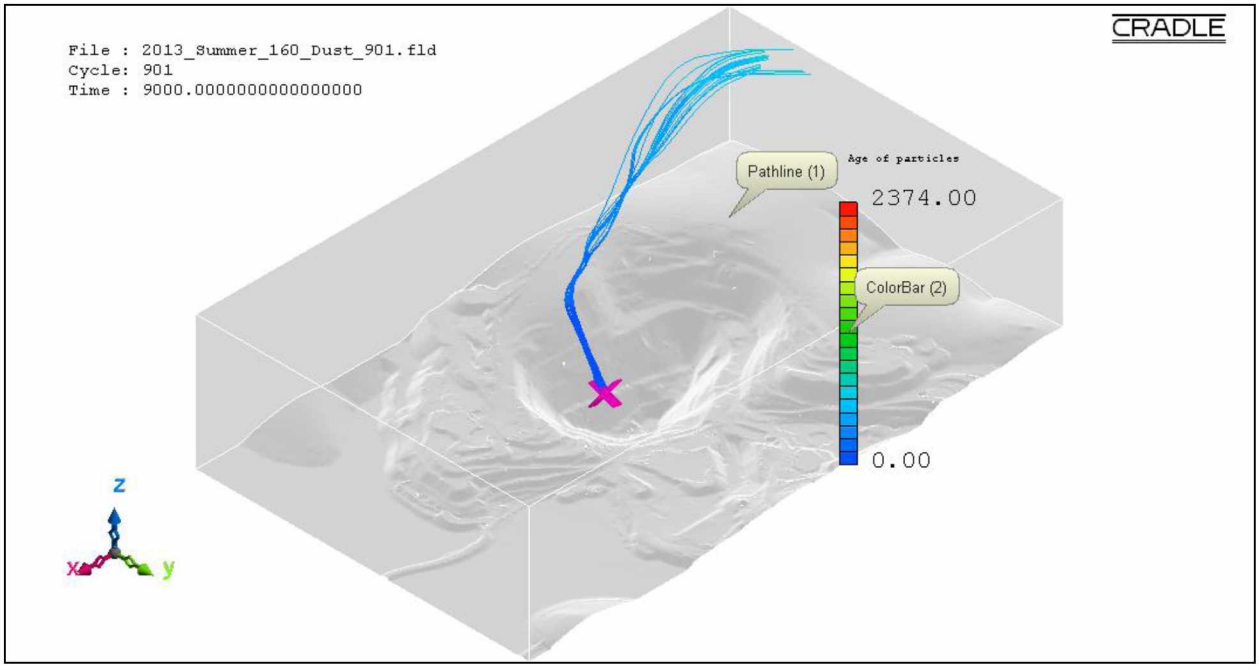

Figure B.30: Pathlines of $PM_{0.1}$ dust particles from source location 14 in the actual open-pit domain for extreme insolation summer condition using the LES method.

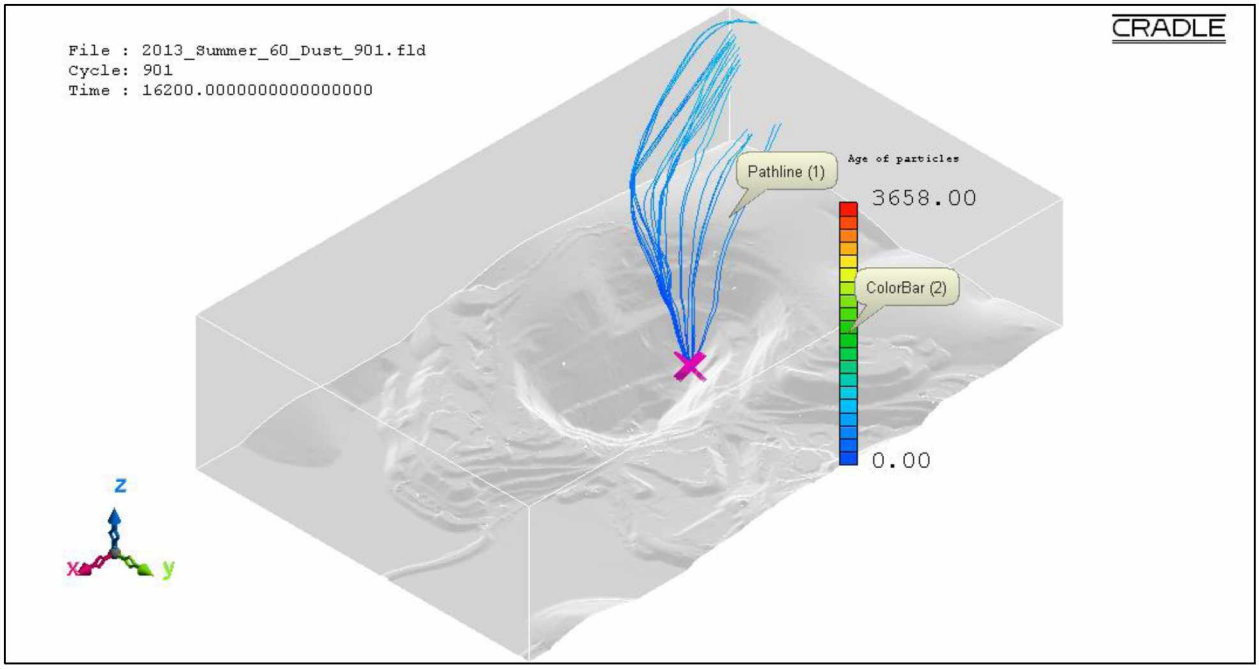

Figure B.31: Pathlines of $PM_{0.1}$ dust particles from source location 15 in the actual open-pit domain for fair insolation summer condition using the LES method.

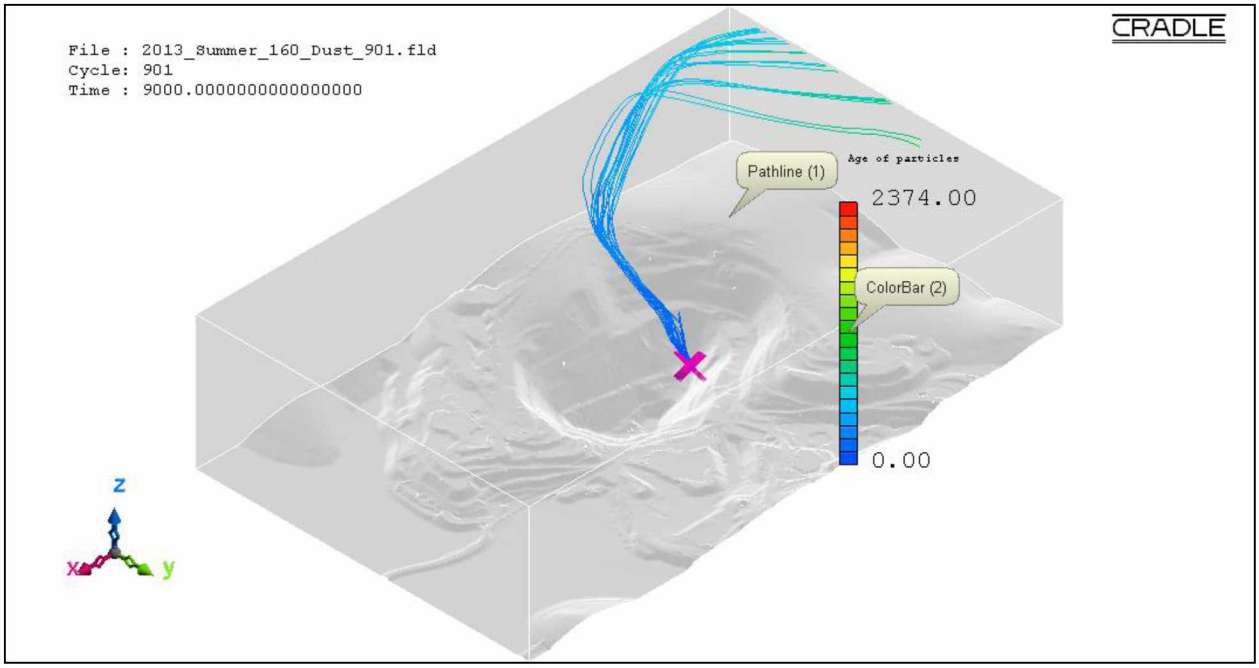

Figure B.32: Pathlines of $PM_{0.1}$ dust particles from source location 15 in the actual open-pit domain for extreme insolation summer condition using the LES method.

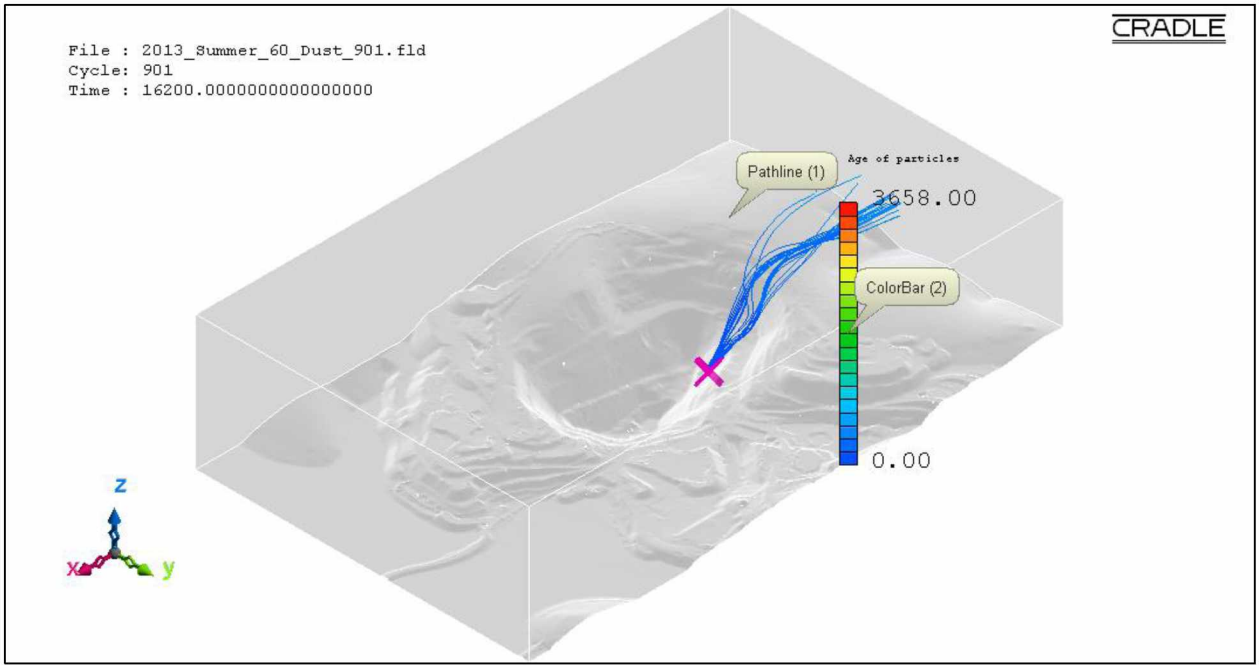

Figure B.33: Pathlines of $PM_{0.1}$ dust particles from source location 16 in the actual open-pit domain for fair insolation summer condition using the LES method.

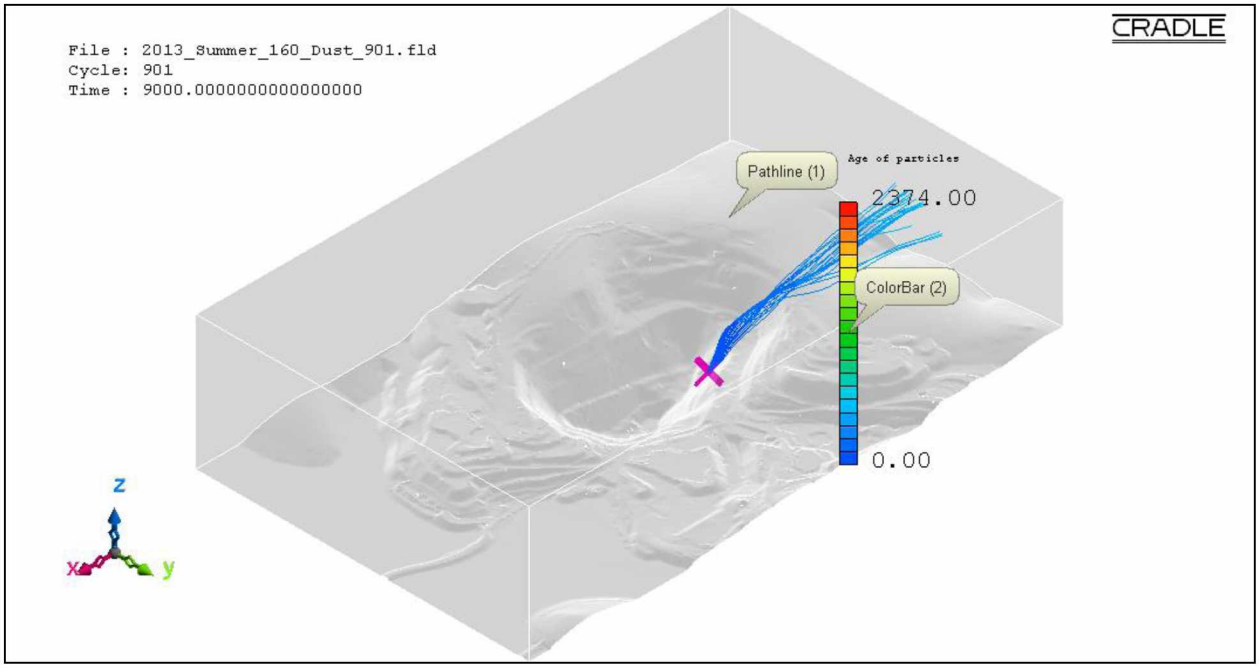

Figure B.34: Pathlines of $PM_{0.1}$ dust particles from source location 16 in the actual open-pit domain for extreme insolation summer condition using the LES method.

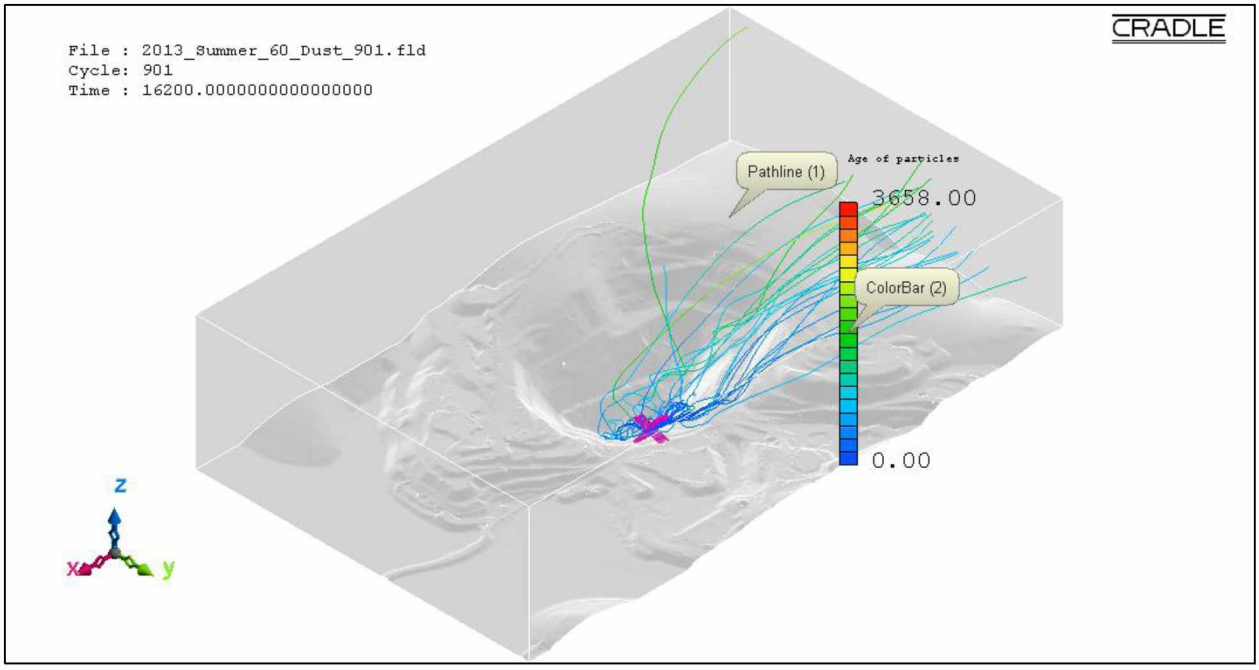

Figure B.35: Pathlines of $PM_{0.1}$ dust particles from source location 17 in the actual open-pit domain for fair insolation summer condition using the LES method.

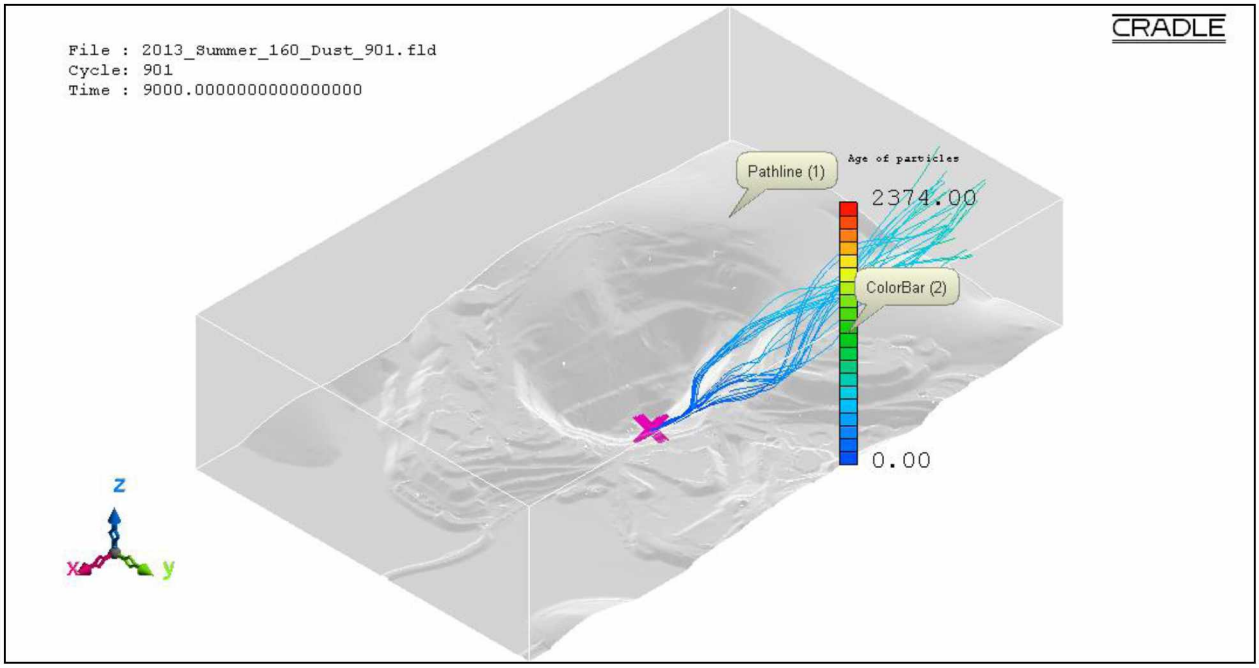

Figure B.36: Pathlines of $PM_{0.1}$ dust particles from source location 17 in the actual open-pit domain for extreme insolation summer condition using the LES method.

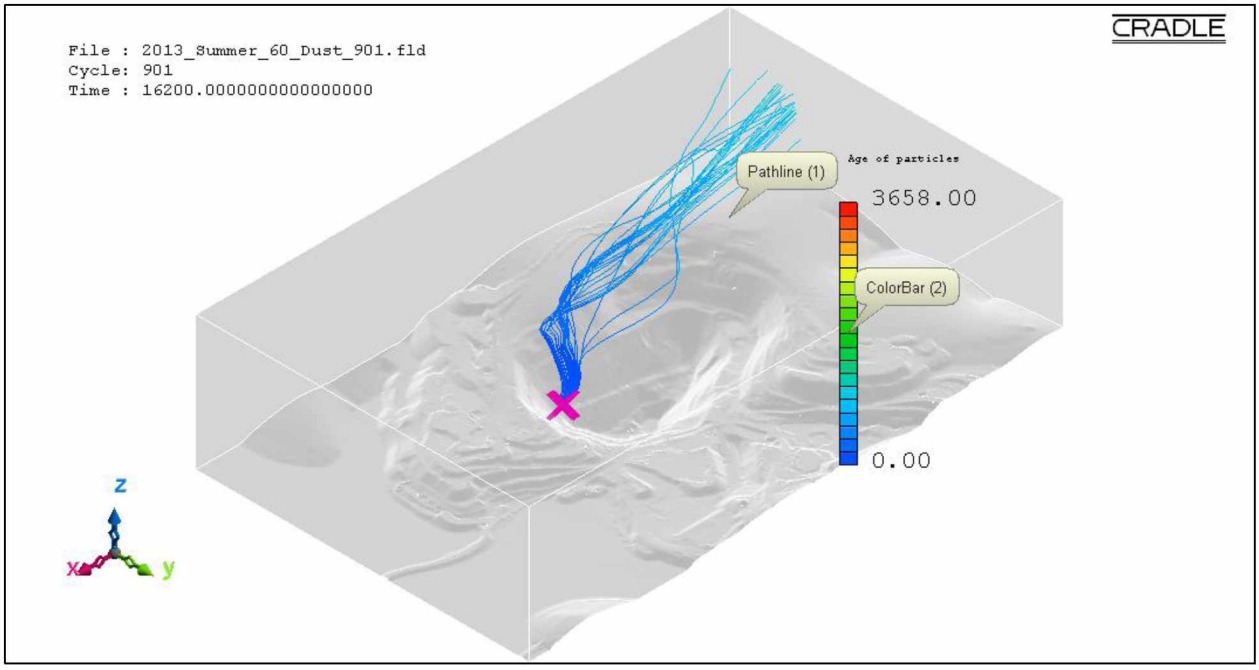

Figure B.37: Pathlines of $PM_{0.1}$ dust particles from source location 18 in the actual open-pit domain for fair insolation summer condition using the LES method.

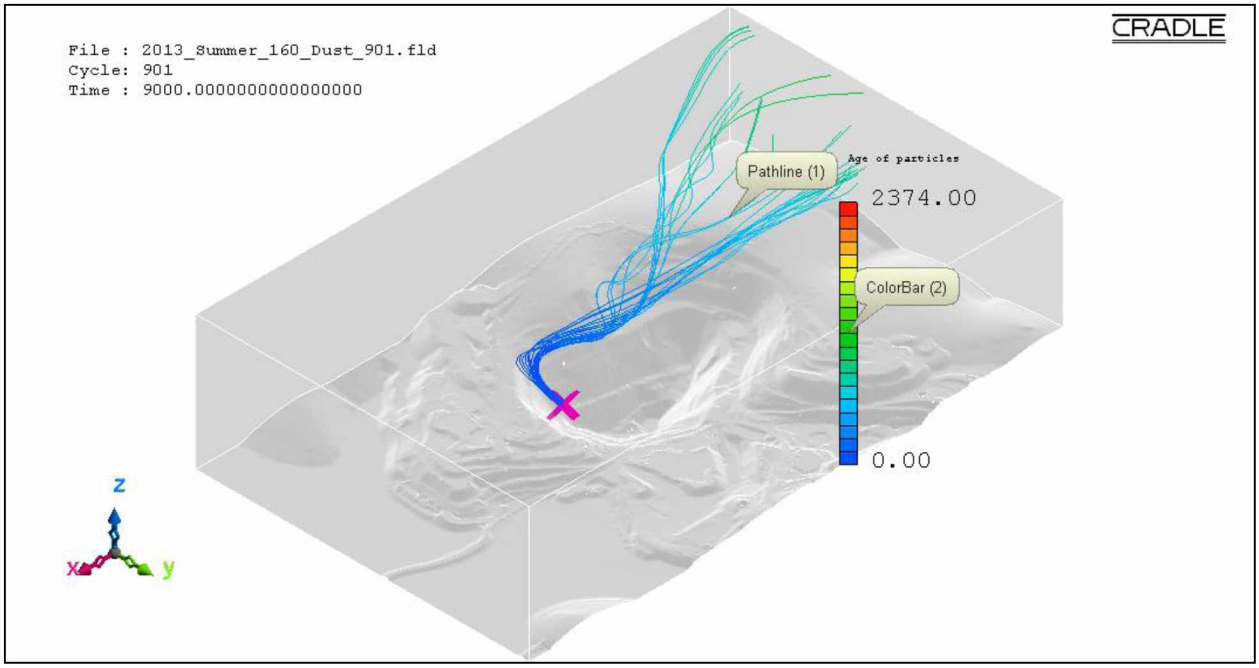

Figure B.38: Pathlines of $PM_{0.1}$ dust particles from source location 18 in the actual open-pit domain for extreme insolation summer condition using the LES method.

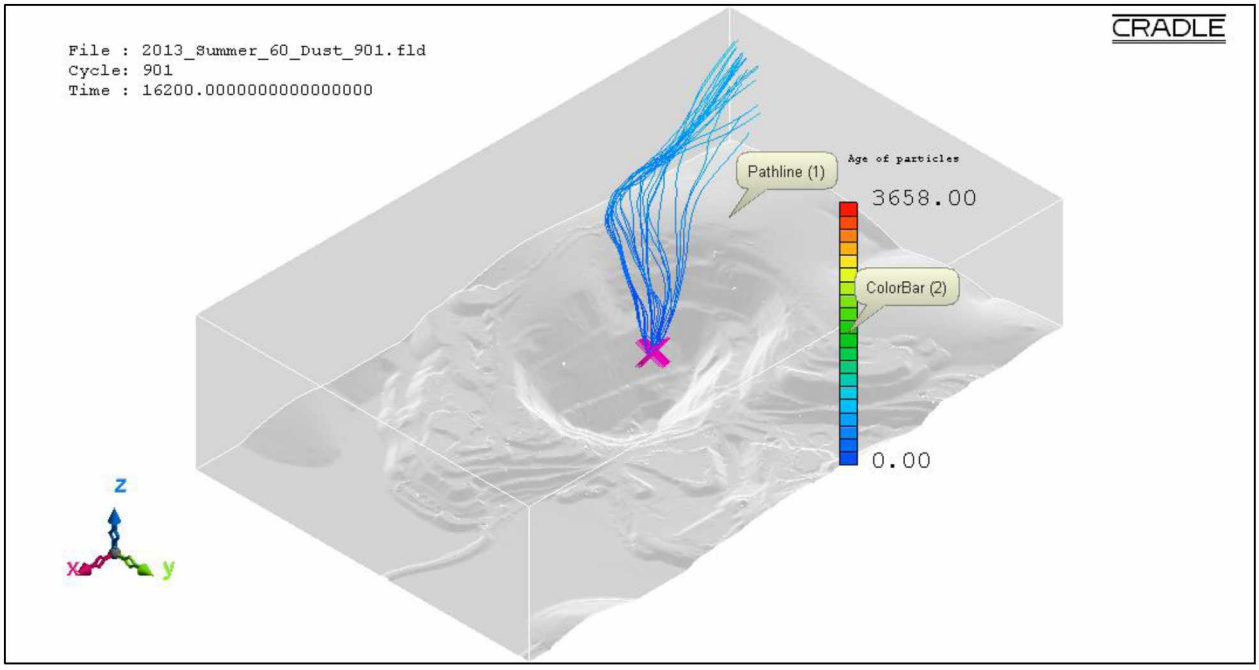

Figure B.39: Pathlines of $PM_{0.1}$ dust particles from source location 19 in the actual open-pit domain for fair insolation summer condition using the LES method.

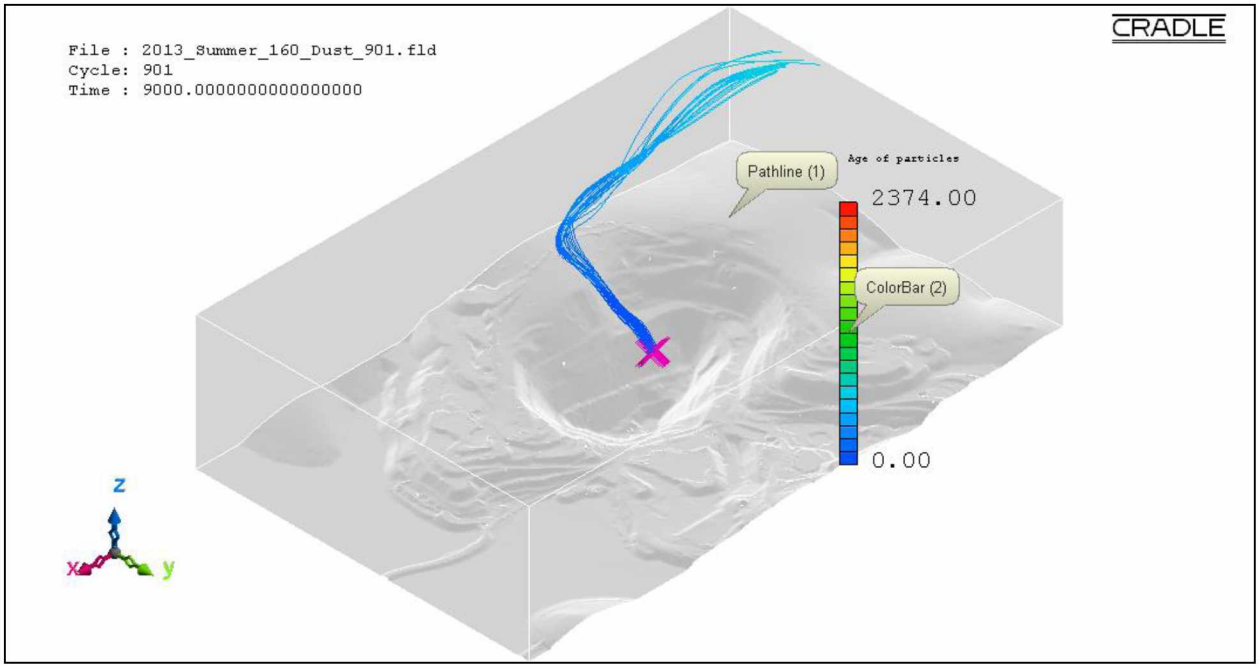

Figure B.40: Pathlines of $PM_{0.1}$ dust particles from source location 19 in the actual open-pit domain for extreme insolation summer condition using the LES method.

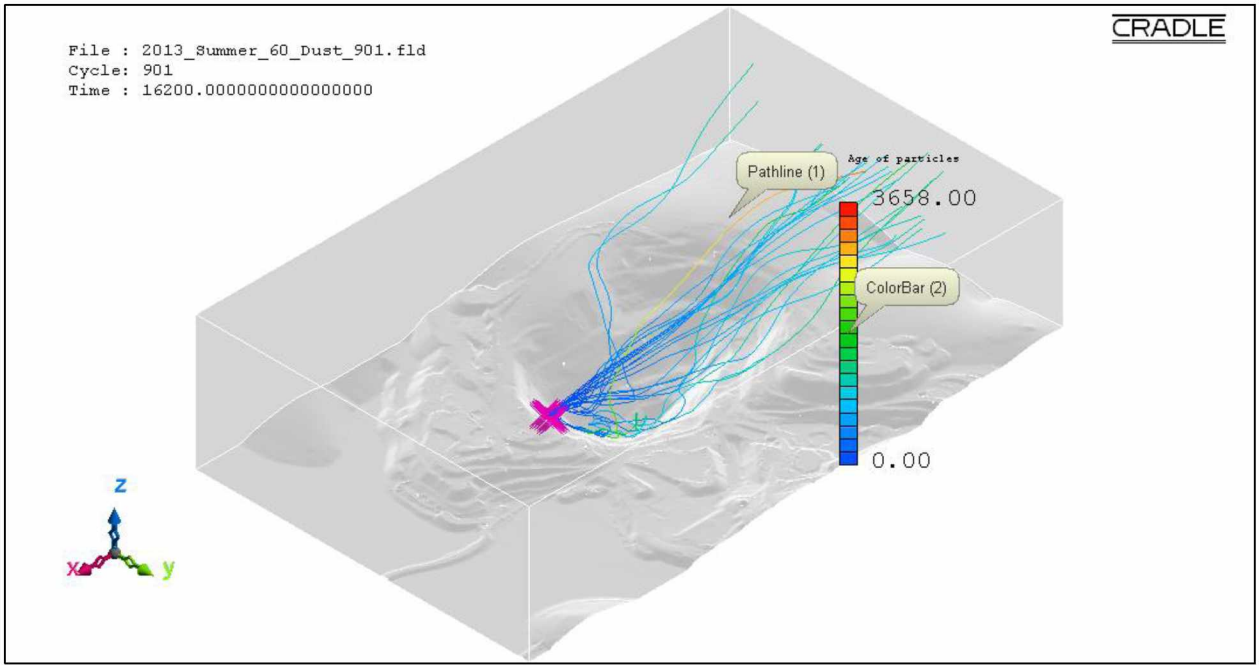

Figure B.41: Pathlines of $PM_{0.1}$ dust particles from source location 20 in the actual open-pit domain for fair insolation summer condition using the LES method.

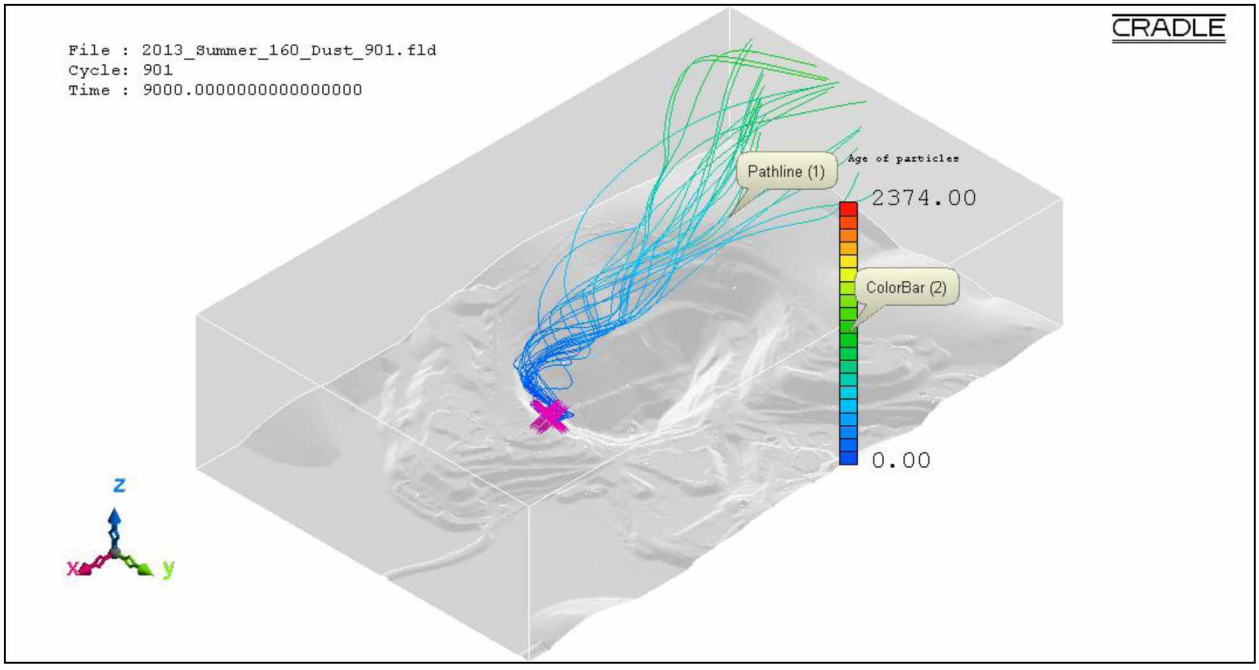

Figure B.42: Pathlines of $PM_{0.1}$ dust particles from source location 20 in the actual open-pit domain for extreme insolation summer condition using the LES method.

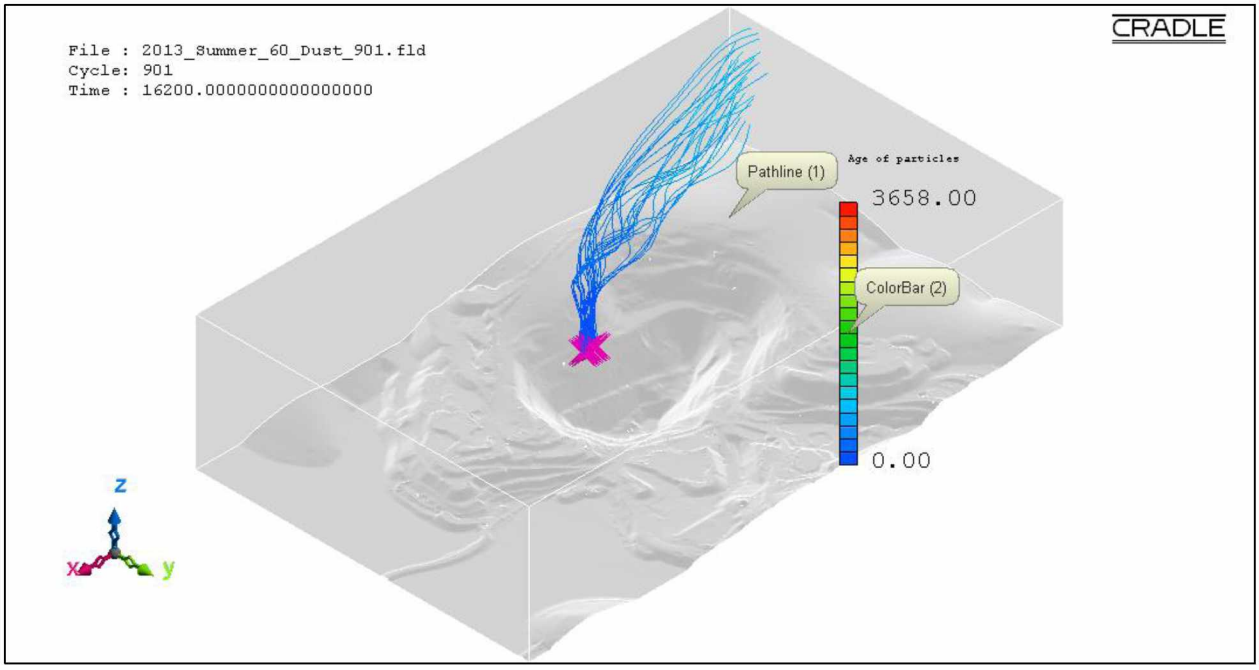

Figure B.43: Pathlines of $PM_{0.1}$ dust particles from source location 21 in the actual open-pit domain for fair insolation summer condition using the LES method.

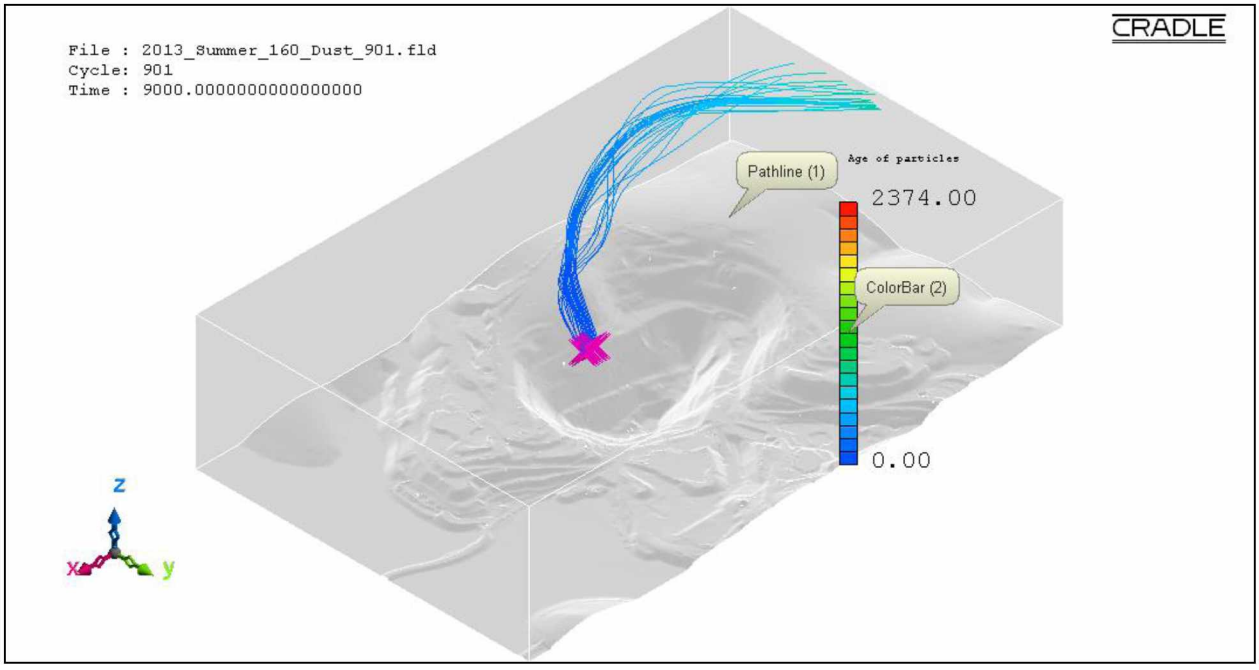

Figure B.44: Pathlines of $PM_{0.1}$ dust particles from source location 21 in the actual open-pit domain for extreme insolation summer condition using the LES method.

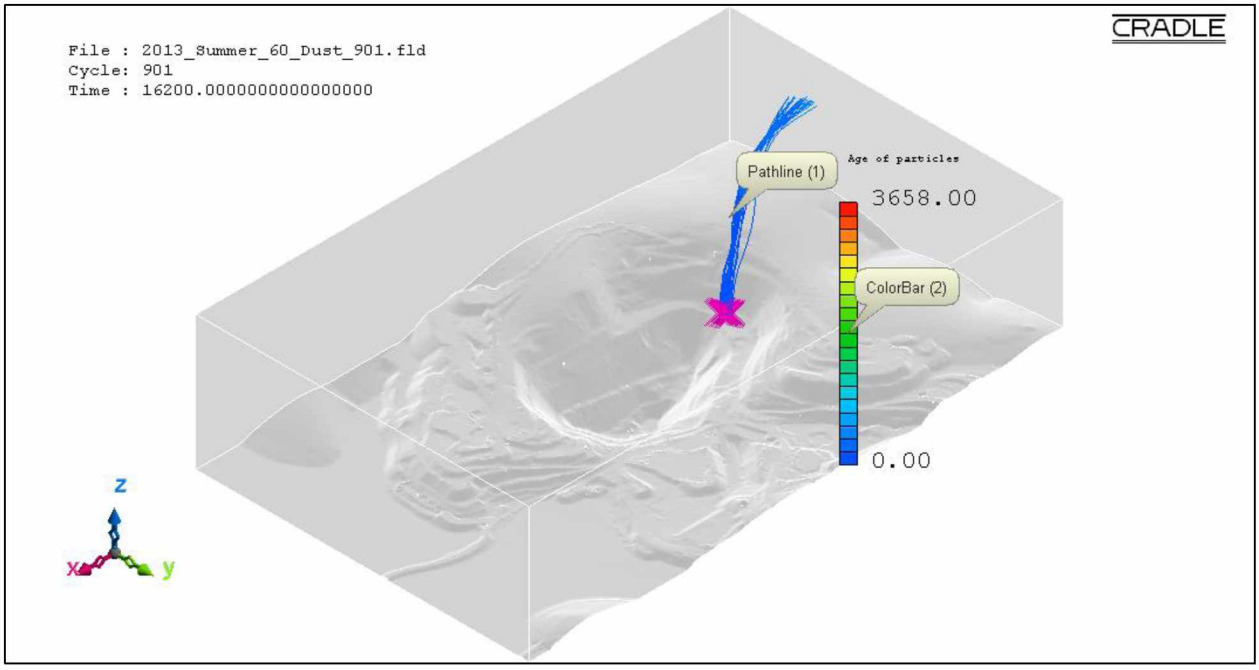

Figure B.45: Pathlines of $PM_{0.1}$ dust particles from source location 22 in the actual open-pit domain for fair insolation summer condition using the LES method.

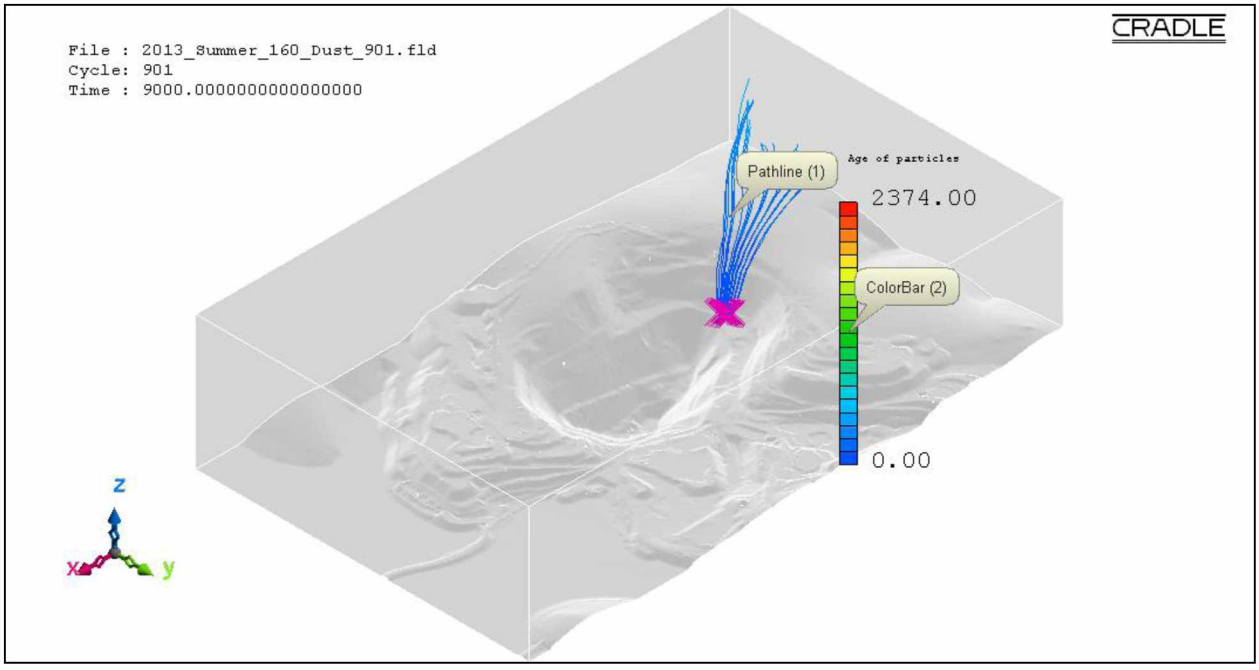

Figure B.46: Pathlines of $PM_{0.1}$ dust particles from source location 22 in the actual open-pit domain for extreme insolation summer condition using the LES method.

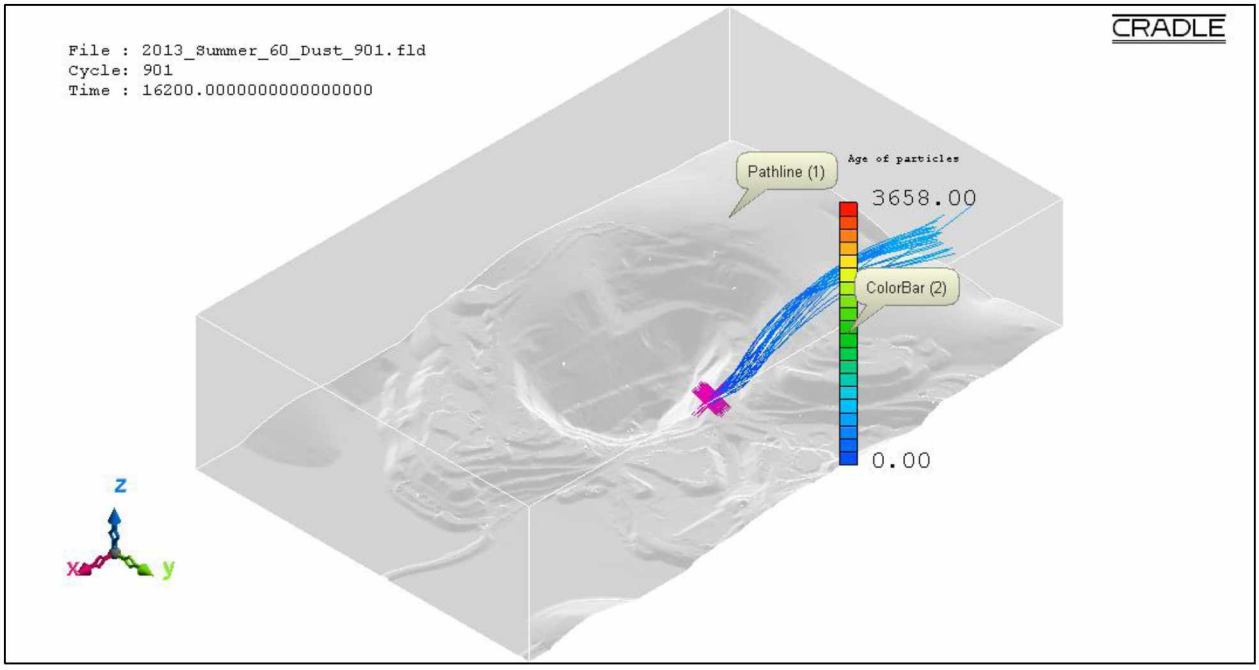

Figure B.47: Pathlines of $PM_{0.1}$ dust particles from source location 23 in the actual open-pit domain for fair insolation summer condition using the LES method.

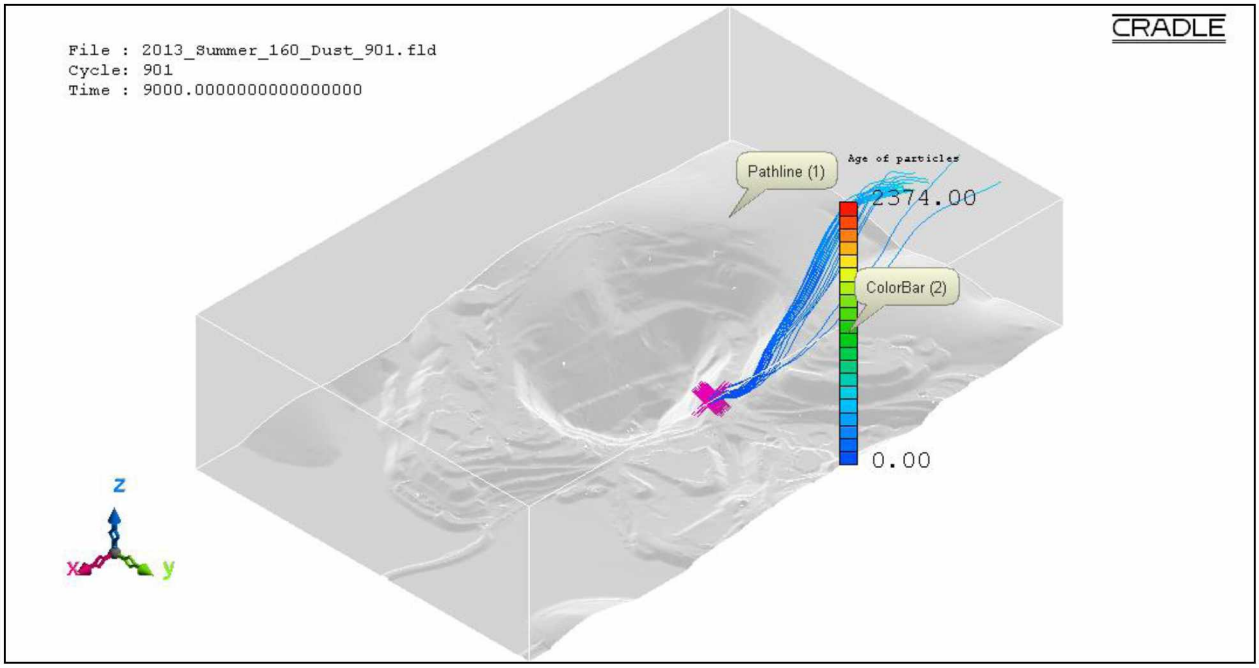

Figure B.48: Pathlines of $PM_{0.1}$ dust particles from source location 23 in the actual open-pit domain for extreme insolation summer condition using the LES method.

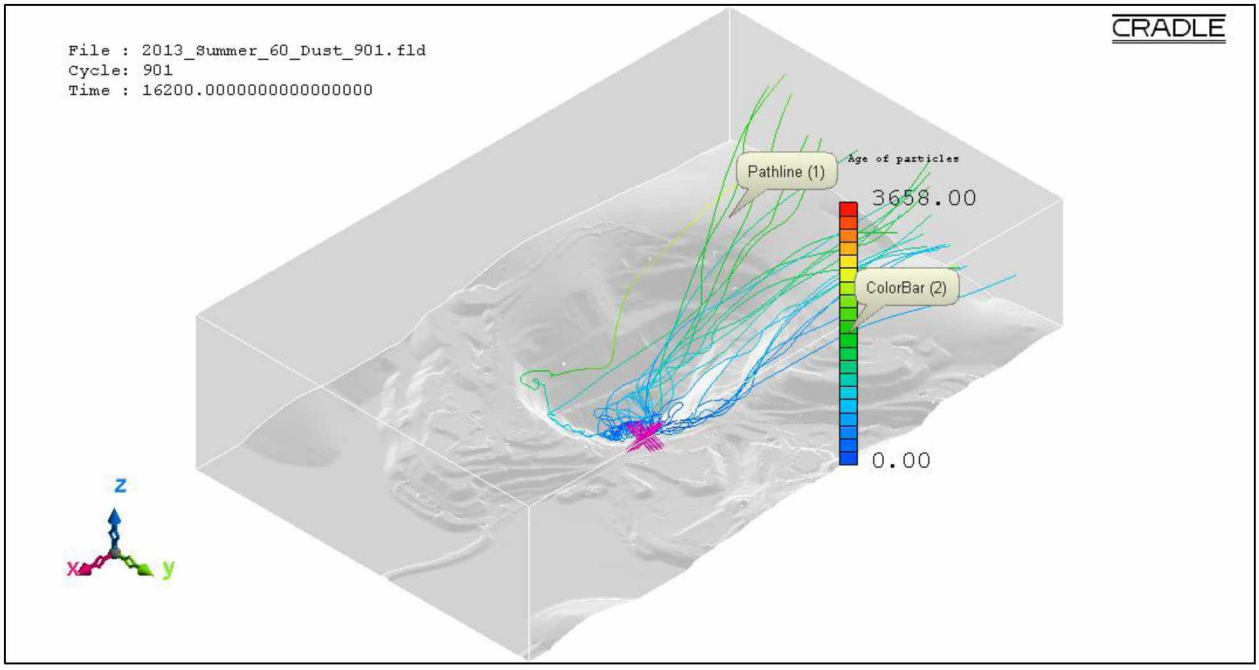

Figure B.49: Pathlines of $PM_{0.1}$ dust particles from source location 24 in the actual open-pit domain for fair insolation summer condition using the LES method.

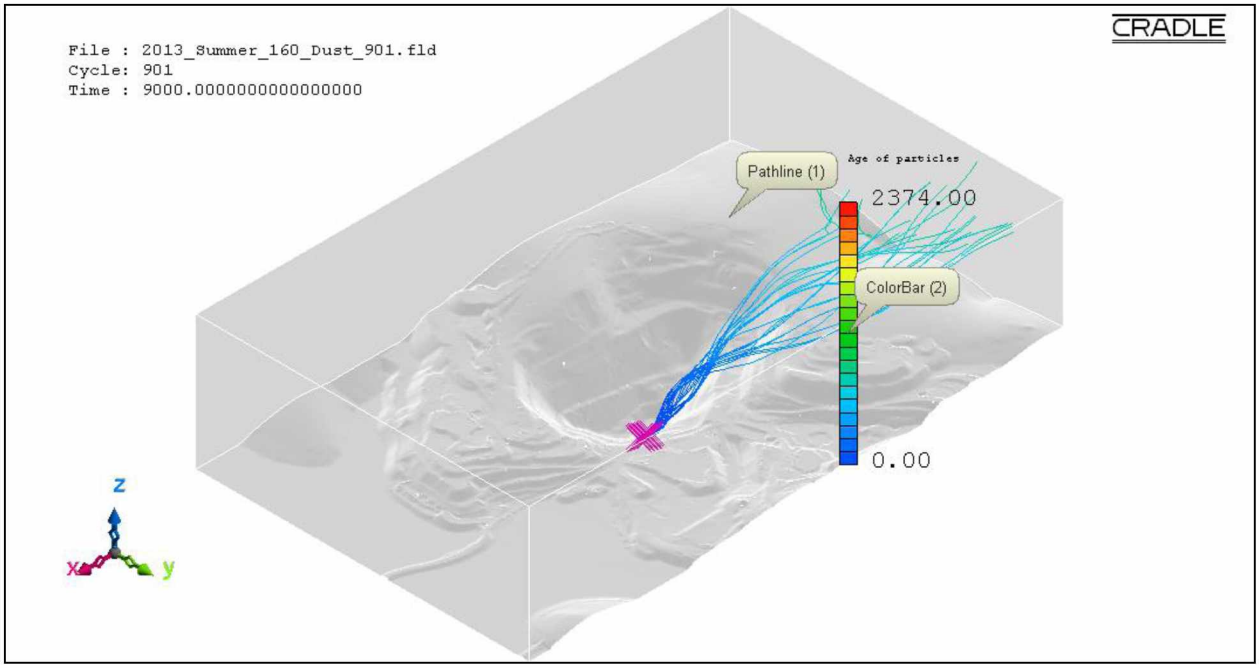

Figure B.50: Pathlines of $PM_{0.1}$ dust particles from source location 24 in the actual open-pit domain for extreme insolation summer condition using the LES method.

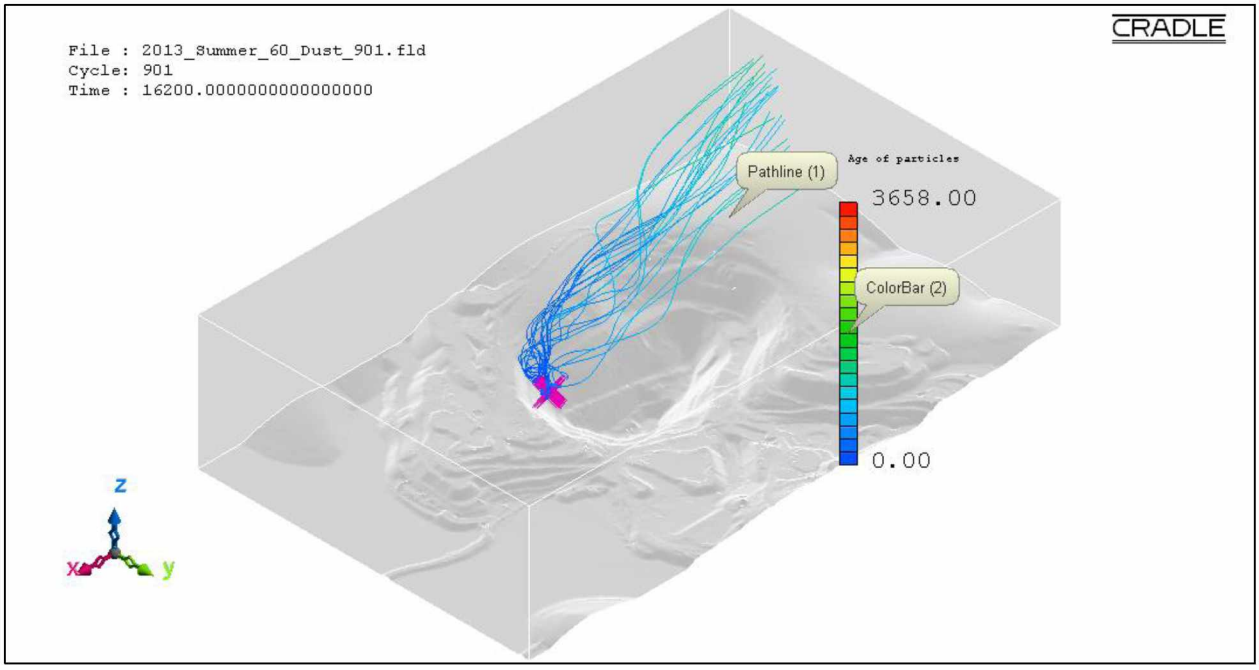

Figure B.51: Pathlines of $PM_{0.1}$ dust particles from source location 25 in the actual open-pit domain for fair insolation summer condition using the LES method.

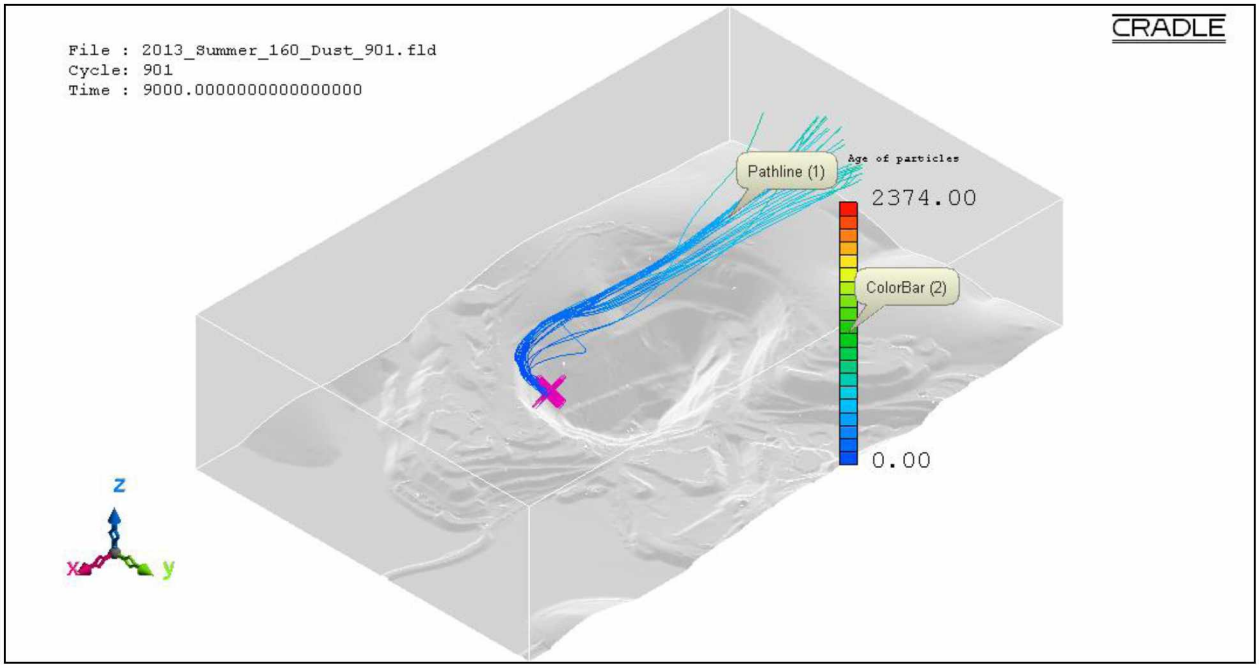

Figure B.52: Pathlines of $PM_{0.1}$ dust particles from source location 25 in the actual open-pit domain for extreme insolation summer condition using the LES method.

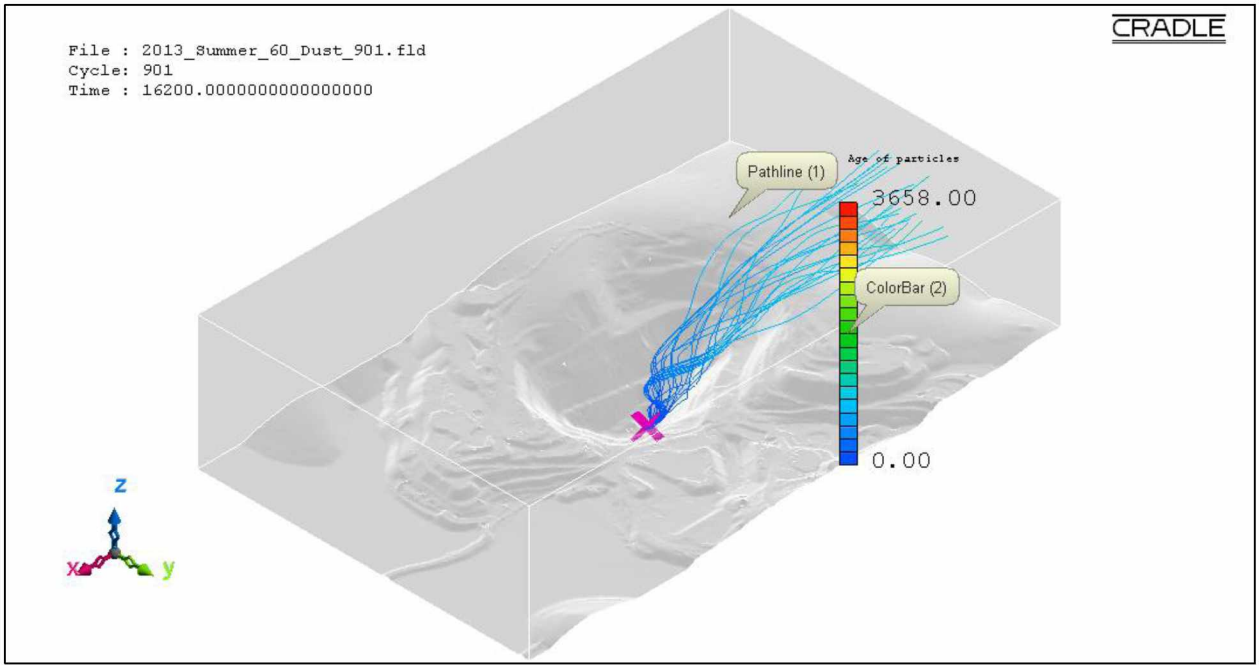

Figure B.53: Pathlines of $PM_{2.5}$ dust particles from source location 1 in the actual open-pit domain for fair insolation summer condition using the LES method.

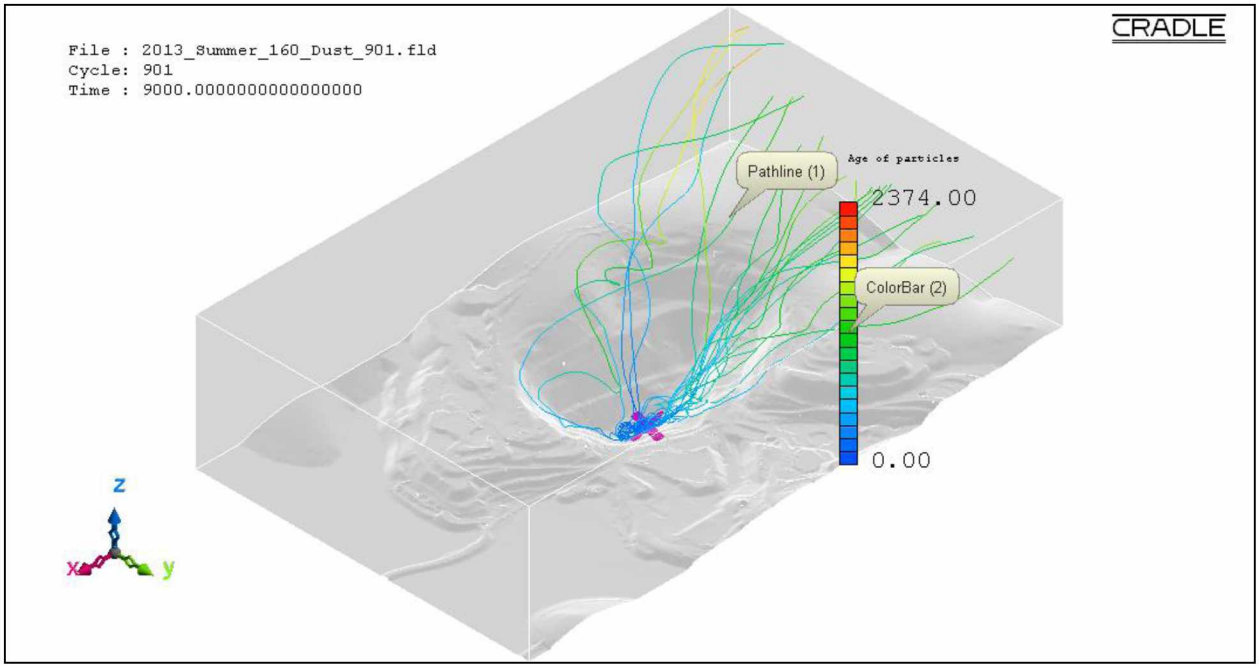

Figure B.54: Pathlines of $PM_{2.5}$ dust particles from source location 1 in the actual open-pit domain for extreme insolation summer condition using the LES method.

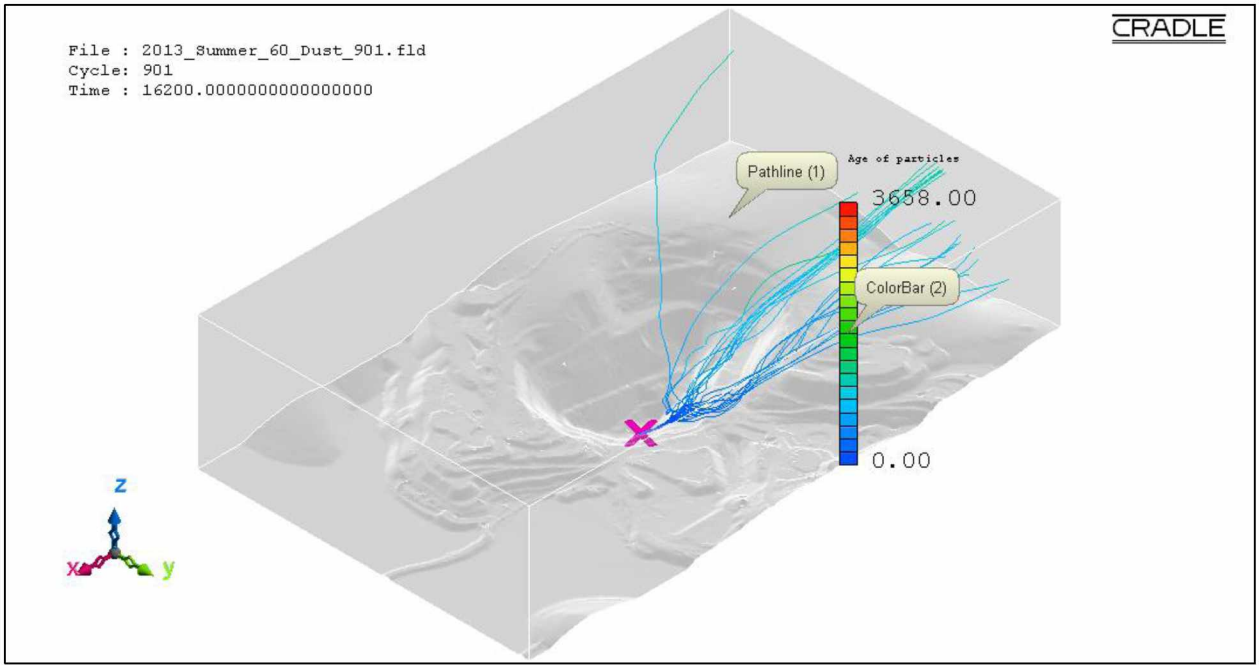

Figure B.55: Pathlines of $PM_{2.5}$ dust particles from source location 2 in the actual open-pit domain for fair insolation summer condition using the LES method.

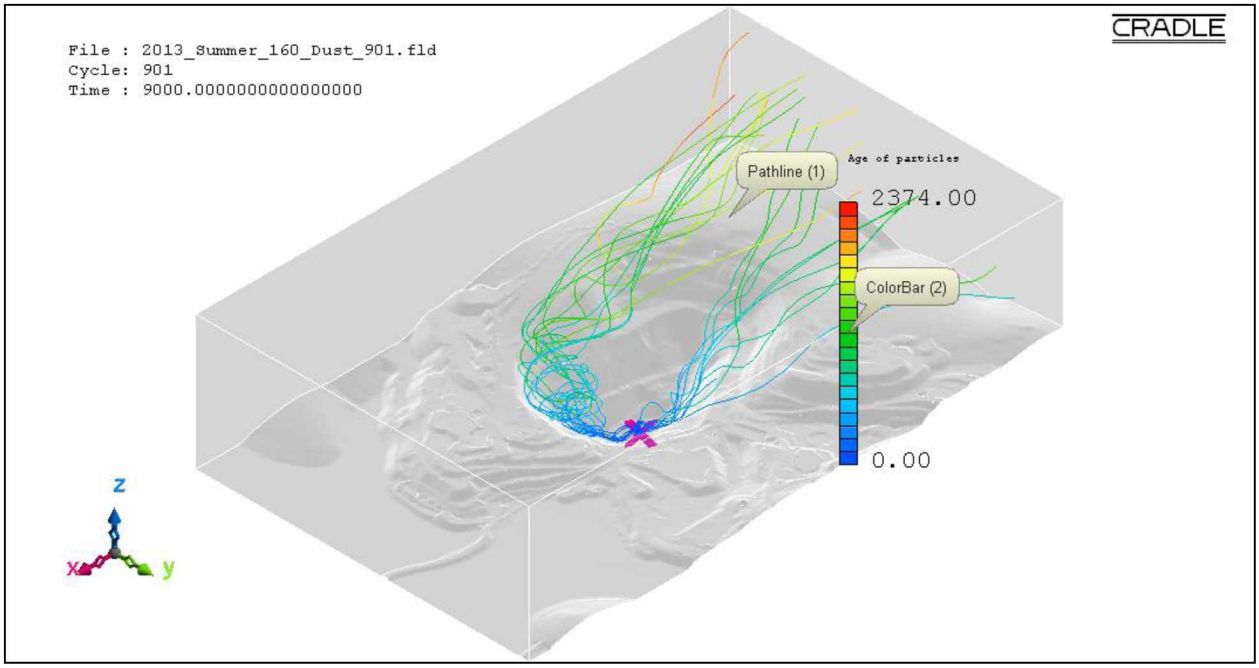

Figure B.56: Pathlines of $PM_{2.5}$ dust particles from source location 2 in the actual open-pit domain for extreme insolation summer condition using the LES method.

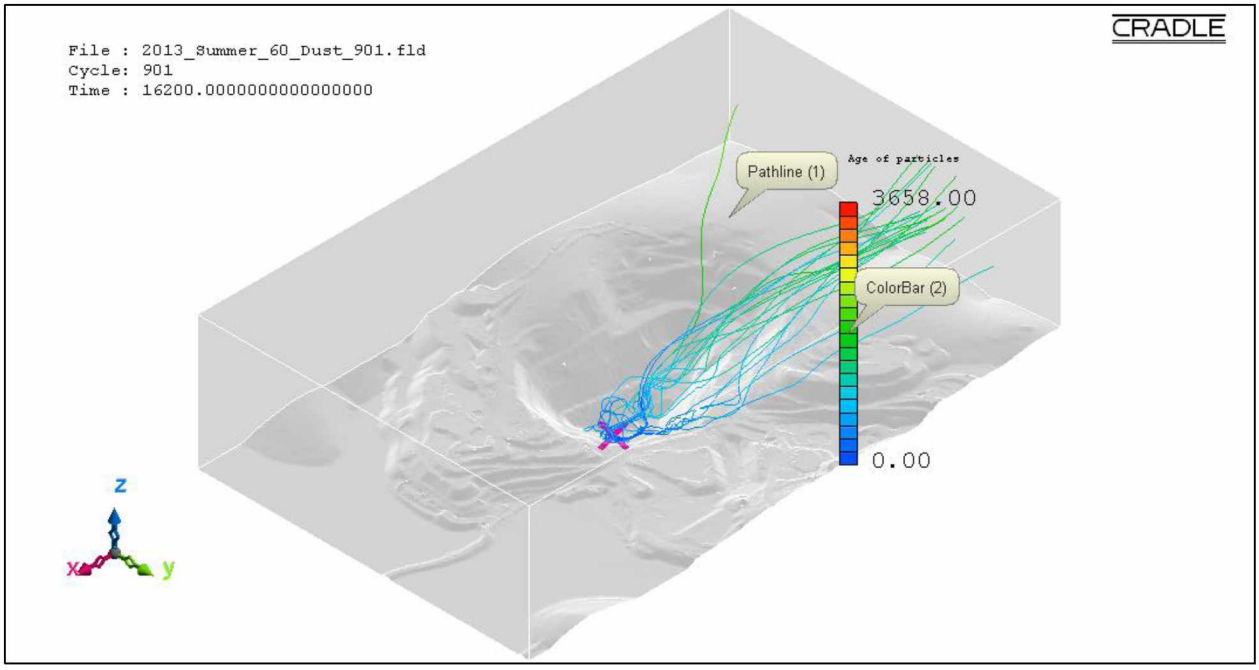

Figure B.57: Pathlines of $PM_{2.5}$ dust particles from source location 3 in the actual open-pit domain for fair insolation summer condition using the LES method.

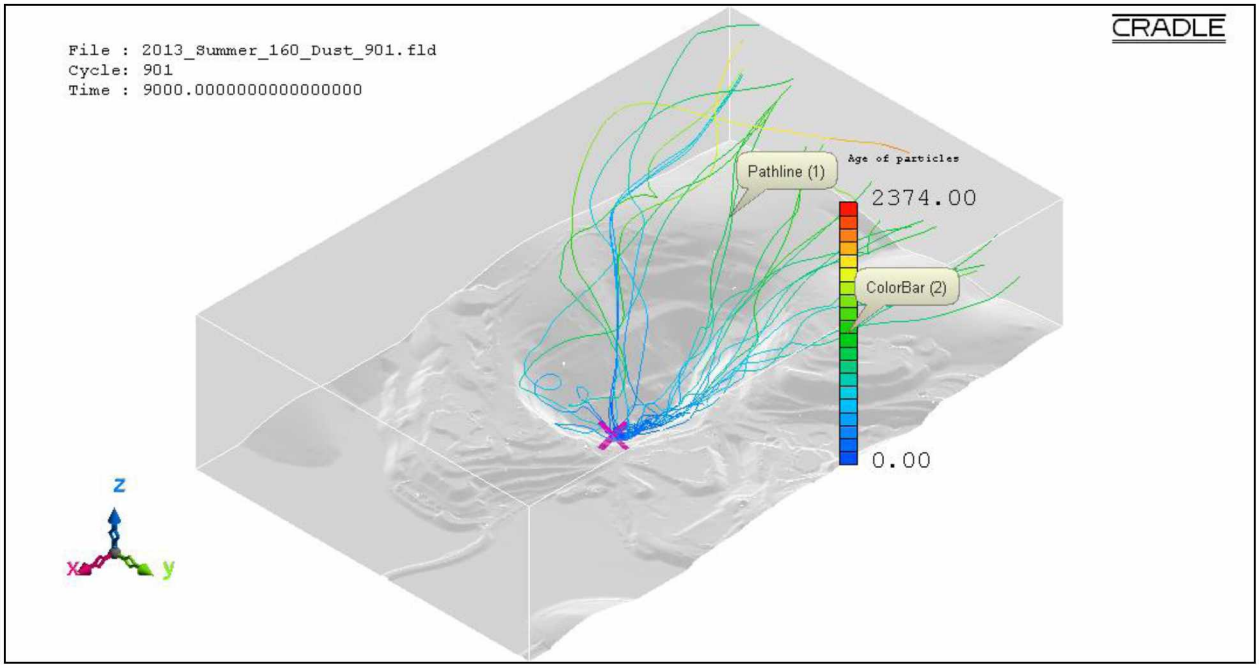

Figure B.58: Pathlines of $PM_{2.5}$ dust particles from source location 3 in the actual open-pit domain for extreme insolation summer condition using the LES method.

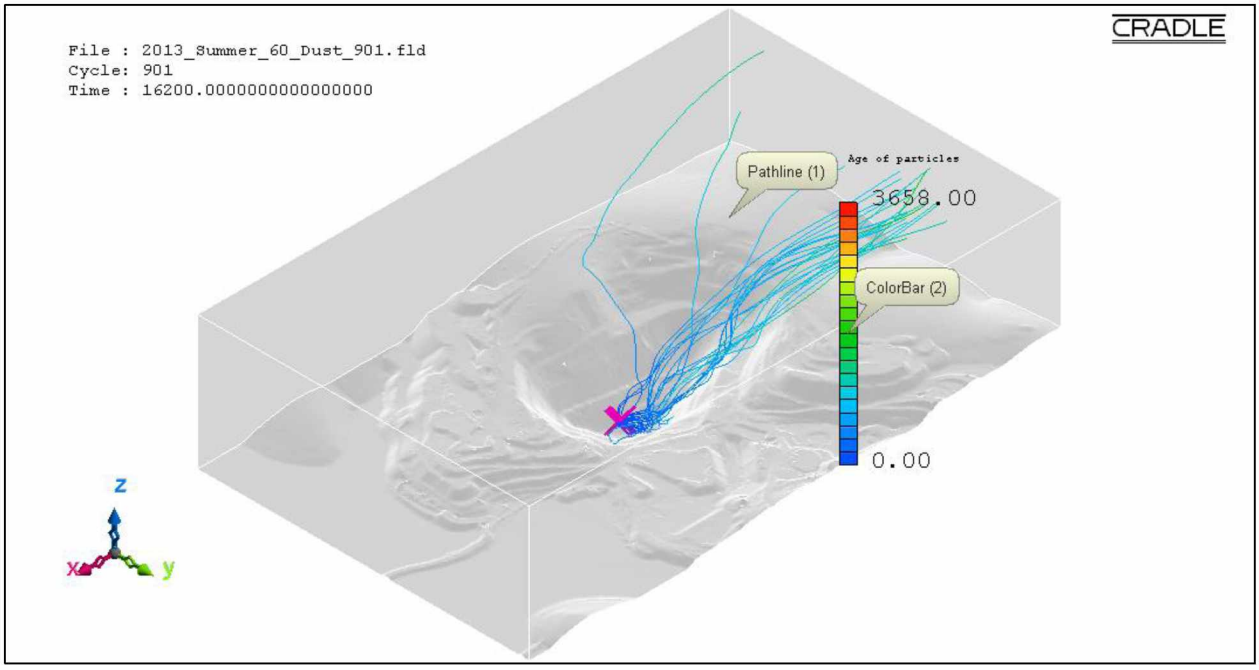

Figure B.59: Pathlines of $PM_{2.5}$ dust particles from source location 4 in the actual open-pit domain for fair insolation summer condition using the LES method.

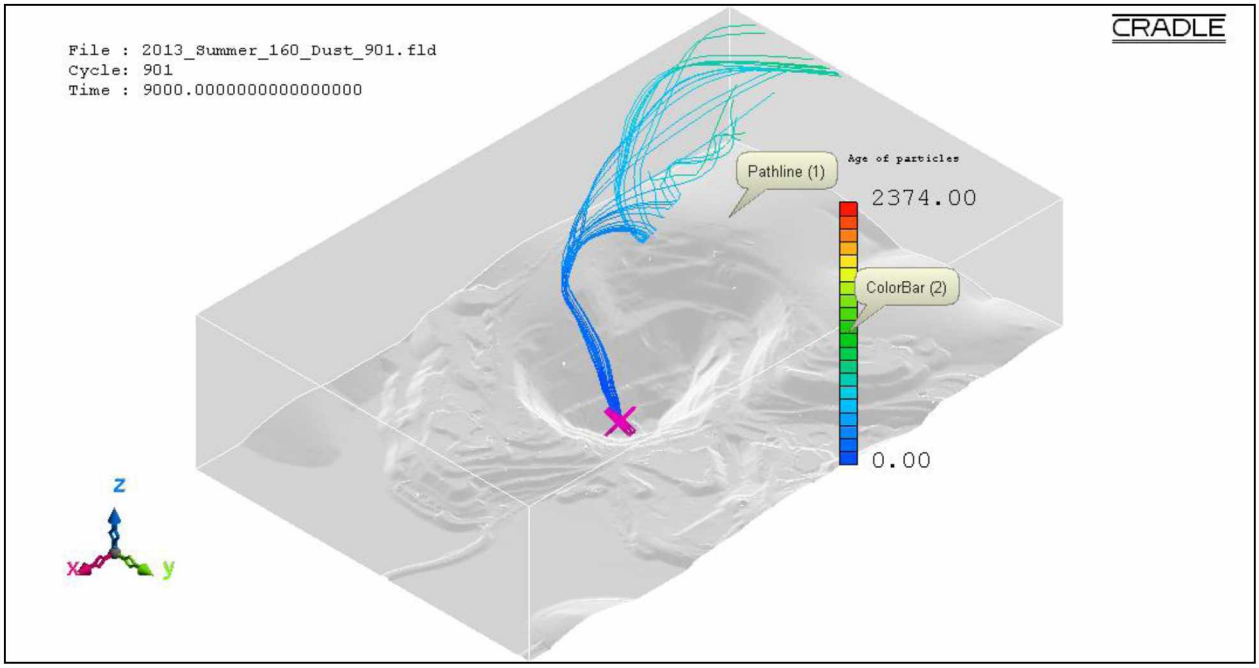

Figure B.60: Pathlines of $PM_{2.5}$ dust particles from source location 4 in the actual open-pit domain for extreme insolation summer condition using the LES method.

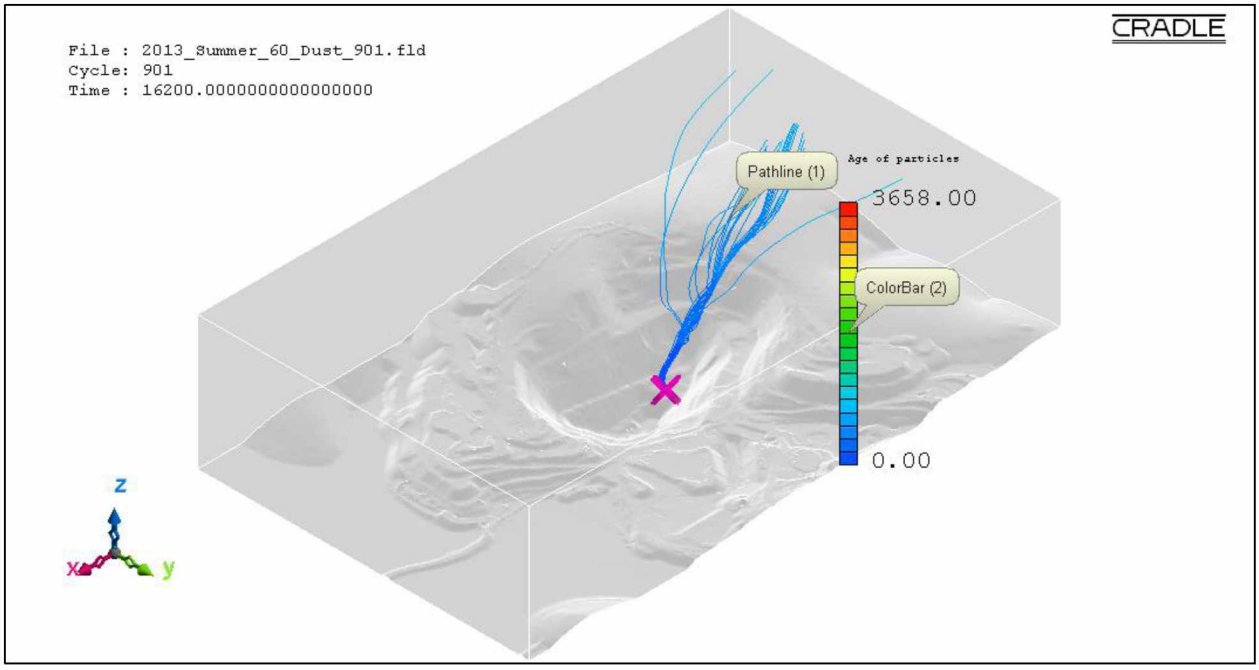

Figure B.61: Pathlines of $PM_{2.5}$ dust particles from source location 5 in the actual open-pit domain for fair insolation summer condition using the LES method.

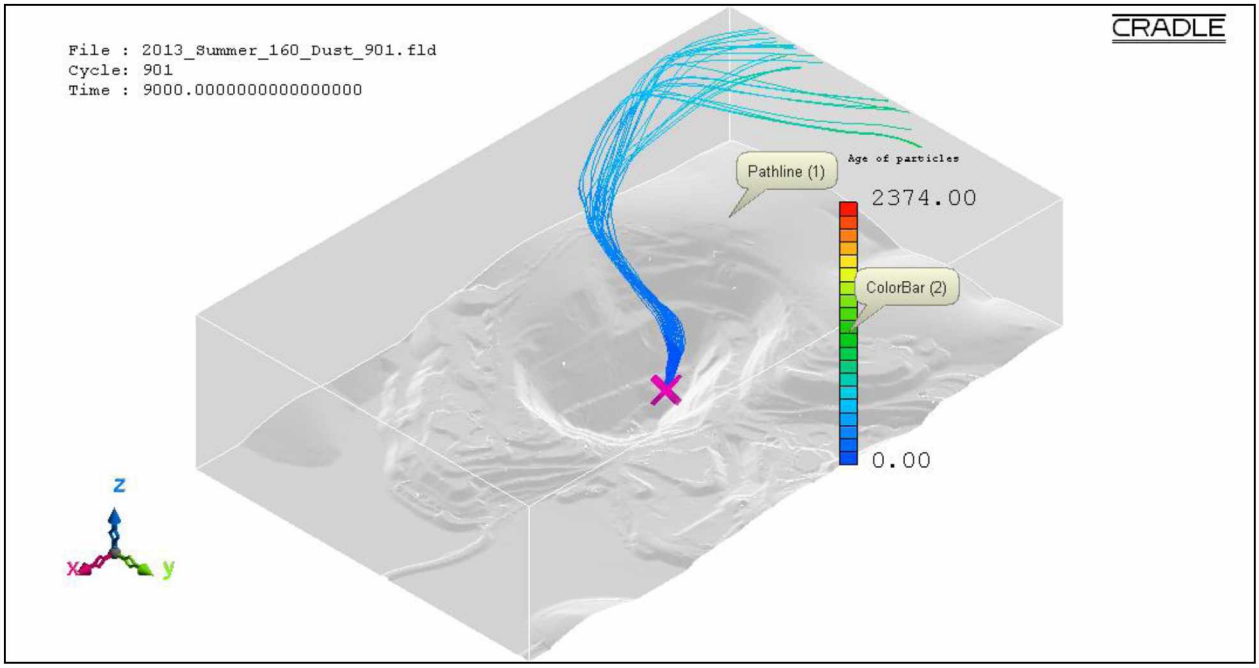

Figure B.62: Pathlines of $PM_{2.5}$ dust particles from source location 5 in the actual open-pit domain for extreme insolation summer condition using the LES method.

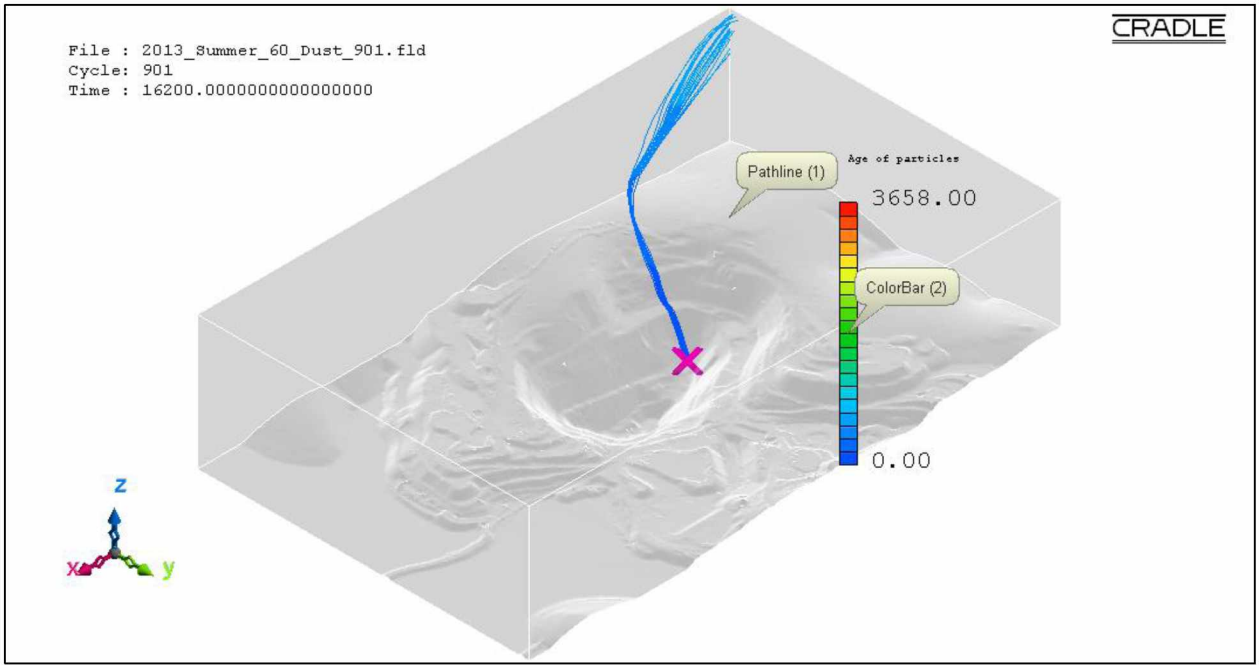

Figure B.63: Pathlines of $PM_{2.5}$ dust particles from source location 6 in the actual open-pit domain for fair insolation summer condition using the LES method.

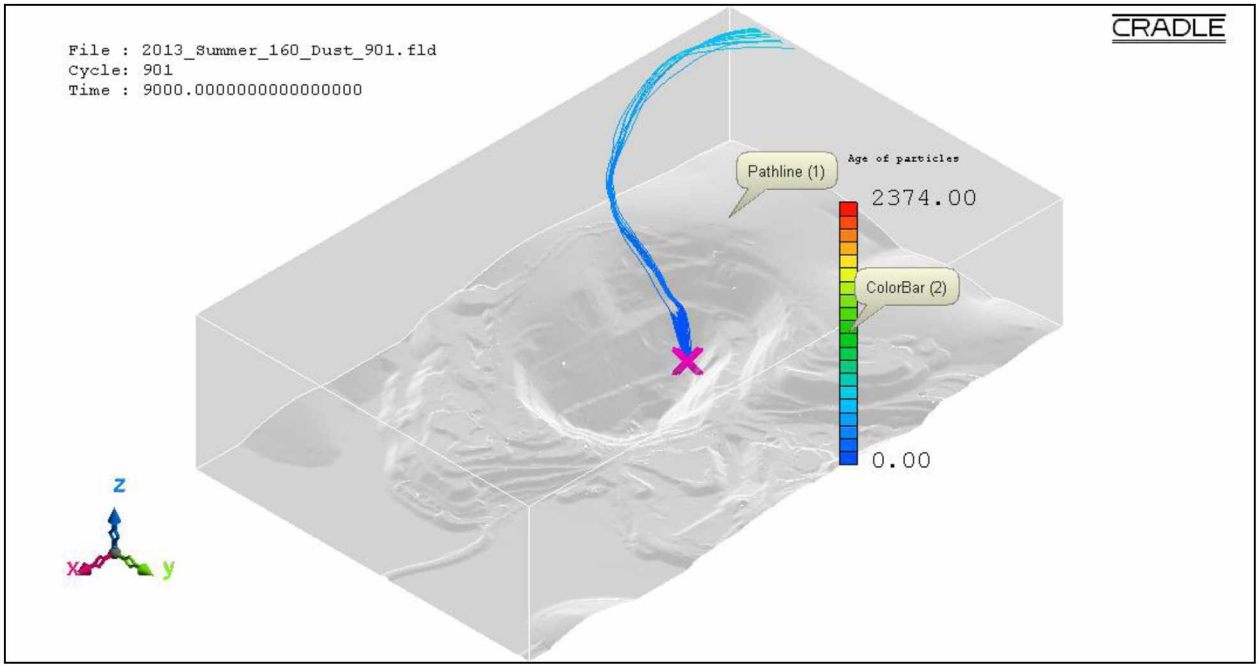

Figure B.64: Pathlines of $PM_{2.5}$ dust particles from source location 6 in the actual open-pit domain for extreme insolation summer condition using the LES method.

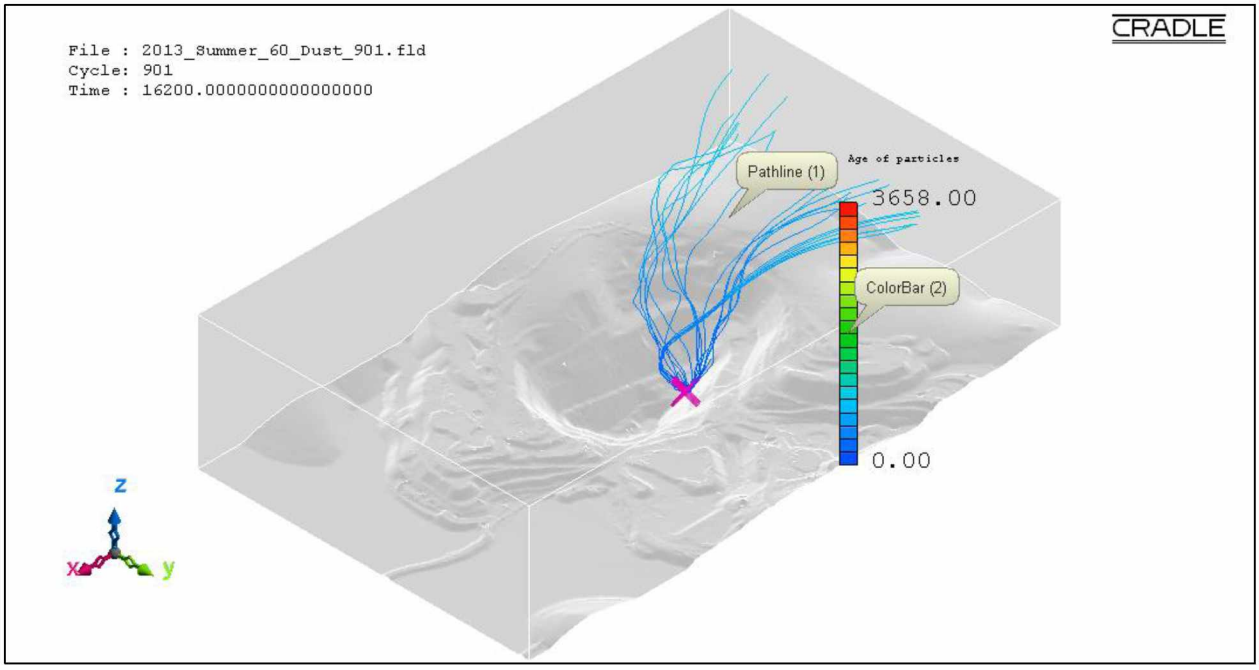

Figure B.65: Pathlines of $PM_{2.5}$ dust particles from source location 7 in the actual open-pit domain for fair insolation summer condition using the LES method.

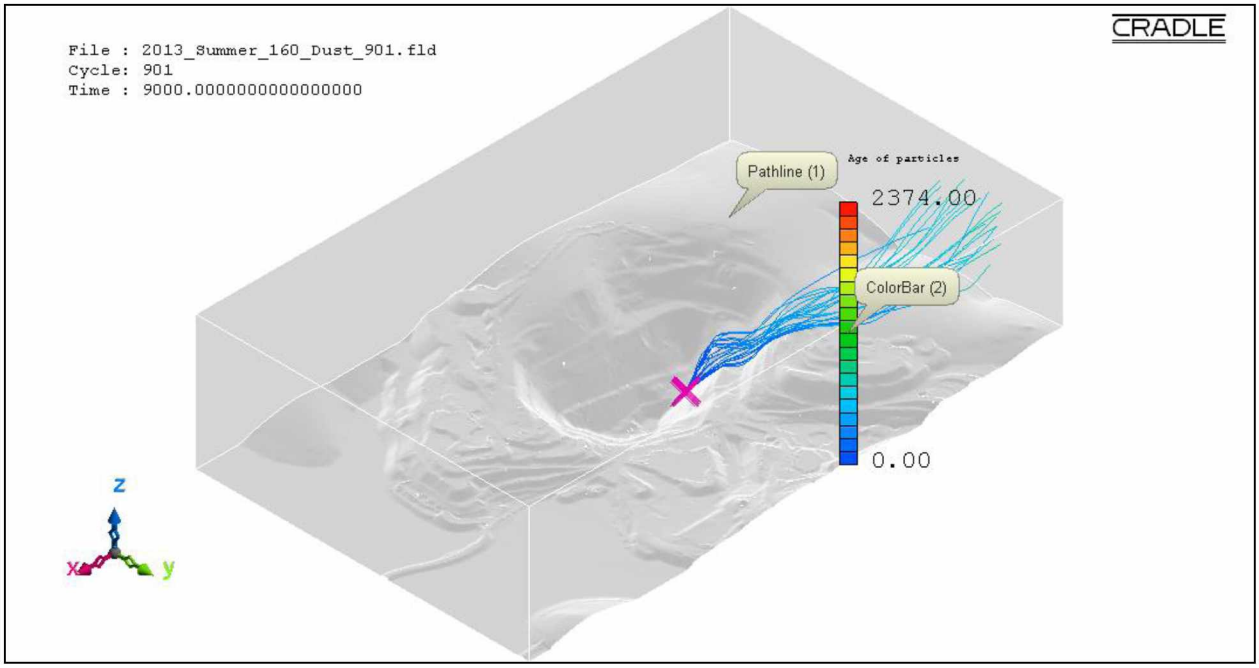

Figure B.66: Pathlines of $PM_{2.5}$ dust particles from source location 7 in the actual open-pit domain for extreme insolation summer condition using the LES method.

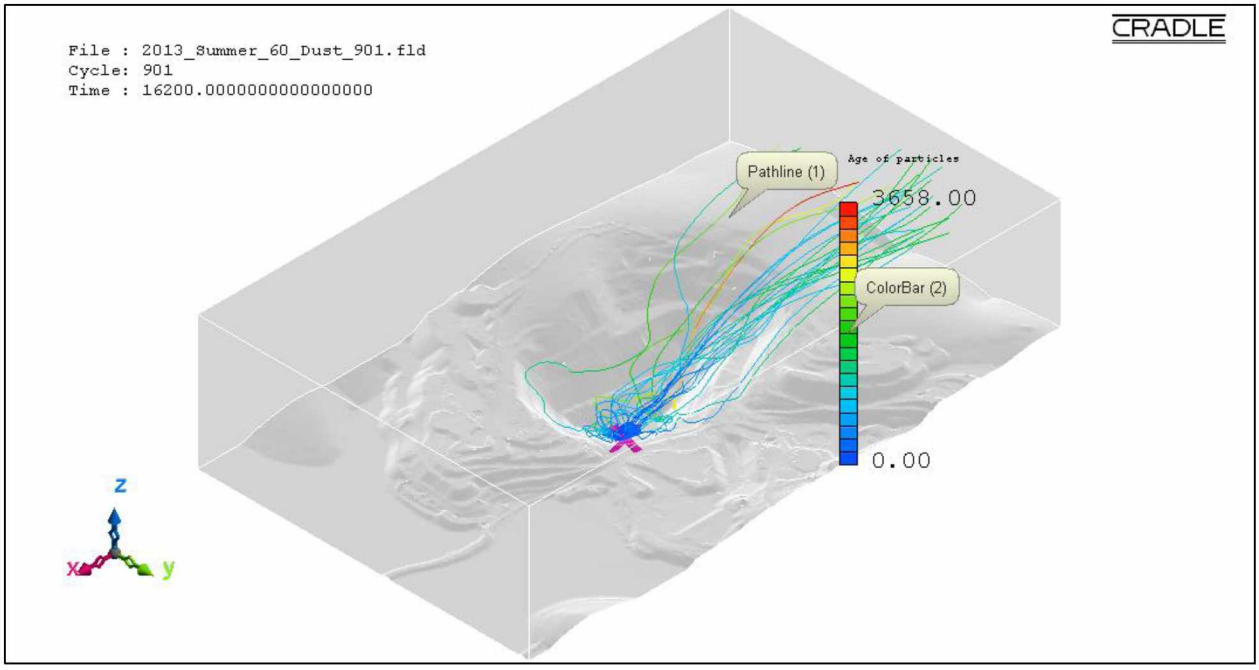

Figure B.67: Pathlines of $PM_{2.5}$ dust particles from source location 8 in the actual open-pit domain for fair insolation summer condition using the LES method.

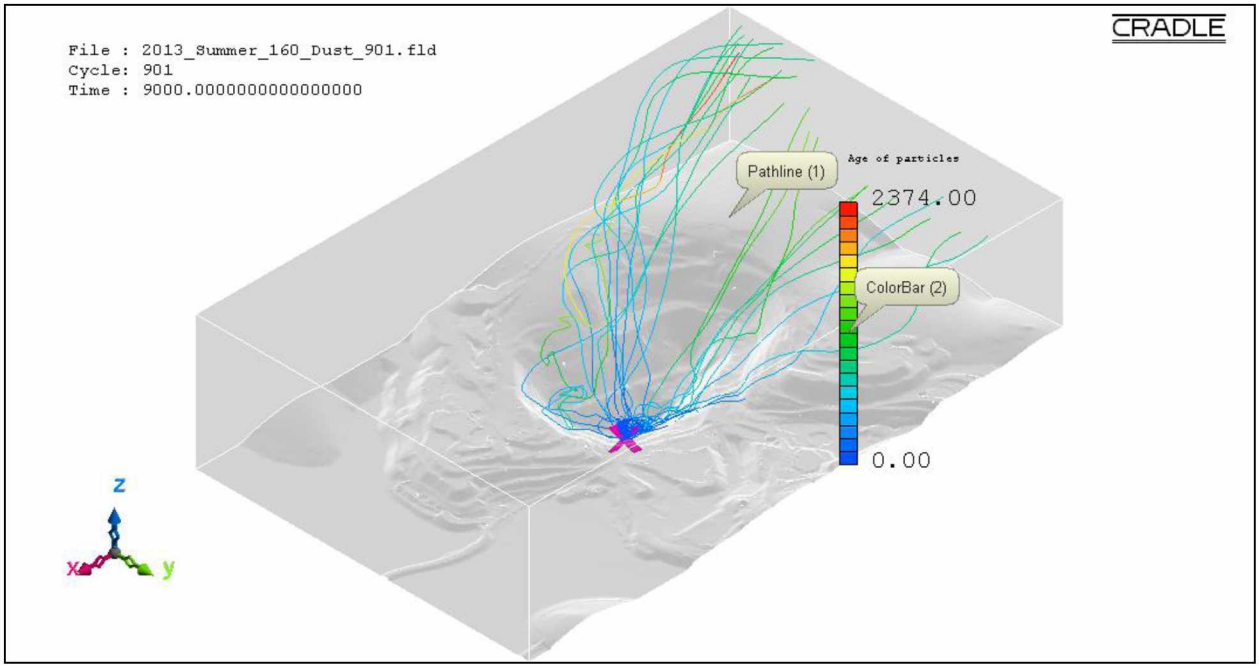

Figure B.68: Pathlines of $PM_{2.5}$ dust particles from source location 8 in the actual open-pit domain for extreme insolation summer condition using the LES method.

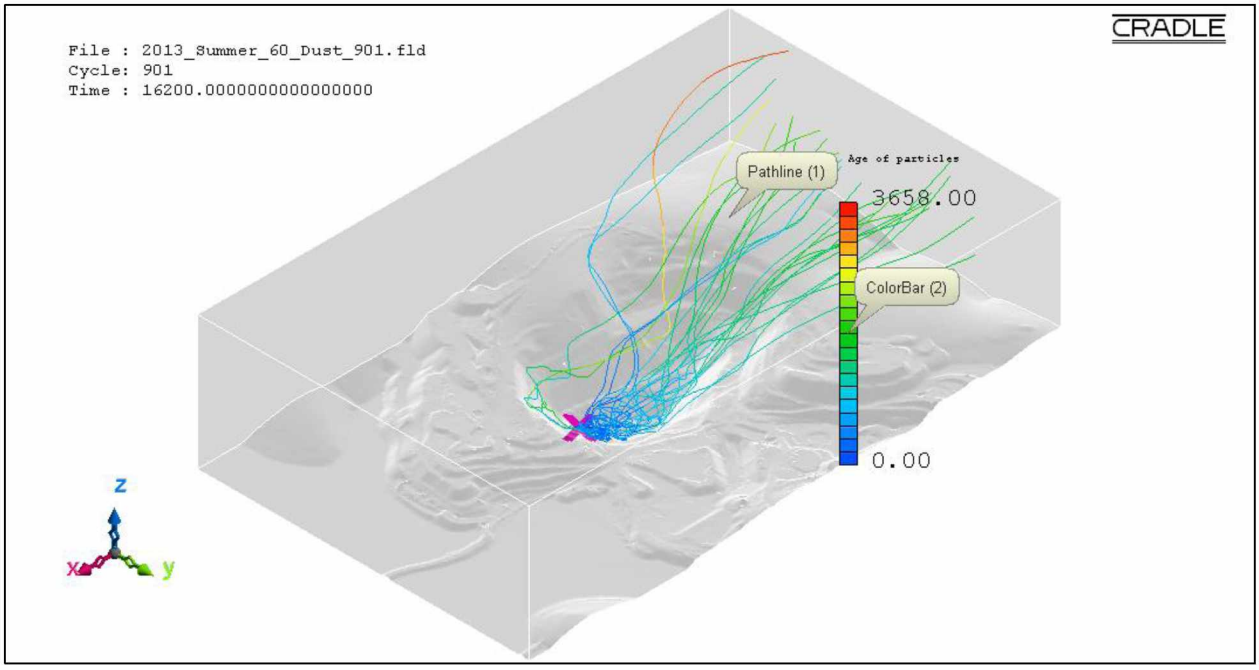

Figure B.69: Pathlines of $PM_{2.5}$ dust particles from source location 9 in the actual open-pit domain for fair insolation summer condition using the LES method.

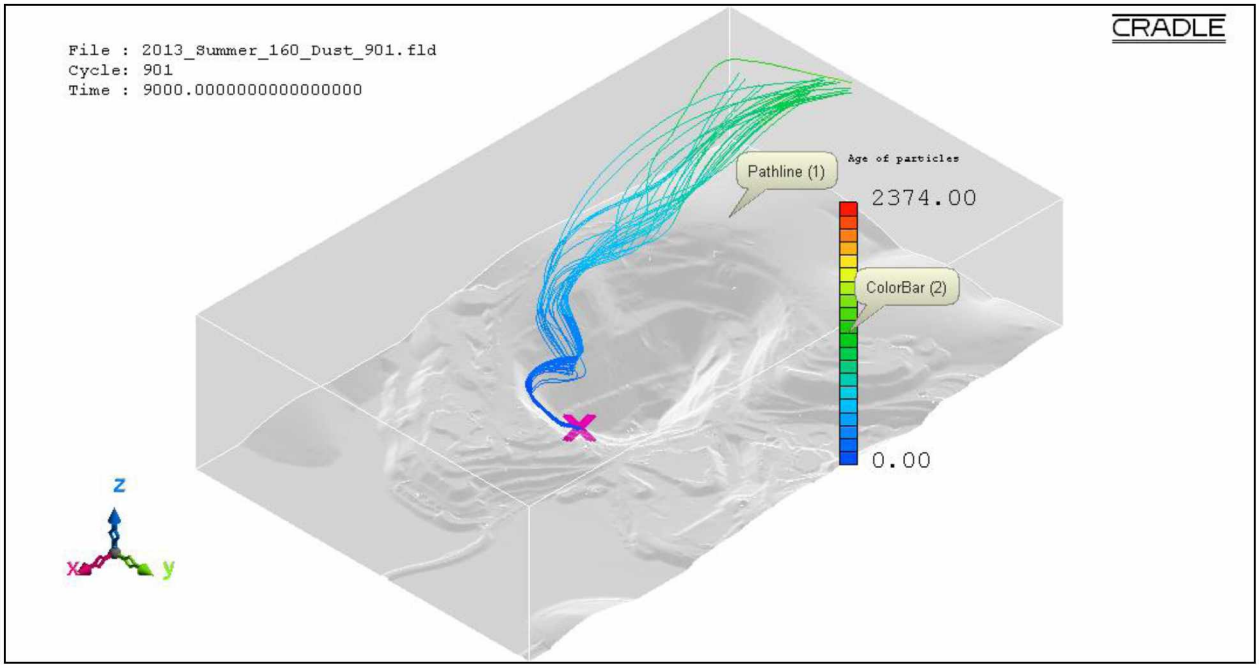

Figure B.70: Pathlines of $PM_{2.5}$ dust particles from source location 9 in the actual open-pit domain for extreme insolation summer condition using the LES method.

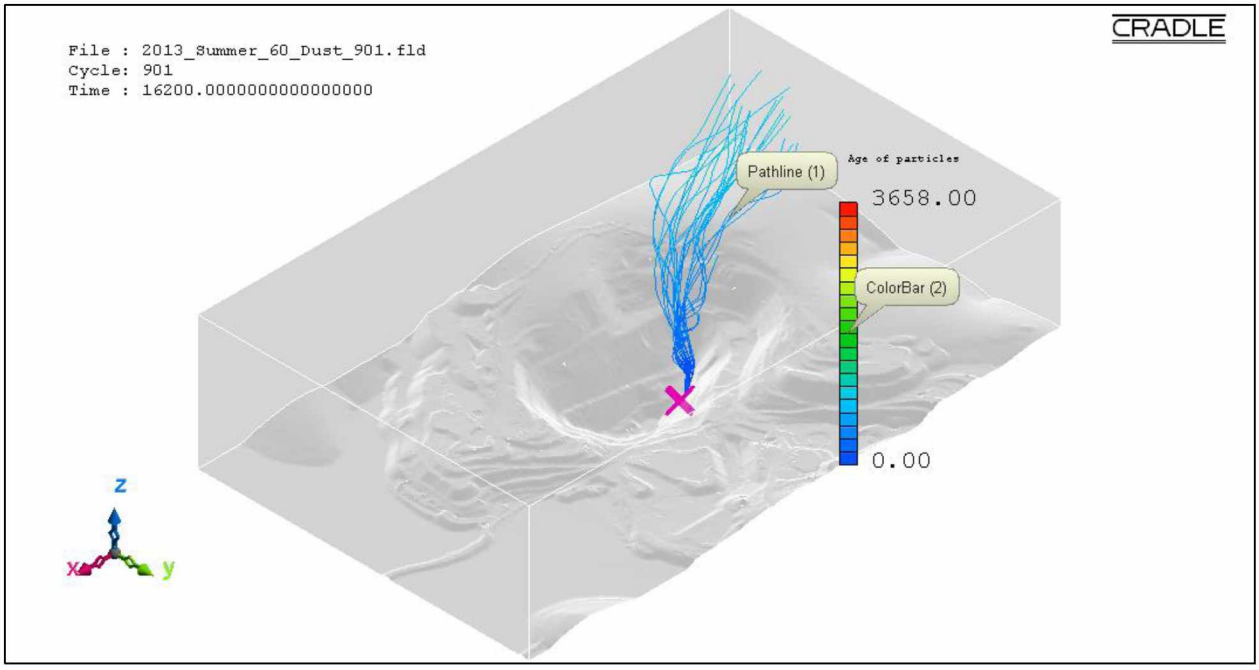

Figure B.71: Pathlines of $PM_{2.5}$ dust particles from source location 10 in the actual open-pit domain for fair insolation summer condition using the LES method.

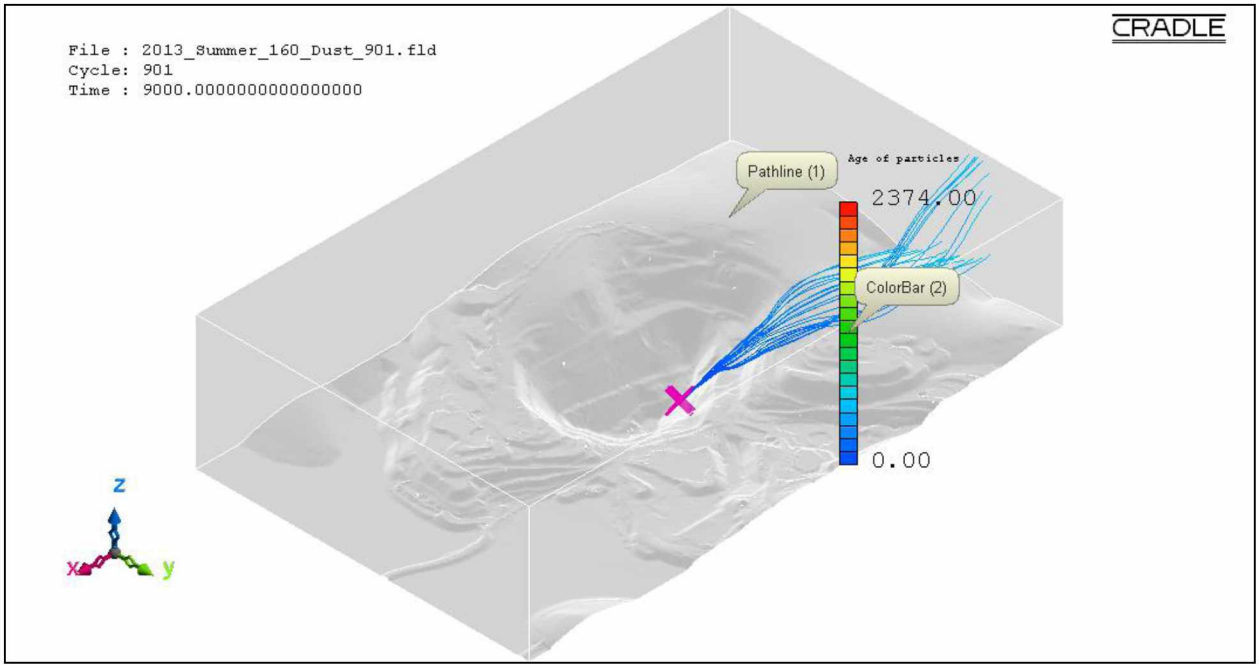

Figure B.72: Pathlines of $PM_{2.5}$ dust particles from source location 10 in the actual open-pit domain for extreme insolation summer condition using the LES method.

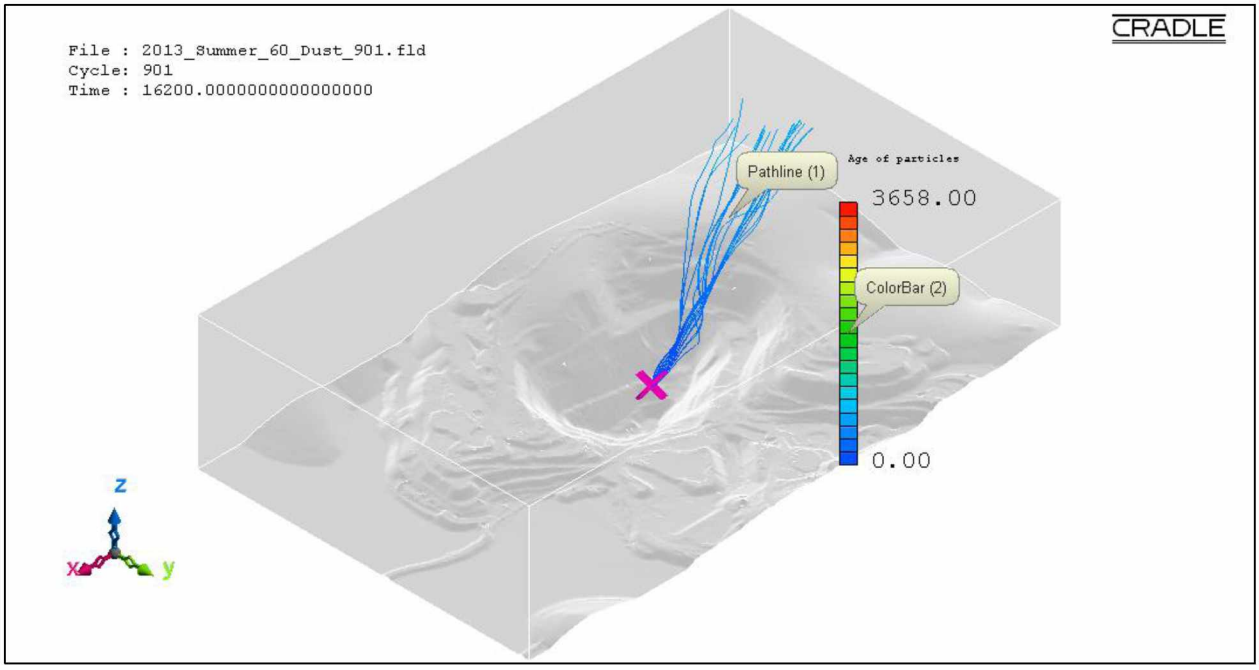

Figure B.73: Pathlines of $PM_{2.5}$ dust particles from source location 11 in the actual open-pit domain for fair insolation summer condition using the LES method.

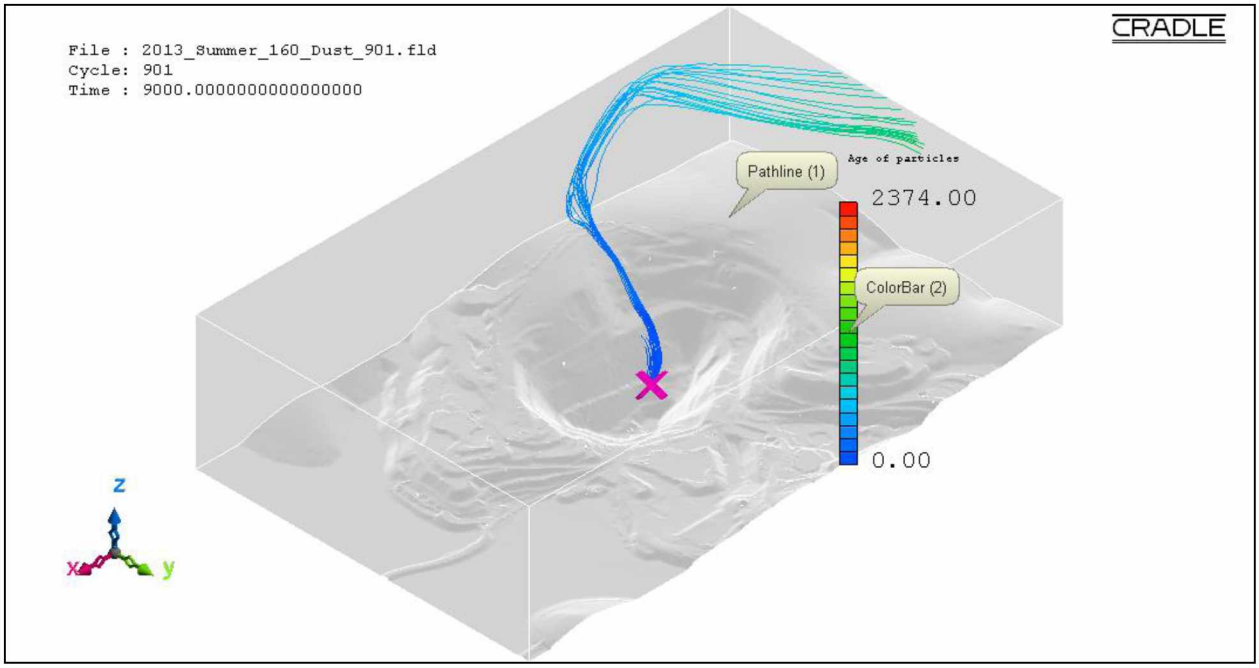

Figure B.74: Pathlines of $PM_{2.5}$ dust particles from source location 11 in the actual open-pit domain for extreme insolation summer condition using the LES method.

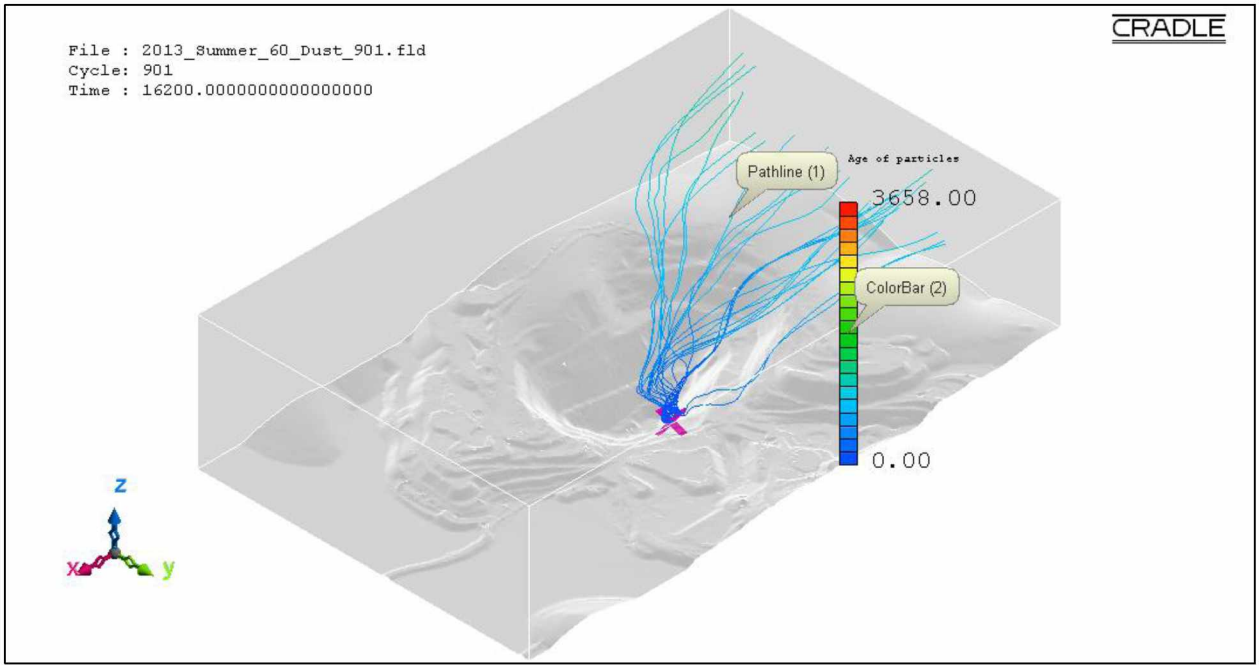

Figure B.75: Pathlines of $PM_{2.5}$ dust particles from source location 12 in the actual open-pit domain for fair insolation summer condition using the LES method.

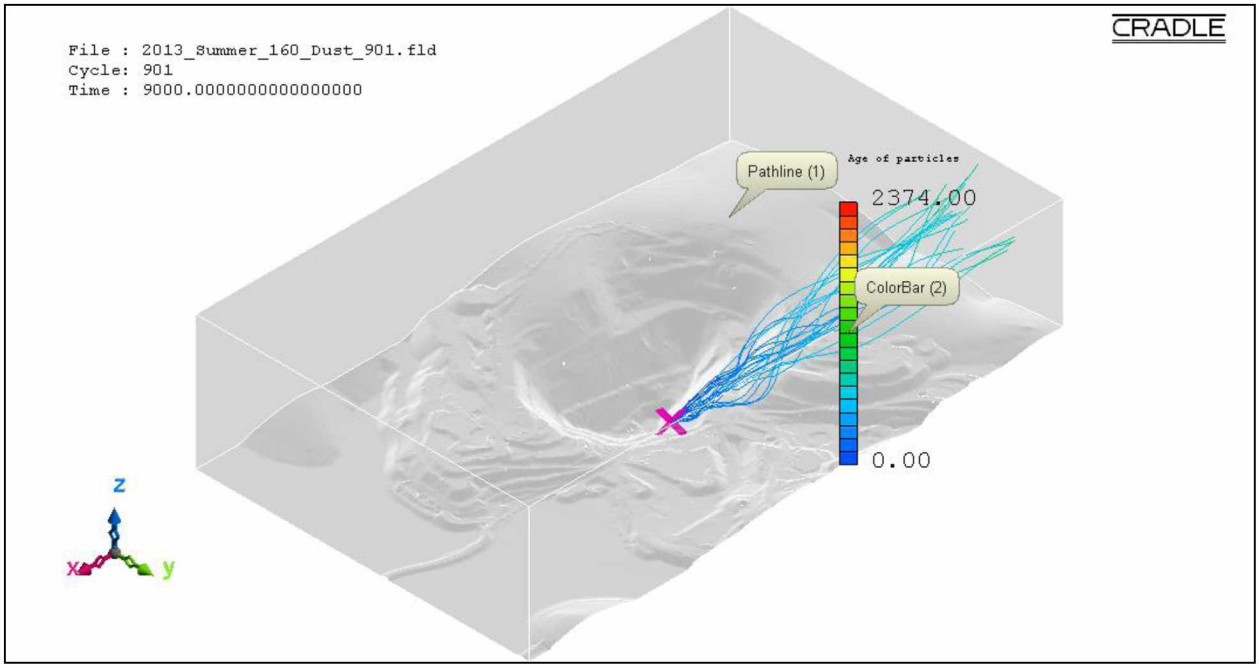

Figure B.76: Pathlines of $PM_{2.5}$ dust particles from source location 12 in the actual open-pit domain for extreme insolation summer condition using the LES method.

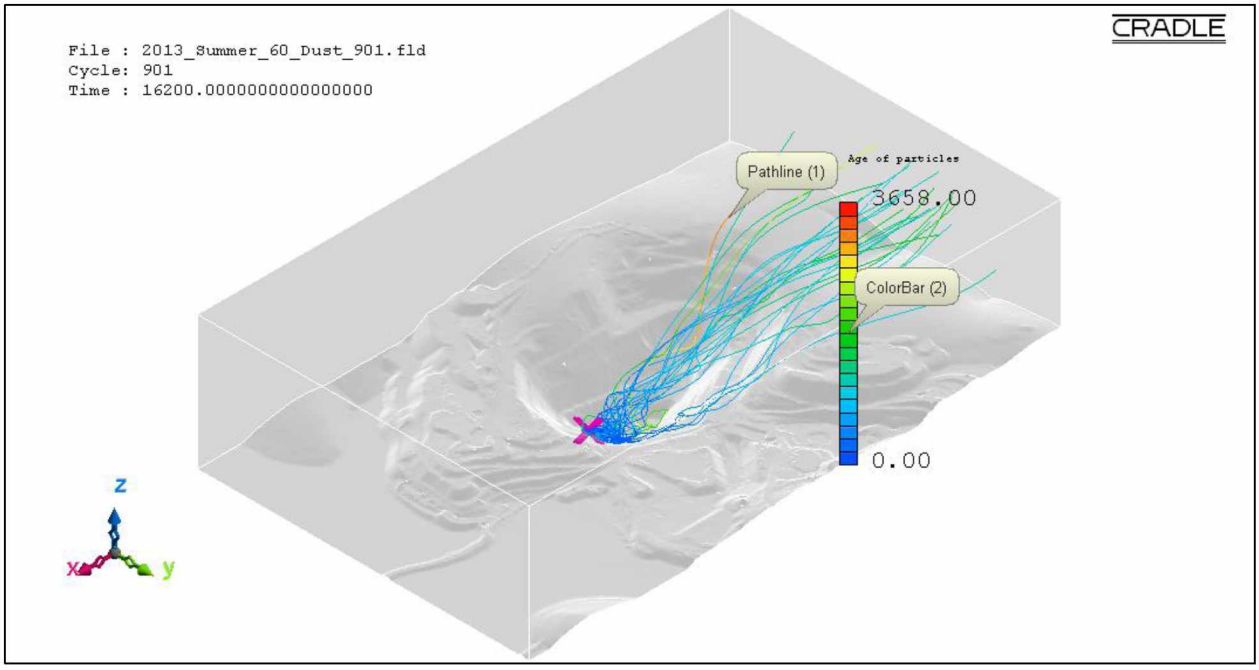

Figure B.77: Pathlines of $PM_{2.5}$ dust particles from source location 13 in the actual open-pit domain for fair insolation summer condition using the LES method.

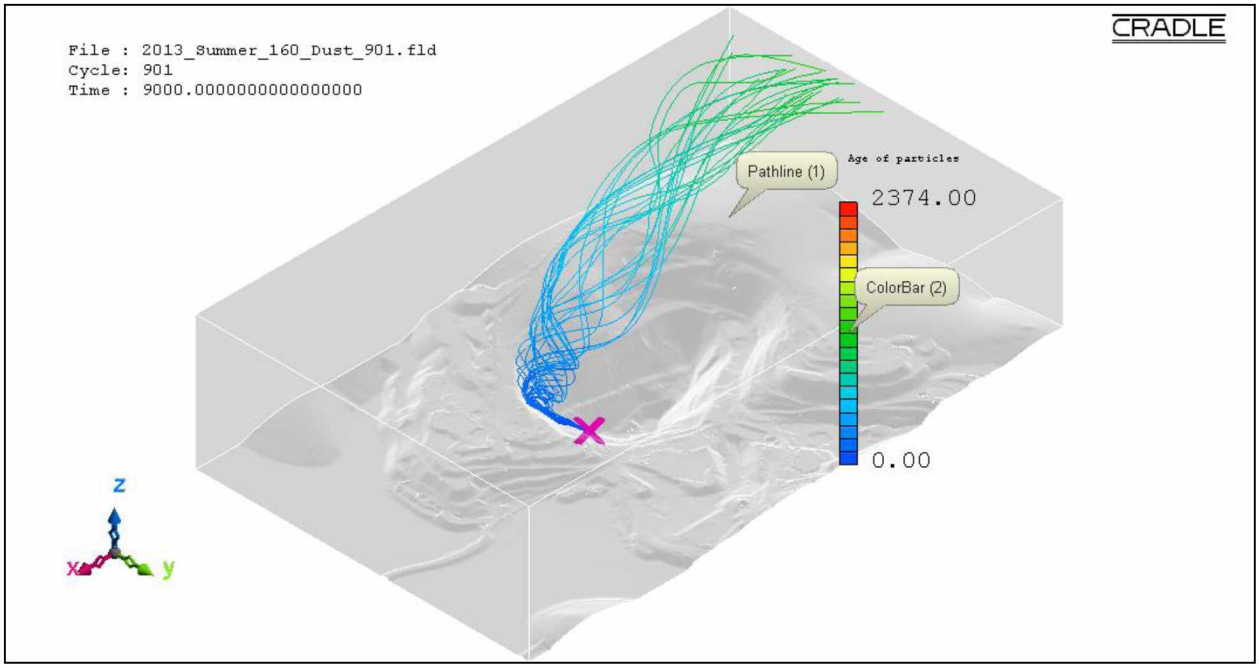

Figure B.78: Pathlines of $PM_{2.5}$ dust particles from source location 13 in the actual open-pit domain for extreme insolation summer condition using the LES method.

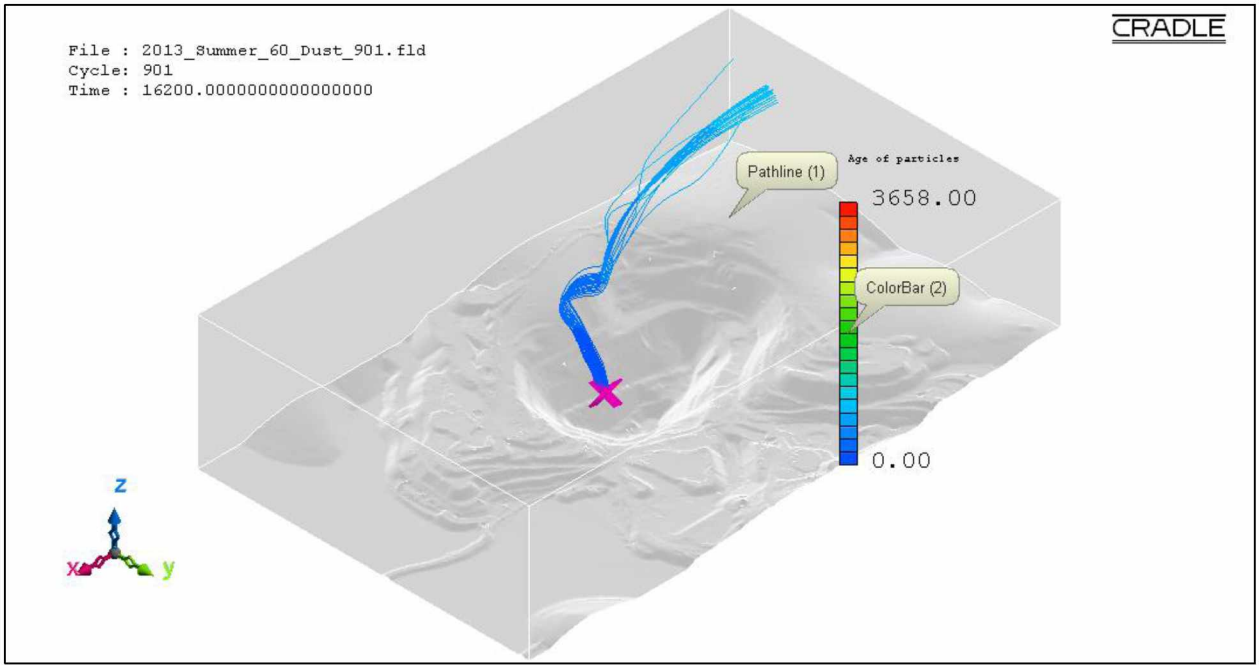

Figure B.79: Pathlines of $PM_{2.5}$ dust particles from source location 14 in the actual open-pit domain for fair insolation summer condition using the LES method.

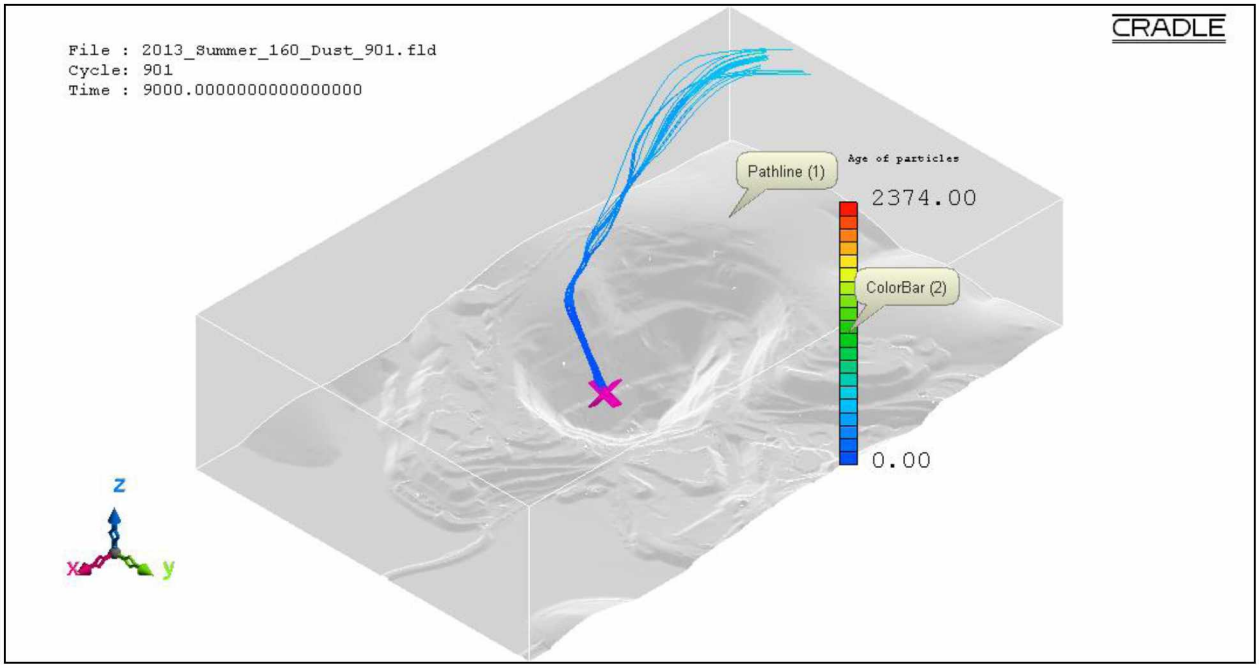

Figure B.80: Pathlines of $PM_{2.5}$ dust particles from source location 14 in the actual open-pit domain for extreme insolation summer condition using the LES method.

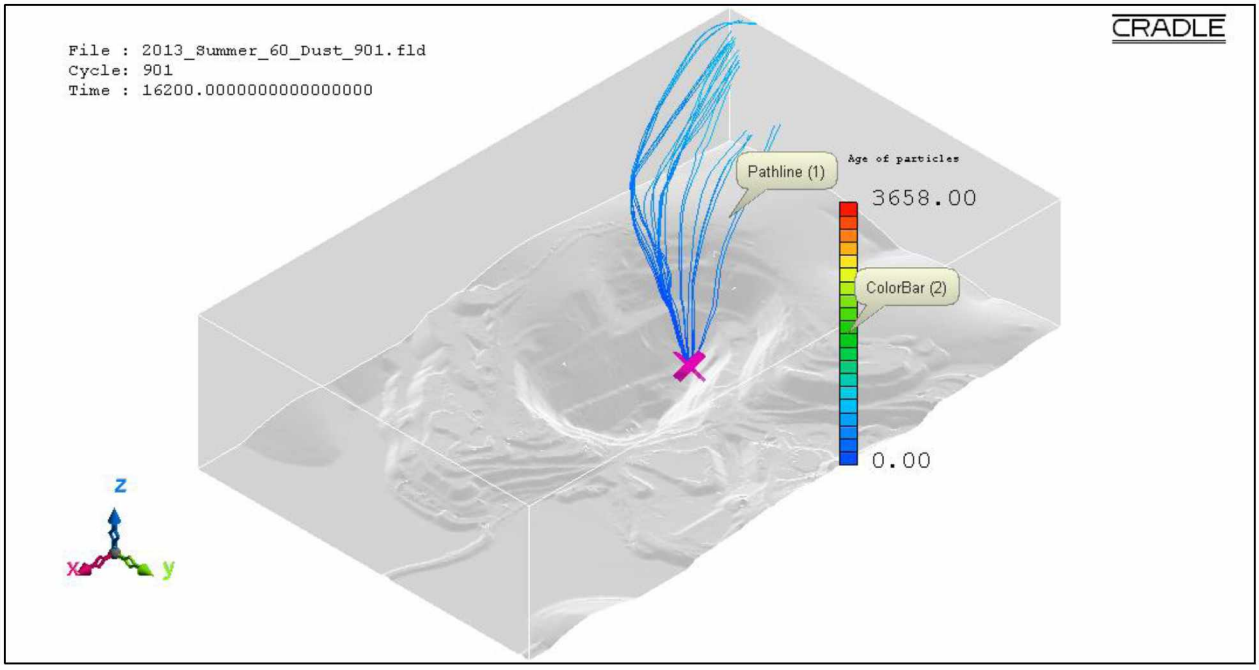

Figure B.81: Pathlines of $PM_{2.5}$ dust particles from source location 15 in the actual open-pit domain for fair insolation summer condition using the LES method.

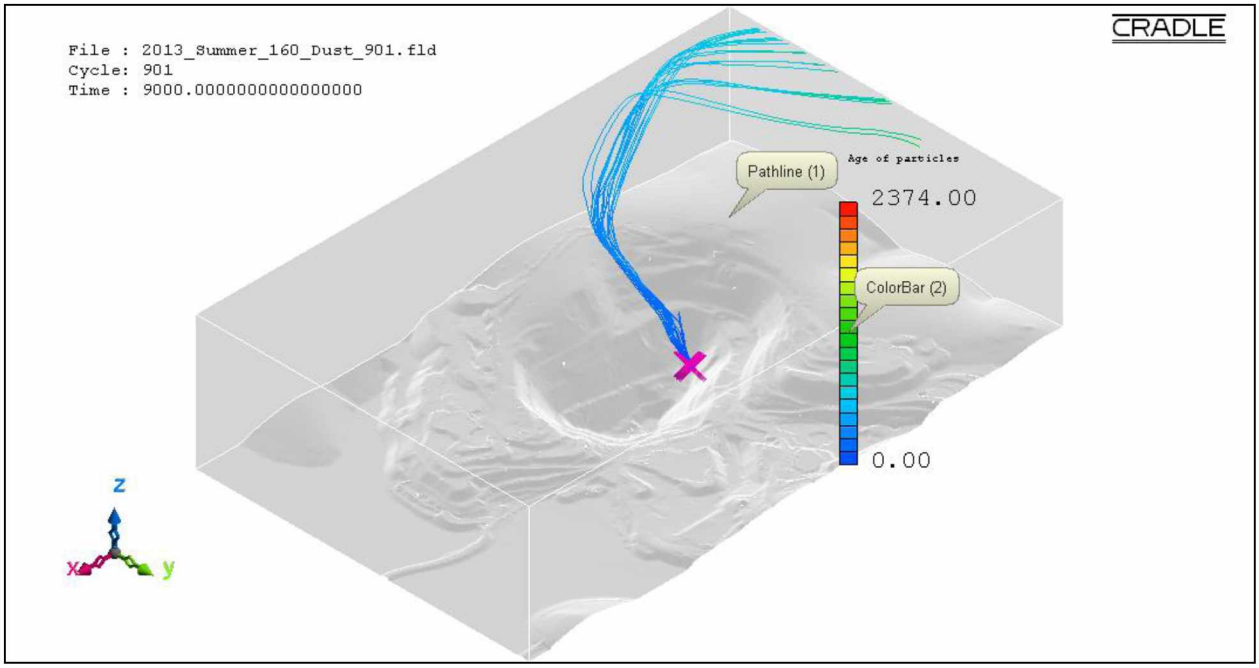

Figure B.82: Pathlines of $PM_{2.5}$ dust particles from source location 15 in the actual open-pit domain for extreme insolation summer condition using the LES method.

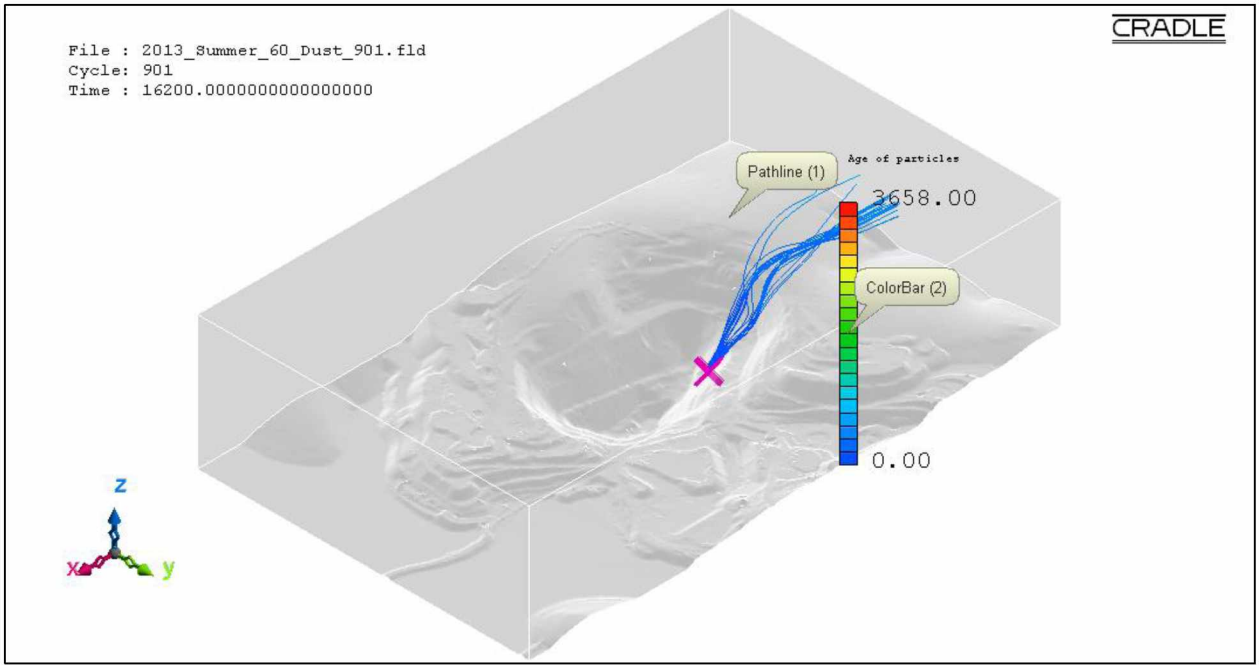

Figure B.83: Pathlines of $PM_{2.5}$ dust particles from source location 16 in the actual open-pit domain for fair insolation summer condition using the LES method.

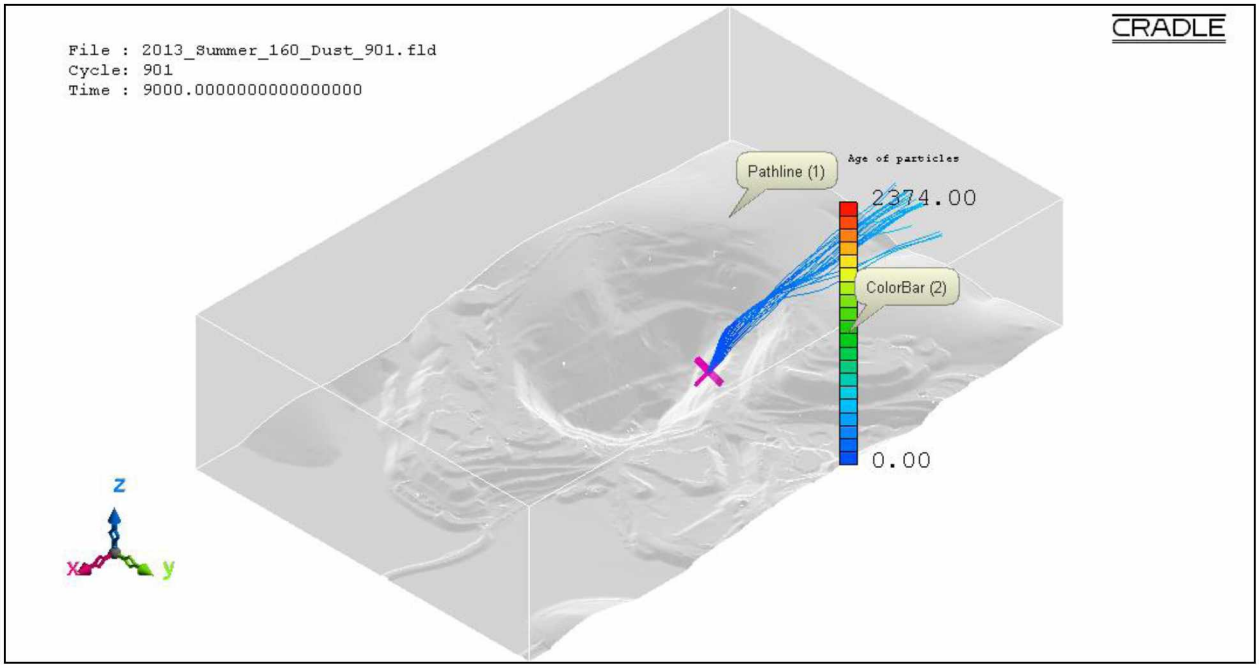

Figure B.84: Pathlines of $PM_{2.5}$ dust particles from source location 16 in the actual open-pit domain for extreme insolation summer condition using the LES method.

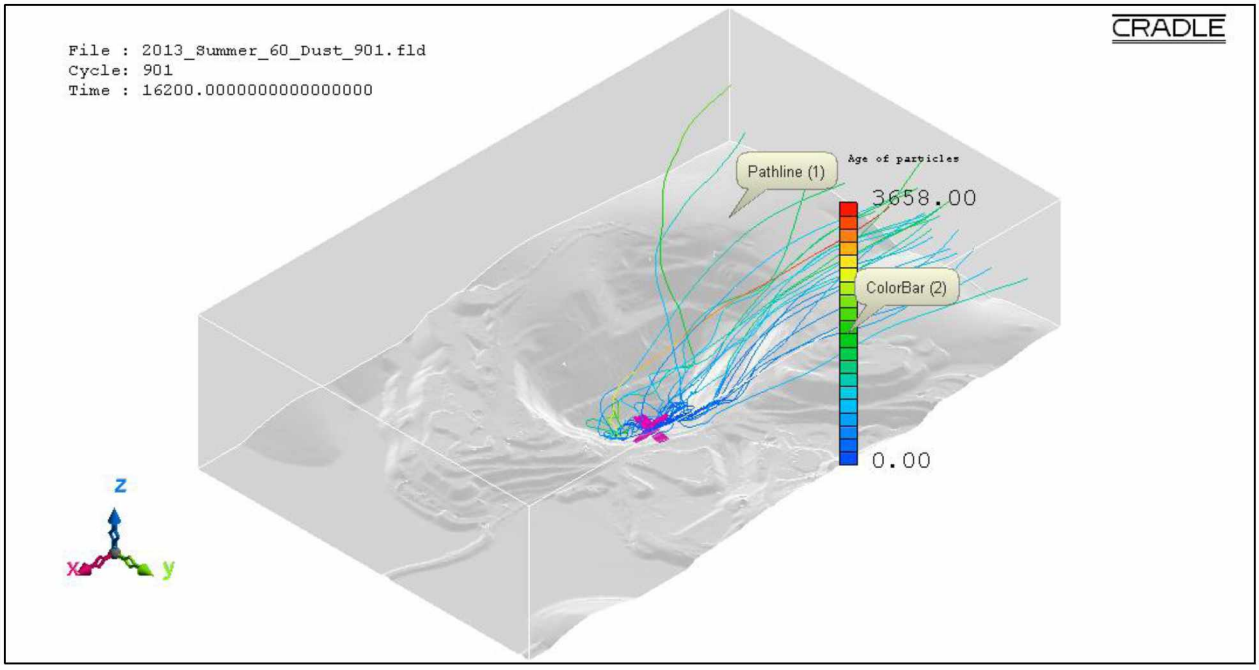

Figure B.85: Pathlines of $PM_{2.5}$ dust particles from source location 17 in the actual open-pit domain for fair insolation summer condition using the LES method.

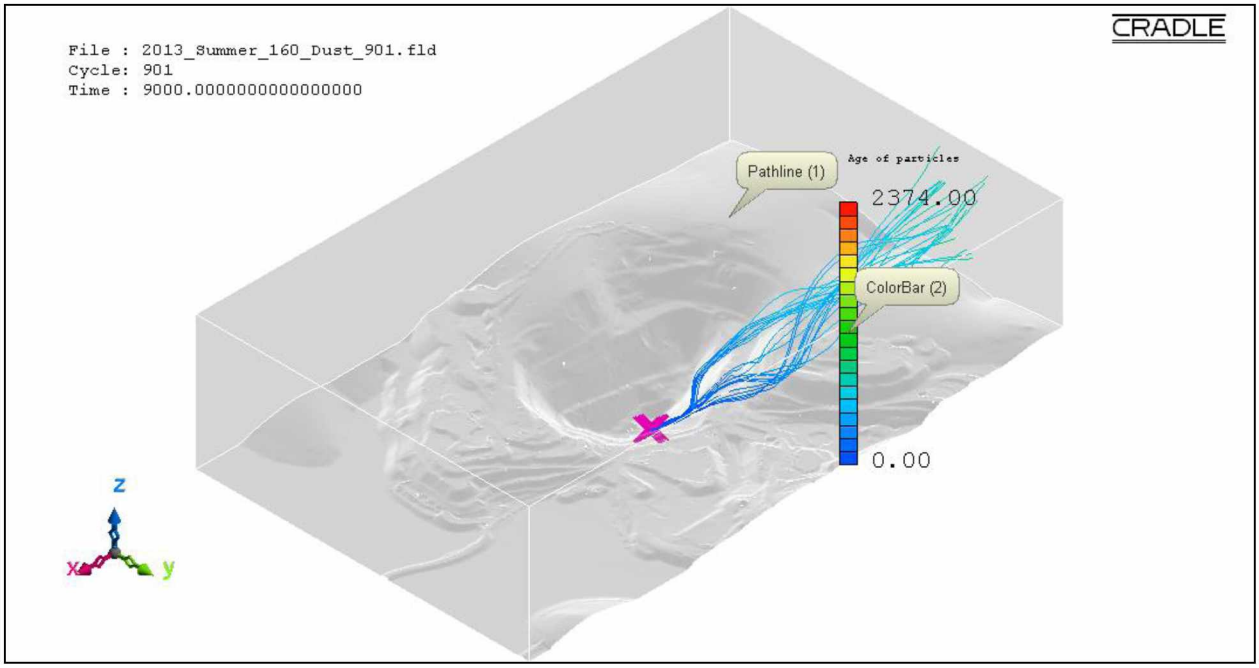

Figure B.86: Pathlines of $PM_{2.5}$ dust particles from source location 17 in the actual open-pit domain for extreme insolation summer condition using the LES method.

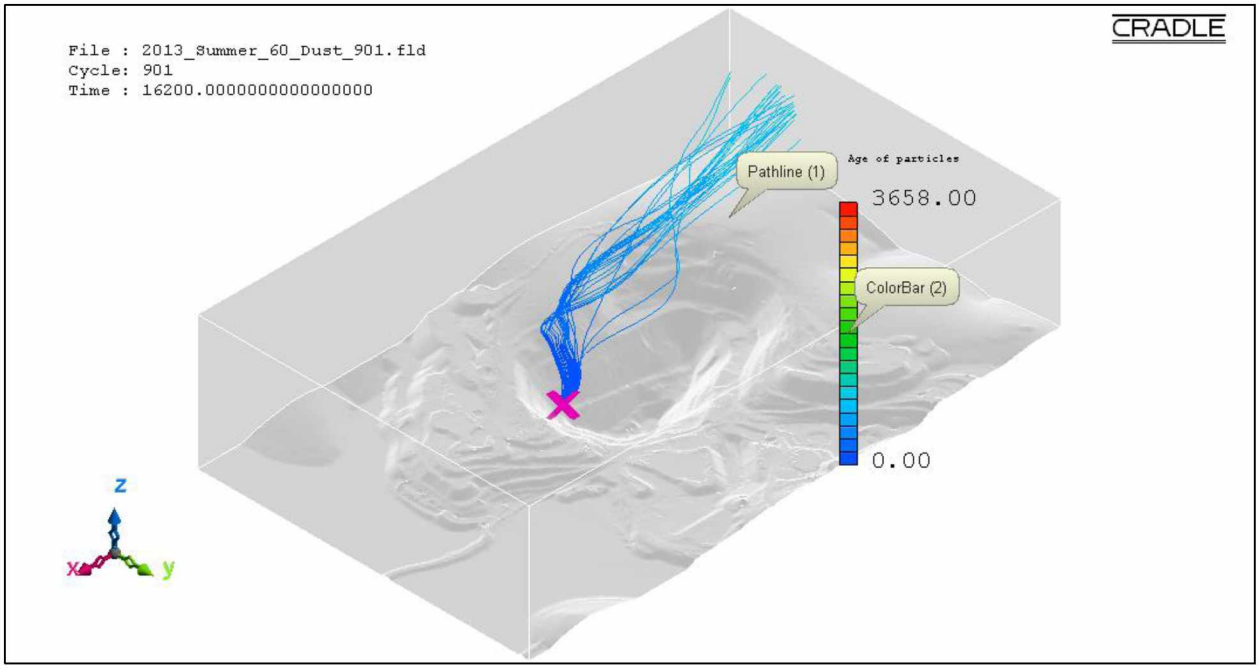

Figure B.87: Pathlines of $PM_{2.5}$ dust particles from source location 18 in the actual open-pit domain for fair insolation summer condition using the LES method.

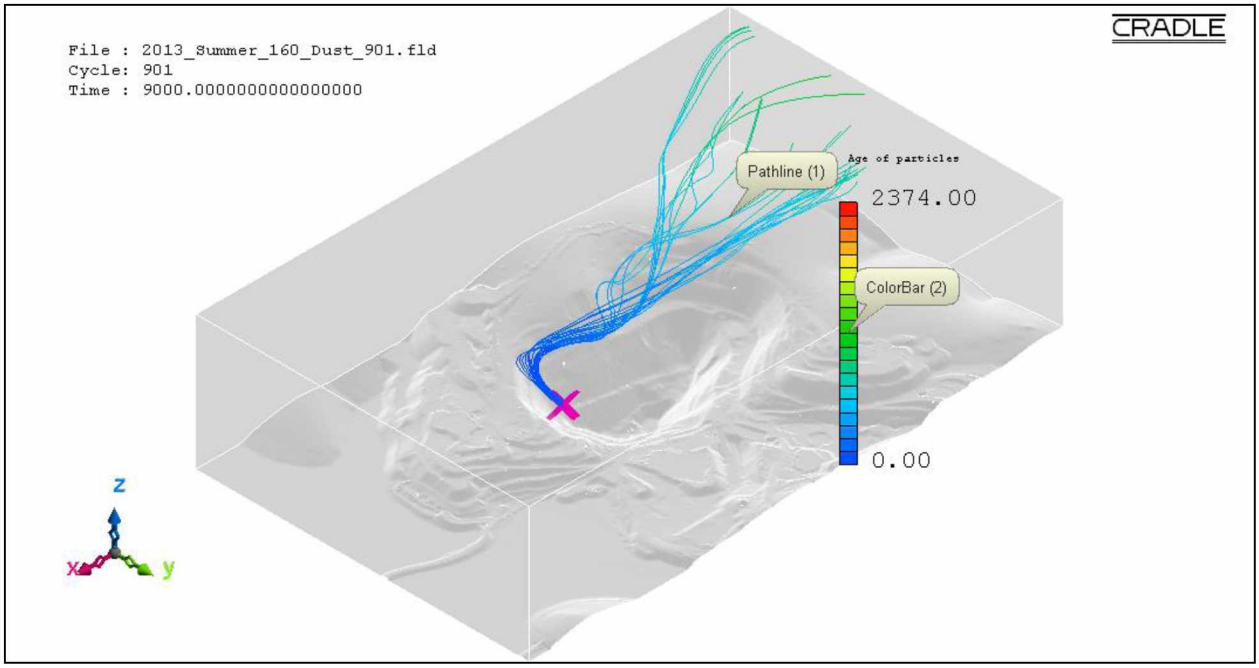

Figure B.88: Pathlines of $PM_{2.5}$ dust particles from source location 18 in the actual open-pit domain for extreme insolation summer condition using the LES method.

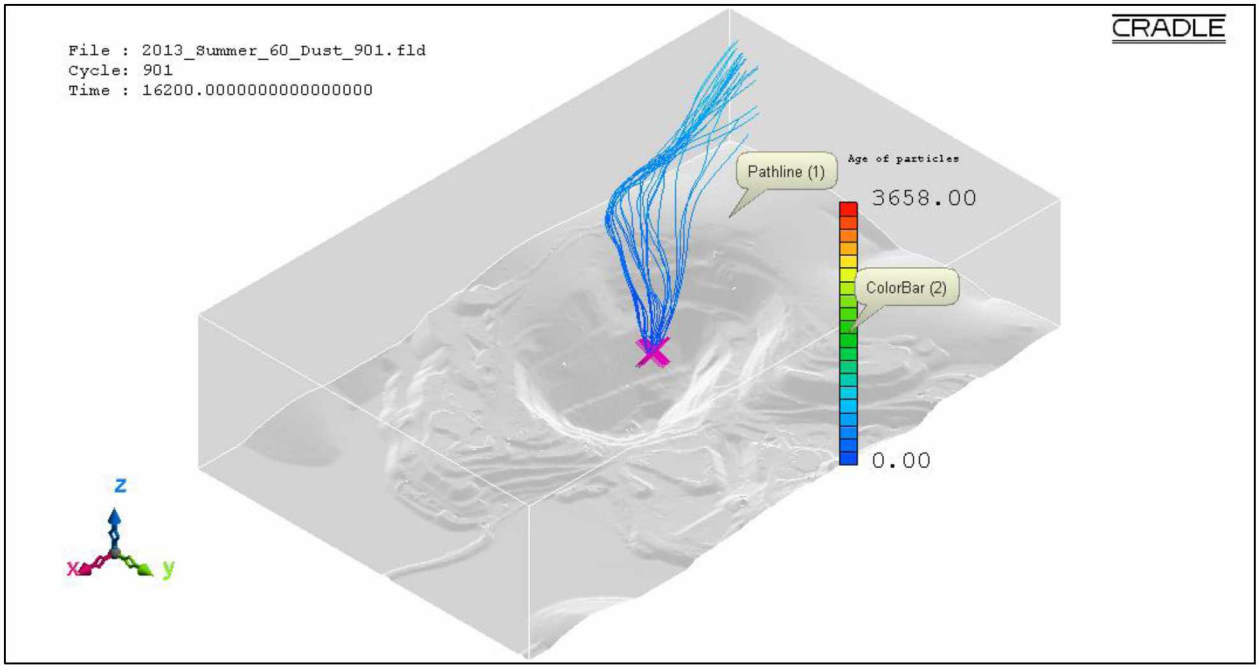

Figure B.89: Pathlines of $PM_{2.5}$ dust particles from source location 19 in the actual open-pit domain for fair insolation summer condition using the LES method.

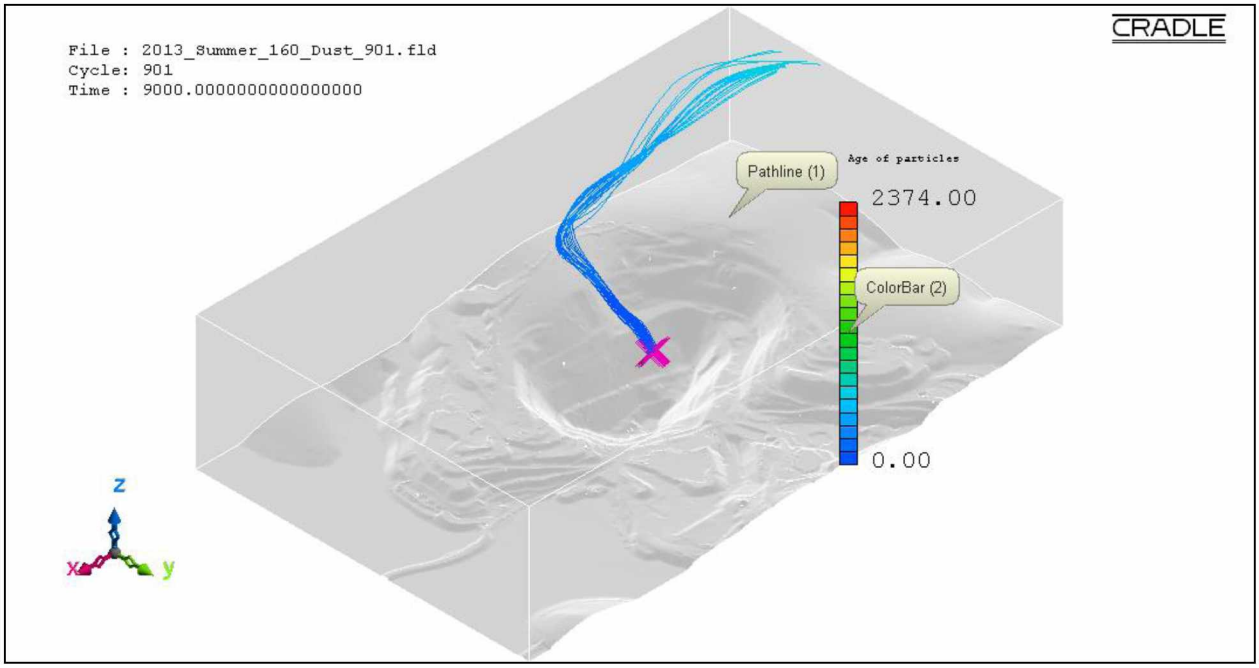

Figure B.90: Pathlines of $PM_{2.5}$ dust particles from source location 19 in the actual open-pit domain for extreme insolation summer condition using the LES method.

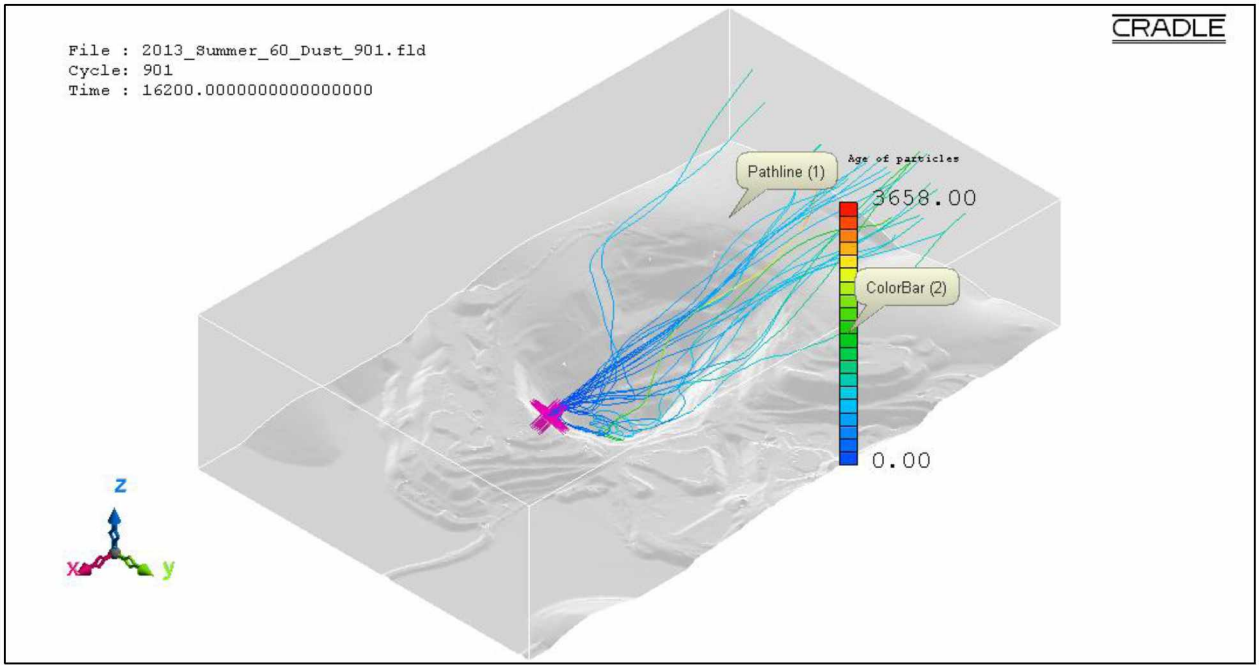

Figure B.91: Pathlines of $PM_{2.5}$ dust particles from source location 20 in the actual open-pit domain for fair insolation summer condition using the LES method.

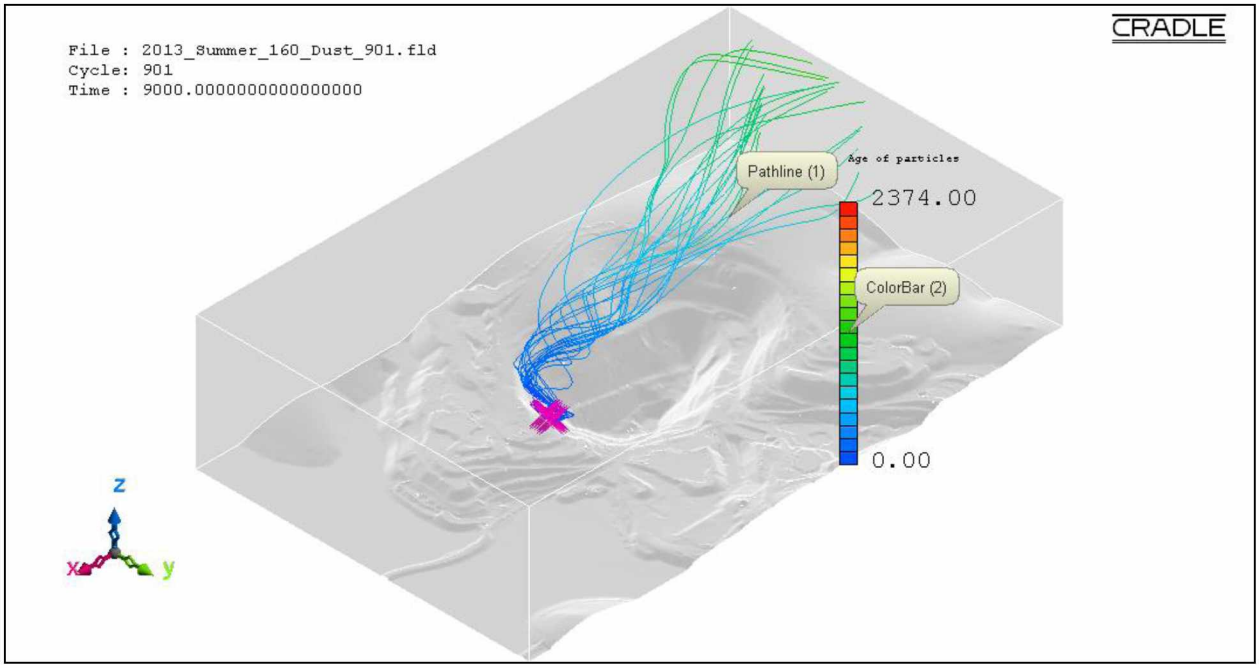

Figure B.92: Pathlines of $PM_{2.5}$ dust particles from source location 20 in the actual open-pit domain for extreme insolation summer condition using the LES method.

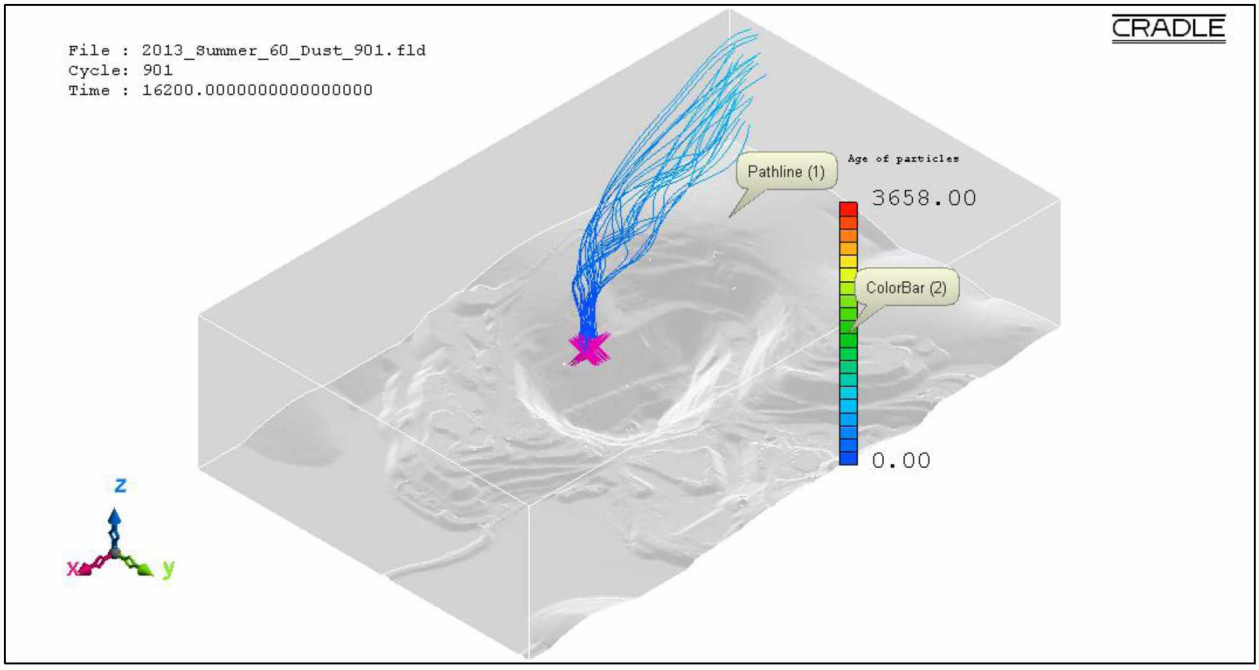

Figure B.93: Pathlines of $PM_{2.5}$ dust particles from source location 21 in the actual open-pit domain for fair insolation summer condition using the LES method.

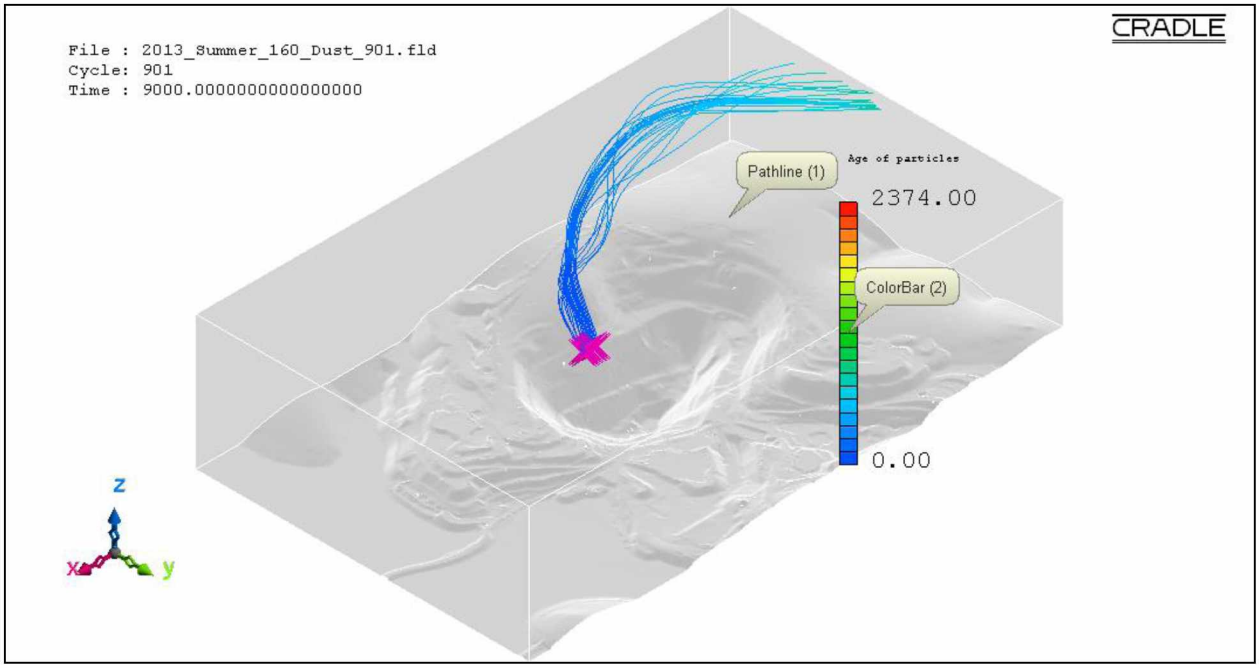

Figure B.94: Pathlines of $PM_{2.5}$ dust particles from source location 21 in the actual open-pit domain for extreme insolation summer condition using the LES method.

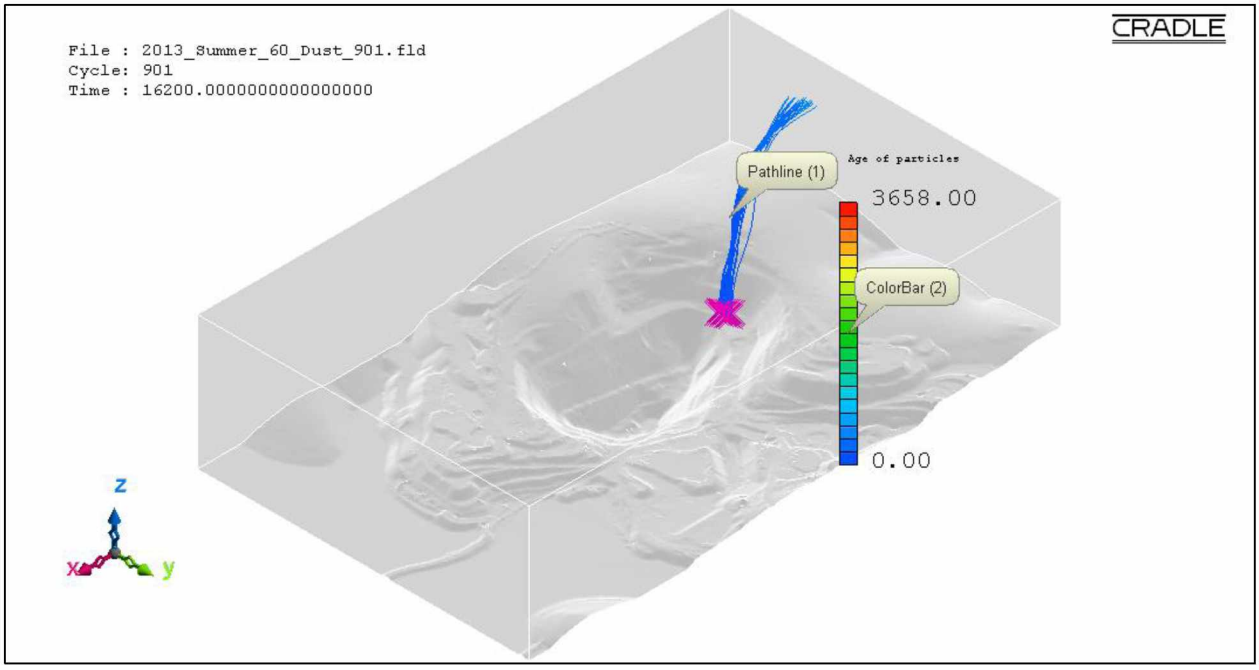

Figure B.95: Pathlines of $PM_{2.5}$ dust particles from source location 22 in the actual open-pit domain for fair insolation summer condition using the LES method.

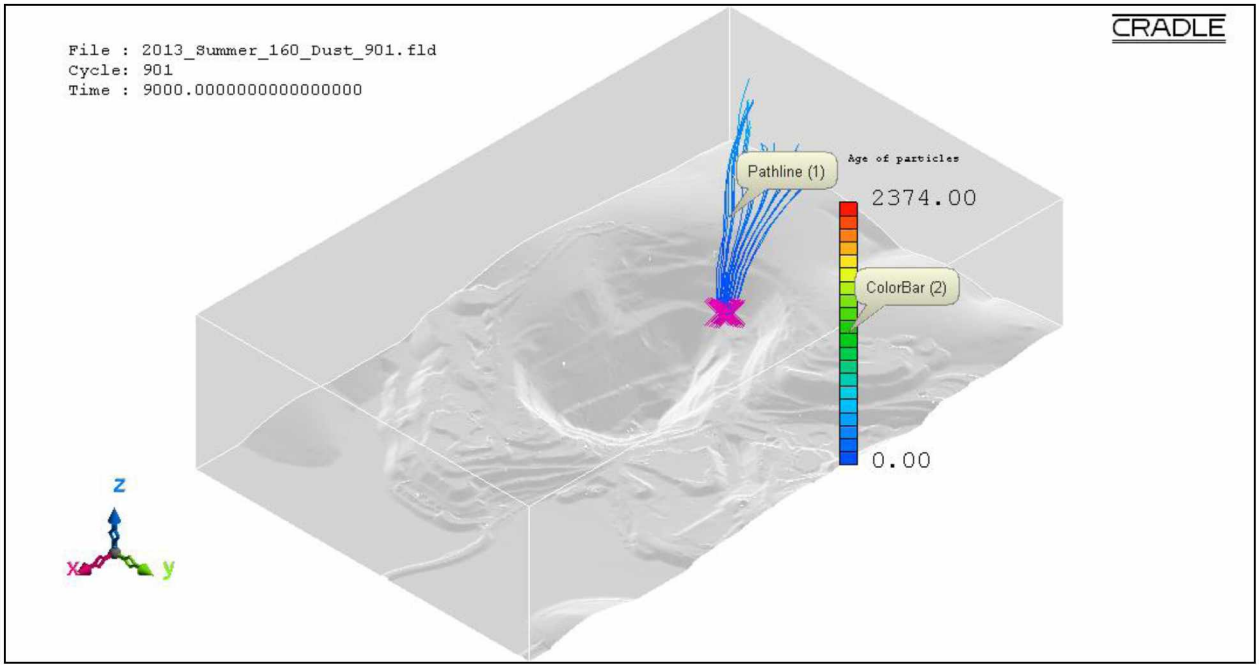

Figure B.96: Pathlines of $PM_{2.5}$ dust particles from source location 22 in the actual open-pit domain for extreme insolation summer condition using the LES method.

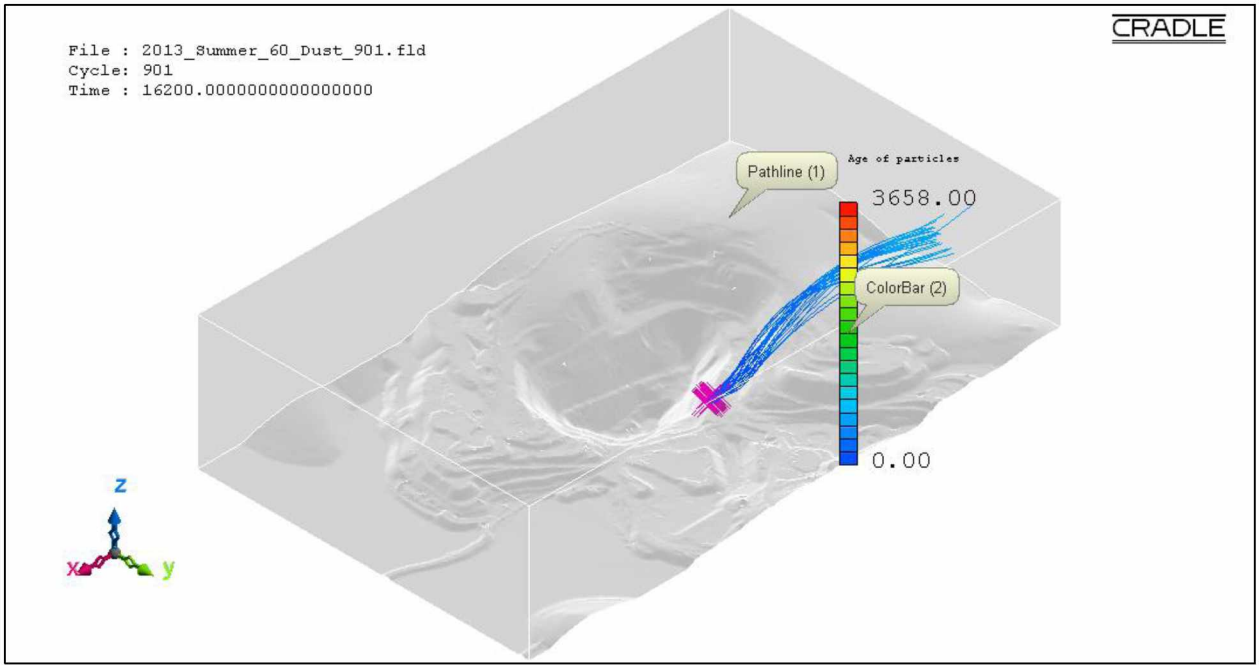

Figure B.97: Pathlines of $PM_{2.5}$ dust particles from source location 23 in the actual open-pit domain for fair insolation summer condition using the LES method.

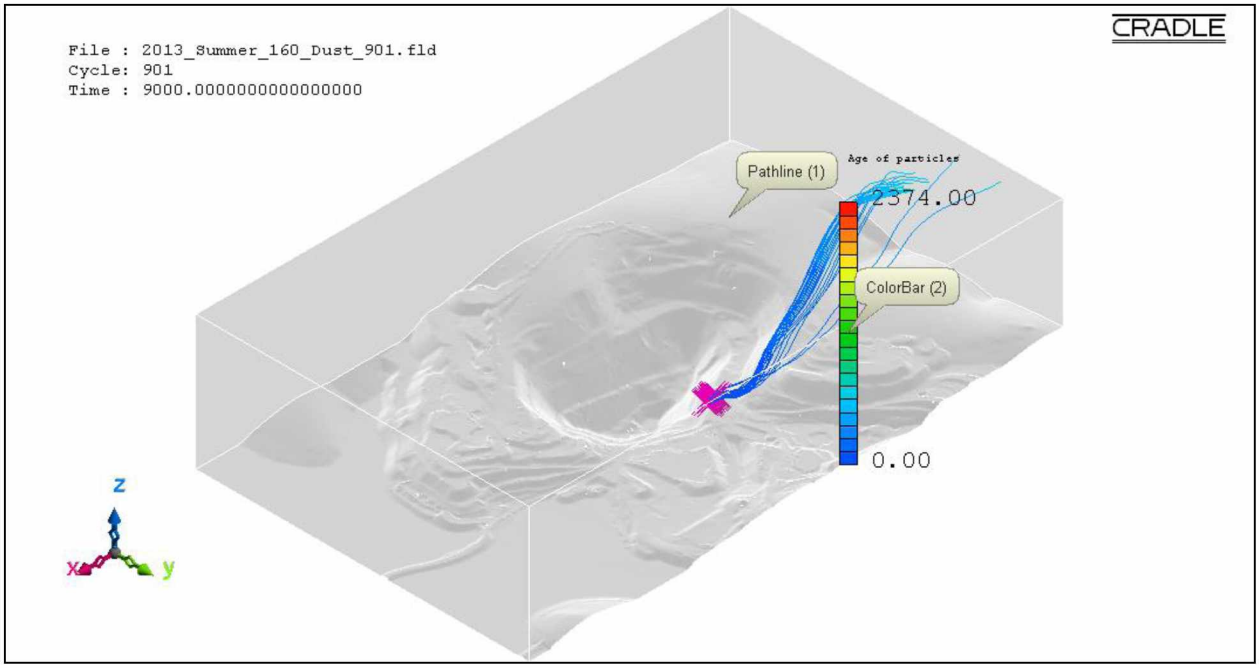

Figure B.98: Pathlines of $PM_{2.5}$ dust particles from source location 23 in the actual open-pit domain for extreme insolation summer condition using the LES method.

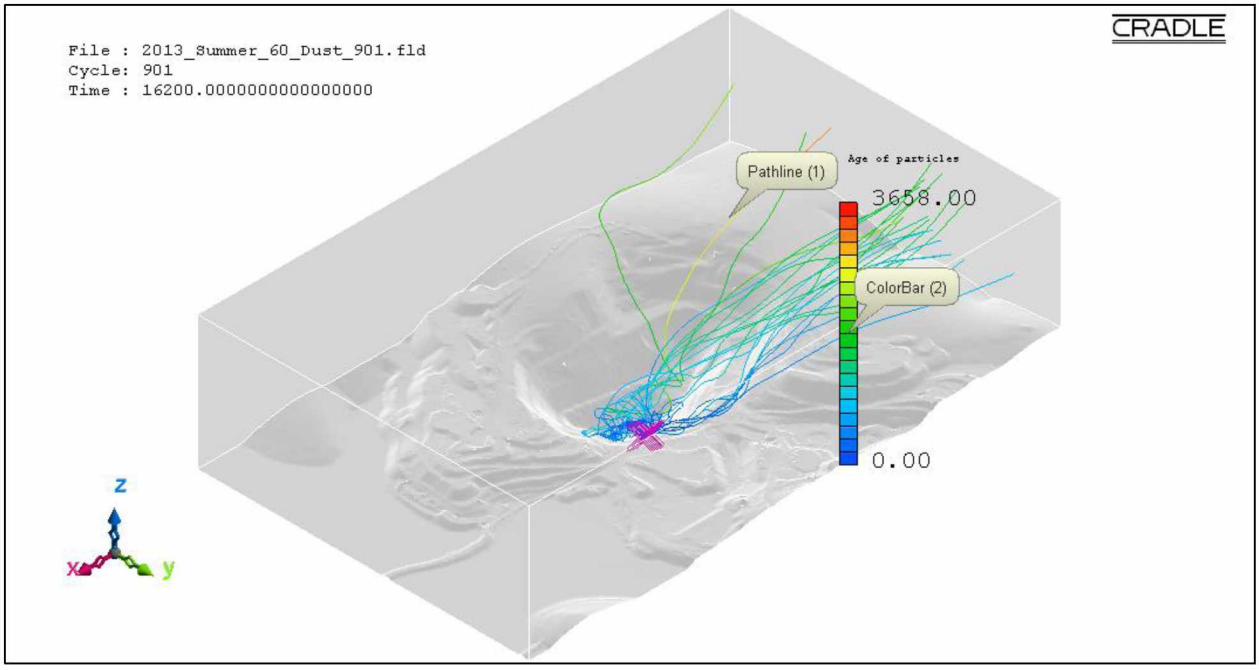

Figure B.99: Pathlines of $PM_{2.5}$ dust particles from source location 24 in the actual open-pit domain for fair insolation summer condition using the LES method.

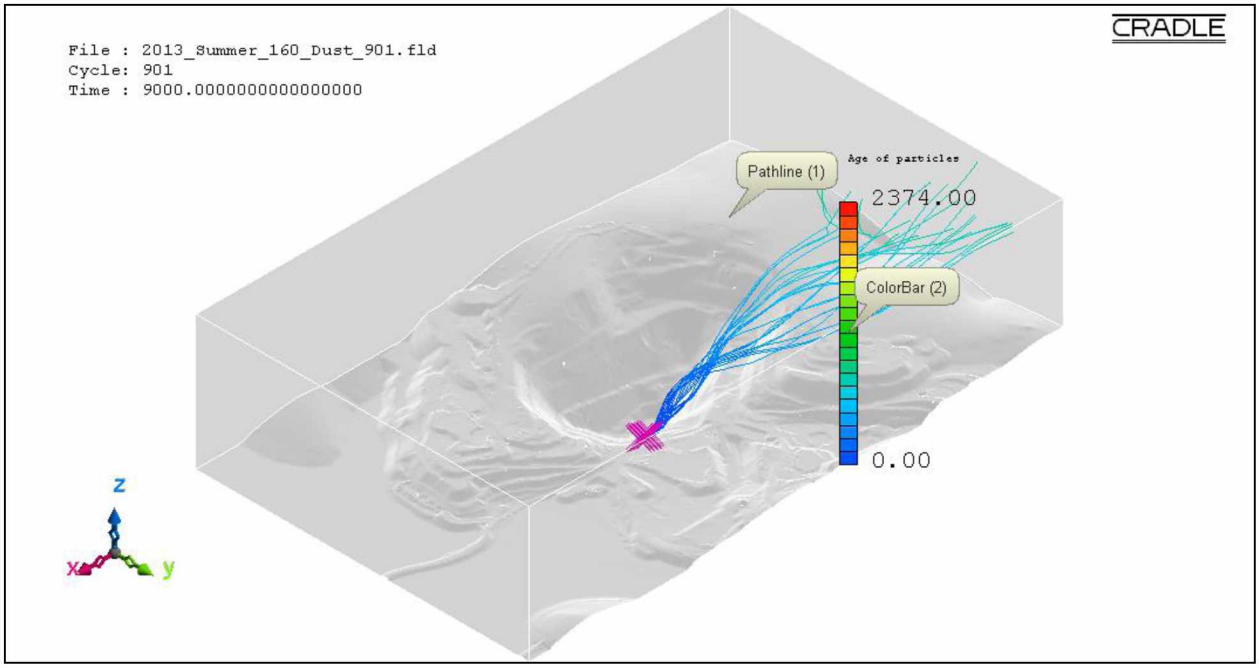

Figure B.100: Pathlines of $PM_{2.5}$ dust particles from source location 24 in the actual open-pit domain for extreme insolation summer condition using the LES method.

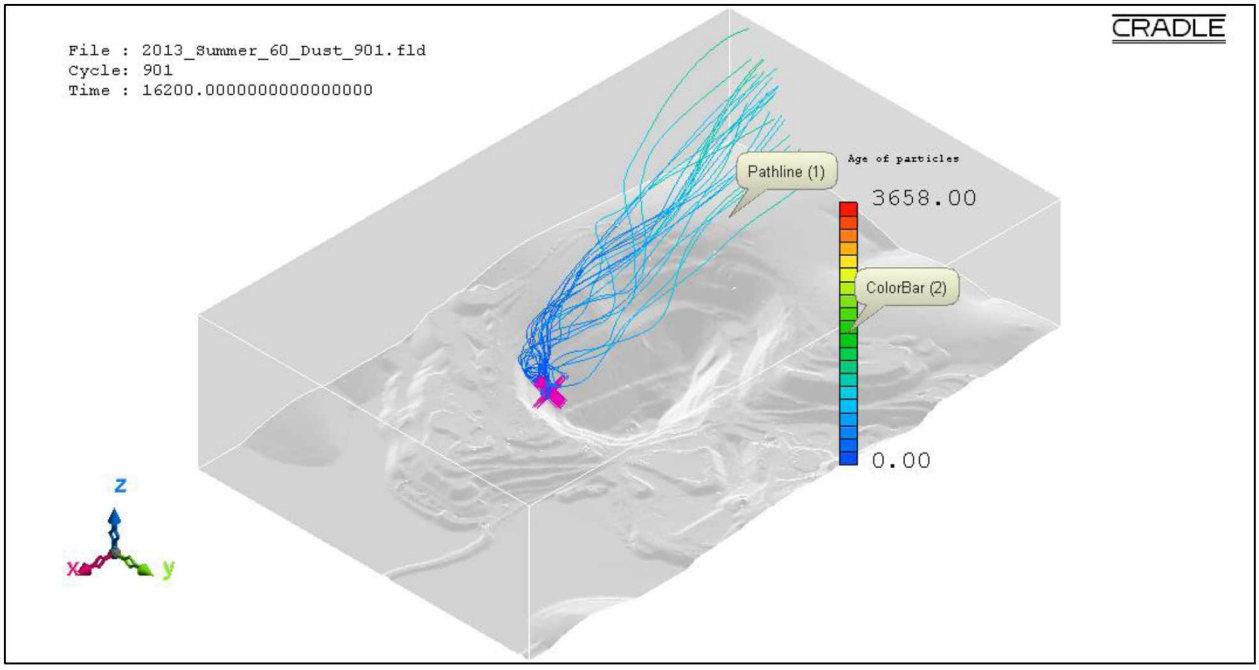

Figure B.101: Pathlines of $PM_{2.5}$ dust particles from source location 25 in the actual open-pit domain for fair insolation summer condition using the LES method.

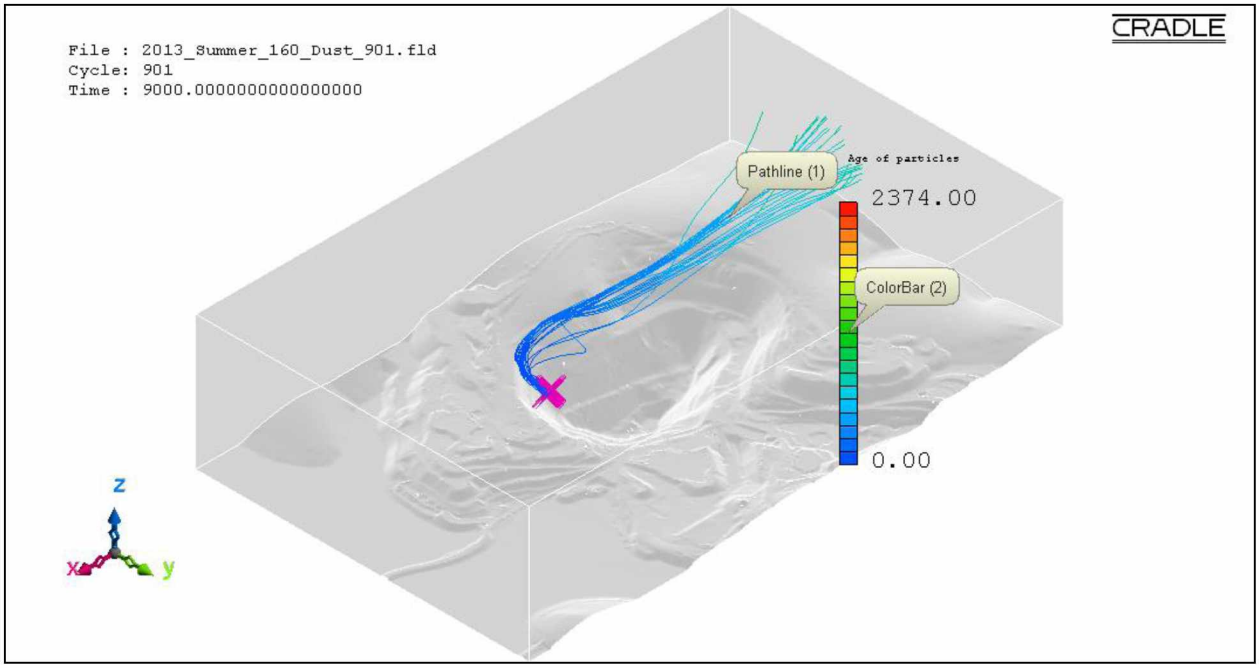

Figure B.102: Pathlines of $PM_{2.5}$ dust particles from source location 25 in the actual open-pit domain for extreme insolation summer condition using the LES method.

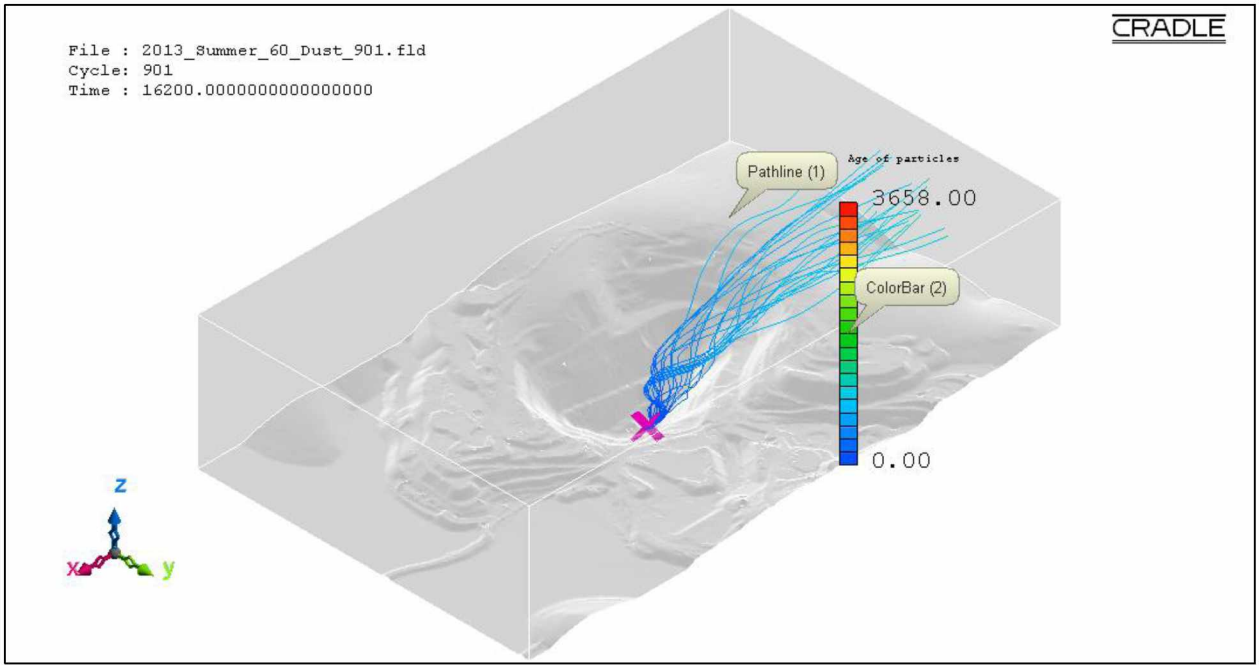

Figure B.103: Pathlines of PM_5 dust particles from source location 1 in the actual open-pit domain for fair insolation summer condition using the LES method.

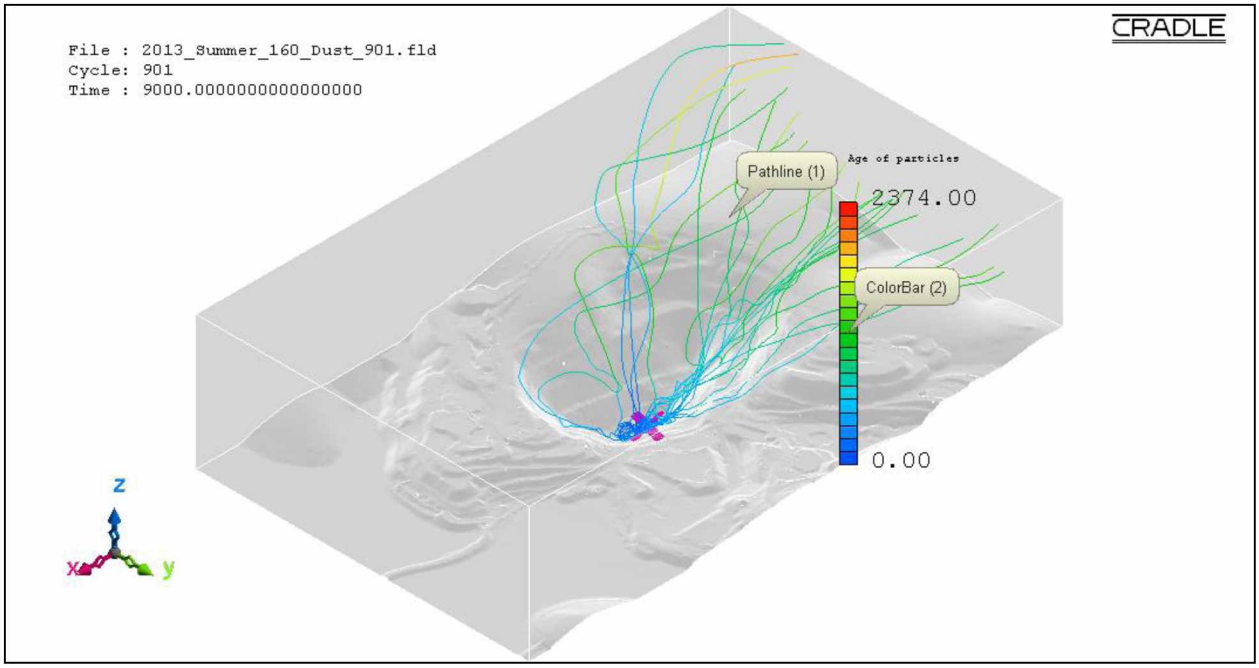

Figure B.104: Pathlines of PM_5 dust particles from source location 1 in the actual open-pit domain for extreme insolation summer condition using the LES method.

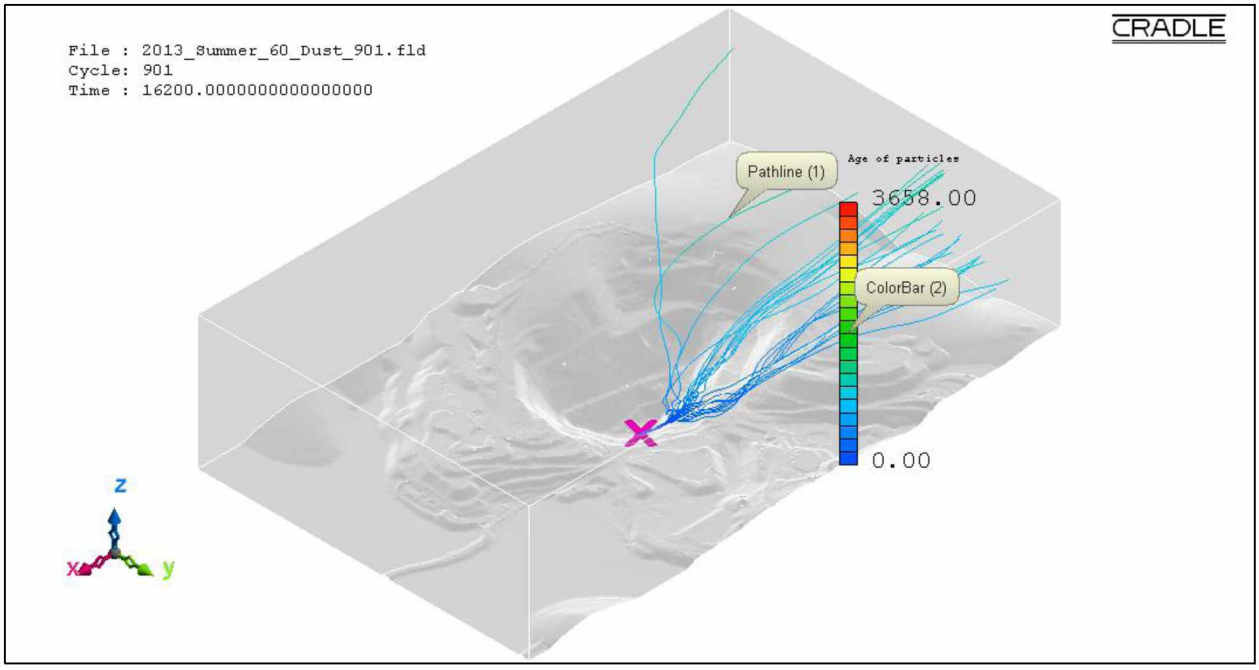

Figure B.105: Pathlines of PM_5 dust particles from source location 2 in the actual open-pit domain for fair insolation summer condition using the LES method.

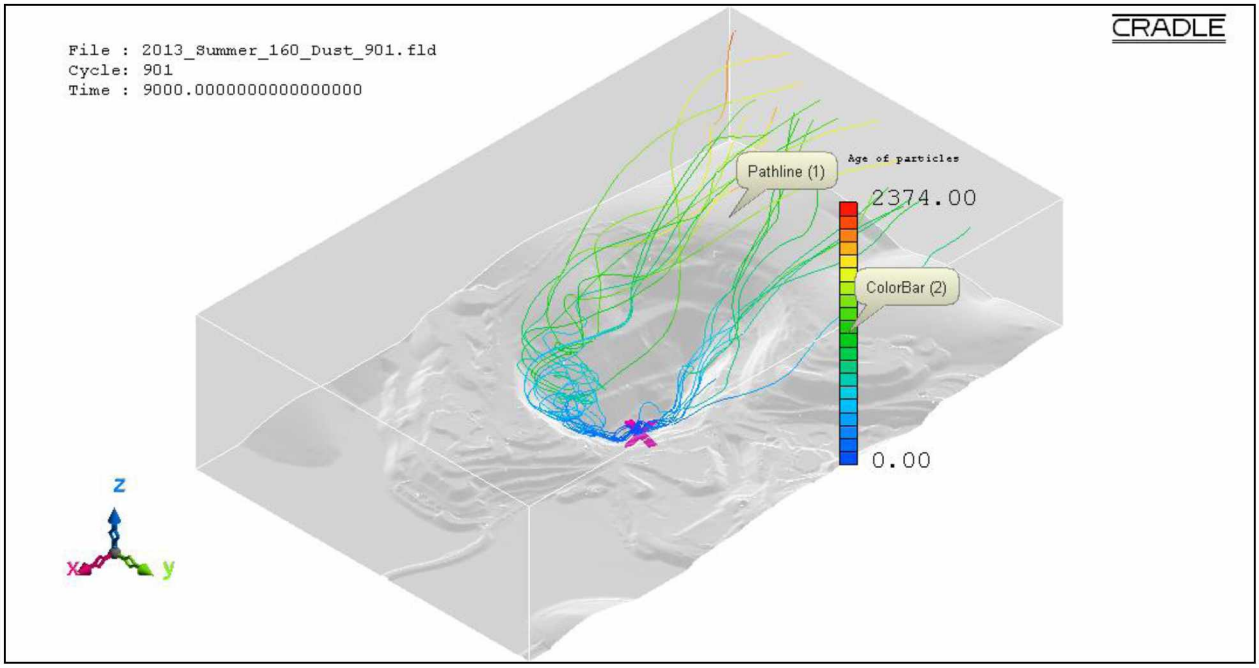

Figure B.106: Pathlines of PM_5 dust particles from source location 2 in the actual open-pit domain for extreme insolation summer condition using the LES method.

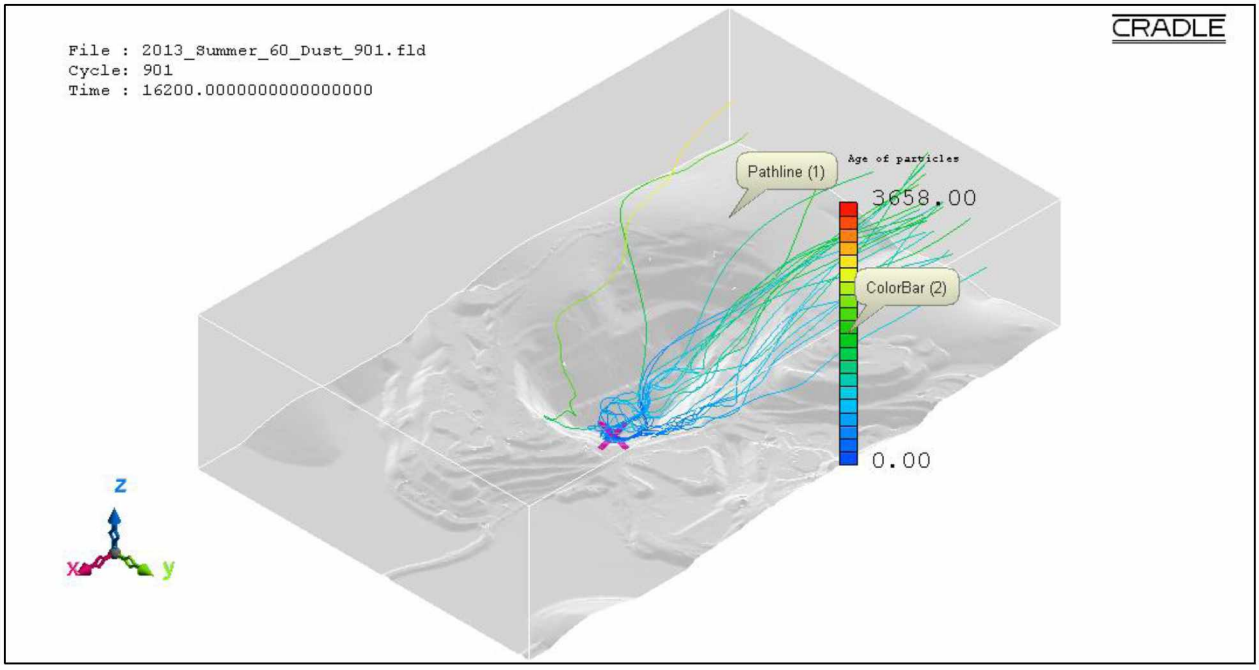

Figure B.107: Pathlines of PM_5 dust particles from source location 3 in the actual open-pit domain for fair insolation summer condition using the LES method.

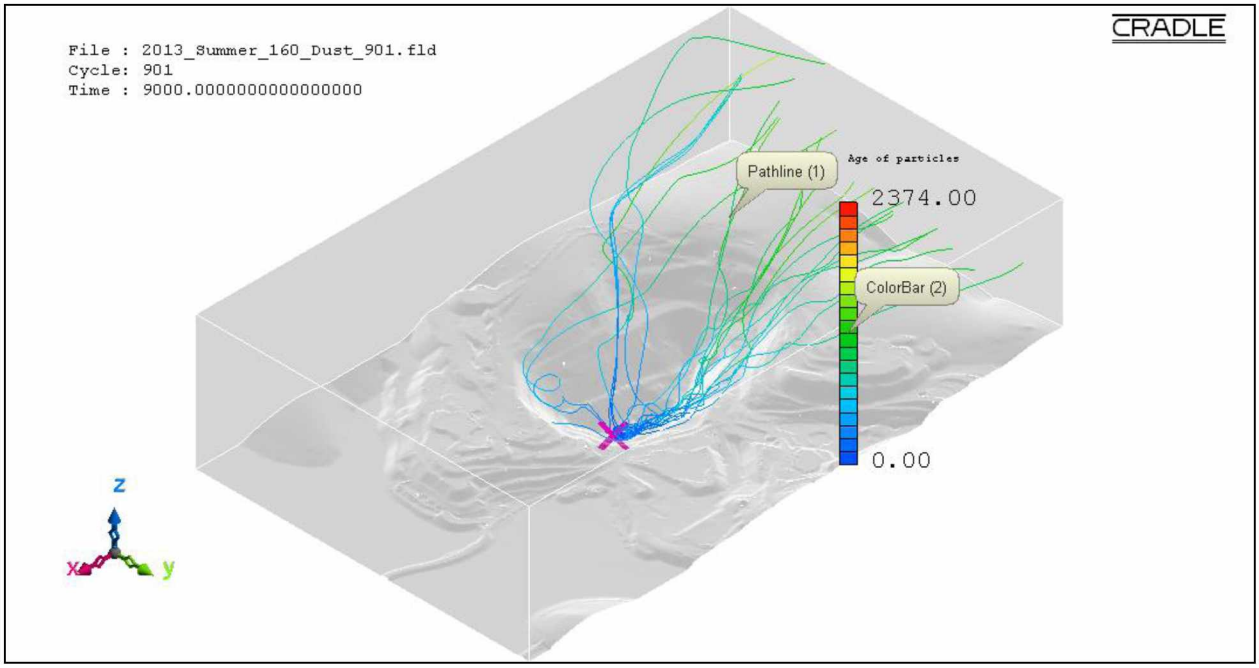

Figure B.108: Pathlines of PM_5 dust particles from source location 3 in the actual open-pit domain for extreme insolation summer condition using the LES method.

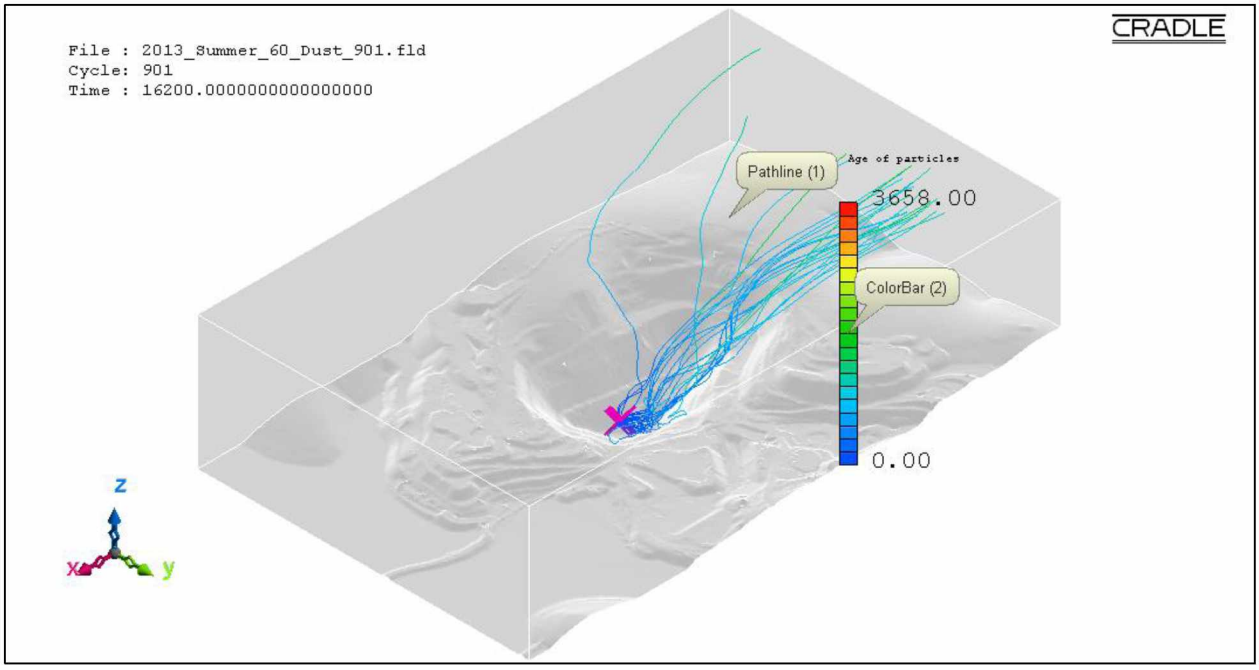

Figure B.109: Pathlines of PM_5 dust particles from source location 4 in the actual open-pit domain for fair insolation summer condition using the LES method.

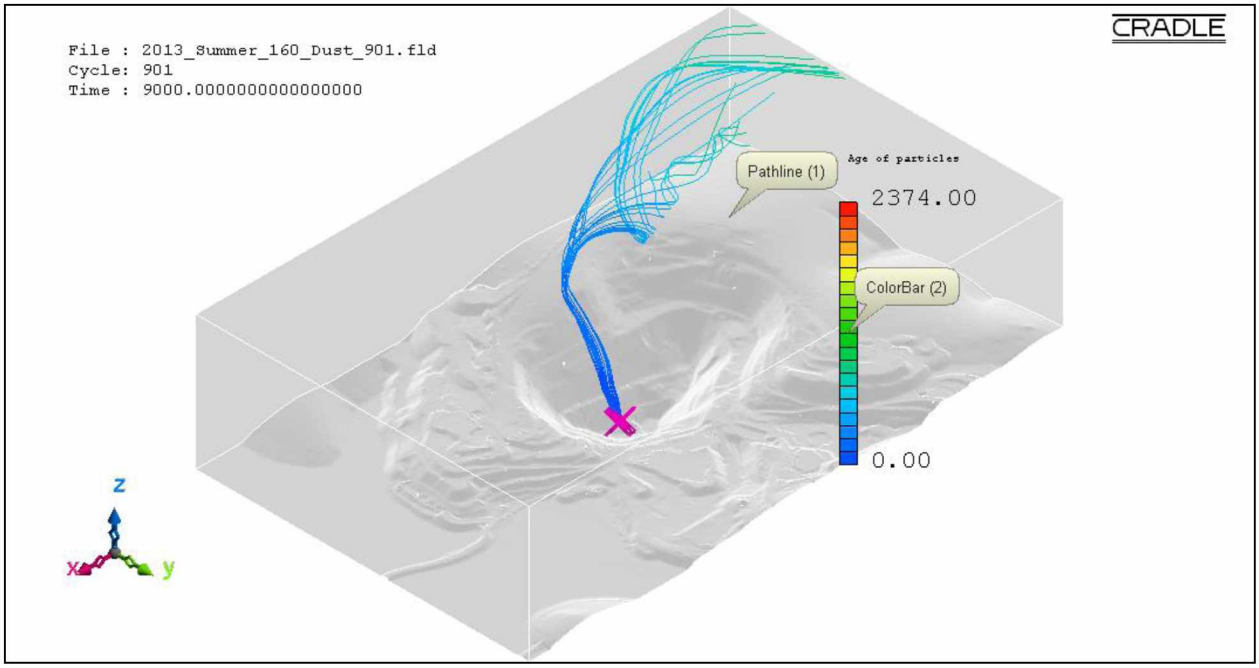

Figure B.110: Pathlines of PM_5 dust particles from source location 4 in the actual open-pit domain for extreme insolation summer condition using the LES method.

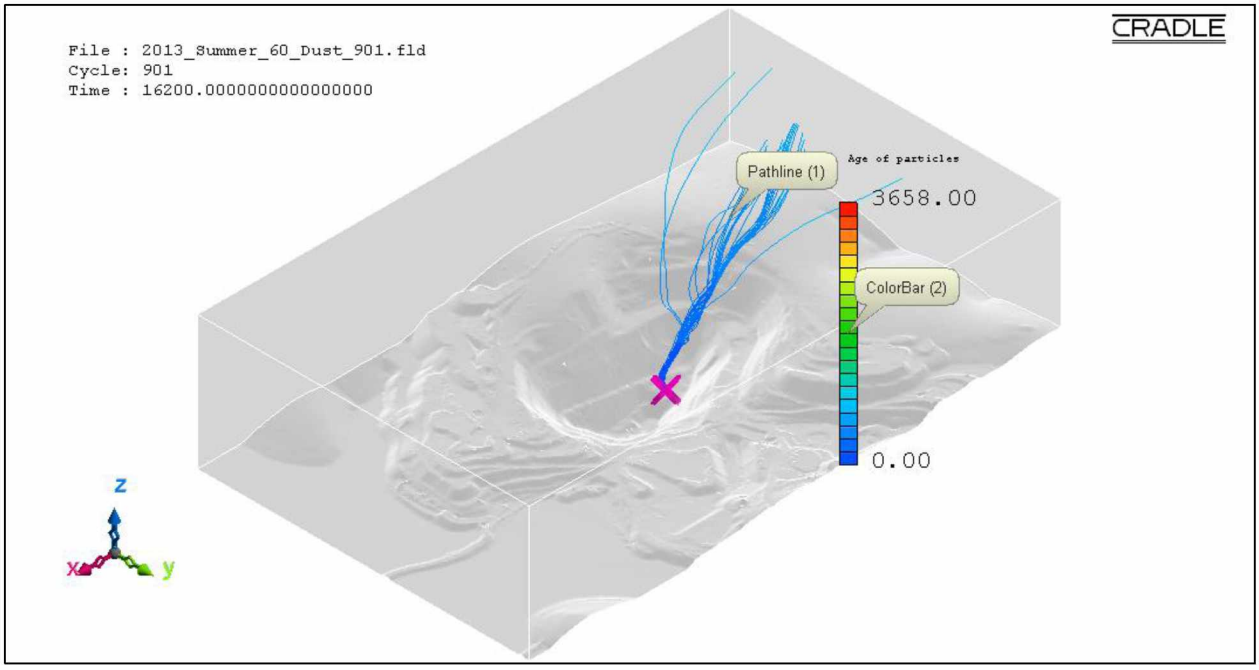

Figure B.111: Pathlines of PM_5 dust particles from source location 5 in the actual open-pit domain for fair insolation summer condition using the LES method.

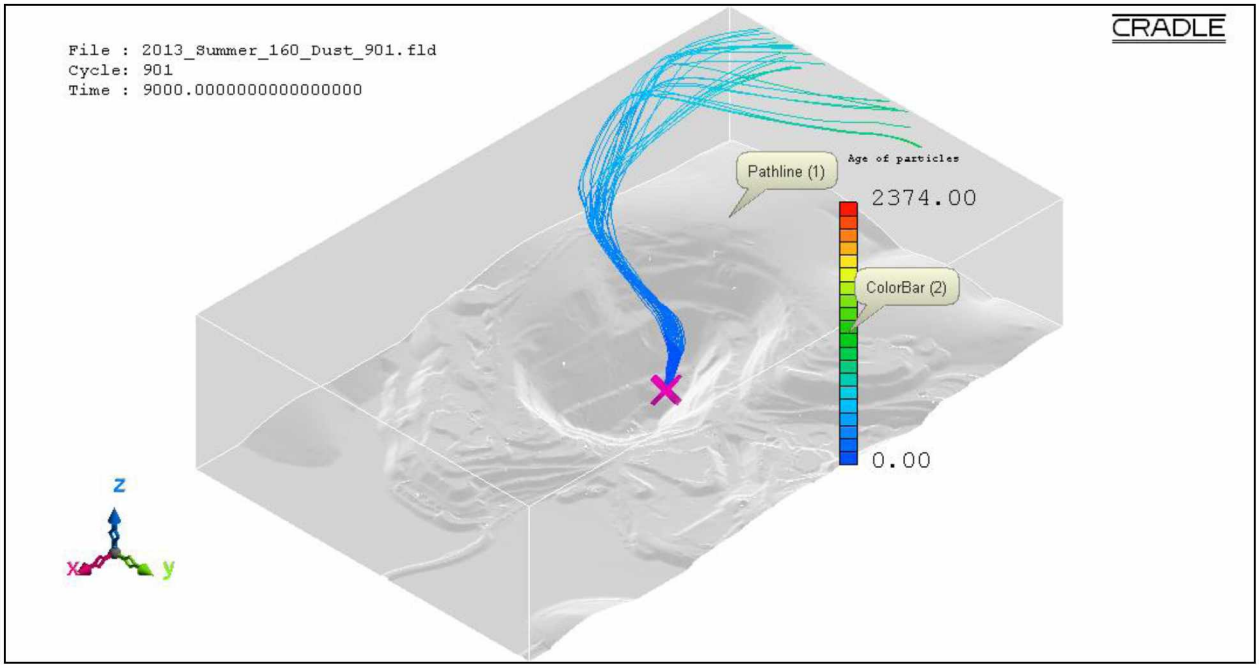

Figure B.112: Pathlines of PM_5 dust particles from source location 5 in the actual open-pit domain for extreme insolation summer condition using the LES method.

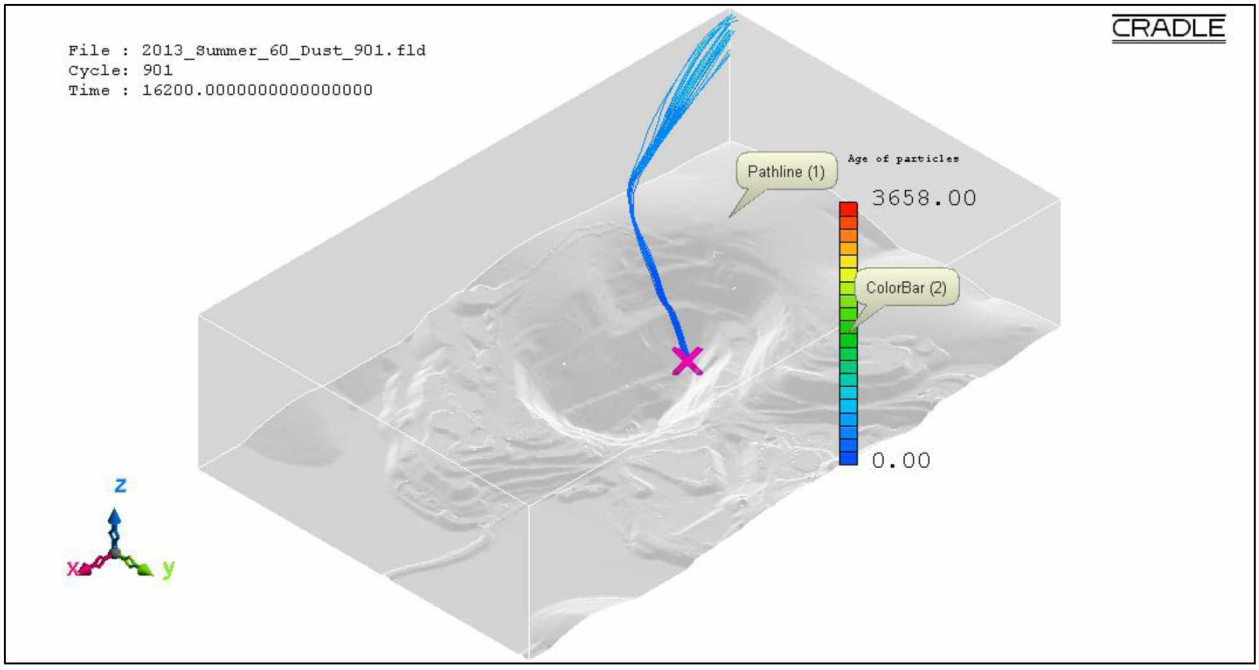

Figure B.113: Pathlines of PM_5 dust particles from source location 6 in the actual open-pit domain for fair insolation summer condition using the LES method.

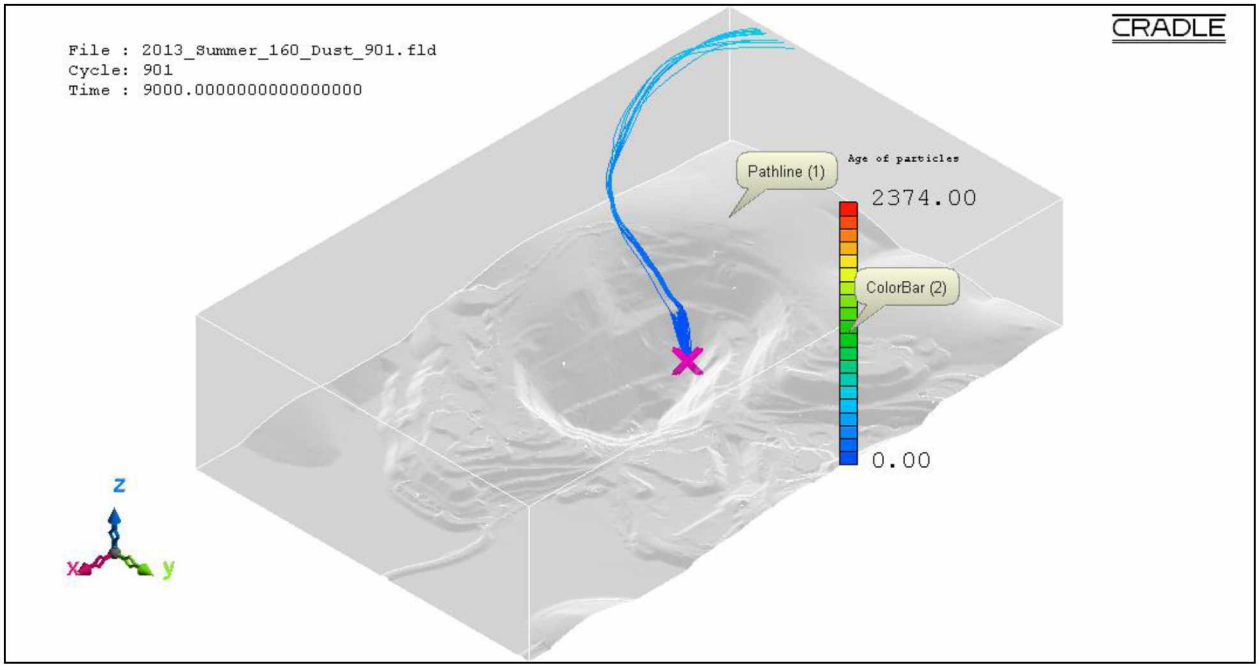

Figure B.114: Pathlines of PM_5 dust particles from source location 6 in the actual open-pit domain for extreme insolation summer condition using the LES method.

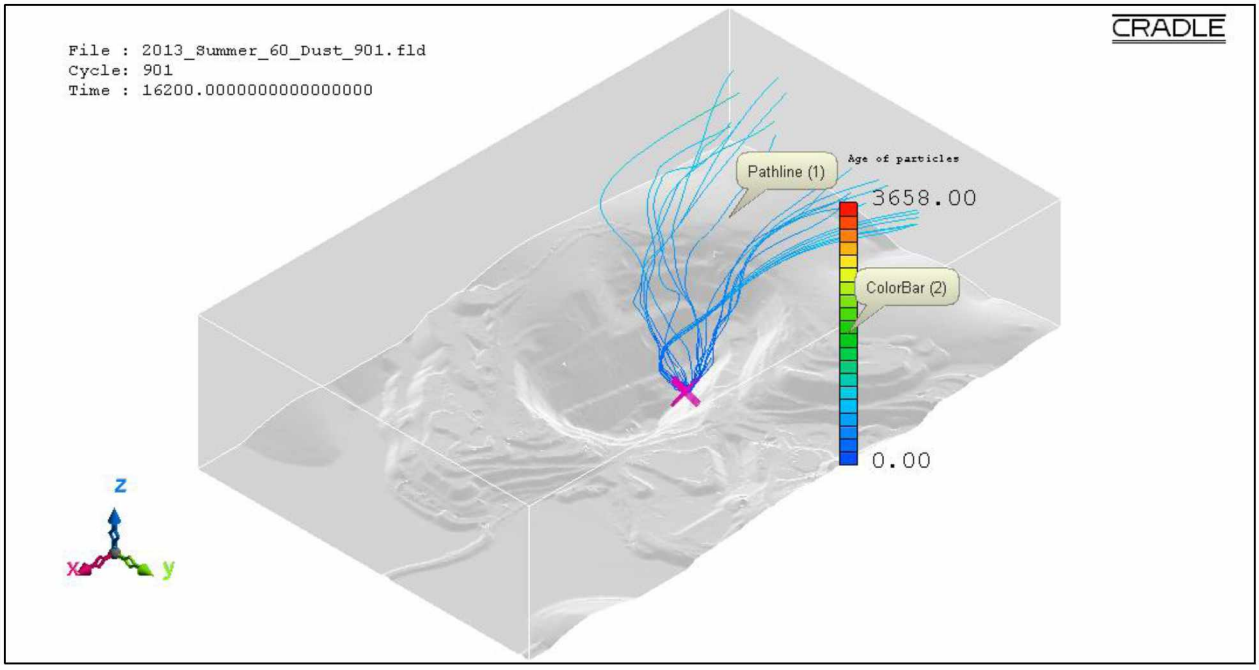

Figure B.115: Pathlines of PM_5 dust particles from source location 7 in the actual open-pit domain for fair insolation summer condition using the LES method.

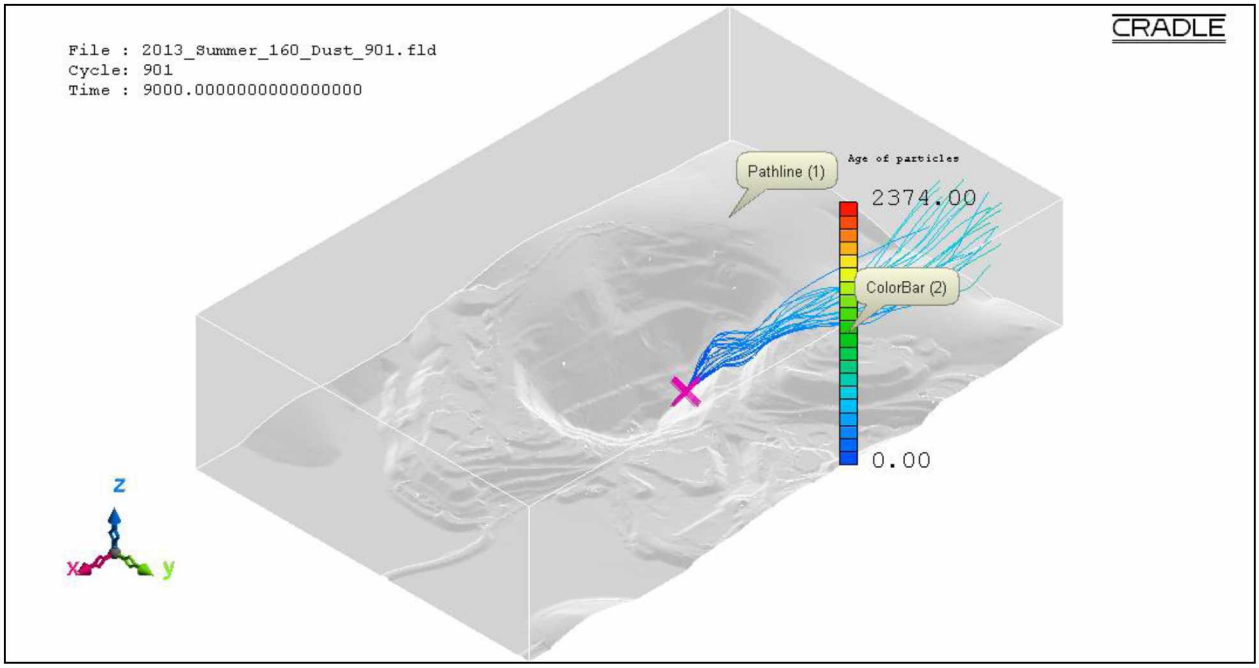

Figure B.116: Pathlines of PM_5 dust particles from source location 7 in the actual open-pit domain for extreme insolation summer condition using the LES method.

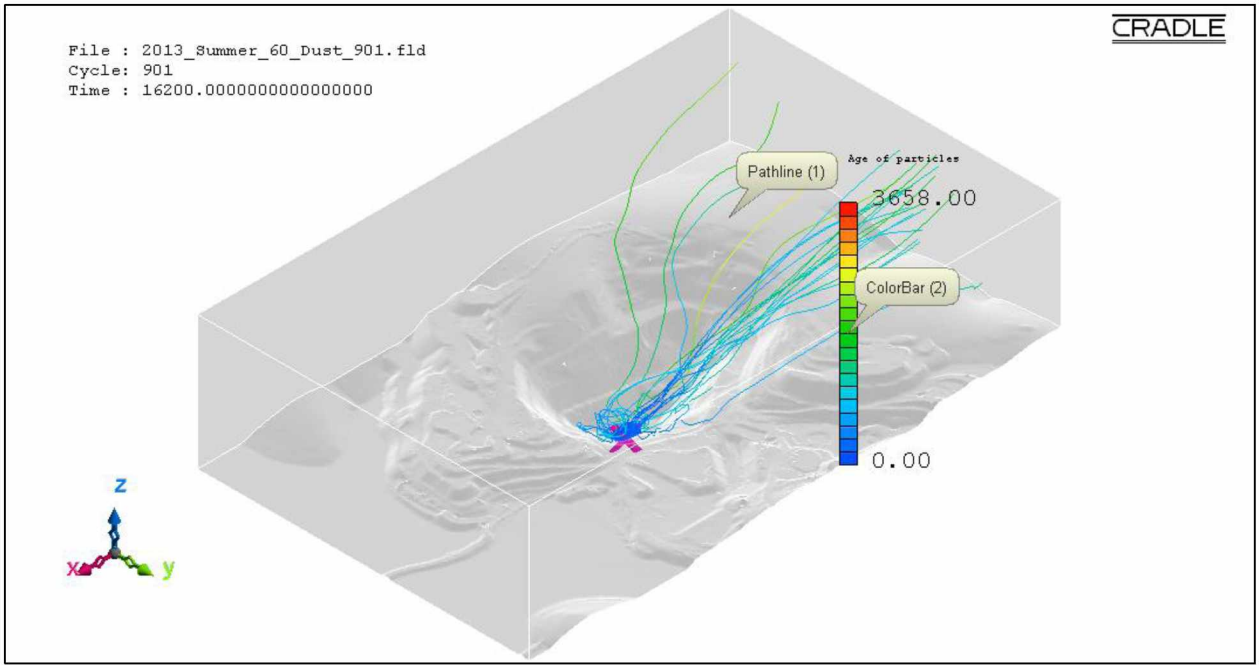

Figure B.117: Pathlines of PM_5 dust particles from source location 8 in the actual open-pit domain for fair insolation summer condition using the LES method.

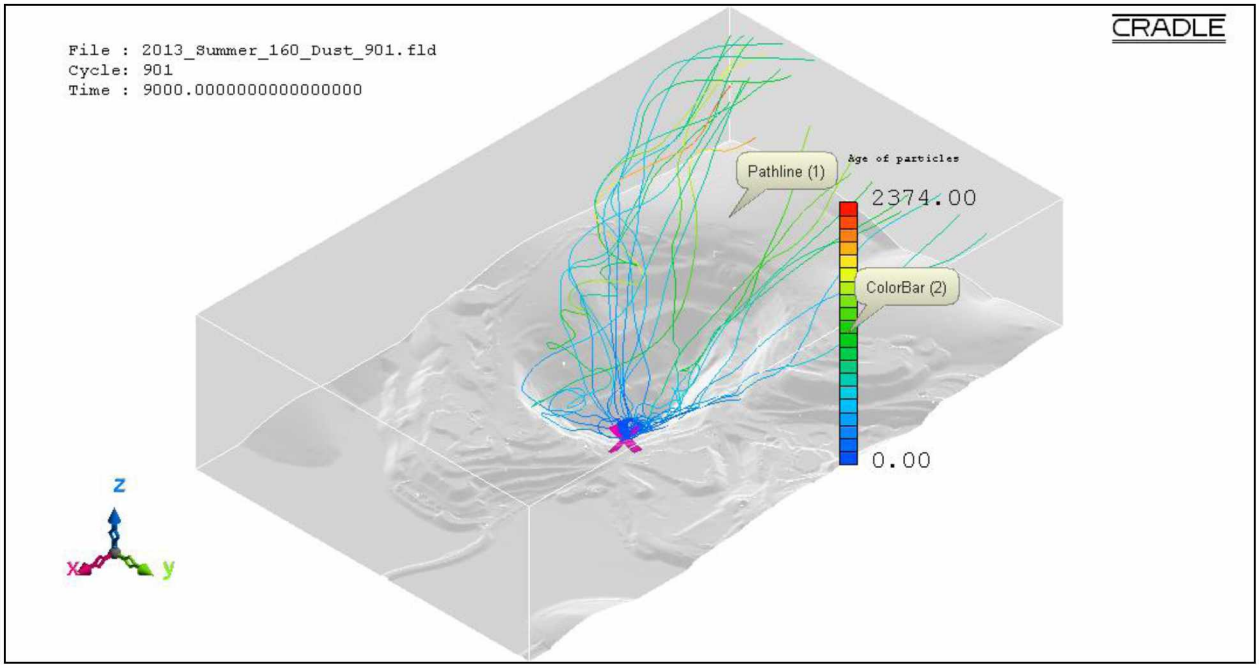

Figure B.118: Pathlines of PM_5 dust particles from source location 8 in the actual open-pit domain for extreme insolation summer condition using the LES method.

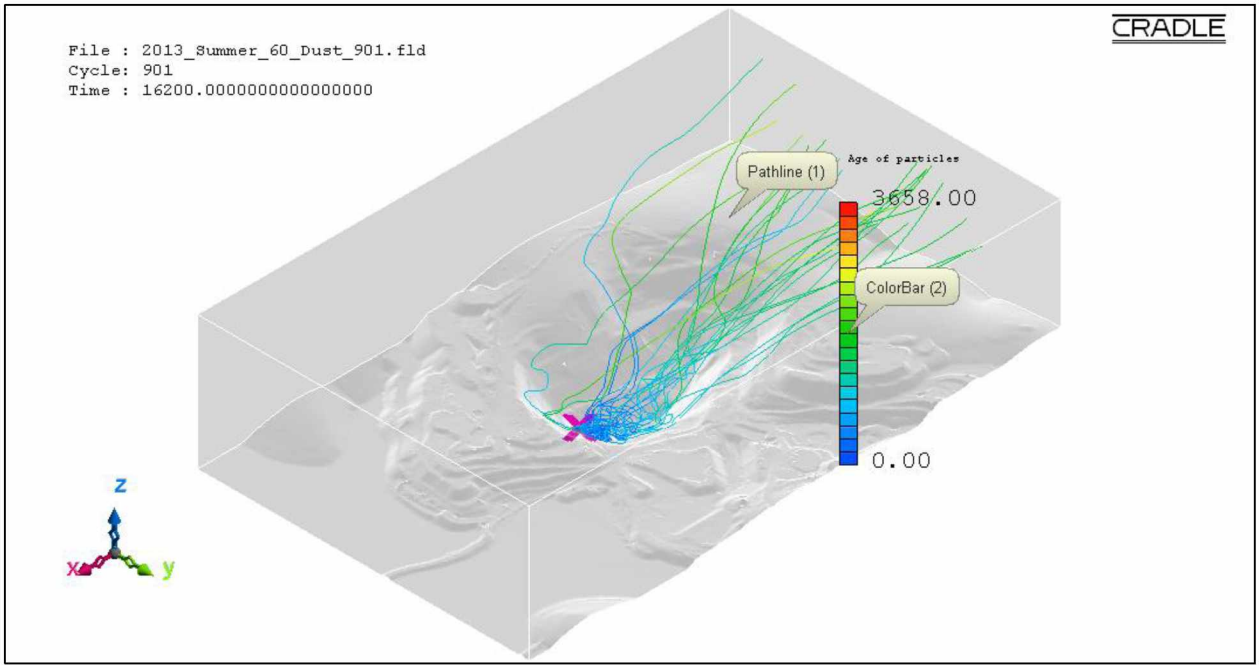

Figure B.119: Pathlines of PM_5 dust particles from source location 9 in the actual open-pit domain for fair insolation summer condition using the LES method.

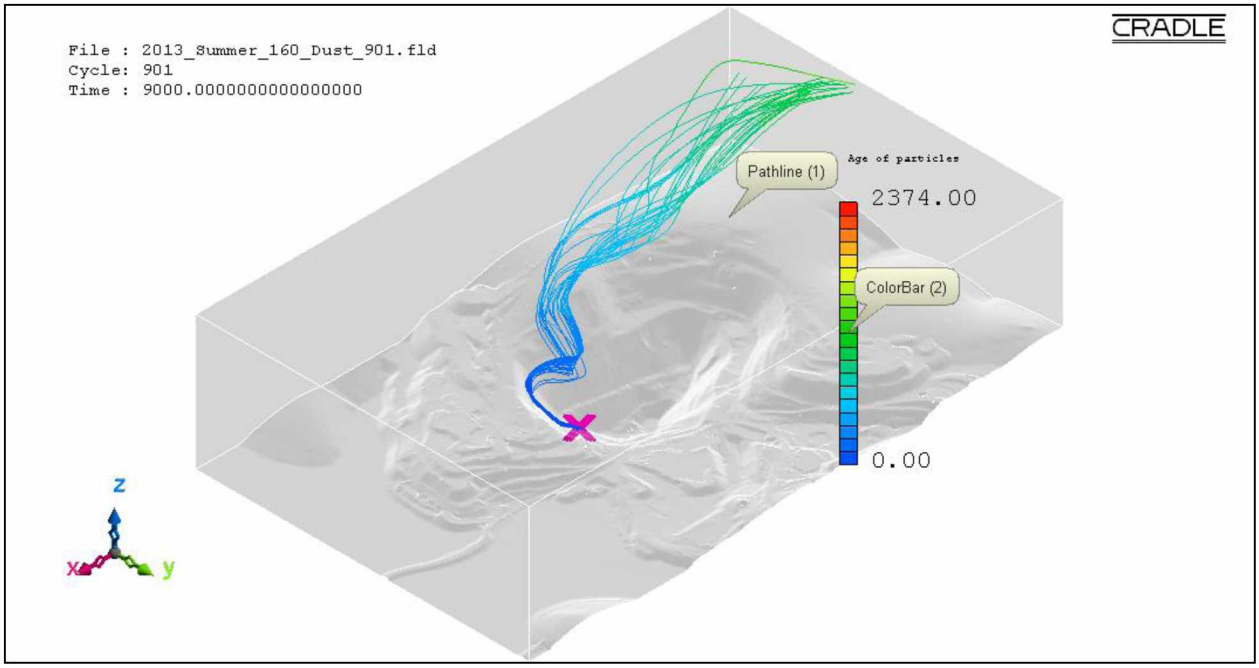

Figure B.120: Pathlines of PM_5 dust particles from source location 9 in the actual open-pit domain for extreme insolation summer condition using the LES method.

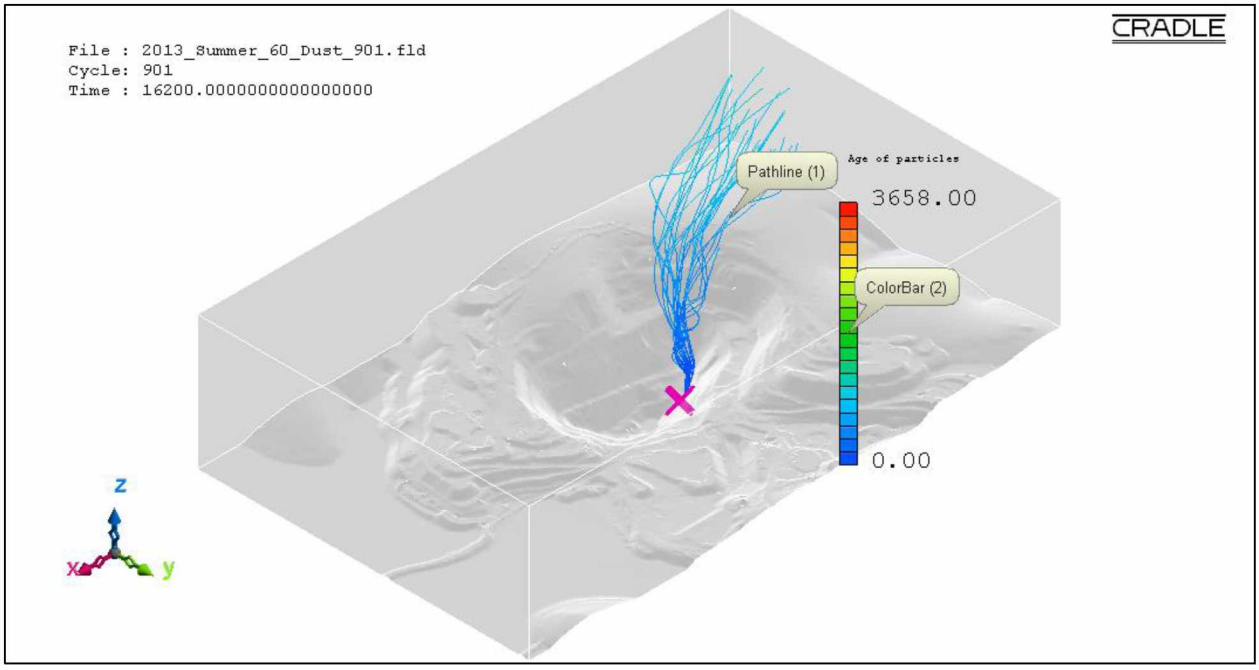

Figure B.121: Pathlines of PM_5 dust particles from source location 10 in the actual open-pit domain for fair insolation summer condition using the LES method.

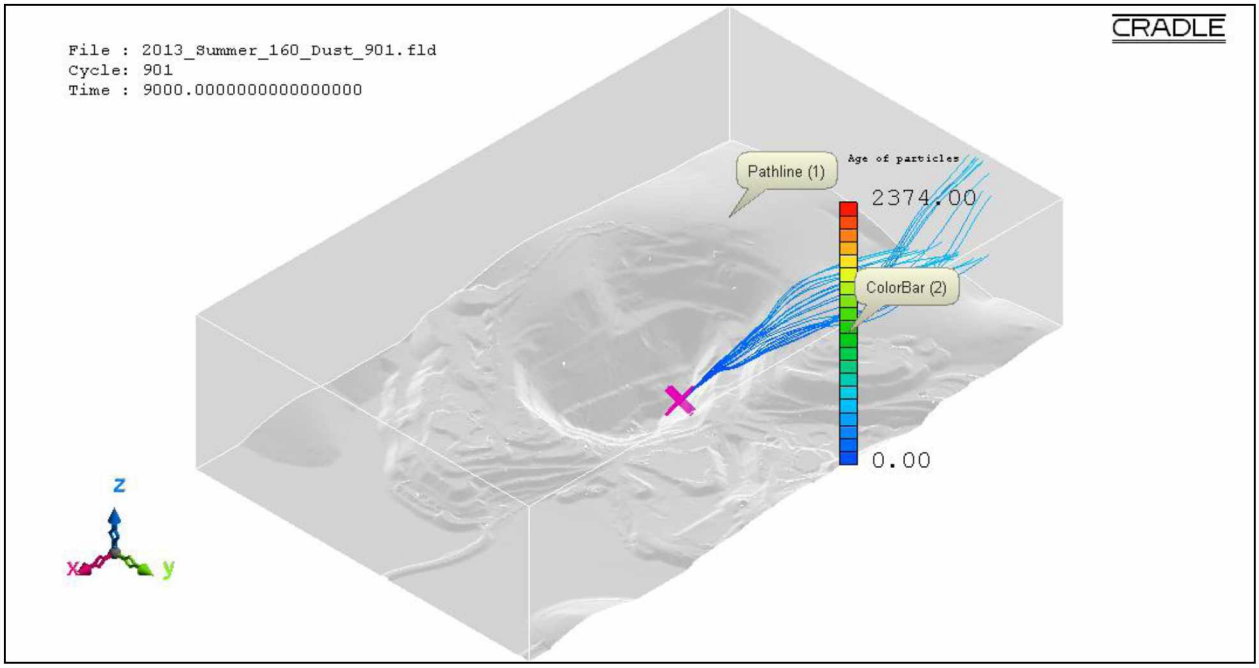

Figure B.122: Pathlines of PM_5 dust particles from source location 10 in the actual open-pit domain for extreme insolation summer condition using the LES method.

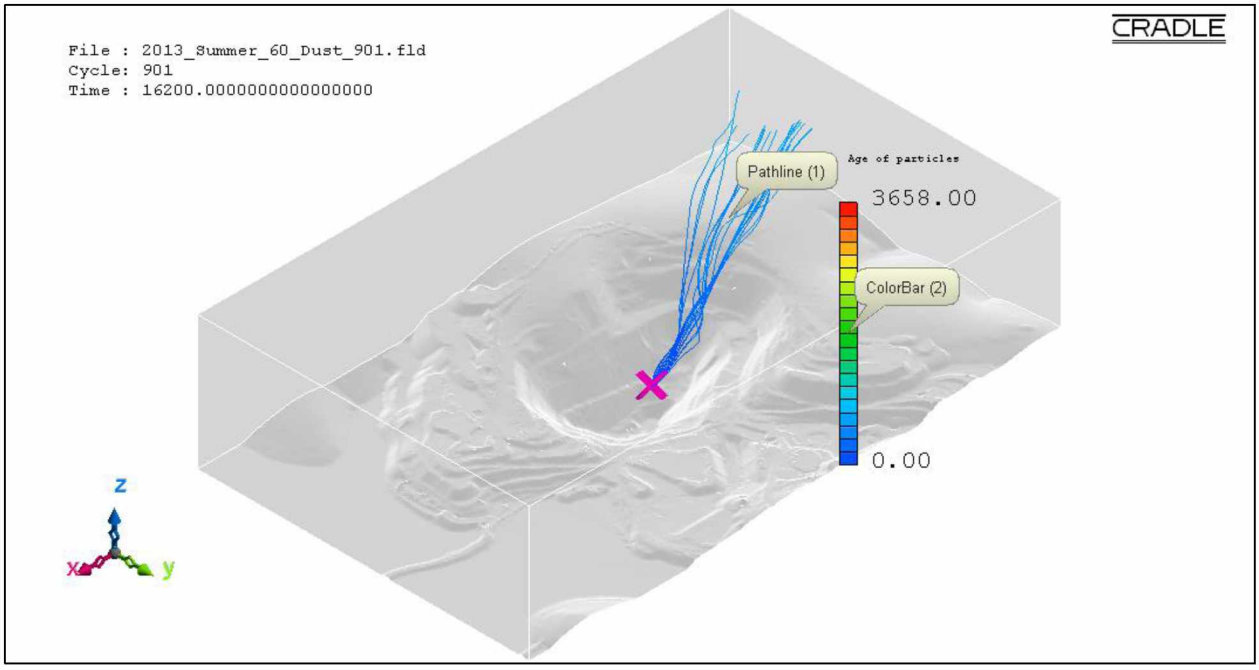

Figure B.123: Pathlines of PM_5 dust particles from source location 11 in the actual open-pit domain for fair insolation summer condition using the LES method.

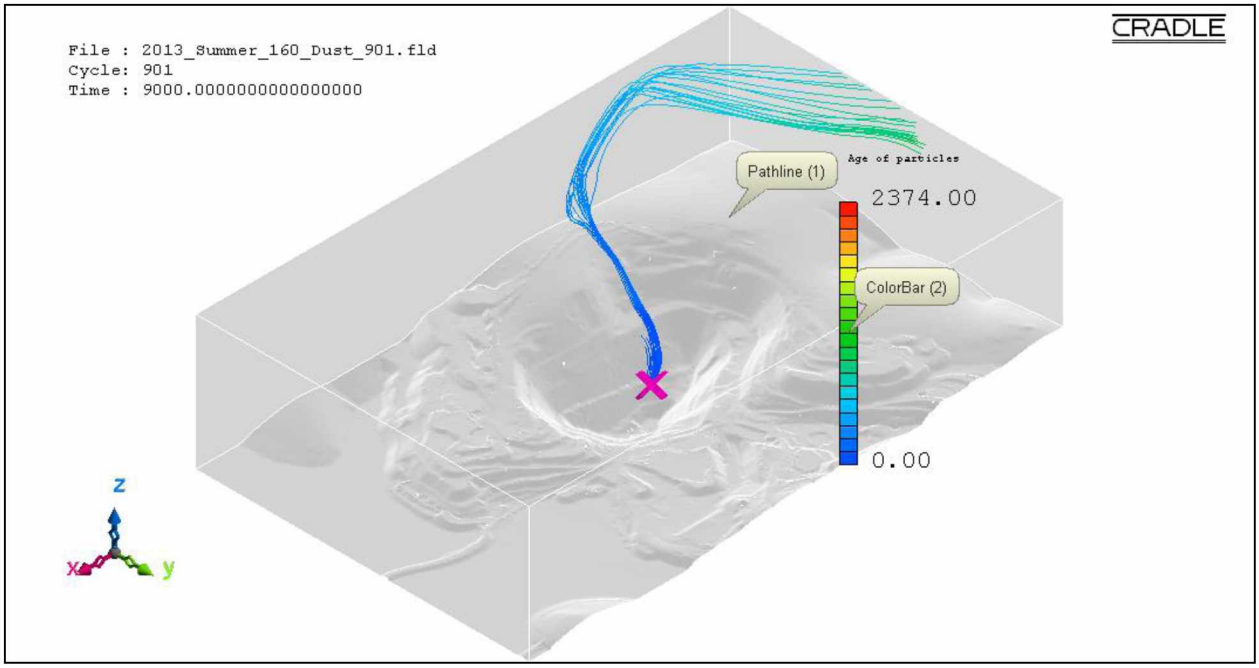

Figure B.124: Pathlines of PM_5 dust particles from source location 11 in the actual open-pit domain for extreme insolation summer condition using the LES method.

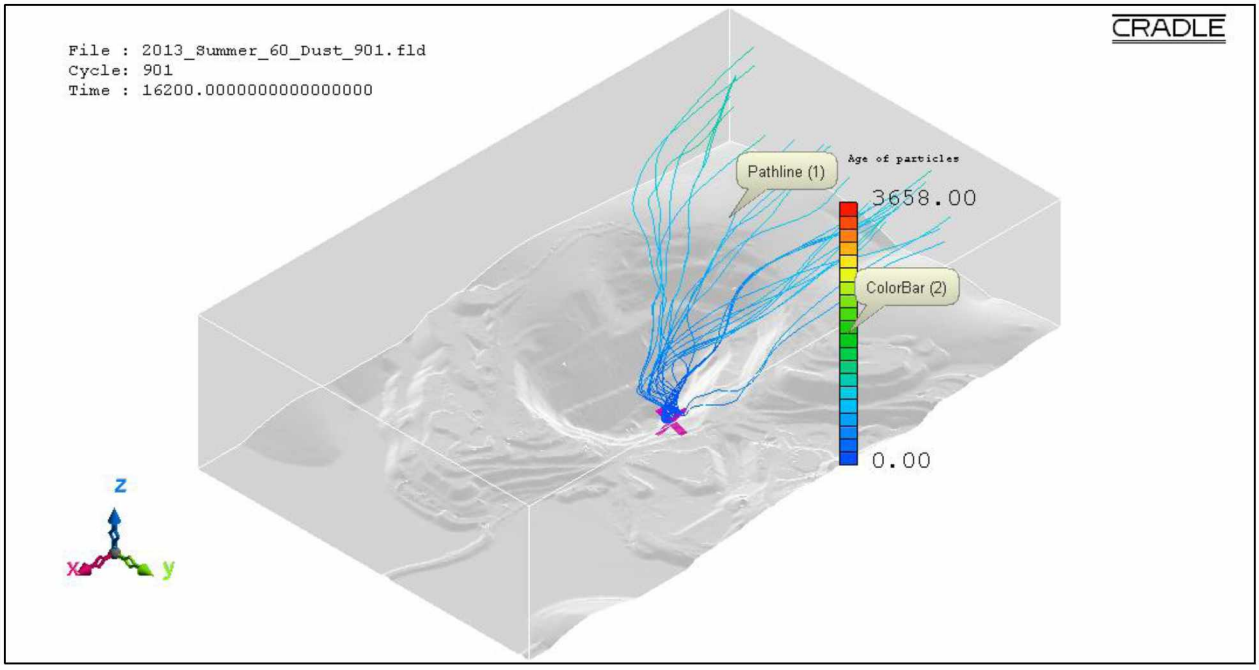

Figure B.125: Pathlines of PM_5 dust particles from source location 12 in the actual open-pit domain for fair insolation summer condition using the LES method.

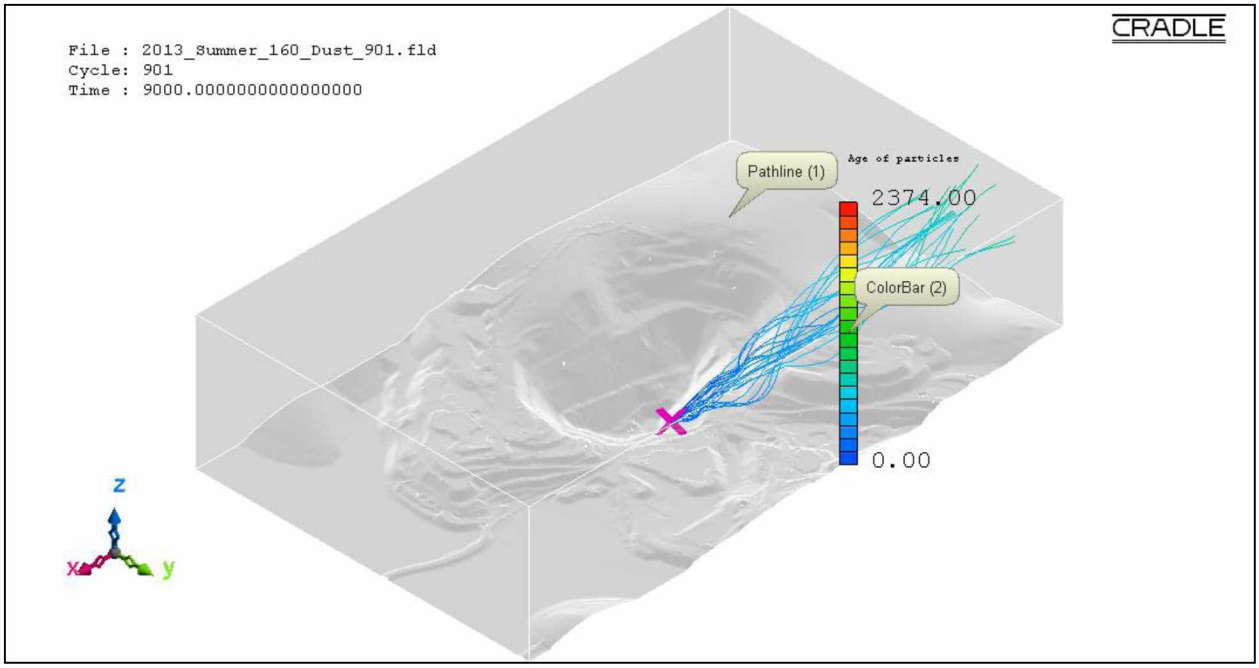

Figure B.126: Pathlines of PM_5 dust particles from source location 12 in the actual open-pit domain for extreme insolation summer condition using the LES method.

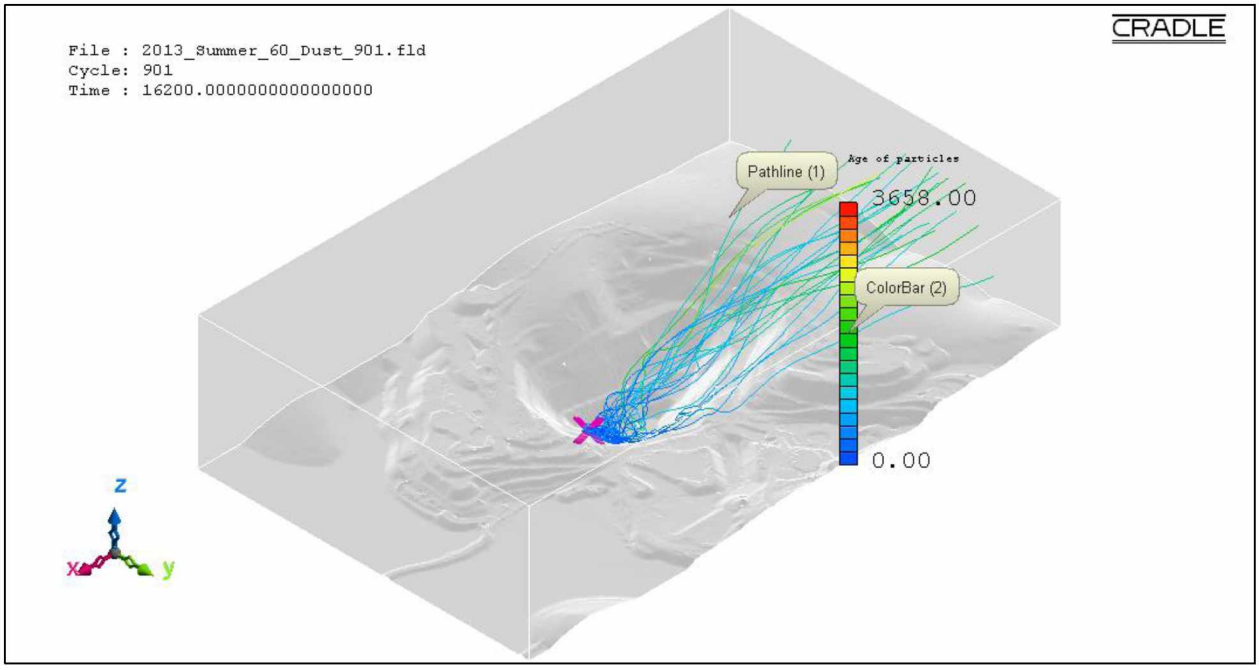

Figure B.127: Pathlines of PM_5 dust particles from source location 13 in the actual open-pit domain for fair insolation summer condition using the LES method.

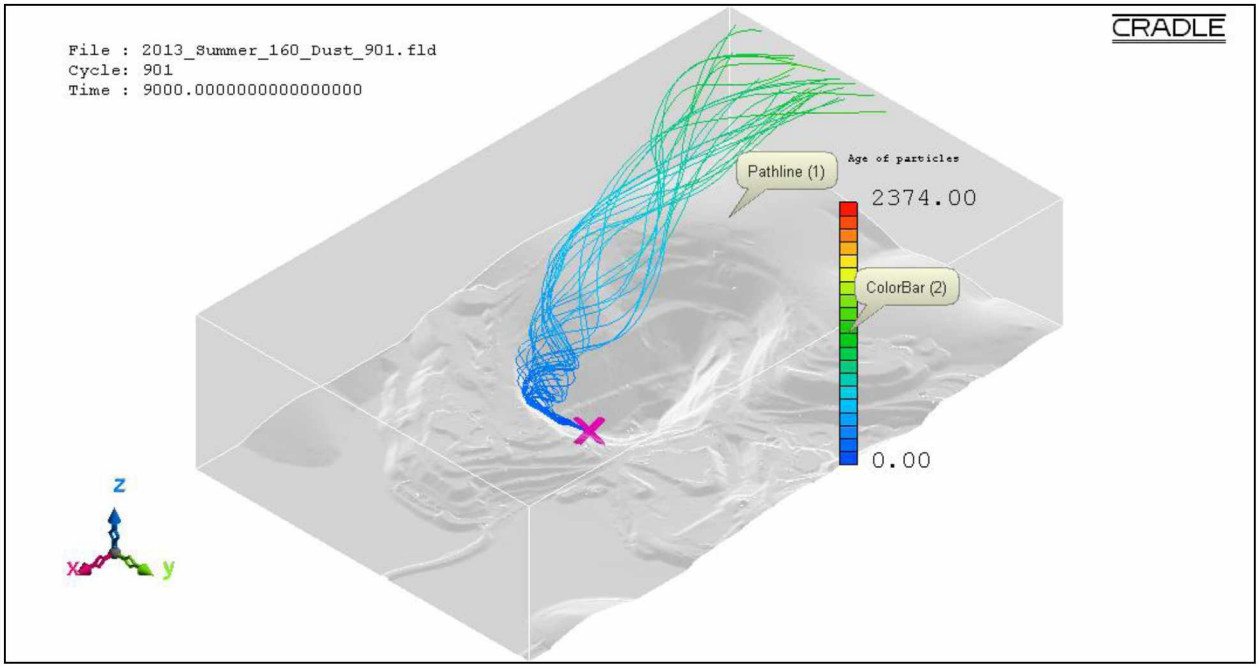

Figure B.128: Pathlines of PM_5 dust particles from source location 13 in the actual open-pit domain for extreme insolation summer condition using the LES method.

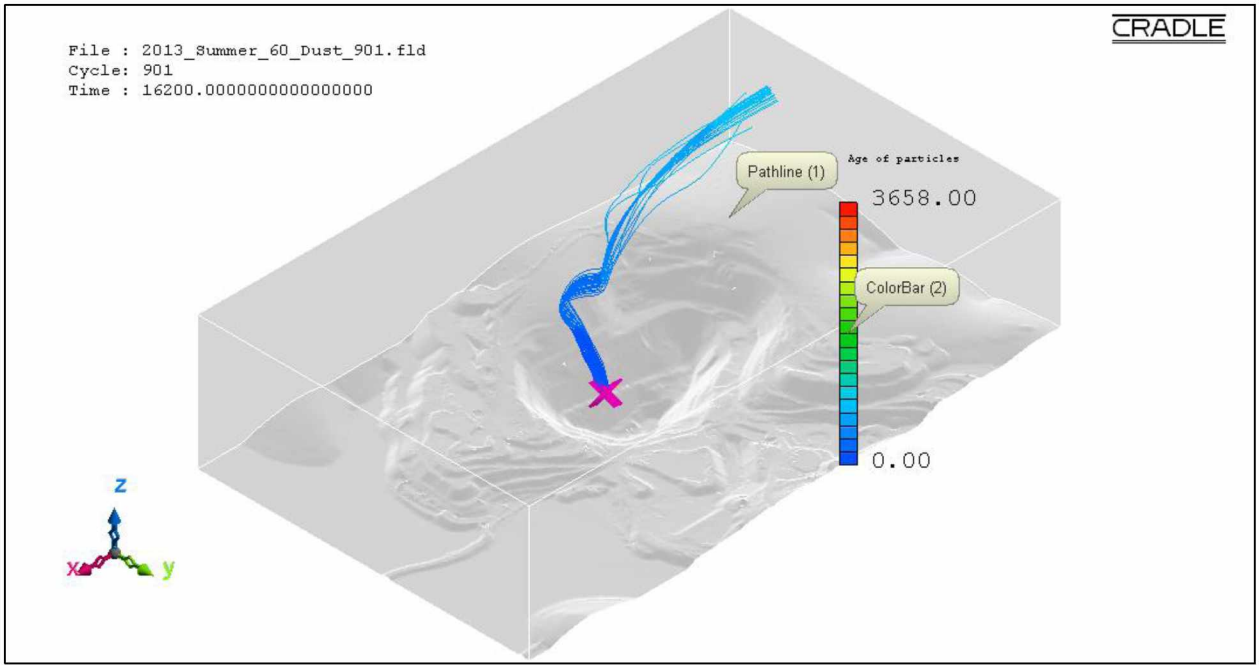

Figure B.129: Pathlines of PM_5 dust particles from source location 14 in the actual open-pit domain for fair insolation summer condition using the LES method.

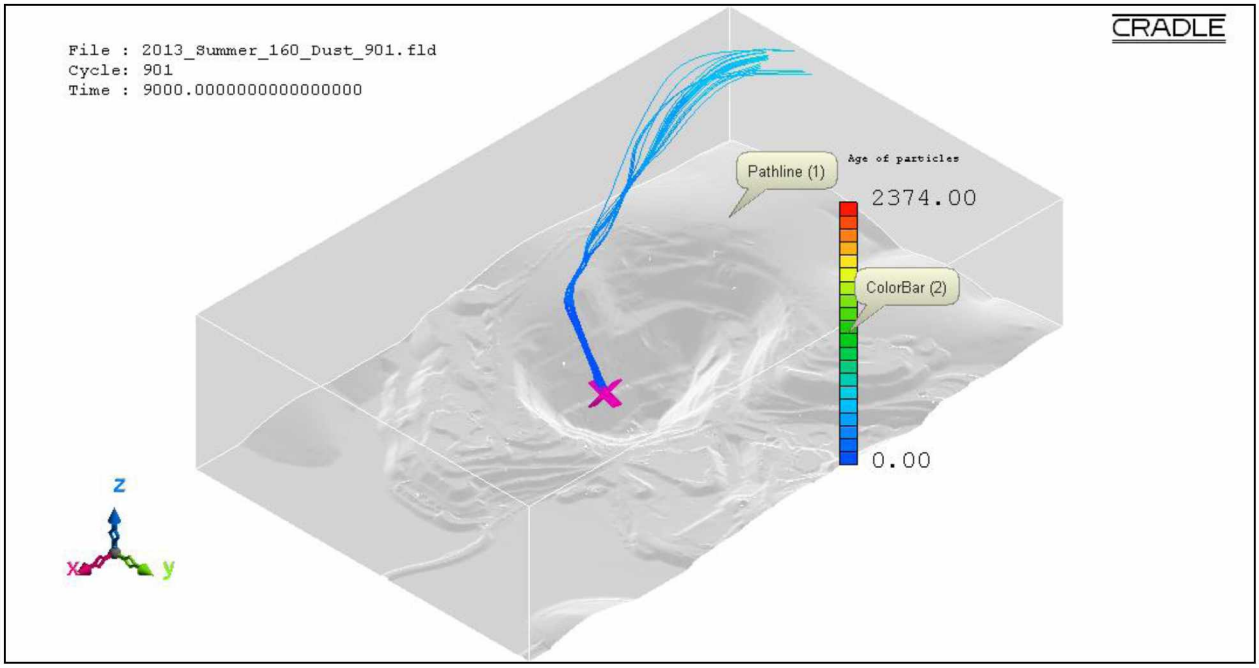

Figure B.130: Pathlines of PM_5 dust particles from source location 14 in the actual open-pit domain for extreme insolation summer condition using the LES method.

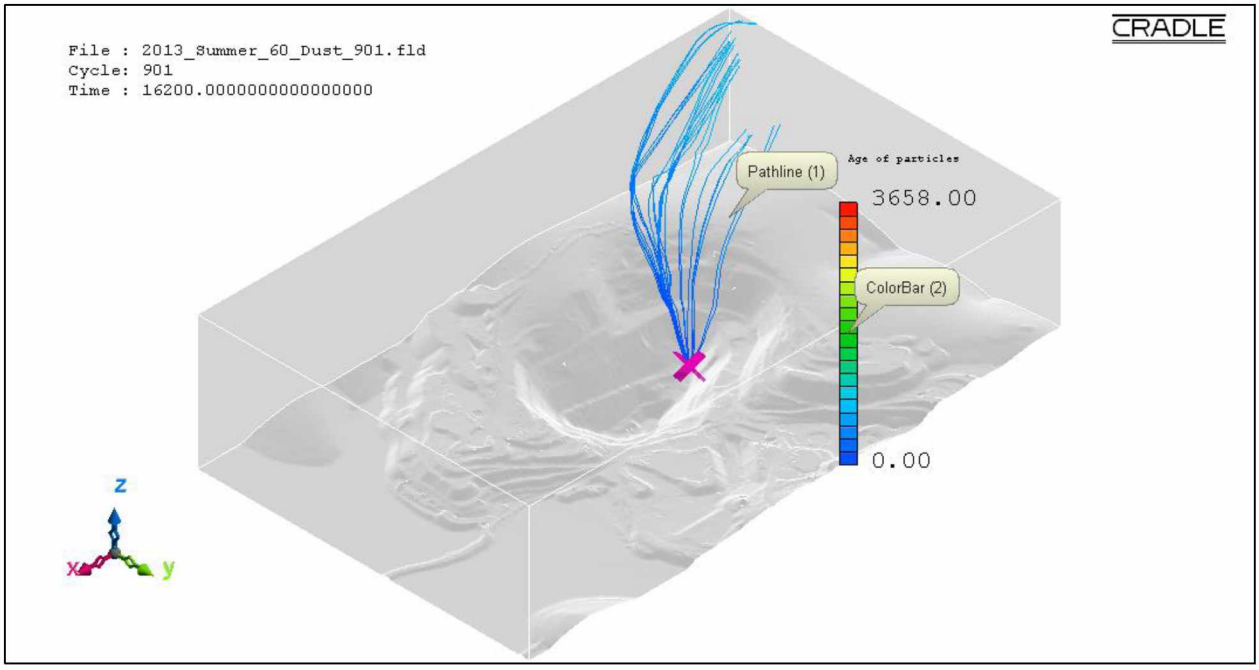

Figure B.131: Pathlines of PM_5 dust particles from source location 15 in the actual open-pit domain for fair insolation summer condition using the LES method.

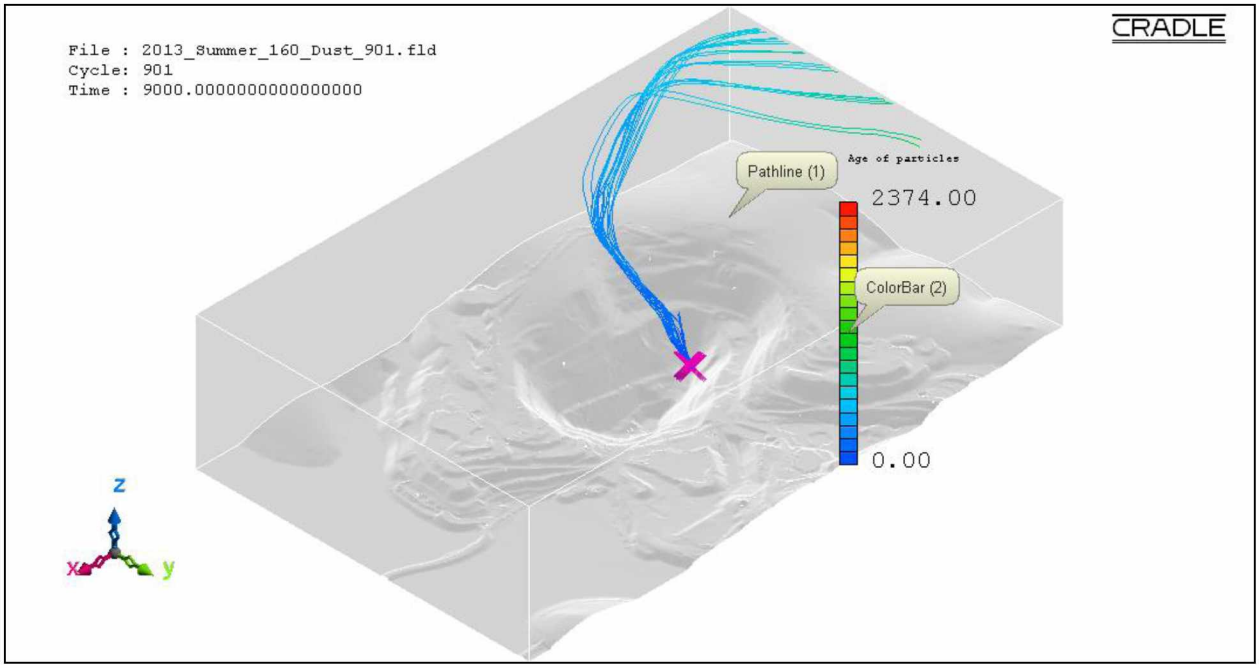

Figure B.132: Pathlines of PM_5 dust particles from source location 15 in the actual open-pit domain for extreme insolation summer condition using the LES method.

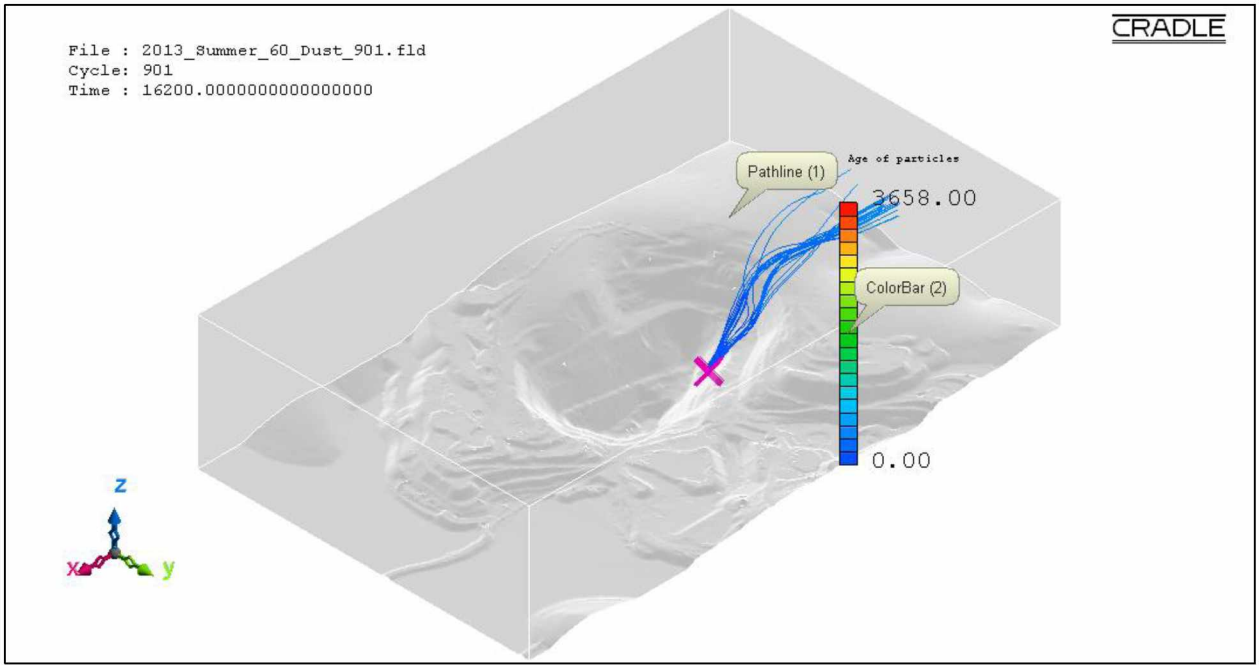

Figure B.133: Pathlines of PM_5 dust particles from source location 16 in the actual open-pit domain for fair insolation summer condition using the LES method.

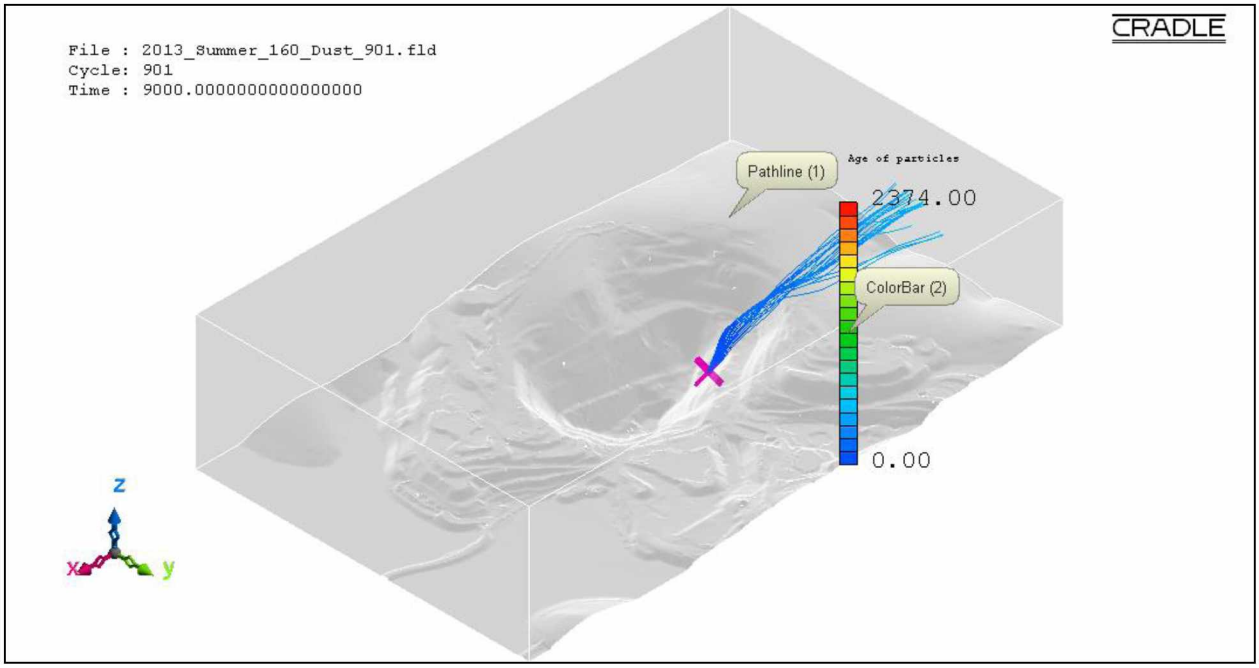

Figure B.134: Pathlines of PM_5 dust particles from source location 16 in the actual open-pit domain for extreme insolation summer condition using the LES method.

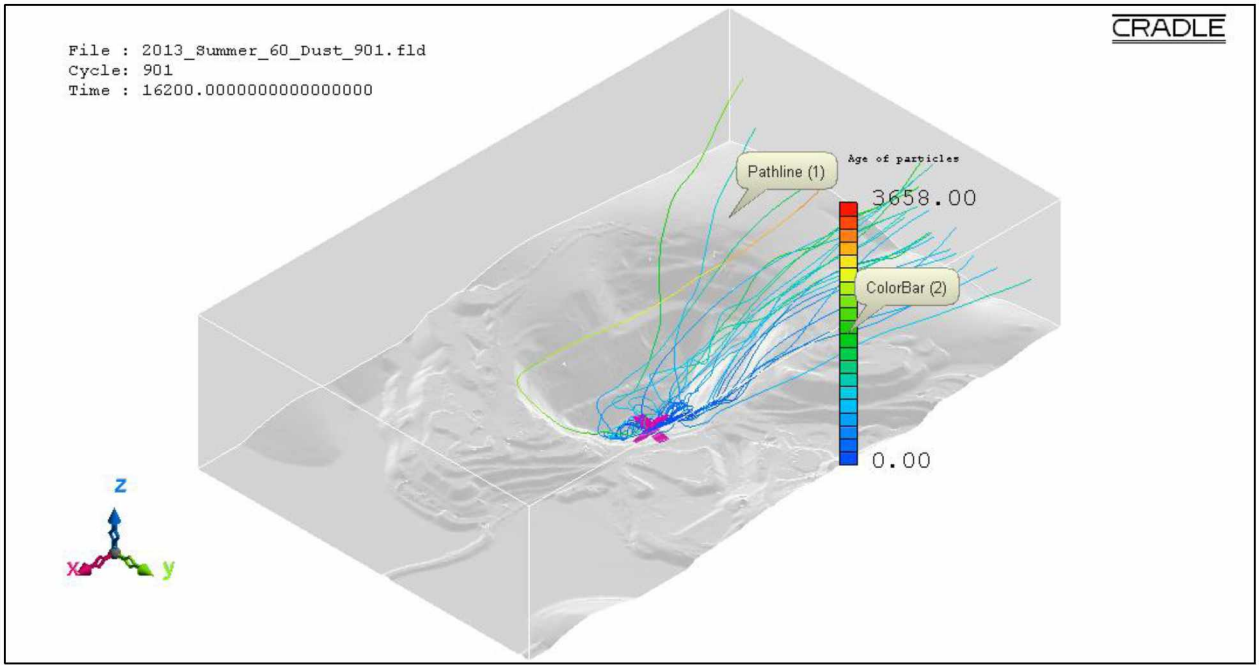

Figure B.135: Pathlines of PM_5 dust particles from source location 17 in the actual open-pit domain for fair insolation summer condition using the LES method.

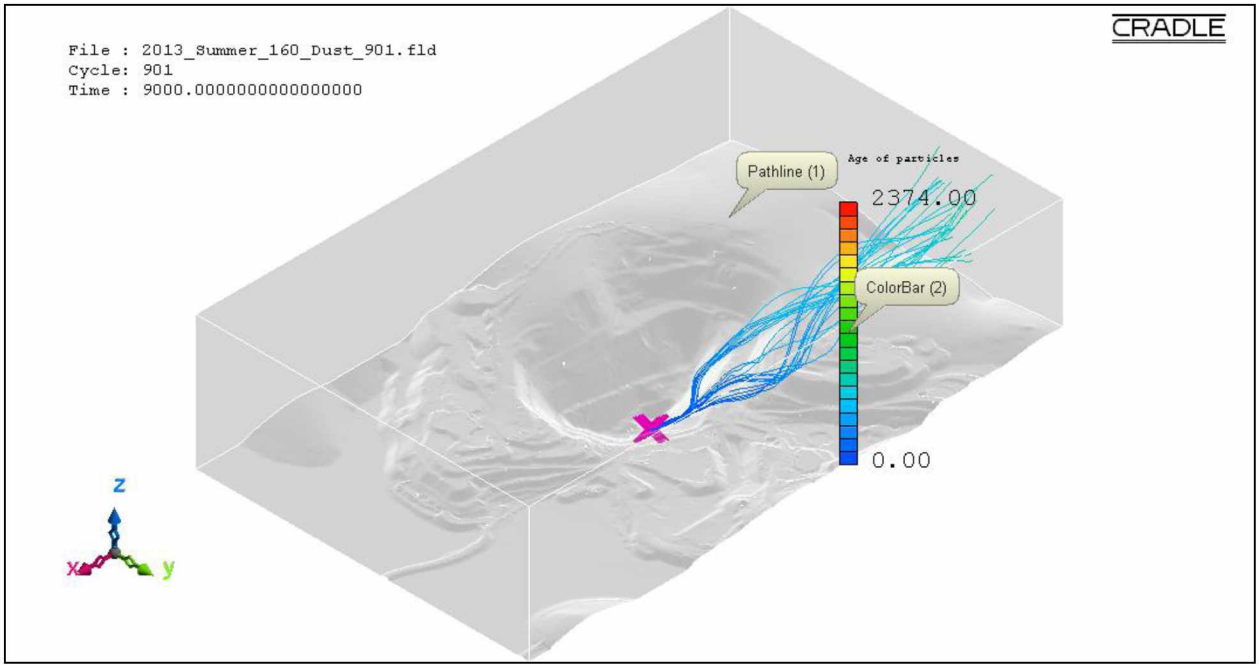

Figure B.136: Pathlines of PM_5 dust particles from source location 17 in the actual open-pit domain for extreme insolation summer condition using the LES method.

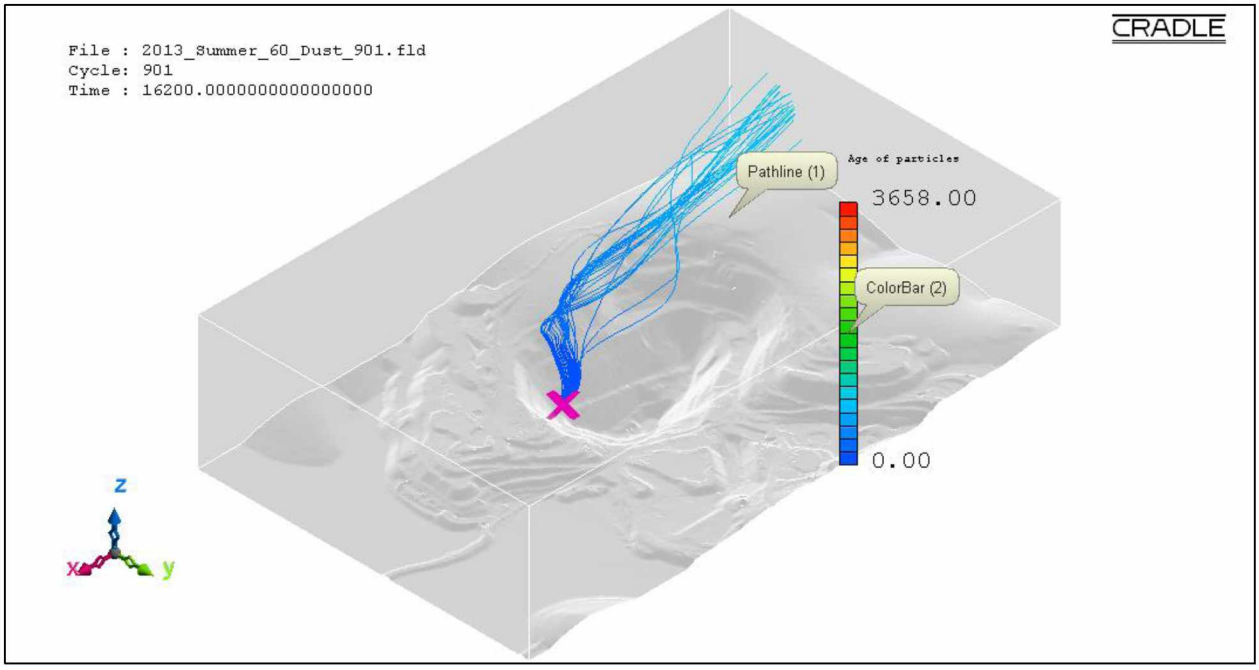

Figure B.137: Pathlines of PM_5 dust particles from source location 18 in the actual open-pit domain for fair insolation summer condition using the LES method.

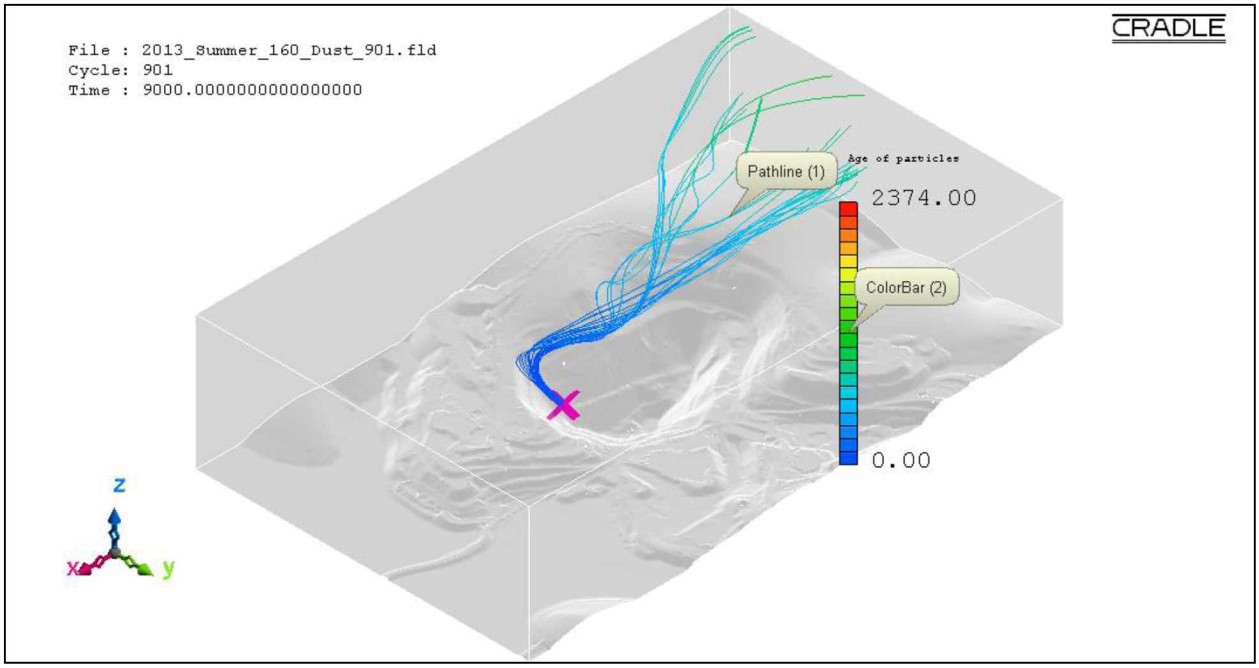

Figure B.138: Pathlines of PM_5 dust particles from source location 18 in the actual open-pit domain for extreme insolation summer condition using the LES method.

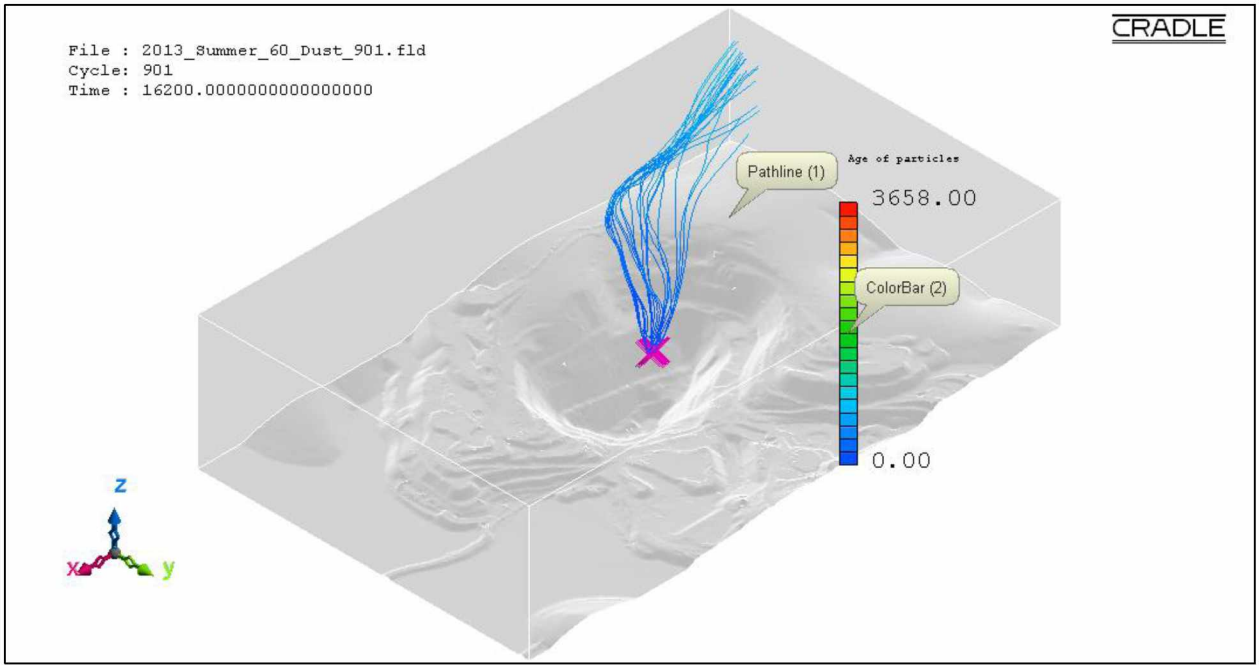

Figure B.139: Pathlines of PM_5 dust particles from source location 19 in the actual open-pit domain for fair insolation summer condition using the LES method.

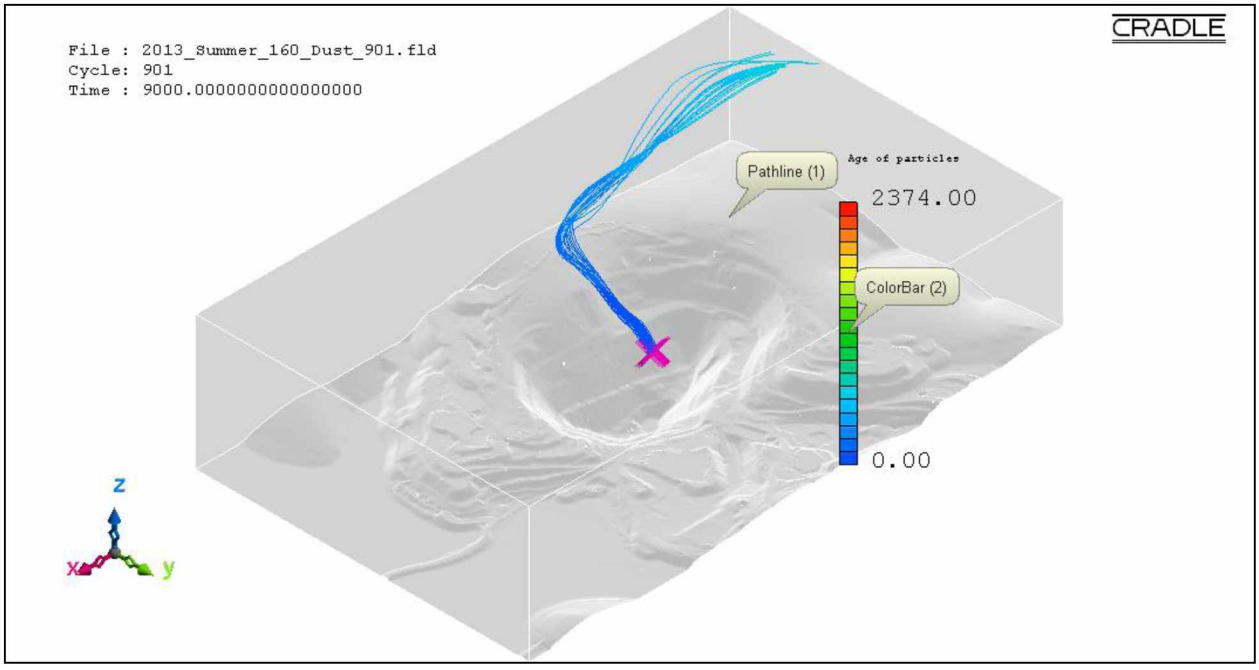

Figure B.140: Pathlines of PM_5 dust particles from source location 19 in the actual open-pit domain for extreme insolation summer condition using the LES method.

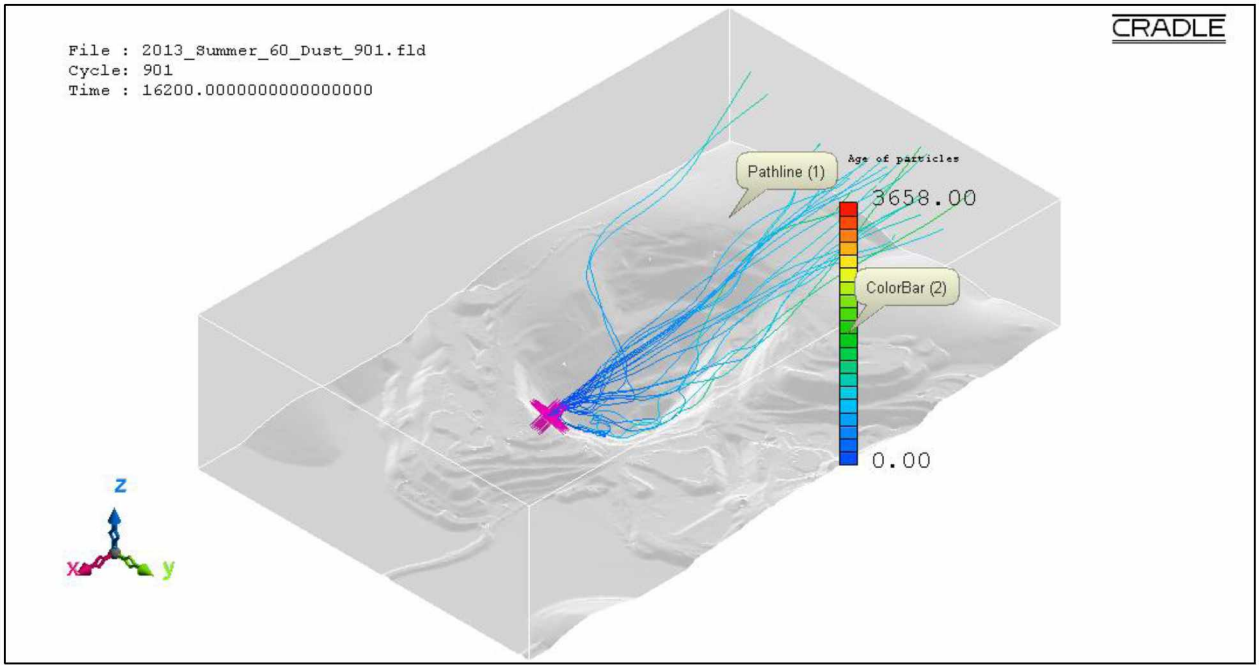

Figure B.141: Pathlines of PM_5 dust particles from source location 20 in the actual open-pit domain for fair insolation summer condition using the LES method.

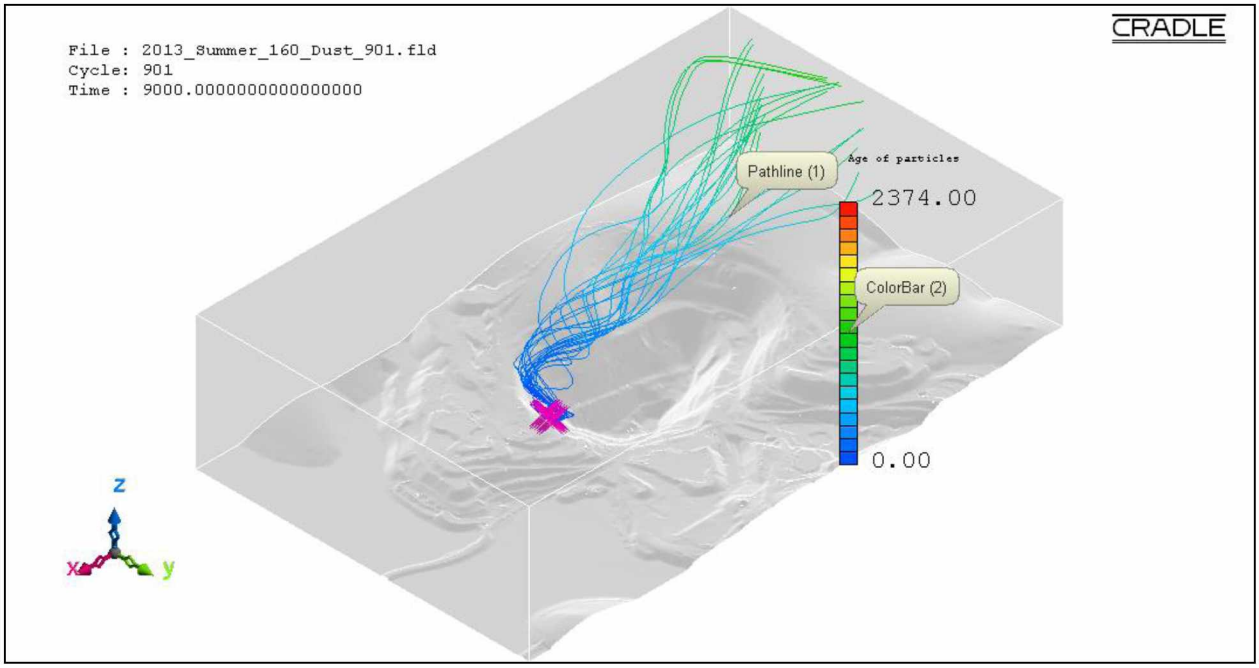

Figure B.142: Pathlines of PM_5 dust particles from source location 20 in the actual open-pit domain for extreme insolation summer condition using the LES method.

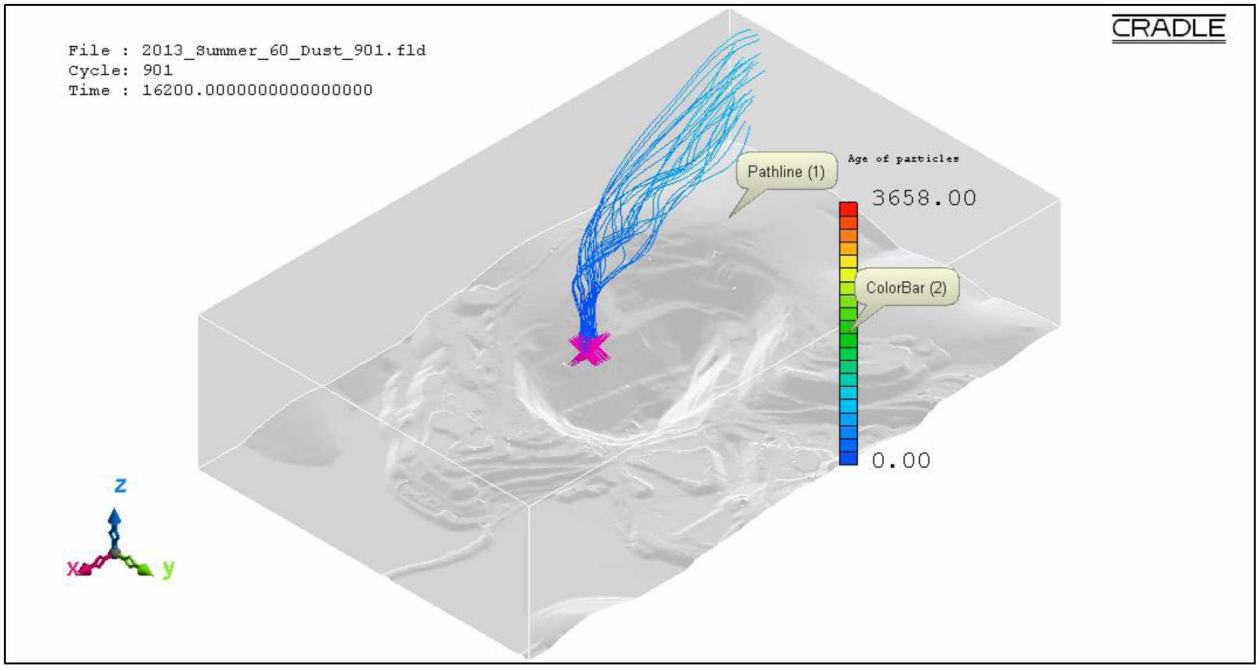

Figure B.143: Pathlines of PM_5 dust particles from source location 21 in the actual open-pit domain for fair insolation summer condition using the LES method.

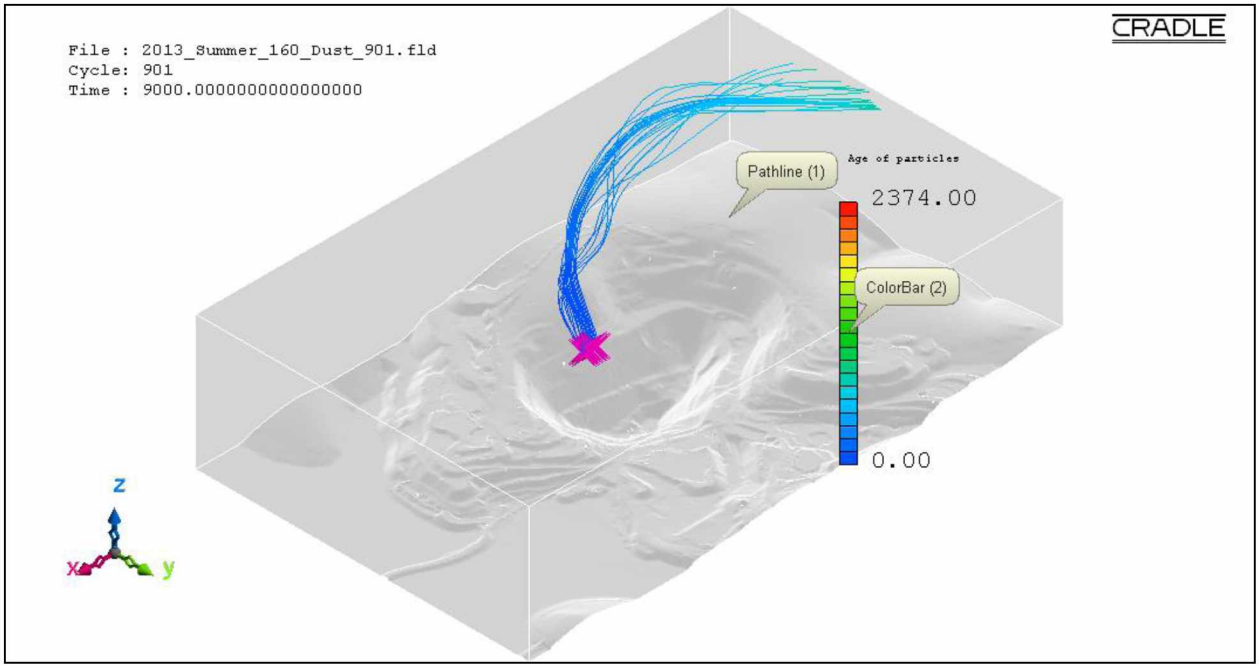

Figure B.144: Pathlines of PM_5 dust particles from source location 21 in the actual open-pit domain for extreme insolation summer condition using the LES method.

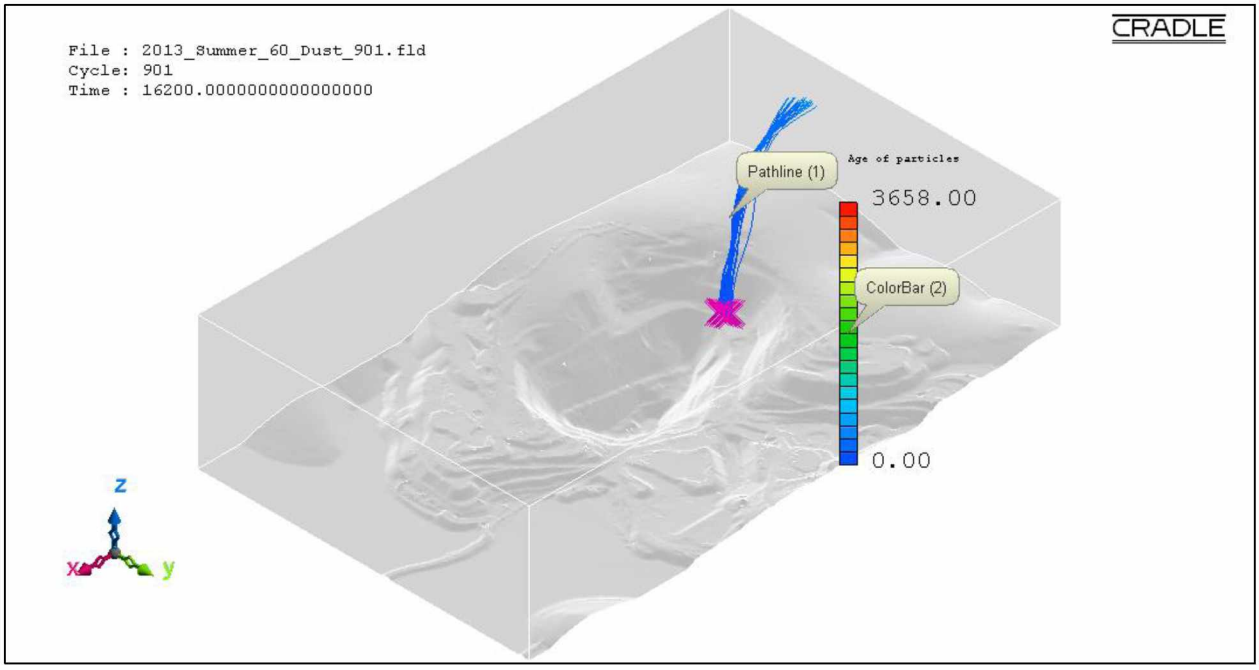

Figure B.145: Pathlines of PM_5 dust particles from source location 22 in the actual open-pit domain for fair insolation summer condition using the LES method.

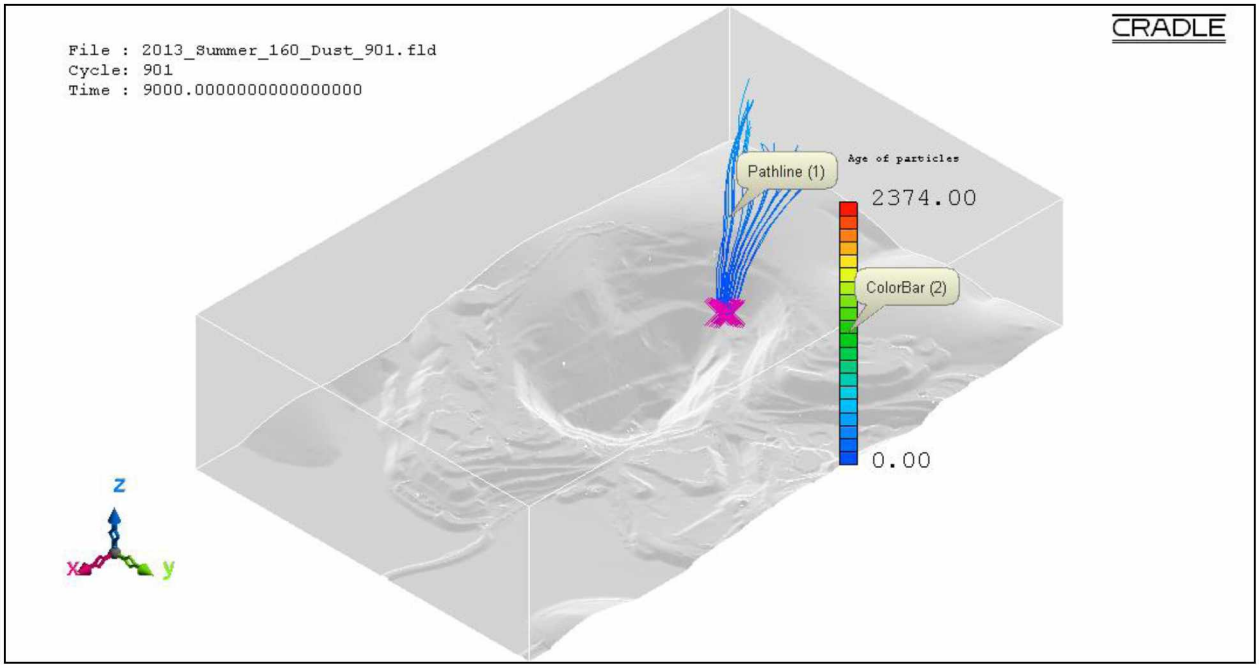

Figure B.146: Pathlines of PM_5 dust particles from source location 22 in the actual open-pit domain for extreme insolation summer condition using the LES method.

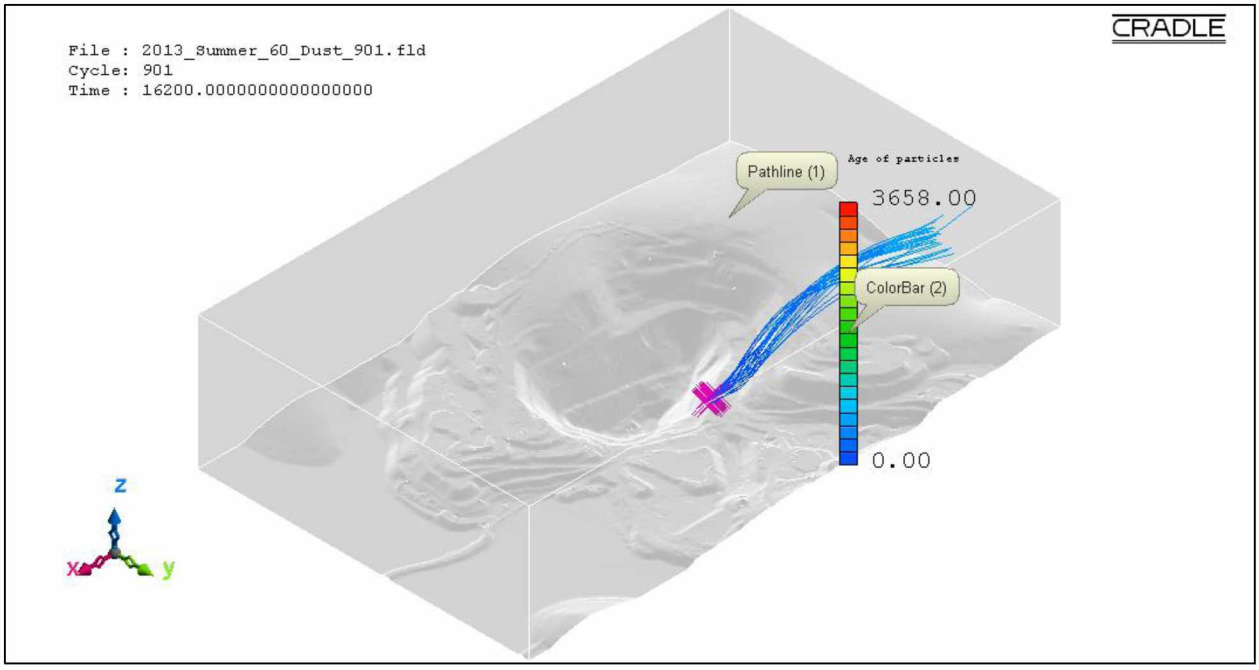

Figure B.147: Pathlines of PM_5 dust particles from source location 23 in the actual open-pit domain for fair insolation summer condition using the LES method.

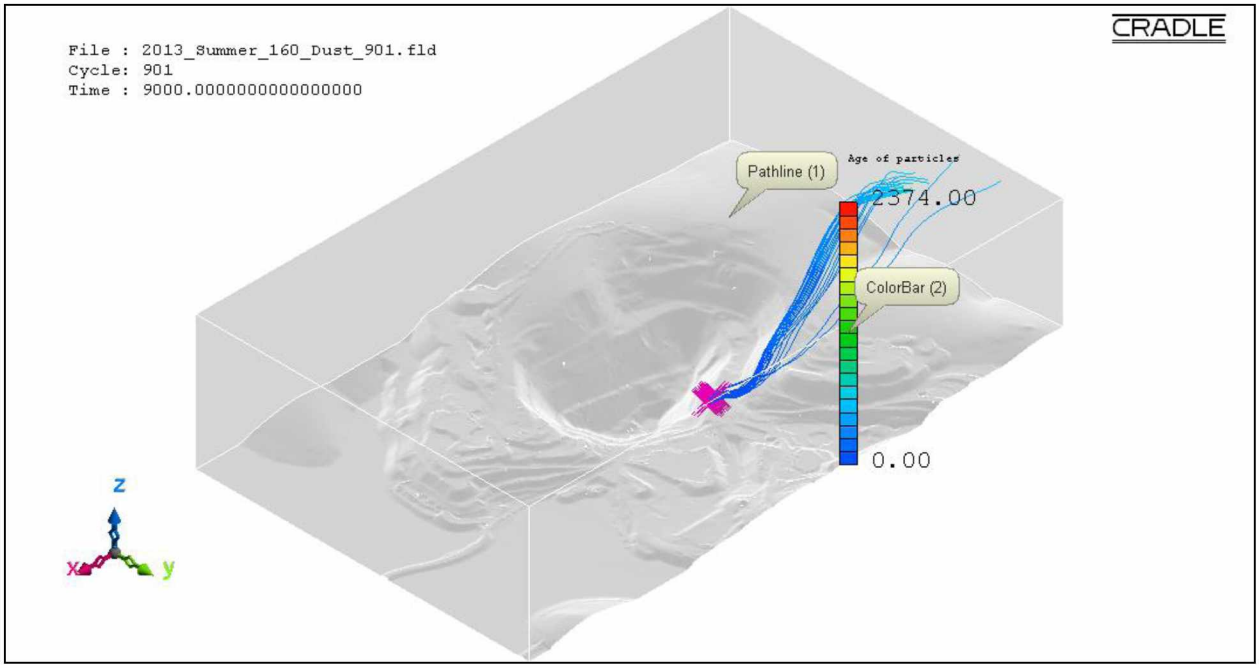

Figure B.148: Pathlines of PM_5 dust particles from source location 23 in the actual open-pit domain for extreme insolation summer condition using the LES method.

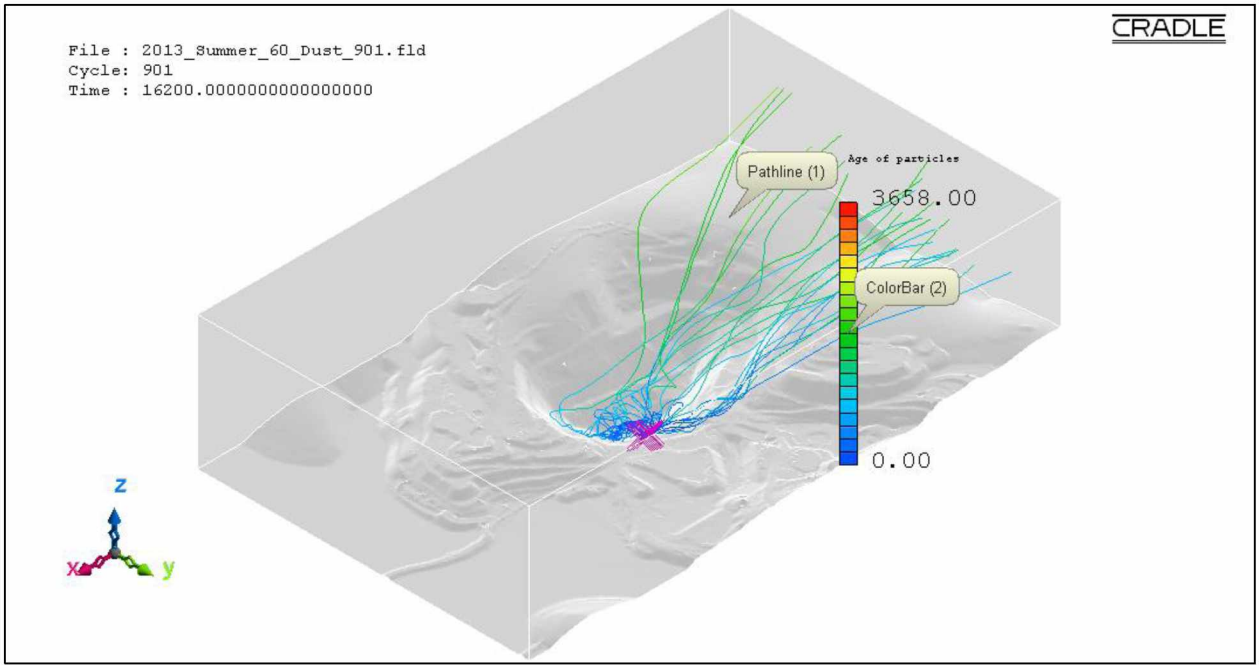

Figure B.149: Pathlines of PM_5 dust particles from source location 24 in the actual open-pit domain for fair insolation summer condition using the LES method.

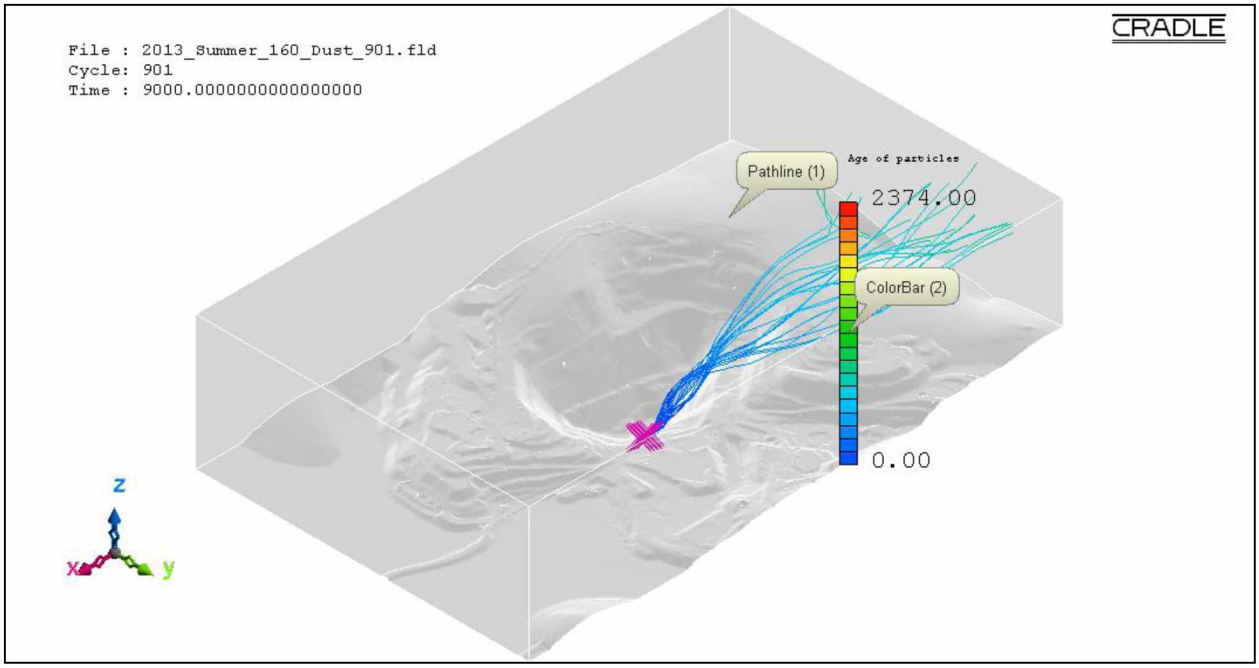

Figure B.150: Pathlines of PM_5 dust particles from source location 24 in the actual open-pit domain for extreme insolation summer condition using the LES method.

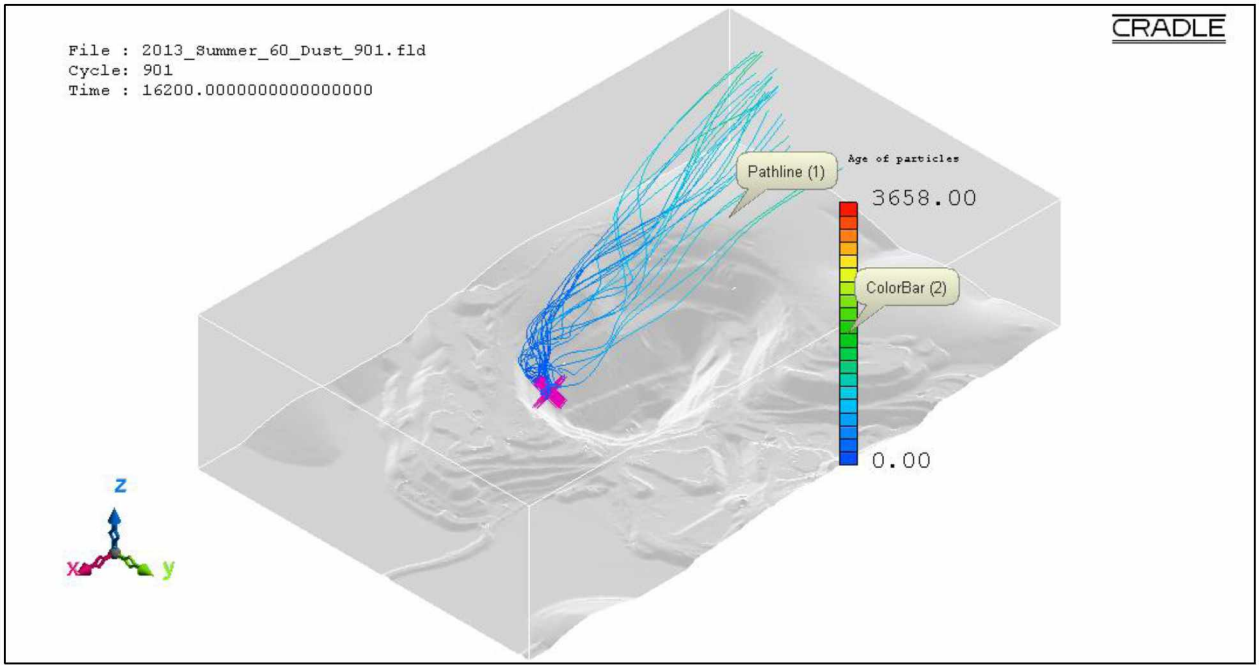

Figure B.151: Pathlines of PM_5 dust particles from source location 25 in the actual open-pit domain for fair insolation summer condition using the LES method.

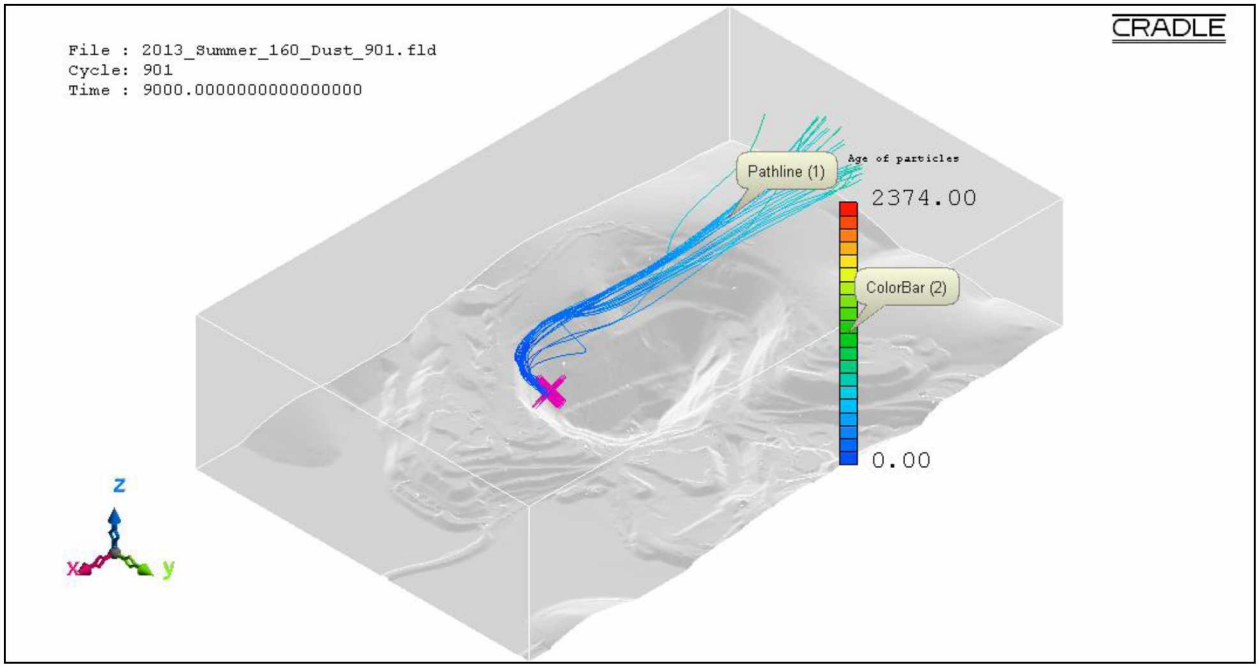

Figure B.152: Pathlines of PM_5 dust particles from source location 25 in the actual open-pit domain for extreme insolation summer condition using the LES method.

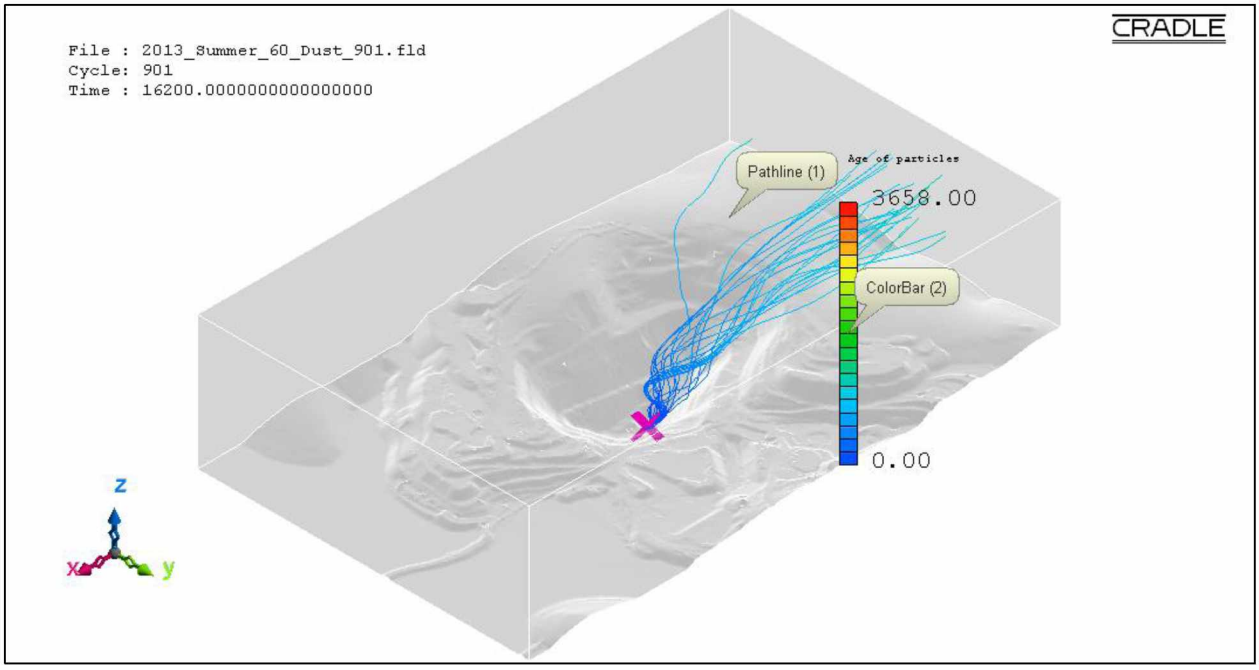

Figure B.153: Pathlines of PM_{10} dust particles from source location 1 in the actual open-pit domain for fair insolation summer condition using the LES method.

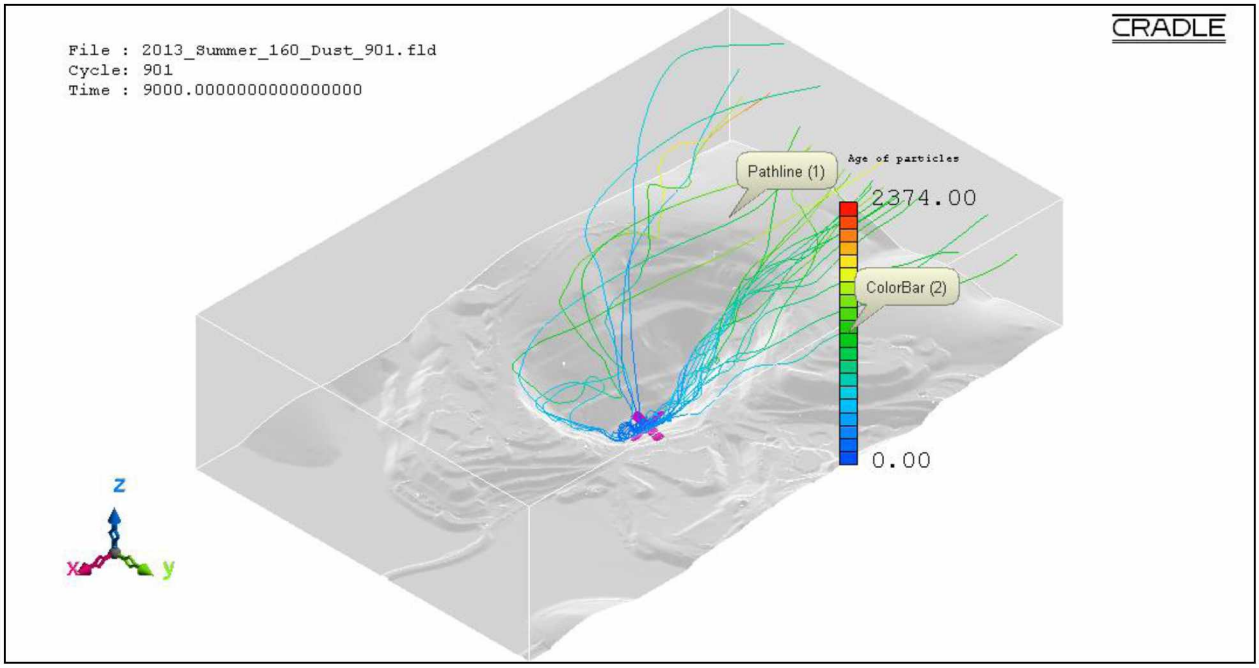

Figure B.154: Pathlines of PM_{10} dust particles from source location 1 in the actual open-pit domain for extreme insolation summer condition using the LES method.

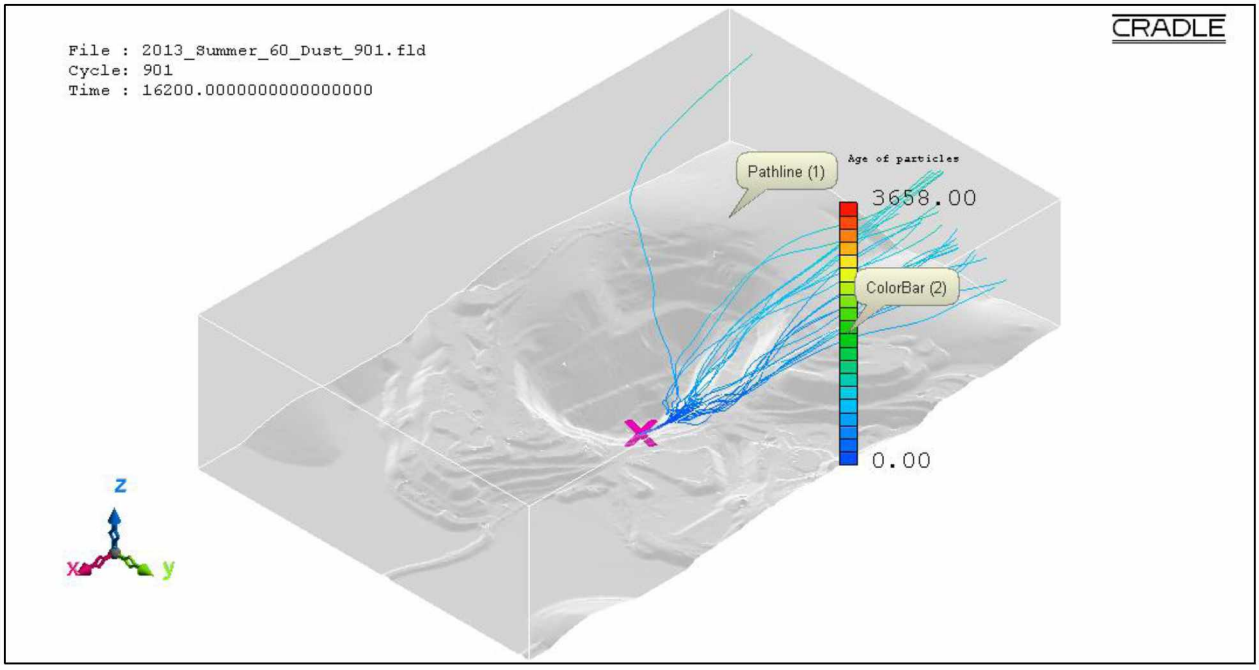

Figure B.155: Pathlines of PM_{10} dust particles from source location 2 in the actual open-pit domain for fair insolation summer condition using the LES method.

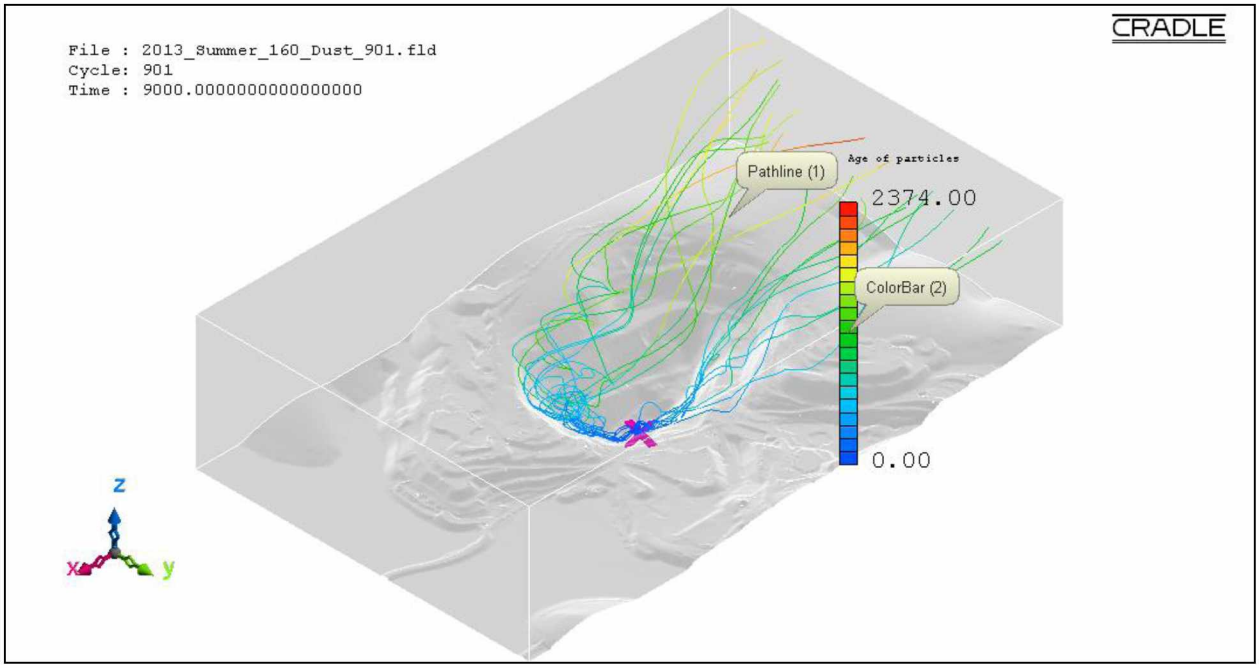

Figure B.156: Pathlines of PM_{10} dust particles from source location 2 in the actual open-pit domain for extreme insolation summer condition using the LES method.

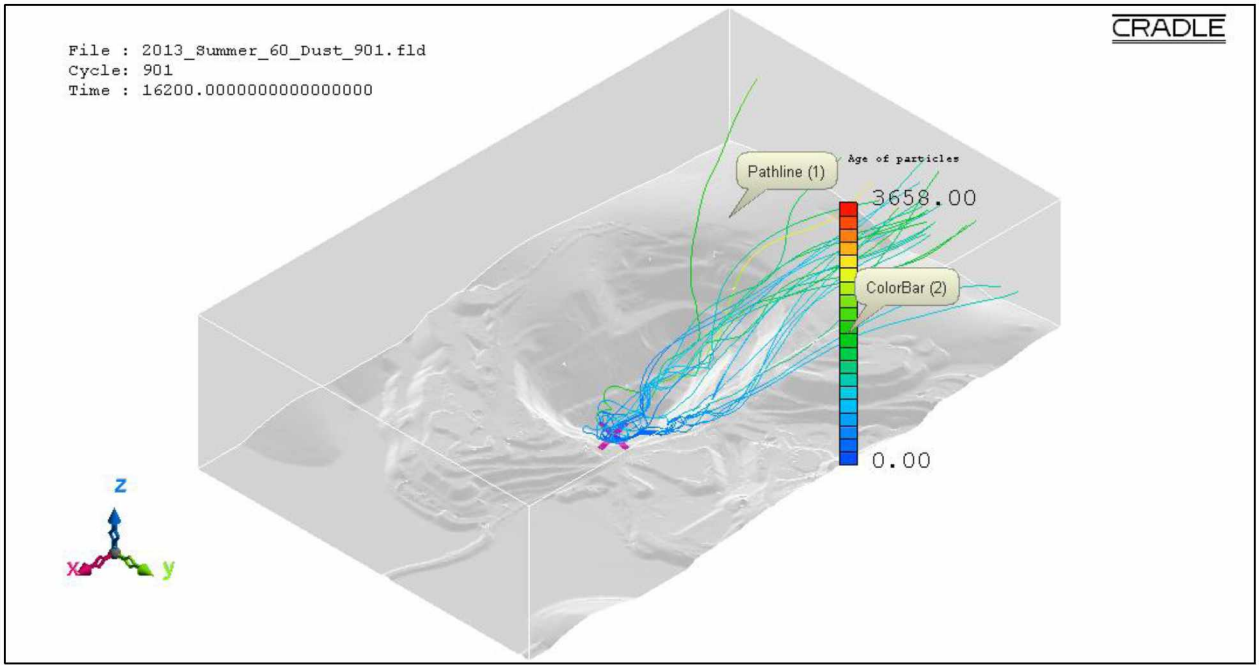

Figure B.157: Pathlines of PM_{10} dust particles from source location 3 in the actual open-pit domain for fair insolation summer condition using the LES method.

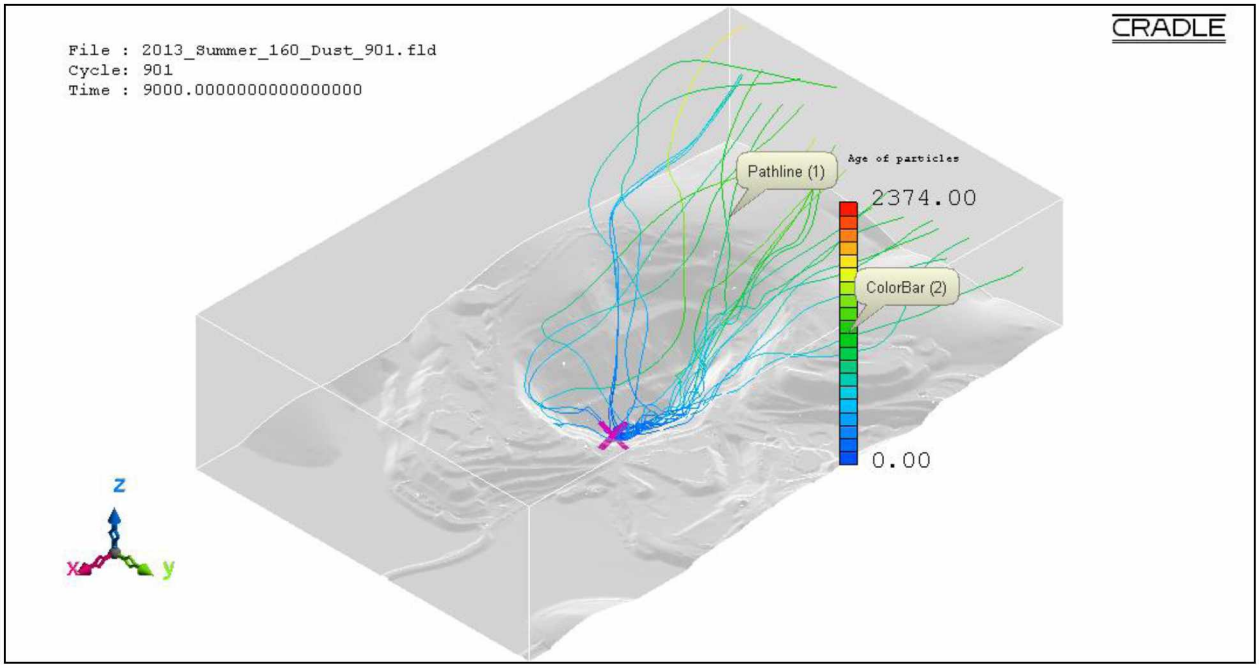

Figure B.158: Pathlines of PM_{10} dust particles from source location 3 in the actual open-pit domain for extreme insolation summer condition using the LES method.

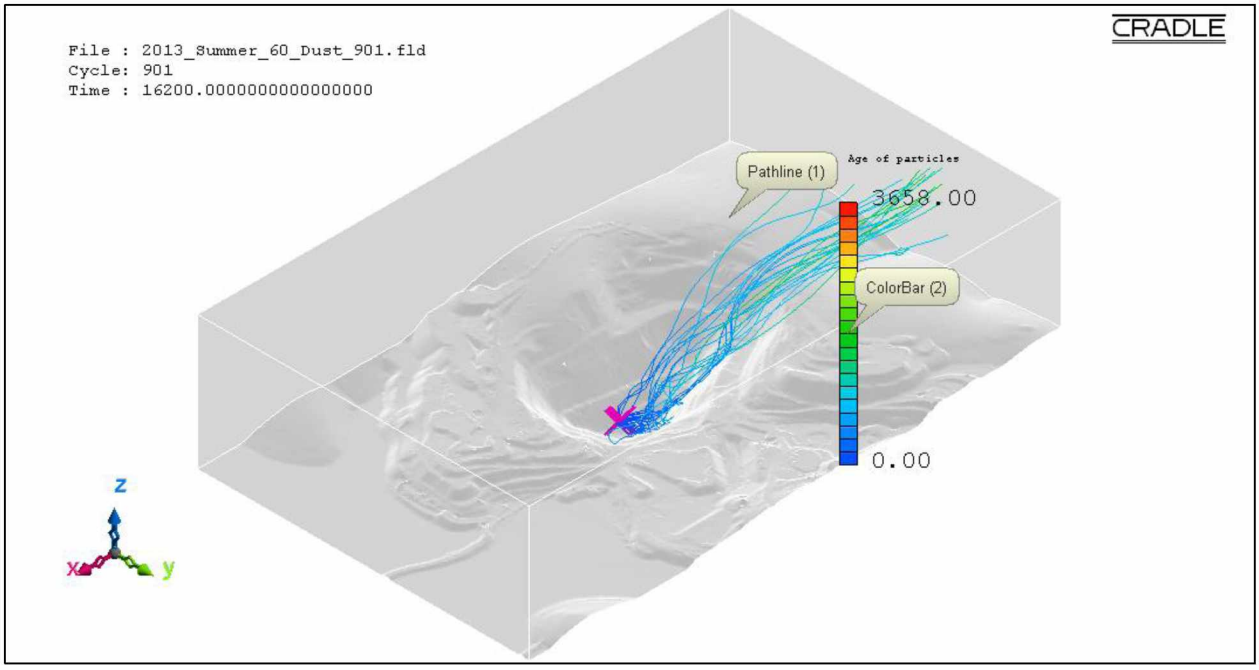

Figure B.159: Pathlines of PM_{10} dust particles from source location 4 in the actual open-pit domain for fair insolation summer condition using the LES method.

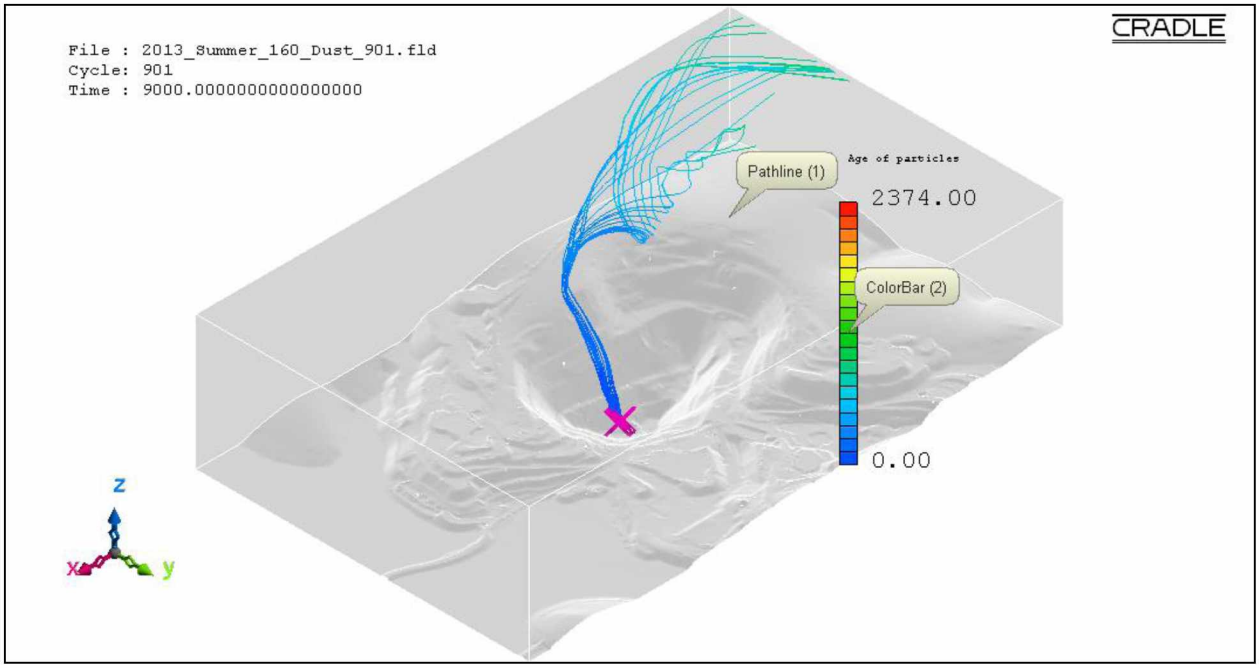

Figure B.160: Pathlines of PM_{10} dust particles from source location 4 in the actual open-pit domain for extreme insolation summer condition using the LES method.

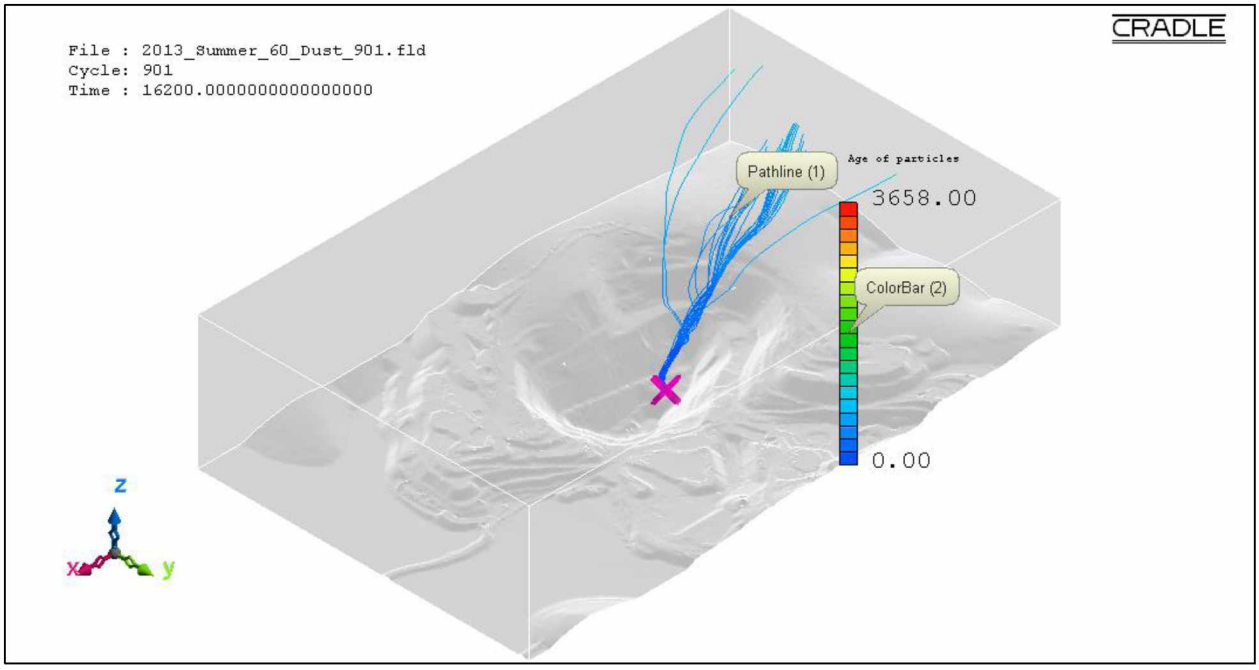

Figure B.161: Pathlines of PM_{10} dust particles from source location 5 in the actual open-pit domain for fair insolation summer condition using the LES method.

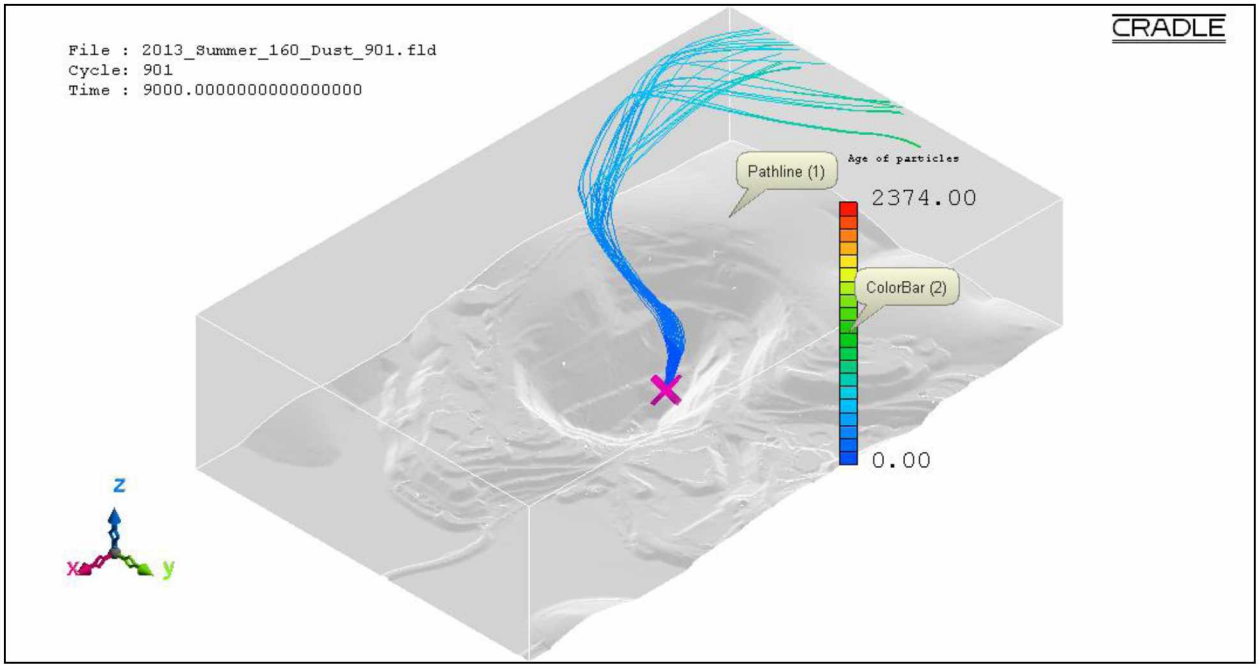

Figure B.162: Pathlines of PM_{10} dust particles from source location 5 in the actual open-pit domain for extreme insolation summer condition using the LES method.

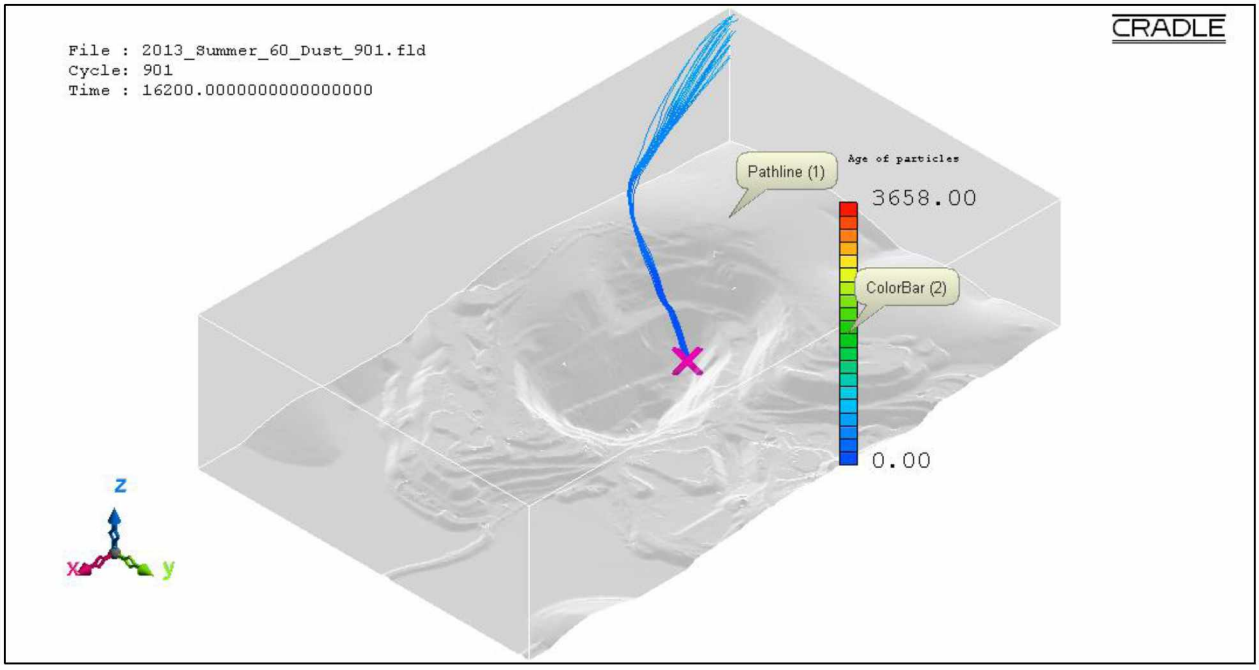

Figure B.163: Pathlines of PM_{10} dust particles from source location 6 in the actual open-pit domain for fair insolation summer condition using the LES method.

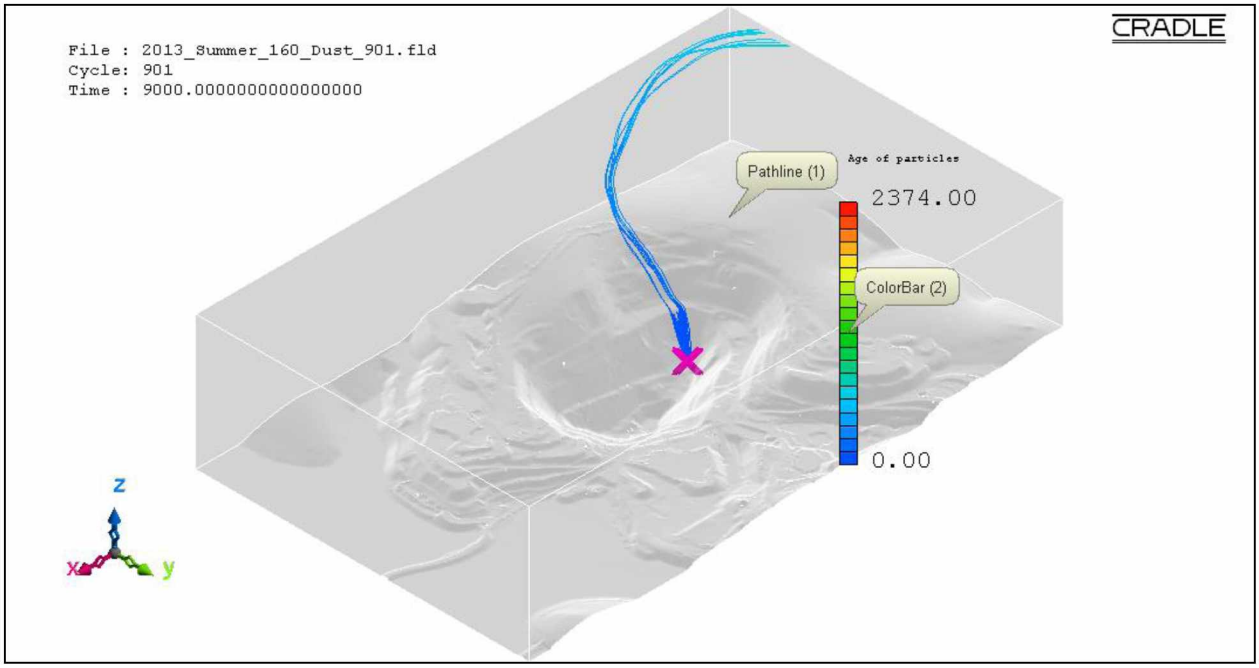

Figure B.164: Pathlines of PM_{10} dust particles from source location 6 in the actual open-pit domain for extreme insolation summer condition using the LES method.

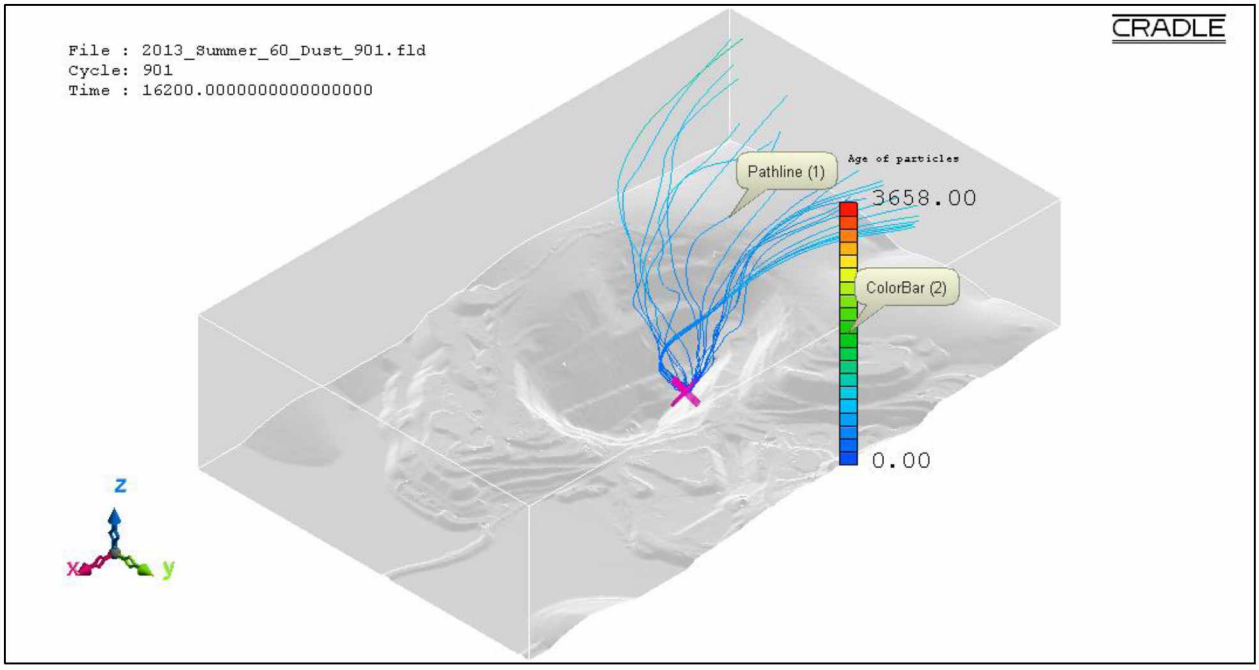

Figure B.165: Pathlines of PM_{10} dust particles from source location 7 in the actual open-pit domain for fair insolation summer condition using the LES method.

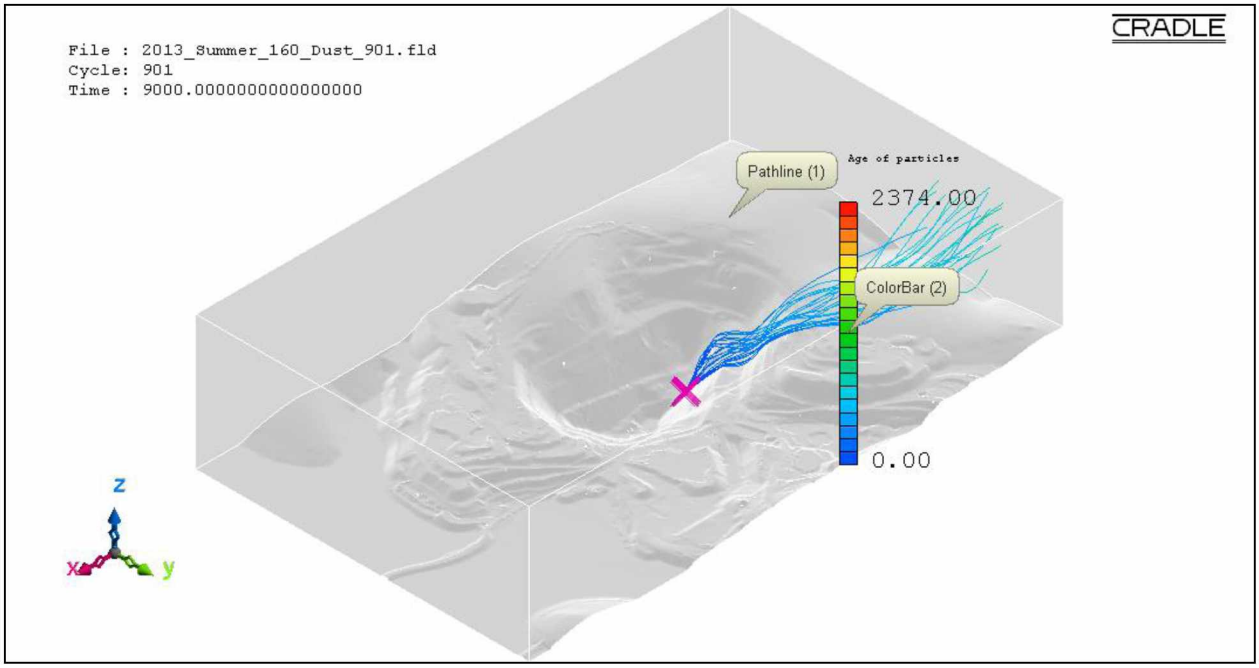

Figure B.166: Pathlines of PM_{10} dust particles from source location 7 in the actual open-pit domain for extreme insolation summer condition using the LES method.

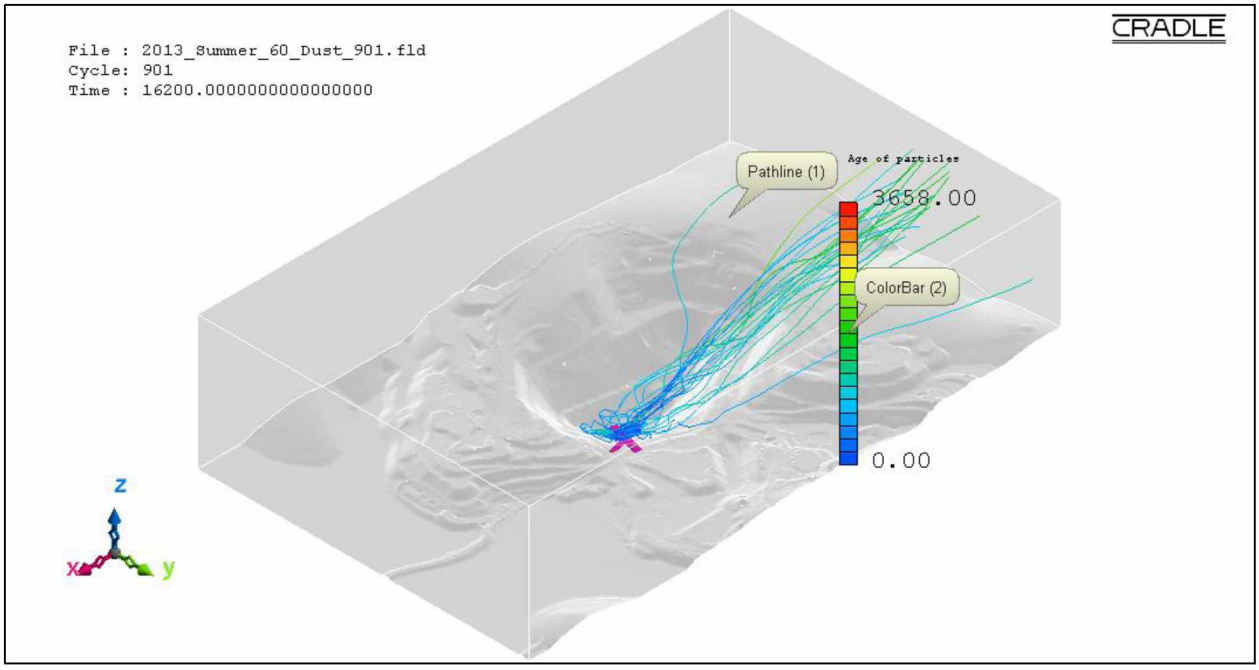

Figure B.167: Pathlines of PM_{10} dust particles from source location 8 in the actual open-pit domain for fair insolation summer condition using the LES method.

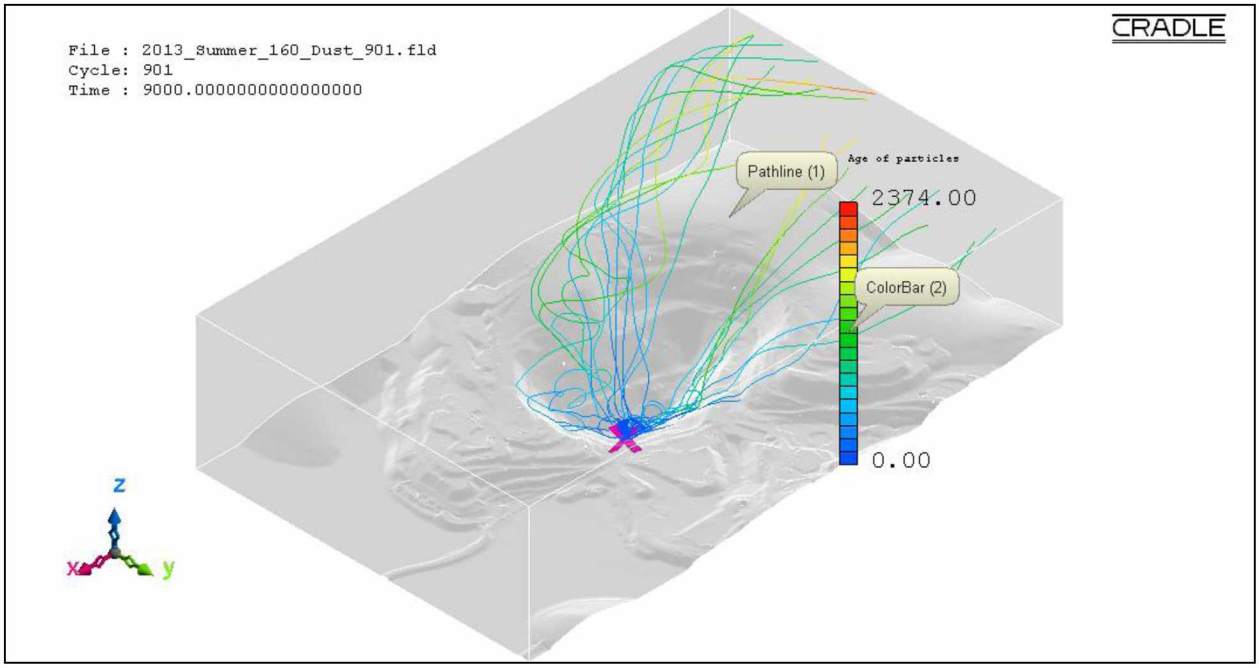

Figure B.168: Pathlines of PM_{10} dust particles from source location 8 in the actual open-pit domain for extreme insolation summer condition using the LES method.

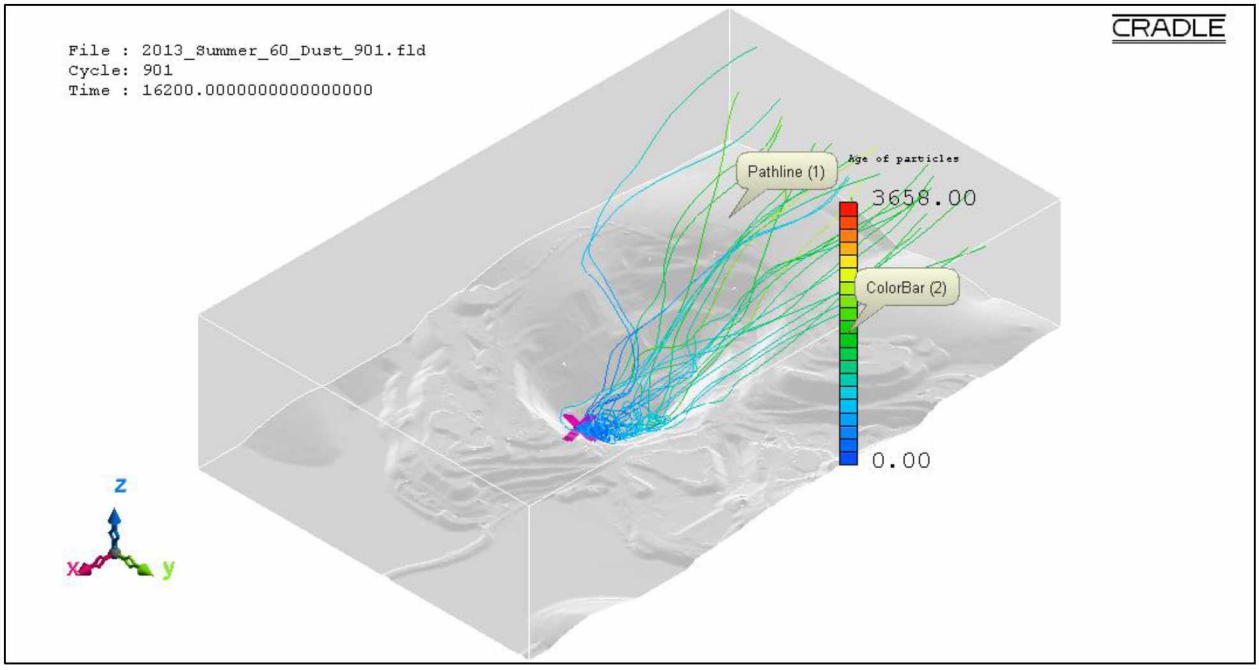

Figure B.169: Pathlines of PM_{10} dust particles from source location 9 in the actual open-pit domain for fair insolation summer condition using the LES method.

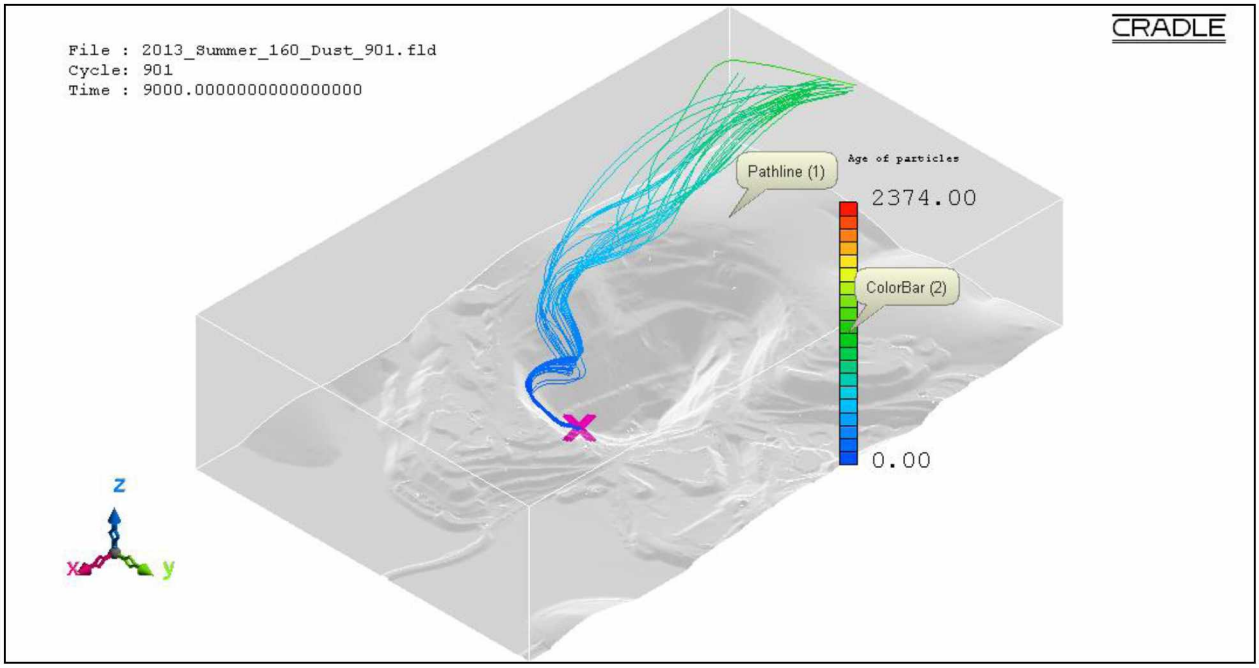

Figure B.170: Pathlines of PM_{10} dust particles from source location 9 in the actual open-pit domain for extreme insolation summer condition using the LES method.

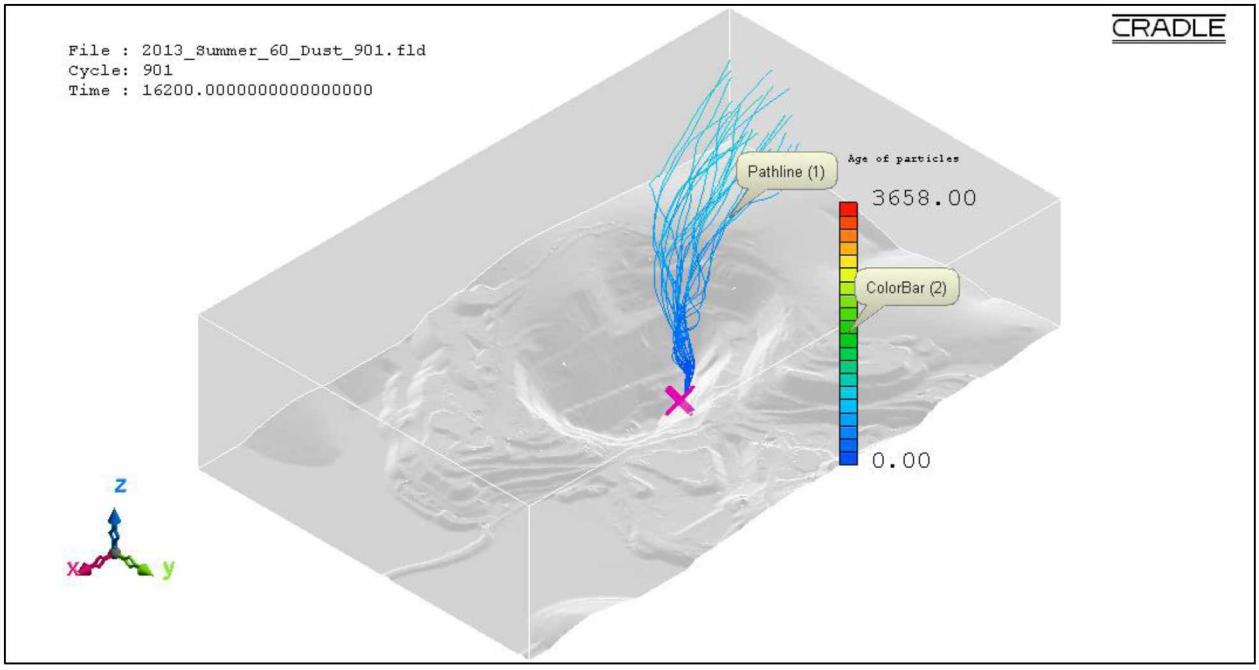

Figure B.171: Pathlines of PM_{10} dust particles from source location 10 in the actual open-pit domain for fair insolation summer condition using the LES method.

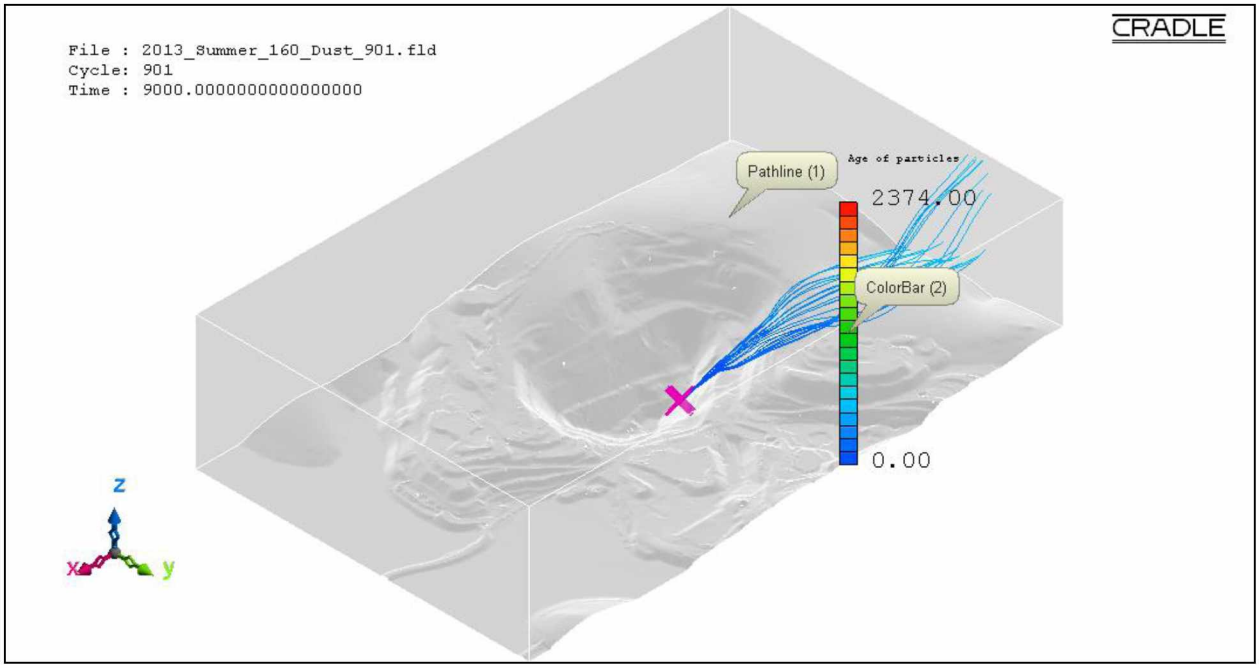

Figure B.172: Pathlines of PM_{10} dust particles from source location 10 in the actual open-pit domain for extreme insolation summer condition using the LES method.

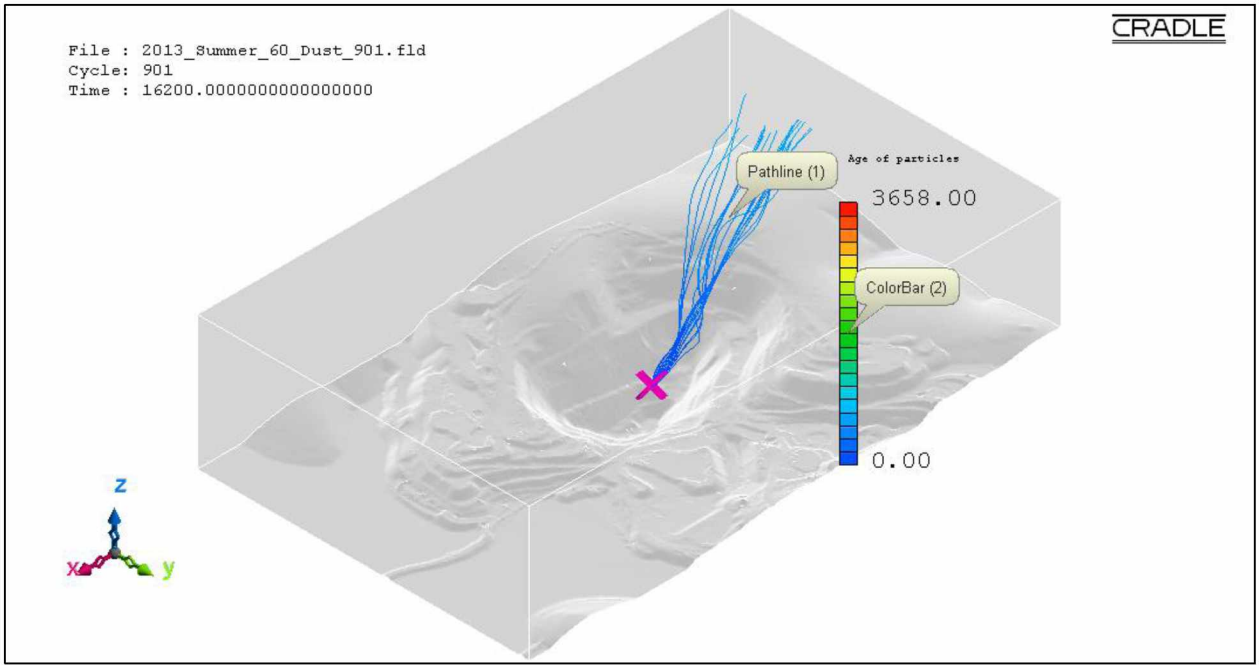

Figure B.173: Pathlines of PM_{10} dust particles from source location 11 in the actual open-pit domain for fair insolation summer condition using the LES method.

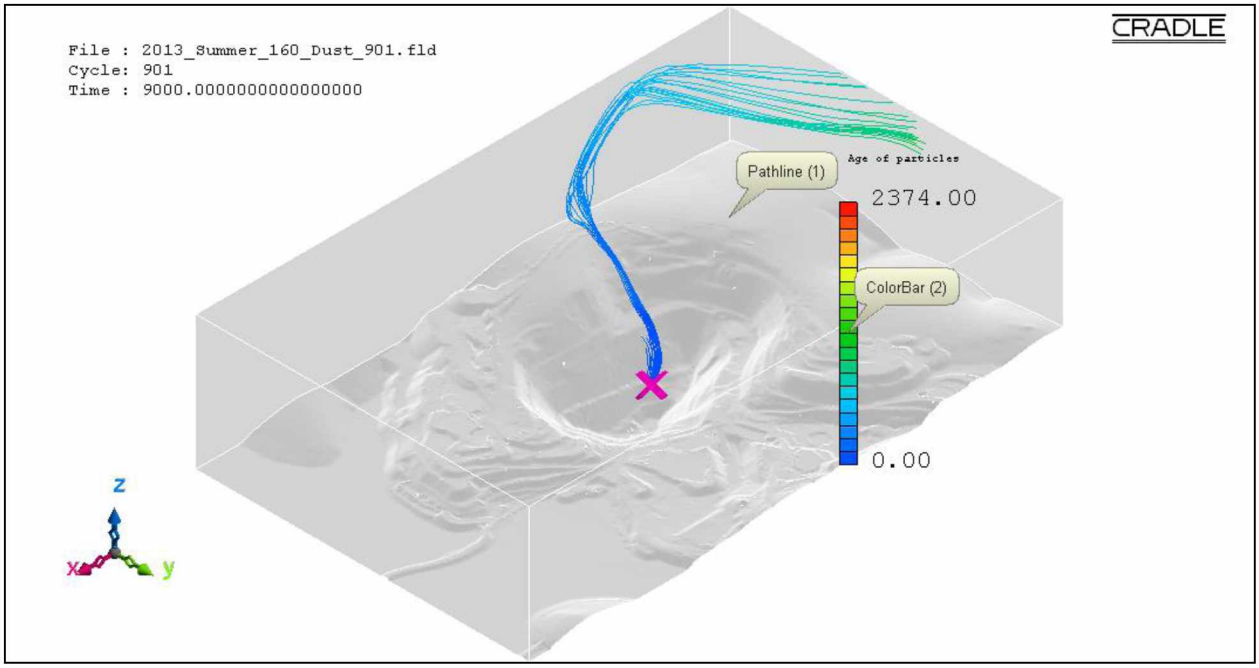

Figure B.174: Pathlines of PM_{10} dust particles from source location 11 in the actual open-pit domain for extreme insolation summer condition using the LES method.

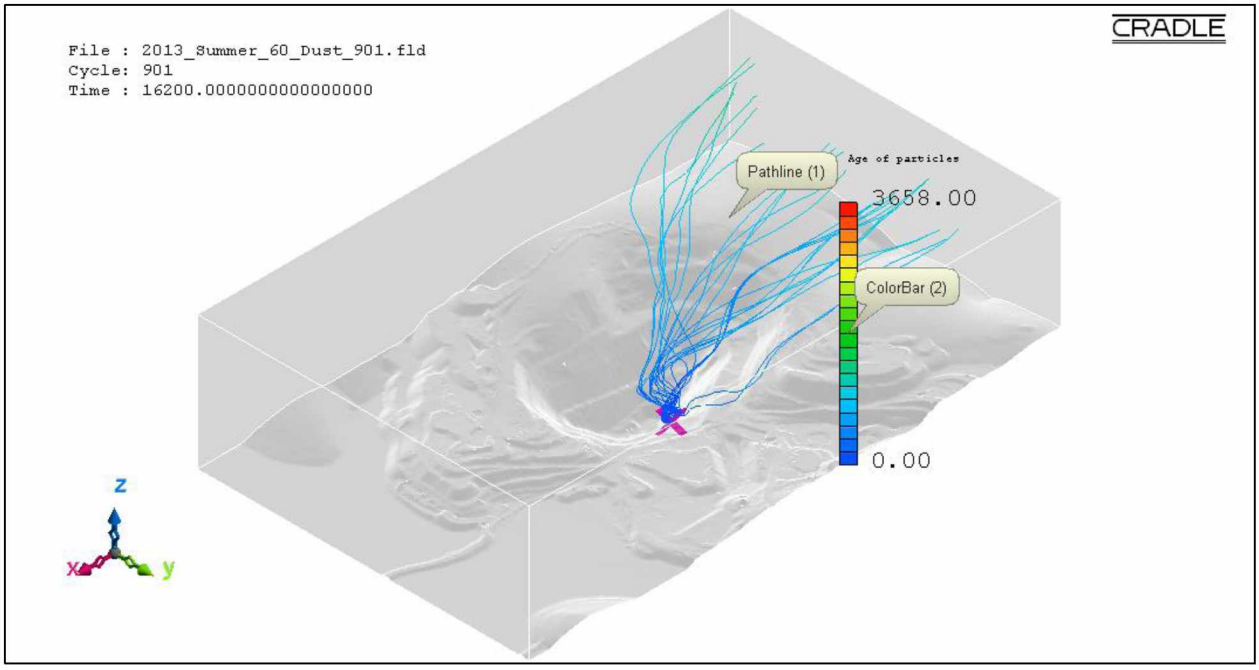

Figure B.175: Pathlines of PM_{10} dust particles from source location 12 in the actual open-pit domain for fair insolation summer condition using the LES method.

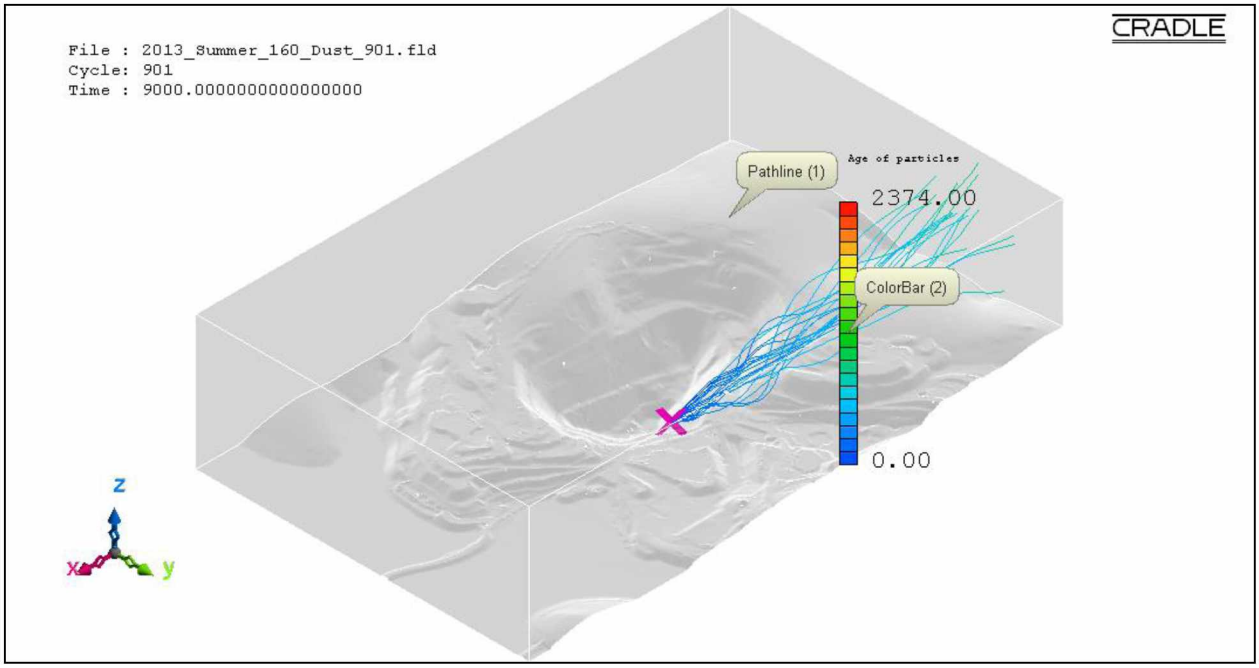

Figure B.176: Pathlines of PM_{10} dust particles from source location 12 in the actual open-pit domain for extreme insolation summer condition using the LES method.

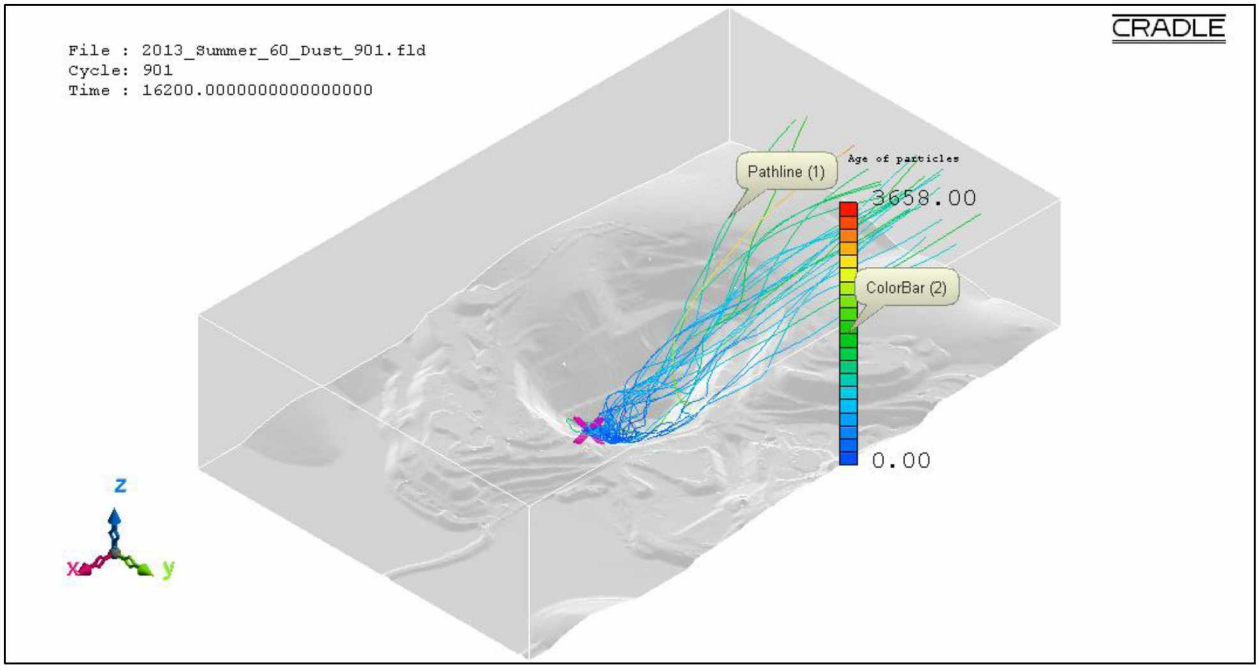

Figure B.177: Pathlines of PM_{10} dust particles from source location 13 in the actual open-pit domain for fair insolation summer condition using the LES method.

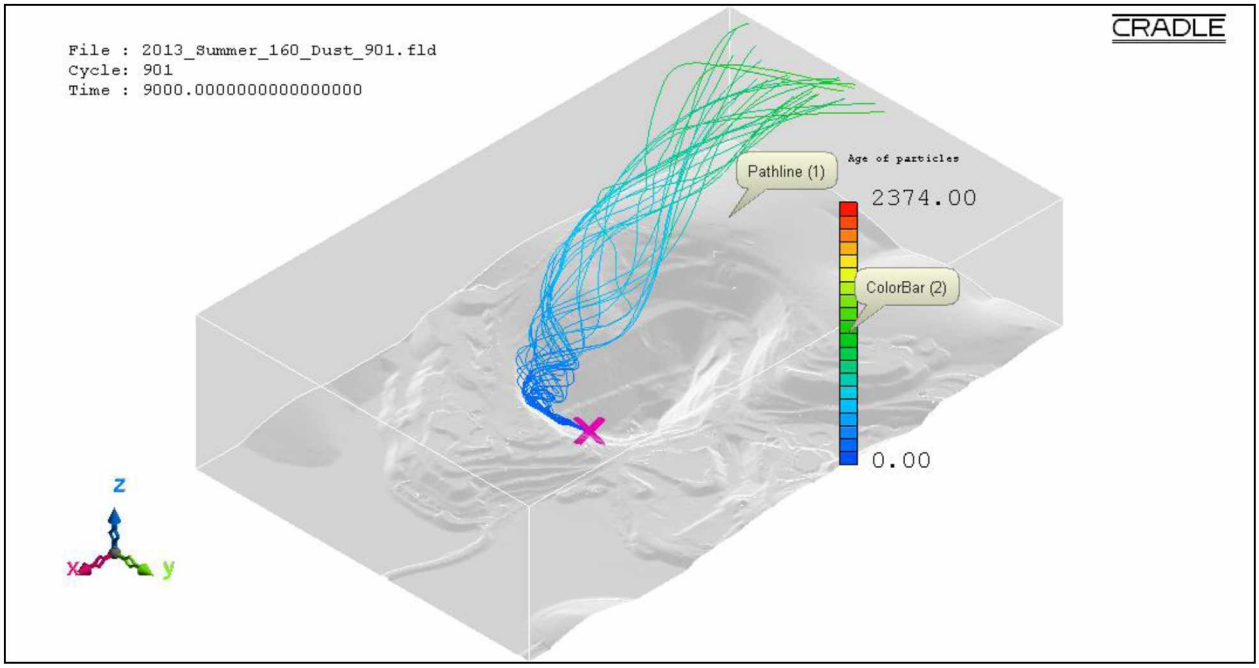

Figure B.178: Pathlines of PM_{10} dust particles from source location 13 in the actual open-pit domain for extreme insolation summer condition using the LES method.

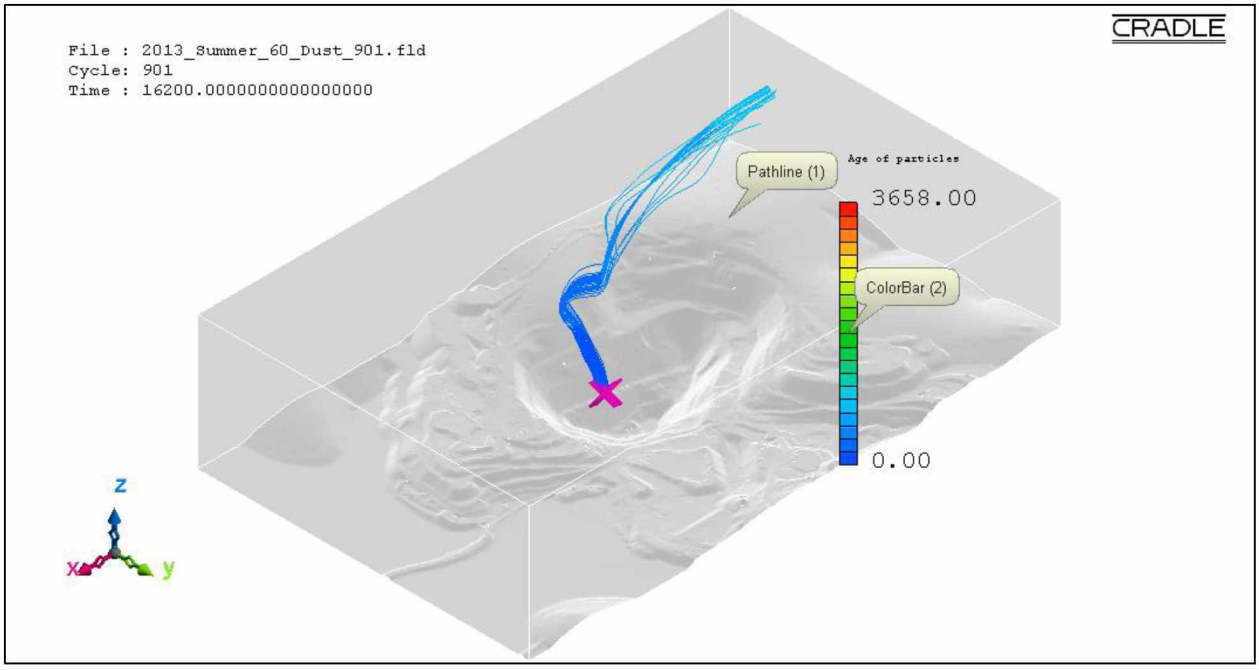

Figure B.179: Pathlines of PM_{10} dust particles from source location 14 in the actual open-pit domain for fair insolation summer condition using the LES method.

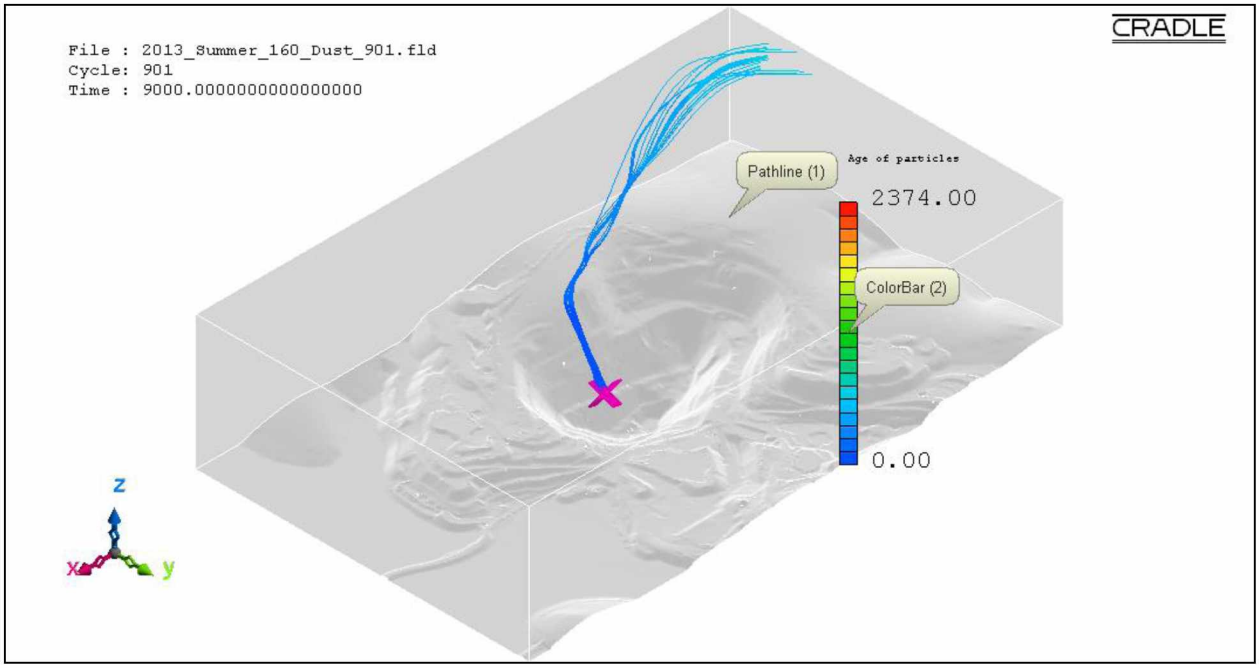

Figure B.180: Pathlines of PM_{10} dust particles from source location 14 in the actual open-pit domain for extreme insolation summer condition using the LES method.

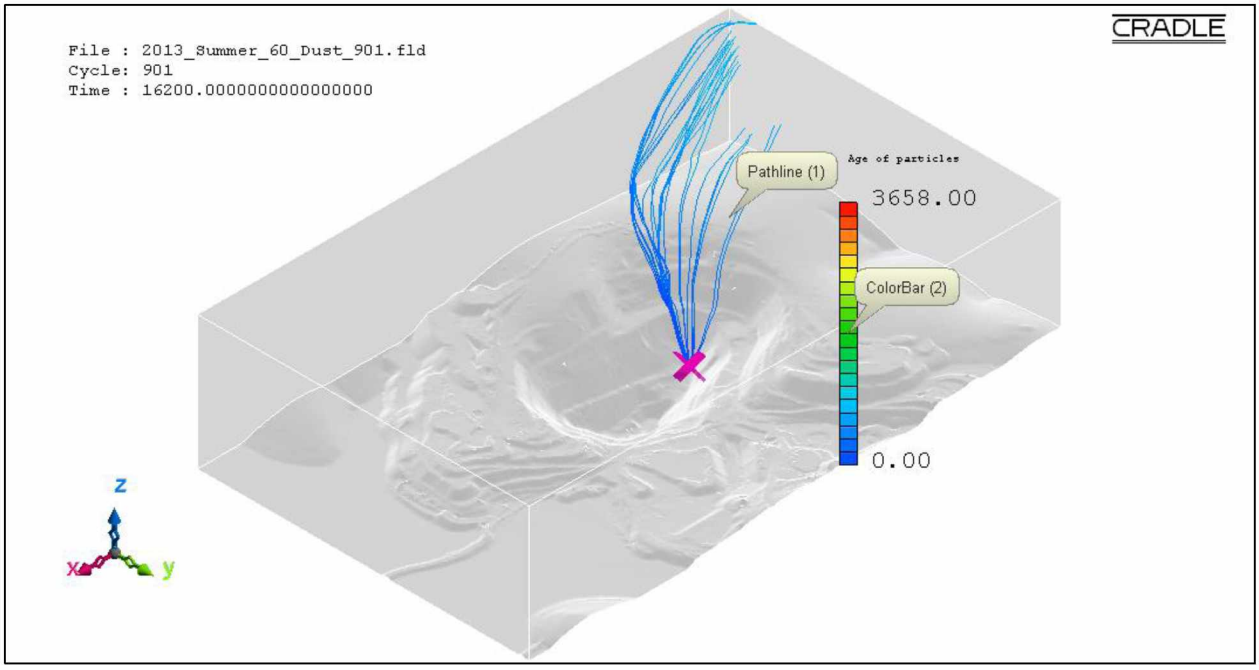

Figure B.181: Pathlines of PM_{10} dust particles from source location 15 in the actual open-pit domain for fair insolation summer condition using the LES method.

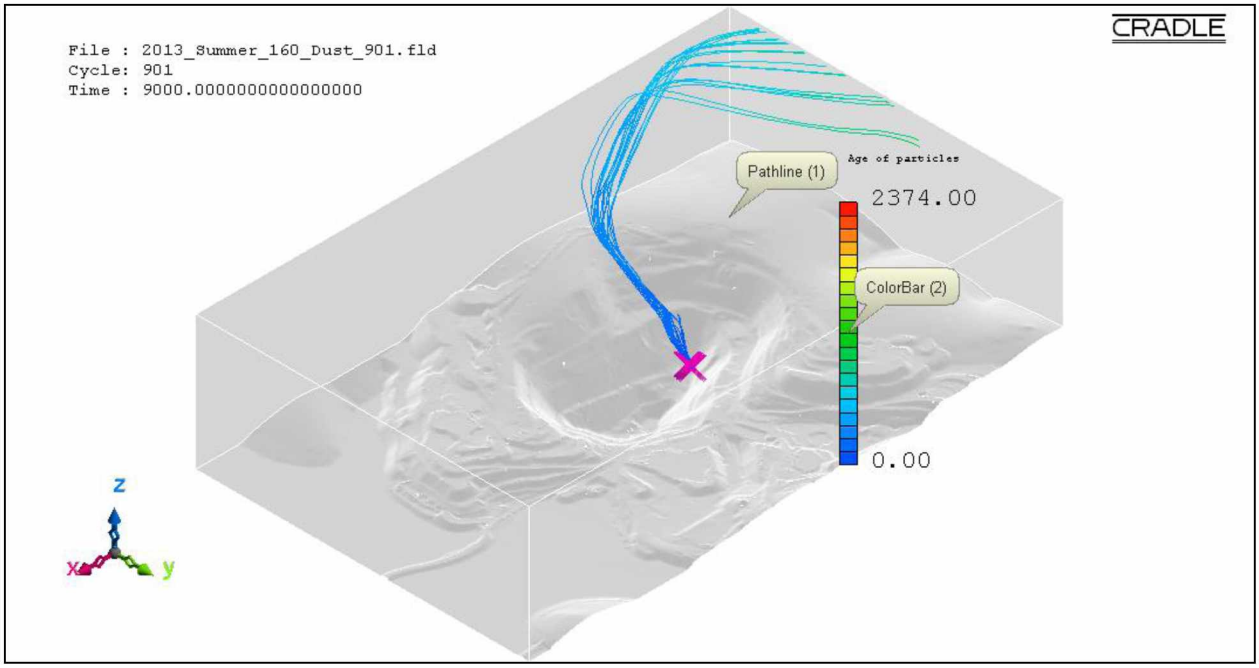

Figure B.182: Pathlines of PM_{10} dust particles from source location 15 in the actual open-pit domain for extreme insolation summer condition using the LES method.

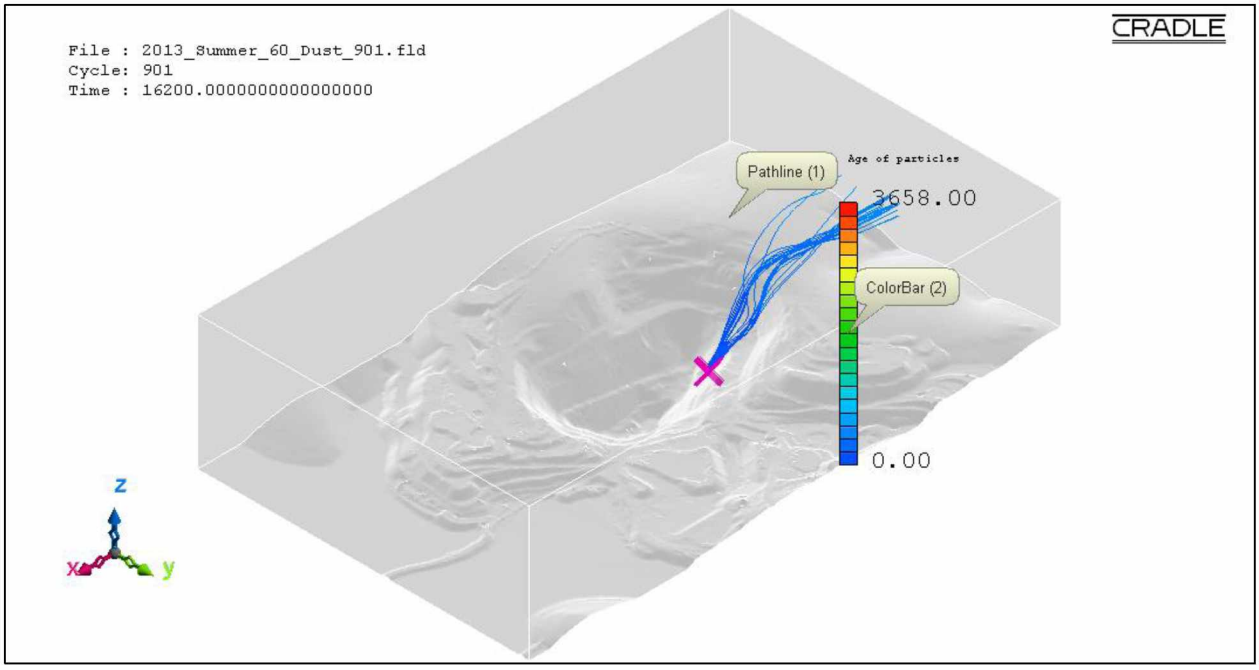

Figure B.183: Pathlines of PM_{10} dust particles from source location 16 in the actual open-pit domain for fair insolation summer condition using the LES method.

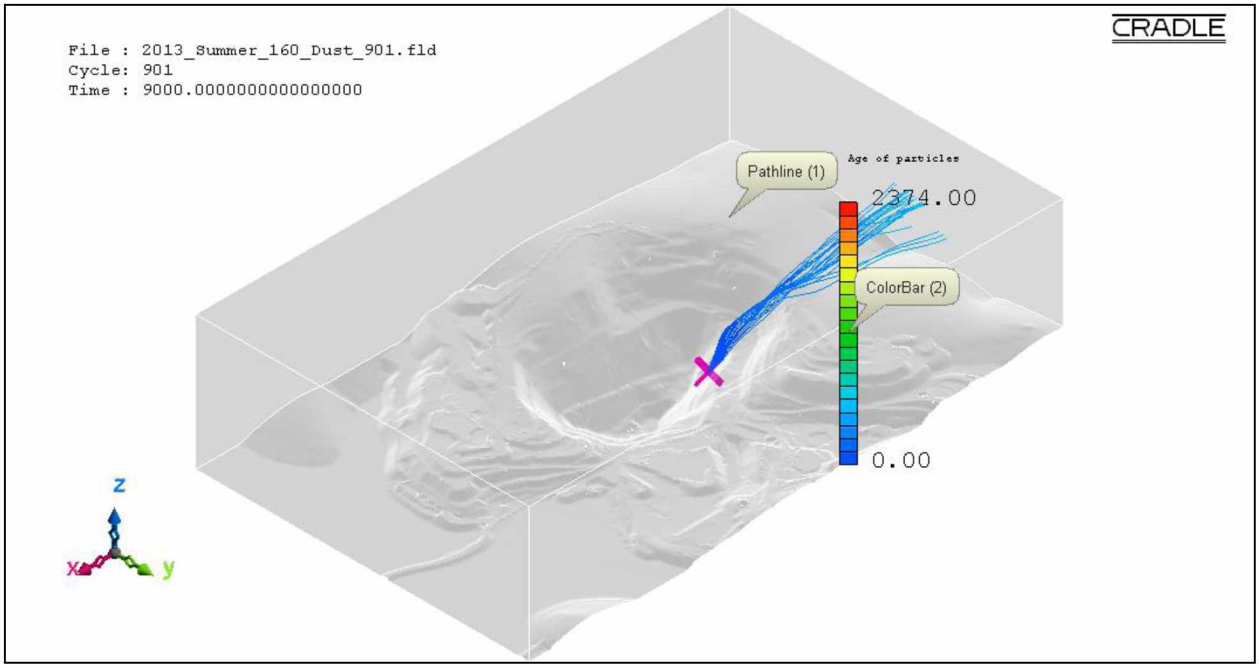

Figure B.184: Pathlines of PM_{10} dust particles from source location 16 in the actual open-pit domain for extreme insolation summer condition using the LES method.

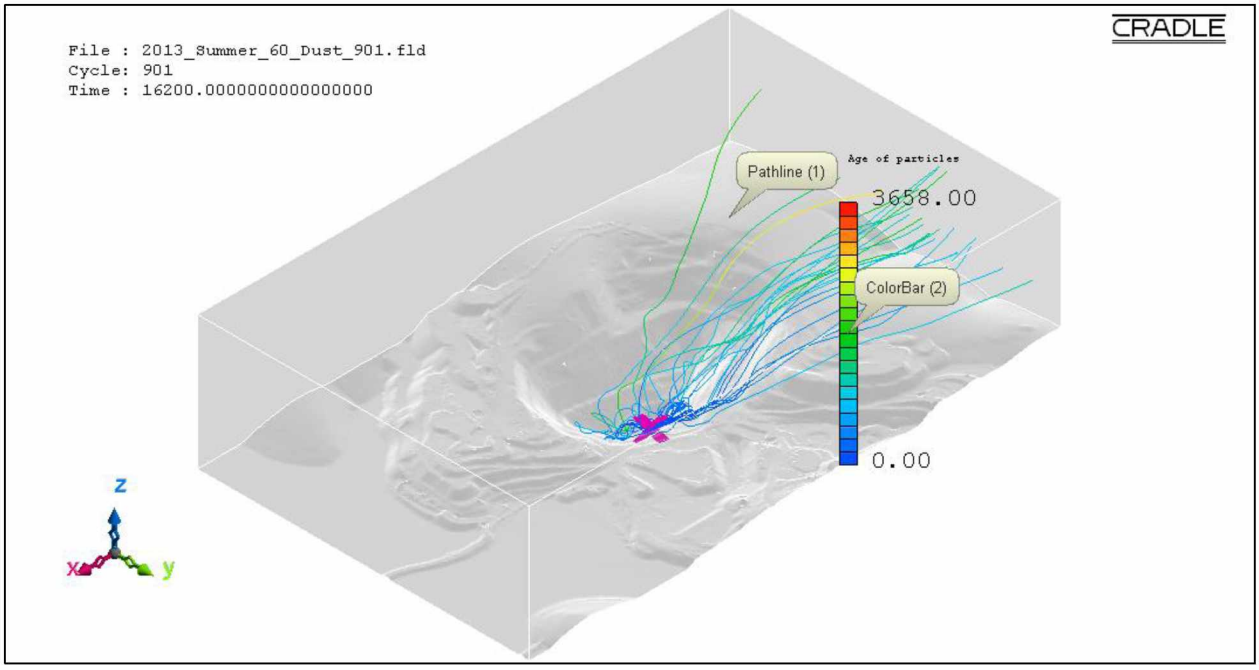

Figure B.185: Pathlines of PM_{10} dust particles from source location 17 in the actual open-pit domain for fair insolation summer condition using the LES method.

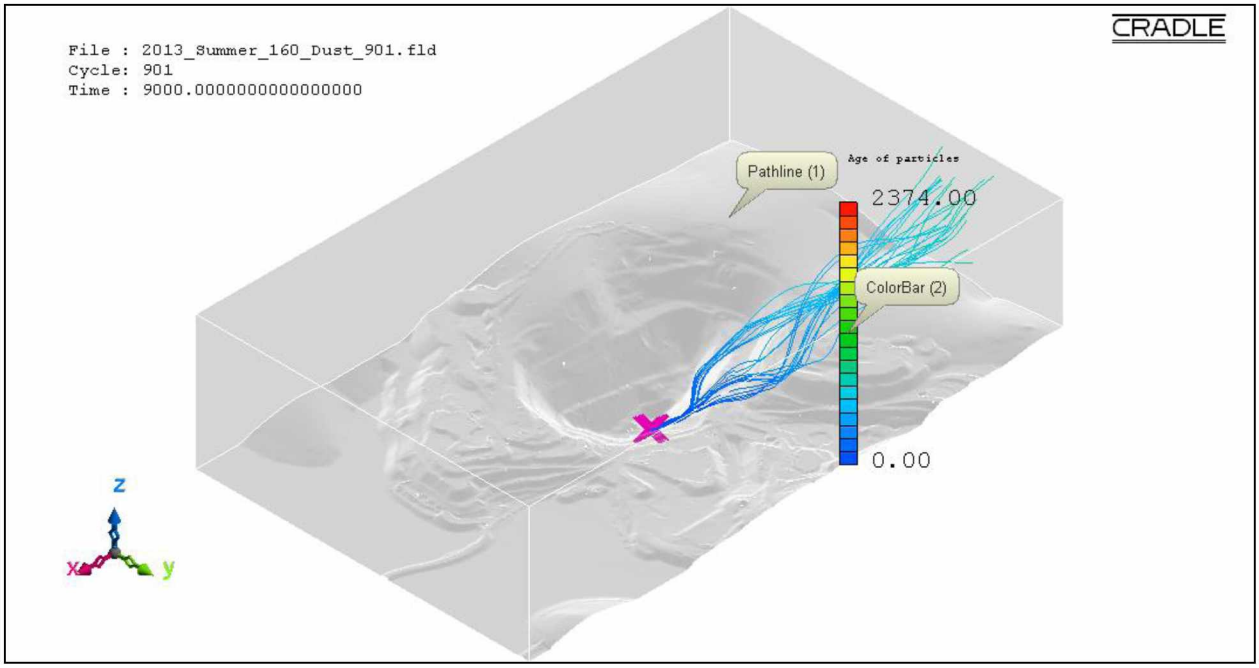

Figure B.186: Pathlines of PM_{10} dust particles from source location 17 in the actual open-pit domain for extreme insolation summer condition using the LES method.

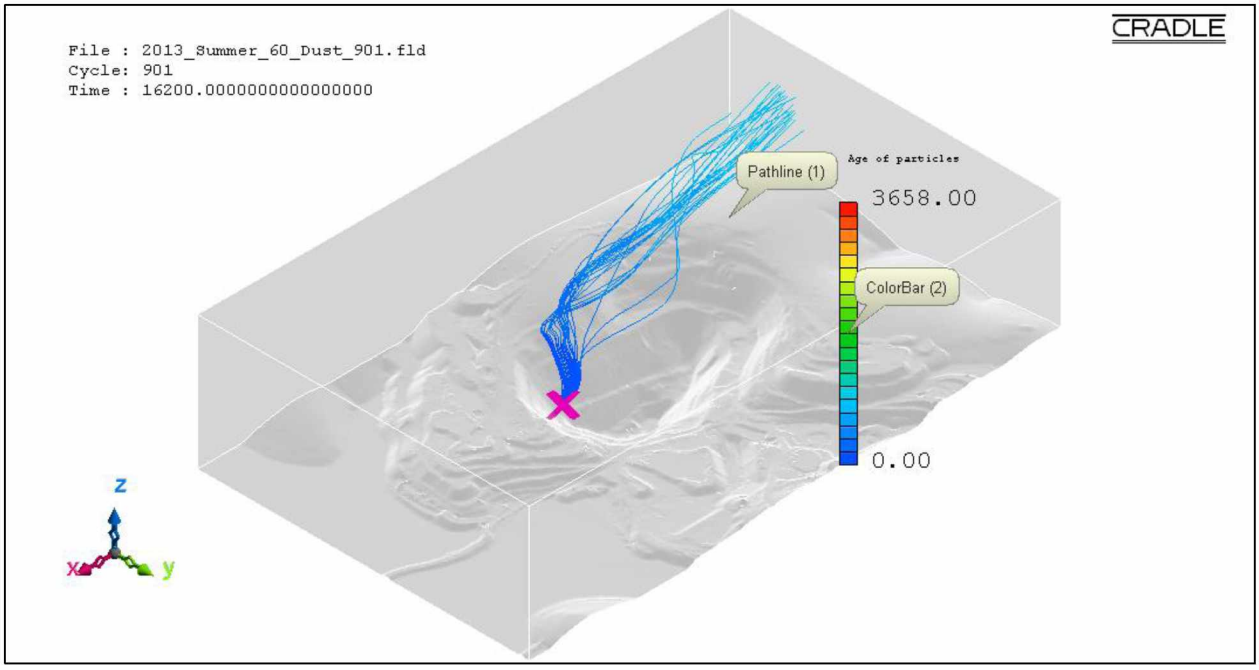

Figure B.187: Pathlines of PM_{10} dust particles from source location 18 in the actual open-pit domain for fair insolation summer condition using the LES method.

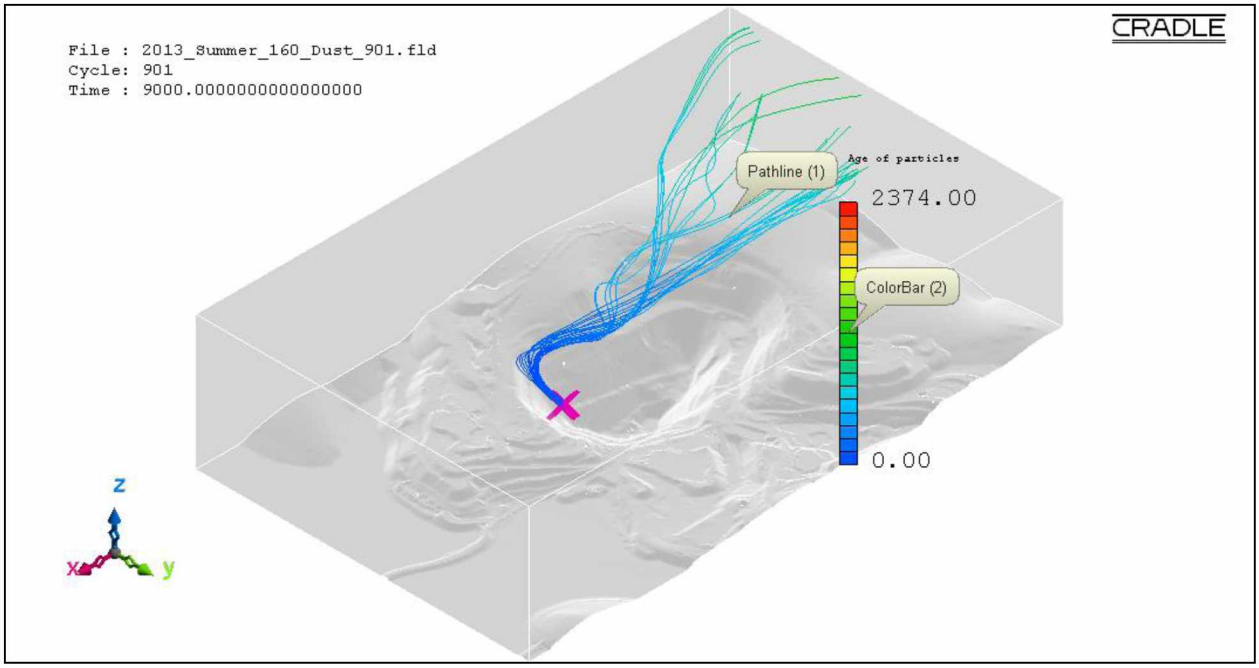

Figure B.188: Pathlines of PM_{10} dust particles from source location 18 in the actual open-pit domain for extreme insolation summer condition using the LES method.

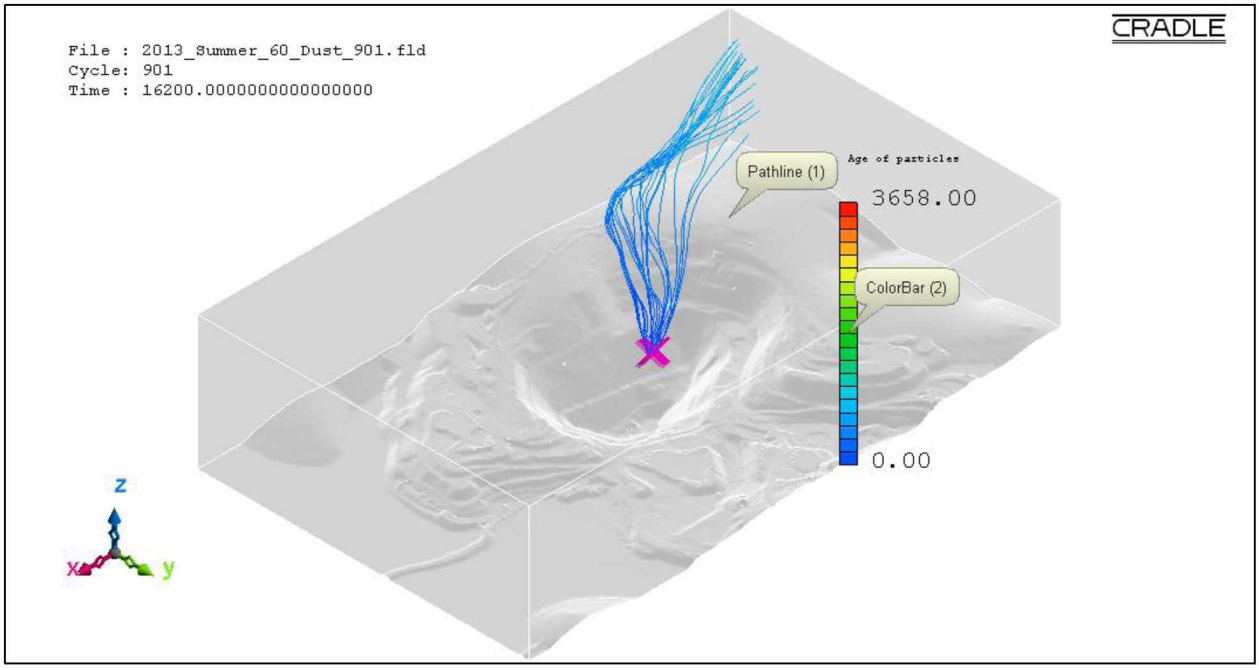

Figure B.189: Pathlines of PM_{10} dust particles from source location 19 in the actual open-pit domain for fair insolation summer condition using the LES method.

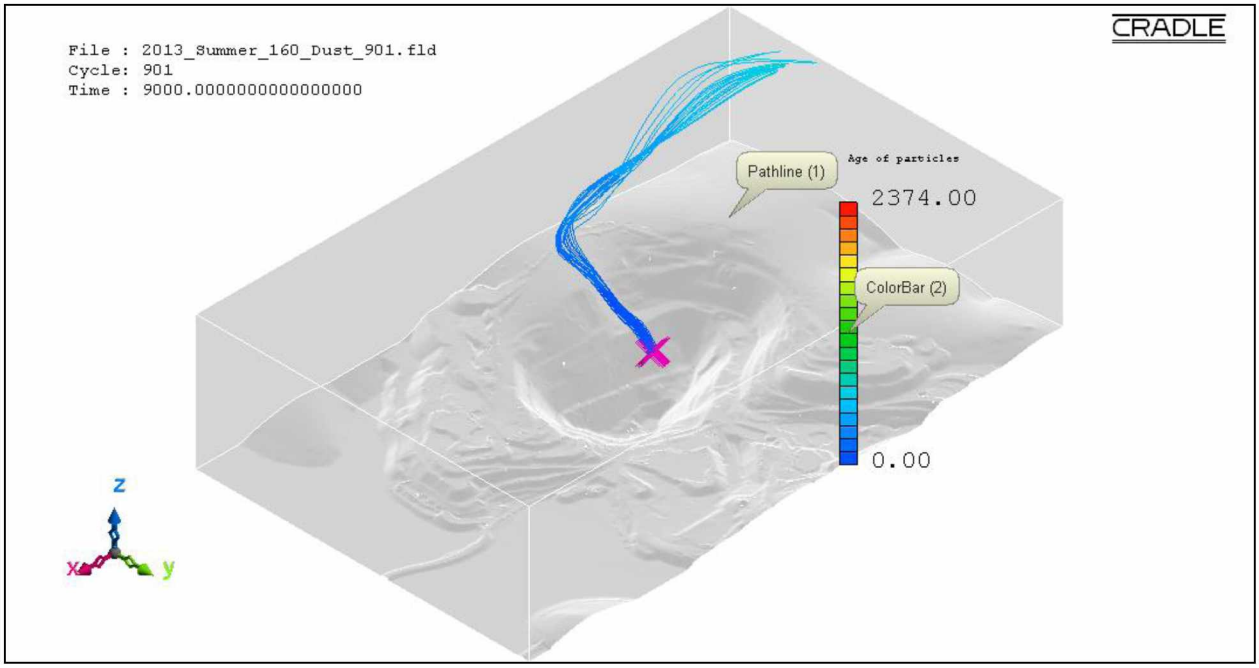

Figure B.190: Pathlines of PM_{10} dust particles from source location 19 in the actual open-pit domain for extreme insolation summer condition using the LES method.

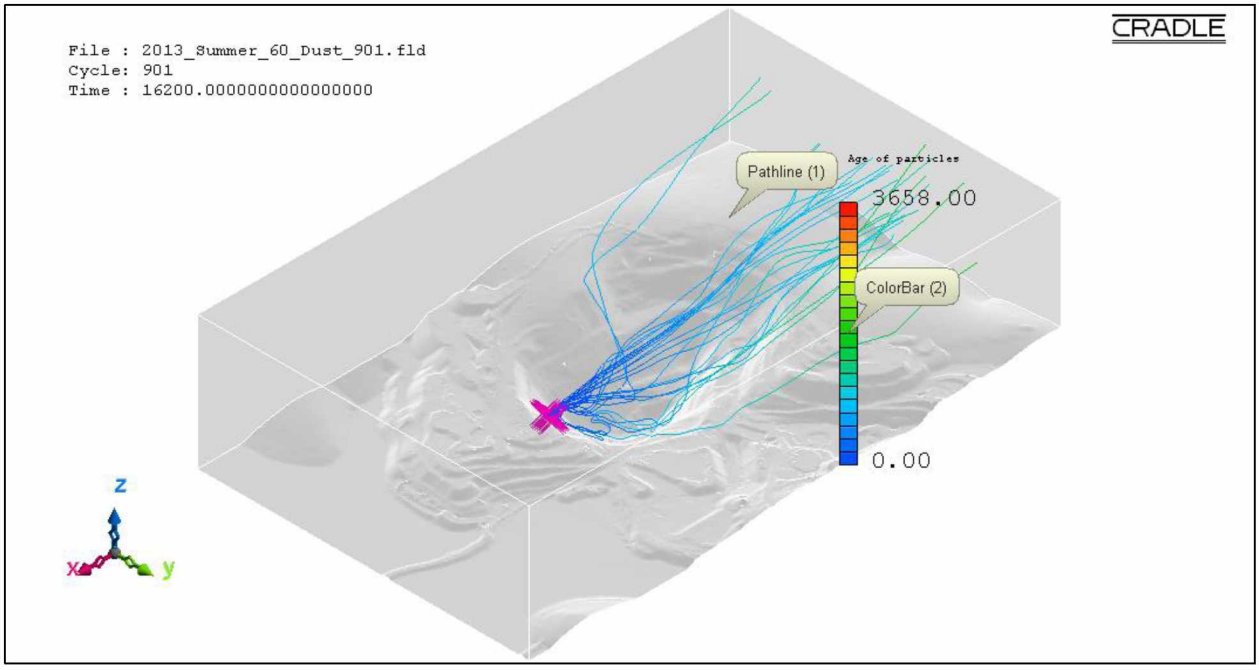

Figure B.191: Pathlines of PM_{10} dust particles from source location 20 in the actual open-pit domain for fair insolation summer condition using the LES method.

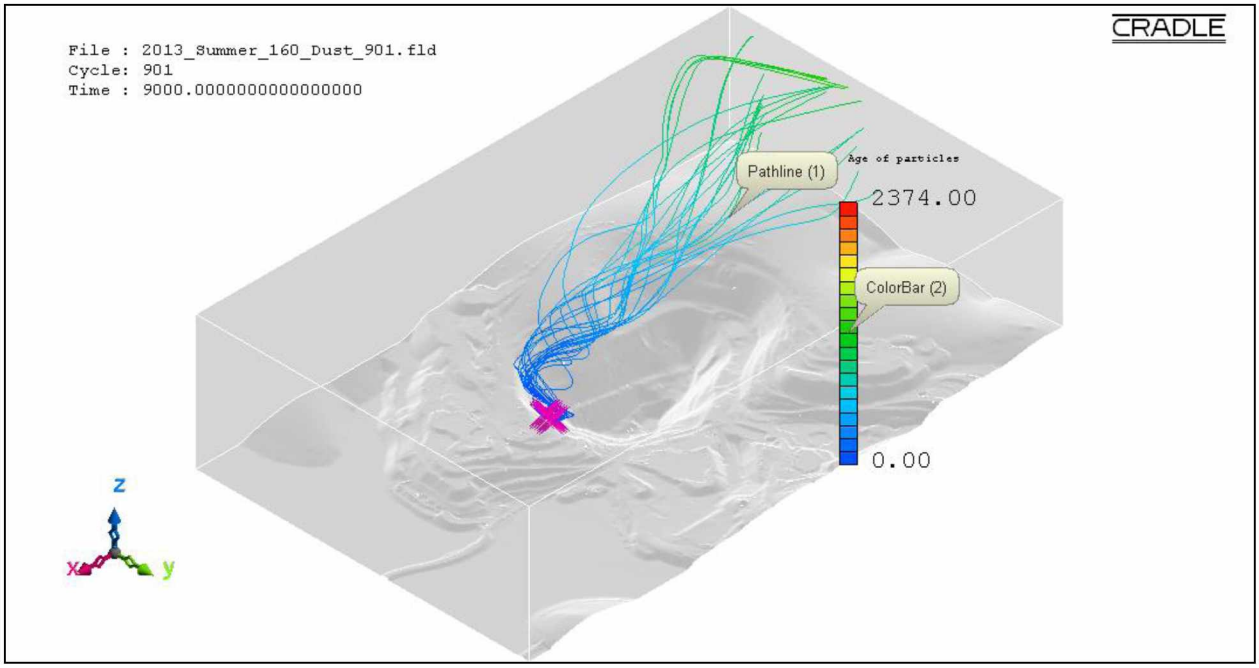

Figure B.192: Pathlines of PM_{10} dust particles from source location 20 in the actual open-pit domain for extreme insolation summer condition using the LES method.

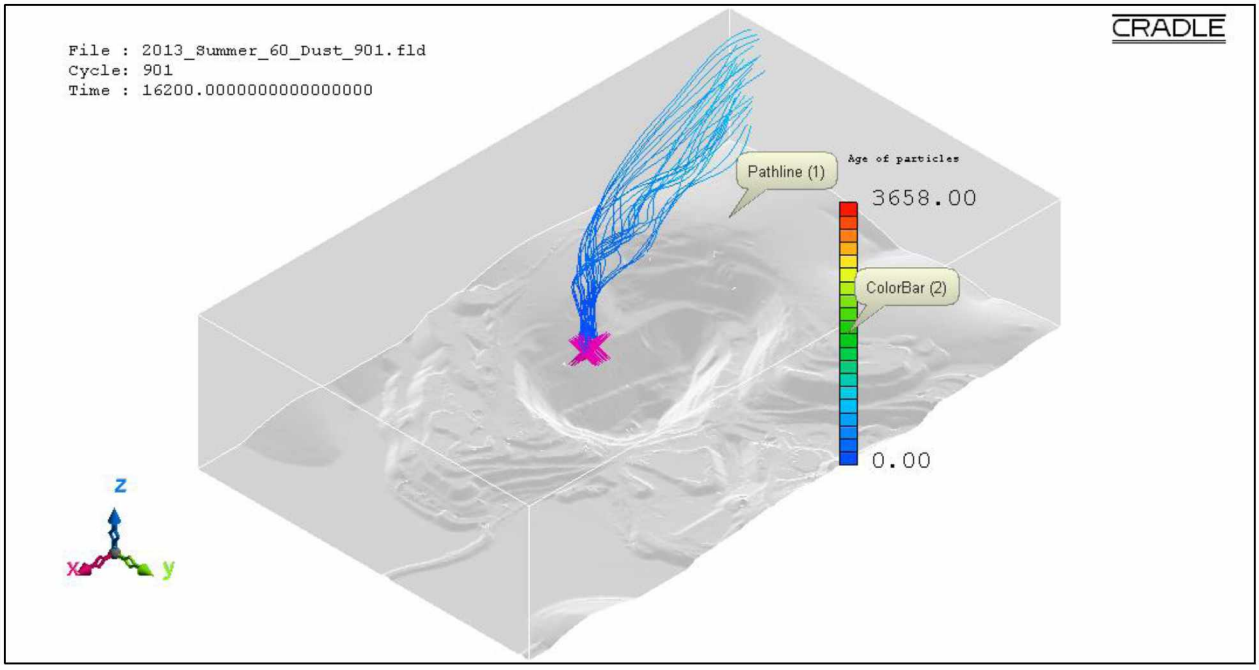

Figure B.193: Pathlines of PM_{10} dust particles from source location 21 in the actual open-pit domain for fair insolation summer condition using the LES method.

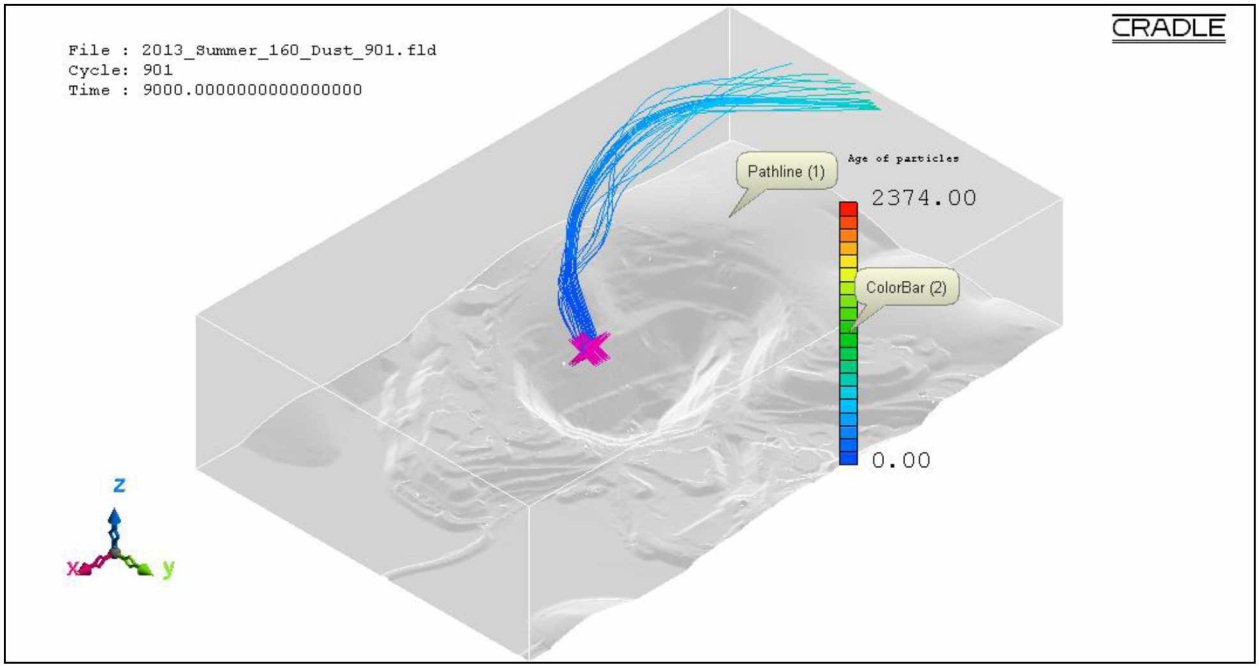

Figure B.194: Pathlines of PM_{10} dust particles from source location 21 in the actual open-pit domain for extreme insolation summer condition using the LES method.

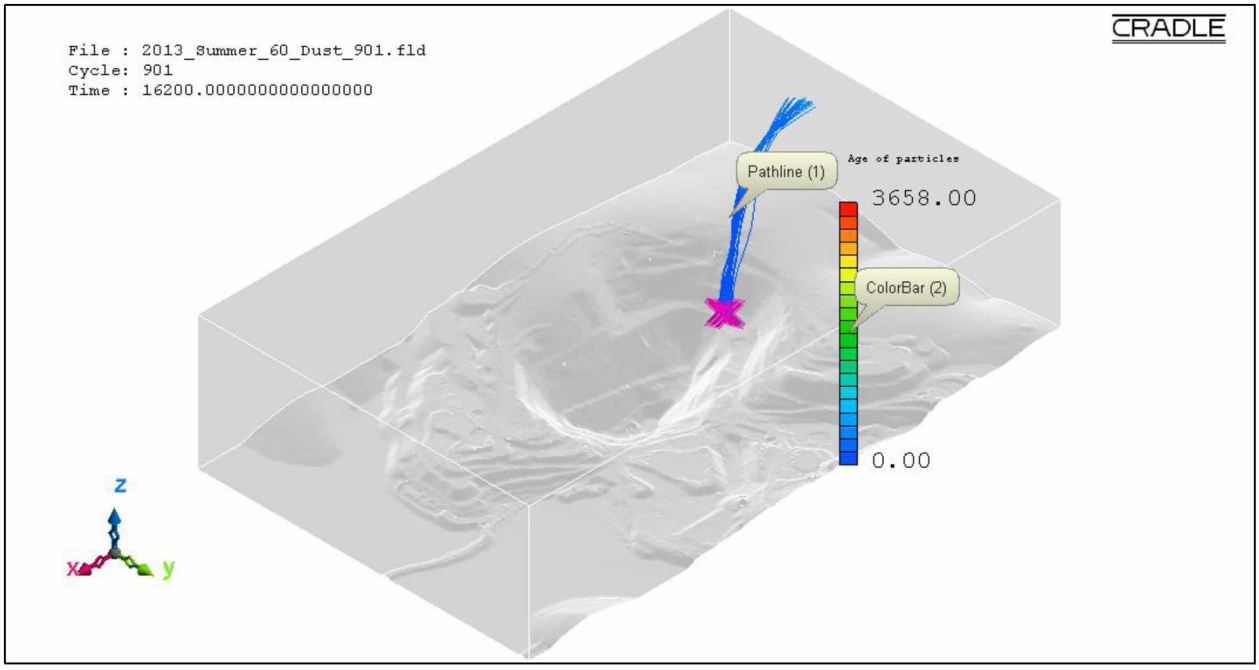

Figure B.195: Pathlines of PM_{10} dust particles from source location 22 in the actual open-pit domain for fair insolation summer condition using the LES method.

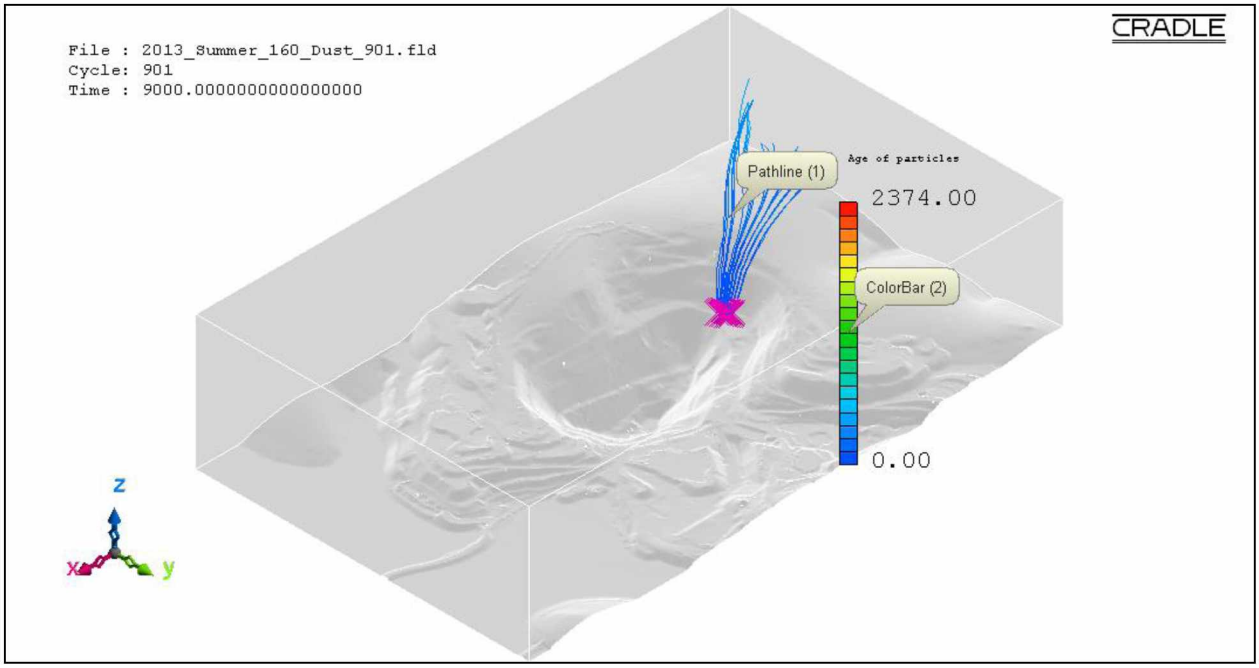

Figure B.196: Pathlines of PM_{10} dust particles from source location 22 in the actual open-pit domain for extreme insolation summer condition using the LES method.

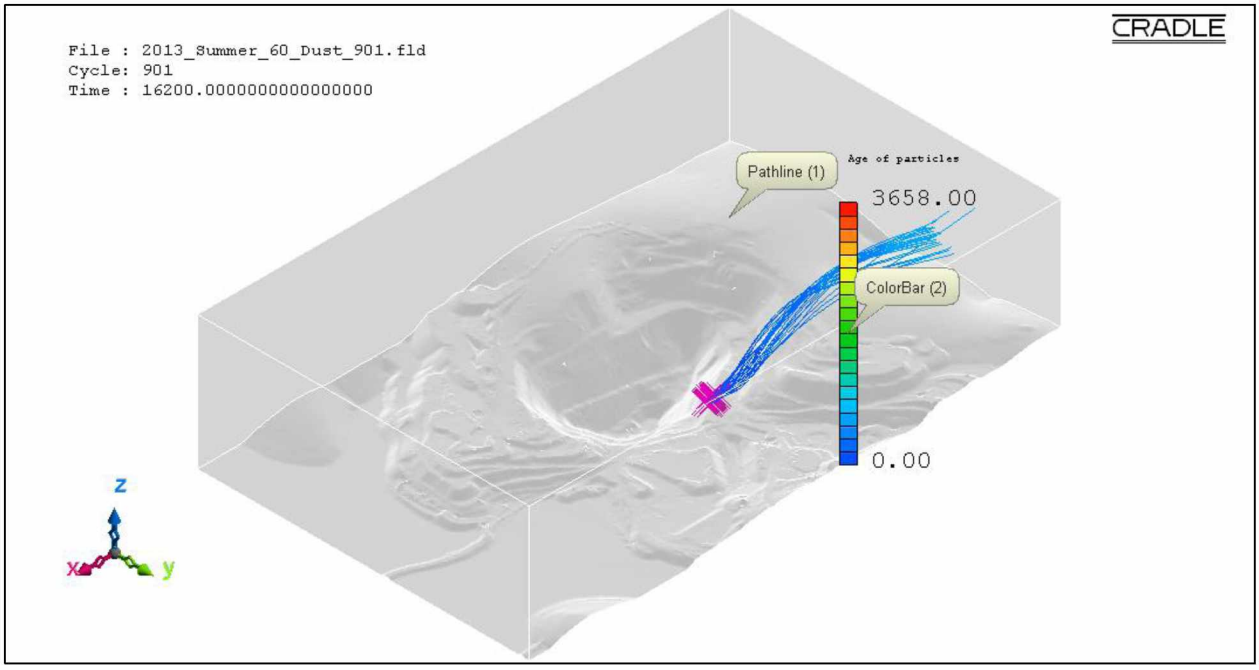

Figure B.197: Pathlines of PM_{10} dust particles from source location 23 in the actual open-pit domain for fair insolation summer condition using the LES method.

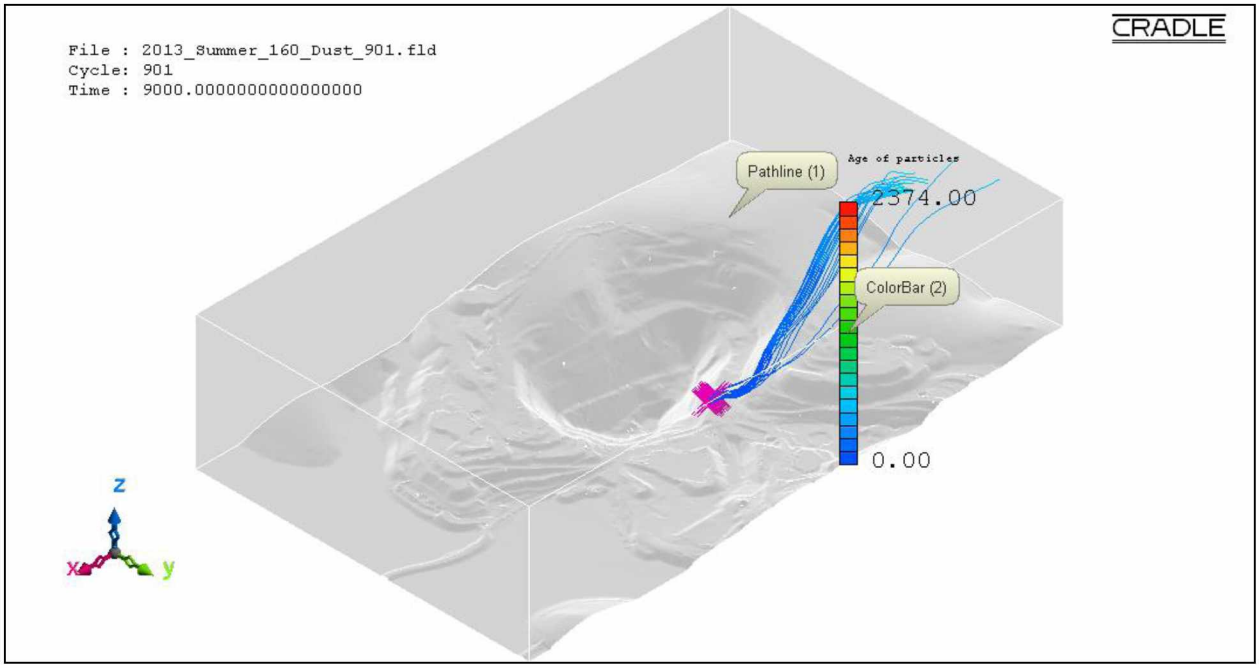

Figure B.198: Pathlines of PM_{10} dust particles from source location 23 in the actual open-pit domain for extreme insolation summer condition using the LES method.

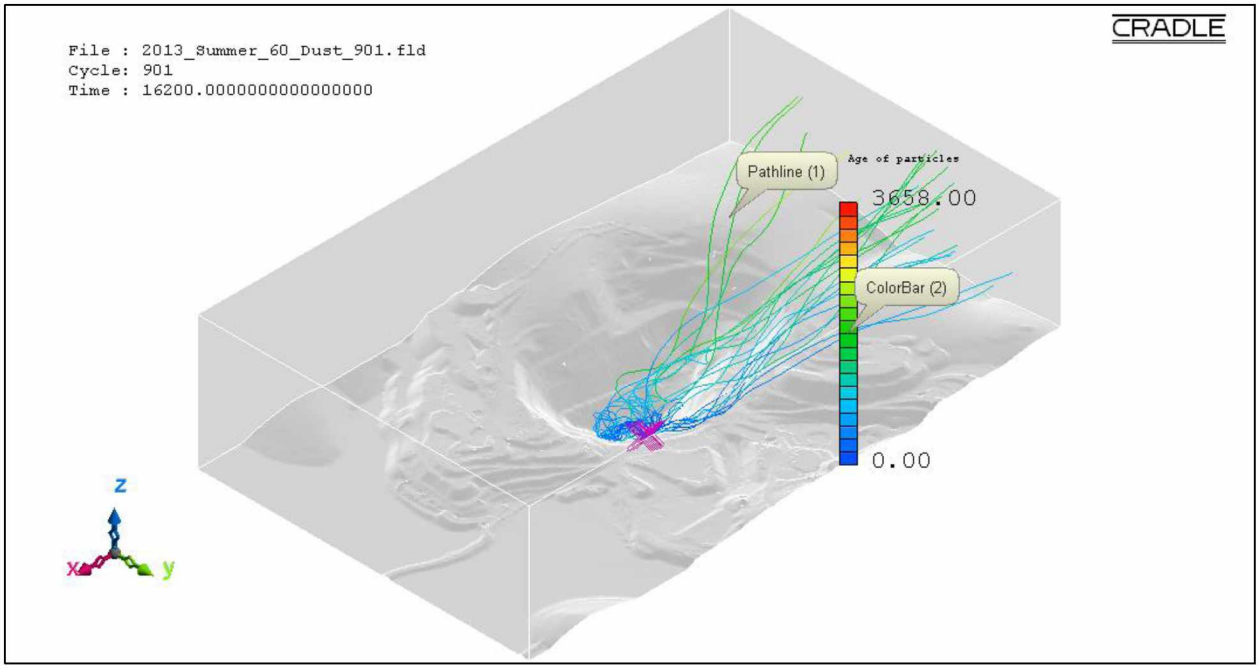

Figure B.199: Pathlines of PM_{10} dust particles from source location 24 in the actual open-pit domain for fair insolation summer condition using the LES method.

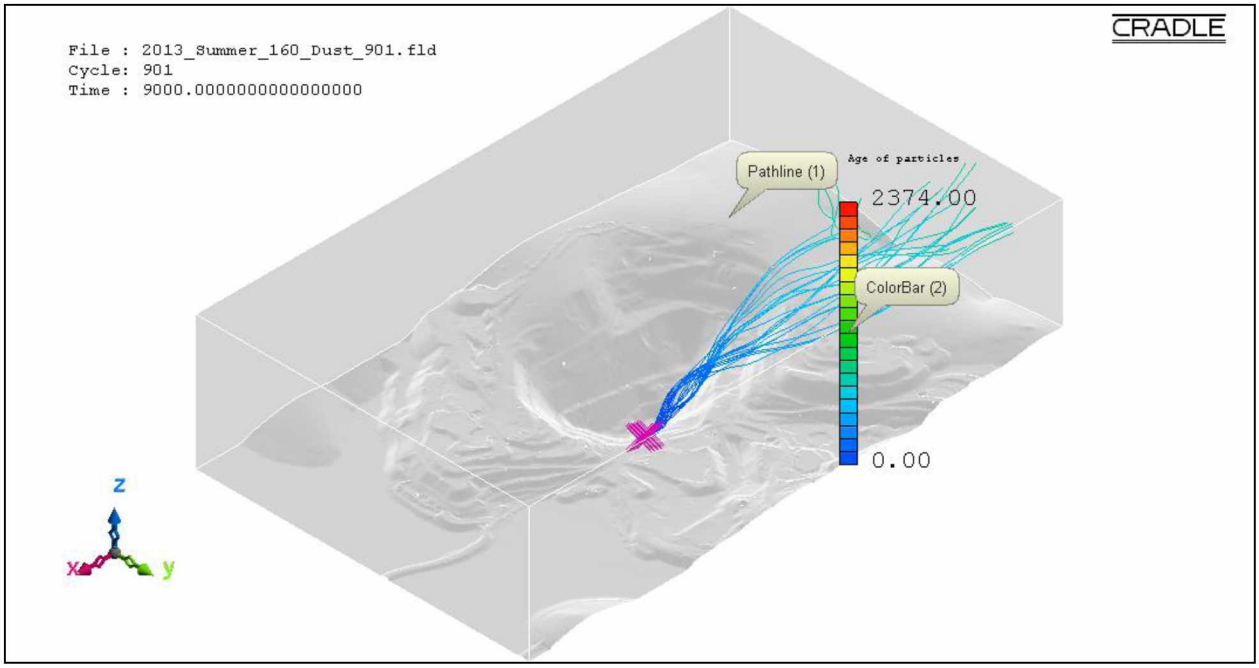

Figure B.200: Pathlines of PM_{10} dust particles from source location 24 in the actual open-pit domain for extreme insolation summer condition using the LES method.

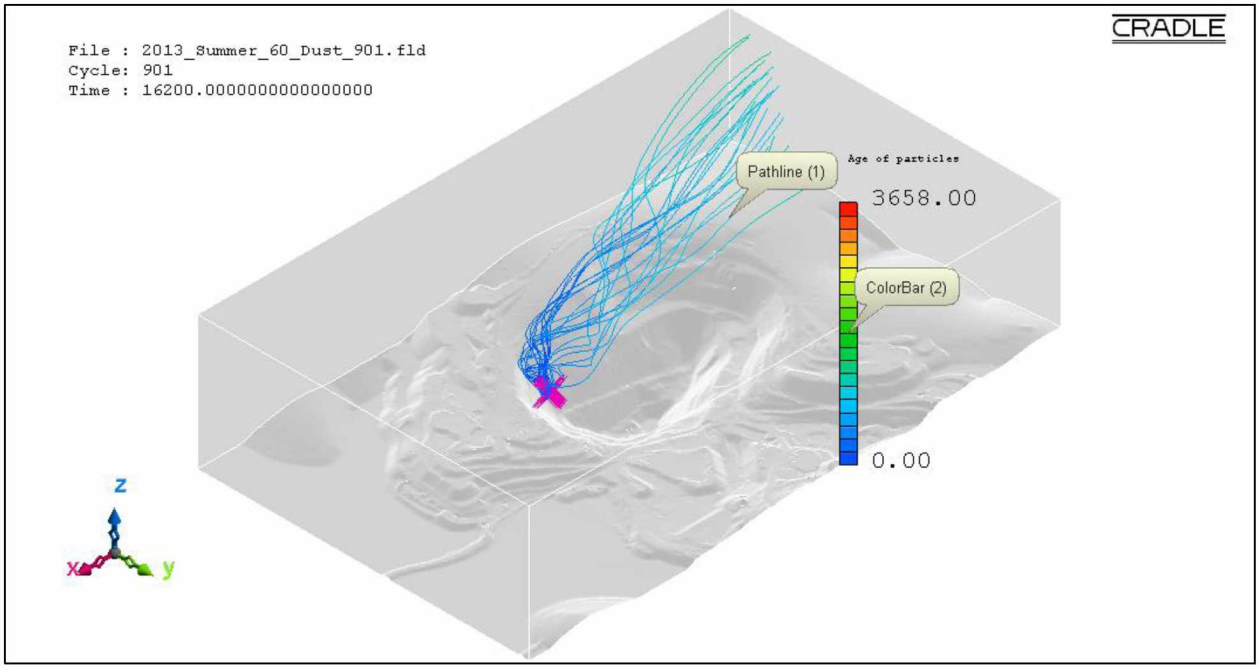

Figure B.201: Pathlines of PM_{10} dust particles from source location 25 in the actual open-pit domain for fair insolation summer condition using the LES method.

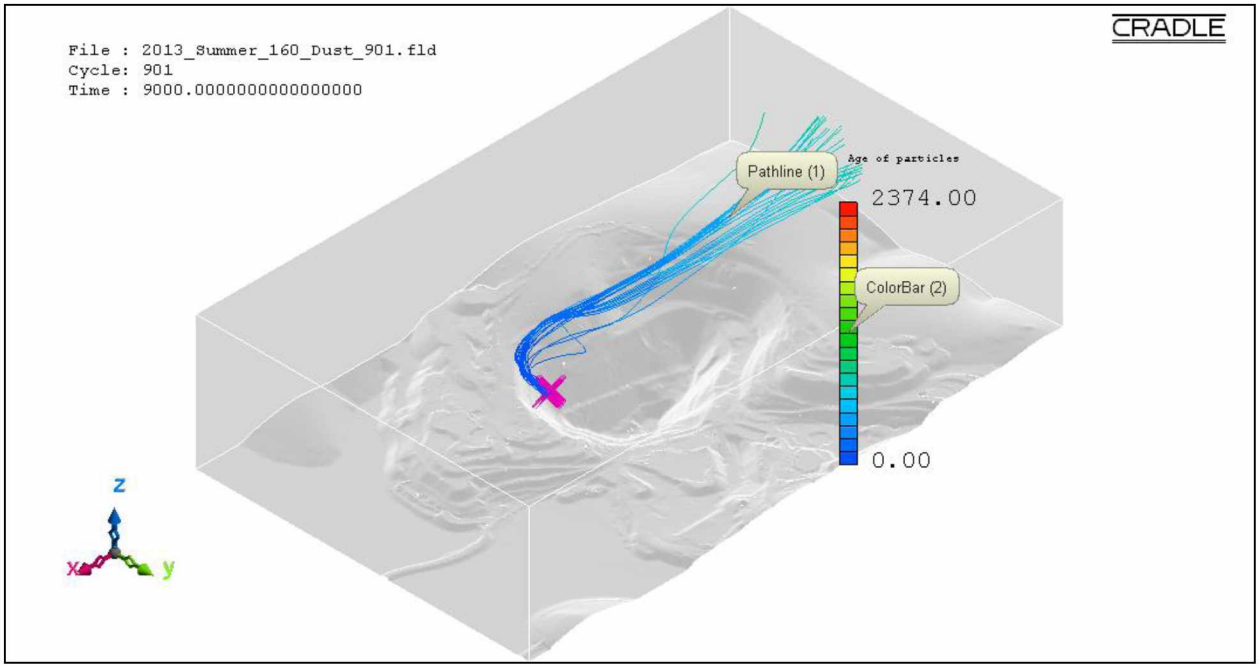

Figure B.202: Pathlines of PM_{10} dust particles from source location 25 in the actual open-pit domain for extreme insolation summer condition using the LES method.